

Sepember 2022 Vol:8 Issue:3
Eylül 2022 Cilt:8 Sayı:3



T.C.
ÇANAKKALE ONSEKİZ MART ÜNİVERSİTESİ
LİSANSÜSTÜ EĞİTİM ENSTİTÜSÜ

***CANAKKALE ONSEKİZ MART UNIVERSITY
JOURNAL OF ADVANCED
RESEARCH IN NATURAL AND
APPLIED SCIENCES***



ISSN 2757-5195

**Journal of Advanced Research in Natural
and Applied Sciences**

e-ISSN: 2757-5195

**Volume 8 / Issue 3
Sayı 8 / Cilt 3**

2022 Eylül/September

Yayıncı/Publisher: Çanakkale Onsekiz Mart Üniversitesi

Rektör /Rector: Prof. Dr. Sedat MURAT

Dergi Editör Kurulu/Editorial Board

Doç. Dr. Filiz UĞUR NİĞİZ (Editor-in-Chief)

Dr. Öğretim Üyesi Ayça AYDOĞDU EMİR

Doç. Dr. Tuğba GÜNGÖR

Doç. Dr. Deniz ŞANLIYÜKSEL YÜCEL

Doç. Dr. Necati KAYA

Doç. Dr. Mehmet Ali YÜCEL

Doç. Dr. Özgür Turay KAYMAKÇI

Dr. Öğretim Üyesi Gülçin ÖZCAN ATEŞ

Dr. Öğretim Üyesi Şebnem ÖNDER

Dr. Öğretim Üyesi Doğukan TAŞER

Mizanpaj Editörü

Semanur BELEN

Önsöz:

Journal of Advanced Research in Natural and Applied Sciences Dergisi Fen, Mühendislik, Doğa ve Temel bilimler alanlarında daha önce yayımlanmamış orijinal araştırma makalesi, derleme yazılar, teknik not türünde araştırmaları yayımlayan ulusal ve uluslararası indekslerde taranan, hakemli ve bilimsel bir dergidir. Journal of Advanced Research in Natural and Applied Sciences Dergisi Mart, Haziran, Eylül, Aralık olmak üzere yılda dört sayı yayınlanacaktır. Tr-Dizin’de taranan Journal of Advanced Research in Natural and Applied Sciences Dergisi’nin 8.cilt 3.sayısında 15 adet araştırma makalesi yayına kabul edilmiştir.

	<ul style="list-style-type: none"> • TÜBİTAK TR DİZİN tarafından taranmaktadır • Indexed by TR-DİZİN Database.
	<ul style="list-style-type: none"> • TÜBİTAK-ULAKBİM DergiPark Akademik tarafından yayımlanmaktadır. • Published by TÜBİTAK-ULAKBİM Turkish Journal Park Academic Database.
	<ul style="list-style-type: none"> • CROSSREF® Veri Tabanı Tarafından Taranmakta ve Makaleler DOI numarası ile yayımlanmaktadır. • Indexed by CROSSREF® Database and Articles are published with DOI number.
	<ul style="list-style-type: none"> • Google Scholar'da ve SOBIAD'da taranmaktadır • Indexed by Google Scholar and SOBIAD Database.

İletişim Adresi / Publisher Address: Çanakkale Onsekiz Mart Üniversitesi Lisansüstü Eğitim Enstitüsü
Terzioğlu Yerleşkesi Çanakkale (Sağlık Hizmetleri Meslek Yüksekokulu Binası)

Tel: 0286 218 05 23, Belgegeçer / Fax: 0286 218 05 24

E-posta / E-mail: jarnas.journal@gmail.com

Dergi Web Sayfası / Journal Home Page:

<http://jarna.dergi.comu.edu.tr/>

<https://dergipark.org.tr/tr/pub/jarnas>

Printing and Graphics Department

PUNTO
AJANS

Adres / Address: Seyrantepe Mah. İbrahim Karaoğlanoğlu Cd. İspar İş Merkezi,

D:No:105 D:124, 34418 Kâğıthane/İstanbul

Web: www.puntoajans.com



Çanakkale Onsekiz Mart University Journal of Advanced Research in Natural and Applied Sciences

Eylül (September) 2022 / Cilt (Volume) 8 / Sayı (Issue) 3 / e-ISSN 2757-5195

Çanakkale Onsekiz Mart University Journal of Advanced Research in Natural and Applied Sciences

CONTENTS / İÇİNDEKİLER
(2022, 8:3)

No	Articles & Authors / Makaleler & Yazarlar	Pages / Sayfa No
1	Controllable Electrochemical Synthesis and Photovoltaic Performance of Bismuth Oxide/Graphene Oxide Nanostructure Arrays Fatma Bayrakçeken Nişancı* Research/Araştırma	340-346
2	Shot Peening Effect on Reduced Graphene Oxide-based AA1070 Alloys Produced by Stir Casting Technique İremnur Bülbül1, Remzi Varol, Mehmet Fahri Saraç* Research/Araştırma	347-354
3	Fuzzy Sliding Mode Control with Moving Sliding Surface of Rotary Inverted Pendulum Muhammet Aydın*, Oğuz Yakut Research/Araştırma	355-369
4	Implementation of a Lightweight and Portable Horn Antenna Using 3D Printing Technology Serhan Yamacli* Research/Araştırma	370-379
5	A Sound-Based Monitoring and Evaluation System for Small-Scale Dairy Operations Ünal Kızı1*, Sefa Aksu, Ahmet Cumhuri Kınacı, Ertuğrul Bilgücü, Songül Şentürklü Research/Araştırma	380-390
6	Optimization Tool for Small Hydropower Plant Resource Planning And Development: A Case Study Hasan Huseyin Coban*, Antans Sauhats Research/Araştırma	391-428
7	ZnMnCuO Nanoparçacıkların Karakterizasyonu: Fotokatalitik ve Hemolitik Özellikler Bestenur Yalçın* Research/Araştırma	429-442



8	Türkiye'nin Denizel Çevre Yönetimi Karar Destek Sistemi Cihat Aşan*	443-452
Research/Araştırma		
9	Determination of seed yield, quality and fixed oil components of different basil (<i>Ocimum basilicum</i> L.) genotypes: Evaluation of fatty acid profile by PCA biplot analysis Musa Türkmen*, Yılmaz Eren, Yusuf Ziya Aygün, Esra Nermin	453-462
Research/Araştırma		
10	Ensemble Based Box-Cox Transformation via Meta Analysis Muhammed Ali Yılmaz, Osman Dag*	463-471
Research/Araştırma		
11	Kimyasal Tanker Gemilerinde Emniyet Ekipmanlarını Kullanan Personelin Yeterliği Devran Yazır*, Sefa Yay	472-484
Research/Araştırma		
12	Performance Analysis of Dimming Methods in Visible Light Communication Systems Süleyman Börekoğlu, Mehmet Sönmez*	485-493
Research/Araştırma		
13	Tünel Yangınlarında Jet Fan Diziliminin Duman ve Isı Kontrolüne Olan Etkilerinin İncelenmesi Songül Solmaz, Tolga Demircan*	494-504
Research/Araştırma		
14	Morphometric Analysis of Mount Ararat (Eastern Anatolia, Türkiye) Vedat Avcı*, Murat Sunkar, Ahmet Toprak	505-526
Research/Araştırma		
15	The Effect of Vertical Earthquake Motion on Steel Structures Behaviour in Different Seismic Zones Ercan Işık, Fatma Ülker Peker, Aydın Büyüksaraç*	527-542
Research/Araştırma		



Controllable Electrochemical Synthesis and Photovoltaic Performance of Bismuth Oxide/Graphene Oxide Nanostructure Arrays

Fatma Bayrakçeken Nişancı^{1*}

¹Department of Chemistry, Faculty of Sciences, Atatürk University, Erzurum, Türkiye

Article History

Received: 21.12.2021

Accepted: 18.03.2022

Published: 25.09.2022

Research Article

Abstract – The electrodeposition coated graphene oxide (GO) sheets on semiconductor metal oxide substrates are reduced to produce transparent, flexible, and conductive electrodes. Electrochemically produced bismuth oxide nanoflower films with high crystallinity were characterized by depositing reduced graphene oxide (GO) films on top. The influence of coating period on the shape, structure, and characteristics of electrochemically formed metal oxides was also examined. The graphene oxide modified metal oxide electrode was successfully manufactured using an electrochemical method and characterized using potential controlled electrochemical deposition, atomic force microscopy, scanning electron microscopy, energy dispersive spectroscopy, X-ray diffraction techniques, and Raman measurements. By controlling the deposition period, we can regulate the form and size of electrodeposited bismuth oxide/graphene oxide nanostructures using this electrochemical method from aqueous bismuth oxide/graphene oxide suspensions. The nanostructured bismuth oxide/graphene oxide electrode that results has high photovoltaic characteristics and can be employed in solar energy conversion applications. Our findings suggest that indium tin oxide (ITO) or bismuth oxide-GO films on gold electrodes may be used to enhance surface area in electrochemical synthesis, and that it is conceivable to synthesize semiconductor metal oxides in GO films for future flexible photovoltaic applications.

Keywords – GO, Bi_2O_3 , electrochemical deposition, photovoltaic cell, thin films.

1. Introduction

Nanomaterials including titanium oxide (TiO_2), silicon oxide (SiO_2), silver, iridium oxide, graphene, bismuth (III) oxide (Bi_2O_3), and fullerenes, among others, are commonly employed in electrochemical sensors and biosensors. These biosensors have been effectively employed for sensor preparation, and they are stable and simple to make. Because of its distinctive features such as energy bandgap, wide surface area, electrochemical stability, and excellent catalytic activity applications, Bi_2O_3 is regarded one of the most encouraging electrode substances for electrochemical sensing devices among all nanomaterials. Its sensitivity, electrical conductivity, chemical stability and a favourable electrochemical sensor for voltammetric measurement have all been demonstrated (Anandan et al, 2010). Bismuth(III) oxide is also non-toxic and chemically inert, as well as biocompatible.

Nanoscale bismuth(III) oxide offers more benefits than macroscale bismuth(III) oxide, and its higher surface free energy makes it suited for biomolecule adsorption. The usage areas of GO material are expanding day by day due to its dielectric properties, transparency, ease of solubility in solutions, adjustable electronic properties as well as superior mechanical properties. (McAllister et al., 2007, Anandan et al, 2010, Kim et al, 2012, Mathkar et. al, 2012). It has also turn up as one of the most strong competitors among the most common UV-active TiO_2 photocatalyst, especially Bi_2O_3 (Kamat, 2011). Bismuth is non-poisonous in its oxide shapes and can be used in active apps such as piezoelectric material (Kuma&Devi, 2011), biosensors functional glasses, etc. (Panda, 2009). Current research on the photocatalytic activities of the distinct phases of Bi_2O_3 indicates that they are non-toxic and resistant to photo corrosion (Ünlü et al, 2021, Molinari et al, 2020). In combinations such as Au-loaded α - Bi_2O_3 (Taufik et al, 2011- Eberl& Kisch, 2008).

¹  fbayrakceken@atauni.edu.tr

*Corresponding Author

and Ag-loaded β - Bi_2O_3 (Zhu et al,2011- Jiang et al, 2012), activity is seen to be improved in noble metal nanoparticles. Bi_2O_3 -GO modified electrodes were successfully synthesized on ITO electrochemically. In electrochemically synthesized Bi_2O_3 -GO thin films, GO structures covering Bi_2O_3 nanoflower structures like a transparent sheet will find use in many application areas such as ideal electrochemical performance and superordinate electroactive plane region such as sensors.

2. Materials and Methods

In our electrochemical tests, we employed a BAS 100 B/W electrochemical workstation with three electrodes. For electrochemical studies, we employed an Ag/AgCl electrode as the reference electrode, a platinum wire as the counter, and ITO coated quartz (10 cm^2) as the working electrode in all cases. Dissolved O_2 gas, 1 mM $\text{Bi}(\text{NO}_3)_3$, pH 1.5 At room temperature, electrochemical Bi_2O_3 /GO film deposition was executed. For 30 minutes, maintain a steady voltage of +300 mV. The Bi_2O_3 /GO working electrode was dried at room temperature, and the film was cured for roughly one minute with warm air. The GO (+1000 mV) modification was applied electrochemically to ensure that the surfaces generated by the potential controlled electrolysis process of nanostructured Bi_2O_3 films on ITO substrates at a constant voltage (+300 mV) had a high surface area (Figure 1). The morphological and structural examination of synthesized thin films was performed using atomic force microscopy (AFM), scanning electron microscopy (SEM) and x-ray diffraction (XRD), energy dispersive spectroscopy (EDS) for qualitative and quantitative analysis, and photocurrent spectroscopy for photocurrent measurements. A Rigaku powder X-ray diffractometer with a Cu K X-ray source ($\lambda = 1.5406$) was used to record powder X-ray diffractograms of the deposited films. By performing Bi_2O_3 -GO surface characterization with SEM, AFM images, it was possible to examine the surfaces at atomic and molecular dimensions, and Zeiss/Sigma 300 model SEM, Hitachi HT770 brand TEM, and Hitachi S100N brand AFM systems were used respectively for this. Raman spectra were determined by using the WITech alpha 300R device and the bonds made by the atoms or molecules that make up the Bi_2O_3 -GO in their analysis in the range of $1000\text{-}3500 \text{ cm}^{-1}$.

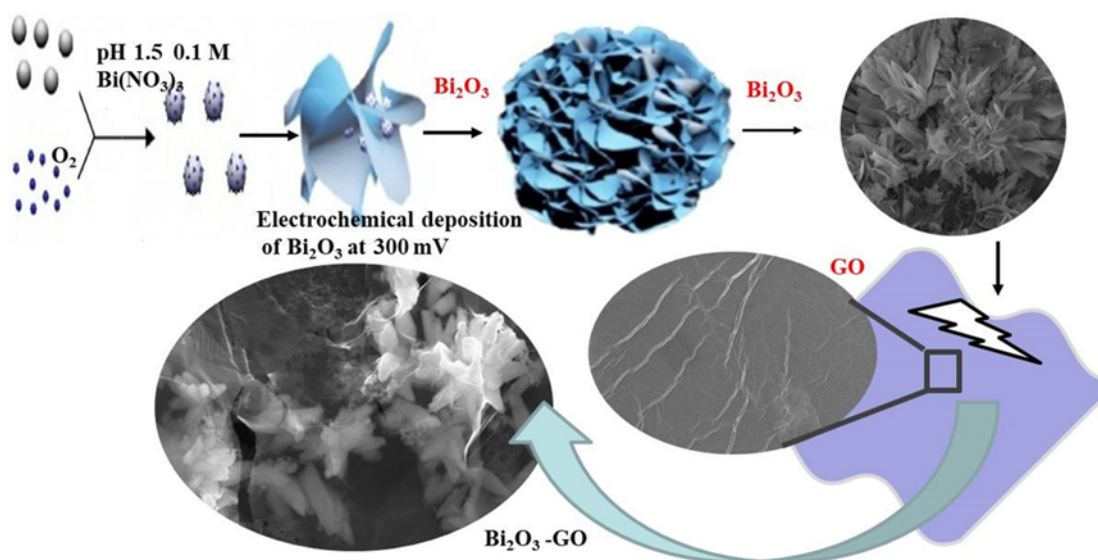


Figure 1. Schematic representation of the electrochemical formation of Bi_2O_3 -GO thin films.

3. Results and Discussion

Figure 2 show the SEM image and EDS spectra taken after electrochemical Bi_2O_3 -GO deposition. Bi_2O_3 -GO nanostructures electrodeposited on ITO electrodes consist of nanoflower and GO film wrapped like a transparent sheet (Figure 2a). This observation shows that the deposition potential and concentration, which provides a significant effect in the morphology-controlled synthesis of Bi_2O_3 nanostructures, remain Bi_2O_3 constant throughout the electrochemical treatment. These results also show that the surface area is increased as much as possible by coating the Bi_2O_3 films with GO films (Cruz-Silva et al. 2016). The EDS spectrum in Figure 2b also indicates that, similar to the XRD spectrum, the Bi_2O_3 -GO nanostructures contain no

impurities other than trace quantities of Cl^- and K^+ induced by reference electrode leakage. XPS analyses were implemented to achieve more detailed split on the type of surface components in Bi_2O_3 -GO films, which were partially analyzed qualitatively by EDS technique, and determine the oxidation steps of these components.

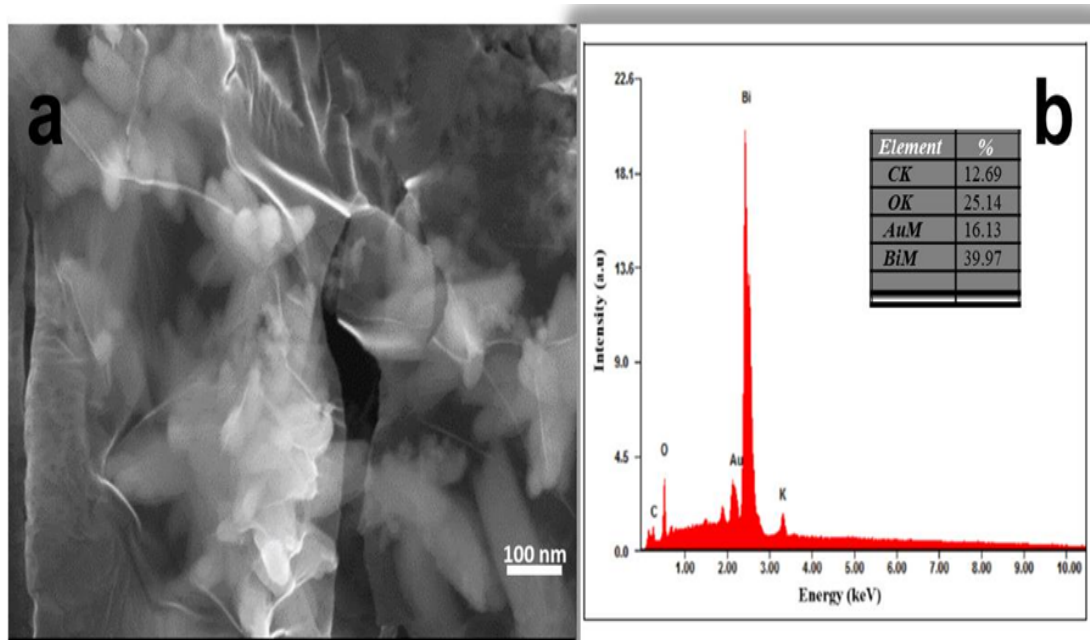


Figure 2. a) SEM image of electrochemically magnified films of Bi_2O_3 -GO on ITO electrode, (b) EDS spectrum of Bi_2O_3 -GO films.

In the XRD diffractogram of the electrodeposited Bi_2O_3 at $2\theta=30,245^\circ$ de, the diffraction peaks of GO at $2\theta=39.838$, Bi_2O_3 -GO at $2\theta=35,468$, and other peaks of the ITO substrate as the working electrode (Figure 3) are clearly seen (Yang&Lin, 2020). The observation of a single and very strong (201) peak belonging to the Bi_2O_3 -GO phase indicates that it has a preferential electrochemical growth orientation.

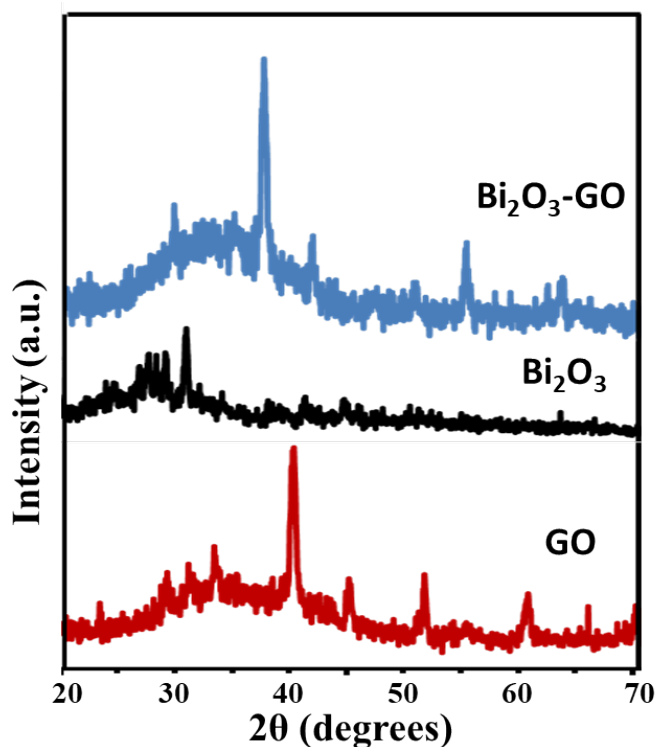


Figure 3. XRD spectrum of GO, Bi_2O_3 , and Bi_2O_3 -GO.

AFM data of GO, Bi_2O_3 , and Bi_2O_3 -GO are given in Figure 4. In the AFM data, as in the 3D images of GO and Bi_2O_3 thin films, GO thin films are homogeneously completely coated on the ITO electrodes, while Bi_2O_3 shows morphological properties like a nanoflower. In the AFM data of Bi_2O_3 -GO, the Bi_2O_3 nanoflower surface is covered with a completely transparent GO film.

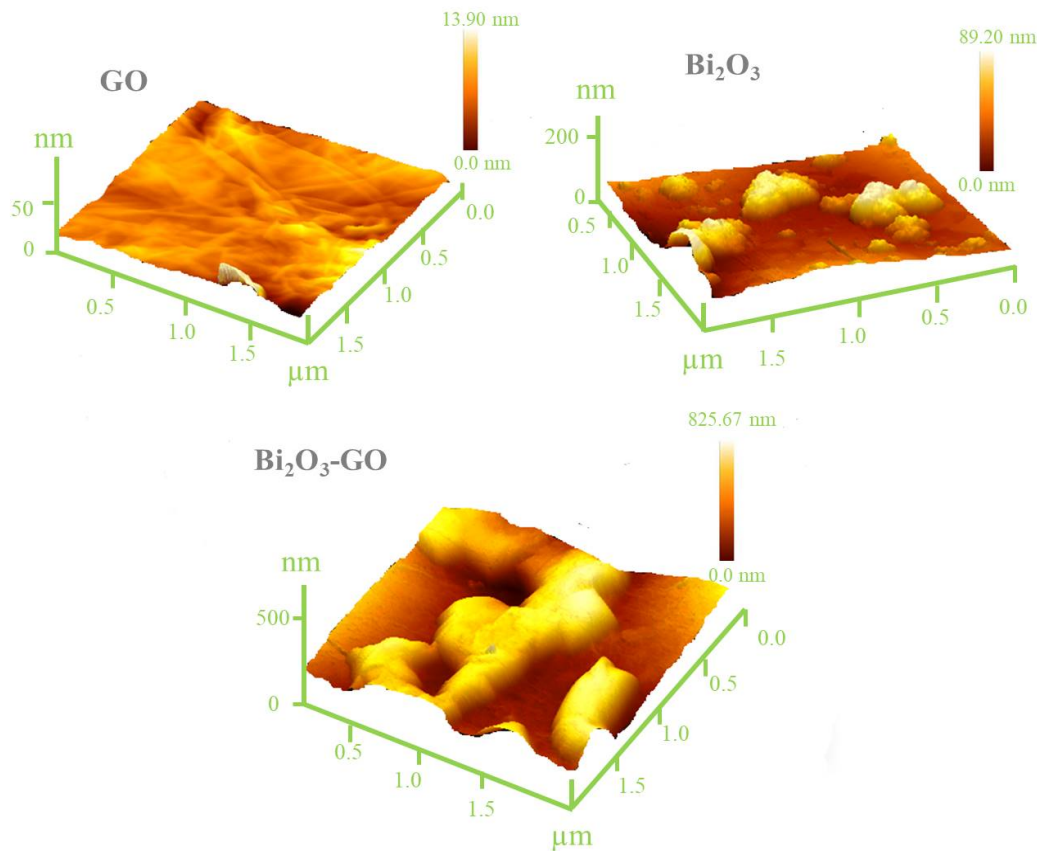


Figure 4. 3D AFM images of GO, Bi_2O_3 , and Bi_2O_3 -GO.

XPS (Figure 5a) analyses were implemented to acquire more detailed diagnose the type of surface components in Bi_2O_3 -GO films and to determine the oxidation steps of the components, which were partially analyzed qualitatively by the Raman technique. The positions of the binding energies of the Bi 4f peaks in the synthesized samples (158.8 eV-164.3 eV for Bi 4f 7/2 and 4f 5/2, seriatim) (Figure 5b) match exactly with the Bi_2O_3 standard data (Oprea et al, 2013). It is clearly seen that the peak in the XPS spectrum obtained for O1s is broad and asymmetrical. The nature of this peak, centered at 530.8 eV, observed for Bi_2O_3 -GO films corresponds to diverse bindings of oxygen in the surfaces. It is formed by the combination of the binding energies of this XPS peak of 529.7 eV, 530.7 eV, and 531.9 eV (Figure 5c). The weak peaks are due to the weakly bonded oxygen and hydroxyl groups to the film surface.

Photoelectrochemical performance of Bi_2O_3 -GO thin films was gauged in a 3 electrode quartz window cell connected to a potentiostat and polar simulator (Figure 6). Photocurrent transitions of Bi_2O_3 -GO structures obtained as a result of illumination at various intervals with artificial sunlight are given in Figure 6. Photocurrents were measured every 8 seconds in the dark and in the light in 0.1 M Na_2SO_4 without any reagents or catalysis. When the Bi_2O_3 -GO electrode is illuminated, a rapid increase is seen in the photocurrent value from 4.9 mA cm^{-2} to 10 mA cm^{-2} . Since the crystal is not ideal, there are entrapment or recombination centers such as defects. When the Bi_2O_3 -GO electrode is illuminated, the photocurrent value increases rapidly and then remains constant, which is explained by the decrease in the trap and recombination centers due to the defects in the electrode structure, thus keeping the carriers in the conduction band less at the defect levels (Sirimanne et al 2002). When the excitation source is turned off, the excess carriers return to the equilibrium value and cause the photocurrent

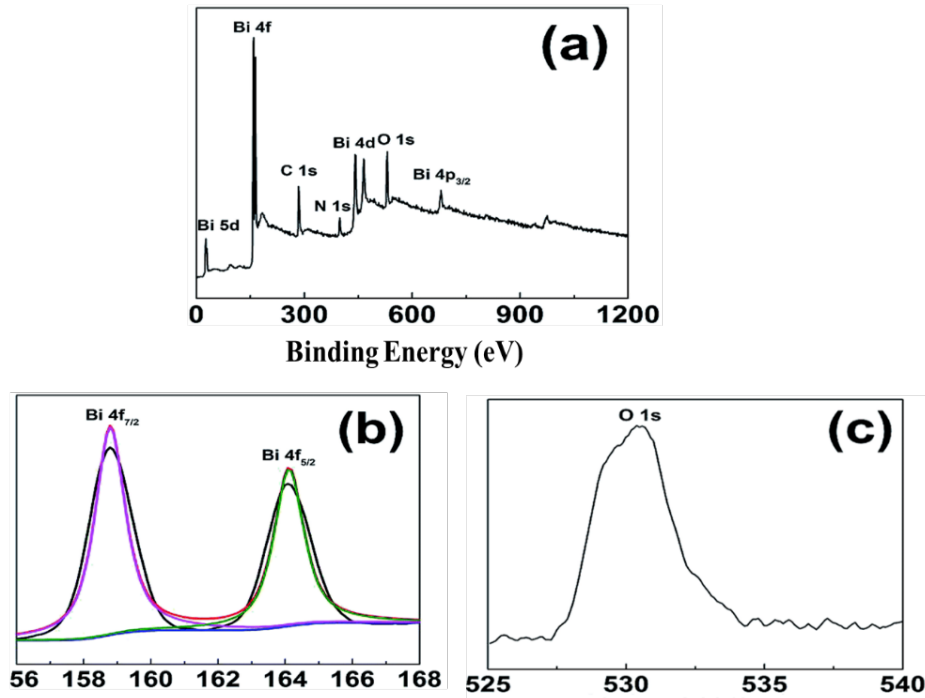


Figure 5. XPS data of Bi₂O₃-GO (a) full-scan XPS spectrum, (b) Bi 4f spectrum and (c) O 1s spectrum.

value to decrease. These fast and homogeneous photocurrent transitions shown indicate that charge transmission in the material is progressing rapidly. This can repeat over many cycles as stable regardless of electrode photocorrosion.

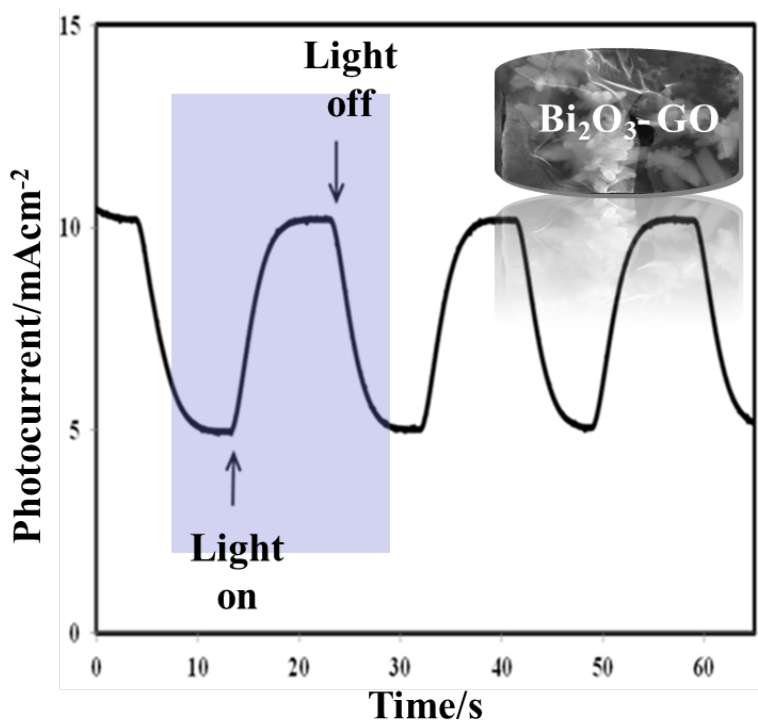


Figure 6. Photocurrent transitions of Bi₂O₃-GO photoanode under discrete artificial sunlight.

Raman spectra of GO, Bi₂O₃, Bi₂O₃-GO structures are given in Figure 7. GO structures have D and G bands available (Qin et al., 2014). Only in Bi₂O₃ films, Bi-O stresses begin in the range of 120-150 cm⁻¹, while coordination vibrations occur in the range of 200-400 cm⁻¹, and weak peaks are caused by oxygen

and hydroxyl groups weakly attached to the film surface. In Bi_2O_3 – GO thin films, the switch of the G band from 1601 cm^{-1} to 1621 cm^{-1} on Bi_2O_3 surfaces coated with GO proves that there is a charge transfer from GO to Bi_2O_3 (Rubbens et al, 2007). Also, this shift from blue to red indicates the existence of an electrical force linking atoms and allogamy between the GO and Bi_2O_3 layers.

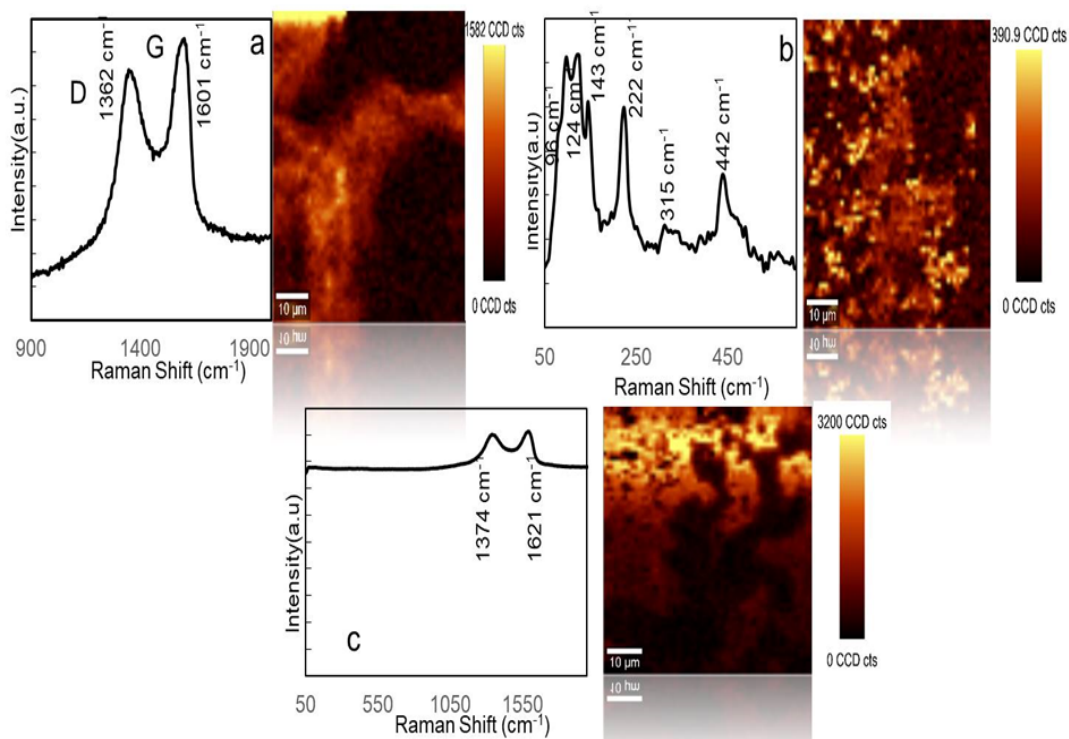


Figure 7. Raman data of (a) GO; (b) Bi_2O_3 ; (c) Bi_2O_3 – GO structures.

4. Conclusion

Bi_2O_3 -GO modified electrodes were successfully synthesized on ITO electrochemically. These heterostructured composites were fully characterized by AFM, SEM, XRD, and Raman spectroscopy and benefited from solar energy applications. The photocurrent transitions of these films also showed homogeneous photocurrent signals, indicating that charge transmission in this material is fast and that the Bi_2O_3 – GO thin films are in a crystalline structure. As a result, metal oxide semiconductor materials have strong photovoltaic characteristics and may be utilized for solar energy conversion and other applications with high performance.

References

- Anandan, S., Lee, G. J., Chen, P. K., Fan, C., & Wu, J. J. (2010). Removal of orange II dye in water by visible light assisted photocatalytic ozonation using Bi_2O_3 and $\text{Au}/\text{Bi}_2\text{O}_3$ nanorods. *Industrial & engineering chemistry research*, 49(20), 9729-9737. DOI: <https://doi.org/10.1021/ie101361c>
- Eberl, J., & Kisch, H. (2008). Visible light photo-oxidations in the presence of α - Bi_2O_3 . *Photochemical & Photobiological Sciences*, 7(11), 1400-1406. DOI: <https://doi.org/10.1039/b811197a>
- Jiang, H. Y., Cheng, K., & Lin, J. (2012). Crystalline metallic Au nanoparticle-loaded α - Bi_2O_3 microrods for improved photocatalysis. *Physical Chemistry Chemical Physics*, 14(35), 12114-12121. DOI: <https://doi.org/10.1039/C2CP42165H>
- Kamat, P. V. (2011). Graphene-based nanoassemblies for energy conversion. *The Journal of Physical Chemistry Letters*, 2(3), 242-251. DOI: <https://doi.org/10.1021/jz101639v>

- Kim, S., Zhou, S., Hu, Y., Acik, M., Chabal, Y. J., Berger, C., ... & Riedo, E. (2012). Room-temperature metastability of multilayer graphene oxide films. *Nature materials*, 11(6), 544-549. DOI: <https://doi.org/10.1038/nmat3316>
- Kumar, S. G., & Devi, L. G. (2011). Review on modified TiO₂ photocatalysis under UV/visible light: selected results and related mechanisms on interfacial charge carrier transfer dynamics. *The Journal of physical chemistry A*, 115(46), 13211-13241. DOI: <https://doi.org/10.1021/jp204364a>
- Molinari, R., Lavorato, C. and Argurio, P. (2020). Visible-Light Photocatalysts and Their Perspectives for Building Photocatalytic Membrane Reactors for Various Liquid Phase Chemical Conversions. *Catalysts*, 10, 1334. DOI: <https://doi.org/10.3390/catal10111334>
- Mathkar, A., Tozier, D., Cox, P., Ong, P., Galande, C., Balakrishnan, K., ... & Ajayan, P. M. (2012). Controlled, stepwise reduction and band gap manipulation of graphene oxide. *The journal of physical chemistry letters*, 3(8), 986-991. DOI: <https://doi.org/10.1021/jz300096t>
- McAllister, M. J., Li, J. L., Adamson, D. H., Schniepp, H. C., Abdala, A. A., Liu, J., ... & Aksay, I. A. (2007). Single sheet functionalized graphene by oxidation and thermal expansion of graphite. *Chemistry of materials*, 19(18), 4396-4404. DOI: <https://doi.org/10.1021/cm0630800>
- Oprea, O. B., Radu, T., Simon, S. (2013). XPS investigation of atomic environment changes on surface of B₂O₃-Bi₂O₃ glasses. *Journal of Non-Crystalline Solids*, 379(1), 35-39. DOI: <https://doi.org/10.1016/j.jnoncrysol.2013.07.024>
- Panda, P. K. (2009). Environmental friendly lead-free piezoelectric materials. *Journal of materials science*, 44(19), 504. DOI: <https://doi.org/10.1007/s10853-009-3643-0>
- Qin, H., Gong, T., Cho, Y., Leeab, C. and Kim, T. (2014). A conductive copolymer of graphene oxide/poly(1- (3-aminopropyl)pyrrole) and the adsorption of metal ions. *Polymer Chemistry*, 5:4466-4473. DOI: <https://doi.org/10.1039/C4PY00102H>
- Rubbens, A., Drache, M., Roussel, P., & Wignacourt, J. P. (2007). Raman scattering characterization of bismuth based mixed oxides with Bi₂O₃ related structures. *Materials research bulletin*, 42(9), 1683-1690.9-5062. DOI: <https://doi.org/10.1016/j.materresbull.2006.11.036>
- Cruz-Silva, R., Endo, M. and Terrones, M. (2016). Graphene oxide films, fibers, and membranes. *Nanotechnol Rev*, 5(4), 377-391. DOI: <https://doi.org/10.1515/ntrev-2015-0041>
- Sirimanne, P. M., Takahashi, K., Sonoyama, N., Sakata, T, (2002). Photocurrent enhancement of wide bandgap Bi₂O₃ by Bi₂S₃ over layers. *Solar Energy Materials & Solar Cells* 73, 175-187. DOI: [https://doi.org/10.1016/S0927-0248\(01\)00123-4](https://doi.org/10.1016/S0927-0248(01)00123-4).
- Taufik, S., Yusof, N. A., Tee, T. W., & Ramli, I. (2011). Bismuth oxide nanoparticles/chitosan/modified electrode as biosensor for DNA hybridization. *Int. J. Electrochem. Sci*, 6, 1880-1891.
- Unlü, U., Kemeç, S., Pozan Soylu, G. S. (2021) The impact of alkaline earth oxides on Bi₂O₃ and their catalytic activities in photodegradation of Bisphenol A. *Turkish Journal of Chemistry*, 45: 683-693. DOI: <https://doi.org/10.3906/kim-2101-30>
- Yang, W. D., & Lin, Y. J. (2020). Highly Oriented β -Bi₂O₃-decorated Reduced Graphene Oxide Composites for Supercapacitor Electrodes. *Int. J. Electrochem. Sci*, 15, 1915-1929. DOI: <https://doi.org/10.20964/2020.03.64>
- Zhu, G., Que, W., & Zhang, J. (2011). Synthesis and photocatalytic performance of Ag-loaded β -Bi₂O₃ microspheres under visible light irradiation. *Journal of alloys and compounds*, 509(39), 9479-9486. DOI: <https://doi.org/10.1016/j.jallcom.2011.07.046>



Shot Peening Effect on Reduced Graphene Oxide-based AA1070 Alloys Produced by Stir Casting Technique

İremnur Bülbül¹, Remzi Varol¹, Mehmet Fahri Saraç^{2,*}

¹ Department of Mechanical Engineering, Faculty of Engineering, Suleyman Demirel University, Isparta, Türkiye

² Department of Automotive Engineering, Faculty of Engineering, Suleyman Demirel University, Isparta, Türkiye

Article History

Received: 22.03.2022

Accepted: 26.05.2022

Published: 25.09.2022

Research Article

Abstract – The shot peening effects of reduced graphene oxide (rGO) additive on the structural, residual stress, hardness and surface roughness of AA1070 composites were investigated and reported in detail for the first time. It can be said that with increasing amounts of rGO added into AA1070 alloy, rGO is randomly distributed into the Al matrix with increasing amounts. The XRD analysis shows that there is no trace of carbon in the Al matrix, showing the the carbon structure did not diffuse into Al matrix during casting. However, in the EDS analysis, it was deter-mined that the carbon value increased due to the increased presence of rGO. Although it has been studied ac-cording to the differences in ball diameters, it has been observed that the relative differences between the ball forging times affect the surface roughness changes in the samples. It was also observed that the hardness values were directly related to the ball forging times. On the other hand, the surface area of the forged matrix decreases in the presence of increasing rGO. While the hardness should increase after shot peening, cold deformation is not expected on the surface with the increase in the presence of rGO, and therefore, a decrease in the hardness value of the shot peened surface occurs. This is compatible with the residual stress results as well.

Keywords – AA1070, reduced graphene oxide, residual stress, stir casting, severe shot peening.

1. Introduction

Graphite oxides as reinforcement material in different composite structures has become very popular in recent years (Naseer et al., 2019; Zhan et al., 2020a; Zheng et al. 2020b). Due to its high surface area and superior mechanical properties make the use of this structure for aluminium matrix composites much more interesting. It is also of great importance for applications in the automotive components where excessive motion is occurred, such as cylinder liners, crankshaft, tappets, pistons in order to increase the desired properties such as lightweight, surface hardness and mechanical strength in aluminium matrix composites (AMC) using a very small amount of reinforcement material (Naseer et al., 2019).

Due to the structural dissimilarity of graphene oxide in the aluminium matrix, there are difficulties in its homogeneous distribution in the matrix. For that reason, the studies on surface strengthening of graphene oxide added AMC have been carried out by using techniques such as stirred casting, liquid metal impregnation, sprayed deposition casting and so on (Toptan et al., 2010; Fadavi Boostani et al., 2018; Wu et al., 2019; Zheng et al., 2020a; Pehlivanlı & Pul, 2021). However, no study has been found on the graphene oxide-added AMCs with stirred casting so far using surface hardening processes like shot peening (Sun et al., 2018; Zhu et al., 2019; Rozhbiany & Jalal, 2019; Sasikumar et al., 2020)

With the shot peening process, the surface of the graphene oxide structured AMC will be hardened by a massive amount of high hardness and high-speed kinetic energy projectiles (Zhu et al., 2016; Zhan et al., 2018a; Zhan et al., 2018b). After shot peening, residual stress field and microstructure enhance its fatigue, surface hardness, resistance to stress corrosion cracks or high temperature oxidation resistance. However,

¹ bulbul.irem09@gmail.com

² remzivarol@sdu.edu.tr

³ fahrisarac@sdu.edu.tr

*Corresponding Author

residual stress distribution, microstructure and surface roughness will also differ depending on shot peening properties such as diameter of balls, Almen intensity, time and projectile material (Sasikumar et al., 2020; Avcu et al., 2021). In this study, the effect of shot peening with increasing rGO (0.25%, 0.5% and 1% wt.) on AA1070 composites were empirically investigated by scanning electron microscopy, electron diffraction scattering, x-ray diffraction, microhardness, residual stress and surface roughness.

2. Materials and Methods

2.1 Material

AA1070 was purchased from ISM Foreign Trade, Turkey and its chemical composition of the AA1070 alloy is presented in Table 1. The main reason for choosing the specified alloy is to examine the interaction of aluminum with the highest possible purity against rGO. In the synthesis of rGO, graphite (<20 μm powder), sulfuric acid (H_2SO_4 , 98%), sodium nitrate (NaNO_3), hydrogen peroxide (H_2O_2 , 30%) and potassium permanganate (KMnO_4 , 98%) were obtained from Sigma Aldrich.

Table 1

Chemical composition of AA1070 alloy, % weight

Element	Al	Cu	Fe	Mg	Mn	Si	Ti	V	Zn
% wt	rmn	0.04	0.25	0.03	0.03	0.2	0.03	0.05	0.04

2.2 Experimental Procedure

Reduced graphene oxide was produced by the modified Hummers method (Ciğeroğlu et al., 2020). To explain shortly, 3 g of natural graphite was mixed with sodium nitrate (1.2 g) for 30 minutes in a beaker placed in an ice bath at 1°C , and 150 mL of sulfuric acid was then added. Afterwards, potassium permanganate (12 g) was added to oxidize the graphite. After the resulting solution was removed from the ice bath, it was subjected to magnetic stirring at 35°C for 90 minutes. So, it was observed that a rapid increase in temperature occurred with the addition of ultrapure water. The temperature was kept below 100°C . After these procedures, the solution, which is stirred for another 30 minutes, is diluted with 300 mL of ultrapure water and the reaction is terminated by adding 20 mL of 30% hydrogen peroxide. Finally, the mixture is washed sequentially with HCl and H_2O , then centrifuged at 4000 rpm for 10 minutes to separate the solid and dried under vacuum at 80°C overnight to yield GO powder. After obtaining GO powder, it was subjected to ascorbic acid with volume ratio of 1:1 and then heated for 30 min at 90°C . Finally, the aqueous solution was re-centrifuged at 8000rpm, washed three times with ethanol and water, respectively, and dried at 120°C for 60 min. in the oven. As it is seen in Figure 1, the presence of rGO is located close to 26.8° at the reflection plane (002) which was previously reported in Soomro et al. (2019) study. This peak also distinct rGO from GO as well.

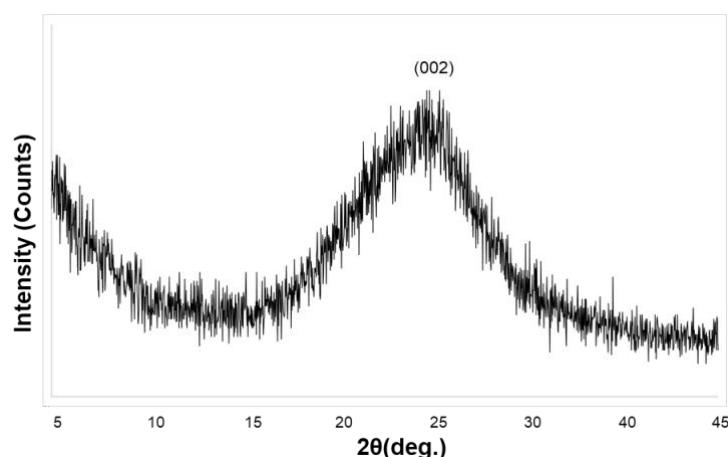


Figure 1. XRD analysis of synthesized rGO powder

Reduced graphene oxide with 0.25%, 0.5% and 1%wt. was separately added to the melted AA1070 alloy in a graphite crucible with a graphite probe, and after mixing at 4000 rpm for 5 minutes. Afterwards, a melted sample poured into the mold of a tubular shape of 10 mm in diameter and 10 cm in length and waited for cooling. Afterwards, each sample with a length of 10 mm was cut and made ready for structural and mechanical tests.

Severe shot peening process were applied with three Almen intensities of A10-12, A14-16 and A16-18 with other parameters remain constant. Severe shot peening treatment was conducted in accordance with MIL-13165 standard under the conditions shown in [Table 2](#).

Table 2

Shot peening parameters

Almen Intensity	Ball type and related hardness	Air pressure (bar)	Flow rate (kg/dk)	Saturation rate	Shot peening time (sn)
A10-12	S110, 45-52 HRc	4.5	5.0	100%	35
A14-16	S170, 45-52 HRc	5.5	5.5	100%	31
A16-18	S230, 45-52 HRc	5.5	5.0	100%	42

3. Results and Discussion

The average shot peened layer under three different Almen intensity was illustrated in [Figure 2](#). The shot peened layer is increased gradually from 0.74mm to 1.08mm. Almen intensity depends on the shot peening parameters. Ball or called projectile diameter, air pressure, saturation rate and shot peening time especially affect shot peening intensity. In this study, Almen intensity values were determined using A strips. As the Forging Intensity values increase, the shot peened layer thickness increases. As the Almen intensity increases, the kinetic energy value transferred to the forged material by the balls used in forging increases. Therefore, the forged or shot peened layer thickness increases.

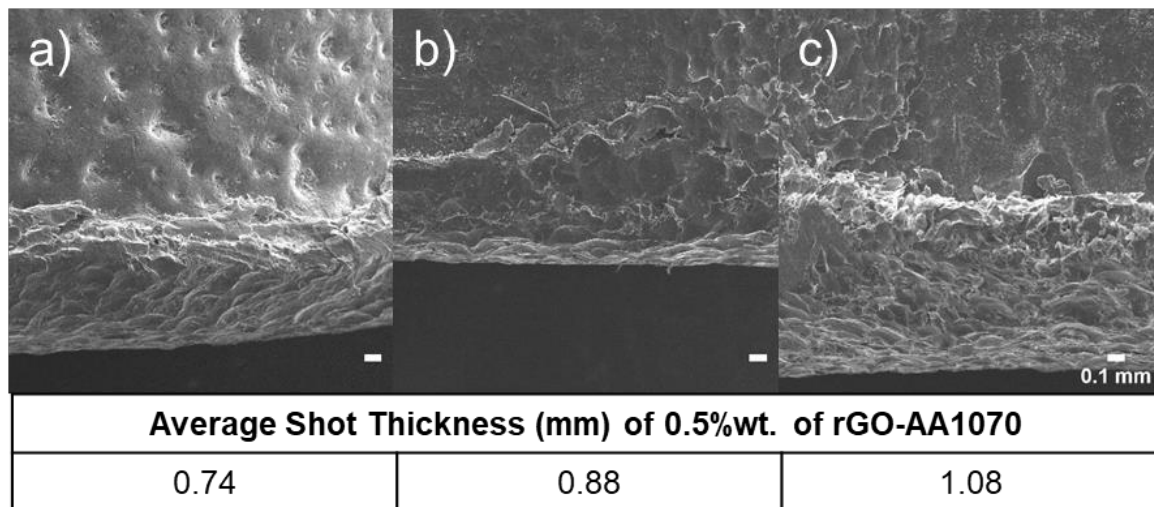


Figure 2. Average Shot Peened Microstructure of a) 0.25%, b) 0.5% and c) 1% wt. of rGO added AA1070 samples after shot peening

For selected 0.25%wt. of rGO added AA1070 samples, the surface roughness's with four different shot peening treatments were shown in [Figure 3](#). The surface roughness of sample at unpeened condition was 2.8 and gradually is increased gradually from 7.5 to 9.2 μ m. Afterwards, the surface roughness suddenly decreases to 8.8 μ m under A16-18 Almen intensity. At the A16-18 Almen intensity, the forging time was 42 seconds. By using S230 ball, the increase in this time causes the improvement of the surface quality. In the case of using S170 ball, since the applied air pressure value is the same, the impact speed was lower

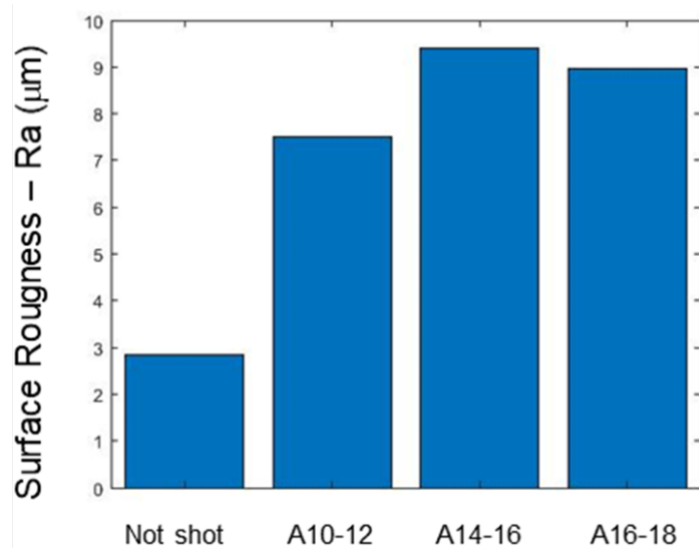


Figure 3. Average surface roughness of selected 0.25%wt. of rGO added AA1070 samples under different Almen intensity

because the mass of the S230 ball was higher. As a result, the surface quality was obtained better than the surface quality obtained under forging conditions using S170 ball diameter.

As seen in Figure 4., xrd analysis of pure and rGO added AA1070 matrix composite shows a single-phase structure of pure aluminium phase identification (JCPDS card no. 04-0787) which are present at 2θ equal to 38.47° , 44.74° and 65.13° , 78.23° and 82.43° . There is no trace of carbon in the Al matrix, so it is evidence that there is no second phase such as Al₃C in the matrix. So, the rGO has not enough time to react with Al matrix during stir casting.

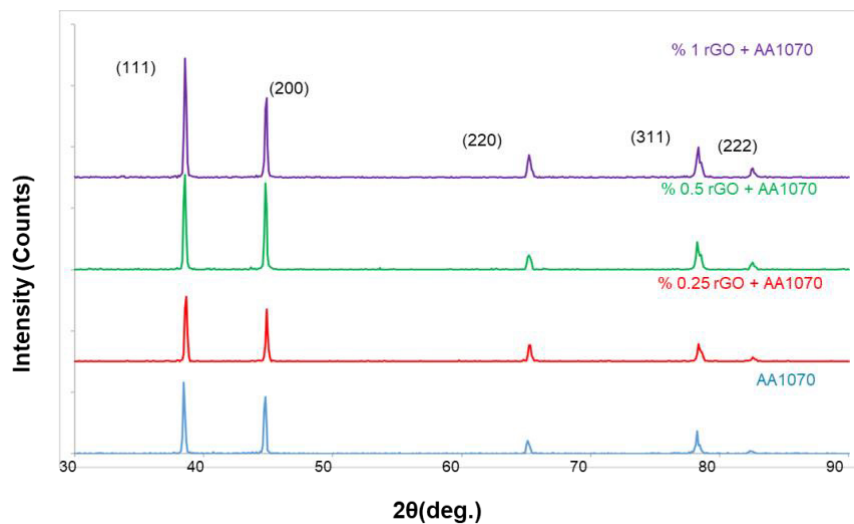


Figure 4. XRD analysis of pure and rGO added AA1070 composites

SEM images and SEM-EDS analysis of pure and rGO added AA1070 samples were shown in Figure 5. It is clearly seen that rGO particles were randomly distributed into Al matrix and the presence of rGO increases with increasing amount of rGO into the Al matrix. It is also seen at the EDS analysis that carbon is observed even at 0.25%wt. of rGO added AA1070 samples and gradually increases from 1.78 %wt to 8.88 %wt of carbon. Apart from AA1070 sample, rGO particles are clearly visible (marked as red circle) on the Al matrix which is compatible with the EDS analysis.

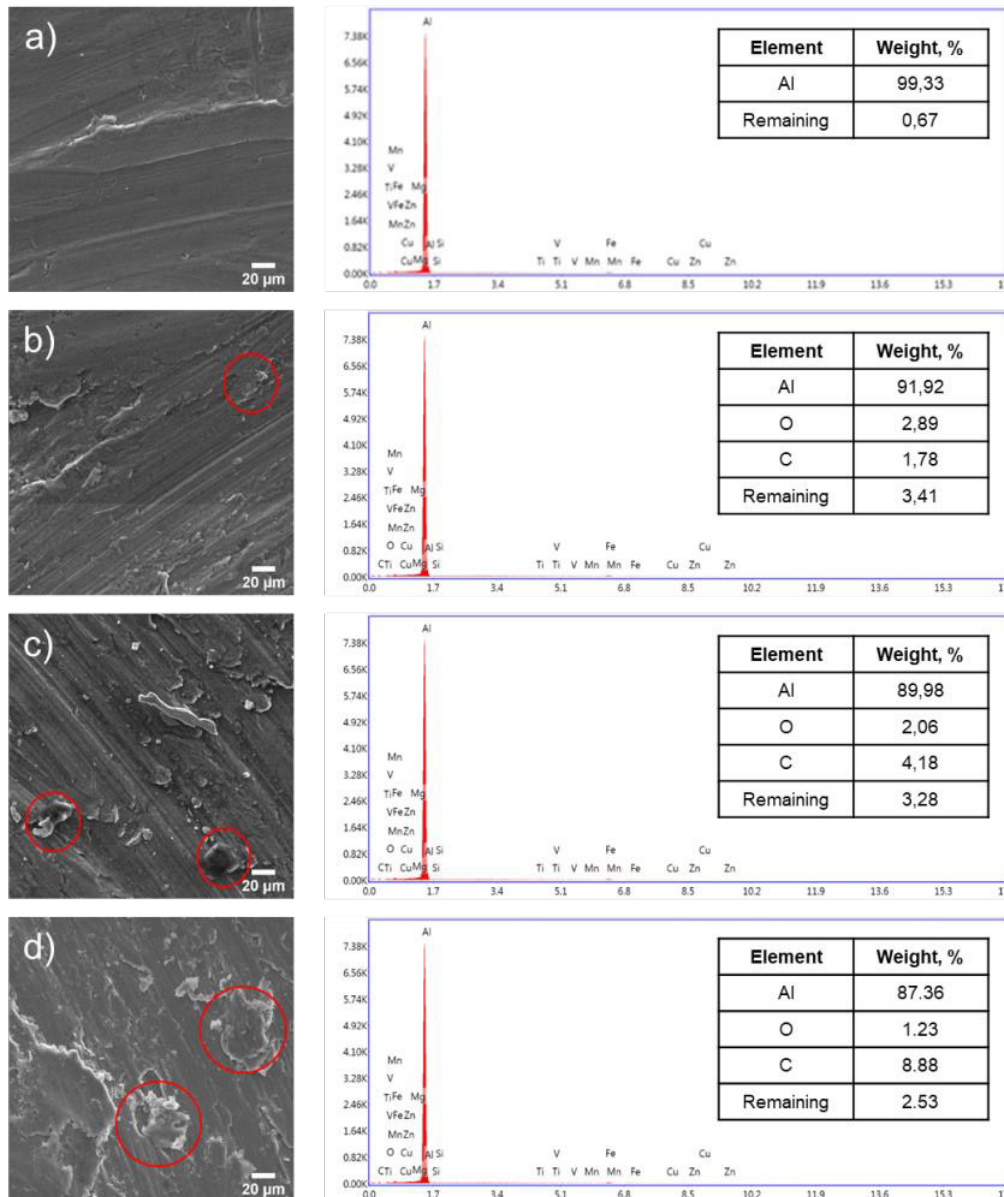


Figure 5. SEM and EDS analysis of pure and rGO added AA1070 samples

As it seen in [Figure 6.](#), the hardness values were decreased with increasing amount of rGO under various shot peening intensity. This observation can be concluded that even 0.25%wt. of rGO amount is still higher because it is not closer to pure AA1070 sample. It could be interpreted that rGO particles were agglomerated during the casting process and lower the hardness at the end. During the shot peening treatment, at least 99% of the surface is struck by the balls. However, as the amount of rGO added into the matrix material (AA1070) increases, the surface area of the forged material decreases. Essentially, it is the hardening that occurs during cold deformation of the surface of the shot peened material that reveals the increase in hardness. However, hardening of rGO should not be expected. Therefore, as the amount of rGO increases, the decrease in the hardness value of the shot peened surface is considered for this situation.

X-ray diffraction residual stress measurements was applied to all samples under different shot peening treatments as tabulated in [Table 3.](#) 0.25%wt. of rGO added AA1070 with increasing shot peening intensity decreases the residual stress which verify that surface area of rGO over 0.25% addition did not make any distinctive change against other samples. Residual stress results match exactly with the hardness values. This shows that the hardening effect is highly dependent on the residual stress as well.

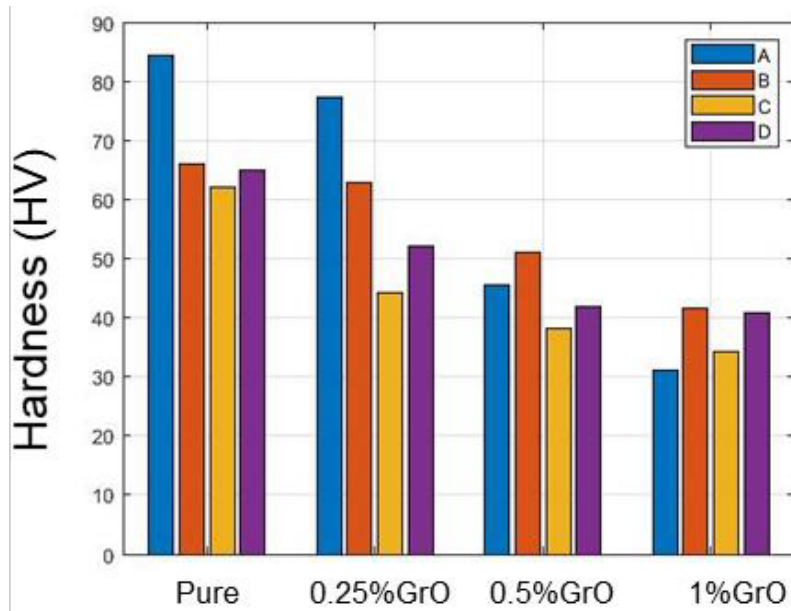


Figure 6. Microvickers hardness values of pure, 0.25%, 0.5% and 1% wt. of rGO added AA1070 samples under Almen intensity (A=not shot peened, B=A10-12, C=A14-16, D=A16-18)

Table 3

Residual stress of rGO added AA1070 samples under three different Almen intensity

Almen Intensity	Residual Stress (MPa)			
	Pure	0.25%wt. rGO	0.5%wt. rGO	1%wt. rGO
A10-12	-37.3±1.8	-44.7±1.6	-37.2±1.1	-36.3±1.9
A14-16	-41.1±1.1	-38.5±2.0	-41.0±1.7	-30.3±4.0
A16-18	-32.7±1.5	-35.5±0.9	-32.6±1.2	-30.3±1.8

4. Conclusion

Pure and three different ratios (0.25, 0.5 and 1%wt.) of rGO added AA1070 composites were produced by stir casting and afterwards, severe shot peening applied for all samples. Under three different Almen intensity, the shot thickness and surface roughness increase up to A14-16 and then decreases. These phenomena are also observed at the hardness and residual stress values. Depending on the various Almen intensity and relative shot time differences, it can be interpreted that A14-16 Almen intensity is the optimum shot intensity value should be used for rGO added AA1070 samples. On the other hand, there is no trace of carbon reacted with Al matrix which is verified by xrd analysis. For SEM observation, rGO is randomly distributed into Al matrix and increases with increasing amount of rGO added into AA1070. Finally, residual stress of 0.25 %wt. of rGO added AA1070 was gradually decreased with increasing Almen intensity while other samples show drastic change. This is a similar situation observed in the change of hardness and surface roughness due to the hardening phenomena observed in presence of rGO added into Al matrix.

Acknowledgement

We would like to thank Süleyman Demirel University Scientific Research Fund for providing financial support to our study within the scope of the project numbered FYL-2021-8294. The casting processes of this study were carried out in Kondöksan Döküm, Konya. We would like to thank Le-vent Çalık who made the foundry available to us, and Murat Çekici, who helped us with the casting processes.

Author Contributions

İremnur Bülbül: Provided the conception and design of the study, acquisition of data, analysis and interpretation of data, drafting of the article

Remzi Varol: Revised it critically for important intellectual content, and final approval of the version to be submitted

Mehmet Fahri Saraç: Provided the revised article critically for important intellectual content and gave final approval of the version to be submitted.

Conflicts of Interest

The authors declare no conflict of interest.

References

- Avcu, Y.Y., Gönül, B., Yetik, O., Sönmez, F., Cengiz, A. Guney, M. & Avcu E. (2021). Modification of Surface and Subsurface Properties of AA1050 Alloy by Shot Peening, *materials*, 14, 6575. DOI: <http://doi.org/10.3390/ma14216575>
- Çiğeroğlu, Z., Haşimoğlu, A., & Özdemir, O.K. (2020). Synthesis, characterization and an application of graphene oxide nanopowder: methylene blue adsorption and comparison between experimental data and literature data. *Journal of Dispersion Science and Technology*, 42, 771-783. DOI: <https://doi.org/10.1080/01932691.2019.1710526>
- Fadavi Boostani, A., Yazdani, S., Azari Khosroshahi, R., Jiang, Z.Y., & Wei, D. (2018). A novel graphene-stimulated semi-solid processing to fabricate advanced aluminium matrix nanocomposites. *Materials Science and Engineering: A*, 736, 316-322. DOI: <https://doi.org/10.1016/j.msea.2018.09.001>
- Naseer, A., Ahmad, F., Aslam, M., Guan, B., Harun, W., Muhamad, N., Raza, M., & German, R. (2019). A review of processing techniques for graphene-reinforced metal matrix composites. *Materials and Manufacturing Processes*, 34, 957-987. DOI: <https://doi.org/10.1080/10426914.2019.1615080>
- Pehlivanlı, Z.O. & Pul, M. (2021). Investigation of the effect of B₄C amount and sintering temperature on the thermal properties of the material in Al 1070–B₄C composites. *Proceedings of the Institution of Mechanical Engineers, Part L: Journal of Materials: Design and Applications*, 235, 2746–2761. DOI: <https://doi.org/10.1177/14644207211035520>
- Rozhbiyani, F.A.R., & Jalal, S.R. (2019). Influence of reinforcement and processing on aluminum matrix composites modified by stir casting route. *Advanced Composites Letters*, 28, 1-8. DOI: <https://doi.org/10.1177/2633366X19896584>
- Sasikumar, K.S.K., Dineshkumar, K., Deeban, K., Sambathkumar, M., & Saravanan, N. (2020). Effect of shot peening on surface properties of Al7075 hybrid aluminum metal matrix composites. *Materials Today: Proceedings*, 33, 2792-2794. DOI: <https://doi.org/10.1016/j.matpr.2020.02.676>
- Soomro, S.A., Gul, I.H., Naseer, H., Marwat, S., & Mujahid, M. (2019). Improved Performance of CuFe₂O₄/rGO Nanohybrid as an Anode Material for Lithium-ion Batteries Prepared Via Facile One-step Method. *Current Nanoscience*, 15, 420-429. DOI: <https://doi.org/10.2174/1573413714666181115122016>
- Sun, Q., Liu, X., Han, Q., Li, J., Xu, R., & Zhao, K. (2018). A comparison of AA2024 and AA7150 subjected to ultrasonic shot peening: Microstructure, surface segregation and corrosion. *Surface and Coatings Technology*, 337, 552-560. DOI: <https://doi.org/10.1016/j.surfcoat.2018.01.072>
- Toptan, F., Kilicarslan, A., Karaaslan, A., Cigdem, M., & Kerti, I. (2010). Processing and microstructural characterisation of AA 1070 and AA 6063 matrix B₄Cp reinforced composites. *Materials & Design*, 31, 87-91. DOI: <https://doi.org/10.1016/j.matdes.2009.11.064>
- Wu, Y., Zhan, K., Yang, Z., Sun, W., Zhao, B., Yan, Y., & Yang, J. (2019). Graphene oxide/Al composites with enhanced mechanical properties fabricated by simple electrostatic interaction and powder metallurgy. *Journal of Alloys and Compounds*, 775, 233-240. DOI: <https://doi.org/10.1016/j.jallcom.2018.10.158>

- Zhan, K., Wu, Y., Li, J., Zhao, B., Yan, Y., & Wang, L. (2018a). Analysis of recrystallization behavior of shot peened graphene reinforced Al composites during isothermal annealing by X-ray diffraction method. *Journal of Alloys and Compounds*, 765, 862-868. DOI: <https://doi.org/10.1016/j.jallcom.2018.06.269>
- Zhan, K., Wu, Y., Li, J., Zhao, B., Yan, Y., Xie, L., Wang, L., & Ji, V. (2018b). Investigation on surface layer characteristics of shot peened graphene reinforced Al composite by X-ray diffraction method. *Applied Surface Science*, 435, 1257-1264. DOI: <https://doi.org/10.1016/j.apsusc.2017.11.242>
- Zheng, Z., Zhang, X., Li, J.C., & Geng, L. (2020a). High-content graphene nanoplatelet reinforced aluminum composites produced by ball milling and hot extrusion. *Science China Technological Sciences*, 63, 1426–1435. DOI: <https://doi.org/10.1007/s11431-020-1670-4>
- Zheng, Z., Zhong, S., Zhang, X., Li, J., & Geng, L. (2020b). Graphene nano-platelets reinforced aluminum composites with anisotropic compressive properties. *Materials Science and Engineering: A*, 798, 140234. DOI: <https://doi.org/10.1016/j.msea.2020.140234>
- Zhu, K., Jiang, C., Li, Z., Du, L., Zhao, Y., Chai, Z., Wang, L., & Chen, M. (2016). Residual stress and microstructure of the CNT/6061 composite after shot peening. *Materials & Design*, 107, 333-340. DOI: <https://doi.org/10.1016/j.matdes.2016.06.030>
- Zhu, K., Li, Z., & Jiang, C. (2019). Surface mechanical properties of shot-peened CNT/Al–Mg–Si alloy composites. *Journal of Alloys and Compounds*, 773, 1048-1053. DOI: <https://doi.org/10.1016/j.jallcom.2018.09.165>



Fuzzy Sliding Mode Control with Moving Sliding Surface of Rotary Inverted Pendulum

Muhammet Aydın^{1,*}, Oğuz Yakut¹

¹Department of Mechatronics Engineering, Faculty of Engineering, Firat University, Elazığ, Türkiye

Article History

Received: 27.10.2021
Accepted: 31.03.2022
Published: 25.09.2022

Research Article

Abstract – In this study, considering the dynamic equations of the rotary inverted pendulum system and the motor dynamics, pendulum angle is controlled with fuzzy logic sliding mode control method which has moving sliding surface using state variables in Matlab program. The sliding surface of sliding mode control method is selected as moving. A fuzzy logic structure is used to calculate the slope of slip surface. The boundary values of the membership functions in the fuzzy logic structure have been optimized using genetic algorithm codes in Matlab program. The sum of the squares of the errors is preferred as the objective function. Inputs of the fuzzy logic structure are the error of the pendulum angle and the derivative of pendulum angle error. In the fuzzy logic structure, the slope of sliding surface of sliding mode control structure is obtained as an output. From the results, it was seen that the pendulum angle reached the desired reference value around the first second and the error was approximately zero. In addition, it has been observed that the motor torque value is at the levels of 20 Nm and the motor current value is at the levels of 3 amperes. It has been obtained from the results that the motor values are at reasonable levels close to the values in practical applications. When the motor is selected according to these obtained values, there won't be a problem with the implementation of this control method in real-time applications of the rotary inverted pendulum system.

Keywords – Fuzzy logic control, genetic algorithm, motor model, moving sliding mode control, rotary inverted pendulum, sliding surface

1. Introduction

Due to its difficult controllability, inverted pendulum systems are one of the preferred systems in the application of control techniques. The single pendulum on a cart (Bugeja,2003) and single rotary inverted pendulum systems (Stimac, 1999), double pendulum on a cart (Zhong & Röck, 2001), and double rotary inverted pendulum systems are some of the inverted pendulum systems developed until today (Krishen & Becerra, 2006; Awtar, S., King, N., Allen, T. & et all, 2002).

One of the preferred inverted pendulum systems in applications is rotary inverted pendulum (rip) system. The Rip system is an excellent test system for working on the control of indirectly driven nonlinear unstable systems. The rip system has been the system of choice for control applications in recent years, where it is more manufacturable and easier to use according to an inverted pendulum on a cart. The rip system has two arms, a horizontally moving rotary arm, and a vertically moving pendulum. Rotary arm takes its motion from DC motor. After the DC motor moves the rotating arm, the pendulum connected to the rotating arm is tried to be stabilized at the upper balance point, that is, where it is unstable (Yan,2003; Kuo, Huang, & Hong 2009).

¹ muhammeta@firat.edu.tr

² oyakut@firat.edu.tr

*Corresponding Author

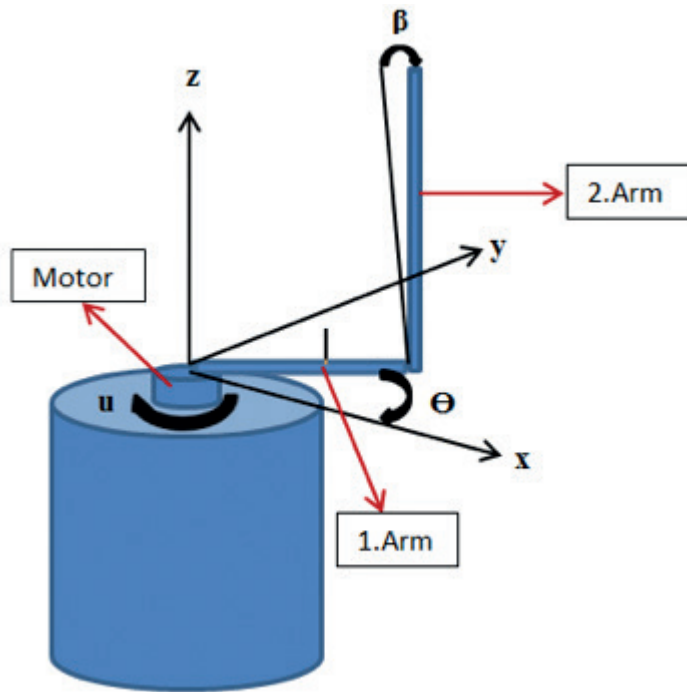


Figure 1. Rotary Inverted Pendulum System

In the studies presented so far in the literature for the angle control of the rotary inverted pendulum system shown in figure 1, classical control methods such as PID (Kuo, Huang, & Hong 2009), PI, PD (Altinoz, Yilmaz, & Weber, 2010), adaptive control methods with sliding mode control (Wang, 2009; Bogdanov, 2004; Aydin, Yakut, & Tutumlu, 2019), fuzzy control (Krishen & Becerra, 2006), sliding mode control (Khanesar, Teshnehlab, & Shoorehdeli, 2007), particle swarm optimization based PID control (Hassanzadeh & Mobayen, 2008; Bogdanov, 2004; Sugie & Fujimoto 1998; Sukontanakarn & Parnichkun 2009) and there are control studies sliding mode control methods via artificial neural network (Aydin, Yakut, & Tutumlu, 2019).

Especially in recent years, development of a Neuro-Fuzzy Friction Estimation Model used to estimate the joint friction coefficients of a Triple Link Rotary Inverted Pendulum system (Hazem, Fotuhi, & Bingül, 2020), controlled of a rotary inverted pendulum by adaptive techniques (Nath & Dewan, 2017), performing stability control of double link rotary inverted pendulum with Fuzzy-LQR and Fuzzy-LQG methods (Hazem, Fotuhi, & Bingül, 2020), developing of a fuzzy logic controller for rotary inverted pendulum (Le, Vo, Van & et all, 2018), controlling the rotary inverted pendulum with incremental sliding mode control (Hong, Nguyen, Hoang & et all 2019), a comparative analysis of the linear quadratic regulator and sliding mode control results for the rotary inverted pendulum (Nath & Dewan, 2018), performing of model-free sliding mode stabilizing control of the real rotary inverted pendulum (Yiğit, 2017), developing of numerical design method by using nonlinear sliding mode control method for Rotary inverted pendulum (Cui, 2019), comparing the PID and sliding mode control results of the rotary inverted pendulum system using PLC (Howimanporn, Chookaew & Silawatchananai, 2020), pole placement controller applied to rotary inverted pendulum system (Muñoz-Poblete, 2018), performing of a rotary inverted pendulum real-time stability control using an LQR-based sliding mode controller (Chawla & Singla, 2021), performing of an adaptive neural network-based control of the rotary inverted pendulum with oscillation compensation (Zabihifar, Yushchenko & Navvabi, 2020) studies have come to the fore.

In this paper, the non-linear model of the rotary inverted pendulum system was obtained and the fuzzy sliding mode control approach, which has a moving sliding surface, was used to control the pendulum. The slope of the slip surface was obtained using a fuzzy logic structure. The values of the coefficients in the fuzzy logic structure are optimized using the genetic algorithm. In the second part, Material and method, Modeling of Rotary Inverted Pendulum System and Sliding Surface Moving Fuzzy Sliding Mode Control

Design are explained. In the third chapter, results and discussion are given. In the last section, the results are mentioned.

2. Materials and Methods

2.1 Modeling of Rotary Inverted Pendulum System

The system in figure 1 is a two-degree-of-freedom system driven by a single motor. Θ and β are variable parameters of the system. The coordinate axis layout of the system is shown in [figure 1](#). If the total kinetic energy of the system is calculated according to this coordinate axis set;

$$T = \frac{1}{2}m_1(\dot{x}_1^2 + \dot{y}_1^2) + \frac{1}{2}I_1\dot{\theta}^2 + \frac{1}{2}m_2(\dot{x}_2^2 + \dot{y}_2^2 + \dot{z}_2^2) + \frac{1}{2}I_2\dot{\beta}^2 \quad (2.1)$$

x_1, y_1 in the equations are the center of gravity coordinates of the first limb., x_2, y_2 and z_2 represent the center of gravity coordinates of the second arm. m_1 and m_2 are the masses of each arm. I_1 and I_2 represent the mass moments of inertia of the arms. The limb dimensions according to their center of gravity are L_1 and L_2 , respectively. The friction coefficients at the joints are b_1 and b_2 . τ represents the control torque applied by the motor.

The equations of the expressions given in [equation 2.1](#) are obtained as follows (see [2.2](#), [2.3](#), [2.4](#), [2.5](#) and [2.6](#)).

$$x_1 = L_1 \cos\theta \quad (2.2)$$

$$y_1 = L_1 \sin\theta \quad (2.3)$$

$$x_2 = x_1 - L_2 \sin\beta \sin\theta \quad (2.4)$$

$$y_2 = y_1 + L_2 \sin\beta \cos\theta \quad (2.5)$$

$$z_2 = L_2 \cos\beta \quad (2.6)$$

If the above expressions are substituted to find the total kinetic energy of the system (see [2.7](#));

$$T = \frac{1}{2}m_1L_1^2\dot{\theta}^2 + \frac{1}{2}I_1\dot{\theta}^2 + \frac{1}{2}m_2(L_1\dot{\theta}^2 + 2L_1L_2\cos\beta\dot{\theta}\dot{\beta} + L_2^2\dot{\beta}^2 + L_2^2\sin^2\beta\dot{\theta}^2) + \frac{1}{2}I_2\dot{\beta}^2 \quad (2.7)$$

Potential energy of the system (see [2.8](#) and [2.9](#)):

$$V = m_2gz_2 \quad (2.8)$$

$$V = m_2gL_2\cos\beta \quad (2.9)$$

From here, the Lagrangian function is created as follows (see [2.10](#) and [2.11](#)).

$$L = T - V \quad (2.10)$$

$$L = \frac{1}{2}(m_1L_1^2 + I_1)\dot{\theta}^2 + \frac{1}{2}m_2[(L_1 + L_2^2\sin^2\beta)\dot{\theta}^2 + 2L_1L_2\cos\beta\dot{\theta}\dot{\beta} + L_2^2\dot{\beta}^2] + \frac{1}{2}I_2\dot{\beta}^2 - m_2gL_2\cos\beta \quad (2.11)$$

The equation of motion for θ (see [2.12](#)):

$$\frac{d}{dt}\left(\frac{\partial L}{\partial \dot{\theta}}\right) - \frac{\partial L}{\partial \theta} = Q_\theta \quad (2.12)$$

If the expressions in this equation are calculated and replaced, the equation of motion for θ is obtained as follows (see [2.13](#)).

$$(m_1L_1^2 + I_1 + m_2L_1 + m_2L_2^2\sin^2\beta)\ddot{\theta} + m_2L_1L_2\cos\beta\ddot{\beta} - m_2L_1L_2\sin\beta\dot{\beta}^2 + 2m_2L_2^2\sin\beta\cos\beta\dot{\beta}\dot{\theta} = \tau - b_1\dot{\theta} \quad (2.13)$$

The equation of motion for β (see [2.14](#)):

$$\frac{d}{dt}\left(\frac{\partial L}{\partial \dot{\beta}}\right) - \frac{\partial L}{\partial \beta} = Q_\beta \quad (2.14)$$

After performing the necessary operations in the above equation, the equation of motion for β is obtained as follows (see [2.15](#)).

$$m_2L_1L_2\cos\beta\ddot{\theta} + (m_2L_2^2 + I_2)\ddot{\beta} - m_2L_2^2\sin\beta\cos\beta\dot{\theta}^2 - m_2gL_2\sin\beta = -b_2\dot{\beta} \quad (2.15)$$

If the expressions θ and β in the equations of motion are separated, the following equations are obtained (see [2.16](#) and [2.17](#)).

$$\ddot{\theta} = \frac{(m_2L_2^2 + I_2)(b_1\dot{\theta} - \tau - m_2L_1L_2\sin\beta\dot{\beta}^2 + 2m_2L_2^2\sin\beta\cos\beta\dot{\beta}\dot{\theta})}{(m_2L_1L_2\cos\beta)^2 - (m_2L_2^2 + I_2)(m_1L_1^2 + I_1 + m_2L_1 + m_2L_2^2\sin^2\beta)} - \frac{m_2L_1L_2\cos\beta(b_2\dot{\beta} - m_2L_2^2\sin\beta\cos\beta\dot{\theta}^2 - m_2gL_2\sin\beta)}{(m_2L_1L_2\cos\beta)^2 - (m_2L_2^2 + I_2)(m_1L_1^2 + I_1 + m_2L_1 + m_2L_2^2\sin^2\beta)} \quad (2.16)$$

$$\ddot{\beta} = \frac{(m_1L_1^2 + I_1 + m_2L_1 + m_2L_2^2\sin^2\beta)(b_2\dot{\beta} - m_2L_2^2\sin\beta\cos\beta\dot{\theta}^2 - m_2gL_2\sin\beta)}{(m_2L_1L_2\cos\beta)^2 - (m_2L_2^2 + I_2)(m_1L_1^2 + I_1 + m_2L_1 + m_2L_2^2\sin^2\beta)} - \frac{m_2L_1L_2\cos\beta(b_1\dot{\theta} - \tau - m_2L_1L_2\sin\beta\dot{\beta}^2 + 2m_2L_2^2\sin\beta\cos\beta\dot{\beta}\dot{\theta})}{(m_2L_1L_2\cos\beta)^2 - (m_2L_2^2 + I_2)(m_1L_1^2 + I_1 + m_2L_1 + m_2L_2^2\sin^2\beta)} \quad (2.17)$$

The equation of motion of the DC motor that provides the rotational motion of the first arm can be written as follows (see [2.18](#)). Here, V_a is the motor supply voltage and also the control signal, K_b is the back electromotive voltage coefficient, N is the gear ratio, R is the motor winding ohmic resistance, L is the motor inductance coefficient and i is the electrical current flowing through the motor windings.

$$\frac{di}{dt} = \frac{V_a - Ri}{L} - \frac{K_b\dot{\theta}}{LN} \quad (2.18)$$

If we convert the expressions in the equations into state variables is obtained as [2.19](#), [2.20](#), [2.21](#), [2.22](#) and [2.23](#):

$$\theta = x(1) \quad (2.19)$$

$$\dot{\theta} = x(2) \quad (2.20)$$

$$\beta = x(3) \quad (2.21)$$

$$\dot{\beta} = x(4) \quad (2.22)$$

$$\frac{di}{dt} = x(5) \quad (2.23)$$

The motor control torque is calculated as 2.24:

$$\tau = \frac{K_t i}{N} \quad (2.24)$$

Where K_t is the motor torque coefficient.

For the rotary inverted pendulum system, using these state variables, the moving sliding mode control method was applied with the help of the program written in the Matlab program. With this control method, it will be ensured that the pendulum angle β goes to the desired zero reference point. The Values of used system parameters are given in table 1.

Table 1
System Parameter Values

Parameter	Value	Unit
m_1	0.15	kg
m_2	0.1	kg
L_1	0.4	m
L_2	0.4	m
b_1	0.01	Ns/m
b_2	0.01	Ns/m
I_1	0.0248	kgm ²
I_2	0.00386	kgm ²
L	0.1	Henry
R	1.4	Ohm
K_t	0.25	-
K_b	0.05	-
N	1/20	-

2.2 Sliding Surface Moving Fuzzy Sliding Mode Control Design

The sliding mode control method is a nonlinear and robust control method. Compared to other control methods, it is a method that is not affected by external disturbances. Thanks to the oscillations on the sliding surface to reach the desired reference, it can reach the result quickly with high accuracy (Young, Utkin, & Ozguner, 1999). Because the system parameters are unknown or constantly changing and there are external disturbances affecting the system, the sliding mode control allows long-term controllability as long as the limit values of the system are known.

While performing the sliding mode control design, the slip surface must first be determined and a control rule must be created to reach the determined slip surface. The time taken to reach the slip surface is called the reach time. This region of the phase trajectory is called the reach mode. In reach mode, the system is sensitive to parameter uncertainty and external noise (Edwards & Spurgeon, 1998). When the slip surface is reached, the slip mode starts, in which the trajectory of the system is insensitive to uncertain parameters and external factors. Chattering in sliding mode control applications is caused by oscillations around the system's desired equilibrium point, and it discloses the system's unmodeled high-frequency dynamics. Sliding mode control expression with sign function can be written as 2.25:

$$U = -k \operatorname{sign}(S) \quad (2.25)$$

S in equation 25 is the slip surface function and it can be expressed as given in equation (2.26), depending on the error (e) that occurs according to the response of the system and the variation of the error with time (de). When choosing S, the slope of the slip surface C is taken as a time variable. The slope value is updated instantly by looking at the answers of the system.

$$S = C e + de \tag{2.26}$$

An example of the sliding surface of the sliding mode control is shown in figure 2. As can be seen from the given figure, the slip surface has a certain slope. The coefficient C in equation (2.26) represents this slope.

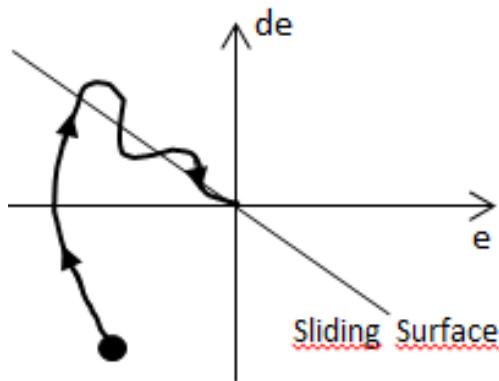


Figure 2. Sliding surface

The controller’s success is ensured by determining the best value for this defined slope. The sliding mode controller’s slip surface slope coefficients are treated as moving in this investigation. Fuzzy logic was used to calculate the slope coefficient C. Mamdani type was used as fuzzy inference method. Center of gravity was used as the defuzzification method. The error of the pendulum angle and the derivative of the pendulum error are given as an introduction to the fuzzy logic structure. As an output, the slope coefficient of the sliding surface of the sliding mode control is obtained. The optimum values of the base coefficients of the membership functions in the fuzzy logic structure were calculated using a genetic algorithm. Genetic algorithm parameters were used as FitnessLimit 1e-10, Generations 100 and PopulationSize 20. Figure 3 shows the block diagram in which the coefficients of the controller are optimized by the genetic algorithm technique.

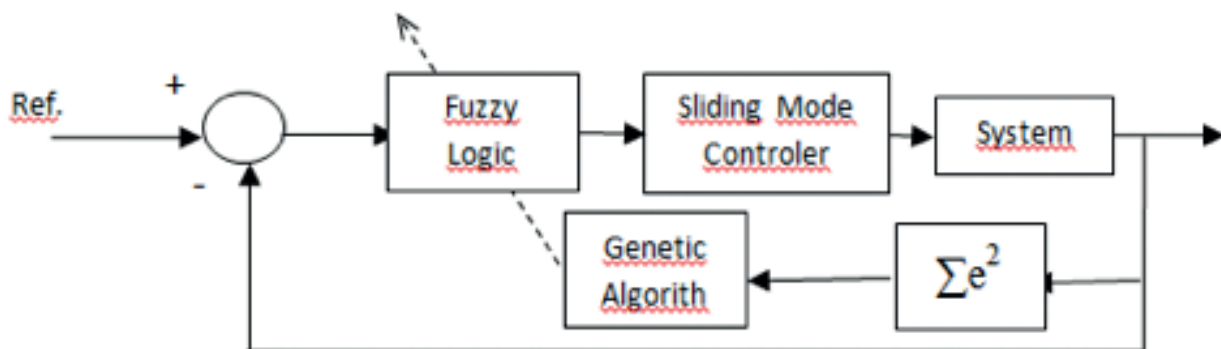


Figure 3. Controller Block Diagram

Since the C coefficient obtained will vary each time, the control method has a moving sliding surface. Below is the [Figure 4](#) showing the mobility of the C coefficient.

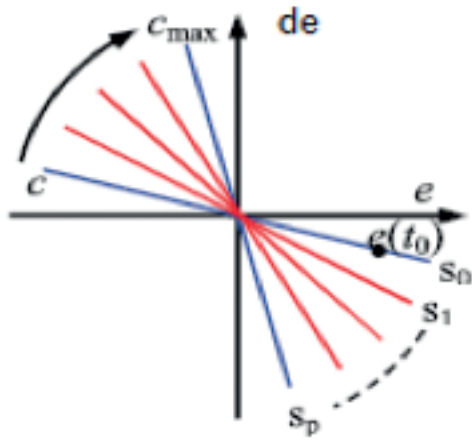


Figure 4. Variation of the C coefficient

The rule table for the inputs and the output for the fuzzy logic structure, membership functions are shown in [table 2](#), [figure 5](#), [figure 6](#), and [figure 7](#), respectively. Triangular membership functions are used for each input and output.

Table 2

Rule table of fuzzy logic structure for slip surface C

e \ de/dt	NB_{de}	Z_{de}	PB_{de}
NB_e	Z	NB	NB
Z_e	NB	Z kg	PB
PB_1	PB	PB	PB

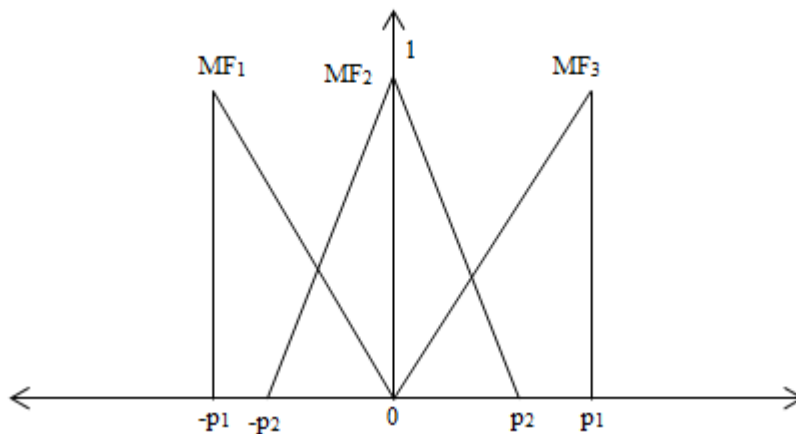


Figure 5. Membership functions for input1(e)

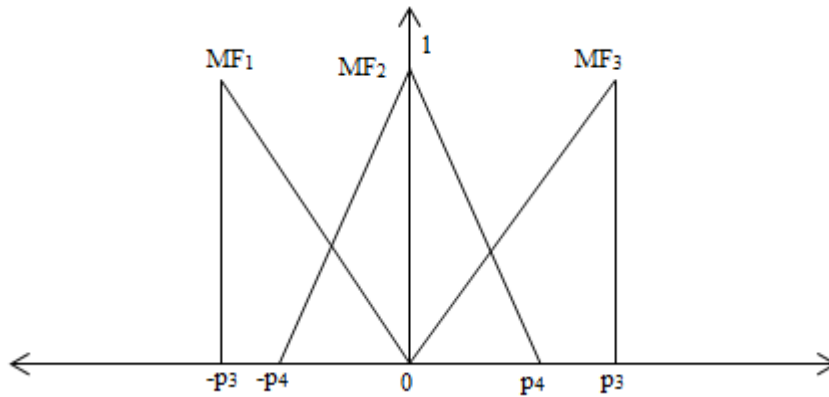


Figure 6. Membership functions for input2(de/dt)

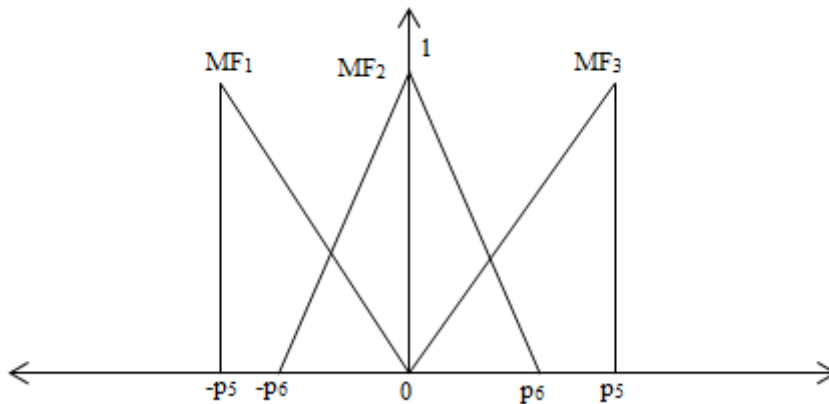


Figure 7. Membership functions for output (C)

The $p_1, p_2, p_3, p_4, p_5,$ and p_6 values of the base coefficients of the membership functions used in the fuzzy structures were calculated by genetic algorithm and obtained as given in [table 3](#)

Table 3

Base values of membership functions

P_1	P_2	P_3	P_4	P_5	P_6
20.7646	0.4166	0.7657	11.0061	91.7301	8.4752

The sign function in the sliding mode control expression causes the control signal to crackle. Various types of functions are used instead of this sign function to solve this problem. The widely used saturation function was chosen to replace the sign function in this study. As a result, equation (2.27) calculates the sliding mode control expression with saturation function.

$$U = -k \cdot \text{SAT}(S / \text{epsilon}) \tag{2.27}$$

Where the epsilon value was found to be 74.55 by genetic algorithm. The Fitness value-Generation (Iteration) graph of the optimization process performed while calculating the unknown coefficients with the genetic algorithm is given in [figure 8](#).

3. Results and Discussion

In [figure 9](#), the variation of the angular position of the first arm connected to the motor with respect to time is seen. It started from the zero point at the beginning and changed direction in the first seconds. This is an expected result to raise the pendulum.

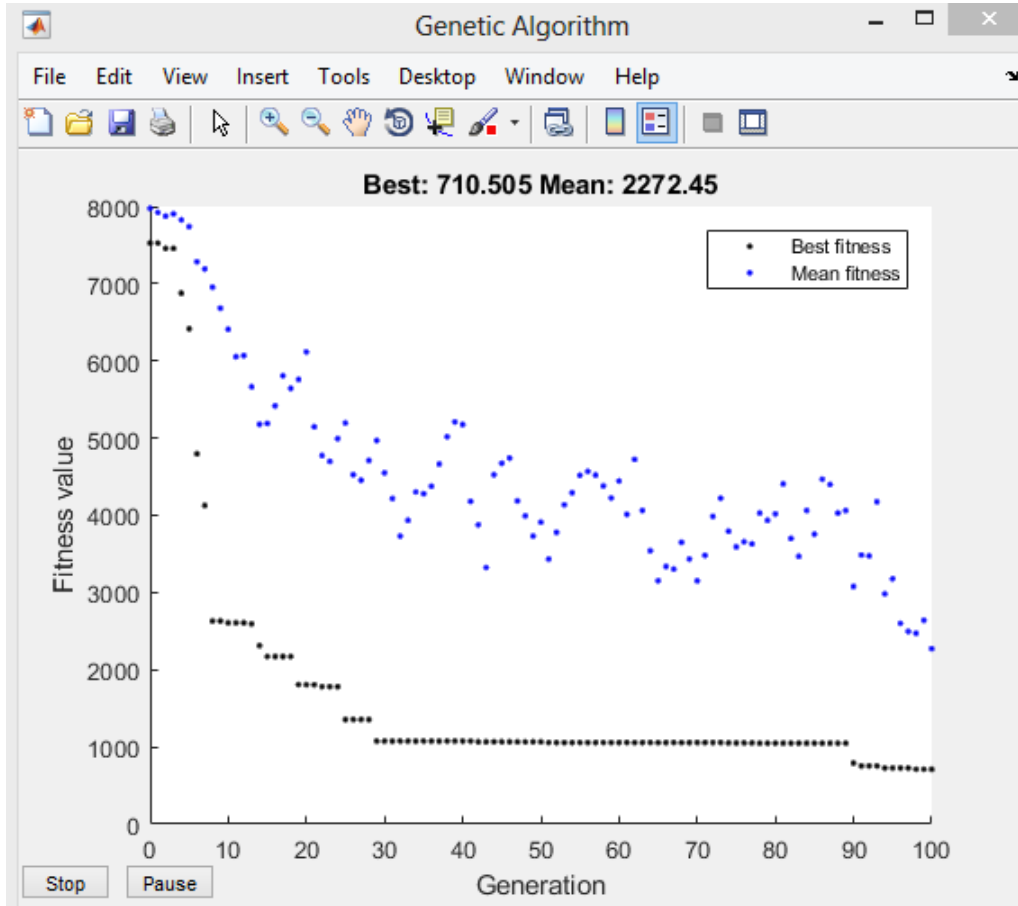


Figure 8. The Fitness value-Generation (Iteration) graph of the genetic algorithm optimization process

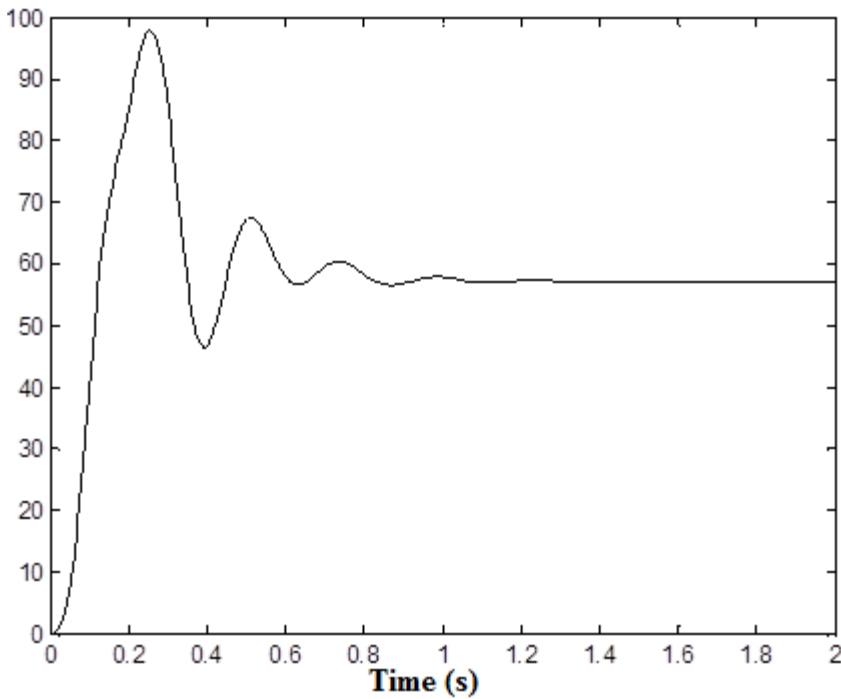


Figure 9. Variation of theta angle according to time

The graph in [figure 10](#) shows the angular velocity of the first arm to time. It is seen that the angular velocity value reaches 14 rad/s at the beginning and is fixed at 0 rad/s.

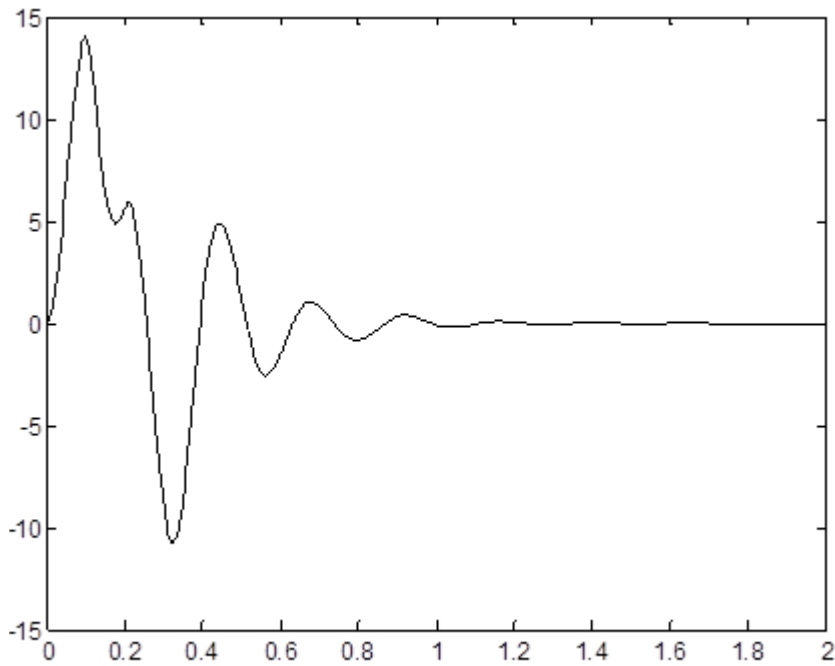


Figure 10. Angular velocity change of the first arm according to time

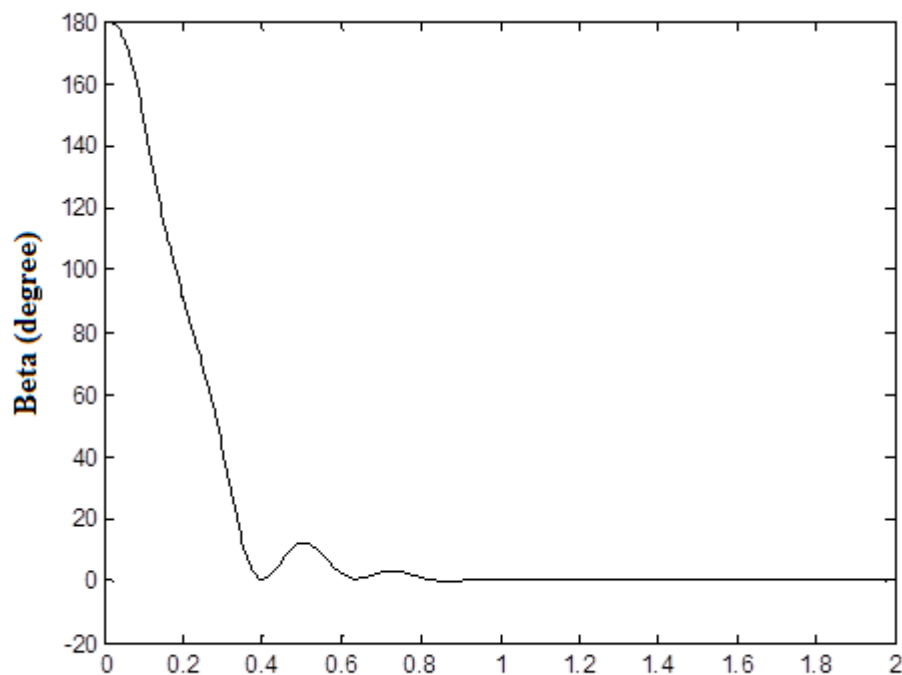


Figure 11. Variation of beta angle (pendulum angle) according to time

In [figure 11](#), there is a graph showing the change of pendulum angle with respect to time. The pendulum is required to stop at the unstable upper balance point. Therefore, the pendulum angle must reach the desired zero reference point. As seen in the figure, the pendulum reaches the desired reference value in about 1 second.

In [figure 12](#), the variation of the angular velocity of the pendulum with time is shown. As can be seen from the graph, the angular velocity of the pendulum reaches zero after 1 second.

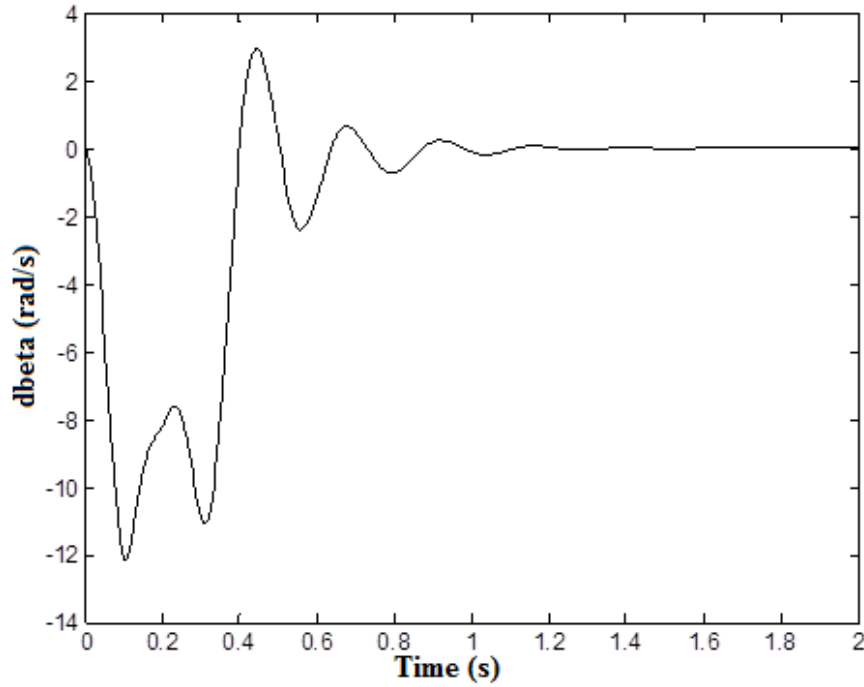


Figure 12. Angular velocity change of the pendulum according to time

In [figure 13](#) and [14](#), respectively, the torque value of the DC motor to be applied to the first arm and the graph of the slope values of the slip surface are given. When the DC motor torque graph in [figure 13](#) is examined, it is clear that approximately 20 Nm of motor torque will be sufficient to bring the pendulum to the desired reference value. It can be said that this torque value is reasonable for real applications. After about 1 second, the control signal reaches zero. When the slip surface slope graph in [figure 14](#). is examined, it is seen that it takes values between 0-50 values.

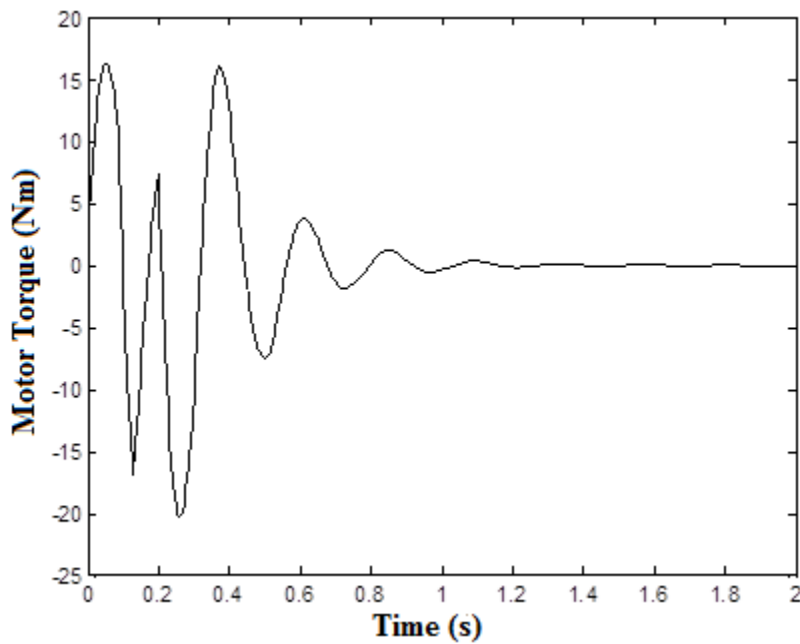


Figure 13. Variation of DC motor's torque according to time

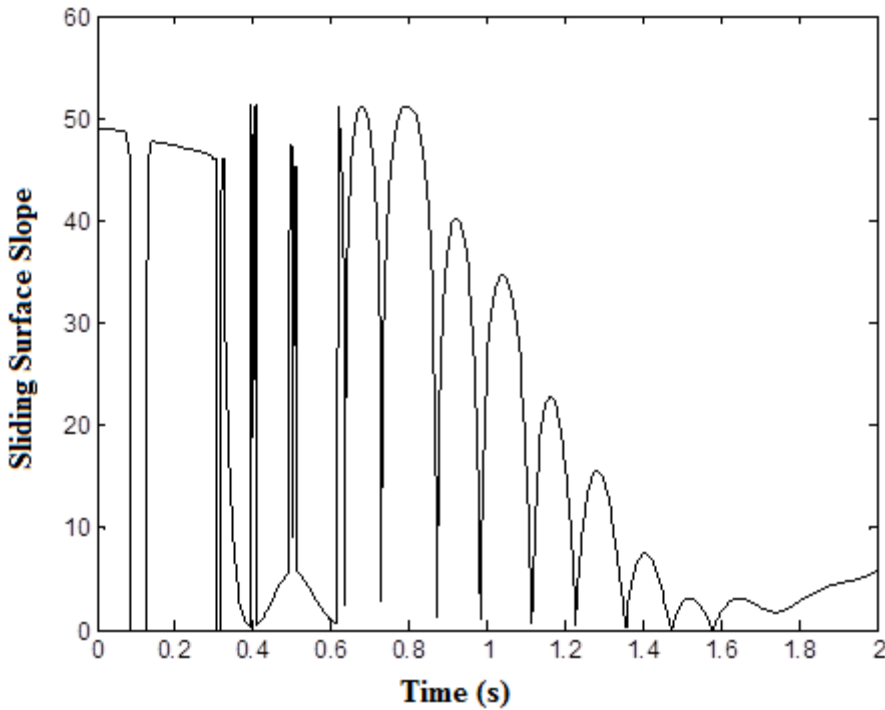


Figure 14. Sliding surface slope graph

Figure 15 shows the time variation of the supply voltage signal that should be applied to the DC motor. It can also be seen from the graph that the DC motor supply voltage source is limited to 12 volts. In figure 16, the variation of the current passing through the DC motor windings with time is shown. It is seen that the current drawn by the motor reaches zero value after about 1 second.

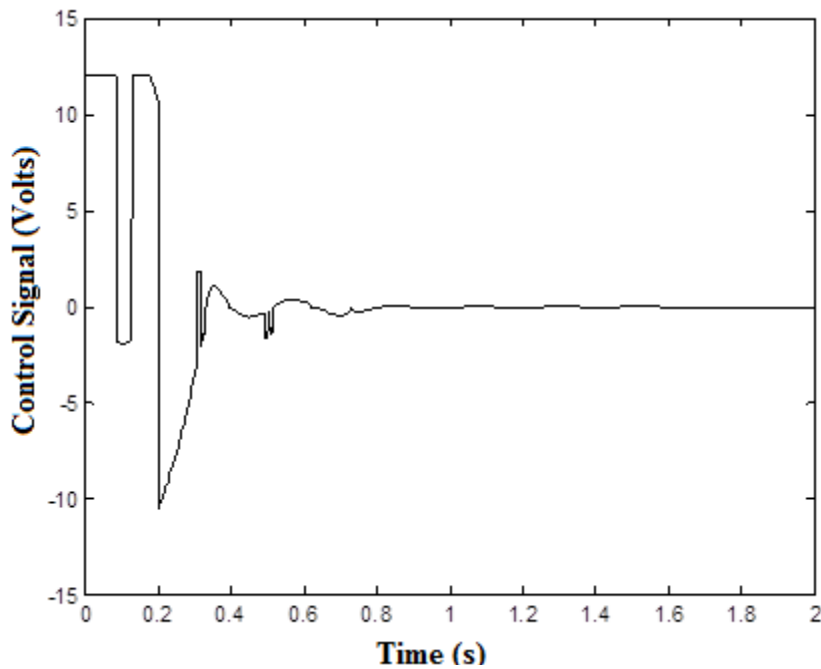


Figure 15. Graph of DC Motor Control Signal according to Time

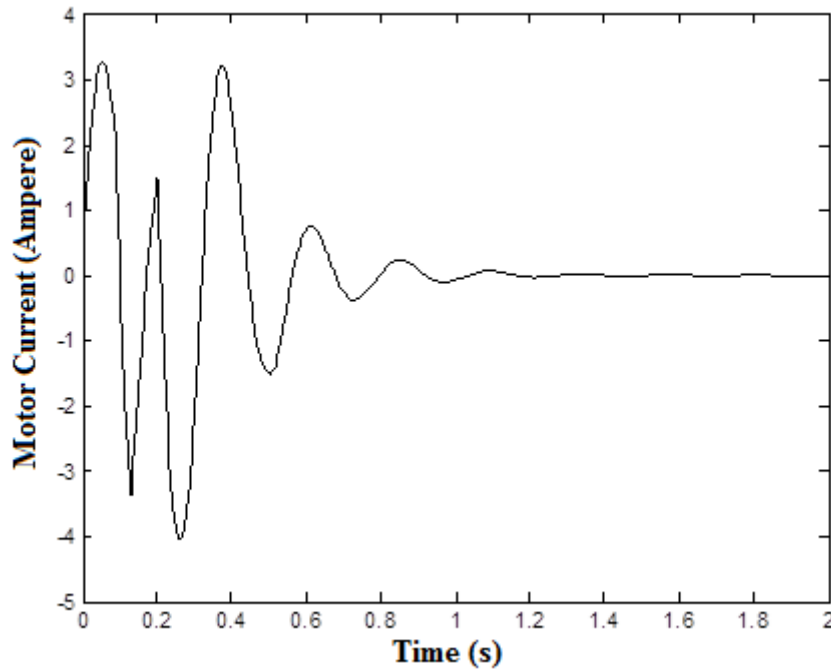


Figure 16. Graph of DC Motor Current according to Time

In Table 4, the results of the study conducted in this research article and a publication in the literature are compared. As can be seen in the table, the pendulum angle of the system achieved a better settling time of 0.9 s in the current study (Nath & Dewan 2018)..

Table 4

Comparison of between work in the literature and the present work

	Method	Settling Time (s)	Max. Overshoot (rad)	Max. Undershoot (rad)
Rotary inverted pendulum arm angle results	LQR	0.80	0.1260	-
	SMC	0.80	0.1460	-
	Present Work	1.05	0.6981	0.1523
Pendulum angle results	LQR	1.25	0.0072	- 0.003
	SMC	1.25	0.0130	- 0.004
	Present Work	0.90	0.1745	- 0.035

4. Conclusion

In this study, the nonlinear model of the rotary inverted pendulum system, which has a single degree of freedom, was first obtained using the Lagrangian method. The pendulum angle was controlled by the program created in Matlab with the help of state variables on the model obtained. For this reason, the system has been controlled using the moving sliding mode control approach. The variability of the slope of the slip surface was calculated by the fuzzy logic method. The coefficients of the fuzzy logic structure were calculated with the help of the genetic algorithm. At the end of the study, it was observed that the pendulum reached the desired reference value in about 1 second, the error was zero, and the control signal reached zero. It has been observed that the motor torque value reaches up to 20 Nm and the motor draws a maximum of 4 amperes. From these results, it has been obtained that the moving sliding mode control can be applied to the system without any problems if the motor is selected considering the obtained motor values in the real-time motor selection.

Author Contributions

Muhammet Aydin: Modeling of rotary inverted pendulum system.

Oğuz Yakut: Sliding surface moving fuzzy sliding mode control design.

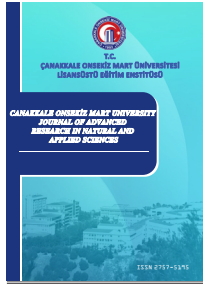
Conflicts of Interest

The authors declare no conflict of interest.

References

- Altinoz, O. T., Yilmaz, A. E., & Weber, G. W. (2010). Chaos particle swarm optimized PID controller for the inverted pendulum system. In *2nd international conference on engineering optimization*. http://www.dem.ist.utl.pt/engopt2010/Book_and_CD/Papers_CD_Final_Version/pdf/01/01454-01.pdf
- Awtar, S., King, N., Allen, T., Bang, I., Hagan, M., Skidmore, D., & Craig, K. (2002). Inverted pendulum systems: rotary and arm-driven-a mechatronic system design case study. *Mechatronics*, 12(2), 357-370. [https://doi.org/10.1016/S0957-4158\(01\)00075-7](https://doi.org/10.1016/S0957-4158(01)00075-7)
- Aydin, M., Yakut, O., & Tutumlu, H. (2019). Implementation of the Network-Based Moving Sliding Mode Control Algorithm to the Rotary Inverted Pendulum System. *Journal of Engineering and Technology*, 3(1), 32-41. <https://dergipark.org.tr/en/download/article-file/721111>
- Bogdanov, A. (2004, Aralık) Optimal control of a double inverted pendulum on a cart, Health and Science University Technical Report.
- Bugeja, M. (2003, September). Non-linear swing-up and stabilizing control of an inverted pendulum system. In *The IEEE Region 8 EUROCON 2003. Computer as a Tool*. (Vol. 2, pp. 437-441). IEEE. <https://doi.org/10.1109/EURCON.2003.1248235>
- Chawla, I., & Singla, A. (2021). Real-Time Stabilization Control of a Rotary Inverted Pendulum Using LQR-Based Sliding Mode Controller. *Arabian Journal for Science and Engineering*, 46(3), 2589-2596. <https://doi.org/10.1007/s13369-020-05161-7>
- Cui, J. (2019, July). Numerical Design Method for Nonlinear Sliding Mode Control of Inverted Pendulum. In *2019 Chinese Control Conference (CCC)* (pp. 2646-2649). IEEE. <http://doi.org/10.23919/ChiCC.2019.8865123>
- Edwards, C., & Spurgeon, S. (1998). *Sliding mode control: theory and applications*. Crc Press.
- Hassanzadeh, I., & Mobayen, S. (2008). PSO-based controller design for rotary inverted pendulum system. *Journal of Applied Sciences*, 8(16), 2907-2912. <https://docsdrive.com/pdfs/ansinet/jas/2008/2907-2912.pdf>
- Hazem, Z. B., Fotuhi, M. J., & Bingül, Z. (2020). A comparative study of the joint neuro-fuzzy friction models for a triple link rotary inverted pendulum. *Ieee Access*, 8, 49066-49078. <http://doi.org/10.1109/ACCESS.2020.2978025>
- Hazem, Z. B., Fotuhi, M. J., & Bingül, Z. (2020). Development of a Fuzzy-LQR and Fuzzy-LQG stability control for a double link rotary inverted pendulum. *Journal of the Franklin Institute*, 357(15), 10529-10556. <https://doi.org/10.1016/j.jfranklin.2020.08.030>
- Hong, G. B., Nguyen, H. T., Nguyen, M. T., Hoang Le, T. T., & Hai Nguyen, V. D. (2019). TRAJECTORY TRACKING FOR FUTUR APENDULUM BY INCREMENTAL SLIDING MODE CONTROL. *Robotica & Management*, 24(1). <https://web.p.ebscohost.com/ehost/pdfviewer/pdfviewer?vid=0&sid=6590e51f-2bfb-4b30-b7aa-5aa088f805fc%40redis>
- Howimanporn, S., Chookaew, S., & Silawatchananai, C. (2020, October). Comparison between PID and Sliding Mode Controllers for Rotary Inverted Pendulum Using PLC. In *2020 4th International Conference on Automation, Control and Robots (ICACR)* (pp. 122-126). IEEE. <http://doi.org/10.1109/ICACR51161.2020.9265510>

- Khanesar, M. A., Teshnehlab, M., & Shoorehdeli, M. A. (2007, June). Sliding mode control of rotary inverted pendulum. In *2007 Mediterranean Conference on Control & Automation* (pp. 1-6). IEEE. <https://doi.org/10.1109/MED.2007.4433653>
- Krishen, J., & Becerra, V. M. (2006, October). Efficient fuzzy control of a rotary inverted pendulum based on LQR mapping. In *2006 IEEE Conference on Computer Aided Control System Design, 2006 IEEE International Conference on Control Applications, 2006 IEEE International Symposium on Intelligent Control* (pp. 2701-2706). IEEE. <https://doi.org/10.1109/CACSD-CCA-ISIC.2006.4777066>
- Kuo, T. C., Huang, Y. J., & Hong, B. W. (2009, July). Adaptive PID with sliding mode control for the rotary inverted pendulum system. In *2009 IEEE/ASME International Conference on Advanced Intelligent Mechatronics* (pp. 1804-1809). IEEE. <http://doi.org/10.1109/AIM.2009.5229784>
- Le, T. T. H., Vo, A. K., Van Nguyen, T., Vu, D. H., & Tran, M. S. (2018). FUZZY CONTROLLER FOR ROTARY INVERTED PENDULUM. *Robotica & Management*, 23(2). <https://web.p.ebscohost.com/ehost/pdfviewer/pdfviewer?vid=2&sid=0f28d825-27ec-4362-a82b-dd944bf02a20%40redis>
- Muñoz-Poblete, C. (2018, October). Pole placement controller applied to a Rotary Inverted Pendulum System. A didactic view. In *2018 IEEE International Conference on Automation/XXIII Congress of the Chilean Association of Automatic Control (ICA-ACCA)* (pp. 1-6). IEEE. <http://doi.org/10.1109/ICA-ACCA.2018.8609824>
- Nath, K., & Dewan, L. (2017, November). Control of a rotary inverted pendulum via adaptive techniques. In *2017 International Conference on Emerging Trends in Computing and Communication Technologies (ICETCCT)* (pp. 1-6). IEEE. <http://doi.org/10.1109/ICETCCT.20178280315>
- Nath, K., & Dewan, L. (2018, March). A comparative analysis of linear quadratic regulator and sliding mode control for a rotary inverted pendulum. In *2018 International Conference on Recent Trends in Electrical, Control and Communication (RTECC)* (pp. 302-307). IEEE. <http://doi.org/10.1109/RTECC.2018.8625648>
- Stimac, A. K. (1999). *Standup and stabilization of the inverted pendulum* (Doctoral dissertation, Massachusetts Institute of Technology, Dept. of Mechanical Engineering). <https://ocw.mit.edu/courses/mechanical-engineering/2-003-modeling-dynamics-and-control-i-spring-2005/study-materials/andrew.pdf>
- Sugie, T., & Fujimoto, K. (1998). Controller design for an inverted pendulum based on approximate linearization. *International Journal of Robust and Nonlinear Control: IFAC-Affiliated Journal*, 8(7), 585-597. [https://doi.org/10.1002/\(SICI\)1099-1239\(199806\)8:7<585::AID-RNC331>3.0.CO;2-B](https://doi.org/10.1002/(SICI)1099-1239(199806)8:7<585::AID-RNC331>3.0.CO;2-B)
- Sukontanakarn, V., & Parnichkun, M. (2009). Real-time optimal control for rotary inverted pendulum. *American journal of applied sciences*, 6(6), 1106. <http://citeseerx.ist.psu.edu/viewdoc/download?doi=10.1.1.1020.5634&rep=rep1&type=pdf>
- Wang, W. (2009). Adaptive fuzzy sliding mode control for inverted pendulum. In *Proceedings. The 2009 International Symposium on Computer Science and Computational Technology (ISCSCI 2009)* (p. 231). Academy Publisher. <https://citeseerx.ist.psu.edu/viewdoc/download?doi=10.1.1.648.7484&rep=rep1&type=pdf>
- Yan, Q. (2003, December). Output tracking of underactuated rotary inverted pendulum by nonlinear controller. In *42nd IEEE International Conference on Decision and Control (IEEE Cat. No. 03CH37475)* (Vol. 3, pp. 2395-2400). IEEE. <http://doi.org/10.1109/CDC.2003.1272978>
- Yiğit, İ. (2017). Model free sliding mode stabilizing control of a real rotary inverted pendulum. *Journal of Vibration and Control*, 23(10), 1645-1662. <https://doi.org/10.1177/1077546315598031>
- Young, K. D., Utkin, V. I., & Ozguner, U. (1999). A control engineer's guide to sliding mode control. *IEEE transactions on control systems technology*, 7(3), 328-342. <http://doi.org/10.1109/87.761053>
- Zhong, W., & Rock, H. (2001, September). Energy and passivity based control of the double inverted pendulum on a cart. In *Proceedings of the 2001 IEEE International Conference on Control Applications (CCA'01)(Cat. No. 01CH37204)* (pp. 896-901). IEEE. <http://doi.org/10.1109/CCA.2001.973983>
- Zabihifar, S. H., Yushchenko, A. S., & Navvabi, H. (2020). Robust control based on adaptive neural network for Rotary inverted pendulum with oscillation compensation. *Neural Computing and Applications*, 32(18), 14667-14679. <https://doi.org/10.1007/s00521-020-04821-x>



Implementation of a Lightweight and Portable Horn Antenna Using 3D Printing Technology

Serhan Yamacli^{1,*}

¹Department of Electrical-Electronics Engineering, Faculty of Engineering, Nuh Naci Yazgan University, Kayseri, Türkiye

Article History

Received: 27.12.2021
Accepted: 26.05.2022
Published: 25.09.2022

Research Article


Abstract – In this study, a horn antenna operating at 5.8GHz centre frequency, which is an ISM operating frequency, is designed and manufactured. The novelty of the antenna is that it is produced using a 3D printer with a conductive filament containing carbon nanotube particles. The geometric dimensions of the antenna were calculated by means of an antenna design software. Then, the size of the radiating element of the antenna was optimized to set the centre frequency to 5.8GHz. It has been verified by electromagnetic simulations that the proposed antenna exhibits this centre frequency. Then, the antenna geometry was sketched in a 3-dimensional drawing program and made ready for printing. This antenna was fabricated on an Ultimaker 3D printer with a PLA filament containing conductive carbon nanotubes. The radiation element of the antenna and the SMA connector were finally attached to the printed antenna. The frequency response of the antenna is then measured using a vector network analyser and it has been shown that the produced pyramidal horn antenna works in the desired frequency band. The printed antenna has the desired frequency characteristic without the need for any additional coating or conductive spray thanks to the PLA filament containing conductive carbon nanotubes. The produced antenna has a weight of only 64.53 grams, including the SMA connector and the radiation element. The proposed lightweight and practical horn antenna design concept may have important applications considering the advances and needs of mobile defence and telecommunication systems.

Keywords – Antenna design, 3-dimensional printing, conductive filament, electromagnetic simulation, horn antenna,

1. Introduction

Antennas are used for the propagation and reception of electromagnetic waves in radio frequency (RF) systems. Electromagnetic wave propagation and reception are needed in many application areas such as telecommunications, defence and medical systems. Antennas with various parameters are needed for the propagation of high frequency signals in telecommunication systems, for the transition of the telecommunication signal from the transmitting system to the transmission medium and again from the transmission medium to the receiver system; in defence systems especially in radars that are used to determine position, speed and shape; and in medical systems where medical imaging signals are transmitted and received. In recent years, the demand for small and lightweight components is increasing especially in mobile telecommunication and defence systems. For instance, the use of mobile base stations in the form of drones in times of natural disasters are being implemented successfully (Bor-Yaliniz et al., 2018). Another contemporary example is mobile defence systems, and it is predicted that the use of these systems will increasingly continue (Hui et al., 2018). It is obvious that such applications will require components that are as small, compact and lightweight as possible. On the other hand, 3-dimensional (3D) printing methods are also being improved continuously and its application areas are widespread (Shahrubudin et al., 2019).

Apart from the engineering applications of 3D printing technology, their utilization areas are expanding to medical systems (Wang et al., 2019), drug delivery systems (Matthew et al., 2020) and many other areas (Phillips et al., 2020). In the engineering field, the application areas are expanding by diversifying the filaments, which are the raw materials of 3D printing (Hu et al., 2018).

¹  syamacli@nny.edu.tr

*Corresponding Author

Various antenna implementations employing 3D printing technique exist in the literature. For example, (Yao et al., 2017) proposed a horn antenna with a centre frequency of 28GHz and printed on a 3D printer using insulating filament. Then, copper-containing conductive spray paint and conductive tape were adhered to insulating plastic antennas, and the measurements were performed and then the performance of the antennas were compared for these two cases. Similarly, an antenna with a circular reflector operating in the microwave X-band was printed with a polylactic acid (PLA) filament, and its measurements were performed after painting it with conductive spray paint. This antenna has been concluded to operate properly at the centre frequency of 10GHz (Tak et al., 2017). In another study, a horn antenna was printed with PLA filament using a 3D printer to operate in the 14-18 GHz band, then electrochemical deposition technique was used for metallic coating (Kyovtorov et al. 2017). It has been shown by measurements that this antenna works properly in the planned frequency band. In another study, an antenna was implemented to operate in the microwave D-band and the performances of conductive coated polymer and direct metallic printing were compared (Gu et al., 2020). In (Esfahani et al., 2018), a capsule-shaped antenna is printed using a 3D printer with silver and copper plating, and this antenna has been shown to work as expected. In another study, a 2x1 horn antenna array structure was given and the entire structure, including the feeding elements, was implemented using a 3D printer with acrylonitrile butadiene styrene (ABS) filament; and then copper electroplating was applied on the structure (Genç, 2019). The measurements showed that the antenna worked as expected. In another study, the gains of horn antennas, which are implemented on a 3D printer using ABS filament, are experimentally investigated for the cases where they are coated with copper, chrome and nickel (Genç et al., 2017). On the other hand, a double-backed horn antenna was implemented in (Lee et al., 2018) to operate in the 6-18 GHz range, printed on a 3D printer, and its performance was measured after coating it with silver-containing conductive paint. It has been shown that this antenna also works as expected. In another study, a 16x16 dipole antenna array was printed on a 3D printer, coated using electrodeposition method and then the characteristics of this printed antenna and the equivalent antenna made of standard aluminium were compared (So et al., 2018). In (Zhang et al., 2018), horn antennas were produced as prototypes, copper alloy and aluminium alloy horn antennas were produced with metallic 3D printing technique and then performance tests were conducted. Although these types of metallic antennas outperform coated antennas, manufacturing costs are seen as a drawback. In (Kwon et al., 2017), fractal antennas were proposed, the insulating frame part was produced with 3D ABS filament, the conductive parts were made using copper strips, and then performance tests were carried out. In a paper reviewing the production of 3D high-frequency elements, it has been reported that elements produced with the metallic 3D writing technique have better thermal and physical stability than plastic elements that are subsequently painted with conductive paint (Zhang et al., 2017). Information about the antenna and other supporting RF components implemented with silver-containing paint and PLA printing was given by (Kiesel et al., 2020) and it was concluded that the silver paint was successful for providing adequate conductivity. A horn antenna design for ultra-wideband applications was demonstrated by (Midtboen et al., 2017). Another horn antenna operating in the microwave X-band (8-12GHz) is 3D printed using insulating ABS filament, then silver-containing conductive paint, copper-containing adhesive tape and copper plating processes are utilized to provide conductivity (Chuma et al. 2019). The performances of these antennas are compared and it was concluded that the performance of the horn antenna implemented with copper coating performs better than the others.

In this study, a horn antenna with a 5.8GHz centre frequency is designed and implemented using 3D printing technique. This centre frequency is selected to be used in Industrial, Scientific and Medical (ISM) applications (Mishra et al., 2019; Mazar, 2014). The antenna dimensions is firstly computed and optimized using antenna design and electromagnetic simulation tools. Then, the planned antenna geometry was laid out in the 3D modelling program and then printed with a 3D printer using a PLA filament containing conductive carbon nanotube particles. No other coating or deposition is applied to the implemented antenna. Then, a subminiature version A (SMA) connector is attached to the antenna and then calibrated measurements were performed using a vector network analyser (VNA) device. The measurements have shown that the antenna works as expected at the expected frequency range. Thus, it has been shown that 3D antennas can be implemented using carbon nanotube doped conductive PLA filament with accurate electromagnetic characteristics. The weight of the produced antenna is 64.53 grams, which it is much lighter than its metallic counterparts. It is concluded that the use of conductive carbon nanotube doped PLA filament for the implementation of 3D printed antennas can be deployed for the fast production of lightweight antennas in mobile defence and telecommunication systems.

2. Materials and Methods

2.1. The Design and Simulation of the Pyramidal Horn Antenna

In this study, a pyramidal horn antenna, which is a widely used antenna type, was designed and implemented. The model of a typical pyramidal horn antenna is given in Figure 1.

A typical pyramidal horn antenna consists of three sections as can be seen in Figure 1 (Balanis, 2016) The first section is the waveguide part shown in green, the second is the aperture section shown in blue, and the third is the radiation element shown inside the waveguide. Descriptions of the geometric parameters shown in Figure 1 are presented in Table 1. In this study, an antenna design that can be used in ISM systems is aimed. Therefore, the centre frequency of the antenna was chosen as $f_c=5.8\text{GHz}$. In addition, the input impedance is taken as the standard 50Ω reference level and the minimum gain is selected as 10dBi. These design parameters were entered to an antenna design software and the geometric dimensions of the antenna were obtained as in Table 1.

In order to test the proper functioning of the design before the manufacturing of the antenna, the antenna geometry was imported as shown in Figure 2a and simulated in an electromagnetic simulation software. In the simulation program, the frequency range is selected 5-7GHz, the iteration residual limit is -40dB , and the boundary conditions are chosen as space. After the simulations, the length of the radiation element was optimized as 14.02mm, and the S_{11} characteristic obtained according to this value is shown in Figure 3. As it can be seen from this simulation result, the proposed antenna operates in a wide band around the 5.8GHz centre frequency.

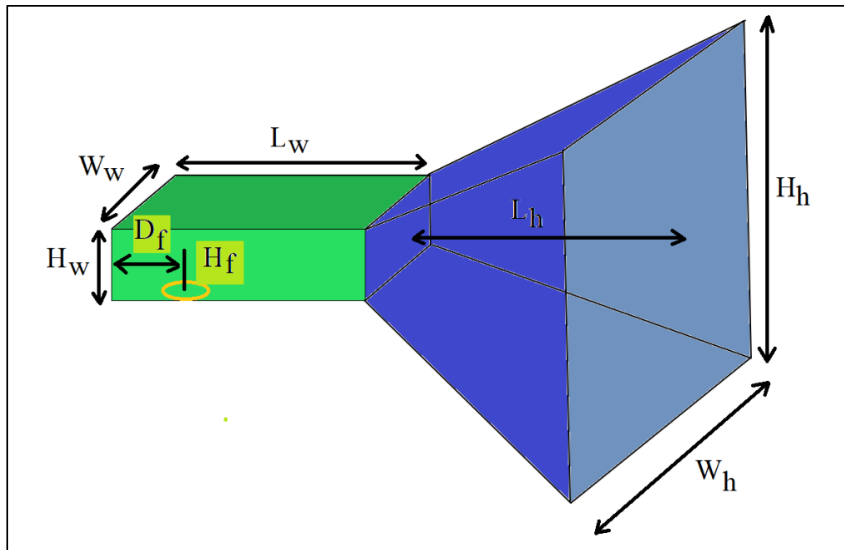


Figure 1. Pyramidal horn antenna model.

Table 1

Geometric parameters of the pyramidal horn antenna and the values for $f_c=5.8\text{GHz}$ centre frequency.

Parameter shown in Figure 1	Explanation	Value obtained by the design software
H_w	Height of the waveguide section	19.91mm
W_w	Width of the waveguide section	39.81mm
L_w	Length of the waveguide section	50.86mm
H_h	Height of the aperture section	76.17mm
W_h	Width of the aperture section	105.27mm
L_h	Length of the aperture section	31.22mm
H_f	Length of the radiation element	14.47mm
D_f	Distance of the radiation element to the back surface of the antenna	9.56mm

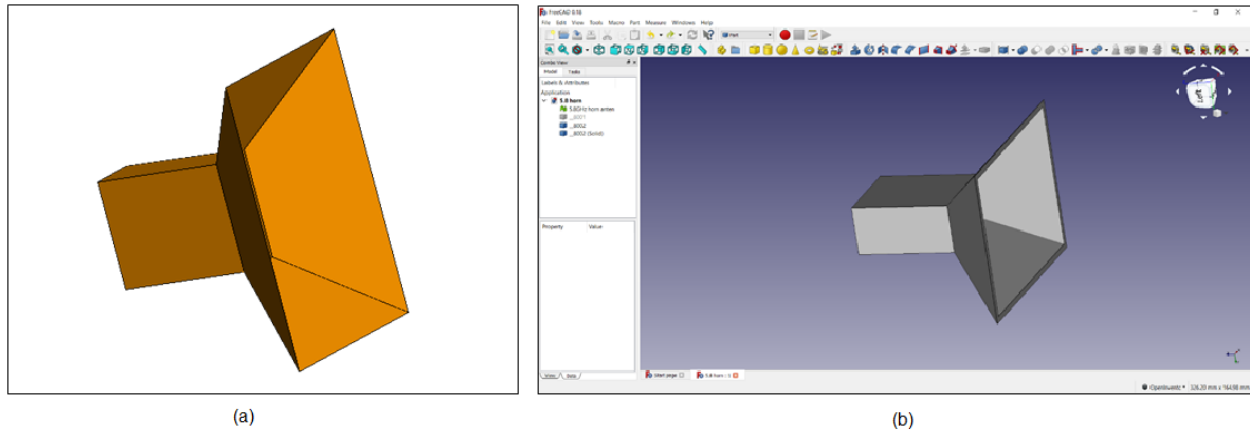


Figure 2. a) The view of the designed pyramidal horn antenna in the simulation software, b) FreeCad drawing of the 3D printing of pyramidal horn antenna.

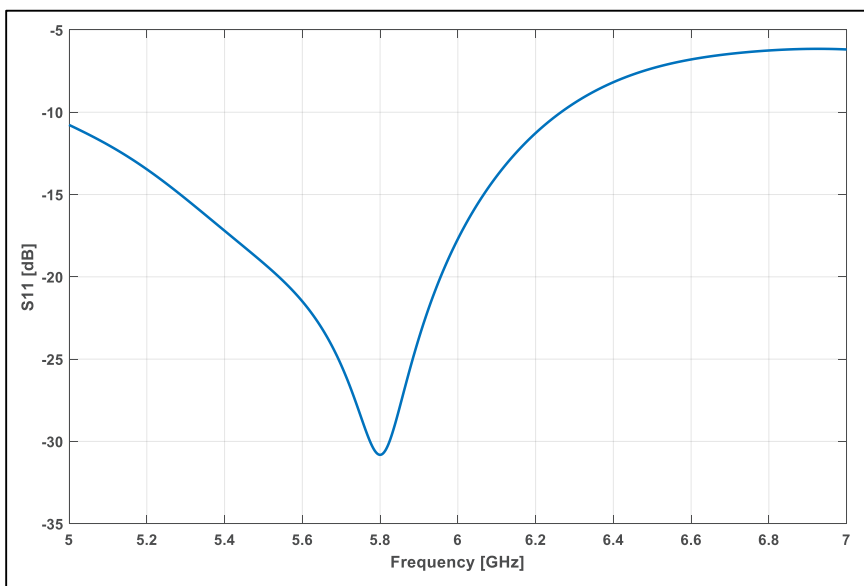


Figure 3. The S_{11} characteristic of the antenna obtained from electromagnetic simulations.

2.2. Manufacturing of the Designed Horn Antenna Using 3D Printing Technique

The pyramidal horn antenna, which was designed in the previous section and whose center frequency is fine-tuned with simulations, has been drawn in a way that can be printed in 3D. FreeCad software, a free program, was used for the 3D drawing process (FreeCad, 2021). The parametrically drawn antenna is shown in Figure 2b.

The 3D drawn antenna was printed on an Ultimaker 3D printer. The .stl file for the drawing was imported to the Ultimaker Cura software and the output was adjusted with 0.1mm layer thickness and 30% filling rate. Functionalized F-Electric® PLA filament, which has high conductivity, was used as the conductive filament. This filament can be used in applications that require high conductivity thanks to the included conductive carbon nanotube particles making it to have a volume resistivity of $0.75\Omega\cdot\text{cm}$ which corresponds to the volume conductivity of $1.33\text{S}/\text{cm}$ (Functionalize, 2021). In the 3D printed antenna geometry, the relevant holes were carefully drilled at the position of the radiation element and then the SMA type connector, on which the radiation element was soldered, was attached to the antenna. No solder or conductive material is applied between the SMA connector and the antenna body. Photographs of the manufactured antenna are shown in Figure 4. 48.94 cm³ conductive PLA filament was used for the production of this antenna. The resulting antenna, including the SMA connector, is 64.53 grams and provides a significant weight advantage over its metallic counterparts (ETS, 2021; NS-MI, 2021; Pasternack, 2021) that is around 500~700 grams.

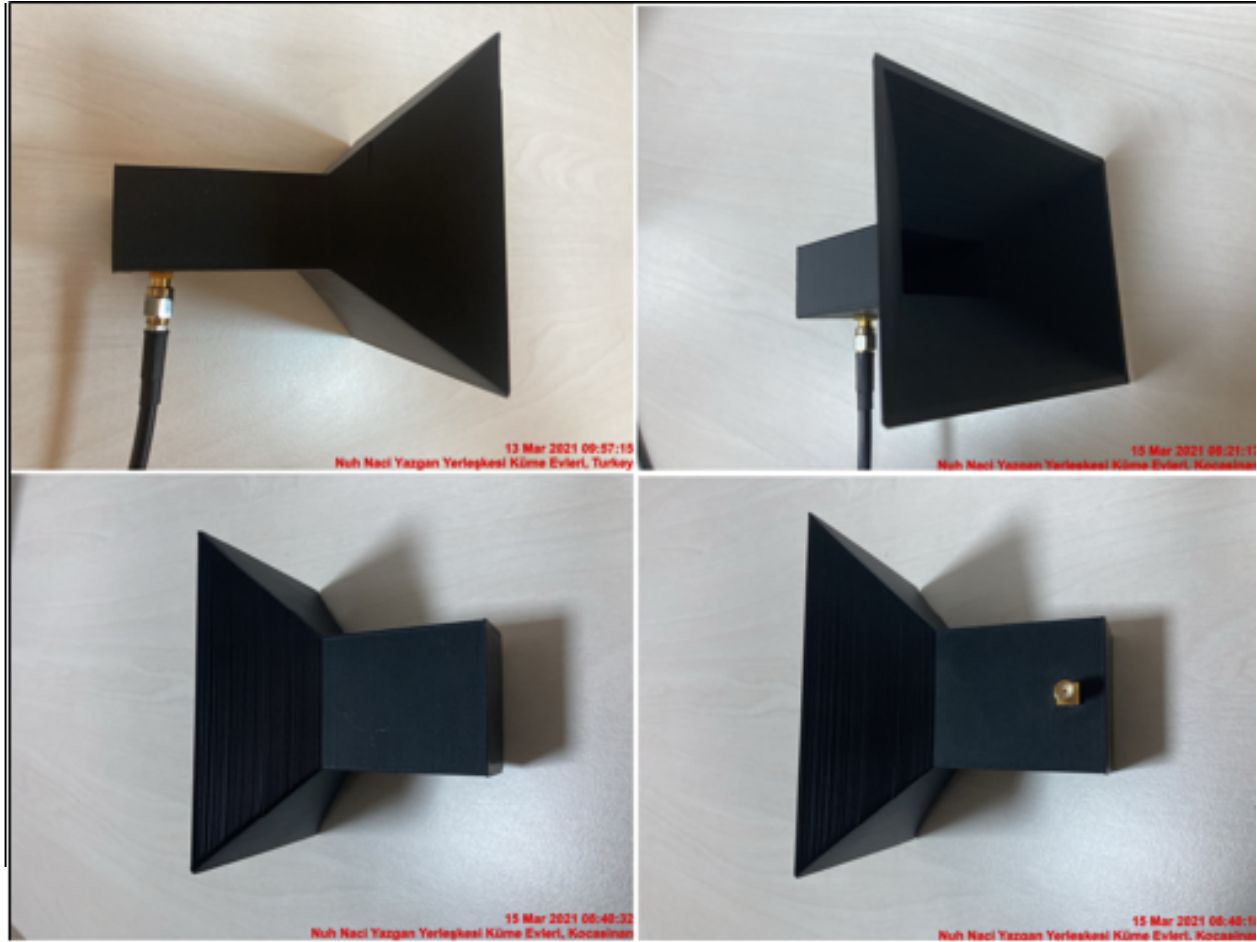


Figure 4. Images of the manufactured antenna.

3. Results and Discussion

A Rohde&Schwarz ZVH8 vector circuit analyser (VNA) was used to measure the manufactured pyramidal horn antenna. In order to increase the accuracy of the measurements, a 201-point calibration between 5-7GHz was performed with the ZV-Z135 SMA calibration kit before the measurements. The scattering parameters of the produced antenna were then measured as shown in Figure 5. During the measurements, the screenshot of the device was recorded as shown in Figure 6. In addition, the measurement data are saved and plotted in the MATLAB environment as shown in Figure 7.

According to the measurement results, the frequency range in which the antenna's reflection coefficient (S_{11}) is below the reference value of -10dB is between 5.22GHz and 6.55GHz, and the centre frequency value of the S_{11} is determined to be 5.79GHz at which the S_{11} has the lowest value of -40.52dB . From this point of view, it is seen that the measured centre frequency is very close to the targeted centre frequency of 5.8GHz. Moreover, it has been shown that the operating range of the produced antenna readily covers 5.725GHz-5.875GHz, which is the range of the ISM 5.8GHz band. Hence, the experimental results verify that the implemented antenna has the desired frequency characteristic without the need for any additional coating or conductive spray thanks to the utilization of the PLA filament containing conductive carbon nanotubes. Furthermore, the produced antenna including the SMA connector and the radiation element has the weight of only 64.53 grams, making it a feasible alternative for a variety of applications demanding lightweight antenna components.

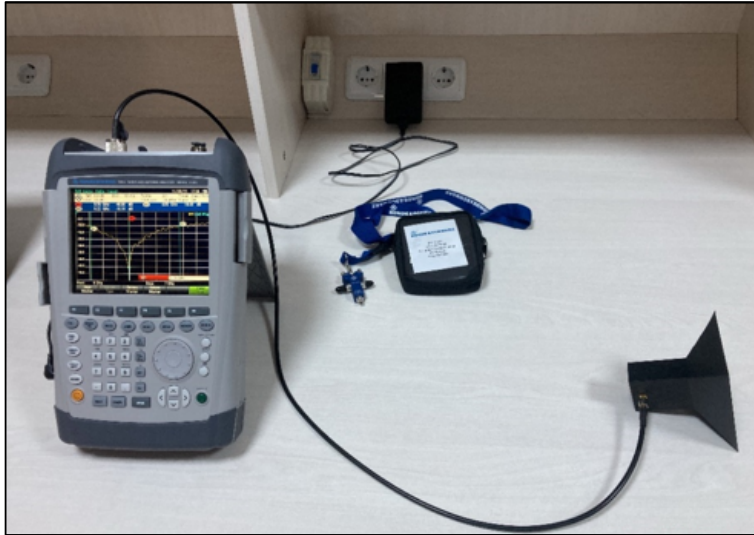


Figure 5. Experimental setup



Figure 6. The screenshot of the VNA screen during the measurement of the manufactured antenna

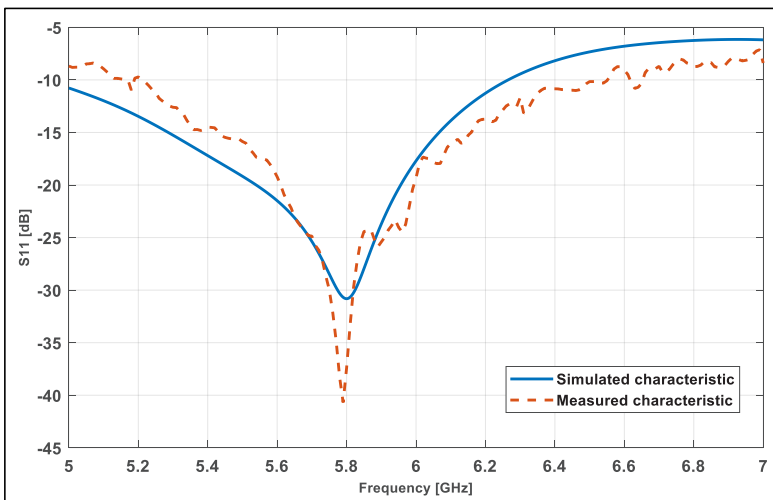


Figure 7. The measured and simulated S_{11} characteristics of the manufactured antenna

As the next step, the gain-frequency characteristic of the antenna is measured in anechoic chamber using the ZVH8 VNA. A Pasternack standard gain horn antenna is employed as the reference antenna which is placed at a distance of 1m from the 3D printed antenna. The obtained gain-frequency plot of the antenna is shown in Figure 8. As it can be seen from Figure 8, the measured antenna gain closely follows the simulated gain. The simulated antenna gain at the centre frequency of 5.8GHz has the value of 12.7025dB where the measured gain is 12.6341dB at the same frequency point.

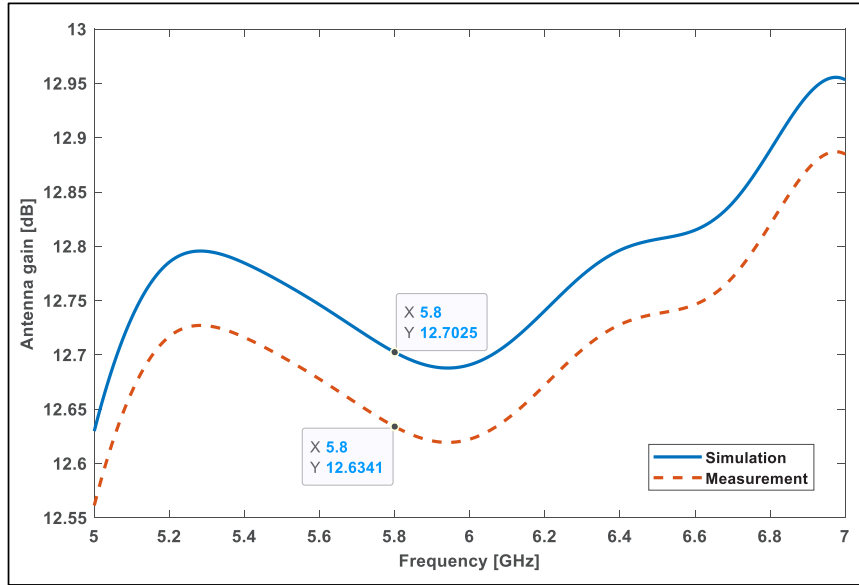


Figure 8. Gain-frequency characteristic of the manufactured antenna

The E-plane ($\phi=90^\circ$) farfield radiation pattern of the antenna is obtained in polar coordinates as given in Figure 9. From this figure, the antenna gain is confirmed as 12.7dB at 5.8GHz and the direction of the main lobe is in line with the +z axis. The 3dB beamwidth has the angle of 36.6° and the side lobe level has the value of -17.1dB.

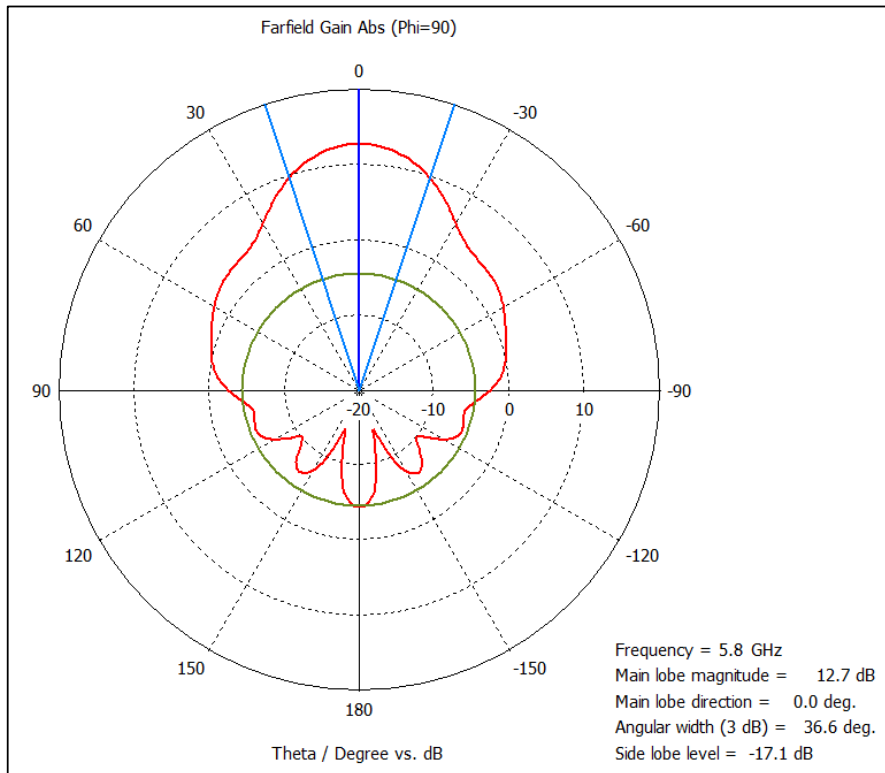


Figure 9. E-plane farfield radiation pattern of the antenna in polar coordinates

Finally, the normalized gain of the manufactured antenna is obtained and plotted as shown in [Figure 10](#) for the centre frequency of 5.8GHz. It is seen from [Figure 10](#) that the measured normalized gain of the antenna is close to the simulated case demonstrating the versatility of the filaments containing conductive carbon nanotube particles for use in 3D printing of antennas.

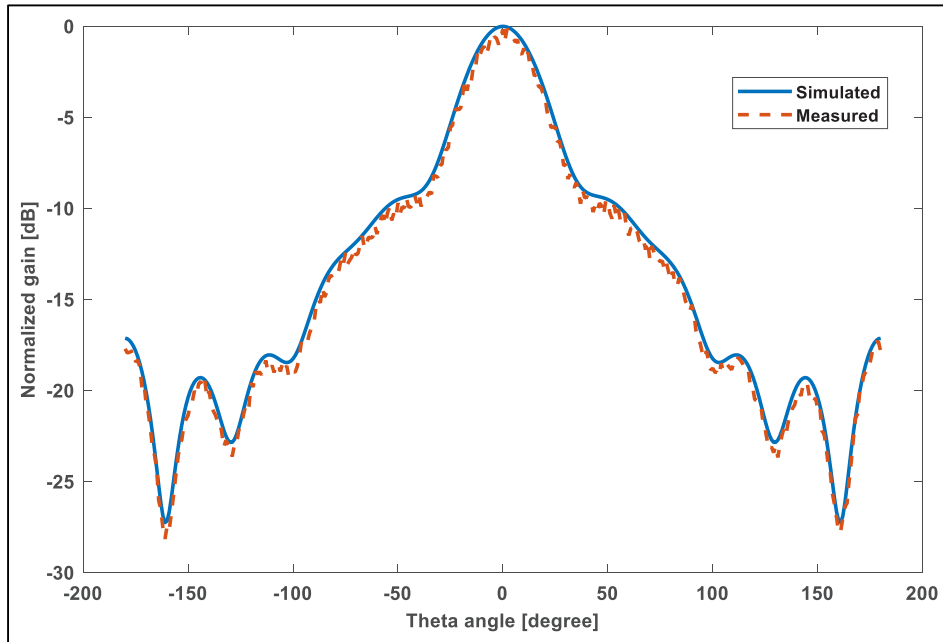


Figure 10. Normalized gain of the antenna at 5.8GHz centre frequency

4. Conclusion

In this study, a pyramidal horn antenna is designed and manufactured for the 5.8GHz ISM frequency band. First of all, the antenna dimensions were computed according to the required frequency band and then the size of the radiation element was optimized by simulating the antenna via an electromagnetic simulation software. As the next step, the proposed antenna was modelled on FreeCad, a 3D drawing program, according to the final geometric dimensions. The antenna geometry was manufactured on an Ultimaker 3D printer with a conductive PLA filament containing carbon nanotube particles. Then, the antenna production was completed by adding the SMA connector and the radiation element to the antenna. The calibrated Rohde & Schwarz ZVH8 VNA device was used for the measurement of the produced antenna. The measurement results show that the antenna operates in the 5.22GHz-6.55GHz range. The antenna provides a reflection coefficient lower than -20 dB in the 5.725GHz-5.875GHz frequency range, which is the targeted 5.8GHz ISM band. Moreover, the gain-frequency characteristic and the farfield radiation pattern of the manufactured antenna are obtained and presented. The simulated and measured antenna gains are 12.7025dB and 12.6341dB, respectively, at the centre frequency of 5.8GHz. The normalized antenna gain with respect to the theta angle is also given, which shows that the characteristic of the 3D printed antenna closely follows the simulated values demonstrating the versatility of the filaments containing conductive carbon nanotube particles for the manufacturing of 3D printed antennas. Therefore, it has been concluded that the designed and manufactured pyramidal horn antenna works as expected. As a result, it has been shown that conductive filaments containing carbon nanotube particles can be used in 3D antenna production and the antennas manufactured in this way possess a weight advantage thus their use in mobile defence and telecommunication systems can be advantageous.

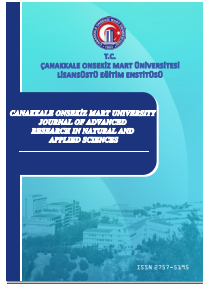
Conflicts of Interest

The authors declare no conflict of interest.

References

- Balanis, C.A. (2016). *Antenna theory: Analysis and design* (4th ed.). Wiley.
- Bor-Yaliniz, I., Szyszkowicz, S., & Yanikomeroglu, H. (2018). Environment-aware drone-base-station placements in modern metropolitans. *IEEE Wireless Communication Letters*, 7, 372–375. DOI: <https://doi.org/10.1109/LWC.2017.2778242>
- Chuma, E.L., Iano, Y., Roger, L.L.B., Scroccaro, M., Frazatto, F., & Manera, L.T. (2019). Performance analysis of X band horn antennas using additive manufacturing method coated with different techniques. *Journal of Microwaves, Optoelectronics and Electromagnetic Applications*, 18, 263–269. DOI: <https://doi.org/10.1590/2179-10742019v18i21337>
- Esfahani, M.R.N., Shuttleworth, M.P., Harris, R.A., Kay, R.W., Doychinov, V., Robertson, I.D., Marques-Hueso, J., Jones, T.D.A., Ryspayeva, A., & Desmullieux, M.P.Y. (2018). Hybrid additive manufacture of conformal antennas. *Proc. of IEEE MTT-S International Microwave Workshop Series on Advanced Materials and Processes for RF and THz Applications*, 1, 17–19. DOI: <https://doi.org/10.1109/IMWS-AMP.2018.8457128>
- ETS-Lindgren standard antenna datasheet. (2020). Retrieved from: www.ets-lindgren.com.
- FreeCad 3D parametric modeller. (2021). Retrieved from: www.freecadweb.org.
- Functionalize F-Electric PLA. (2021). Retrieved from: www.functionalize.com/about/functionalize-f-electric-highly-conductive-filament.
- Genç, A. (2019). Gain increase of horn antenna with waveguide feeding network by using 3D printing technology. *Bayburt Üniversitesi Fen Bilimleri Dergisi*, 2, 18–25. Retrieved from: <https://dergipark.org.tr/en/pub/bufbd/issue/46478/534593>
- Genç, A., Başıyigit, İ., Göksu, T., & Helhel, S. (2017). Investigation of the performances of X-Ku band 3D printing pyramidal horn antennas coated with the different metals. *Proc. of 10th International Conference on Electrical and Electronics Engineering (ELECO)*, 1, 1012–1016. Retrieved from: <https://ieeexplore.ieee.org/document/8266200>
- Gu, C., Gao, S., Fusco, V., Gibbons, G., Sanz-Izqueirido, B., Standaert, A., Raynaert, P., Bosch, W., Gadringer, M., Xu, R., & Yang, X. (2020). A D-band 3D printed antenna. *IEEE Transactions on Terahertz Science and Technology*, 10, 433–442. DOI: <https://doi.org/10.1109/TTHZ.2020.2986650>
- Hu, K., Duan, Y., Zhang, H., Liu, D., Yan, B., & Peng, F. (2018). Manufacturing and 3D printing of continuous carbon fiber prepreg filament. *Composites*, 53, 1887–1898. DOI: <https://doi.org/10.1007/s10853-017-1624-2>
- Hui, K-P., Philips, D., & Kekirigoda, A. (2017). Beyond line-of-sight range extension with OPAL using autonomous un-manned aerial vehicles. *Proc. of IEEE Military Communications Conference*, 1, 279–284. DOI: <https://doi.org/10.1109/MILCOM.2017.8170774>
- Kiesel, G., Bowden, P., Cook, K., Habib, M., Marsh, J., Reid, D., Phillips, C., & Baker, B. (2020). Practical 3D printing of antennas and RF electronics. *Aerospace and Defense Technology*, 1, 403–406. Retrieved from: <https://apps.dtic.mil/sti/pdfs/AD1041830.pdf>
- Kwon, O., Park, W.B., Lee, S., Lee, J.M., Park, Y.M., & Hwang, K.C. (2017). 3D-printed super-wideband spidron fractal cube antenna with laminated copper. *Applied Sciences*, 7, 979–988. DOI: <https://doi.org/10.3390/app7100979>
- Kyovtorov, V., Georgiev, I., Margenov, S., Stoychev, D., Oliveri, F., & Tarchi, D. (2017). New antenna design approach–3D polymer printing and metallization experimental test at 14–18 GHz. *AEU International Journal of Electronics and Communications*, 73, 119–128. DOI: <https://doi.org/10.1016/j.aeue.2016.12.017>
- Lee, S., Yang, Y., Lee, K-Y., Jung, K-Y., & Hwang, K.C. (2018). Robust design of 3D-printed 6–18 GHz double-ridged TEM horn antenna. *Applied Sciences*, 8, 1582–1592. DOI: <https://doi.org/10.3390/app8091582>

- Matthew, E., Pitzanti, G., Larraneta, E., & Lamprou, D. A. (2020). 3D printing of pharmaceuticals and drug delivery devices. *Pharmaceutics*, 12, 266–275. DOI: <https://dx.doi.org/10.3390/2Fpharmaceutics12030266>
- Mazar, H. (2014). International, regional and national regulation of SRDs. *Proc. of ITU Workshop on Short Range Devices and Ultra Wide Band*, 1, 27–32. Retrieved from: <https://www.itu.int/en/ITU-R/study-groups/workshops/RWP1B-SRD-UWB-14/Presentations/International,%20regional%20and%20national%20regulation%20of%20SRDs.pdf>
- Midtboen, V., Kjelgard, K. G., & Lande, T. S. (2017). 3D printed horn antenna with PCB microstrip feed for UWB radar applications. *Proc. of IEEE MTT-S International Microwave Workshop Series on Advanced Materials and Processes for RF and THz Applications (IMWS-AMP)*, 1, 146–151. DOI: <https://doi.org/10.1109/IMWS-AMP.2017.8247374>
- Mishra, A., & Li, C. (2019). A Low Power 5.8-GHz ISM-band intermodulation radar system for target motion discrimination. *IEEE Sensors Journal*, 19, 9206–9214. DOI: <https://doi.org/10.1109/JSEN.2019.2926189>
- NS-MI standard gain horns. (2021). Retrieved from: www.ns-mi.com.
- Pasternack standard gain horn antennas. (2021). Retrieved from: www.pasternack.com/antennas-category.aspx.
- Phillips, B. T., Alder, J., Bloan, G., Nagle, R. S., Redington, A., Hellebrekers, T., Borden, J., Pawlenko, N., & Licht, S. (2020). Additive manufacturing aboard a moving vessel at sea using passively stabilized stereolithography (SLA) 3D printing. *Additive Manufacturing*, 31, 100969. DOI: <https://doi.org/10.1016/j.addma.2019.100969>
- Shahrubudin, N., Lee, T., & Ramlan, R. (2019). An overview on 3D printing technology: technological, materials and applications. *Procedia Manufacturing*, 35, 1286–296. DOI: <https://doi.org/10.1016/j.promfg.2019.06.089>
- So, K., Luk, K., Chan, C. H., & Chan, K. F. (2018). 3D printed high gain complementary dipole/slot antenna array. *Applied Sciences*, 8, 1410–1417. DOI: <https://doi.org/10.3390/app8081410>
- Tak, J., Kang, D-G., & Choi, J. (2017). A lightweight waveguide horn antenna made via 3d printing and conductive spray coating. *Microwave and Optical Technology Letters*, 59, 727–729. DOI: <https://doi.org/10.1002/mop.30374>
- Wang, K., Ho, C., Zhang, C., & Wang, B. (2017). A review on the 3D printing of functional structures for medical phantoms and regenerated tissue and organ applications. *Engineering*, 3, 653–662. DOI: <https://doi.org/10.1016/J.ENG.2017.05.013>
- Yao, H., Sharma, S., Henderson, R., Ashrafi, S., & MacFarlane, D. (2017). Ka band 3D printed horn antennas. *Proc of Texas Symposium on Wireless and Microwave Circuits and Systems*, 1, 21–24. DOI: <https://doi.org/10.1109/WMCaS.2017.8070701>
- Zhang, B., Chen, W., Wu, Y., Ding, K., & Li, R. (2017). Review of 3D printed millimeter-wave and terahertz passive devices. *International Journal of Antennas and Propagation*, 1, 1297931. DOI: <https://doi.org/10.1155/2017/1297931>
- Zhang, B., Guo, Y-X., Sun, H., & Wu, Y. (2018). Metallic, 3D-printed, K-band-stepped, double-ridged square horn antennas. *Applied Sciences*, 8: 33–40. DOI: <https://doi.org/10.3390/app8010033>



A Sound-Based Monitoring and Evaluation System for Small-Scale Dairy Operations

Ünal Kızıllı^{1,*}, Sefa Aksu¹, Ahmet Cumhur Kınacı², Ertuğrul Bilgücü³, Songül Şentürklü⁴

¹Department of Agricultural Structures and Irrigation, Faculty of Agriculture, Çanakkale Onsekiz Mart University, Çanakkale, Türkiye

²Department of Computer Engineering,, Faculty of Engineering, Çanakkale Onsekiz Mart University, Çanakkale, Türkiye

³Department of Food Processing, Biga Vocational School, Çanakkale Onsekiz Mart University, Biga, Çanakkale, Türkiye

⁴Department of Crop and Livestock Production, Biga Vocational School, Çanakkale Onsekiz Mart University, Biga, Çanakkale, Türkiye

Article History

Received: 06.03.2022

Accepted: 26.05.2022

Published: 25.09.2022

Research Article

Abstract – Continuous monitoring of livestock operations is vitally important for a sustainable production system. Monitoring systems based on cameras are not sufficient in livestock barns since they require visual inspection and ignore vocal conditions within the barn. These systems are also quite expensive for most small family operations. A prototype device that costed \$ 470 developed to remotely monitor the barn based on sound sensors (microphones) data. This device also warns the operator by sending an SMS at sound intensities exceeding the predetermined durations and threshold values. It also makes it possible to listen to the barn by phone if needed. The device and associated web database was tested in this study. The main challenge was the determination of threshold values at which sensors are to generate warning SMS messages. As a method, Z-score of 2.33 which corresponds to area left of the 99% of the normally distributed data curve was determined representing the highest values with a possibility of 1% observation for each sensor. An average value of 97 dB was determined to be a threshold suggestion for future studies. A customizable web-based MySQL database was created to monitor and evaluate the long term data collected via the system.

Keywords – Arduino, dairy housing, sound sensor, noise monitoring.

1. Introduction

Modern herd management practices and technologies cause animals to become more sensitive to environmental stimuli and stress (Demirören and Taşkın, 2004). It may not be adequate to explain or reveal stress and animal welfare with discrete methods. For example, it is not enough to state that the animal is 'in harmony' with the surrounding conditions (Lorz, 1973; Hughes, 1976). Nor are these explanations useful in the scientific view of livestock wellbeing. Other measures related to the livestock's responses to control the relevant environmental conditions that cause stress and are more descriptive (Wiepkema, 1982; Broom, 1986). These terms measure the welfare of the animal and the effort of the animal to cope with the environmental factors that cause stress with perceptible parameters (Broom, 1996; Duncan, 1996).

In this context, there has been many research conducted to explain the stress-induced behaviors among livestock under the influence of environmental stimuli. If these behaviors are not detected correctly and in a timely manner, overall animal performance may be affected. In recent years, there are many studies on the use of information technologies to minimize these effects (Chung et al., 2013a; Chung et al., 2013b; Lee et al., 2014; Lee et al., 2015; Mendes et al., 2015; Ahmed, Mun, Islam, Yoe & Yang., 2016). Observing animal behavior by placing a camera in the barn for visual evaluation of livestock welfare is one of the simplest

¹ unal@comu.edu.tr

² aksusefa@comu.edu.tr

³ cumhur.kinaci@comu.edu.tr

⁴ ebilgucu@comu.edu.tr

⁵ ssenturklu@comu.edu.tr

*Corresponding Author

and first imaginable methods. Moreover, it is possible to obtain different information by analyzing animal behavior in computer using different algorithms ([Rushen, Chapinal & Passillé, 2012](#)).

One of the environmental factors that cause stress in animals is noise. Mammals show startle, freeze or move away from the sound source response above 90 decibel (dB). Animals are more comfortable at intensities below this value. It is also reported that reactive behaviors to sound vary according to sound type and content, and that mammals can adapt to sound with some minimal differences ([Anthony, Ackerman & Lloyd, 1959](#); [Bond, Winchester, Campbell & Webb, 1963](#); [Ames and Arehart, 1972](#); [Espmark, Falt & Falt, 1974](#); [Ames, 1978](#)). The acceptable noise level in the barns is reported as 85 dB in the regulations. However, it is reported that the measured intensity can reach up to 106.8 dB due to the different works done inside the barn with a background noise level of 72 dB. Hence, acceptable sound intensity in the barn may vary between 72 and 85 dB ([Anonymous, 2006](#)).

Animals not only develop stress due to environmental sound, but also make sound as an indicator of stress. Vocalization of cattle is an indicator of stress. The cattle sound has a frequency range of 50-1,250 Hz ([Kiley, 1972](#); [Watts and Stookey, 2000](#)). Newly weaned calves have been noted to make sounds at frequencies as low as 31 Hz ([Watts and Stookey, 2000](#)). Average sound levels from cattle may vary between 80 and 90 dB ([Weeks et al., 2009](#)). In fact, cattle can detect sounds as low as 25-35 kHz ([Heffner and Heffner, 1992](#)). Therefore, knowing these threshold values reveals the potential of using today's technologies to determine stress based on animals' sound.

Sound levels of dairy cattle barns must be monitored, as it is a sign of conditions related to loss of life beyond the loss of productivity and welfare. Operations are usually monitored by security cameras. However, it is not possible to continuously monitor the security camera images. Therefore, they can't be aware of the conditions that may occur in the barn and to take the necessary precautions when the operator is out of the operation. Approximately 99% of dairy farms in Turkey are small family businesses with 50 heads or less. It is very expensive for these small businesses to have the technology to continuously monitor and evaluate noise in the barn. Producers are looking for low-cost solutions that can warn them based on the sound level inside the barn rises above normal levels and allow them to listen inside the barn. In this sense, the most important problem is the lack of technology to intervene in a timely manner in cases where animals get sick, injured or even when there are security problems in the barn.

In this study it was aimed to develop an easy-to-use; low-cost barn noise tracking system that can work with the most widely used smart mobile phones. The features of the system were to monitor the environmental conditions related to the sound in the barn via a mobile phone, to intervene in a timely manner when needed, to listen to the barn from outside the operation, and to collect sound-related data for further analysis. The proposed technology also provided a database to evaluate the overall noise level that cause environmental stress on both animals and workers.

2. Materials and Methods

2.1. Experimental Setup

The prototype device was developed in the Digital Agricultural Laboratory in Çanakkale Onsekiz Mart University, Faculty of Agriculture, Department of Agricultural Structures and Irrigation. The device was fixed in a double row free stall dairy barn housing 80 Simmental cattle located in Çanakkale Province, Biga District, Çınarköprü Village, Turkey. Average milk yield in the enterprise was 20 lt.day⁻¹. Seven microphone sensors were placed in the 30 m long and 15 m wide barn. The main station (prototype device) was fixed to the middle bar of the roof truss at the center of the barn on the service road. Microphones installation plan and cross-sectional view of the barn showing the microphones and main station is given in [Figure 1](#). The microphone fixed to the main station is denoted as Mic-0 and the remainders are numbered through Mic-1 to Mic-6. It was observed that the replacement height (2.5 m from the ground) of the microphones had ignorable effects on the recorded data.

The main station device recorded microphone data in the database at specified intervals. In addition, the automatic answering system which was used to listen to any microphones was also in the main station.

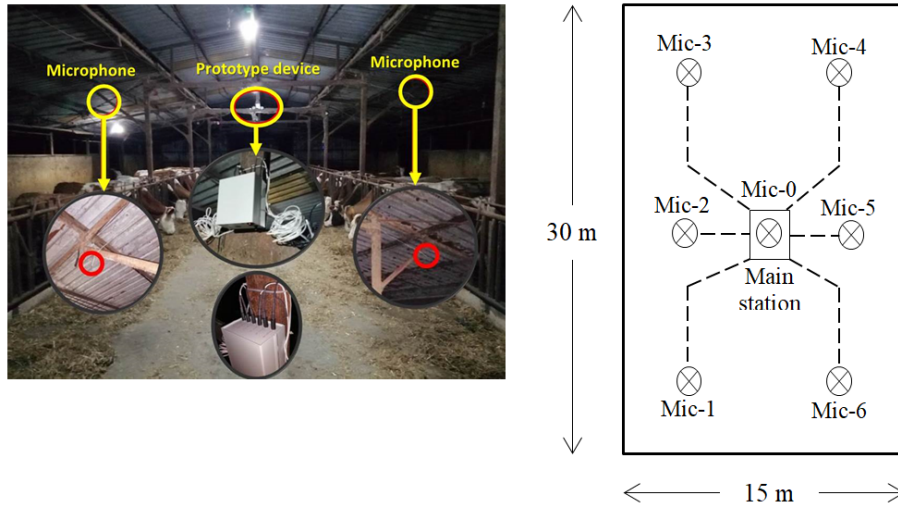


Figure 1. Microphone installation plan

2.2. Development of the Prototype Device

The system consists of a main station (prototype device), software, and a web-based database. It is essential that these three components communicate with each other continuously in order to allow real-time sound monitoring, collecting the sound data and generating instant alerts based on the alarm set points. The schematic representation of the prototype is given in [Figure 2](#).

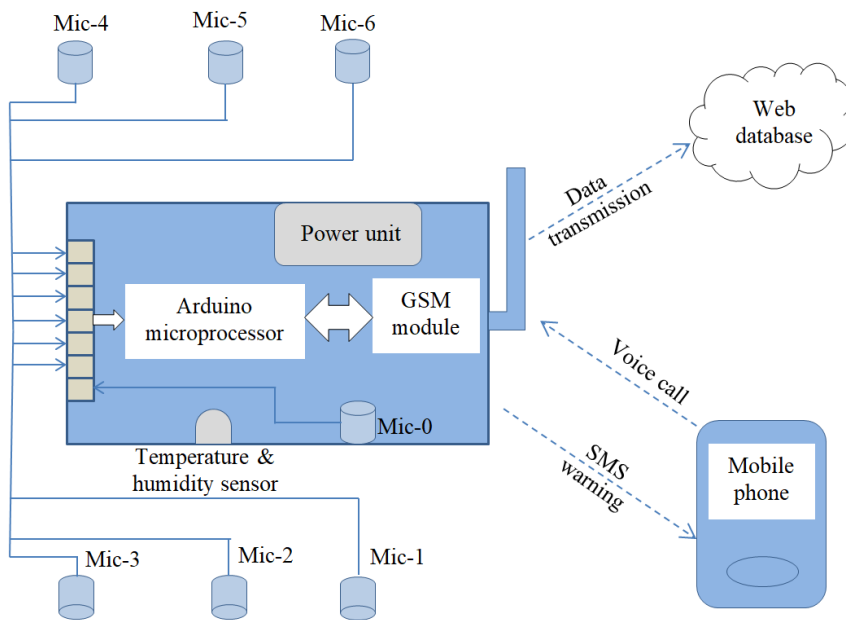


Figure 2. Schematic representation of prototype

An Arduino microcontroller was used to integrate all sensors and related electronics. Six sensors (Mic-1 to Mic-6) transmitting the sound data to the main station via cables and the central sensor (Mic-0) were soldered to the relevant analog inputs. It was also expected to listen to the real-time sound in the barn when needed. The microphone located near the loudest sound source should be selected automatically. Since there were 7 microphones connected to a single output, it was inevitable for the sounds at different points to overlap. To prevent such situation, a digital channel selector (multiplexer) was used to listen to the

microphone closest to the sound source. This module has 4 selective channels depending on the sound data obtained from the analog inputs. Based on the combinations of on-off information sent to these channels, the relevant microphone was listened.

Microphone module (ON Semiconductors, Phoenix, Arizona, USA) integrated on the Arduino microcontroller is a low-cost technology consisting of an amplifier circuit card with three different outputs including analog audio output, sound detection and level outputs. In this way, the sound can be output directly, the presence of any sound in the environment can be detected and the level of the sound can be measured. Each output works independently of each other and can all be used at the same time. In this way, sound levels at different points could be recorded and the microphone that detects the highest intensity could be selected for listening. The components on the microprocessor have different energy demands in the stationary and active phases. It is vitally important to maintain consistent power to the system at all times. Using an external power supply module that only meets the energy needs of the sensors has eliminated the potential power problem.

The prototype system can also record the temperature and relative humidity at desired time intervals. The aim here was to observe temperature/humidity, which is another important stress factor, along with the stress that noise can cause. A SHT11 sensor that can measure both temperature and relative humidity ([Sensirion AG, Staefa ZH, Switzerland](#)) was used in the prototype. This sensor measures the air temperature and relative humidity with high accuracy and sends them to the microprocessor unit. Although temperature and humidity data were recorded, they were not evaluated in this study.

Arduino GSM Shield-Simcom/Sim800C unit was used in order to send the data received from the sound and temperature/humidity sensors to the server via the mobile network. Due to its ability to operate in four different bands and its internal antenna, data transmission can be prevented from being interrupted in areas where the network signal is weak. Unlike other components, the GSM module needs a consistent power supply. If it cannot get enough power, it stops the communication in order to protect the system. An uninterruptible power supply was built into the prototype device to prevent power surges and short-term interruptions inside the barn from blocking the system. This unit consists of 6 lithium batteries and a battery recharge module. This power supply not only protects the device from fluctuations caused by the city current, but makes it possible to operate during interruptions that may occur up to 4 hours.

2.3. Sensor Calibration

The microphones produce digital output of 8-bit integers varying between 0 and 1024. Therefore, the microphone data should be calibrated to obtain sound levels in decibel (dB). In order to develop a calibration setup, a unit that will produce constant sound and another unit where sound data can be monitored were designed. The sound generator to be used in the experimental setup must provide sound with a constant frequency and intensity. For this reason, active piezo speaker was preferred. The piezo speaker works with the logic that the two-layer plate inside is deformed under electrical load and then returns to its original form. Depending on the applied electrical load, the intensity of the sound produced remains constant. In addition, its active operation ensures that the sound frequency is equal to that of the electric charge.

The electric charge passing over the piezo speaker must be controlled in terms of frequency and intensity. These parts, called drivers in sound generators, require a microcontroller. Considering the power demand of the unit an Arduino Nano ([Arduino LLC., Italy](#)) control card working with ATmega328P microcontroller was used. The operation of the digital output terminal at 1 ms intervals was specified. In this way, it was ensured that the piezo speaker remains constant at a frequency of 1000 Hz. Another component required in the design of the unit is an interface where sensor data can be monitored simultaneously. In order to ensure the flexibility of the experimental setup and the continuity of the data flow, it was needed to be directed to a mobile device wirelessly. For this purpose, HC-05 Bluetooth Module ([ITEAD Intelligent Systems Co. Ltd., China](#)) was used. Since this module uses the serial communication channels of the microprocessor control card, it does not cause any interference in the sensor data. Schematic representation of the calibration unit is shown in [Figure 3](#).

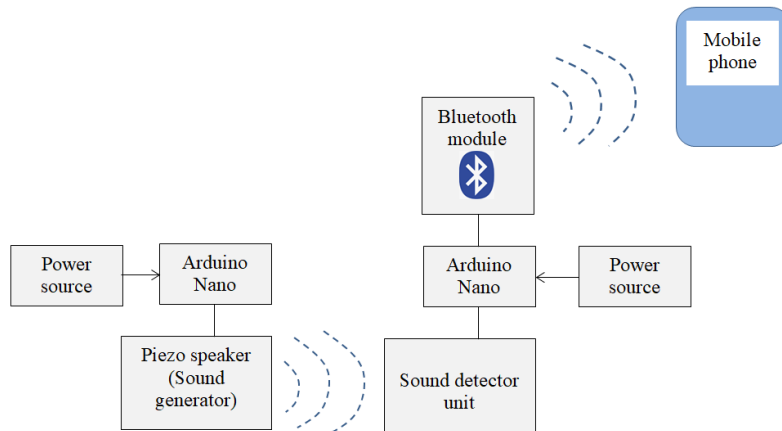


Figure 3. Assembly diagram of the calibration unit

2.4. Software and Database Development

The open source platform (Arduino IDE) provided by the microcontroller card was used to develop the software. Arduino IDE employs C/C++ programming language. Each microphone continuously transfers the sound data to the Arduino mainboard. In addition, they transmit the ambient sound to the audio input jack of the GSM unit. The sensor directed to the audio input jack of the GSM unit was also determined by the multiplexer module. On the other hand, the correct sensor command was given to the channel selector module via the Arduino. In this case, time should be allowed to channel selector to operate by monitoring the level data from the microphone modules in 3-second cycles. In each cycle, the selector combination required for the sensor module with the highest loudness was transmitted to the channel selector module. Apart from the resting cycle of the sensors, the frequency of the data to be transmitted to the database was another cycle in the software. The shortest interval allowed for login in the web database was 1 minute. Hence, data is recorded in 1-minute intervals.

Another expected capability from the prototype was to create a warning SMS in case the threshold values are exceeded, which is provided by another cycle specified in the software. Accordingly, 5 minutes of sound level above the threshold values should create a warning SMS. When the GSM module is called to listen to the voice in the barn after the warning SMS is received, the call should be answered automatically. The command to provide automatic response must be active continuously between sending data and sending SMS. Therefore, this command is associated with the starting point of the first loop of 3 seconds. Thus, when the barn is monitored, it was automatically directed to the microphone with the loudest sound, and as long as the call continues, all microphones were tested every 3 seconds and if the sound source was in motion, the relevant microphone was activated.

It was aimed that the sensor data obtained from the barn is collected in the web database. There are different options for creating and running an online database. However, in the selection of database management system, bandwidth demands of the collected data and easiness of the transmitting the data in a uniform variable format was considered. Hence, PHP that creates customizable databases associated with MySQL, which is the most preferred open source management system for the creation of web interfaces was selected. The PHP can work with all internet-enabled devices. In this respect, a customized table has been created in the PHP database, which allows the data to be followed from almost any device. The data transferred over the GSM unit were analyzed in a table format and placed in the relevant columns together with the timestamp for further data processing. The flowchart of the software is given in [Figure 4](#).

3. Results and Discussion

3.1. Calibration Results

The units prepared for the calibration experiment were fixed to the upper edges of the 65 cm high stands. The stands were aligned so that the direction of the generator was right between the sound sensor and the

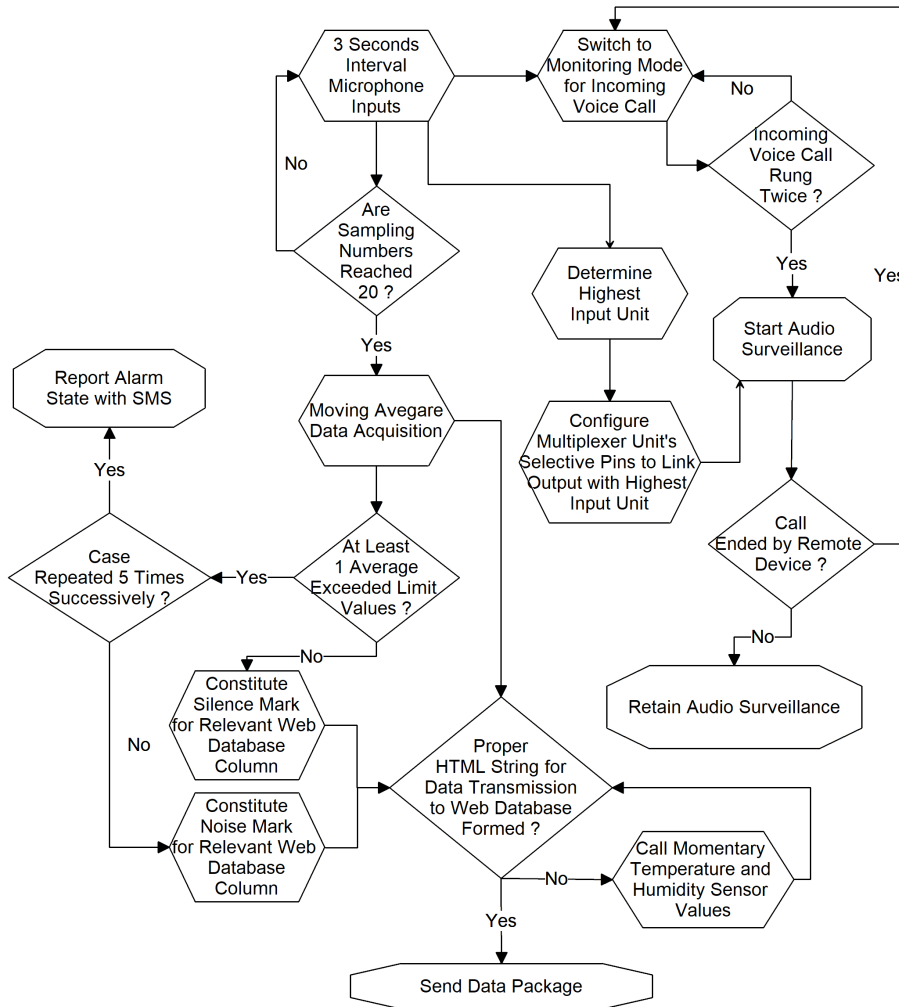


Figure 4. Flowchart of the software

UT-353 decibelmeter (Uni-Trend Technology Co.Ltd., China). In this way, it was ensured that the sound intensity can be perceived equally by both devices.

A standard 5V power supply was connected with a USB cable to provide the energy needed by the sensor unit and the sound generator during the experiment. Then, a mobile phone was connected via Bluetooth and placed on the stand where the decibelmeter was located (Figure 5).

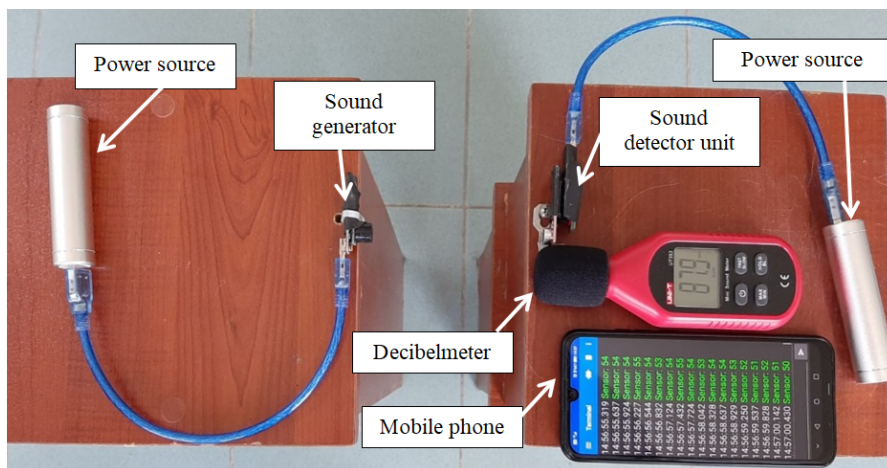


Figure 5. Calibration experiment

During the experiment, generator unit was removed from the measuring unit to create decreasing amplitudes. The sound generator unit produced 20 measurements per second. The moving average method was used to calculate average sound intensity for each second. In this way, the effect of instantaneous fluctuations that may cause deviations in sound intensity data was eliminated. Each 1 dB change in the decibel meter and corresponding 8-bit integer values were monitored and recorded to create a calibration equation. Using the logarithmic calibration equation each sensor readings were converted to dB units for further processing (Figure 6).

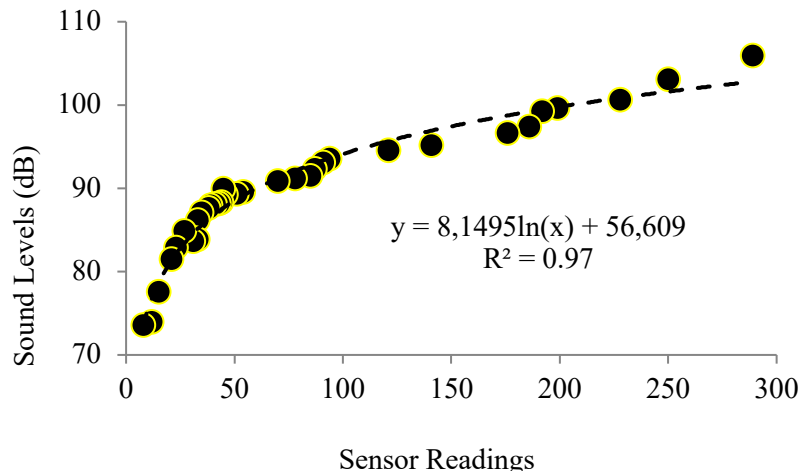


Figure 6. Calibration equation

3.2. Statistical Analysis

The main purpose of the developed prototype was to monitor the unusual changes in ambient sound level regarding animal and barn safety and send a warning SMS to the producer. The most important challenge faced with the developed method was the determination of threshold values for warning SMSs. No such threshold value has been found in the literature. As an approach, using the highest recorded value in the barn could be considered. *Anonymous (2006)* stated that the noise level in a dairy barn can reach up to 106 dB. Therefore, when the system was installed in the barn, 106 dB was used as the threshold until sufficient data was obtained. It was observed that in the first 4 months of the study 106 dB was exceeded only by Mic-5 and Mic-6, 1 and 25 times, respectively.

The 4-month-data were used to calculate the maximum, minimum and mean values for each sensor. The aim here was to determine whether the mean or maximum values could be used as threshold. The statistical parameters and the number of times they were exceeded calculated in MS Excel (*Table 1*).

Table 1

Statistical parameters for the first 4 month of study

Parameter	Mic-0	Mic-1	Mic-2	Mic-3	Mic-4	Mic-5	Mic-6
Average:	86.0	93.6	90.2	93.0	93.8	91.0	94.0
Maximum:	96.8	103.6	105.4	105.9	102.2	106.0	107.3
Minimum:	79.2	79.2	79.2	78.1	79.7	79.2	79.2
Times average value exceeded:	47,313	44,165	51,486	51,896	48,666	48,241	48,566
Times maximum value exceeded:	0	0	1	0	1	1	6

As can be seen from *Table 1*, if the sensor average values are accepted as the threshold, more SMS will be sent than necessary. On the other hand using the maximum values may cause almost no warnings. It is very difficult to determine a realistic threshold value. Considering the past experiences of the owner, unusual conditions

such as sick animals or the entry of other animals such as dogs or wild birds into the barn are observed about a few times a month. It was aimed to determine the noise level that continues for 5 minutes and above, which will cause an average of 2-3 SMS to be sent per month based on the producers demand and experiences.

For this purpose, Z-score test was applied. For each sensor, it was determined by trial and error method that the highest decibel value, which is likely to be seen with a probability of 1% was selected as threshold. Normality test (confidence level 95%) applied to the sensor values for testing the suitability of Z-score test in MS Excel ([Table 2](#)). Considering the values listed in [Table 2](#), all sensor values were normally distributed.

Table 2

Normality test results

Parameter	Mic-0	Mic-1	Mic-2	Mic-3	Mic-4	Mic-5	Mic-6
Mean	86.0	93.6	90.2	93.0	93.8	91.0	94.0
Standard Error	0.0037	0.0087	0.0069	0.0085	0.0086	0.0066	0.0094
Median	85.8	93.6	90.1	93.0	93.9	91.0	93.9
Mode	85.6	93.3	88.3	91.6	93.6	89.7	93.3
Standard Deviation	1.1596	2.7512	2.1886	2.7121	2.7226	2.0829	2.9800
Sample Variance	1.3447	7.5690	4.7903	7.3554	7.4128	4.3383	8.8774
Kurtosis	6.1307	0.7127	1.0434	0.4918	1.1364	0.7973	1.6521
Skewness	1.3299	-0.5455	0.1524	-0.4241	-0.71624	-0.0020	-0.6275
Range	17.6	24.4	26.2	27.8	22.5	26.8	28.1
Minimum	79.2	79.2	79.2	78.1	79.7	79.2	79.2
Maximum	96.8	103.6	105.4	105.9	102.2	106.0	107.3
Confidence Level (95.0%)	0.0072	0.0170	0.0135	0.0167	0.0168	0.0129	0.0184

With Z-score which corresponds to area left of the 99% of the normal distribution curve of 2.33 was determined representing the highest values with a possibility of 1% observation for each sensor. Then the following equation was applied to determine actual sensor values corresponding to this Z-score ([3.1](#)) ([Blaisdell, 1998](#)).

$$Y = Z_{value} \times \sigma + \mu \quad (3.1)$$

where, Y is the sensor value observed with a possibility of 1% of all population, σ is standard deviation, μ is mean sensor value. Based on the Z-score test threshold values were determined for each sensor. The system generated SMS messages when the threshold values exceeded for 5 minutes. The threshold values and the number of SMSs that producer received during the second 4-month-period study are listed in [Table 3](#).

Table 3

Threshold values

	Mic-0	Mic-1	Mic-2	Mic-3	Mic-4	Mic-5	Mic-6
Threshold value (dB)	89	100	95	99	100	96	101
No of SMSs sent	21	13	15	25	11	12	9

As explained above, the multiplexer used in the system does not allow the sensors to send SMS simultaneously. Therefore, the values in [Table 3](#) were obtained with the largest sensor values recorded for 5 minutes. This means more than one sensor may reach the threshold values but only the highest was allowed to generate SMS. Based on the data the prototype caused total of 106 SMS during the 4-month period.

3.3. System Performance

The producer reported that the warning SMS was sent generally during the feeding and milking times when the animals were active. This is an expected result due to the use of machinery and staff mobility in the barn. During the study no SMS received at night when there were almost no activities. Although there was a power outage at least once a week, continuous data could be obtained from the system, which can work with both AC and DC power supplies. Minute-based data is collected for 8 months, yet the database limits were not exceeded. Collected daily data volume was around 76 bytes which is an acceptable capacity. In addition, the data in the database can be downloaded in MS Excel format, allowing it to be used directly for data analysis for various purposes. Accordingly, the existing database can be recorded for more than 10 years without any limit problem. When the minimum and maximum sound intensity values created by the sensors were compared, there was a $\pm 8\%$ difference, including the module inside the device whose microphone was not removed. This difference decreases to 2% between the sensors on the right and left of the service road and which were symmetrical to each other. In this case, it can be concluded that the length of the cable used for the microphones has some ignorable effect on the generated sound intensity data. The fact that each sensor was handled separately while determining the threshold value for the sensors prevented possible errors.

The most important factor determining the performance of the system was the threshold value to be used. As a method in this study, the values corresponding to 1% or less of the recorded values were accepted as the threshold. However, it should not be forgotten that different times and lower sound levels may also indicate unfavorable conditions in the barn. In such cases, if the owner or employees are in the business, the device can be completely deactivated and unnecessary SMSs can be prevented. In addition, both shorter alerts (less than 5 minutes) and lower threshold values can be easily defined in the system when the owner is outside and has to check the barn more often. Hence the developed system provides a flexibility to monitor the barn under various situations. The overall cost of the system should also be considered in the performance evaluations. All the electronics and associated materials that were needed to assemble the system can be easily obtained from the electronics market at low costs. The prototype costed \$ 470 including the 1 year webhosting service fee for database.

4. Conclusion

One of the most important problems encountered in small livestock operations is the remote monitoring of the barn, especially regarding safety and animal health. Visual monitoring based on cameras is not possible when the producer is out of operation. It is also an expensive solution for small scale operations. Based on the principle that animals make sounds at different frequencies and durations when under stress, a low-cost sound-based monitoring system was developed. The device was assembled in the laboratory and sound data was collected in a small-scale dairy barn for 8 months. It was aimed to send SMS warnings in case of emergencies when the pre-set threshold values are exceeded and listen to the barn if needed. The main challenge was the determination of threshold values for each microphone sensors that causes SMS warnings. It can be suggested to adjust threshold values depending on the presence of operator within the operation. Accordingly, the SMS warnings should be suspended for the time intervals in the daily routine of feeding, manure cleaning and milking processes. This may be a solution to unnecessary SMS warnings or missed situations. The prototype device not only provides a tool to monitor noise conditions it is also a useful tool to evaluate the overall noise levels within and outside the barn. The results show that this particular operation maintains the limits of noise exposure for both animals and labors.

Acknowledgement

This work was supported by the Çanakkale Onsekiz Mart University, Scientific Research Projects Coordination Unit (BAP) [Grant number FBA-2019-3080].

Author Contributions

Ünal Kızıl: Planned the study, established the design criteria.

Sefa Aksu: Designed the electronics/sensors, applied the system to the dairy barn.

Ahmet Cumhuri Kınacı: Designed the database.

Ertuğrul Bilgücü: Helped finding experimental barn and collecting data.

Songül Şentürklü: Helped design, conducted literature review, and collect data.

Conflicts of Interest

The authors declare no conflict of interest.

References

- Ahmed, S.T., Mun, H.S., Islam, M.M., Yoe, H., & Yang, C.J. (2006). Monitoring activity for recognition of illness in experimentally infected weaned piglets using received signal strength indication ZigBee-based wireless acceleration sensor. *Asian Australian Journal of Animal Science*, 29, 149–156. DOI: <https://doi.org/10.5713/ajas.15.0221>
- Ames, D.R. (1978). *Physiological responses to auditory stimuli*. In J.L. Fletcher and R.G. Busnel, eds. *Effects of noise on wildlife*. Academic Press, New York.
- Ames, D.R., & Arehart, L.A. (1972). Physiological response of lambs to auditory stimuli. *Journal of Animal Science*, 34, 994 – 998. DOI: <https://doi.org/10.2527/jas1972.346994x>
- Anonymous (2006). *The Act No. 148/2006 Coll.*, On Health Protection from the Adverse Effects of Noise and Vibration. Retrieved from: <https://www.ilo.org/dyn/natlex/docs/ELECTRONIC/91003/105285/F-1423016467/91003.pdf>
- Anthony, A., Ackerman, E., & Lloyd, J.A. (1959). Noise stress in laboratory rodents. I. Behavioral and endocrine responses of mice, rats, and guinea pigs. *Journal of Acoustical Society of America*, 31, 1430–1437. DOI: <https://doi.org/10.1121/1.1907645>
- Blaisdell, E.A. (1998). *Statistics in Practice 2nd Edition*. Saunders College Publishing, Fort Worth.
- Bond, J., Winchester, C.F., Campbell, L.E., & Webb J.C. (1963). *Effects of loud sounds on the physiology and behavior of swine*. U.S. Department of Agriculture, Agricultural Research Service Technical Bulletin No. 1280. Retrieved from: <https://naldc.nal.usda.gov/download/CAT87201269/pdf>
- Broom, D.M. (1986). Indicators of poor welfare. *British Veterinary Journal*, 142, 524 – 526. DOI: [https://doi.org/10.1016/0007-1935\(86\)90109-0](https://doi.org/10.1016/0007-1935(86)90109-0)
- Broom, D.M. (1996). Animal welfare defined in terms of attempts to cope with the environment. *Acta Agriculturae Scandinavica Section A, Animal Supplement*, 27, 22 – 28. Retrieved from: <https://www.neuroscience.cam.ac.uk/publications/download.php?id=31975>
- Chung, Y., Oh, S., Lee, J., Park, D., Chang, H., & Kim, S. (2013a). Automatic detection and recognition of pig wasting diseases using sound data in audio surveillance systems. *Sensors* 13, 12929–12942. DOI: <https://doi.org/10.3390/s131012929>
- Chung, Y., Lee, J., Oh, S., Park, D., Chang, H., & Kim, S. (2013b). Automatic detection of cow's oestrus in audio surveillance system. *Asian Australian Journal of Anim. Sci.*, 26, 1030–1037. DOI: <https://doi.org/10.5713/ajas.2012.12628>
- Espmark, Y., Falt, L., & Falt B. (1974). Behavioral responses in cattle and sheep exposed to sonic booms and low-altitude subsonic flight noise. *Veterinary Record*, 94(6), 106–113. DOI: <https://doi.org/10.1136/vr.94.6.106>

- Heffner, R.S., & Heffner, H.E. (1992). Auditory perception. In C. Phillips, and D. Piggins (Ed.) *Farm Animals and the Environment*. CAB International: Wallingford, UK.
- Hughes, B.O. (1975). Spatial preference in the domestic hen. *British Veterinary Journal*, 131, 560– 564. DOI: [https://doi.org/10.1016/S0007-1935\(17\)35188-6](https://doi.org/10.1016/S0007-1935(17)35188-6)
- Kiley, M. (1972). The vocalizations of ungulates, their causation and function. *Zeitschrift fur Tierpsychologie*, 31, 171– 222. DOI: <https://doi.org/10.1111/j.1439-0310.1972.tb01764.x>
- Lee, J., Zuo, S., Chung, Y., Park, D., Chang, H.-H., & Kim, S. (2014). Formant-based acoustic features for cow's estrus detection in audio surveillance system. *The 11th IEEE International Conference on Advanced Video and Signal Based Surveillance (AVSS 2014)* (pp. 236-240), Seoul, Korea. DOI: <https://doi.org/10.1109/AVSS.2014.6918674>
- Lee, J., Noh, B., Jang, S., Park, D., Chung, Y., & Chang, H.-H. (2015). Stress detection and classification of laying hens by sound analysis. *Asian Australian Journal of Anim. Sci*, 28, 592–598. DOI: <https://doi.org/10.5713%2Fajas.14.0654>
- Mendes, L.B., Ogink, N.W., Edouard, N., Van Dooren, H.J.C., Tinôco, I.D.F.F., & Mosquera, J. (2015). NDIR gas sensor for spatial monitoring of carbon dioxide concentrations in naturally ventilated livestock buildings. *Sensors*, 15, 11239–11257. DOI: <https://doi.org/10.3390/s150511239>
- Rushen, J., Chapinal, N., & Passillé, A.M de. (2012). Automated monitoring of behavioural-based animal welfare indicators. *Animal Welfare*, 21, 339 – 350. DOI: <https://doi.org/10.7120/09627286.21.3.339>
- Watts, J.M., & Stookey, J.M. (2000). Vocal behaviour in cattle: the animal's commentary on its biological processes and welfare. *Applied Animal Behaviour Science*, 67,15 – 33. DOI: [https://doi.org/10.1016/S0168-1591\(99\)00108-2](https://doi.org/10.1016/S0168-1591(99)00108-2)
- Weeks, C. A., Brown, S. N., Lane, S., Heasman, L., Benson, T., & Warriss, P. D. (2009). Noise levels in lairages for cattle, sheep and pigs in abattoirs in England and Wales. *Veterinary Record*, 165, 308 – 314. DOI: <https://doi.org/10.1136/vr.165.11.308>
- Wiepkema, P.R. (1982). On the identity and significance of disturbed behaviour in vertebrates. In W. Bessei (Ed.), *Disturbed behaviour in farm animals* (pp. 7-17). Hohenheimer Arbeiten 121, Verlag Eugen Ulmer, Stuttgart. Retrieved from: <http://library.wur.nl/WebQuery/wurpubs/75640>



Optimization Tool for Small Hydropower Plant Resource Planning And Development: A Case Study

Hasan Huseyin Coban^{1,*}, Antans Sauhats²

¹Department of Electrical Engineering, Faculty of Engineering, Ardahan University, Ardahan, Türkiye

²Institute of Power Engineering, Faculty of Power and Electrical Engineering, Riga Technical University, Riga, Latvia

Article History

Received: 05.03.2022
Accepted: 26.05.2022
Published: 25.09.2022

Research Article

Abstract – In recent years, the use of renewable energy sources in electricity networks; has shown a rapid increase thanks to their clean, environment-friendly, and most importantly the supportive policies of the countries. As the production and distribution of energy resources become more complex, there is an increasing need for mathematical modelling and optimization problems, especially for designing clean energy systems and establishing clear and systematic decision-making mechanisms in the operation of these systems. The models created within the scope of this study include decisions such as the capacity of the systems to be created in order to support long-term investment decisions for energy infrastructure planning, and where, how much, and when energy should be generated. In addition to the purpose of the models and the elements they contain, one of the most important factors that complicate the problem is that the problem is stochastic and contains uncertainty. It is possible to get an idea about the electricity market prices and the flow rate and amounts of the rivers that supply water to the production in hydroelectric power plants, with estimation methods, but it is impossible to determine them precisely. All these uncertainties should be taken into account when the capacity of the infrastructure of the energy systems is created. In this respect, in this study, systems are modelled and compared using both deterministic and stochastic programming. The quasi-Newton method is used for nonlinear optimization tasks to plan energy production under the uncertainties in the nature of renewable energy. In the feasibility study, the Monte-Carlo method, which is a mathematical technique used to predict the possible outcomes of an uncertain event, was applied.

Keywords – Cost-benefit analysis, cost correlation, cost optimization, net present value, small hydropower plant.

1. Introduction

The need for energy, which has increased in parallel with production with the Industrial Revolution, has been a current issue since the 18th century (Teck et al., 2019). Every government, every home, every business, and every major issue is underpinned by energy. The increase of power consumption day by day, climate change, and the need to manage diminishing fossil fuels such as natural gas and oil reserves; these three main factors create an enormous problem in power engineering and it gives us reasons to develop power systems and their management, which influence market conditions and to be depended from other countries. But the situation is not easy to understand and resolve as power systems are among the hardest issues that exist for human activities. As seen in Figure 1; according to the International Energy Agency, world energy demand is estimated to increase by approximately 60% in the next 30 years (Kober et al., 2020). The most pressing issue is determining how to fulfil this demand.

Because of the rapid decrease in the number of conventional resources and increasing demand, some countries will not be able to meet the demand by conventional primary resources until 2030 (Matzenberger et al., 2015). As conventional energy sources (fossil fuels) are decreasing day by day, governments should adopt two strategies: reducing energy demand and increasing supply. In this context energy reliability, efficiency and renewable energy are notably relevant. Renewable energy serves two main targets: protecting

¹ huseyincoban@ardahan.edu.tr

² antans.sauhats@rtu.lv

*Corresponding Author

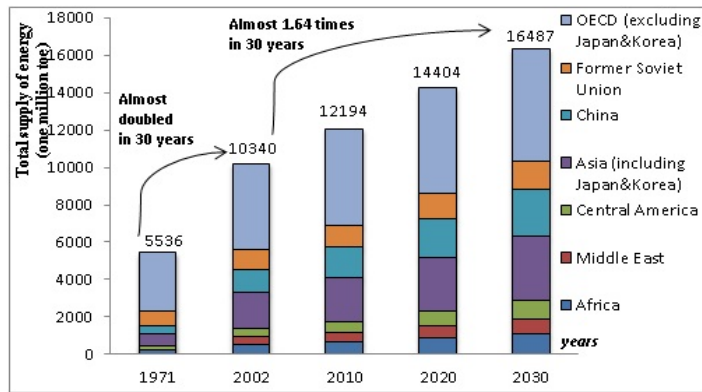


Figure 1. Global energy demand between 1971-2030 (Ranaraja et al., 2020)

the environment with emissions-free energy and generating energy to meet the demand (Davis et al., 2018). The efficiency of energy addresses using energy most accurately without any reduction in production, comfort, and workforce.

Furthermore, currently, a lot of the countries are developing policies and trying to determine attainable targets in this area (Shukla et al., 2017). Comprising features mentioned above, small hydropower plants (SHPP) have been getting attention in both developed and developing countries. Western countries such as North America and Europe have already exploited most of their hydropower potential. However, South America, Africa, and Asia have still substantial unused potential for hydropower. Small hydro can be the cure and help of the insufficient energy in developing countries, as China did with 43000 small schemes and 265 GW of total installed power capacity (Bachir, 2017). In terms of fossil fuel sources, Turkey cannot be considered a rich country; this condition creates economical and political barriers to the development of the country (Kok & Benli, 2017). Beyond these problems; Turkey has a large renewable energy sources potential for electricity generation (Bulut & Muratoglu, 2018). The participation of the private sector in the energy field started a new era in energy generation from renewable sources in Turkey.

Hydroelectric energy constitutes the most important renewable energy source in Turkey (Bulut & Muratoglu, 2018; Erdin & Ozkaya, 2019). Considering its geomorphological structure and climatological/hydrological characteristics, Turkey is among the countries that can be considered lucky in terms of both its head and water level. Disregarding that potential, mainly large-scale hydroelectricity and thermal (non-renewable) has been widely exploited. To handle the potential of other renewables, a feed-in tariff (FIT) scheme has been implemented since 2001 (Kural & Ara, 2020) and it has experienced several revisions over the last decade.

One of the world's biggest problems faced in the 21st century is a secure energy supply (Asif & Muneer, 2007). In our country, where the demand is increasing quite rapidly, meeting the energy demand in a reliable manner as well as peak power is of great importance in terms of ensuring the supply security of the system and hydropower can handle this issue. Large numbers of papers (Alvarez et al., 1994; Asif & Muneer, 2007; Jiang et al., 2018; Marchand et al., 2019; Xu, J., Liu, Z., Jiang, 2021; Y. Yang et al., 2020; Z. Yang et al., 2022) are devoted to solving the generation plan problems. It is important to note that the HPP operating mode should be selected based on uncertain and random factors. Summarizing the above can be noted that despite the efforts of researchers and governments, there are still many unresolved issues, especially to maximize profits through an optimal selection of HPP parameters and operation mode.

For the purposes of this study, objective research is defined as research that aims to develop short- and long-term planning models for price takers generating in the market environment while pursuing profit maximization while taking into account energy market conditions, uncertainties, and joint working opportunities. To achieve the stated goal four main tasks need to be considered:

- development of stochastic optimization algorithm for hydroelectric power plant;
- a cost-benefit analysis (CBA) to measure the benefits of a decision;
- presentation of CBA findings of total project costs for installed power capacity and reservoir alternatives; establishing a long-term SHP to evaluate qualifications and find the best alternative;

- synthesis of a model for the benefit of hydroelectric power plant operators; testing of models during the solution of optimization tasks; description of the volume and resources of information required; the possibility of applying models has been proven by the Quasi-Newton method.

The first chapter describes the topicality of the study, formulates the goal and tasks of the work. The chapter contains an introduction to the problem and deals with the research methods which are used for the acquisition of the results of the work, as well as the basic levels of research. Chapter two describes general knowledge about small hydropower plants and their equipment. Chapter three starts with information about SHPP design and continues to describe the formulation of SHPP operations. Also, feasibility scenario the Chapter offers an optimization technique purposeful by maximizing income for hydropower which has limited water to use. The economic part of the feasibility study of power plants in terms of a particular feed-in tariff and market conditions is formulated. Chapter four presents the application of the considered methods with examples and a case study for a Turkish SHPP. The suggested algorithm of power plant working condition optimization is approved on the Saf HPP. Chapter five represents conclusions and devoted an outline of the future work. Finally, several conclusions and suggestions for future work are given and the solution algorithm is presented to solve the hydropower generation coordination problem at market conditions.

1.1 The objectives of power supply development

Sustainable energy is the model of energy acquired from non-exhaustible resources so the provision of this model of energy distributes the needs of the present without compromising the ability of future generations' capacity to satisfy their own. Electricity generation, distribution, and consumption have many unfavourable environmental consequences at the global, regional, and local levels, including indoor air pollution in global warming, blighted area communities, and land degradation. Green energy organizations are needed to direct all of these towards environmental sustainability ([Zhang et al., 2021](#)). The sustainability topic covers the three pillars of issues – environmental, economic, and social– and includes issues such as indigenous peoples, downstream flow regimes, resettlement, infrastructure safety, water quality, sedimentation, and erosion ([Ranjbari et al., 2021](#)).

Sustainability prevents the rising of oil prices; it helps provide cheap and environment-friendly energy. Overall, the sustainable development of the hydropower sector is based on three important principles: ([Zhang et al., 2021](#))

- economic sustainability means delivering the maintenance of the renewable resource base, and the use of non-renewable resource rents to encourage structure the improvement of other factors of generation. Cost-benefit analysis and evaluation of long-term economic performance are the keys to the achievement of economic sustainability;
- social sustainability is based on how effective regions and countries are in the building of new projects, which means people involvement during erection and generation for working and improvement of self-knowledge.
- the avoidance of unavoidable environmental causes such as biodiversity loss and the buildup of persistent pollutants is essential for ecological (environmental) sustainability. Technology and economics are also related to resource management, decision-making, acquisitions, etc ([Alterach et al., 2010](#)). [Figure 2](#) represents a definition of the space of feasible solutions, considering the legal, technical, and economic aspects or boundary conditions.

Hydropower energy technologies are important contributors to sustainable energy because they help to provide global energy security by lowering reliance on fossil fuels and giving chances to reduce greenhouse gas emissions. Sustainable energy sources and efficient use of energy as a whole cannot be considered separately. The basic aim of sustainable energy sources and efficient use of energy is a reduction of carbon dioxide emissions. Small-scale hydropower is a promising alternative for producing inexpensive and sustainable energy in rural or developing areas. The case study of this thesis aims at investigating the useful tools for operation and management for small-scale hydropower in rural areas for sustainable development. ([Demirtas, 2013](#))

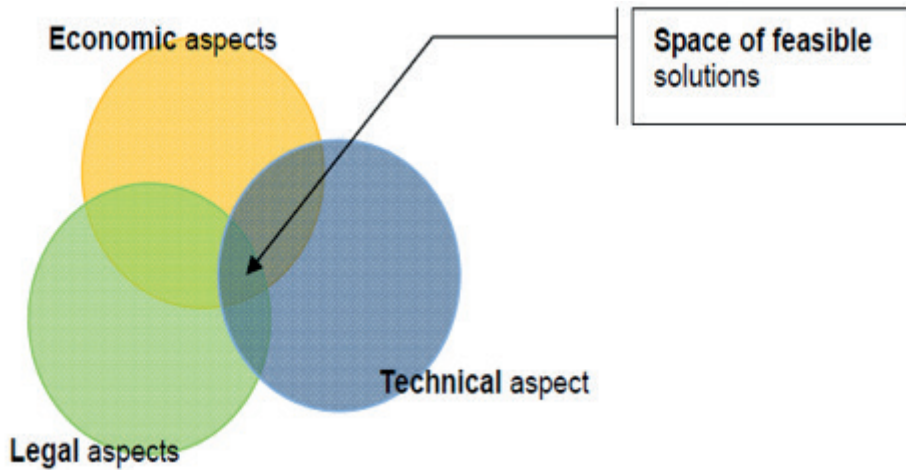


Figure 2. The space of SHPP feasible solutions (Alterach et al., 2010)

A sustainable hydropower project is possible, but it needs careful system design and proper planning to control the objections (Kaunda et al., 2012). The hydropower projects which are planned well can contribute to the supply of sustainable energy. It is important that up-to-date information (knowledge) is necessary for investors, energy planners, and other stakeholders to make informed decisions concerning hydropower projects. Hydropower can considerably provide towards diminishing effects of global warming and mitigation of climate change, increased national energy access and security, creation of economic opportunities, and thus completely leading to sustainable development (De Jong et al., 2018).

1.2 Hydropower in Turkey

The technical potential provided current and expected local economic conditions in developing technology but can be part of the so-called developed and economically feasible hydropower potential of increasing energy prices, technical and economic potential of the technical potential of the approach. Figure 3 shows Turkey’s annual energy generation percentages.

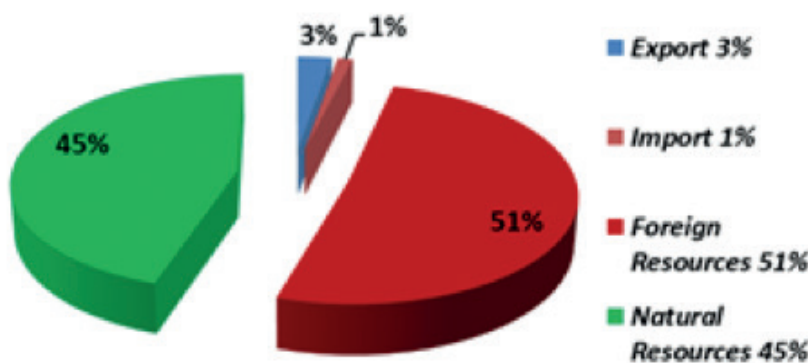


Figure 3. Turkey’s annual energy generation percentages (Ministry of Energy and Natural Resources, 2022)

As a result of climate change, and due to the effects of Covid-19; electricity production in Turkey decreased by 16% in HPPs in 2021 compared to the previous period (Coban, 2021). As seen in Figure 3, developing domestic and renewable energy resources is very important for Turkey in ensuring sustainable development because the country imports 51% of the total energy it consumes, according to the statistical data of the General Directorate of Renewable Energy. The country’s premier domestic and renewable energy resource is hydropower. Figure 4 below presents the distribution of Turkey's installed power resources as of the end of 2021. About 46% of the installed capacity belongs to renewable energy sources. The renewable installed capacity of a very large portion is constituted by hydraulic capacity. The share of solar and geothermal power is limited. The share of natural gas is 27% (Ministry of Energy and Natural Resources, 2022).

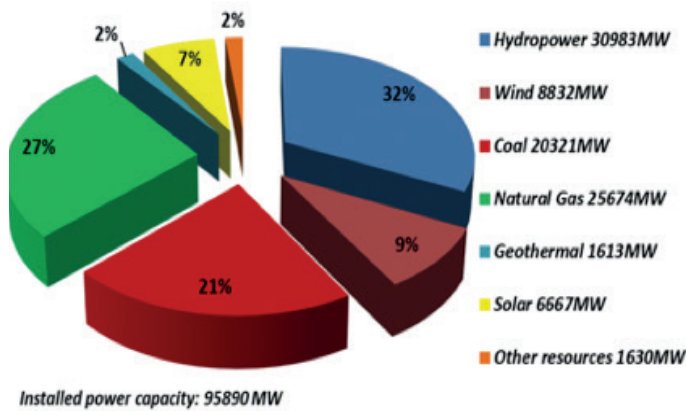


Figure 4. Turkey's installed power as distributed among resource types (*Ministry of Energy and Natural Resources, 2022*)

- Turkey's annual potential hydroelectric energy capacity is 128 billion kWh. Nevertheless, only 36% of this capacity is being used; currently, the amount of electricity annually produced from hydroelectric power plants is 46 billion kWh. Also, many hydropower plants are under construction by the private and the public sector. (*Yuksel et al., 2017*)
- Especially Northern of the country (the Black Sea region) is rich in terms of altitude and rivers. Most of the Black Sea region is hilly; it can be possible to develop higher heads by way of non-expensive civil works so that smaller flow rates are needed to achieve the power aimed at. Renewable energy will play a critical role as Turkey's development for accession to the European Union is in progress. (*Yuksel et al., 2017*)
- Turkey has about 1.5% of the world's total hydroelectric potential, with an average altitude three times higher than the European average, with an average elevation of 1132 m, and the location, the country is ringed on three sides by seas, is highly favourable for hydroelectric power production. This topography favours the formation of high gradient mountain streams, which are applicable locations for small-scale hydropower development. (*Kaygusuz, 2018*)
- Turkey, which has the sixth-largest electricity market in Europe, has a rapid growth rate in electricity consumption above the GDP per capita growth as a result of population growth, economic, and industrialization growth in the last two twenty years (*M. Şahin, 2021*).
- Privatization efforts of the government were notably fruitful in Turkey's hydropower environment. The very quick growth in the number of privately financed small to medium-sized hydroelectric power plants helped the country to develop a more secure, efficient, and reliable energy supply as well as progress towards its goal of producing 100% of its total energy from renewables by 2050 (*Coban, 2020a*).
- Turkey has Europe's highest hydroelectric potential with its 216 billion kWh/year technical hydropower potential and the economically viable potential is 140 billion kWh/year; but was using only 24.58% (67,259 GWh) of hydropower potential as of the year 2015 (*Bilgili et al., 2018; Erat et al., 2021*). However, many European countries are trying to reach the production target of over 70% of their economically viable hydroelectric potential. (*Lund & Østergaard, 2018*).

The support scheme and the day-ahead market:

Unfortunately, Turkey's markets are still inadequate when compared to the EU countries that are leading the utilization of renewable energy sources. For example, according to the German Renewable Energy Law for different energy sources government offers different feed-in tariffs. Still, the Turkish government guarantees to purchase the produced electricity for 10 years and offers a feed-in tariff of 7.3\$cents (6.4€cents)/kWh (*Yalılı et al., 2020*). In addition, the Law provides additional bonus income for each domestically produced component of mechanical or electro-mechanical equipment used in power plants. This is called "local contribution" (*Yalılı et al., 2020*). The feed-in tariff for some of the European countries is shown in [Table 1](#).

Table 1

Feed-in tariff rates in Europe €/kWh (Legal Sources on Renewable Energy, 2021)

Country	Biomass	Biogas	Hydropower	Wind	PV
Lithuania	8.6	8.6	7.0	7.5	44.0
Latvia	18.5	19.5	18.8	10.5	42.6
Germany*	5.76	8.3	3.5 – 12.5	3.5-19	8.92
Turkey	10.4	10.4	6.4	6.4	10.3
Turkey*	11.8	13.3	9.5	9.5	15.2

Germany*: offshore wind €ct 3.5 – 19 per kWh, onshore wind €ct 4.72 – 8.66; Turkey*: with an additional payment for “Made in Turkey” components

Every day, the national load distribution center publishes a demand forecast determined on an hourly basis for the next day on the Market Management System. Participants need information such as seasonal conditions, precipitation, various factors such as occupancy rates, and system constraints when the dam produces electricity for the next day considering their estimates. The aim is to increase production at times when the demand is high and to reduce and stop production at times when the demand is low. As in all markets, in the electricity market, if the demand is greater than the supply, the price increases at that time; night hours, weekends, and holidays represent examples of electricity prices going down. Market participants can submit hourly, block, and flexible bids at the day-ahead market. The amount and price of bids can differ for different hours. The maximum and minimum amount of power and price that can be traded is determined by the Market Financial Settlement Center (C. Şahin, 2021). Figure 5 abstracts the process of the day-ahead electricity market.

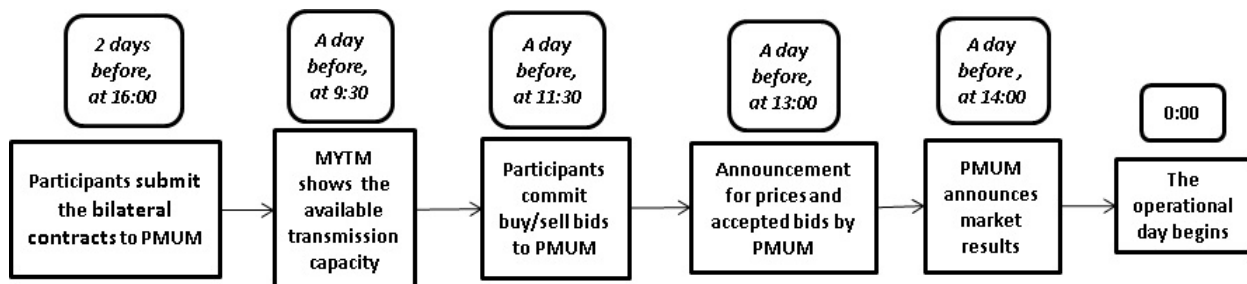


Figure 5. A timeline of the Turkish day-ahead market

1.3 The methodology of a cost-benefit analysis

The CBA is the heart of a feasibility study for a small hydropower project (Wendle, 2019). The costs and benefits that an investment project will provide over its entire life are determined in monetary terms. The discount rate plays a critical role in the choice of whether or not a proposed project is economically feasible and should accordingly be carried out. Furthermore, the longer the life of an investigated power plant project, the greater the impact that the discount rate has on costs and future benefits (Wendle, 2019). The main objective of the CBA is to provide alternatives that are economically best appropriated for the improvement of an aging hydropower plant. The primary objective of the analysis is to collect all the costs associated with all the alternatives and to determine the relationship between the returns and the investment. The initial stage of this analysis is to calculate the total cost for each alternative, then the present worth of the revenues is calculated and the relationship established; if the alternative is economically viable and is best suited for both the investment or returns ratio and the reliability of the unit, then the project application stage begins (Wendle, 2019).

Figure 6 summarizes the economic methodology for calculating the annual net income. To estimate the annual net benefit, project operating and maintenance expenses are subtracted from the sum of revenues, which are gross electricity generation, project services, and additional incomes. Additional annual benefits

relate to being in coalition with irrigation companies, other energy producers, and fishermen. Annual benefits of the project consist of revenues from benefits such as river transportation, water supply, irrigation, and flood control. Annual costs of operation represent interest payment, past and future investment costs on the project, and current operation and maintenance costs. (Bin, 2021)

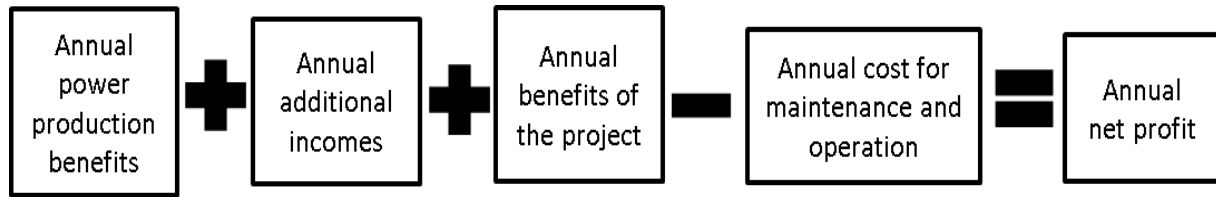


Figure 6. An income calculation of a hydropower plant

A thorough search and review have been carried out for relevant published reports and journal papers; several studies exist that reveal the costs of production for run-of-river, storage, and pumped-storage hydropower plants (Belbo, 2016; Kotchen et al., 2006; Wessel et al., 2020; Yildiz & Vrugt, 2019). One of the existing cost equations and associated work is summarized below.

The authors of (Kotchen et al., 2006) draw on three studies of environmental constraints, which are, firstly, electricity production costs, secondly, air quality benefits, and, thirdly, recreational fishing benefits on hydroelectricity production costs and benefits related to the run of river flow. The authors investigated the economic impact of increases in electricity production from other resources. As a result, the best approximate calculation offers that the aggregate benefits are more than two times as large as the producer’s costs.

A review of the literature shows that several empirical equations have been developed worldwide to estimate electromechanical costs, civil works, and overall project costs. However, each of these studies has certain limitations about being applied to the prediction of costs for new hydropower projects in the United States. Particularly, the cost of a hydropower project is nonlinearly correlated to installed capacity and head; also it is very sensitive to the evolving technologies and site-dependent.

2. The Basics of SHPP Design and Operation

The choice of the most appropriate sites for the hydropower exploitation depends upon the relationship between the construction, operation, and maintenance costs of the entire system and the income from energy selling plus the additional benefits, such as creating a coalition with a public trader and/or local consumers (Sun et al., 2021). According to the hydropower equation (2.1), the power generated is proportional to the product of the head and the release via the turbines, with precise values set by turbine design (Bachir, 2017).

$$P_t = \rho u h \text{ (kgm)}, \tag{2.1}$$

Where;

P_t -potential energy;

ρ - the density of water in kilograms.1000/m³;

u - the amount of water;

h - the height difference between inlet and outlet in meters.

The quantity of water falling (2.2) is called flow. When water supplies u discharge rate some time interval, m³/s:

$$Q = \frac{u}{t} \tag{2.2}$$

In order to obtain the water velocity required to produce energy from a water turbine with the help of water force, a drop height or the kinetic and pressure energy of the water is absolutely needed. The maximum active hydraulic power (installed power) capacity that a facility can produce is expressed in the formula (2.3) below.

$$P = \eta \rho g Q h, \quad (2.3)$$

Where;

P - the power output, measured in Watts;

η - the efficiency rate of the generator and turbine;

Q - the water flow rate m^3/s ;

g - the acceleration of gravity, $9.81 m/s^2$

The real-life model of a power plant is more complicated. Because η is a function of the head-pond of water. This phenomenon can be taken into account when choosing concrete equipment.

2.1 An overview of SHPP optimization procedures

The optimization task of power plant management can be identified with multi-parameter, linear or non-linear, dynamic, stochastic, discrete variables ([Asif & Muneer, 2007](#); [Mahmoudimehr & Sebghati, 2019](#)). No commonly accepted solution to this task. Many simplified approaches are applied. Depending on the objective function, the restrictions on the types and designs, the mathematical task after its formulation can be solved by using the mathematical programming method. A wide range of mathematical programming methods is described in the literature. There are optimization studies in the fields of water resources management and power generation using the solver application, and some of the most frequently used programming models are summarized below.

An optimization model has been developed in the article ([Benli & Kodal, 2003](#)) investigated the optimum plant pattern with the Non-Linear Optimization method they developed in the South-eastern Anatolia Region in their study. The model inputs were transferred to the MS-Excel solver program and the LINDO software package under water potential, crop yield, adequate and limited irrigation conditions. With the same objective function and constraints, they tried to determine the optimum planting area distribution with linear and nonlinear models and showed that the net income obtained from the nonlinear model was higher under limited irrigation conditions.

The article ([Arai et al., 2011](#)) simulated a study in Bangladesh using an Excel Solver application to demonstrate the impact of electricity generation on economic growth. For various power generation schemes, a solver for nonlinear problems in the model was used and six steps were followed. i) the constants and settings were set, ii) a price system calculation was obtained, iii) income and final demand were calculated, iv) production demand was calculated, v) the equilibrium was solved and, vi) future electricity prices and capital accumulation were calculated. Upon comparing the results for various established models, the electricity generation capacities and applicable planning and operating policy were obtained.

The paper ([Tiainen et al., 2008](#)) investigates the optimization of the energy production of a Finnish head-dependent reservoirs in light of market conditions based on the Nord Pool Spot hourly energy price. The optimization algorithm's objective function is to maximize the income in a given period, with the hourly-changing the inflow, electricity price and the current generator states as inputs while keeping the head between the required limits. With varied inflow levels and pricing data, the technique is examined using genetic algorithm-based and steepest ascent-based optimization algorithms. The reservoir was filled to the maximum before the peak time and the head was allowed to drop when the price was high. The optimization is implemented in three versions – Steepest Ascent Hill Climbing, Genetic Algorithm, and Simulated Annealing. The results are compared the income had improved approximately by 0.5-10%.

The authors of (Wu et al., 2008) present the cost of reliability by considering the stochastic nature of power systems in the long term. Random outages of transmission lines and generating units as well as load forecasting errors are designed as scenario trees in the Monte-Carlo simulation. The hourly unit commitment problem is used to solve the reliability model in a successful way. They have applied the Monte-Carlo method to simulate potential contingencies in uncertain security-constrained unit commitment.

The authors of (Desreumaux et al., 2014) aimed to develop a new method to compute the cost-to-go function efficiently and to reduce the computation time of the Stochastic Dynamic Program algorithm applied to a hydropower system optimization. The objective function of the one-stage optimization problem that is solved to evaluate the cost-to-go function includes the summation of two terms, the current benefits function, and the expected water value function.

The article (Howard, 2006) describes the formulation of a hybrid two-stage hourly hydropower generation optimization model that is established on an MS-Excel solver. The first stage determines the hourly total powerhouse discharge that maximizes generation revenue within the operating limitations and constraints, namely the quadratic optimization model. The second stage is a non-linear postprocessor, which disaggregates the optimized plant discharge and simulates the operation of the project using the suitable non-linear curves. The method was used to determine plant and unit operations to maximize revenue.

The authors of (Najarchi & Haghverdi, 2020) would like to attain optimal operation of the hydropower plant, which is a multistage and nonlinear combinatorial optimization problem with many constraints and can be presented as finding a water level change sequence that satisfies all constraints to maximize the annual income by electricity generation. As a result, they found that the differential evolution algorithm is preferable to dynamic programming since it provides a new approach for multi-reservoir combined optimal operation and has better calculation speed.

The nonlinear monthly optimization model proposed by the authors of (Barros et al., 2001) has been developed for the operations and management of a large-scale hydropower system and applied to the hydropower system of Brazil. Their model can be used by two different approaches, a linear approach and a nonlinear one. The linearized model replaces the energy production and tailrace functions by their corresponding average values in a seven-year planning time horizon. Their results showed that the linearized model produced 1.5% and 0.5% more energy.

The authors of (Enoksson & Svedberg, 2015) concentrate their self in master thesis more on the mathematics on a two-stage stochastic optimization model. The objective function aims to maximize the income. The authors developed a model that uses public data that are directly observable from the electricity market for hydropower optimization which takes hydrological uncertainty into account. They have tested different methods which are the normalization approach, where the assumption that inflow to the reservoirs is outcomes from a normal distribution for each time step, and the Bootstrap approach, where scenarios are created by randomly sampling inflows from the historical observations. The author's recommendation is to use one of these two inflow distribution methods.

The article (Soares & Carneiro, 1991) proved the influence of several factors including water inflow seasonality, head-pond, discount rate, and system design on a deterministic optimization. The result showed that these factors have a great effect on the long-term optimization for CBA of hydrothermal power plants. To model the stochastic factors, they have used a deterministic approach because authors could not compute in a stochastic way. Summarizing above, it can be concluded that the HPP optimization problems can be considered as multi-objectives, non-linear and stochastic. These keywords form a base of the algorithm which has been chosen in this study.

3. General mathematical programming

It is assumed that the profit (3.1) of the power facility is any function of head pond, water discharge, market prices, etc. can be defined as below.

$$R_{i\Delta} = \varphi(C_t, D_t, U_{it}, H_{it}, K_t, CH_t, Inv_t, P_{it}, \rho_{it}, OM_t, A_{it}) \quad (3.1)$$

where;

$R_{i\Delta}$ – the profit.

C_t – electricity market prices, Eur/MWh;

D_t – risks ratio for year “t”;

U_{it} – the number of units;

H_{it} – the head-pond, m;

CH_t – the catchment area, km²;

K_t – the discount factor for year “t”;

i – the number of the option (alternatives);

Inv_t – the cost of construction.

P_{it} – the installed capacity;

OM_{it} – operations and maintenance costs in year “t”;

ρ_{it} – efficiency of turbine and generators;

A_{it} – capacity of the reservoir, m³;

t – the time interval, t (year);

A given set of input parameters is known in the deterministic situation, while some of these parameters are uncertain and/or probabilistic in the stochastic case. In this case, the random $R_{i\Delta}$ optimization problem can be formulated as an average profit maximization task as follows:

$$M[R_{i\Delta}] = \Delta t \int_{-\infty}^{+\infty} \dots \int \varphi \left(\begin{matrix} P_{it}, U_{it}, H_{it}, C_t, A_{it}, \rho_{it} \\ OM_t, D_t, K_t, CH_t, Inv_t \end{matrix} \right) dF \quad (3.2)$$

Where;

F – a multidimensional probability distribution function ([Antans Sauhats et al., 2016](#); [R. Varfolomejeva et al., 2014](#)).

The objective function presented in the form (3.2) is not only difficult for maximization, but also very complex to calculate ([Antans Sauhats et al., 2016](#)).

3.1 Constraints of SHPP operation

The main constraints of HPPs operation can be classified into four groups: ([Yuan et al., 2021](#))

I. The reservoir storage volume limits:

The head-pond means the difference in height. It is assumed that H can be any value lying within the domain $[H_{min}, H_{max}]$, where H_{min}, H_{max} are positive constants (3.3) specified in the operation plan:

$$H_{i,min}^t \leq H_i^t \leq H_{i,max}^t, \quad \forall i \in I, \forall t \in T \quad (3.3)$$

where H represents the water level (3.4); the min and max are the allowable lowest and highest-level during time t respectively (3.5, 3.6). is reservoir level at the beginning of period t;

$$H_i^t + A_i^t - Q_i^t = H_i^{t+1} \quad (3.4)$$

$$H_i^t = H_i^{t-1} + \sum_{t=1}^T A_i^t - \sum_{t=1}^T Q_i^t \quad (3.5)$$

$$H_{i,max}^t \geq H_i + \sum_{t=1}^T A_i^t - \sum_{t=1}^T Q_i^t \geq H_{i,min}^t \quad (3.6)$$

$$\forall i \in I, \forall t \in T$$

Where;

T, t - the index and set of hours;

I, i - the index and set of the reservoir;

A_i^t - the water flow rate into the reservoir at hour t ;

H_i^t - the water level at hour t ;

Q_i^t - the volumetric discharge at hour t .

The rate of A water flowing into the dam is a positive variable. It is straightforward to extend water flow can be a deterministic function of t or to follow a stochastic process. The water level relationship can be reformulated as the sum of the initial level storage and the difference between the flow and discharge from periods 1 to T as follows:

II. The water discharge from the reservoir:

Water discharge is the rate of the water flowing through the turbine. It is assumed that Q can be any value residing within the domain $[Q_{min}, Q_{max}]$, where Q_{min} is zero, and Q_{max} (3.7) is determined by the turbine's head.

$$Q_{i,min}^t \leq Q_i^t \leq Q_{i,max}^t, \quad \forall i \in I, \forall t \in T \quad (3.7)$$

where Q_{min} and Q_{max} are water discharge's the lower and the upper limits, respectively. In the case study, the minimum water discharge was considered negligible.

III. The power generation:

P is a function (3.8, 3.9) of the head-pond ΔH and reservoir release Q :

$$P_i^t = n_i^t Q_i^t \Delta H_i^t, \quad \forall i \in I, \forall t \in T \quad (3.8)$$

$$0 \leq P_i^t \leq P_{i,max}^t, \quad \forall i \in I, \forall t \in T \quad (3.9)$$

Where;

ΔH_i^t - the water head at hour t ;

n_i^t - the overall efficiency of the power plant at hour t ;

$P_{i,max}^t$ - the maximum power generation at hour t .

IV. Minimum power generation:

The minimum production (3.10) must be set to a certain amount of the maximum production on each unit, taking into account the efficiency of the turbine and generator, and the cavitation.

$$\%R \cdot P_{i,min}^t \leq P_i^t \leq P_{i,max}^t \quad (3.10)$$

where R is each unit's minimum electricity generation.

The objective function for deterministic approach:

To maximize power generation as one of the operational goals, a way to achieve this is to use water overhead to increase power generation while reducing wastewater. The only way to maximize revenue with the deterministic method is to maximize energy production because electricity prices are fixed.

Mathematically, optimization problem (3.12) can be formulated as:

$$R = \text{Max}(E(\vec{Q}) \cdot c - Ex) \quad (3.11)$$

$$I(P_1, P_2, \dots, P_t) = \text{Max} \sum_{t=1}^T \sum_{i=1}^n P_i^t(\vec{Q}) \cdot c^t \quad (3.12)$$

Where E is the total amount of produced electrical energy as a function of i and t are the index of the reservoir and time, respectively; I_j is income, P is the generated power of the hydropower plant in kWh, Q is the water flow through the turbine in m³/s, c is constant electricity price, Ex represents the expenses; namely interest payments, operations and maintenance costs. According to equation (3.11), the decision variable is the hydroelectric output depending on the reservoir release.

The objective function for stochastic approach:

The purpose of the SHPP owner is to maximize profit from all price forecast scenarios that the turbines/generators are only run during peak load hours, as the prices are higher. SHPP should stop generating power during a period of low price and accumulate water in the reservoir. It is required to consider restrictions and limitations on the natural water flow on small rivers and the possible amount of water that may be consumed by a SHPP during the day. The operation of a reservoir for a hydropower plant is a complex endeavor. The variation of the water pressure on the SHPP is caused by the variation of the upstream and downstream water levels. This is due to the use of water through SHPP's turbines. Therefore, the variation of the water level should be limited from the top and bottom (Berry, 2003; Coban et al., 2015).

The main criterion (the objective function) of the optimization task is income maximization (3.13, 3.14); at market conditions, mathematically, optimization problem can be formulated as:

$$I(P_1, P_2, \dots, P_j) = \sum_{j=1}^J I_j(c_j, P_{SHPP_j}) \rightarrow \max \quad (3.13)$$

$$I(P_1, P_2, \dots, P_j) = \text{argmax} \sum_{j=1}^J I_j(c_j, P_{SHPP_j}) = \max \sum_{j=1}^J c_j \cdot (9,81 \cdot \eta_{turb} \cdot \eta_G \cdot Q_j \cdot H_j) \quad (3.14)$$

Where;

P_{SHPP} - SHPP produced electricity, kWh;

P_j - produced electricity at j-time;

c_j - the electricity market price at the period j, EUR/kWh;

H_j - the headwater level at the intake in m;

Q_j - water inflow through the turbine, m³/s;

h - the efficiency factor of the components: $h_H = h_{turb} \cdot h_G$, where h_{turb} - turbine efficiency factor; h_G - generator efficiency factor (Grigoriu & Popescu, 2010; A. Sauhats et al., 2014).

$I_j(c_j, P_j)$ - the income from the sales of electricity, that is gained on power facility during the time interval

Δt_j by known market price c_j , €;

It is necessary to determine the operating schedule of the SHPP, providing the maximum revenue per regulatory cycle T , hour. The first statement can be applied considering the water level limitations and the usage condition W_j of the set water amount in the reservoir (3.15): (Renata Varfolomejeva, 2014)

$$\sum_{j=1}^J Q_j \cdot \Delta t_j = W_j \tag{3.15}$$

Where;

T – the regulation cycle duration: $T = \sum_{j=1}^J \Delta t_j$

Q_j - the water flow through the SHPP flap during the time interval Δt_j , m³/s;

W_j - the set amount of water (m³) that could be passed through the SHPP flap per regulation cycle T.

The time interval equals to $\Delta t_j = 1$ hour at the daily regulation cycle of SHPP. The power generation on SHPP during to the j -th interval Δt_j is defined as: $P_j \cdot \Delta t_j$. At the known natural inflow of the river Q_{flow} , the used water flow in each time interval of regulation is determined by the value Q_j that depends on the usage of water reservoir capacity (m³) (Renata Varfolomejeva, 2014; Renata Varfolomejeva et al., 2013)

3.2. An overview of the optimization tools

An optimization is a key tool in designing and planning. The purpose of this study can be considered as targeted to not only methodology and algorithm but also the software creation. In this direction, we needed to go a long way. The necessary steps for creating optimization software for power plants are summarized in Figure 7.

The selected path is exhibited by red colour. In the first stage stochastic approach is preferred. Secondly, the time-average method has been applied. The following three steps are associated with optimization procedure selection. A big number of variants are existed and are used. We have selected a mixture of them: linear for part

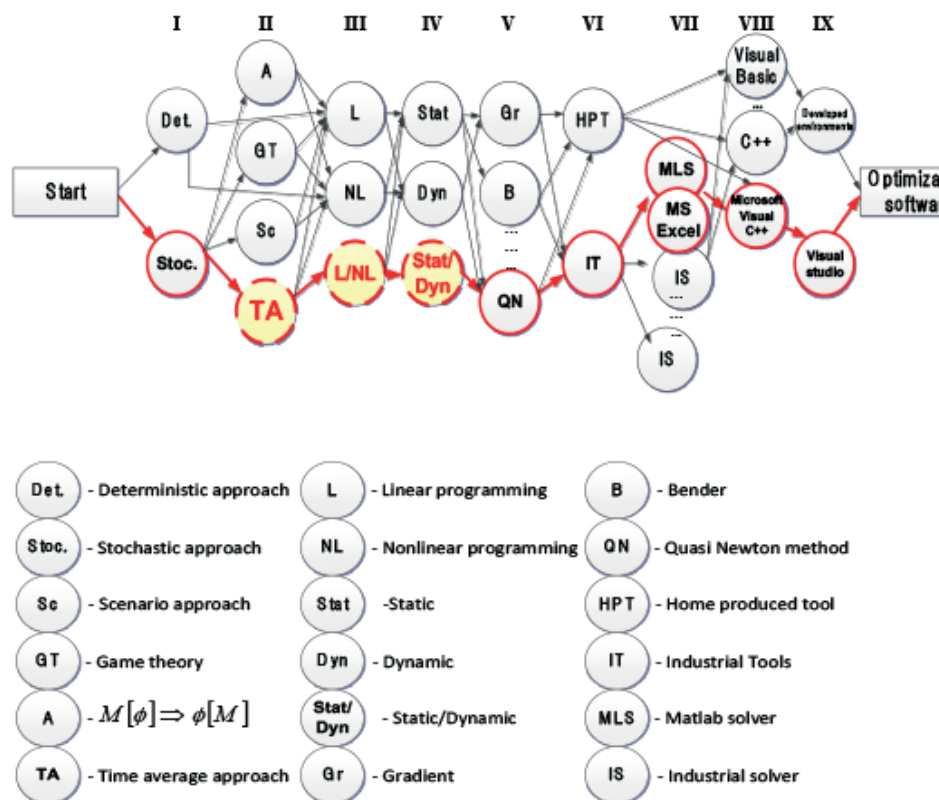


Figure 7. The necessary milestones for creating optimization software of power plants (R. Varfolomejeva et al., 2015)

of tasks and non-linear when accuracy is needed; statistic task statement is applied, but to do enlargement of variables number a dynamic nature of the problem is considered. The Quasi-Newton method is selected for the maximization problem solution (Coban, 2020b; Khaniya et al., 2020). The last three steps are related to software development. The choice of MATLAB and MS-Excel solvers, as well as was determined by university resources.

3.3. SHPP optimization tasks mathematical restatement and reformulation

It is assumed that an electric power system includes consumer Cons, generation companies Gcom, and power network Pnet (3.16):

$$Own(G_{com}, P_{net}, C_{ons}) \tag{3.16}$$

In general, each of these contains many objects managed by different owners (3.17):

$$\begin{aligned} G_{com}(g_{com1}, \dots, g_{comn1}) \\ P_{net}(p_{net1}, \dots, p_{netn1}) \\ C_{ons}(c_{ons1}, \dots, c_{onsn1}) \end{aligned} \tag{3.17}$$

Each owner strives to increase their own profit (or reduce expenses) (3.18):

$$R(Own_j) \Rightarrow \max \tag{3.18}$$

In the general case, it is assumed that the owner’s profit is any of the following nonlinear functions: parameters Π and configuration Σ of the owned objects (3.19);

$$\Sigma_{i-}; \Pi_i \tag{3.19}$$

The part configuration and parameters may change over time (3.20):

$$\Gamma(t) = \Sigma_i(t); \Pi(t) \tag{3.20}$$

Parameters and configurations depend on uncertain and random events and processes (solar radiation, wind speed, ambient temperature, etc.); and they must be selected (in the design phase) before the experiment begins. Considering the parameters listed above, the optimization objectives are formulated as follows:

$$\begin{aligned} R(Own_1) = F_1(\Sigma, \Pi, \Sigma_{i-}, \Pi_{i-}, t, \Gamma(t)) \Rightarrow \max \\ \vdots \\ R(Own_n) = F_{n\Sigma}(\Sigma, \Pi, \Sigma, \Pi, t, \Gamma(t)) \Rightarrow \max \end{aligned} \tag{3.21}$$

subject to: $\delta(\Sigma, \Pi, \Sigma_{i-1}, \Pi_{i-1}, t, \Gamma(t)) \ni \Omega$

Due to each optimization function contains random time processes $\Gamma(t)$, and profit R is time-dependent the form (3.21) cannot be solved. It is necessary to take into account to select indicators that allow describe profit by one number; to create an appropriate statistical model of random processes $\Gamma(t)$; and to choose planning period length. Performance of these steps allows to express the owner’s profits in form (3.2). Using (3.2), it can be re-formed (3.21):

$$\begin{aligned} M[R(Own_1)] \Rightarrow \max \\ \vdots \\ M[R(Own_n)] \Rightarrow \max \end{aligned} \tag{3.22}$$

subject to: $\delta \ni \Omega$

where M is the mathematical expectation of the value.

For the following reasons, statement (3.22) describes an extremely complex problem.

- Equation (3.2) contains a very large integral and highly complicated probability distribution function that should describe a multidimensional random process $\Gamma(t)$;
- The solution of (3.22) is concerned with all owners' decisions. In the event that there is insufficient knowledge regarding the behaviour of rivals, each owner must make own judgments.
- The objective functions of (3.22) are non-linear in the general case and contain discrete variables that describe the configurations of the power system objects under optimization. A large number of configuration variants can be generated.
- Long term planning covers time horizons between 10 and 40 years Meanwhile, the operation conditions are changed each hour.
- The impact of random processes should define the future. Named difficulties lead us to search for appropriated simplifications. Figure 8 represents the proposed general optimization modelling approach.

Analyzing expressions (3.2) and (3.22), the stochastic approach leads to the formulation of an objective function that is extremely complex in terms of required computational effort and wide scope of input data. To estimate the expected profit according to (3.22), the multidimensional integral must be calculated. It should be added that since the typical planning horizon is thousands of hours going into a corresponding dimension of the integral, the size of the integral may be too large for the problem under consideration. The difficulty of computing the integral (3.2) can be considered as the main reason for applying the scenario approach. (Antans Sauhats et al., 2015; R. Varfolomejeva et al., 2015).

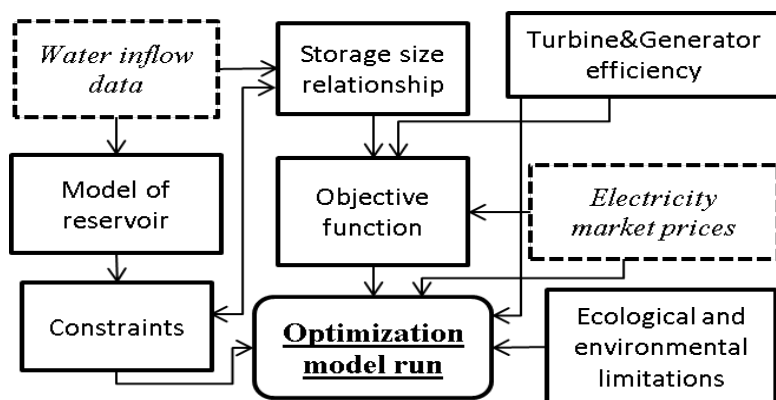


Figure 8. Optimization simulation flow chart

3.4. Decomposition approaches for optimization

It is assumed that the power facility is a player in the day-ahead market. To investigate long-term planning issue; it is necessary to formulate the time period of N_T years profit $M[R(Own_i)]$ maximization problem. The profit for the planning period can be calculated as the sum of the annual profit (3.23).

$$R_{\Sigma} = \sum_{j=1}^{N_T} M[R(Own_i)]_j \tag{3.23}$$

NPV is the difference between the present value of the investment's cash inflows and the present value of the cash outflows. Each year's profit is used when calculating the NPV (3.24) and can be expressed as:

$$NPV = \sum_{j=1}^J \frac{CF_j}{(1+d)^j} = \sum_{j=1}^{8760} \frac{(W_{ej} \cdot C_{ej}) - E_{xj}}{(1+d)^j} \tag{3.24}$$

Where;

CF_j - net the cash inflow during period j ;

d - the discount rate; it is supposed that d is constant during planning time.

j - the number of lifetime periods e.g. years, months;

W_{ej} - produced power at hour j ;

E_x - the expenses.

C_{ej} - electricity market prices at hour j ;

the sum of daily profits represents each annual profit R_i ;

$$R_i = \sum_{K=1}^{365} \sum_{J=1}^{24} M[R(Own_i)]_j \tag{3.25}$$

Analyzing (3.25), the profit of the day is linked with water amount into the reservoirs at the start and the end of the day under the study. The main objective of the model is to estimate the annual income and expenditure of storage facility projects during their lifetime. These parameters can then be used to calculate the payback period, NPV, and IRR for feasibility assessment. Consequently, a simplified profit-based optimization algorithm is presented by the structure of the algorithm in Figure 9.

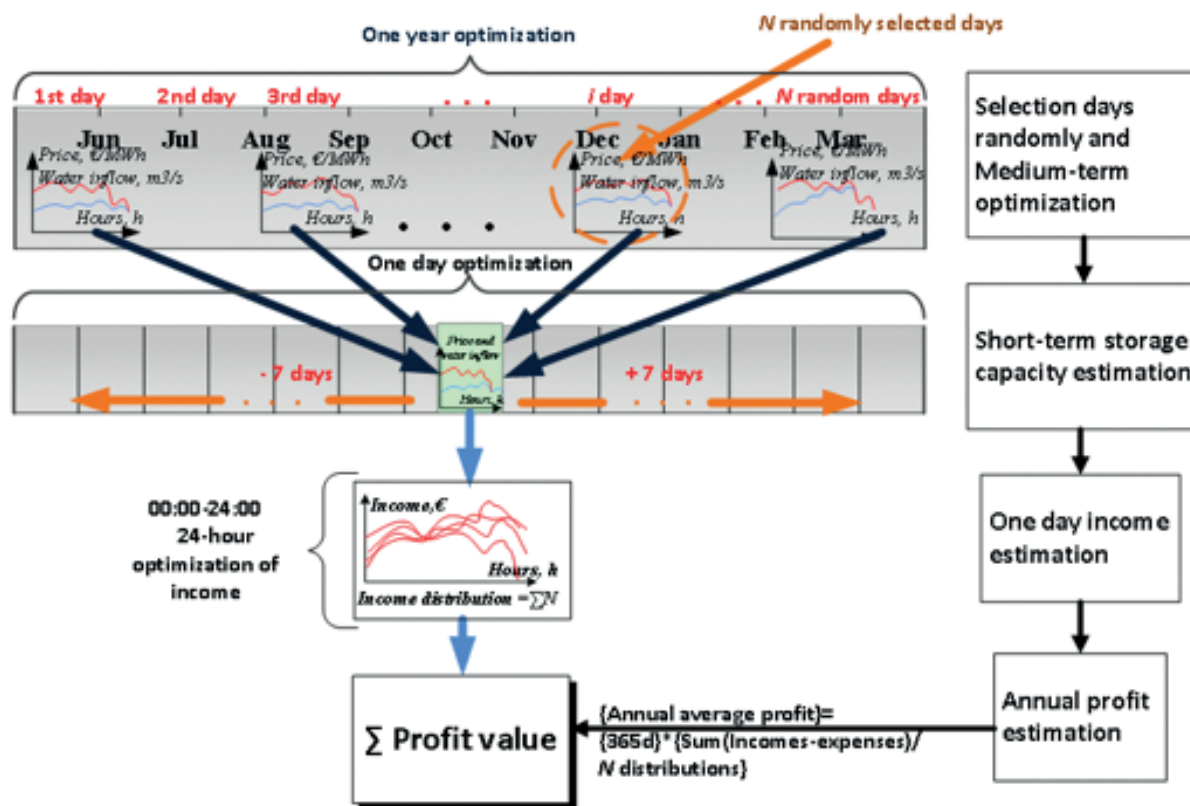


Figure 9. The main algorithm of optimization (Antans Sauhats et al., 2016)

The optimization steps are shown in Figure 10. A concrete day is chosen at random and the level of the reservoir is unknown. To make an accurately estimate of the reservoir level, 7 days before and 7 days after the selected day are selected. In the next step, only the previous reservoir levels are used. Profit maximization of the selected days is accomplished using a more accurate nonlinear model. Next, the short-term optimization results are generalized to the long-term using a time-averaged technique, thus combining long-, medium-, and short-term planning. The number of trials should be large enough to minimize the error rate.

3.5. Multiple probability simulation for profit forecasting

It is considered one day profit R_{ik} , which can be obtained on day i of year ' k '. Due to influence of random and uncertain parameters R_{ik} is also random. The R_{ik} can be expressed as (3.26):

$$R_{ik} = M[R_k] + \underline{R_{ik}} \quad (3.26)$$

where; $M[R_k]$ is the mathematical expectation of average profit in year ' k ';

R_{ik} is a centralized random variable. Also, it is assumed that $M[R_{ik}]$ can be presented as the sum of two components:

$$M[R_{ik}] = d(k)M_1[R_k] + M_2[\underline{R_{ik}}]; \quad (3.27)$$

Where $d(k)$ represents a multiplier that allows to take into account annual profit changes and is affected by price increases over the years. Expression (3.27) can be rewritten as follows:

$$M[R_{ik}] = M_1[R_k] + (1 + d(k)) \quad (3.28)$$

Calculations using (3.28) allow to estimate the mathematical expectation of any day's profit in a year using a statistical model of first-year process. It is supposed that $R_{i1} = R_{i2} = \dots = R_{iR}$. It means that probability distribution function of R_{ik} remains constant over the years. It is assumed that the processes observed in a day are stationary, which means it is possible to calculate the average profit as a time average value. This expression allows to calculate revenue using only a probabilistic representation of processes in the first year. This capability significantly reduces the number of tests in applying the Monte-Carlo method of profit estimation (Dong et al., 2019). If the power producer chooses to work in a market regime, for short-term SHPP optimization, firstly need to know the water flow rate and the electricity market prices which can be forecasted. Then we can decide how to use water resources by linear or non-linear programming. When we decide how much power we can produce on the next day by non-linear programming, then we can deal it with the market.

3.6. Long-term planning problem specifics

A mathematical statement of the problem is to be exhibited. In both cases (market conditions or fixed regime), we assume a nonlinear statement of the problem supposing that the shareholder's revenues $R(t)$ can be described by any nonlinear function as (3.29):

$$R(t) = f(V(t), \rho(t)) \quad (3.29)$$

where $V(t)$ stands for decision variables –the dimensions of the reservoir, the water head pond, the number of aggregates, the type and installed capacity of units, etc.;

$\rho(t)$ stands for the random processes which influence income –the energy prices and the water flow rate to the reservoirs. The annual planning problem is formulated as follows:

$$\text{maximize } \Rightarrow R(T) = \int_0^{T=8760} R(t) dF \quad (3.30)$$

The planning process consists of several steps of alternatives and their evaluation according to the selected time strategy. For HPP feasibility, the planning process is divided into the five following steps for calculating NPV and IRR:

1st step – Identification of the problem: Definition of the problem.

2nd step – Determination of the goals: What goals are to be achieved? What is to be maximized and minimized?

3rd step – Identification of the alternatives: What options are available?

4th step – Evaluation of the alternatives: Evaluation of all the options on a sound basis.

5th step – The final decision: Selection of the best alternative based on the results.

There are so many methodological difficulties in making the final decisions. It is not easy to make a decision and choose the scenario which has information as to, for example, how big is the reservoir, how big is the net head, turbine types, capacities, etc., but only one option, the best one, should be chosen. The optimization procedure is applied to each scenario to reach the goal, which is to maximize the profit for each scenario and to choose the best alternative. Table 2 represents the profit matrix of the strategies and incomes.

The goals of HPP owners:

- profit maximization with reliability and sustainability;
- compliance with legislative, environmental, and technological restrictions;

Table 2

The matrix of income

Strategies	Expected income by generated power				
	P_1	P_2	P_3	...	P_n
S_1	T_{11}	T_{12}	T_{13}	...	T_{1m}
S_2	T_{21}	T_{22}	T_{23}	...	T_{2m}
...
S_n	T_{n1}	T_{n2}	T_{n3}	...	T_{nm}

The mathematical statement of accumulation of profit $P_j(t)$ (3.31) can be considered as the sum of two processes depicting:

- income $I_n(t)$ from produced energy that is sold to consumers;
- expenses $E_x(t)$ that are necessary for energy production.

$$P_j(t) = I_n(t) - E_x(t) \tag{3.31}$$

We can declare that:

- income is a function of produced energy $p(t)$ and market prices $c(t)$;
- expenses are a function of capital investment and expenses for power plant running assessment.

All the processes used in (3.30) should be considered random processes. The numerical characteristics of such processes, particularly the average value, can be estimated based on the prediction of future processes.

The benefit of a supply of hydroelectricity is calculated by multiplying the quantity of electricity generated by the price of electricity. Ecological limitations, changes in the water flow rate, and changes in the electricity prices are also included in the equation. The data on the income from the sale of electricity collected and compared based on published data from the Nord Pool market prices (Day-Ahead Prices, Nordpoolgroup, 2022) and the feed-in tariff, which gives average values of 4.5 Eurocent/kWh.

Let us formulate the problem of investment optimization as maximization of the profit over the planning horizon. Annual profit estimation is calculated by the following formula:

$$AP = \sum_{t=1}^{8760} (AI - E_x) \rightarrow \max \tag{3.32}$$

Where;

AP – annual profit;

AI – annual income;

E_x – annual expenditure.

The objective of maximizing the expected profit $P_j(t)$ of the SHPP can be defined as follows:

$$P_j = \overbrace{\sum_{j=1}^{J.8760} p_j \cdot c_j}^{\text{Expected income}} - \overbrace{(K_i \cdot Inv + E_x)}^{\text{Expenses}} \Rightarrow \max \tag{3.33}$$

Where;

p_j – produced power;

c_j – market price;

K_i – the interest ratio;

Inv – investment amount;

E_x – expenses;

J – length of the planning horizon in years.

The subjects are:

- the highest and lowest level in the reservoir at hour j ;
- the limitation on the water flow through the turbines;
- ecological limitations; which is according to Turkish law, the amount of water released downstream must be at least 10 % of the average flow of the last 10 years (Koç, 2018);
- electricity production at hour j , which is the maximum power level, and generators and turbines are used when the efficiency rate is best;
- the value of the reservoir at the end of the optimization time is taken into account.

The maximization problem (3.32) must be solved by considering various financial, environmental, technical, and legal constraints. The function (3.33) is usually non-linear and depends on uncertain or random variables such as discount rate, electricity price, etc. The solution of the maximization problem by function (3.33) which is generally nonlinear; can be performed by the Monte-Carlo presented in Figure 10.

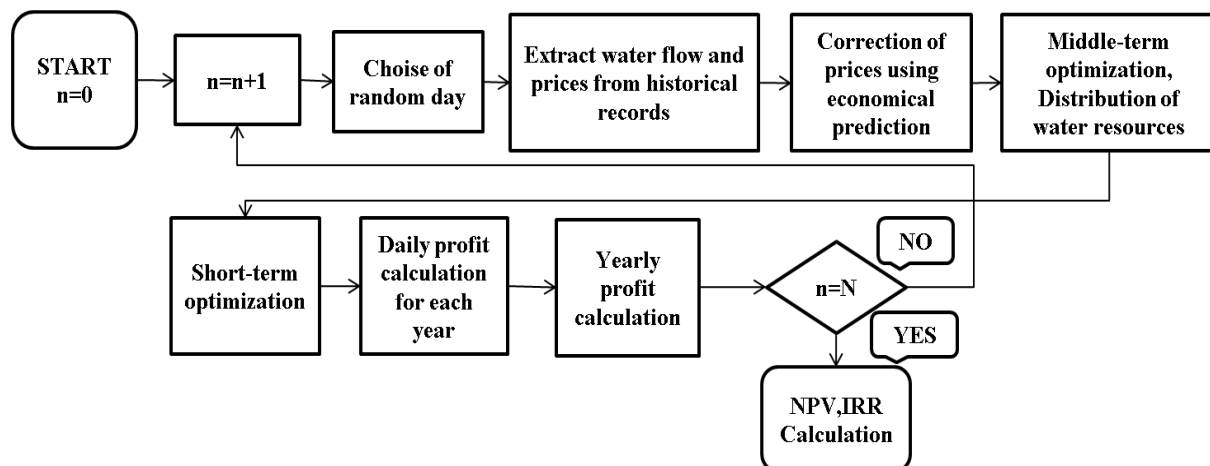


Figure 10. An algorithm based on the Monte-Carlo method to estimate the NPV of a HPP

Annual income must be calculated for HPP feasibility studies. Therefore, it is analyzed of the time period to have as small an error as possible. Firstly, the electricity market prices and water flow rate have to be known; then, it can be performed short and medium-term generation optimization, which allows to calculate annual profit. The Monte Carlo simulation serves to obtain a set of numerical results with a large number of repetitive randomly selected inputs (days). (Dong et al., 2019). When the Monte-Carlo simulation runs are performed by random values, we can analyze the percentage of error each duration outcome between 1 and 365 days. This will be shown graphically in [Figure 21](#).

3.7. The model of the reservoirs

Let us consider water storage models which have to describe H as a function of W_{in} and W_{fl} , (see [Figure 11](#)) namely;

$$H[(W_{in} - W_{fl}), T] \tag{3.34}$$

Where;

W_{in} – water flow in the river;

W_{fl} – water discharge.

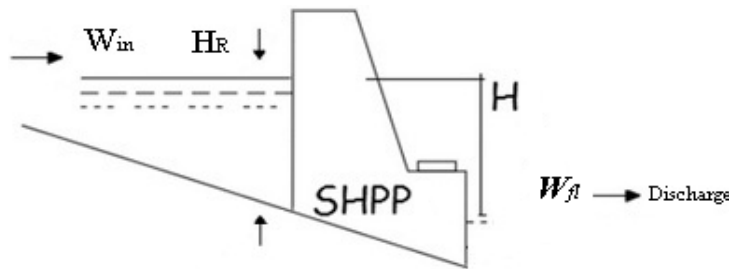


Figure 11. A model of the water reservoir

It is obvious that function (3.34) is non-linear in the common case. Only in the case of a reservoir with strongly vertical borders can this function be described by a linear function. Let us assume that such a reservoir is modelled. Two parameters are needed for model identification –the surface of the reservoirs (S) and the head of the reservoir (H_R). In this case an expression can be written as follows:

$$H = H_0 + (W_{in} - W_{fl}) \cdot \frac{T}{S} \tag{3.35}$$

where H_0 is the initial level of water (t=0)

Expression (3.35) can be used as the basis for the modelling of real-life reservoirs. For that, it is necessary to divide the real reservoir into a sufficient number of parts (sub-reservoirs), which allows to use (3.35) with acceptable accuracy. Let us assume that the length of the reservoir head is divided into n selections but T is short enough for making an additional assumption as follows: during time T, the reservoir level does not exceed the boundaries of the initial sub-reservoir. In this case, the algorithm shown below is obtained. (see [Figure 12](#))

Let us note that the water flow includes two components, water discharge through the turbine(s) and water consumed by the partners.

4. Examples and the Case Study

GoynuK Stream comes from a height of 2000 m in the mountains and is carried from 1700 m down to the KarlioVa district of Turkey. In this mountainous region, both the treated water source itself and the raw water source are under significant pressure that must be discharged at intervals, providing an opportunity to generate energy. The powerhouse and the reservoir have been built on the GoynuK River

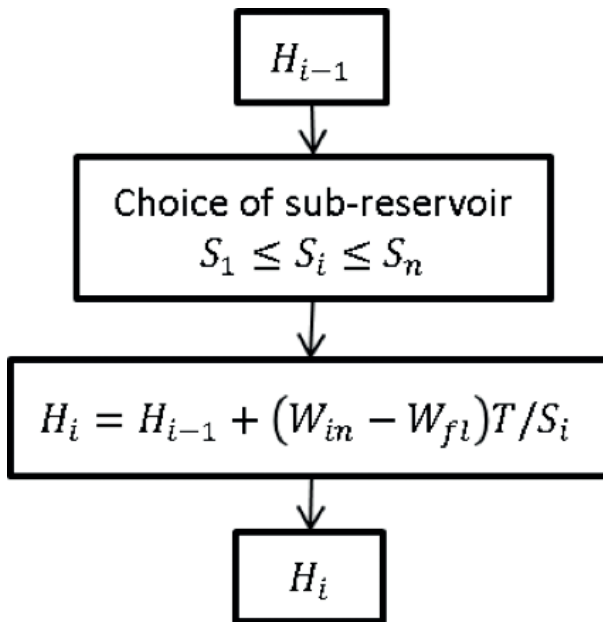


Figure 12. The algorithm of the water reservoir

in the city of Bingol, Eastern Turkey. The powerhouse started to produce electricity in September 2013. The Francis-type turbines at the Saf powerhouse with 2 units of 8.4MW and a unit of 4.2MW power capacity (50Hz). The length of the penstock is 810m. The capacity of the pool is 4605. The main data for Saf HPP is given the yearly average inflow rate is 5.48m³/s; the nominal capacity is 21MW; the head pond is 130m; the maximum water level before the reservoir is 3m; the total efficiency factor of the system set is 90% and the surface of the water in the reservoir is 40000 m². [Table 3](#) represents the technical specifications of Saf HPP.

Table 3

Optimization limitations for Saf HPP

Restrictions	Range
Power	$0 \leq P \leq 21$ MW
Water through the turbine	$0 \leq W \leq 17.03$
The water level in the reservoir	$1 \text{ m} \leq H \leq 3 \text{ m}$
Ecological water use limitation	Max 90%
Reservoir level at the end of day	Min 1 m

Within the feasibility phase, an economically and technically viable reservoir-type hydropower scheme is developed. In the framework of the analysis, the potential schemes were technically evaluated, the construction costs ([Table 4](#)) were estimated and the economic attractiveness was defined. The estimation of the construction costs includes both non-contract costs and field costs. Non-contract costs are related to engineering, environmental studies, site investigations, design, construction management, etc. Replacement, maintenance, and operation costs are not taken into account in construction cost estimates.

Given 21MWh of installed power capacity and 40ha of water storage surface, the total real investment is nearly 15000000€ for the Saf power plant. When the actual cost of the plant is known, it can be compared using the methodology described in the literature ([Fen et al., 2012](#); [Kotchen et al., 2006](#); [Tayefeh Hashemi et al., 2020](#); [Yildiz & Vrugt, 2019](#)). Due to the different economic levels of North America and Turkey; the price of expenses differs and calculation of the total cost of the power plant by (3.35) we received almost three times bigger amount.

Table 4

Estimation of the construction costs of Saf HPP

Type of work	Cost Estimation
Civil works	35%
Penstock	20%
Turbine, generator, switchgear field	20%
Power transmission line	5%
Electromechanical installations	10%
Study, project, consultancy	3%
Expropriation	3%
Insurance expenses	2%
Unknown	2%
Total Cost	15.000.000€

The constraints for Saf HPP:

a) the volume of reservoir (4.1):

$$1 \text{ m} \leq h_i^t \leq 3 \text{ m} \quad (4.1)$$

where h donates the water level; t is the time and i is the reservoir.

b) the discharge (4.2) of water from the reservoir:

$$Q_{i,\min}^t \leq Q_i^t \leq 17.03 \text{ m}^3/\text{s} \quad (4.2)$$

Where Q_{\min} and Q_{\max} are the lowest and highest amount of the water discharge, respectively.

c) the capacity of energy generation (4.3) of the power plant:

$$0 \leq P_i^t \leq 21 \text{ MWh} \quad (4.3)$$

where P donates the produced power.

d) the water balance equation (4.4) of the catchment:

The water flow rate (Q) through the turbine is a positive variable.

$$V_i^{t+1} = V_i^t + (I_i^t - Q_i^t) \cdot \Delta t \quad (4.4)$$

where I donates the naturel inflow and V represents the storage.

e) The limits of the reservoir (4.5, 4.6):

$$H_{i,1} = H_{i,\text{begin}} \quad (4.5)$$

$$H_{i,25} = H_{i,\text{end}} \geq 1 \text{ m} \quad (4.6)$$

where i represents the index of the reservoir, $H_{i,l}$ is the initial (starting point) level of the reservoir; $H_{i,end}$ is the final (ending point) level of the reservoir; it is mandatory that it be minimum 1m because of the fish gate and ecological factors.

f) privatisation of water use rights in Turkey; the amount of water to be released downstream for the continuation of the natural life will be at least 10% of the last ten-year average flow based on the project (4.7). If it is determined that this amount will not be sufficient considering the ecological needs, the amount is increased. If there is less than 10% of the average flow of the last ten years in the river, all of the water is left to the downstream for the continuation of the natural life. The type and properties of the fish gates are assessed at a certain construction phase. (Koc, 2018)

$$I_i^t \cdot 10\% \leq Q_i^t \tag{4.7}$$

The flow duration curve (FDC) represents an important element of hydrology study, which is useful to define different parameters of the hydropower scheme. This curve shows the proportion of time during which the discharge equals or exceeds certain values for a design section of the river. The FDC characterizes the relationship between the amount and frequency of daily, weekly, monthly (or other time interval) flows at a particular station in any stream. All values of a series of flow records from a river determining station (preferably no fewer than 15 years) are ordered from highest to lowest value the curves answer the question: What amount of energy can be generated annually? Regularly, design discharges corresponding to 20% of the time are proper as the design discharge (Kuriqi et al., 2020). The FDC of the multi-year average daily discharges of the Goynuk River is depicted in Figure 13. Following this data, exceeding the multi-year average annual flow for 12% of the time during one year in the design segment equals 17.03 m³/s, this discharge provides full power generation for 44 days throughout the year (see Figure 14). Based on this flow duration curve, different discharges with different exceedance can be selected from a given hydrological series.

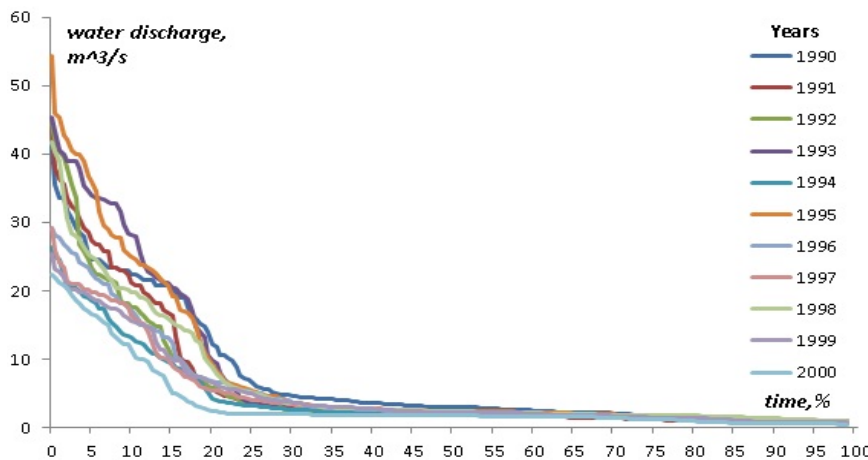


Figure 13. FDC of multi-annual mean daily discharge

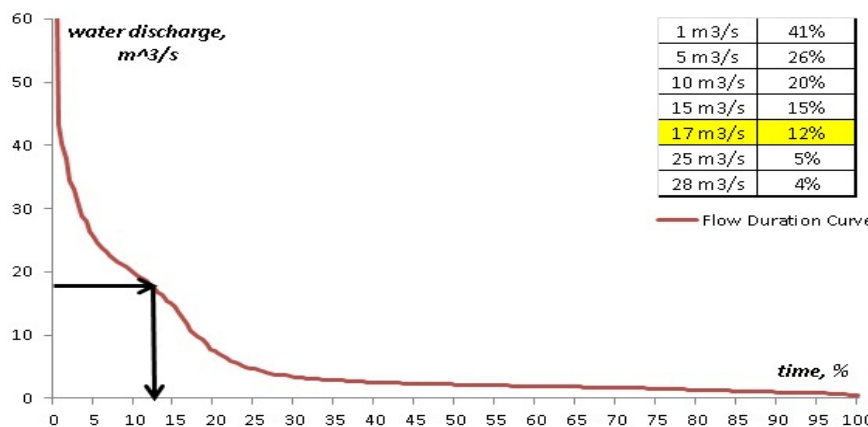


Figure 14. The average FDC for the years 1990–2000

The daily water flow rate of the observed discharge data is recorded by the Hydrology Department of the National Environmental Agency of Turkey (DSG). The initial data contain 35-year of observations which allow us to make reliable statistical analyses. Generally, minimal discharges are observed in the winter and summer periods but overflow appears in springtimes. This data is used for a feasibility study which will be explained in the next subchapter. According to the feasibility report of Saf HPP, the expected annual average electricity production is 42.17 GWh (see [Figure 15](#)). The provided 40 years of data taken between the years of 1965 – 2004 is used in the calculations.

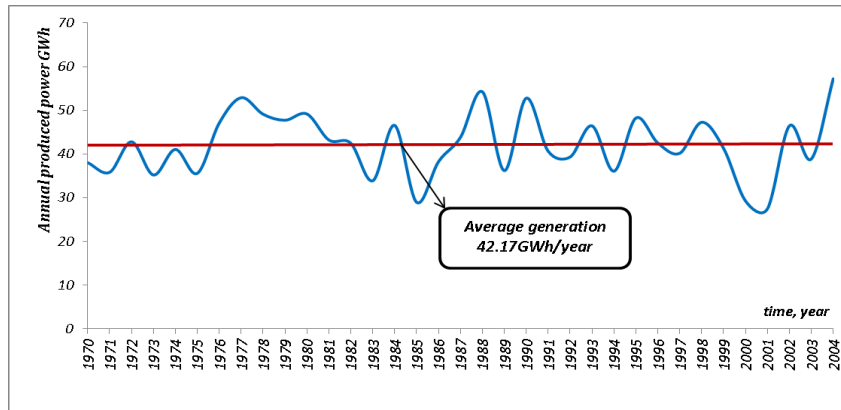


Figure 15. The Saf HPP annual average electricity production estimation

4.1. Application results and comparison of optimization methods

Deterministic models are systems in which there is no randomness in determining the future states of the system. That is, for a well-modeled deterministic system, the system will always give the same result under the same conditions and for the same initial states. On the other hand, Stochastic models contain randomness. This randomness can be in system parameters, dynamics, inputs. Therefore, the output of the system will have similar randomness. In such systems, the same results may not be obtained even if the same experiment is repeated under the same conditions. Let's compare the methods and generating tasks for SHPP feasibility studies. The stochastic and deterministic tasks have common features:

- the main objective function can be formulated as profit maximization in both tasks;
- solutions must be made based on process estimation;
- in both cases, optimization procedures should be non-linear and capable of taking into account a large number of decisions.

a) The result of deterministic method:

The operating method for Saf HPP, which takes into account the constant water flow and electricity price, is shown in [Figure 16](#). With the fixed-price operation, since it is not used in the optimization procedure and the electricity price is fixed, the electricity producer can maximize the income by only increasing the amount of energy produced.

Interpretations of the result obtained will be presented along with an analysis of the stochastic optimization results in the upcoming sub-chapter.

b) The stochastic method:

For decision-making problems under uncertainty, stochastic programming provides a comprehensive framework with the knowledge of stochastic processes that define uncertain parameters such as demand growth. When the parameters of electricity prices with uncertainty and water inflow to reservoirs are defined by stochastic processes, it is possible to formulate the uncertainty of these parameters as a mathematical programming problem. In the stochastic programming model, if the values of the parameters contain

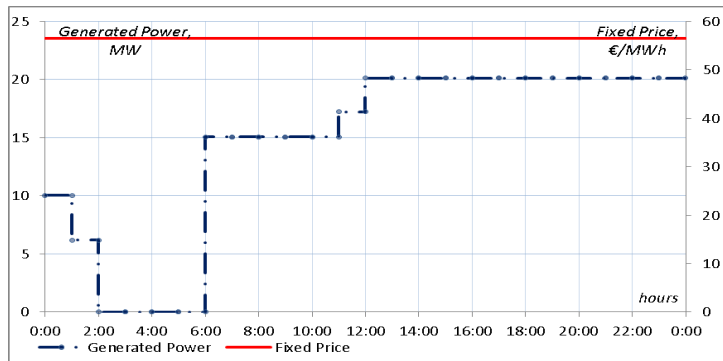


Figure 16. The generation by a fixed price schedule

uncertainty, these parameters can be defined as distributions or multivariate stochastic processes. Thus, the problem turns into an optimization problem in function spaces, and the decisions depend on the observed values of these processes. Figure 17 shows the actual power produced for four consecutive days at Cobanlı HPP, where the production results are not optimal.

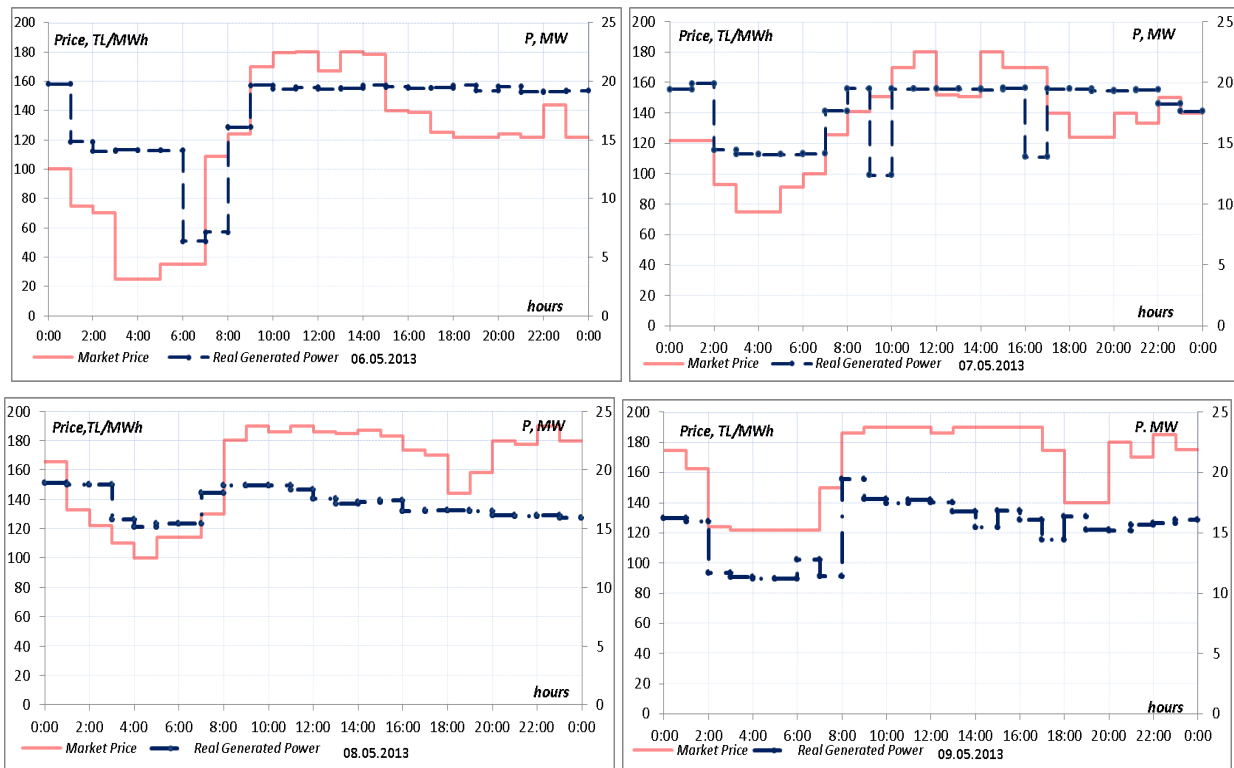


Figure 17. Actual generation in the market conditions from 6 to 9 May (Coban et al., 2015)

The results obtained when electricity generation is optimized according to the market price chart are presented in Figure 18. The SHPPs collect water from the reservoir when market prices are low and use water when market prices are high. The results of the optimization show the similarity of 24-hour power generation with more accurate regime planning to generate maximum revenue. The optimization model has been implemented taking into account the current situation and can be applied to future storage capabilities, which will be explained when discussing the feasibility study of Saf HPP in the next subsection.

As seen from the results, in Figure 18 that water is stored when the market prices are low and starts production when the market price increases. If Cobanlı HPP could operate at a fixed price during these four days (06.-09.05.2013), the income was 2094690 Turkish Lira (TL). The real income of the power plant, which is operated at market prices, was 236809 TL. However, according to the optimization model with

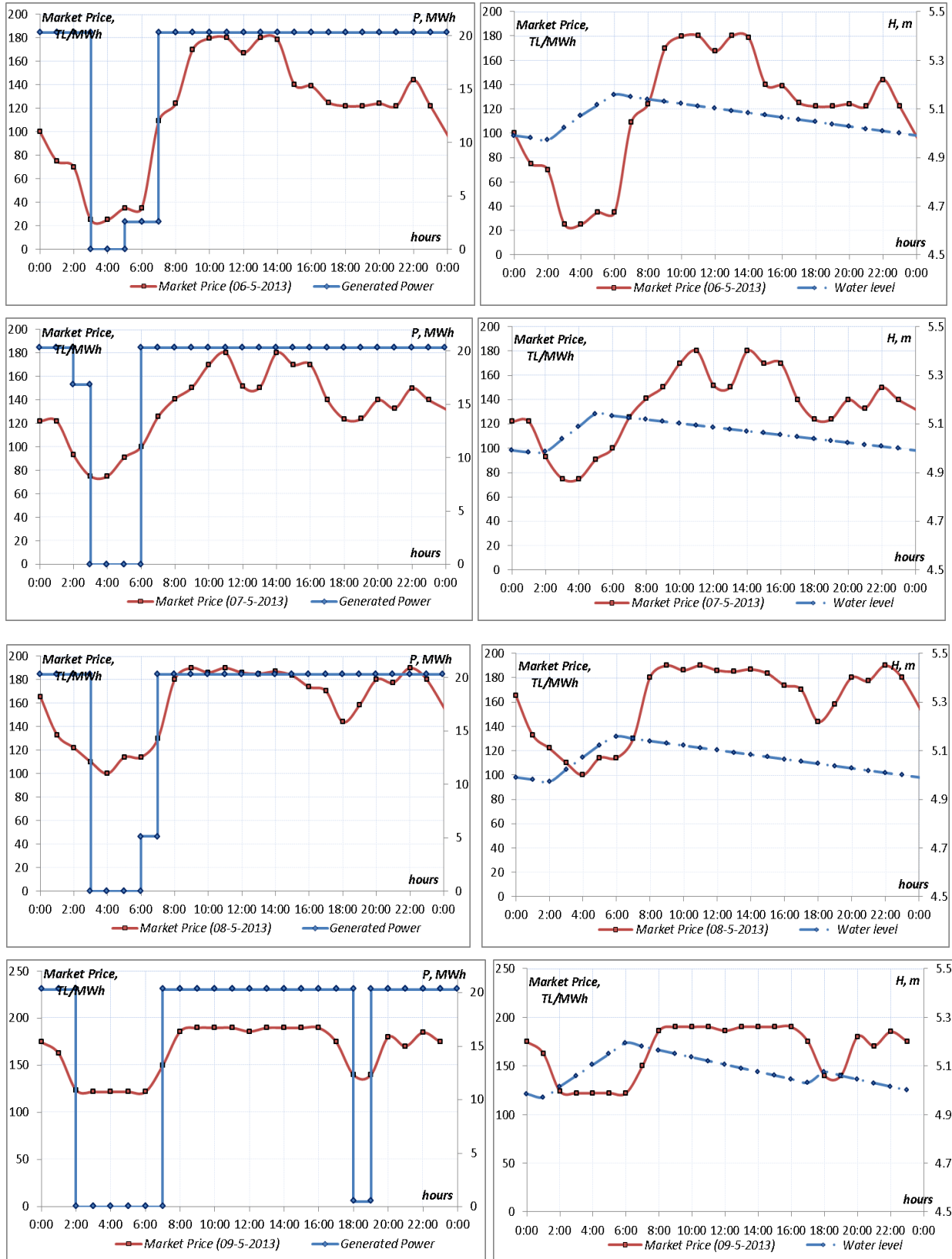


Figure 18. Optimized electricity generation for Cobanlı HPP (6-9 May)

market price, the income reaches 246448 TL. The results allow it to be concluded that in the stochastic case, the power generator provides an opportunity to maximize the amount of income under conditions of limited resources. At the same time, the optimization procedure applied, namely the Quasi-Newton method, succeeded in obtaining the global maximum of the objective function in all cases.

4.2. Cost-benefit analysis for Saf HPP

Estimated costs and input parameters are depicted in Table 4, which summarizes the cost estimate of various reservoir capacities for 21 MW, 35 MW, and 50 MW power capacities. The investigations have been carried out based on the 17 m³, 28 m³/s and 35 m³/s discharges and the head of the pond is constant 130 m (see Table 5). By calculating the profitability for each alternative, there is an opportunity to see if the current design discharge of 17.03 m³/s and the capacity of 21 MW are an optimal choice.

Table 5

Cost estimation (M.Euro) for various design flows, including contingencies

Reservoir Capacity			Power Capacity
200 ha	100 ha	40 ha	
21,16	21,06	21,0	50 MW
18,16	18,06	18,0	35 MW
15,16	15,06	15,0	21 MW

Optimization was carried out at a pre-selected time for three different situations, taking into account the initial and final conditions of the 360-hour period. In the reference case, the initial and final degree of reservoir filling is equal (75%); in the second case, the reservoir level drops from 100% to 33%, and in the third case the level increase from 33% to 100%. The second and third case cause 0.89% and 0.88% respectively income change in 24-hour income. Therefore, it can be concluded that the initial and final state of the reservoir in the medium-term horizon do not have a significant effect on profit. Consequently, all other calculations have been made assuming the degree of reservoir level is 75% at both the beginning and end of any 360-hour period. Figure 19 shows the advanced stochastic optimization method for Saf HPP, which takes into account hourly water flow rates and market prices over 360 hours.

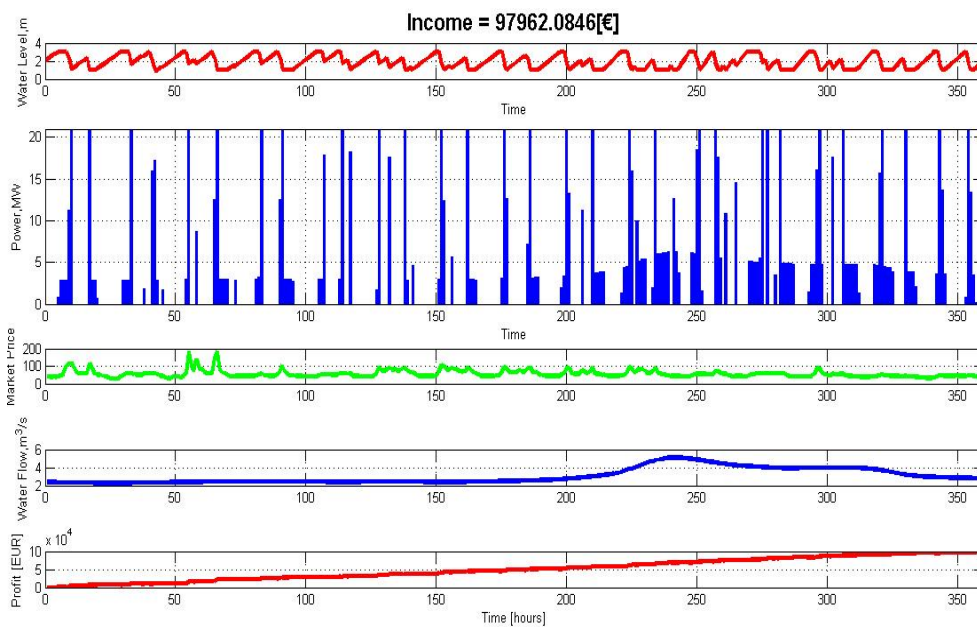


Figure 19. The results obtained from the developed optimization program

The optimization results of the developed algorithm allowed us to choose the best possible alternative for Saf HPP. Finally, the NPV estimate is obtained by summing the discounted total annual revenue estimates. If the NPV of the project is positive, the execution of the project is estimated to be efficient and the CBA method suggests that the project is viable. It is assumed that the production period is 30 years, the total efficiency of the hydroelectric power plant is 90%, the construction plant will last for 2 years, and the annual standstill losses are 2 days, and various interest rates are applied.

Following the existing regulations in Turkey to ensure environmental protection conditions downstream of the intake site of Saf HPP, 10% of the mean annual water discharges shall be selected as the minimum ecological discharges at the design section. The annual escalation rate of the energy price is assumed as 3%. Annual operation and maintenance costs are usually quoted as a percentage of the current year’s income or the investment cost per kW per year. Typical values range between 1% and 4%. The IEA assumes 2.2% for large-scale hydropower and 2.2% to 3% for small-scale projects, with around 2.5% a global average (Irena, 2012; WorldBankGroup, 2015). In this study, it is assumed that annual fixed operating and maintenance costs constitute 3% of the total income.

The optimization model is implemented in MATLAB R2013a with solvers by the Quasi-Newton method in a non-linear optimization procedure. Since the objective function is a non-linear constrained-bounded and multivariable function employed “fmincon” (multidimensional constrained nonlinear minimization) (Singh & Singal, 2018) to find the optimal solution. In optimization, the technical limitation of the turbine as well water reservoir constraints are taken into account. Also, the Monte-Carlo method can be used to avoid difficulties. A large number of trials leads to higher accuracy of calculations, while also increasing the computation time. We ran several simulations per year using a different number of trials to find an appropriate number of Monte-Carlo trials that did not significantly reduce the accuracy and also increase the computational load too much. The reference case is 365 trials (days), and various simulations which are compared with the baseline to determine the error. Figure 20 represents randomly chosen days in a year for Monte-Carlo trials.

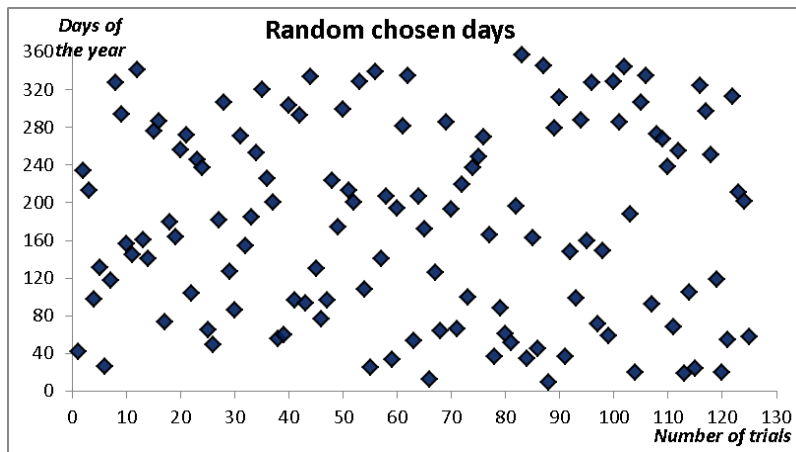


Figure 20. Randomly chosen days in a year for Monte-Carlo trials

The program is run for a single dam operation. All calculations were performed using 2 cores on a Windows PC with Intel I3 CPU processors, 2.53 GHz, 4 GB RAM, and Windows 7 operating system. As seen in Figure 21 it is determined that 120 trials (days) were a sufficient number because it neither introduced a very high estimation error (4.6%) nor required excessive computation time (computation time was 105 minutes). According to the results summarized in Figure 19; a possible improvement can be made by introducing a more efficient algorithm with better performance for a large number of decision variables.

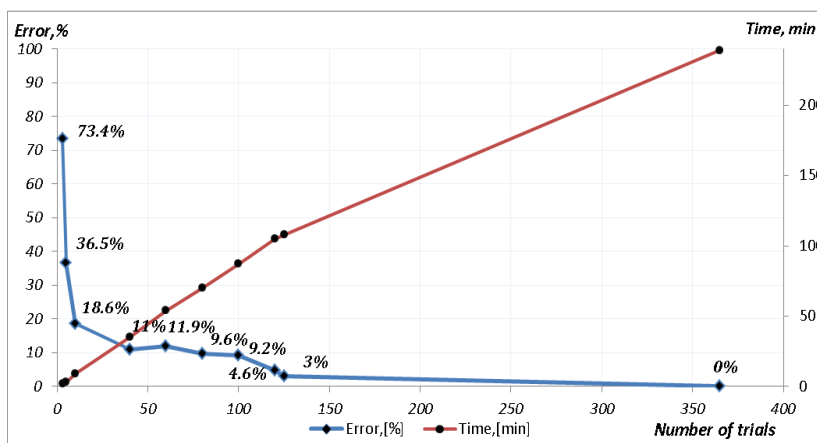


Figure 21. The number of Monte-Carlo trials and calculation error

The results of the IRR and NPV calculations for the 4%, 6%, and 8% interest rates (IR), as well as the cost estimates for the various design flow values, including contingencies, are summarized in Table 6. It is concluded that the best alternative is to choose the 6th one (A6) with a power capacity of 35 MW and a reservoir capacity of 200 ha; The IRR is 15.5% and it takes 12 years to reach the breakeven point.

Table 6

Types of alternatives and the results of IRR and NPV for 30 years

Alternative	Deterministic approach, 8% IR		Stochastic approach, 4% IR		Stochastic approach, 6% IR		Stochastic approach, 8% IR	
	NPV, €	IRR, %	NPV, €	IRR, %	NPV, €	IRR, %	NPV, €	IRR, %
A1	19684434	15.8	21825628	16.2	20587278	15.5	19291375	14.8
A2	19628359	15.8	23429968	16.7	22186664	16.0	20885577	15.3
A3	19534901	15.7	23434537	16.7	22182978	16.0	20873252	15.3
A4	21954523	15.4	25782054	16.2	24296034	15.5	22740950	14.8
A5	21898448	15.4	28024941	16.9	26533967	16.2	24973700	15.4
A6	21804990	15.3	28486431	17.0	26987201	16.3	25418295	15.5
A7	19150785	13.6	24057220	14.6	22323529	13.9	20509265	13.2
A8	19094710	13.6	25972403	15.2	24233758	14.5	22414310	13.7
A9	19001252	13.5	28075139	15.7	26328239	15.0	24500152	14.3

It is difficult to obtain precise results using the deterministic technique because it does not take into account the uncertain and random variables. Figure 22 compares the highest incomes obtained by the stochastic and the deterministic approach for a 30-year horizon.

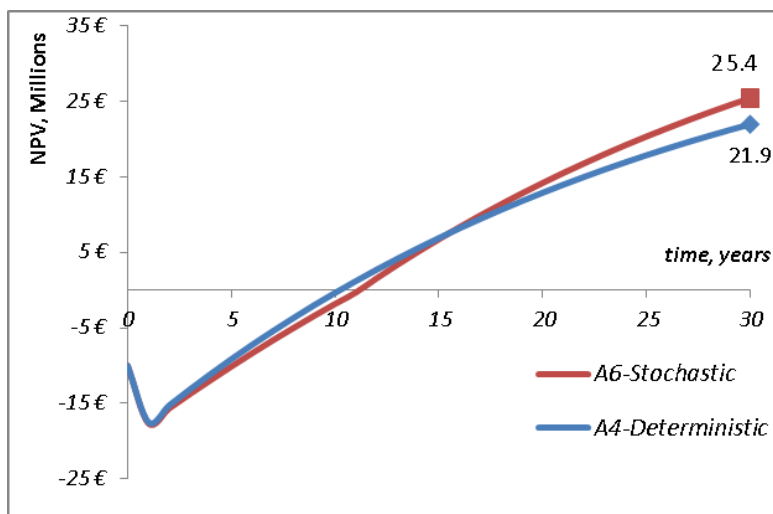


Figure 22. A comparison of deterministic and stochastic approaches

4.3. The influence of reservoir capacity and discount rate on the profit

The construction of hydroelectric plants is a large-scale project that requires a long lead time for site studies, environmental impact assessments, and hydrological studies. Generally, reservoirs are used for water supply, irrigation, electricity generation, flood control, recreation. In order to maximize a reservoir's

usage of a river namely store as much as water, it is essential to prepare the plan that considers all aspects as well as long-term prospects. It is natural that the way of building about the selection of dam sites differs according to the purpose of the project. [Figure 23](#) and [Figure 24](#) verify that stored water in the reservoir is released through the turbine and generates electricity during peak hours in other words when demand is higher. The difference lies in installed power capacity and water storage capacity; [Figure 23](#) represents a reservoir of 40ha and at the end of the day the income is 6518€. [Figure 24](#) represents a reservoir of 200ha and the income is 6699 €; it means that this storage can accumulate a larger amount of water and transform its potential energy into electrical energy during peak hours that increases flexible power generation and maximizes the income.

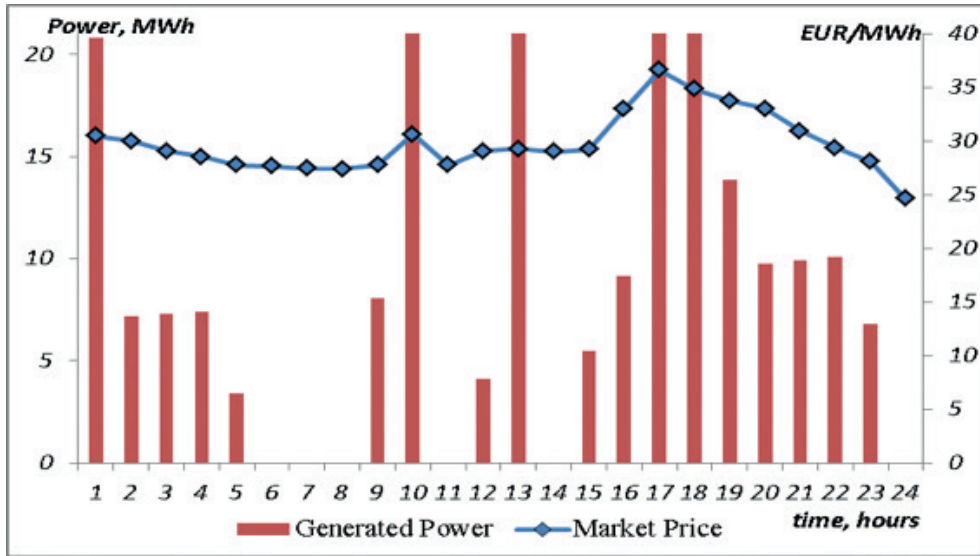


Figure 23. Generation for a 40-ha reservoir capacity

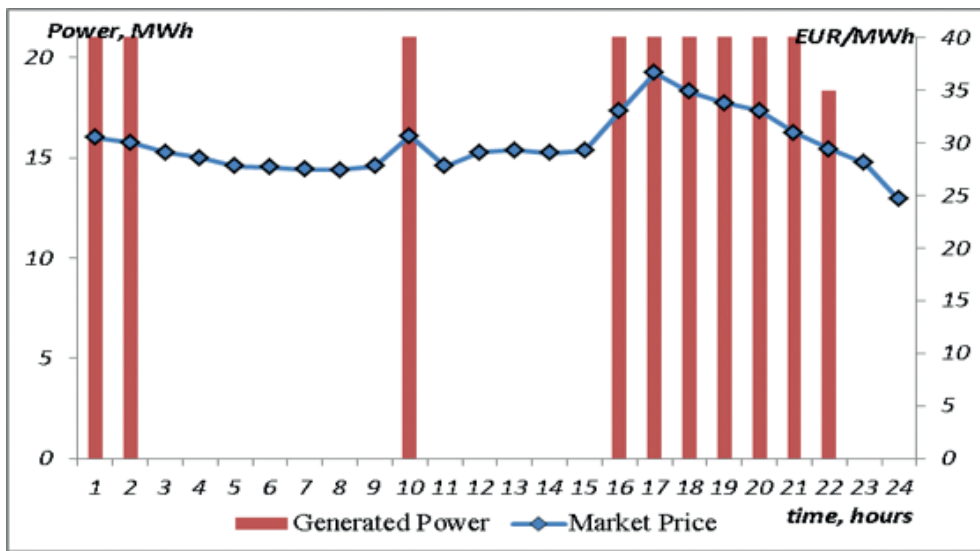


Figure 24. Generation for a 200-ha reservoir capacity

It is assumed four different alternatives for the feasibility study; each of them has various designs which correspond to small, medium, large, and dam-type reservoir capacity. [Figure 25](#) represents the existing reservoir for Saf HPP which has 3 m deep and 40 ha.

Let us consider a dam-type reservoir (see [Figure 26](#)) for Saf HPP with a length of 110 m and a depth of 20 m and a water storage area of 200 ha. It is assumed that the electricity producer is a market player and can export electricity to the grid, the operation of the energy market is based on day-ahead rules, electricity



Figure 25. Existing reservoir for Saf HPP (3 m deep-40 ha)

market prices are exogenous for the power producer, each day, the power producer participates in the day-ahead market. For building, an optimization procedure is performed beforehand to maximize the profit, the behaviour of other market players is neglected.



Figure 26. Dam-type reservoir for Saf HPP

A dam is an obstacle that holds back water; Dams are mainly used to divert, manage and/or prevent excess water flow to certain areas. Dam-type reservoirs are built in a valley based on the natural topography to provide most of the reservoir basin. Dams are often built downstream of a natural basin in a limited part of a valley. The valley sides act as natural walls with the dam located at the narrowest practical point to ensure as low construction cost as possible and as high efficiency as possible. The economic and technical parameters for each alternative are summarized in [Table 7](#).

The feasibility study is related to different numbers of alternatives, and each alternative is based on the expected scenarios. It is underlined ones more that these extensive calculations can be simplified using the Monte-Carlo method which offers average profit. In Turkey private companies get a license for 49 years from the government and the feasibility study is done for 49 years ([Üçüncü, 2018](#)). [Table 8](#) summarizes the

Table 7

Economic and technical parameters of the power plants under the study

Alternative		Cost estimation, €
A1	200 ha-21 MW - Dam	15.660.000
A2	200 ha - 21 MW	15.160.000
A3	100 ha - 21 MW	15.060.000
A4	40 ha - 21 MW	15.000.000

economic feasibility results for Saf HPP; the deterministic approach uses a discount rate of 7%, with an annual interest rate of 6% for a 10-year payback time for each alternative, and the stochastic approach uses three cases with discount rates of 3%, 5%, and 7%, respectively.

Table 8

IRR and NPV results for Saf HPP

Alternative	Deterministic approach, 7% discount rate		Stochastic approach (1), 3% discount rate	Stochastic approach (2), 5% discount rate	Stochastic approach (3), 7% discount rate	Stochastic approach (1, 2, 3) IRR, %
	NPV, €	IRR, %	NPV, €			
A1	24147161	13.91	110484765	63344684	37647625	17.42
A2	24732171	14.26	106767761	61192738	36346641	17.36
A3	24849173	14.33	105420216	60379112	35824568	17.28
A4	24919374	14.38	103154375	58966493	34879630	17.06

The discount rate has a reasonable effect on the NPV level. The NPVs of profit calculated at the 3% interest rate is almost 3 times higher than the 7% discount rate. Figure 27 shows the NPV results for each reservoir model.

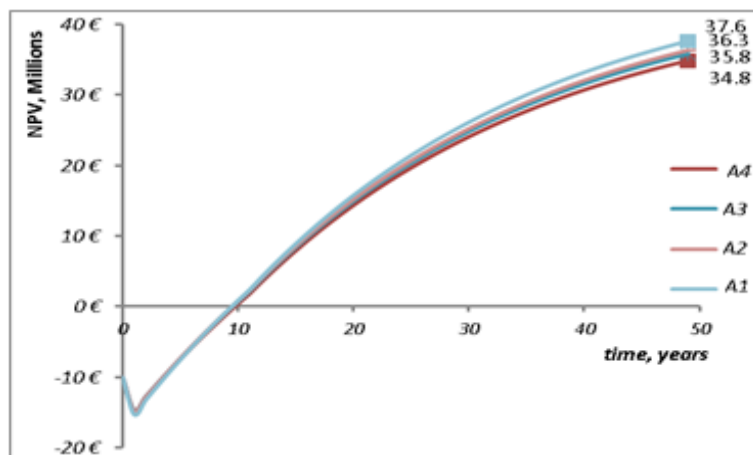


Figure 27. NPV of different reservoirs and varying capital costs

As a conclusion, hydropower plant reservoirs can be created by controlling a water stream that drains an existing body of water. In addition, a dam can be used in river valleys or a reservoir can be constructed by building retaining walls and embankments, or by digging the ground. The results proved that for Saf HPP located in a hilly area, it would be effective to construct a dam type reservoir to store more water to achieve an income maximizing objective function. The discount rates also significantly influence the amount of profit gained. Figure 28 represents the comparison of NPV calculations for various discount rates in the 4th alternative.

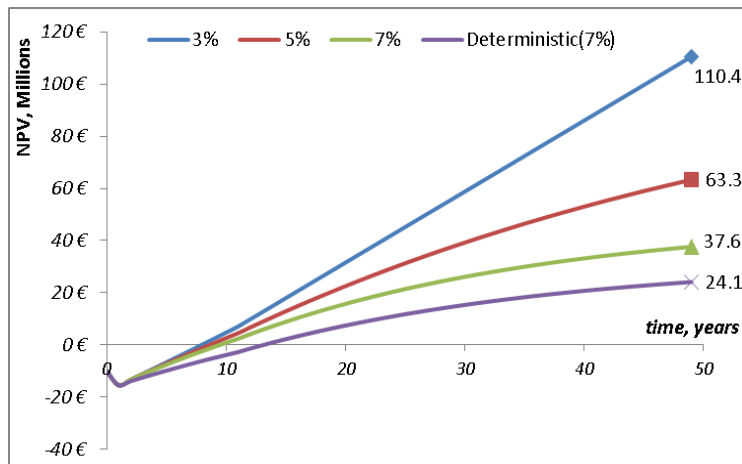


Figure 28. The effect of the interest rate on the investment

Discounted cash-flow analyses are instrumental in investment decision-making during the pre-feasibility stages of the investment and since it is reasonable to formulate an investment strategy that should have an application to the cash flow towards the risk management of the economic part of the investment. The described approach can be easily extended to the more complicated case study, where maybe chosen number and type of turbines, the head-ponds, the deepness of reservoir, and its capability.

To be able to solve the SHPP optimization task, it is necessary to take into account the specific structures and parameters of the power plant and market price. The most widely used methodology (deterministic) of feasibility studies is not useable in market conditions because it does not take into account hourly energy prices and the flexibility of the power plants. The Monte-Carlo method is useful while analyzing income and schedule. With the help of the Monte-Carlo analysis, the calculation of the long-term HPP income planning can be solved. A cost-benefit analysis model has been expanded to cope with social, economic, and environmental factors under uncertainty in order to appraise hydropower projects. In the application to Saf HPP, various discount and interest rates of long-time preference, a positive NPV will likely be obtained. The elaborated algorithm of the problem solution is based on the Quasi-Newton method. A solver program in Matlab R2013a has been developed. The considered numerical examples show its efficiency. Our experience shows that the program works well, and the received results are approved by the requester. A discount and interest rate causes a considerable influence on the number of future benefits and costs.

5. Conclusions

The study discussed the application of the algorithm techniques to find the optimum operating policy for reservoirs and the power plant. The stochastic approach results were compared with the traditional deterministic programming. The optimization problem is formulated in a way that maximizes the total energy income. However, there may be situations where the goal is the maximization of the energy generation or achievement of multiple purposes such as supplying irrigation, flood mitigation, creating a coalition with potential partners, or domestic water together with energy generation. The selection of the optimization procedure is a complicated task. From many of the eventual algorithms, the Quasi-Newton method is selected for further verification and applied for the solution of maximizing obtained profit at Saf and Cobanlı HPP. The developed models are tested by Nord-Pool electricity market prices and satisfactory results are achieved. Comparing the NPV results from the deterministic and stochastic methods, results with the stochastic methods are significantly more accurate than with the deterministic model. The optimization results show that the proposed models perform very well in the absence of volatility. The direction of this economic feasibility assessment is to analyze and determine opportunities for new small hydropower development in Turkey and the developed model can be universally applied to other countries. A CBA is a systematic evaluation of the disadvantages (costs) and economic advantages (benefits) of a set of investment alternatives. The impacts of timing, discount, and interest rate represent a feature of CBA that can significantly affect results. The output of the analysis consists of the NPV and the IRR.

These parameters are used to assess the viability of the investment. Design, hydrology, and alternative solutions have been analyzed and the results from the financial due diligence study indicate that the Saf HPP project is financially viable given a 30-year concession period in an open market perspective. The stochastic statement, which is a scientific and practical model that can be applied around the world and has been successfully tested in the Turkish SHPP in terms of the country's electricity sector, includes an analysis of the potential benefits of generation companies, wholesalers, and investors.

Acknowledgement

This article was produced from the doctoral thesis with title of Optimization Techniques in Short- And Long-Term Power Production at Small Hydropower Plants, prepared by Hasan Huseyin Coban at Riga Technical University, Institute of Power Engineering under the supervision of Prof. Dr. Antans Saulis Sauhats.

Author Contributions

Hasan Huseyin Coban: Methodology, Data curation, Writing-original draft, Visualization, Investigation, Validation, Conceptualization.

Antans Sauhats: Supervision, Conceptualization.

References

- Alterach, J., Popa, B., Magureanu, R., Šantl, S., Kozelj, D., Rak, G., Skroza, A., Steinman, F., Zenz, G., Harb, G., Bostan, I., Dulgheru, V., Bostan, V., & A. Sochirean. (2010). *Manual Addressed to Stakeholders with the Description of Methodologies to Improve SHP Implementation in SEE Countries*.
- Alvarez, M., Cuevas, C. M., Escudero, L. F., Escudero, J. L., García, C., & Prieto, F. J. (1994). Network planning under uncertainty with an application to hydropower generation. *Top*, 2(1), 25–58. DOI: <https://doi.org/10.1007/BF02574759>
- Arai, M., Tanaka, K., Abe, R., & Mogi, G. (2011). Time-Series Analysis in Power Supply System To Achieve a Sustainable Economic Growth in Bangladesh. *Icme2011, December*, 18–20.
- Asif, M., & Muneer, T. (2007). Energy supply, its demand and security issues for developed and emerging economies. *Renewable and Sustainable Energy Reviews*, 11(7), 1388–1413. DOI: <https://doi.org/10.1016/j.rser.2005.12.004>
- Bachir, M. L. (2017). *Impact of Hydrology and Financial Cost Analysis On The Production Of Mini Hydropower: The Case Of Djendjenni, Mali*.
- Barros, M. T., Lopes, J. E., Yang, S. L., & Yeh, W. W. G. (2001). *Large-scale hydropower system optimization*. IAHS Publications.
- Belbo, T. (2016). *Cost Analysis and Cost Estimation Model for 1-10 MW Small-Scale Hydropower Projects in Norway Torfinn Belbo*.
- Benli, B., & Kodali, S. (2003). A non-linear model for farm optimization with adequate and limited water supplies Application to the South-east Anatolian Project (GAP) Region. *Agricultural Water Management*, 62(3), 187–203. DOI: [https://doi.org/10.1016/S0378-3774\(03\)00095-7](https://doi.org/10.1016/S0378-3774(03)00095-7)
- Berry, R. A. (2003). *Ensemble Averaged Conservation Equations For Multiphase, Multi-Component, And Multi-Material FLOws* (Issue August). DOI: <https://doi.org/doi:10.2172/910743>
- Bilgili, M., Bilirgen, H., Ozbek, A., Ekinci, F., & Demirdelen, T. (2018). The role of hydropower installations for sustainable energy development in Turkey and the world. *Renewable Energy*, 126, 755–764. DOI: <https://doi.org/10.1016/j.renene.2018.03.089>

- Bin, D. (2021). Discussion on the development direction of hydropower in China. *Clean Energy*, 5(1), 10–18. DOI: <https://doi.org/10.1093/ce/zkaa025>
- Bulut, U., & Muratoglu, G. (2018). Renewable energy in Turkey: Great potential, low but increasing utilization, and an empirical analysis on renewable energy-growth nexus. *Energy Policy*, 123(September), 240–250. DOI: <https://doi.org/10.1016/j.enpol.2018.08.057>
- Coban, H. H. (2020a). A 100% Renewable Energy System: The Case of Turkey In The Year 2050. *İleri Mühendislik Çalışmaları ve Teknolojileri Dergisi*, 1(2), 130–141. Retrieved from: <https://dergipark.org.tr/en/pub/imctd/issue/59372/817991>
- Coban, H. H. (2020b). Maximizing Income of a Cascade Hydropower with Optimization Modeling Journal of Renewable. *Journal of Renewable Energy and Enviroment*, 7(1), 12–17. DOI: <https://doi.org/http://dx.doi.org/10.30501/jree.2020.105267>
- Coban, H. H. (2021). How is COVID-19 affecting the renewable energy sector and the electric power grid? *European Journal of Science and Technology*, 27, 489–494. DOI: <https://doi.org/10.31590/ejosat.890451>
- Coban, H. H., Varfolomejeva, R., Sauhats, A., & Umbrasko, I. (2015). Hydropower Plant Regime Management According to the Market Conditions. *2nd International Congress on Energy Efficiency and Energy Related Materials (ENEFM2014)*, 141–152.
- Davis, S. J., Lewis, N. S., Shaner, M., Aggarwal, S., Arent, D., Azevedo, I. L., Benson, S. M., Bradley, T., Brouwer, J., Chiang, Y. M., Clack, C. T. M., Cohen, A., Doig, S., Edmonds, J., Fennell, P., Field, C. B., Hannegan, B., Hodge, B. M., Hoffert, M. I., ... Caldeira, K. (2018). Net-zero emissions energy systems. *Science*, 360(6396). DOI: <https://doi.org/10.1126/science.aas9793>
- Day-ahead prices, Nordpoolgroup. (2022). Day-Ahead Prices. Retrieved from: <https://www.nordpoolgroup.com/Market-data1/Dayahead/Area-Prices/LV/Hourly/?view=table>
- De Jong, P., Tanajura, C. A. S., Sánchez, A. S., Dargaville, R., Kiperstok, A., & Torres, E. A. (2018). Hydroelectric production from Brazil's São Francisco River could cease due to climate change and inter-annual variability. *Science of the Total Environment*, 634, 1540–1553. DOI: <https://doi.org/10.1016/j.scitotenv.2018.03.256>
- Demirtas, O. (2013). Evaluating the best renewable energy technology for sustainable energy planning. *International Journal of Energy Economics and Policy*, 3, 23–33.
- Desreumaux, Q., Leconte, R., & Côté, P. (2014). Role of hydrologic information in stochastic dynamic programming: a case study of the Kemano hydropower system in British Columbia. *Canadian Journal of Civil Engineering*, 41(9), 839–844. DOI: <https://doi.org/10.1139/cjce-2013-0370>
- Dong, H., Ye, F., & Fu, W. (2019). Stability reliability of a cutting slope in Laohuzui Hydropower Station in Tibet of China. *Geomatics, Natural Hazards and Risk*, 10(1), 935–957. DOI: <https://doi.org/10.1080/19475705.2018.1554604>
- Enoksson, V., & Svedberg, F. (2015). *Optimization of hydro power on the Nordic electricity exchange using financial derivatives*. Royal Institute of Technology.
- Erat, S., Telli, A., Ozkendir, O. M., & Demir, B. (2021). Turkey's energy transition from fossil-based to renewable up to 2030: milestones, challenges and opportunities. *Clean Technologies and Environmental Policy*, 23(2), 401–412. DOI: <https://doi.org/10.1007/s10098-020-01949-1>
- Erdin, C., & Ozkaya, G. (2019). Turkey's 2023 energy strategies and investment opportunities for renewable energy sources: Site selection based on ELECTRE. *Sustainability (Switzerland)*, 11(7). DOI: <https://doi.org/10.3390/su11072136>
- Fen, Q., Zhang, K., & Smith, B. (2012). *Small Hydropower Cost Reference Model* (Issue October).
- Grigoriu, M., & Popescu, M. C. (2010). Hydropower Preventive Monitoring Action Plan. In *Proceedings of the 5th IASME/WSEAS International Conference on Energy&Environment, Recent Advances in Energy & Environment, Published by WSEAS Press*, 265–270.

- Howard, J. C. (2006). Technical Basis for Optimizing Hydropower Operations with MS-Excel. *Great Wall World Renewable Energy Forum and Exhibition*.
- Irena. (2012). Concentrating Solar Power. In *Renewable energy technologies: Cost analysis series*. DOI: <https://doi.org/10.1016/B978-0-12-812959-3.00012-5>
- Jiang, Z., Li, R., Li, A., & Ji, C. (2018). Runoff forecast uncertainty considered load adjustment model of cascade hydropower stations and its application. *Energy*, 158, 693–708. DOI: <https://doi.org/10.1016/j.energy.2018.06.083>
- Kaunda, C. S., Kimambo, C. Z., & Nielsen, T. K. (2012). Hydropower in the Context of Sustainable Energy Supply: A Review of Technologies and Challenges. *ISRN Renewable Energy*, 2012, 1–15. DOI: <https://doi.org/10.5402/2012/730631>
- Kaygusuz, K. (2018). Small hydropower potential and utilization in Turkey. *Journal of Engineering Research and Applied Science*, 7(1), 791–798.
- Khaniya, B., Karunanayake, C., Gunathilake, M. B., & Rathnayake, U. (2020). Projection of Future Hydropower Generation in Samanalawewa Power Plant, Sri Lanka. *Mathematical Problems in Engineering*, 2020. DOI: <https://doi.org/10.1155/2020/8862067>
- Kober, T., Schiffer, H. W., Densing, M., & Panos, E. (2020). Global energy perspectives to 2060 – WEC’s World Energy Scenarios 2019. *Energy Strategy Reviews*, 31(August), 100523. DOI: <https://doi.org/10.1016/j.esr.2020.100523>
- Koç, C. (2018). A study on operation problems of hydropower plants integrated with irrigation schemes operated in Turkey. *International Journal of Green Energy*, 15(2), 129–135. DOI: <https://doi.org/10.1080/15435075.2018.1427591>
- Kok, B., & Benli, H. (2017). Energy diversity and nuclear energy for sustainable development in Turkey. *Renewable Energy*, 111, 870–877. DOI: <https://doi.org/10.1016/j.renene.2017.05.001>
- Kotchen, M. J., Moore, M. R., Lupi, F., & Rutherford, E. S. (2006). Environmental constraints on hydropower: An ex post benefit-cost analysis of dam relicensing in Michigan. *Land Economics*, 82(3), 384–403. DOI: <https://doi.org/10.3368/le.82.3.384>
- Kural, D., & Ara, S. (2020). An Analysis of the Optimal Design of Feed-in Tariff Policy for Photovoltaic Investments in Turkey. *Sosyoekonomi*, 28(46), 425–444. DOI: <https://doi.org/10.17233/sosyoekonomi.2020.04.20>
- Kuriqi, A., Pinheiro, A. N., Sordo-Ward, A., & Garrote, L. (2020). Water-energy-ecosystem nexus: Balancing competing interests at a run-of-river hydropower plant coupling a hydrologic–ecohydraulic approach. *Energy Conversion and Management*, 223(August). DOI: <https://doi.org/10.1016/j.enconman.2020.113267>
- Legal Sources on Renewable Energy*. (2021). Compare Support Schemes. Retrieved from: <http://www.res-legal.eu/compare-support-schemes>
- Lund, H., & Østergaard, P. A. (2018). Sustainable Towns: The Case of Frederikshavn Aiming at 100% Renewable Energy. *Sustainable Cities and Communities Design Handbook*, 129–146. DOI: <https://doi.org/10.1016/B978-0-12-813964-6.00007-0>
- Mahmoudimehr, J., & Sebghati, P. (2019). A novel multi-objective Dynamic Programming optimization method: Performance management of a solar thermal power plant as a case study. *Energy*, 168, 796–814. DOI: <https://doi.org/10.1016/j.energy.2018.11.079>
- Marchand, A., Gendreau, M., Blais, M., & Emiel, G. (2019). Efficient tabu search procedure for short-term planning of large-scale hydropower systems. *Journal of Water Resources Planning and Management*, 145(7).
- Matzenberger, J., Kranzl, L., Tromborg, E., Junginger, M., Daioglou, V., Sheng Goh, C., & Keramidis, K. (2015). Future perspectives of international bioenergy trade. *Renewable and Sustainable Energy Reviews*, 43, 926–941. DOI: <https://doi.org/10.1016/j.rser.2014.10.106>

- Ministry of Energy and Natural Resources. (2022). The Electricity. Retrieved from: <https://enerji.gov.tr/bilgi-merkezi-enerji-elektrik>
- Najarchi, M., & Haghverdi, A. (2020). Application in optimization of multi-reservoir water systems using improving shuffled complex algorithm. *SN Applied Sciences*, 2(5), 1–9. DOI: <https://doi.org/10.1007/s42452-020-2590-x>
- Ranaraja, C. D., Devasurendra, J. W., Maduwantha, M. I. P., Madhuwantha, G. A. L., & Hansa, R. Y. D. (2020). Optimization of an Industrial Boiler Operation. *Journal of Research Technology and Engineering*, 1(3), 126–134.
- Ranjbari, M., Shams Esfandabadi, Z., Zanetti, M. C., Scagnelli, S. D., Siebers, P. O., Aghbashlo, M., Peng, W., Quatraro, F., & Tabatabaei, M. (2021). Three pillars of sustainability in the wake of COVID-19: A systematic review and future research agenda for sustainable development. *Journal of Cleaner Production*, 297, 126660. DOI: <https://doi.org/10.1016/j.jclepro.2021.126660>
- Şahin, C. (2021). The Development of Renewable Energy in Turkish Electricity Markets. *European Journal of Science and Technology*, 25, 238–246. DOI: <https://doi.org/10.31590/ejosat.893539>
- Şahin, M. (2021). A comprehensive analysis of weighting and multicriteria methods in the context of sustainable energy. *International Journal of Environmental Science and Technology*, 18(6), 1591–1616. DOI: <https://doi.org/10.1007/s13762-020-02922-7>
- Sauhats, A., Varfolomejeva, R., Umbrasko, I., & Coban, H. H. (2014). An additional income of small hydropower plants and a public trader. *International Journal of Energy*, 8.
- Sauhats, Antans, Coban, H. H., Baltputnis, K., Broka, Z., Petrichenko, R., & Varfolomejeva, R. (2016). Optimal investment and operational planning of a storage power plant. *International Journal of Hydrogen Energy*, 41(29), 12443–12453. DOI: <https://doi.org/10.1016/j.ijhydene.2016.03.078>
- Sauhats, Antans, Varfolomejeva, R., Petrichenko, R., & Kucajevs, J. (2015). A stochastic approach to hydroelectric power generation planning in an electricity market. *2015 IEEE 15th International Conference on Environment and Electrical Engineering, IEEEIC 2015 - Conference Proceedings, 2013*, 883–888. DOI: <https://doi.org/10.1109/IEEEIC.2015.7165280>
- Shukla, A. K., Sudhakar, K., & Baredar, P. (2017). Renewable energy resources in South Asian countries: Challenges, policy and recommendations. *Resource-Efficient Technologies*, 3(3), 342–346. DOI: <https://doi.org/10.1016/j.reffit.2016.12.003>
- Singh, V. K., & Singal, S. K. (2018). Optimal Operation of Run of River Small Hydro Power Plant. *BioPhysical Economics and Resource Quality*, 3(3), 1–11. DOI: <https://doi.org/10.1007/s41247-018-0045-4>
- Soares, S., & Carneiro, A. A. F. M. (1991). Optimal operation of reservoirs for electric generation. *IEEE Transactions on Power Delivery*, 6(3), 1101–1107. DOI: <https://doi.org/10.1109/61.85854>
- Sun, L., Niu, D., Wang, K., & Xu, X. (2021). Sustainable development pathways of hydropower in China: Interdisciplinary qualitative analysis and scenario-based system dynamics quantitative modeling. *Journal of Cleaner Production*, 287, 125528. DOI: <https://doi.org/10.1016/j.jclepro.2020.125528>
- Tayefeh Hashemi, S., Ebadati, O. M., & Kaur, H. (2020). Cost estimation and prediction in construction projects: a systematic review on machine learning techniques. *SN Applied Sciences*, 2(10), 1–27. DOI: <https://doi.org/10.1007/s42452-020-03497-1>
- Teck, T. S., Subramaniam, H., & Sorooshian, S. (2019). Exploring challenges of the fourth industrial revolution. *International Journal of Innovative Technology and Exploring Engineering*, 8(9), 27–30. DOI: <https://doi.org/10.35940/ijitee.i7910.078919>
- Tiainen, R., Lindh, T., Ahola, J., Niemelä, M., & Särkimäki, V. (2008). Energy price-based control strategy of a small-scale head-dependent hydroelectric power plant. *Renewable Energy and Power Quality Journal*, 1(6), 514–519. DOI: <https://doi.org/10.24084/repqj06.345>
- Üçüncü, O. (2018). Latest status of hydropower plants in Turkey: Technical, environmental policy and environmental law from the perspective of the evaluation. *A/ZITU Journal of the Faculty of Architecture*, 15(2), 153–171. DOI: <https://doi.org/10.5505/itujfa.2018.79664>

- Varfolomejeva, R., Petrichenko, R., Sauhats, A., & Kucajevs, J. (2015). An optimization algorithm selection to regulate the power plant work. *56th International Scientific Conference on Power and Electrical Engineering of Riga Technical Uni.*
- Varfolomejeva, R., Zima-Bockarjova, M., & Coban, H. H. (2014). Reconsideration of Supporting Scheme for Renewable Energy Producers. *4th International Symposium on Environmental Biotechnology and Engineering (AISEBE)*, 62–63.
- Varfolomejeva, Renata. (2014). *The Aspects of the Planning and Optimization of Electric Stations Operational Regimes under the Conditions of Market Economy*. Riga Technical University.
- Varfolomejeva, Renata, Umbrasko, I., & Mahnitko, A. (2013). The small hydropower plant operating regime optimization by the income maximization. *2013 IEEE Grenoble Conference PowerTech, POWERTECH 2013*. DOI: <https://doi.org/10.1109/PTC.2013.6652497>
- Wendle, C. (2019). *Rights to the River: Implementing A Social Cost-Benefit Analysis in the United States Hydropower Relicensing Process*. Retrieved from: https://scholarship.claremont.edu/scripps_theses/1395/
- Wessel, M., Madlener, R., & Hilgers, C. (2020). Economic Feasibility of Semi-Underground Pumped Storage Hydropower Plants in Open-Pit Mines. *Energies*, 13(6), 1–33. DOI: <https://doi.org/10.3390/en13164178>
- WorldBankGroup. (2015). *Hydroelectric Power, A Guide for Developers and Investors*. Hydroelectric Power. DOI: <https://doi.org/10.1002/9781119204442.ch16>
- Wu, L., Shahidehpour, M., & Li, T. (2008). Cost of reliability analysis based on stochastic unit commitment. *IEEE Transactions on Power Systems*, 23(3), 1364–1374. DOI: <https://doi.org/10.1109/TPWRS.2008.922231>
- Xu, J., Liu, Z., Jiang, H. (2021). Study on Application of Solar Energy in Highway. *E3S Web of Conferences*, 261.
- Yalılı, M., Tiryaki, R., & Gözen, M. (2020). Evolution of auction schemes for renewable energy in Turkey: An assessment on the results of different designs. *Energy Policy*, 145(August). DOI: <https://doi.org/10.1016/j.enpol.2020.111772>
- Yang, Y., Zhou, J., Liu, G., Mo, L., Wang, Y., Jia, B., & He, F. (2020). Multi-plan formulation of hydropower generation considering uncertainty of wind power. *Applied Energy*, 260(December 2019). DOI: <https://doi.org/10.1016/j.apenergy.2019.114239>
- Yang, Z., Wang, Y., & Yang, K. (2022). The stochastic short-term hydropower generation scheduling considering uncertainty in load output forecasts. *Energy*, 241, 122838. DOI: <https://doi.org/10.1016/j.energy.2021.122838>
- Yildiz, V., & Vrugt, J. A. (2019). A toolbox for the optimal design of run-of-river hydropower plants. *Environmental Modelling and Software*, 111(August 2017), 134–152. DOI: <https://doi.org/10.1016/j.envsoft.2018.08.018>
- Yuan, W., Wang, X., Su, C., Cheng, C., Liu, Z., & Wu, Z. (2021). Stochastic optimization model for the short-term joint operation of photovoltaic power and hydropower plants based on chance-constrained programming. *Energy*, 222, 119996. DOI: <https://doi.org/10.1016/j.energy.2021.119996>
- Yuksel, I., Arman, H., & Demirel, I. H. (2017). As a clean, sustainable and renewable energy - Hydropower in Turkey. *MATEC Web of Conferences*, 120, 1–5. DOI: <https://doi.org/10.1051/mateconf/201712008004>
- Zhang, Y., Ma, H., & Zhao, S. (2021). Assessment of hydropower sustainability: Review and modeling. *Journal of Cleaner Production*, 321(September), 128898. DOI: <https://doi.org/10.1016/j.jclepro.2021.128898>



ZnMnCuO Nanoparçacıkların Karakterizasyonu: Fotokatalitik ve Hemolitik Özellikler

Bestenur Yalçın^{1*}

¹Tıbbi Laboratuvar Teknikleri Programı, Sağlık Hizmetleri Meslek Yüksek Okulu, Bahçeşehir Üniversitesi, İstanbul, Türkiye

Makale Tarihi

Gönderim: 28.01.2022
Kabul: 27.05.2022
Yayın: 25.09.2022

Araştırma Makalesi

Öz – Çinko oksit (ZnO) temelli nano boyutlu parçacıklar, fotokatalitik etkileri, birim hacim başına oldukça yüksek olan yüzey alanları ve foto-kararlılıklarının yanı sıra, biyolojik potansiyelleri nedeniyle de özellikle son yıllarda oldukça dikkat çekmektedirler. Bu makalede, bakır asetat, çinko asetat ve mangan asetat öncülleri kullanılarak sol-jel yöntemiyle sentezlenmiş nano-boyutlu mangan katkılı çinko-bakır oksit nano-parçacıkların ($Zn_{0.99-x}Mn_xCu_{0.01}O$ $x = 0.00, 0.01, 0.03, 0.05, 0.10$), kristal özellikleri, morfolojik yapıları, fotokatalitik performansları ve hemolitik özellikleri araştırılmıştır. Elde edilen sonuçlar, yine sol-jel yöntemiyle sentezlenmiş nano boyutlu ZnCuO parçacıklara ait bulgular ile kıyaslamalı olarak verilmiştir. Örneklerin kristal yapı özellikleri ile yüzeylere ait morfolojik özellikler, sırasıyla x-ışını kırınım spektroskopisi (XRD) ve taramalı elektron mikroskopu (SEM) kullanılarak incelenmiştir. Yapısal karakterizasyonlara ek olarak, $Zn_{0.99-x}Mn_xCu_{0.01}O$ nanoparçacıkların fotokatalitik özellikleri de model organik molekül olarak kristal viyole (crystal violet - CV) kullanılarak incelenmiş, CV'nin fotokatalitik bozunma süreci ultraviyole-görünür alan (UV-vis) spektroskopisi ile takip edilmiştir. Ayrıca, $Zn_{0.99-x}Mn_xCu_{0.01}O$ nanoparçacıkların biyomedikal uygulamalar açısından potansiyele sahip olup olmadığını tespiti amacıyla kan uyumluluğu testleri de gerçekleştirilmiştir. Sentezlenen numuneler içerisinde en yüksek fotokatalitik aktivite ve en yüksek kan uyumluluğunun $Zn_{0.94}Mn_{0.05}Cu_{0.01}O$ nanoparçacıklar tarafından gösterildiği tespit edilmiştir. $Zn_{0.94}Mn_{0.05}Cu_{0.01}O$ nanoparçacıklar, 330 dakika sonunda CV başlangıç miktarının %78.1'ini degrade ederken, çalışılan her iki konsantrasyonda (1.0 mg mL^{-1} ve 5.0 mg mL^{-1}) %5'in altında hemolize sebep olarak belirgin bir kan uyumluluğu göstermiştir.

Anahtar Kelimeler – Çinko oksit, fotokataliz, kan uyumluluğu, kristal viyole, sol-jel

Characterization of ZnMnCuO Nanoparticles: Photocatalytic and Hemolytic Properties

¹Department of Medical Laboratory Techniques, Vocational School of Health Services, Bahcesehir University, Istanbul, Türkiye

Article History

Received: 28.01.2022
Accepted: 27.05.2022
Published: 25.09.2022

Research Article

Abstract – Zinc oxide (ZnO)-based nano-sized particles have attracted a lot of interest in recent years due to their photocatalytic effects, their relatively high surface/volume ratio and photo-stability, as well as their biological potential. In this study, nano-sized manganese doped zinc-copper oxide nanoparticles ($Zn_{0.99-x}Mn_xCu_{0.01}O$ $x = 0.00, 0.01, 0.03, 0.05, 0.10$) were synthesized by sol-gel method. Morphological structures, photocatalytic performances and hemolytic properties of $Zn_{0.99-x}Mn_xCu_{0.01}O$ nanoparticles synthesized by using copper, zinc and manganese acetates precursors were investigated. The obtained results are given in comparison with the findings of nano-sized ZnCuO particles synthesized by the same method. The crystal structure properties of the samples and the morphological properties of the surfaces were investigated using x-ray diffraction spectroscopy (XRD) and scanning electron microscopy (SEM), respectively. In addition to the structural characterizations, the photocatalytic properties of $Zn_{0.99-x}Mn_xCu_{0.01}O$ nanoparticles were also investigated using crystal violet (CV) as a model organic molecule and the photocatalytic degradation process of CV had been followed by ultraviolet-visible (UV-vis) spectroscopy. In addition, blood compatibility tests were carried out to determine whether $Zn_{0.99-x}Mn_xCu_{0.01}O$ nanoparticles have potential for biomedical applications. It was determined that the highest photocatalytic activity and the highest blood compatibility among the synthesized samples were shown by $Zn_{0.94}Mn_{0.05}Cu_{0.01}O$ nanoparticles. It has been shown that $Zn_{0.94}Mn_{0.05}Cu_{0.01}O$ degraded 78.1% of the initial amount of CV after 330 minutes, and caused hemolysis below 5% at both nanoparticle concentrations corresponding to a significant blood compatibility.

Keywords – Blood compatibility, crystal violet, sol-gel, zinc oxide, photocatalysis,

¹ bestenur.yalcin@eng.bau.edu.tr

*Sorumlu Yazar / Corresponding Author

1. Giriş

Makro boyutlu malzemelerle karşılaştırıldıklarında, nano malzemeler, herhangi bir kimyasal algılama sistemi veya katalitik reaksiyonların temel alındığı uygulamalar için temel kriterler olan yüksek yüzey/hacim oranına ve uygulama alanına özel şekilde tasarlanabilen özelliklere sahiptirler. Çinko oksit (ZnO), endüstri, bilim ve teknoloji gibi farklı alanlardaki uygulamaları nedeniyle büyük ilgi görmekte olan bir yarı iletkenidir (Al-Buriah vd., 2022). ZnO temelli nano malzemeler, sensörler, biyogörüntüleme sistemleri, terapötik, fotokatalitik ve enerji dönüşüm uygulamaları gibi birçok alan için geniş çapta araştırılmaktadır (Beitollahi vd., 2020, Li vd., 2020, Yi vd., 2020). ZnO nanoparçacıkların sentezi ve karakterizasyonuna olan ilgi özellikle son yirmi yılda oldukça artmış, ZnO ve türevlerinin farklı elektriksel ve optik özellikleri, çeşitli sentez yöntemleri, çeşitli reaksiyon öncüleri ve bileşimleri kullanılarak iyileştirilmeye çalışılmıştır. ZnO (3.3 eV), önemli sayıda elektron boşluğu oluşturması nedeniyle atık sulardan tekstil boya ve antibiyotik kalıntıları gibi kirleticilerin giderilmesinde kullanılabilir yüksek potansiyelli bir malzeme olarak öne çıkmaktadır (Bopape vd., 2022, Islam vd., 2018). ZnO nanoparçacıkların fotokatalitik özellik gösteren diğer malzemelere (TiO₂, Fe₂O₃, WO₃ vb.) kıyasla en büyük avantajı parçacık boyutunun yanısıra, kristal yapıya katılan Al³⁺, Cd²⁺, Cu²⁺, Mn²⁺, Ni²⁺ gibi çeşitli metal iyonları sayesinde ayarlanabilen bir bant aralığı değerine sahip olmasıdır. Bu özellik ZnO türevi nano yapıların birçok alanda kullanılabilir olmasını sağlar. Bunun yanında, fotokatalitik özellikleri ve yarı iletken davranışı da, ZnO'ü özellikle antimikrobiyal çalışmaları içeren biyolojik alanlarda, nano-antibiyotikler ve antikanser ilaçların tasarımında ve yeni nesil erken teşhis ve tedavi süreçlerinde kullanılabilir potansiyel bir aday haline getirmektedir (Ahmad vd., 2022, Thirumoorthy vd., 2021, Carofiglio vd., 2020). Öte yandan, ZnO, kimyasal kararlılığı, geniş bant aralığı ve belirgin elektron transfer hızı nedeniyle elektro-kimyasal algılama sistemlerinde de yaygın olarak kullanılmaktadır (Sha vd., 2017a, Hasan ve Hussein, 2021).

ZnO'nun çevre dostu özellikleri ve n-tipi yarı iletken yapısı, yüksek ışık duyarlılığı, biyoyumluluk ve kimyasal kararlılık gibi önemli özelliklerinin temelini oluşturur (Li vd., 2022). Diğer nano boyutlu iletkenlerle karşılaştırıldığında, ZnO, oda sıcaklığındaki termal enerjiden (25 meV) yaklaşık 2.4 kat daha yüksek olan 60 meV'lik eksiton bağlanma enerjisi gösterir (Titov vd., 2019, Hou vd., 2022, Aggarwal vd., 2018). Bu, ZnO nanoparçacıklar için eksitonik geçişin oda sıcaklığında da mümkün olduğu anlamına gelir. ZnO nanoparçacıklar, UV ışığa karşı sağladıkları geniş spektrumlu koruma nedeniyle güneşten koruyucu ürünlerde de kullanılmaktadır (Lee vd., 2021). ZnO nanoparçacıklar, yüksek yüzey alanları, düşük maliyetleri, önemli kimyasal kararlılıkları, antioksidan özellikleri ve fotokatalitik aktiviteleri nedeniyle, kontrollü ilaç salım sistemlerinde, biyosensörlerde, elektrokimyasal sensör uygulamalarında ve atık su arıtımında yüksek potansiyele sahip bir malzeme olarak ilgi çekmektedir (Pillai vd., 2020, Jha ve Shimpi 2018, Sha vd., 2017b).

Bununla birlikte, ZnO nanoparçacıklar kısmen geniş bant aralığı ve sınırlı elektriksel özellikleri sebebiyle, biyolojik ortamda sınırlı fotostabilite göstermekte ve beklenmedik sitotoksik etkilere yol açabilmektedirler. ZnO nanoparçacıkların bu zayıf yönlerinin iyileştirilebilmesi için, geniş spektrumlu katkı maddeleri kullanılarak, metal ya da ametal katkılar yapılması uygun çözümlerden biri olarak görünmektedir (Reynolds ve Reynolds, 2014). "Katkılama" ifadesi kristal yapı içerisine ZnO'nun her türlü fizikokimyasal özelliğini değiştirmek/geliştirmek için kasıtlı olarak safsızlıkların eklenmesi anlamına gelir. Bu safsızlıklar, katyonik ve anyonik yapıda olabilen ve ZnO kristal yapısındaki sırasıyla Zn²⁺ ve O²⁻'nin yerini alan katkılamalardır. Katkılamanın türü ve miktarı, özellikle ZnO kristal yapısına ilave edilen Al³⁺, Cd²⁺, Cu²⁺, Mn²⁺, Ni²⁺ gibi metal iyonları, ZnO'nun fonksiyonel davranışları üzerinde doğrudan etkili olan elektronik özelliklerini kuvvetle etkiler (Ozcelik vd., 2021, Senol vd., 2020, Zhou vd., 2018, Acharya vd., 2012). Katkılama, ZnO ve diğer metal oksitlerin bant aralığını, kristal yapısını, yüzey alanını, kristal boyutunu ve morfolojisini de önemli ölçüde değiştirir. Genel olarak, katkılama sonrası bant aralığındaki bir artış, orijinal yapının stabilitesinin artması, kimyasal aktivitenin azalması ve daha düşük elektrik iletkenliği anlamına gelirken, bant aralığındaki bir azalma, yüksek elektrik iletkenliği, iyileştirilmiş fotokatalitik özellikler ve yüksek miktarda reaktif oksijen türü oluşturabilme gibi farklı malzeme özelliklerinin elde edilmesi anlamına gelmektedir (Khan vd., 2022, He vd., 2020).

Bu çalışmada, Mn elementinin değişen oranları (Zn_{0.99-x}Mn_xCu_{0.01}O x=0.00, 0.01, 0.03, 0.05, 0.10) katkılanarak, fotokatalitik ve biyolojik uygulamalar için ZnCuO nanoparçacıkların özellikleri iyileştirilmeye çalışılmıştır. XRD ve SEM analizleri ile Zn_{0.99-x}Mn_xCu_{0.01}O nanoparçacıkların sırasıyla kristal yapı

özellikleri ve yüzey morfolojileri incelenmiştir. $Zn_{0.99-x}Mn_xCu_{0.01}O$ varlığında CV fotokatalitik bozunma süreci ultraviyole-görünür alan (UV-vis) spektroskopisi ile takip edilmiş ve nanoparçacıkların fotokatalitik aktiviteleri incelenmiştir. Eritrosit hücre zarı, biyolojik sistemi oluşturan diğer dokuların hücre zarlarıyla benzer bir moleküler organizasyon ilkesine dayandığından, bu çalışmada, $Zn_{0.99-x}Mn_xCu_{0.01}O$ - eritrosit etkileşimleri de incelenmiş, $Zn_{0.99-x}Mn_xCu_{0.01}O$ nanoparçacıkların biyomedikal uygulamalar açısından potansiyele sahip olup olmadığının tespiti amacıyla kan uyumluluğu testleri gerçekleştirilmiştir.

2. Materyal ve Yöntem

2.1. Kullanılan kimyasallar

Bu çalışmada başlangıç maddeleri olarak analitik saflıkta bakır asetat ($Zn(CH_3COO)_2$, Merck), çinko asetat dihidrat ($Zn(CH_3COO)_2 \cdot 2H_2O$, Merck) ve mangan asetat tetrahidrat ($Mn(CH_3COO)_2 \cdot 4H_2O$, Alfa Aesar) kullanılmıştır. Metanol (Merck) ve monoetanolamin (Merck) sırasıyla çözücü ve sol stabilize edici olarak kullanılmıştır. Kan uyumluluğu testlerinde kullanılacak fosfat tampon çözelti (Phosphate buffer solution (PBS)) NaCl (8 g/L), KCl (0.2 g/L), $Na_2HPO_4 \cdot 2H_2O$ (1.78 g/L) ve KH_2PO_4 (0.24 g/L) kimyasalları kullanılarak pH 7.35 olacak şekilde hazırlanmıştır. Hazırlanan PBS 1 atm basınçta ve 121°C sıcaklıkta 15 dakika süreyle otoklavlanarak sterilize edilmiştir. $Zn_{0.99-x}Mn_xCu_{0.01}O$ nanoparçacıkların fotokatalitik özellikleri, model organik molekül olarak seçilen CV'nin ($C_{16}H_{18}N_3ClS \cdot 3H_2O$) nanoparçacıklar varlığında ilerleyen fotokatalitik bozunma tepkimeleri takip edilerek aydınlatılmıştır. Tüm deneylerde, Human marka Zener Power1 model saf su cihazından sağlanan destile deiyonize su kullanılmıştır.

2.2. $Zn_{0.99-x}Mn_xCu_{0.01}O$ nanoparçacıkların sentezi

$Zn_{0.99-x}Mn_xCu_{0.01}O$ nanoparçacıkların sol-jel yöntemi ile sentezinde ilk adım, başlangıç maddeleri olarak kullanılan bakır asetat, çinko asetat dihidrat ve mangan asetat tetrahidratın uygun tartımlarının bir beher içerisinde birleştirilmesidir. Yapılan tartımlar, nanoparçacık bileşimindeki her bir element için mol oranları dikkate alınarak hesaplanmıştır. Ardından çözücü olarak etanol ve sol sabitleştirici olarak monoetanolamin ilave edilmiştir. Hazırlanan çözelti, parafilm ile kapatılmış beher içerisinde 8 saat boyunca oda sıcaklığında bir manyetik karıştırıcı kullanılarak berrak bir çözelti elde edilene kadar karıştırılmış ve jel faz metanol içerisinde hazır hale getirilmiştir. Karıştırma süresi sonunda beherlerin üzeri açılmış ve yine oda sıcaklığında manyetik karıştırma altında çözücünün uzaklaşması sağlanmıştır. Bu adımın ardından kuruluğa ulaşmış olan jel faz, 400°C'da 10 dakika, ardından 600°C'da 30 dakika süreyle kalsine edilmiş ve kristal örgünün oluşumu tamamlanmıştır.

2.3. Yapısal Analiz

$Zn_{0.99-x}Mn_xCu_{0.01}O$ nanoparçacıkların kristal yapı özellikleri, XRD (PANalytical X'pert³) analizleri ile aydınlatılmıştır. Difraktometre, $\lambda = 1.5418 \text{ \AA}$ dalga boyu $CuK\alpha$ radyasyonu kullanmakta olup, ölçümler oda sıcaklığında, $2\theta = 10^\circ - 90^\circ$ aralığında, 3° dk^{-1} tarama hızı ile ve $0.02^\circ \text{ s}^{-1}$ hızla yapılmıştır. $Zn_{0.99-x}Mn_xCu_{0.01}O$ nanoparçacıkların yüzey morfolojileri SEM (JEOL, JSM-5910LV) ile incelenmiştir.

2.4. Fotokatalitik aktivite ölçümleri

$ZnCuO$ ve Mn katkılı $ZnCuO$ ($Zn_{0.99-x}Mn_xCu_{0.01}O$) nanoparçacıkların fotokatalitik aktiviteleri, 254 nm dalga boyu elektromanyetik radyasyon etkisi altında model organik boya olarak CV kullanılarak araştırılmıştır. Yöntem, nanoparçacıkların yüzeyinde üretilen reaktif oksijen türleri tarafından CV'nin renksizleştirilmesine dayanmaktadır. Nanoparçacık dispersiyonları ve CV çözeltisinin konsantrasyonu sırasıyla 1.0 mg mL^{-1} ve $2.5 \times 10^{-6} \text{ mol L}^{-1}$ olarak belirlenmiştir. $ZnCuO$ ve $Zn_{0.99-x}Mn_xCu_{0.01}O$ nanoparçacıklarının uygun tartımları 30 mL'lik CV çözeltisine ilave edilmiş, ardından fotoreaksiyon karışımı karanlıkta oda sıcaklığında 30 dakika sürekli manyetik karıştırma altında tutularak yüzey adsorpsiyon-desorpsiyon dengesine getirilmiştir. Daha sonra nanoparçacık dispersiyonları, 254 nm dalga boyuna sahip ışık altında sürekli karıştırılarak ışınlanmıştır. Işınlama, reaksiyon kaplarına 40 cm mesafede yatay olarak yerleştirilmiş bir çift UV lamba

(her biri 45 W) kullanılarak gerçekleştirilmiştir. Fotokatalitik aktivite ölçümleri sırasında nanoparçacık dispersiyonlarının sıcaklığı 25°C’da sabit tutulmuştur.

Belirlenen zaman aralıklarında alınan, 1.75 mL’lik fotoreaksiyon çözeltisi örnekleri asılı kalan nanoparçacıkların çökmesini sağlamak için 4000 rpm’de 3 dakika santrifüjlenmiştir. Ardından süpernatantın absorpsiyon spektrumu, Shimadzu UV mini 1240 UV-vis spektrofotometre kullanılarak ölçülmüş ve fotobozunmaya uğramamış CV konsantrasyonu, 594 nm’deki karakteristik absorpsiyon maksimumu dikkate alınarak ve CV için önceden çizilmiş kalibrasyon grafiği kullanılarak belirlenmiştir. Tüm denemelerde referans çözelti olarak destile deiyonize su kullanılmıştır.

CV’nin fotokatalitik bozunma kinetiği, birinci derece kinetik kullanılarak incelenmiş ve bozunma reaksiyonları için hız sabitleri Eşitlik 2.1 ile hesaplanmıştır (Karthik vd., 2017).

$$\ln(C_0/C) = k.t \quad (2.1)$$

Eşitlik 2.1’de, C_0 ve C , sırasıyla CV için yüzey adsorpsiyon dengesi kurulduktan hemen sonra ($t = 0$ anında) ve belirli bir fotodegradasyon süresinin (t) sonunda çözeltideki CV konsantrasyonu (mol L^{-1}), k ise fotokatalitik bozunma için birinci dereceden hız sabitidir (dak^{-1}).

2.5. Kan uyumluluğu ölçümleri

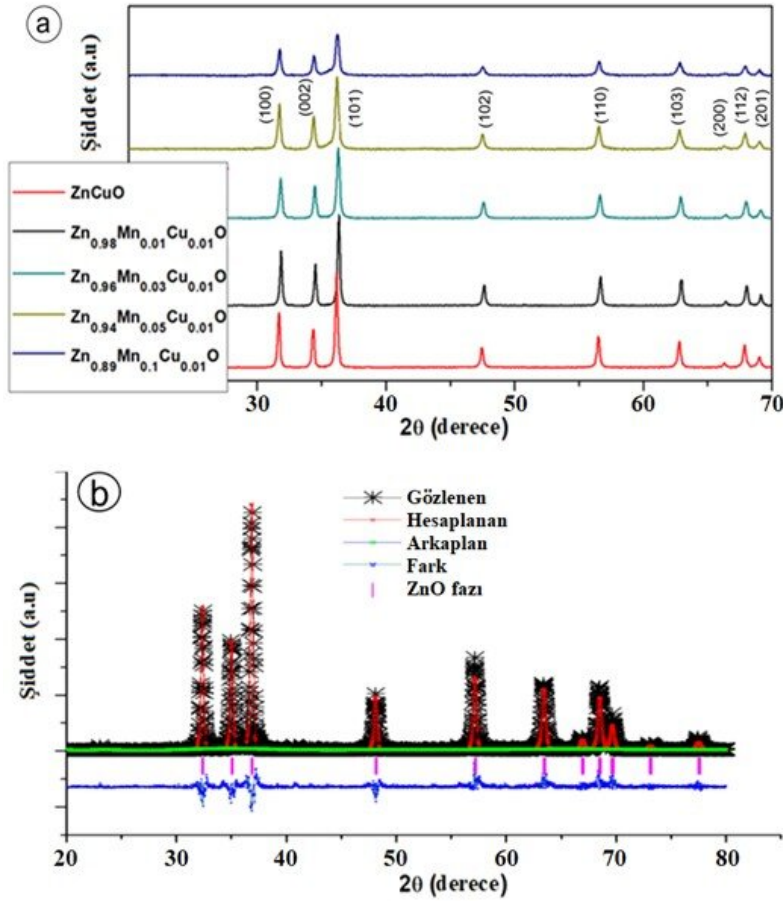
$\text{Zn}_{0.99-x}\text{Mn}_x\text{Cu}_{0.01}\text{O}$ nanoparçacıklarının kan uyumlulukları sağlıklı yetişkin gönüllülerden alınan tam kan örnekleri kullanılarak araştırılmıştır. Kan örnekleri 5 mL’lik tek kullanımlık şırınga ile alınmış ve hemen ardından 0.108 mM sulu trisodyum sitrat çözeltisi kullanılarak antikoagüle edilmiştir. Kan: antikoagülan oranı (9:1) olarak ayarlanmıştır. Antikoagüle edilmiş tam kan örnekleri, PBS ile seyreltilmiş, ardından eritrositlerin kan plazmasından ayrılması için 4000 rpm’de 5 dakika santrifüjlenmiştir. Süpernatantın dekantasyonundan sonra, sediment oluşturan eritrositler PBS kullanılarak 50 mL’ye seyreltilmiş ve eritrosit stok çözelti hazır hale getirilmiştir. Eritrosit stok çözeltiden alınan uygun hacimler, 1.0 mg mL^{-1} ve 5.0 mg mL^{-1} konsantrasyonlarında 5.0 mL hacimli $\text{Zn}_{0.99-x}\text{Mn}_x\text{Cu}_{0.01}\text{O}$ nanoparçacık süspansiyonları ile karıştırılmıştır. Nanoparçacık-eritrosit dispersiyonları manyetik karıştırma altında fizyolojik sıcaklık olan 37°C’de 3 saat inkübe edildikten sonra, numuneler 3000 rpm’de 5 dakika santrifüjlenmiş ve eritrosit lizisinin bir sonucu olarak ortama salınan hemoglobinin varlığını göstermek üzere UV-görünür alan spektrofotometre kullanılarak 200 nm - 800 nm arasında süpernatant absorbansları ölçülmüştür. Tüm testler iki tekrar olacak şekilde yapılmıştır. Pozitif kontrol (%100 hemoliz) ve negatif kontrol (%0 hemoliz) testleri sırasıyla destile deiyonize su ve PBS kullanılarak gerçekleştirilmişlerdir. Her bir $\text{Zn}_{0.99-x}\text{Mn}_x\text{Cu}_{0.01}\text{O}$ bileşimi için hemoliz yüzdesi, Eşitlik 2.2 ile verilen denklem kullanılarak 540 nm’de ölçülen süpernatant absorbans değerine (ABS) bağlı olarak hesaplanmıştır (Yalcin ve Erbil, 2018).

$$\%Hemoli = \frac{\text{ABS}_{\text{numune}} - \text{ABS}_{\text{negatif kontrol}}}{\text{ABS}_{\text{pozitif kontrol}} - \text{ABS}_{\text{negatif kontrol}}} \quad (2.2)$$

3. Bulgular ve Tartışma

3.1. Yapısal Özellikler

$\text{Zn}_{0.99-x}\text{Mn}_x\text{Cu}_{0.01}\text{O}$ nanoparçacıklarının kristal yapı özelliklerini ve mevcut fazlarını aydınlatmak için XRD yöntemi kullanılmış, analizler $10^\circ \leq 2\theta \leq 80^\circ$ aralığında gerçekleştirilmiştir. $\text{Zn}_{0.99-x}\text{Mn}_x\text{Cu}_{0.01}\text{O}$ ($x=0.00, 0.01, 0.03, 0.05, 0.10$) nanoparçacıklarının XRD spektrumları Şekil 1a’da gösterilmektedir. XRD spektrumları, altıgen bir yapının varlığını gösteren ZnCuO kafesinin tüm karakteristik piklerini göstermektedir (Shi vd., 2022). Wurtzite yapılı $\text{Zn}_{0.99-x}\text{Mn}_x\text{Cu}_{0.01}\text{O}$ için karakteristik pik noktaları; $2\theta = 32^\circ, 34^\circ, 36^\circ, 57^\circ$ ve 63° ’de ortaya çıkmış olup, (100), (002), (101), (110) ve (103) kırınım noktalarına karşılık gelmektedir. Elde edilen bulgular JCPDS kart No.36-1451 ile uyumludur. Şekil 1, tüm Mn katkı oranları için tek fazlı bir kristal örgü elde edilmiş olduğunu göstermekte olup, MnO veya başka bir fazın varlığını gösteren ilave hiçbir pik göstermemektedir. Bulgular, Şekil 1b’de yapılan Rietveld analizleri ile elde edilen sonuçlarla uyumludur.



Şekil 1. a) $Zn_{0.99-x}Mn_xCu_{0.01}O$ nanoparçacıkları için X-ışını kırınım spektrumları, b) $Zn_{0.98}Mn_{0.01}Cu_{0.01}O$ nanoparçacıklar için Rietveld analizi.

$Zn_{0.99-x}Mn_xCu_{0.01}O$ kristal yapıları için örgü parametreleri, a ve c, kırınım desenlerinden [Eşitlik 3.1](#) ve [Eşitlik 3.2](#) yardımıyla hesaplanmıştır ([Bilgili vd., 2019](#), [Guler vd., 2019](#)).

$$a_{exp} = d_{hkl} (h^2 + k^2 + l^2)^{1/2} \quad (3.1)$$

$$\frac{1}{d_{hkl}^2} = \frac{4}{3} \left(\frac{h^2 + k^2 + hk}{a^2} \right) + \frac{l^2}{c^2} \quad (3.2)$$

$Zn_{0.99-x}Mn_xCu_{0.01}O$ nanoparçacıklarının çapları (D), en yoğun pikin (101) yarı maksimumunda (full-width at half maximum - FWHM) tam genişliği dikkate alınarak ve Debye-Scherrer denklemi ([Eşitlik 3.3](#)) kullanılarak hesaplanmıştır.

$$D = 0.9\lambda/\beta\cos\theta_B \quad (3.3)$$

[Eşitlik 3.3](#)'de λ , β ve θ_B sırasıyla $CuK\alpha$ 'nın X-ışını dalga boyu (1.5418 Å), kırınım zirvesinin (101) FWHM'si ve Bragg kırınım açısıdır.

Ortalama partikül boyutlarının Mn katkı oranına bağlı değişimleri [Tablo 1](#)'de gösterilmiştir. Mn^{2+} (0.83 Å) katkı elementinin Zn^{2+} (0.60 Å) ile kısmen değiştirilmesiyle yapısal bozulmanın ortaya çıkmadığı ve artan Mn katkılama oranlarının ($x=0.03-0.10$) parçacık boyutları ortalamalarında azalmaya sebep olduğu gözlenmiştir. ZnCuO yapısına Mn katkılanması, örgü parametresi a üzerinde belirgin bir etki yaratmazken, c değerlerinin artan Mn katkı oranı ile ZnCuO'ya kıyasla hafifçe azaldığı gözlenmiştir. $Zn_{0.99-x}Mn_xCu_{0.01}O$ nanoparçacıklar için konsantrasyona bağlı parçacık çapları (D), örgü parametreleri (a ve c), birim hücre hacmi, dislokasyon

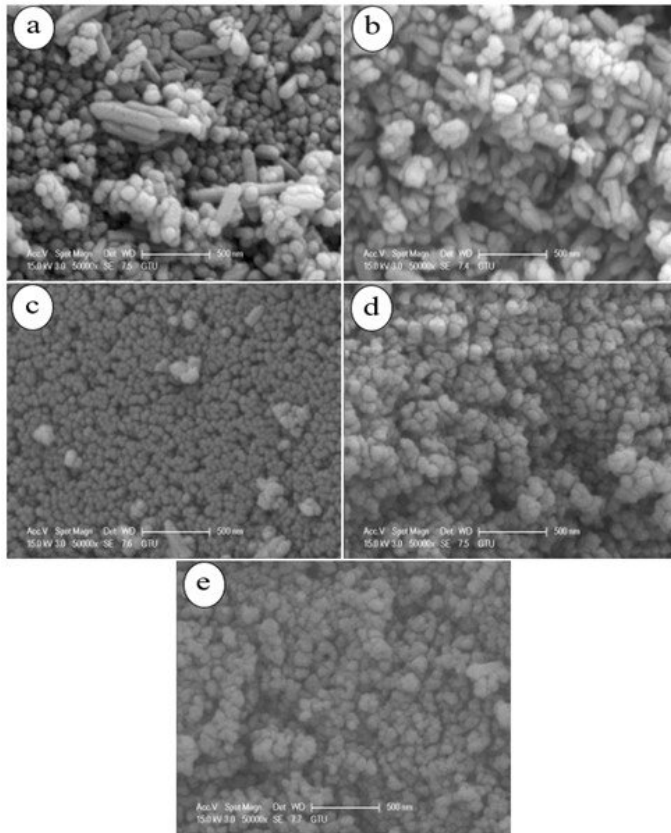
yoğunluğu (δ) (numunedeki kusur miktarı), yer değiştirme faktörü (u) ve bağ uzunluğu (L) Tablo 1'de verilmiştir. Tablo 1 içinde sunulan değerler, Şekil 1b'de verilen Rietveld analizi değerleri ile uyusmaktadır.

Tablo 1

$Zn_{0.99-x}Mn_xCu_{0.01}O$ nanoparçacıklar için konsantrasyona bağlı parçacık çapları (D), örgü parametreleri (a ve c), birim hücre hacmi (V), dislokasyon yoğunluğu (δ), yer değiştirme faktörü (u) ve bağ uzunluğu (L) değerleri.

Nanoparçacık	a (Å)	c (Å)	D (nm)	V (nm ³)	δ (nm) ⁻²	u	L (nm)
$Zn_{0.99}Cu_{0.01}O$	3.253	5.210	35.48	47.731	0.000637	0.3799	1.9793
$Zn_{0.98}Mn_{0.01}Cu_{0.01}O$	3.245	5.201	38.05	47.423	0.000824	0.3797	1.9750
$Zn_{0.96}Mn_{0.03}Cu_{0.01}O$	3.248	5.203	30.72	47.525	0.000835	0.3799	1.9765
$Zn_{0.94}Mn_{0.05}Cu_{0.01}O$	3.245	5.201	28.73	47.418	0.001130	0.3797	1.9750
$Zn_{0.89}Mn_{0.10}Cu_{0.01}O$	3.247	5.195	26.88	47.420	0.001393	0.3802	1.9751

Sol-jel yöntemiyle sentezlenmiş $Zn_{0.99-x}Mn_xCu_{0.01}O$ nanoparçacıkların yüzey morfolojileri, SEM kullanılarak incelenmiştir. Şekil 2'de nanoparçacıkların küre şekilli ve aglomere halde oldukları gözlenmektedir.



Şekil 2. $Zn_{0.99-x}Mn_xCu_{0.01}O$ nanoparçacıkların SEM görüntüleri, (a) $Zn_{0.99}Cu_{0.01}O$, (b) $Zn_{0.98}Mn_{0.01}Cu_{0.01}O$, (c) $Zn_{0.96}Mn_{0.03}Cu_{0.01}O$, (d) $Zn_{0.94}Mn_{0.05}Cu_{0.01}O$, (e) $Zn_{0.89}Mn_{0.10}Cu_{0.01}O$.

3.2. Fotokataliz sonuçları

Oksidatif stresin çeşitli biyolojik sistemler üzerinde olumsuz etkileri olmasına rağmen, metal oksit parçacıkları tarafından üretilen reaktif oksijen türleri, boya, antibiyotik ve biyolojik atıklar gibi çeşitli kirleticileri fotokatalitik bozunma yoluyla ortamdaki uzaklaştırmak için de kullanılabilir. Çeşitli endüstriyel atıkların ve özellikle tekstil boyalarının doğal su kaynaklarına uygun olmayan şekilde deşarj edilmesi,

su kütlelerinin kirlenmesine sebep olmaktadır. Organik boyalar, biyolojik olarak parçalanmamaları ve yüksek kanserojen potansiyelleri nedeniyle insanlar, hayvanlar ve su ekosistemi için büyük tehdit oluşturmakta olup, başlıca çevre kirleticileri olarak değerlendirilirler (Saleh ve Djaja, 2014, Balcha vd., 2016). Bu çalışmada model organik boya olarak seçilen CV, diğer birçok organik boya gibi, mide-bağırsak rahatsızlıkları, hemoliz sonucu kansızlık ve daha birçok rahatsızlığa neden olabilir (Balcha ve ark. 2016). Ancak tekstil endüstrisinde özellikle boyama aşamasında CV kullanımını oldukça yaygındır. ZnO ve türevi nano malzemeler, boyalar dahil organik maddelerle kirlenmiş suların arıtılması için uygun bir alternatif malzeme olarak giderek daha fazla dikkat çekmektedir. Bunun nedeni, titanyum dioksit gibi diğer yaygın oksitlere kıyasla nispeten yüksek yüzey alanı ve kuantum verimi ile iyi foto aktivite ve fotoluminesans özellikleri sergilemesidir (Bijang vd., 2022).

Literatüre sunulmuş çeşitli çalışmalar, metal oksit nanoparçacıklar tarafından açığa çıkarılan reaktif oksijen türlerinin kirlenmiş su kaynaklarında bulunabilecek hidrokarbonlar, boyalar ve farmasötikler gibi organik kirleticilerin bozunmasını sağlayabileceğini ifade etmektedir (Rani ve Shanker, 2022, Murali vd., 2021, Wolski vd., 2019). Özellikle CV gibi organik kirleticiler, elektromanyetik radyasyon tarafından tetiklenen bir dizi redoks reaksiyonu nedeniyle esas olarak nanopartiküllerin yüzeyinde bozunur (Naik vd., 2018). Boya molekülleri fotokatalizörlerin yüzeyine adsorbe de edilebilir ve literatür çalışmalarının çoğunda gerçek boya konsantrasyonu, ışınlama süresinin başlangıcında çözeltideki boya moleküllerinin denge konsantrasyonuna eşit olarak kabul edilir (Saravanan vd., 2013, Rao vd., 2009). Bu çalışmada, CV'nin yüzey adsorpsiyon/desorpsiyon dengesi sağlandıktan sonra boya-nanopartikül süspansiyonu 254 nm dalga boylu ışık kullanılarak ışınlanmıştır. Bazı CV molekülleri nanopartiküllerin yüzeyine adsorbe edildiğinden, gerçek CV konsantrasyonu, ışınlama süresinin başlangıcında çözeltide CV'nin denge konsantrasyonuna eşit olarak kabul edilmiştir (Shen vd., 2008).

$Zn_{0.99-x}Mn_xCu_{0.01}O$ nanoparçacıkların fotokatalitik özellikleri, CV'nin fotodegradasyon sürecinin takibi yoluyla değerlendirilmiştir. $Zn_{0.99-x}Mn_xCu_{0.01}O$ nanoparçacıkların sulu bir süspansiyonundaki fotodegradasyona uğramamış CV'nin UV-görünür alan spektrumunun zamana bağlı değişimi, 0-330 dakika aralığında 590 nm'de karakteristik bant şiddetinin azaldığını göstermektedir. 254 nm ışınlamanın etkisi altındaki bu değişiklik, CV'nin $Zn_{0.99-x}Mn_xCu_{0.01}O$ nanoparçacıkların tarafından başarıyla fotodegradasyona uğratıldığını gösterir. Şekil 3a, $Zn_{0.94}Mn_{0.05}Cu_{0.01}O$ varlığında, 0-330 dakika aralığındaki CV foto-bozunma dinamiğini göstermektedir. İncelenen tüm $Zn_{0.99-x}Mn_xCu_{0.01}O$ nanoparçacıkların birinci merteye foto-bozunma kinetikleri Şekil 3b'de gösterilmiştir. $Zn_{0.94}Mn_{0.05}Cu_{0.01}O$ nanoparçacıkları, 330 dakikalık bir fotodegradasyon süresi için 0.0046 dak^{-1} 'lık birinci dereceden hız sabiti ile yüksek bir fotodegradasyon verimliliği göstermiştir.

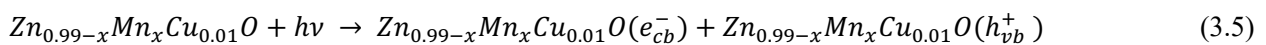
$Zn_{0.99-x}Mn_xCu_{0.01}O$ nanoparçacıklarının fotokatalitik özellikleri, CV'ye karşı gösterdikleri dekolorizasyon etkinlikleri takip edilerek incelenmiştir (Eşitlik 3.4) (Li vd., 2017).

$$\text{Dekolorizasyon yüzdesi} = ((C_0 - C)/C_0) \times 100 \quad (3.4)$$

Eşitlikte, C_0 ve C sırasıyla ışınlama öncesi CV konsantrasyonuna ve belirli bir ışınlama süresinden (t) sonra CV konsantrasyonuna karşılık gelmektedir.

$Zn_{0.99-x}Mn_xCu_{0.01}O$ nanoparçacıklarının zamana bağlı dekolorizasyon etkinlikleri ve gram nanoparçacık başına uzaklaştırılan CV kütlesi (mg) sırasıyla Şekil 4a ve Şekil 4b'de verilmiştir. 330 dakika sonunda $Zn_{0.94}Mn_{0.05}Cu_{0.01}O$ nanoparçacıklarının toplam CV'nin %78.1'ini parçalayabildiği gözlenmiştir.

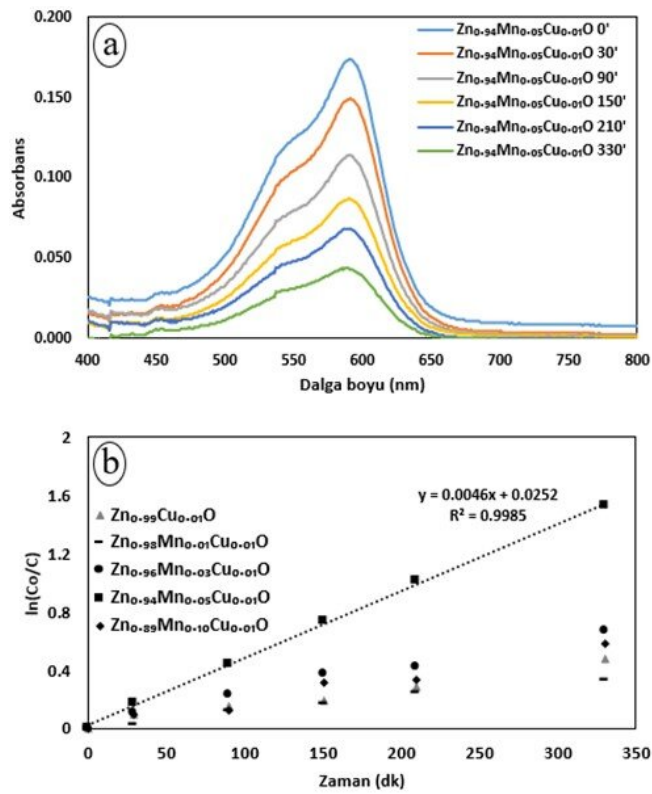
Metal oksit nanoparçacıklardan reaktif oksijen türlerinin oluşumu oksidatif bir süreç olup, CV'nin de dahil olduğu çeşitli organik moleküllerin parçalanmasına sebep olmaktadır. $Zn_{0.99-x}Mn_xCu_{0.01}O$ nanoparçacıklar varlığında CV'nin foto-bozunma süreci aşağıda belirtilen 3 temel basamaktan oluşan mekanizmayı takip eder. İlk basamak değerlik bandı elektronlarının uyarılmasıdır. Bu adımda, değerlik bandı (valence band - vb) elektronları, $Zn_{0.99-x}Mn_xCu_{0.01}O$ nanoparçacıklarının bant aralığından daha fazla enerjiye sahip elektromanyetik radyasyon tarafından foto-uyarılır. Elektronlar (e^-), değerlik bandında eşit sayıda elektron boşluğu bırakarak boş bir iletkenlik bandına (conduction band - cb) göç eder (Eşitlik 3.5).



İkinci adım, malzemenin yüzeyine göç eden elektronların hidroksil (HO^*) ve süperoksit (O_2^{*-}) gibi reaktif oksijen türlerini oluşturmak üzere HO^- , O_2 veya HO_2 ile reaksiyona girmesidir (Eşitlikler 3.6-3.8).

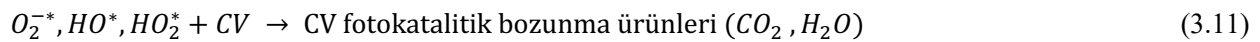


Bu adımda ortaya çıkan radikalleri, hidrojen peroksit (H_2O_2) ve hidroperoksil (HO_2^*) radikalleri gibi diğer bazı reaktif ara ürünlerin oluşumu ile sonuçlanan Eşitlik 3.9 ve Eşitlik 3.10 ile verilmiş olan bazı reaksiyonlara da katılabilir.

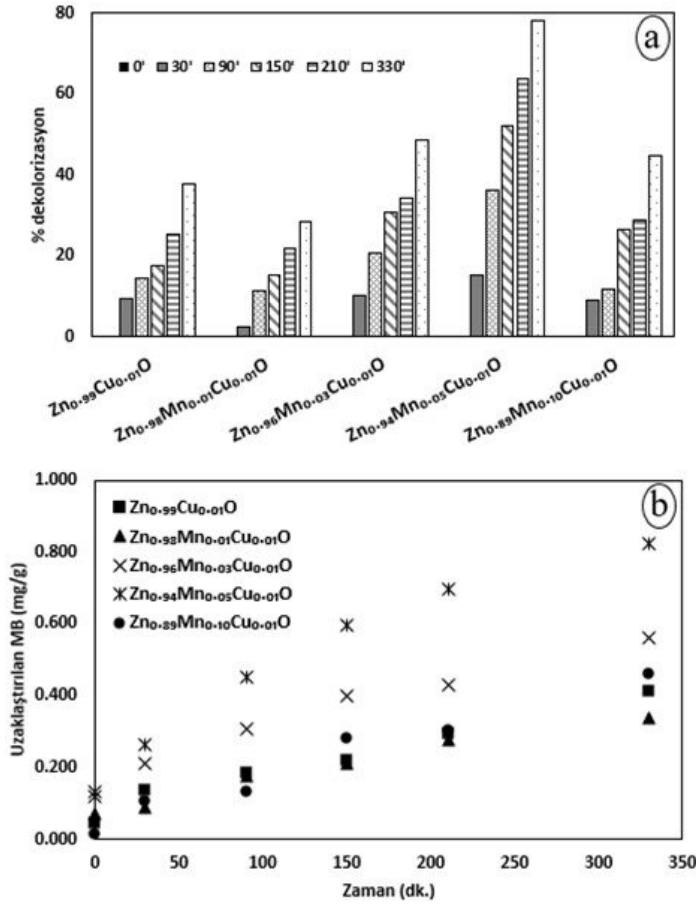


Şekil 3. (a) 254 nm ışınlatma altında $Zn_{0.99-x}Mn_xCu_{0.01}O$ varlığında zamanın bir fonksiyonu olarak CV foto-bozunmasını gösteren UV-görünür alan spektrumları ve (b) $Zn_{0.99-x}Mn_xCu_{0.01}O$ nanoparçacıkları üzerinde CV'nin fotokatalitik bozunması için birinci mertebe bozunma kinetiği.

Üçüncü ve son basamakta organik moleküllerin reaktif oksijen türleri tarafından H_2O ve CO_2 gibi daha az zararlı moleküllere fotokatalitik bozunması meydana gelir (Eşitlik 3.11).



$Zn_{0.99-x}Mn_xCu_{0.01}O$ nanoparçacıkların özellikle $x=0.03$, 0.05 ve 0.10 Mn katkı oranlarında foto uyarılmış elektronların değerlik bandından iletim bandına geçişi yoluyla üretilen ve temelde ve radikallerinin oluşumuna kuvvetle bağlı olan fotokatalitik aktivite sergilediği belirlenmiştir. Belirtilen Mn katkı oranları için 330 dakikalık ışınlatma süresi sonunda foto-bozunmaya uğrayan CV yüzdeleri sırasıyla, %48.7, %78.1 ve %44.6'dır. Gram nano parçacık başına bozulan CV kütlesi (mg), $Zn_{0.94}Mn_{0.05}Cu_{0.01}O$ varlığında gerçekleşen foto-bozunma sürecinde 0.826 mg g^{-1} değerine kadar ulaşmıştır (Şekil 4b).



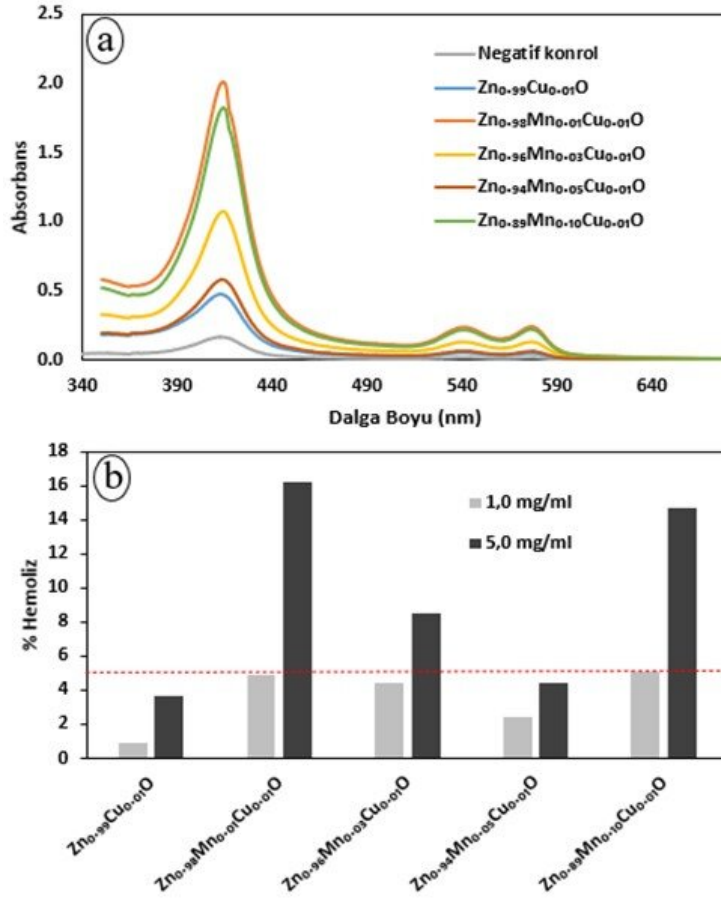
Şekil 4. (a) Zn_{0.99-x}Mn_xCu_{0.01}O nanoparçacıkların zamana bağlı dekolorizasyon etkinlikleri ve (b) gram nanoparçacık başına uzaklaştırılan CV kütlelerinin zamana bağlı değişimi.

3.3. Kan Uyumluluğu Sonuçları

Biyolojik uygulamalar için kullanılmak üzere tasarlanan malzemeler, biyoyumlulukları açısından iyi tanımlanmalıdır. Kan uyumluluğu testleri, sentetik bir malzeme ile canlı dokular arasındaki biyoyumluluğun değerlendirilmesi için bilimsel olarak kabul görmekte olan testlerdir (Markiewicz vd., 2016, Li vd., 2013). Sentetik nano boyutlu malzemeler eritrosit yapısını etkileyebilir, fizyolojik fonksiyonlarını değiştirebilir ve hücrelerin parçalanmasına neden olabilir (Zhang, 2016). Hemotoksik özellikler, bu sentetik malzemelere elementel düzeyde katkılar yapmak yoluyla ayarlanabilir, nanoparçacık kaynaklı hemoliz azaltılabilir ve biyoyumluluk artırılabilir.

Bu çalışmada, Zn_{0.99-x}Mn_xCu_{0.01}O nanoparçacıkların eritrositler üzerindeki etkilerini incelemek için hemolitik aktivite testleri yapılmıştır. Sağlıklı insan eritrositleri iki farklı konsantrasyonda (1.0mg mL⁻¹ ve 5.0mg mL⁻¹) Zn_{0.99-x}Mn_xCu_{0.01}O nanoparçacıklarına maruz bırakılmış ve nanoparçacık kaynaklı hemoliz oranları belirlenmiştir.

Zn_{0.99-x}Mn_xCu_{0.01}O nanoparçacıkları ile muamele edilmiş eritrosit süspansiyonlarının UV-görünür alan süpernatant spektrumları ve hemoliz oranları sırasıyla Şekil 5a ve Şekil 5b'de verilmiştir. Oksihemoglobin için 418 nm'de gözlenen soğutma bantı ile 540 nm ve 577 nm'de gözlenen Q bantlarında gözlenen intensite artışı nanoparçacıkların sebep olduğu hemolizin spektral göstergesi olarak izlenmiştir. Deney sonuçlarına göre 37°C'da 3 saat inkübasyona tabi tutulan eritrositler, 1.0 mg mL⁻¹ Zn_{0.99-x}Mn_xCu_{0.01}O konsantrasyonunda nanoparçacıkların etkisiyle farklı yüzdelerde hafifçe hemolize uğramışlardır (Şekil 5b). Zn_{0.99-x}Mn_xCu_{0.01}O, tüm Mn katkı oranları için 1.0 mg mL⁻¹ nanoparçacık konsantrasyonunda düşük *in vitro* toksisite ve ihmal edilebilir hemolitik aktivite göstergesi olarak kabul edilen %5'ten daha düşük hemoliz oranları gözlenmiştir (Kokila vd., 2022). Zn_{0.94}Mn_{0.05}Cu_{0.01}O her iki konsantrasyonda da %5'in altında hemolize sebep olarak belirgin bir kan uyumluluğu gösterirken, x=0.01, 0.03 ve 0.10 Mn katkı oranlarıyla sentezlenen nanoparçacıklarda 1.0 mg mL⁻¹ konsantrasyonda sırasıyla %16.2, %8.5 ve %14.6 oranlarında hemoliz ortaya çıkmıştır.



Şekil 5. (a) Tek başına PBS (negatif kontrol) ve 5.0mg ml⁻¹ konsantrasyonlarda Zn_{0.99-x}Mn_xCu_{0.01}O nanoparçacıkları ile muamele edilmiş eritrosit süspansiyonlarının UV-görünür alan süpernatant spektrumları. (b) Zn_{0.99-x}Mn_xCu_{0.01}O nanoparçacıklarının 1.0mg ml⁻¹ ve 5.0mg ml⁻¹ konsantrasyonlarda yarattıkları hemoliz yüzdeleri.

Yüksek nanoparçacık konsantrasyonunda ortaya çıkan daha belirgin hemolitik etki başlıca, nanoparçacıklar tarafından oluşturulan reaktif oksijen türlerinin daha baskın hale gelmiş oksidan etkilerinden ve nanoparçacıklar ile eritrosit hücre duvarı arasındaki daha yoğun hale gelmiş etkileşimlerden kaynaklanmaktadır. Eritrosit hücre zarı, temel olarak lipid ve protein kısımlarının hemen hemen aynı konsantrasyonlarını taşıyan bir fosfolipid çift tabakasından oluşan kompozit bir yapıdır (Cho vd., 2019, Sathi vd., 2014). Nanoparçacıklar, eritrosit hücre zarındaki proteinleri etkisiz hale getirerek hücre ölümüne neden olur. Nanoparçacıklar, başta sistein gibi sülfidril (-SH) gruplarını taşıyanlar olmak üzere membran yapısındaki proteinlerle etkileşerek R-S-(Cu)²⁺-S-R kompleksleri oluştururlar. Bu etkileşimler, eritrosit membran geçirgenliğini azaltır ve nihayetinde eritrosit hücre duvarının parçalanmasına neden olur (Tkachenko vd., 2020, Azzam ve Zaki, 2016).

Bu çalışmadan elde edilen hemolitik aktivite deney sonuçları, tüm Mn katkı oranları için, Zn_{0.99-x}Mn_xCu_{0.01}O nanoparçacıklarının 1.0mg ml⁻¹ konsantrasyonda ZnCuO'ya kıyasla hafifçe yüksek olmakla birlikte, kan uyumluluğu sınırları içerisinde kabul edilen %5 altında hemoliz oranlarına sebep olduğunu göstermiştir.

4. Sonuç ve Öneriler

Bu çalışmada, farklı oranlarda mangan katkılanmış nano-boyutlu çinko-bakır oksit (Zn_{0.99-x}Mn_xCu_{0.01}O x=0.00, 0.01, 0.03, 0.05, 0.10) sol-jel yöntemiyle sentezlenmiş, bu yeni malzeme kristal özellikler, yüzey morfolojisi, fotokatalitik performans ve kan uyumluluğu bakımından araştırılmıştır. Bulgular, aynı yöntemle sentezlenmiş nano boyutlu ZnCuO parçacıklarla kıyaslamalı olarak verilmiştir. XRD analizleri, tek fazlı ve Wurtzite yapının varlığını göstermiş olup, nanoparçacıkların Mn katkı oranına göre değişen ve 26.88 nm-35.48 nm aralığında olan ortalama çap değerlerine sahip oldukları tespit edilmiştir. Zn_{0.99}

$Zn_xMn_{0.99-x}Cu_{0.01}O$ nanoparçacıkların fotokatalitik performansları CV foto-bozunma süreci UV-görünür alan spektroskopisiyle takip edilerek incelenmiş ve sentezlenen numuneler içerisinde en yüksek fotokatalitik aktivitenin $Zn_{0.94}Mn_{0.05}Cu_{0.01}O$ nanoparçacıklar tarafından gösterildiği tespit edilmiştir. $Zn_{0.94}Mn_{0.05}Cu_{0.01}O$ nanoparçacıklar, 330 dakikalık ışınlama süresi sonunda CV başlangıç miktarının %78.1'ini degrade ederken $Zn_{0.96}Mn_{0.03}Cu_{0.01}O$ ve $Zn_{0.89}Mn_{0.10}Cu_{0.01}O$ nanoparçacıklarda bu oran sırasıyla %48.7 ve %44.6 olmuştur. $Zn_{0.94}Mn_{0.05}Cu_{0.01}O$ nanoparçacıkları, 330 dakikalık bir fotodegradasyon süresi için 0.0046 dak^{-1} 'lık birinci dereceden hız sabiti ile yüksek bir fotodegradasyon verimliliği göstermiş, gram nano parçacık başına bozulan CV kütlesi (mg), $Zn_{0.94}Mn_{0.05}Cu_{0.01}O$ varlığında gerçekleşen foto-bozunma sürecinde 0.826 mg g^{-1} değerine ulaşmıştır. **İki farklı $Zn_{0.99-x}Mn_xCu_{0.01}O$ nanoparçacık konsantrasyonunda (1.0mg ml^{-1} ve 5.0mg ml^{-1}) gerçekleştirilen kan uyumluluğu testleri ile, numunelerin Mn katkı oranı ile değişen ve nanoparçacık konsantrasyonuna bağlı olan hemolitik aktiviteler gösterdikleri belirlenmiştir.** $Zn_{0.99-x}Mn_xCu_{0.01}O$ nanoparçacıkların tamamı 1.0 mg ml^{-1} konsantrasyonda düşük in vitro toksisite ve potansiyel biyoyumluluk göstergesi olarak %5'ten daha düşük hemoliz oranları göstermiştir. $Zn_{0.94}Mn_{0.05}Cu_{0.01}O$ her iki konsantrasyonda da %5'in altında hemolize sebep olarak belirgin bir kan uyumluluğu gösterirken, $x=0.01, 0.03$ ve 0.10 Mn katkı oranlarıyla sentezlenen nanoparçacıklarda 1.0 mg ml^{-1} konsantrasyonda sırasıyla %16.2, %8.5 ve %14.6 oranlarında hemoliz gözlenmiştir. Sonuç olarak, $Zn_{0.99-x}Mn_xCu_{0.01}O$ nanoparçacıklar için hem fotokatalitik özellikler hem de kan uyumlulukları bakımından optimum Mn katkı oranı $x=0.05$ olarak tespit edilmiştir. Bu çalışmanın, ileri araştırmalar ve modifikasyonlar ile gelişmiş biyoyumluluk ve yeterli yapısal özelliklere sahip nano boyutlu metal oksitlerin geliştirilmesine öncülük etmesi ümit edilmektedir.

Yazar Katkıları

Bestenur Yalçın: Deneyleri planlamış, tasarlamış, verileri toplamış, değerlendirmelerini yapmış ve makaleyi yazmıştır.

Çıkar Çatışması

Yazar çıkar çatışması bildirmemiştir.

Kaynaklar

- Acharya, A. D., Moghe, S., Panda, R., Shrivastava, S. B., Gangrade, M., Shripathi, T., Ganesan, V. (2012). Effect of Cd dopant on electrical and optical properties of ZnO thin films prepared by spray pyrolysis route. *Thin Solid Films*, 525, 49-55. <https://doi.org/10.1016/j.tsf.2012.10.100>
- Aggarwal, N., Vasishth, A., Singh, B., & Singh, B. (2018). Investigation of room temperature ferromagnetic behaviour in dilute magnetic oxides. *Integrated Ferroelectrics*, 186(1), 10-16. <https://doi.org/10.1080/10584587.2017.1369317>
- Ahmad, S., Aadil, M., Ejaz, S. R., Akhtar, M. U., Noor, H., Haider, S., Yasmin, G. (2022). Sol-gel synthesis of nanostructured ZnO/SrZnO₂ with boosted antibacterial and photocatalytic activity. *Ceramics International*, 48(2), 2394-2405. <https://doi.org/10.1016/j.ceramint.2021.10.020>
- Al-Buriah, A. K., Al-Gheethi, A. A., Kumar, P. S., Mohamed, R. M. S. R., Yusof, H., Alsharif, A. F., & Khalifa, N. A. (2022). Elimination of rhodamine B from textile wastewater using nanoparticle photocatalysts: A review for sustainable approaches. *Chemosphere*, 287, 132162. <https://doi.org/10.1016/j.chemosphere.2021.132162>
- Azzam, E. M. S., & Zaki, M. F. (2016). Surface and antibacterial activity of synthesized nonionic surfactant assembled on metal nanoparticles. *Egyptian Journal of Petroleum*, 25(2), 153-159. <https://doi.org/10.1016/j.ejpe.2015.04.005>
- Balcha, A., Yadav, O. P., & Dey, T. (2016). Photocatalytic degradation of methylene blue dye by zinc oxide nanoparticles obtained from precipitation and sol-gel methods. *Environmental Science and Pollution Research*, 23(24), 25485-25493. <https://doi.org/10.1007/s11356-016-7750-6>

- Beitollahi, H., Tajik, S., Nejad, F. G., & Safaei, M. (2020). Recent advances in ZnO nanostructure-based electrochemical sensors and biosensors. *Journal of Materials Chemistry B*, 8(27), 5826-5844. <https://doi.org/10.1039/D0TB00569J>
- Bijang, C. M., Nurdin, M., Latupeirissa, J., Aziz, T., & Talapessy, F. (2022). The Ouw Natural Clay Impregnation Using Titanium Dioxide as a Rhodamine B Dyestuff Degradation. *Indonesian Journal of Chemical Research*, 9(3), 144-149. <https://doi.org/10.30598/ijcr>
- Bilgili, A. K., Akpınar, Ö., Kurtuluş, G., Öztürk, M. K., Özcelik, S., & Ozbay, E. (2019). Lattice parameters a-, c-, strain-stress analysis and thermal expansion coefficient of InGaN/GaN solar cell structures grown by MOCVD. *Politeknik Dergisi*, 22(1), 33-39. <https://doi.org/10.2339/politeknik.403978>
- Bopape, D. A., Motaung, D. E., & Hintsho-Mbita, N. C. (2022). Green synthesis of ZnO: Effect of plant concentration on the morphology, optical properties and photodegradation of dyes and antibiotics in wastewater. *Optik*, 251, 168459. <https://doi.org/10.1016/j.ijleo.2021.168459>
- Carofiglio, M., Barui, S., Cauda, V., & Laurenti, M. (2020). Doped zinc oxide nanoparticles: Synthesis, characterization and potential use in nanomedicine. *Applied Sciences*, 10(15), 5194. <https://doi.org/10.3390/app101551944>
- Cho, Y., Woo, J. H., Kwon, O. S., Yoon, S. S., & Son, J. (2019). Alterations in phospholipid profiles of erythrocytes deep-frozen without cryoprotectants. *Drug testing and analysis*, 11(8), 1231-1237. <https://doi.org/10.1002/dta.2600>
- Guler, A., Arda, L., Dogan, N., Boyraz, C., & Ozugurlu, E. (2019). The annealing effect on microstructure and ESR properties of (Cu/Ni) co-doped ZnO nanoparticles. *Ceramics International*, 45(2), 1737-1745. <https://doi.org/10.1016/j.ceramint.2018.10.056>
- Hasan, F. A., & Hussein, M. T. (2021). Study of some electronic and spectroscopic properties of ZnO nanostructures by density functional theory. *Materials Today: Proceedings*, 42, 2638-2644. <https://doi.org/10.1016/j.matpr.2020.12.593>
- He, X., Gui, Y., Xie, J., Liu, X., Wang, Q., & Tang, C. (2020). A DFT study of dissolved gas (C₂H₂, H₂, CH₄) detection in oil on CuO-modified BNNT. *Applied Surface Science*, 500, 144030. <https://doi.org/10.1016/j.apsusc.2019.144030>
- Hou, Q., Qi, M., Yin, X., Wang, Z., & Sha, S. (2022). First principles study of carrier activity, lifetime and absorption spectrum to investigate effects of strain on the photocatalytic performance of doped ZnO. *Current Applied Physics*, 33, 41-50. <https://doi.org/10.1016/j.cap.2021.09.012>
- Islam, S. E., Hang, D. R., Chen, C. H., & Sharma, K. H. (2018). Facile and Cost-Efficient Synthesis of Quasi-0D/2D ZnO/MoS₂ Nanocomposites for Highly Enhanced Visible-Light-Driven Photocatalytic Degradation of Organic Pollutants and Antibiotics. *Chemistry—A European Journal*, 24(37), 9305-9315. <https://doi.org/10.1002/chem.201801397>
- Jha, M., & Shimpi, N. G. (2018). Spherical nanosilver: Bio-inspired green synthesis, characterizations, and catalytic applications. *Nano-Structures & Nano-Objects*, 16, 234-249. <https://doi.org/10.1016/j.nanoso.2018.07.004>
- Karthik, K., Dhanuskodi, S., Gobinath, C., Prabukumar, S., & Sivaramakrishnan, S. (2017). Photocatalytic and antibacterial activities of hydrothermally prepared CdO nanoparticles. *Journal of Materials Science: Materials in Electronics*, 28(15), 11420-11429. <https://doi.org/10.1007/s10854-017-6937-z>
- Khan, U., Jan, F. A., Ullah, R., & Ullah, N. (2022). Comparative photocatalytic performance and therapeutic applications of zinc oxide (ZnO) and neodymium-doped zinc oxide (Nd-ZnO) nanocatalysts against Acid Yellow-3 dye: kinetic and thermodynamic study of the reaction and effect of various parameters. *Journal of Materials Science: Materials in Electronics*, 1-20. <https://doi.org/10.1007/s10854-021-07483-0>
- Kokila, N. R., Mahesh, B., Roopa, K. P., Prasad, B. D., Raj, K., Manjula, S. N., Ramu, R. (2022). Thunbergia mysorensis mediated Nano Silver Oxide for Enhanced Antibacterial, Antioxidant, Anticancer potential and in vitro Hemolysis Evaluation. *Journal of Molecular Structure*, 132455. <https://doi.org/10.1016/j.molstruc.2022.132455>

- Lee, D., Park, D., Shin, K., Seo, H. M., Lee, H., Choi, Y., & Kim, J. W. (2021). ZnO nanoparticles-laden cellulose nanofibers-armored Pickering emulsions with improved UV protection and water resistance. *Journal of Industrial and Engineering Chemistry*, 96, 219-225. <https://doi.org/10.1016/j.jiec.2021.01.018>
- Li, H. C., Hsieh, F. J., Chen, C. P., Chang, M. Y., Hsieh, P. C., Chen, C. C., Chang, H. C. (2013). The hemocompatibility of oxidized diamond nanocrystals for biomedical applications. *Scientific reports*, 3(1), 1-8. <https://doi.org/10.1038/srep03044>
- Li, H., Liu, J., Wang, C., Yang, H., & Xue, X. (2022). Oxygen vacancies-enriched and porous hierarchical structures of ZnO microspheres with improved photocatalytic performance. *Vacuum*, 110891. <https://doi.org/10.1016/j.vacuum.2022.110891>
- Li, Y., Liao, C., & Tjong, S. C. (2020). Recent advances in zinc oxide nanostructures with antimicrobial activities. *International Journal of Molecular Sciences*, 21(22), 8836. <https://doi.org/10.3390/ijms21228836>
- Li, X., Lu, H., Zhang, Y., & He, F. (2017). Efficient removal of organic pollutants from aqueous media using newly synthesized polypyrrole/CNTs-CoFe₂O₄ magnetic nanocomposites. *Chemical Engineering Journal*, 316, 893-902. <https://doi.org/10.1016/j.cej.2017.02.037>
- Markiewicz, K. H., Zembko, P., Póltorak, K., Misztalewska, I., Wojtulewski, S., Majcher, A. M., Wilczewska, A. Z. (2016). Magnetic nanoparticles with chelating shells prepared by RAFT/MADIX polymerization. *New Journal of Chemistry*, 40(11), 9223-9231. <https://doi.org/10.1039/C6NJ01938B>
- Murali, M., Kalegowda, N., Gowtham, H. G., Ansari, M. A., Alomary, M. N., Alghamdi, S., Amruthesh, K. N. (2021). Plant-Mediated Zinc Oxide Nanoparticles: Advances in the New Millennium towards Understanding Their Therapeutic Role in Biomedical Applications. *Pharmaceutics*, 13(10), 1662. <https://doi.org/10.3390/pharmaceutics13101662>
- Naik, M. M., Naik, H. B., Nagaraju, G., Vinuth, M., Vinu, K., & Rashmi, S. K. (2018). Effect of aluminium doping on structural, optical, photocatalytic and antibacterial activity on nickel ferrite nanoparticles by sol-gel auto-combustion method. *Journal of Materials Science: Materials in Electronics*, 29(23), 20395-20414. <https://doi.org/10.1007/s10854-018-0174-y>
- Ozcelik, S., Yalcin, B., Arda, L., Santos, H., Sáez-Puche, R., Angurel, L. A., Ozcelik, B. (2021). Structure, magnetic, photocatalytic and blood compatibility studies of nickel nanoferrites prepared by laser ablation technique in distilled water. *Journal of Alloys and Compounds*, 854, 157279. <https://doi.org/10.1016/j.jallcom.2020.157279>
- Pillai, A. M., Sivasankarapillai, V. S., Rahdar, A., Joseph, J., Sadeghfar, F., Rajesh, K., & Kyzas, G. Z. (2020). Green synthesis and characterization of zinc oxide nanoparticles with antibacterial and antifungal activity. *Journal of Molecular Structure*, 1211, 128107. <https://doi.org/10.1016/j.molstruc.2020.128107>
- Rani, M., & Shanker, U. (2022). Green nanomaterials: An overview. *Green Functionalized Nanomaterials for Environmental Applications*, 43-80. <https://doi.org/10.1016/B978-0-12-823137-1.00026-9>
- Rao, A. N., Sivasankar, B., & Sadasivam, V. (2009). Kinetic studies on the photocatalytic degradation of Direct Yellow 12 in the presence of ZnO catalyst. *Journal of Molecular Catalysis A: Chemical*, 306(1-2), 77-81. <https://doi.org/10.1016/j.molcata.2009.02.028>
- Reynolds, J. G., & Reynolds, C. L. (2014). Progress in ZnO acceptor doping: what is the best strategy?. *Advances in Condensed Matter Physics*, 2014. <https://doi.org/10.1155/2014/4570588>
- Saleh, R., & Djaja, N. F. (2014). UV light photocatalytic degradation of organic dyes with Fe-doped ZnO nanoparticles. *Superlattices and Microstructures*, 74, 217-233. <https://doi.org/10.1016/j.spmi.2014.06.013>
- Saravanan, R., Karthikeyan, S., Gupta, V. K., Sekaran, G., Narayanan, V., & Stephen, A. J. M. S. (2013). Enhanced photocatalytic activity of ZnO/CuO nanocomposite for the degradation of textile dye on visible light illumination. *Materials Science and Engineering: C*, 33(1), 91-98. <https://doi.org/10.1016/j.msec.2012.08.011>
- Sathi, A., Viswanad, V., Aneesh, T. P., & Kumar, B. A. (2014). Pros and cons of phospholipid asymmetry in erythrocytes. *Journal of pharmacy & bioallied sciences*, 6(2), 81. <https://doi.org/10.4103/0975-7406.129171>

- Senol, S. D., Yalcin, B., Ozugurlu, E., & Arda, L. (2020). Structure, microstructure, optical and photocatalytic properties of Mn-doped ZnO nanoparticles. *Materials Research Express*, 7(1), 015079. <https://doi.org/10.1088/2053-1591/ab5eea>
- Sha, R., Puttapati, S. K., Srikanth, V. V., & Badhulika, S. (2017a). Ultra-sensitive phenol sensor based on overcoming surface fouling of reduced graphene oxide-zinc oxide composite electrode. *Journal of Electroanalytical Chemistry*, 785, 26-32. <https://doi.org/10.1016/j.jelechem.2016.12.001>
- Sha, R., Puttapati, S. K., Srikanth, V. V., & Badhulika, S. (2017b). Ultra-sensitive non-enzymatic ethanol sensor based on reduced graphene oxide-zinc oxide composite modified electrode. *IEEE Sensors Journal*, 18(5), 1844-1848. <https://doi.org/10.1109/JSEN.2017.2787538>
- Shen, W., Li, Z., Wang, H., Liu, Y., Guo, Q., & Zhang, Y. (2008). Photocatalytic degradation for methylene blue using zinc oxide prepared by codeposition and sol-gel methods. *Journal of Hazardous Materials*, 152(1), 172-175. <https://doi.org/10.1016/j.jhazmat.2007.06.082>
- Shi, Y., Liu, Q. G., Chen, Y., & Wang, M. H. (2022). Synthesis and properties of rod-like ZnO composite powders by the reflux method. *Journal of Materials Science: Materials in Electronics*, 1-10. <https://doi.org/10.1007/s10854-021-07548-0>
- Thirumoorthy, G. S., Balasubramaniam, O., Kumaresan, P., Muthusamy, P., & Subramani, K. (2021). Tetraselmis indica mediated green synthesis of zinc oxide (ZnO) nanoparticles and evaluating its antibacterial, antioxidant, and hemolytic activity. *BioNanoScience*, 11(1), 172-181. <https://doi.org/10.1007/s12668-020-00817-y>
- Titov, V. V., Lisachenko, A. A., Akopyan, I. K., Labzovskaya, M. E., & Novikov, B. V. (2019). Long-Lived Photocatalysis Centers Created in ZnO via Resonant Exciton Excitation. *Physics of the Solid State*, 61(11), 2134-2138. <https://doi.org/10.1134/S1063783419110398>
- Tkachenko, A., Onishchenko, A., Klochkov, V., Kavok, N., Nakonechna, O., Yefimova, S., Posokhov, Y. (2020). The impact of orally administered gadolinium orthovanadate GdVO₄: Eu³⁺ nanoparticles on the state of phospholipid bilayer of erythrocytes. *Turkish Journal of Biochemistry*, 45(4), 389-395. <https://doi.org/10.1515/tjb-2019-0427>
- Wolski, L., Walkowiak, A., & Ziolk, M. (2019). Formation of reactive oxygen species upon interaction of Au/ZnO with H₂O₂ and their activity in methylene blue degradation. *Catalysis Today*, 333, 54-62. <https://doi.org/10.1016/j.cattod.2018.04.004>
- Yalcin, B., & Erbil, C. (2018). Effect of sodium hydroxide solution as polymerization solvent and activator on structural, mechanical and antibacterial properties of PNIPAAm and P (NIPAAm-clay) hydrogels. *Polymer Composites*, 39, E386-E406. <https://doi.org/10.1002/pc.24490>
- Yi, C., Yu, Z., Ren, Q., Liu, X., Wang, Y., Sun, X., Huang, X. (2020). Nanoscale ZnO-based photosensitizers for photodynamic therapy. *Photodiagnosis and photodynamic therapy*, 30, 101694. <https://doi.org/10.1016/j.pdpdt.2020.101694>
- Zhang, H. (2016). Erythrocytes in nanomedicine: an optimal blend of natural and synthetic materials. *Biomaterials science*, 4(7), 1024-1031. <https://doi.org/10.1039/C6BM00072J>
- Zhou, D., Wang, P., Roy, C. R., Barnes, M. D., & Kittilstved, K. R. (2018). Direct evidence of surface charges in n-type Al-doped ZnO. *The Journal of Physical Chemistry C*, 122(32), 18596-18602. <https://doi.org/10.1021/acs.jpcc.8b04718>



Türkiye'nin Denizel Çevre Yönetimi Karar Destek Sistemi

Cihat Aşan^{1*}

¹Deniz Ulaştırma ve İşletme Mühendisliği Bölümü, Denizcilik Fakültesi, Piri Reis Üniversitesi, İstanbul, Türkiye

Makale Tarihiçesi

Gönderim: 20.01.2022
Kabul: 26.04.2022
Yayın: 25.09.2022

Araştırma Makalesi

Öz – “Denizel Çevre”, kapsamı içerisindeki değişkenlerin dinamik yapısı dolayısıyla, sorumlu makamlar tarafından süratli ve etkin kararlar alınması gerekli bir sahadır. Denizde meydana gelebilecek bir kaza sonrası, deniz durumu, akıntı ve rüzgâr, gemi trafiği, kirlilik yaratan yakıtın hareketleri vb. değişkenler nedeniyle doğru ve zamanında tedbirlerle müdahale gerekmekte, aksi durumda ortaya çıkacak can ve mal kayıplarının boyutu artmaktadır. Küresel çapta hacmi artan lojistik ve taşımacılık sektörü içerisinde deniz taşımacılığının artan payı, denizlerdeki gemi trafiğini de artırmıştır. Artan trafik, her ne kadar sayıca azalmış gibi görünse de kazaları da beraberinde getirmiş, kazaya sebep olan gemilerin büyüklüğü ise ortaya çıkan can ve mal kayıpları ile çevre kirliliğinin boyutlarını da artırmıştır. Denizel çevrenin yapısı ülkelerin büyük boyutta deniz kazalarına tek başlarına müdahale etmelerini imkânsız kılmış, bu kapsamda bilginin ve teknik imkân kabiliyetlerin ülkeler arası paylaşımı ile koordineli müdahalede plan ve organizasyon yapısına yönelik 2000’li yılların başından itibaren bir dizi uluslararası sözleşme yürürlüğe sokulmuştur. Denizde oluşan bu olaylara müdahalede kararların sürat ve etkinliği, değişkenlerin gerçek zamanlı üretimi ve paydaşlar arasında akışını sağlayacak kapsamlı bir mekanizmayı gerektirmektedir. Bu çalışma; Türkiye’nin denizel çevresinin yönetiminden sorumlu makamların gerçek zamanlı entegrasyon ve bilgi paylaşımı sağlayacak bir karar destek sistemi öngörmektedir. Bu maksatla, süreç içerisindeki paydaşlar ve değişkenler ile bunların nasıl bir organizasyonda entegre edilebileceği ortaya konmuştur.

Anahtar Kelimeler – Deniz kirliliği, denizel çevre, karar destek sistemi, organizasyon, yönetim.

Turkish Marine Environment Management Decision Making System

¹Department of Maritime Transportation and Management Engineering, Maritime Faculty, Piri Reis University, İstanbul, Türkiye

Article History

Received: 20.01.2022
Accepted: 26.04.2022
Published: 25.09.2022

Research Article

Abstract – Due to the dynamic nature of the variables within its scope, “Marine Environment” is a field that requires quick and effective decisions by the responsible authorities. After an accident at sea, due to the variables such as, sea condition, current and wind, ship traffic, movements of polluting fuel, etc. it is necessary to intervene with correct and timely measures, otherwise the size of the loss of life and property increases. The increasing share of maritime transport among the modes of transport has also increased the ship traffic in the seas. The structure of the marine environment has made it impossible for countries to intervene in large-scale maritime accidents on their own, and in this context, a number of international conventions have been put into effect since the beginning of the 2000s on the plan and organizational structure of the coordinated response with the sharing of information and technical capabilities between countries. The speed and efficiency of decisions in responding to these events at sea requires a comprehensive mechanism that will ensure the real-time production of variables and their flow between stake-holders. This study; It envisages a decision support system that will enable real-time integration and information sharing of authorities responsible for the management of Turkey’s marine environment. For this purpose, the stakeholders and variables in the process and how they can be integrated in an organization are revealed.

Keywords – Decision making system, organization, marine pollution, marine environment, management.

¹ casan@pirireis.edu.tr

*Sorumlu Yazar / Corresponding Author

1. Giriş

20'nci yüzyılın ikinci yarısı ile bu yüzyılın başlangıcından itibaren meydana gelen büyük çaplı deniz kazaları beraberinde, bazılarında geri döndürülemez ölçekte olmak üzere, felaket boyutunda çevre kirlilikleri yaratmıştır. Torrey Canyon-1967, Amoco Cadiz-1976, Independenta-1979, Exxon Valdez-1989, Sea Empress-1996, Erika-1999, Prestige-2002, Tasman Spirit-2003 kazaları bu konudaki örnekler olup, meydana gelen can ve mal kayıpları ile deniz kirliliğinin yarattığı ekolojik denge bozuklukları bir dizi önlemin alınmasını gerekli kılmıştır.

Kirliliği meydana getiren kimyasalların hava ve deniz suyuyla etkileşimi neticesinde yapılarında değişiklik meydana gelmekte ve doğal dağılıma, batma, çökme, buharlaşma vb. farklı davranış biçimleri ortaya çıkmaktadır (Fingas, 2014). Kimyasalların yapılarında meydana gelen bu değişiklikler, zaman geçtikçe müdahaleyi daha da güçleştirmektedir. Bu kapsamda kirleten maddelerin bertarafına yönelik müdahale süresinin kısalığı, ekolojik dengeye verilen zararın asgari seviyede tutulması için hayati önem taşımaktadır. Şu ana kadar meydana gelen deniz kirliliklerinden çıkartılan dersler ışığında; benzer olayların oluşmasını önlemek, oluştuktan sonra ise etkin ve süratli müdahale etmek üzere kirliliğin olası hareketlerini öngörecektir yayılım modelleri, kontrol, değerlendirme ve karar destek sistemleri gibi teknolojik imkânlar geliştirilmiştir. Bu teknolojik imkânların karar süreçlerine etkisini ortaya koymak üzere daha önce yapılmış çalışmalar incelenmiştir: Garello ve Kerbaol (2017) yaptıkları çalışmada, denizdeki yakıt kirliliğinin tespiti, izlenmesi ve etkin bir müdahalenin sağlanabilmesi için, kirliliğe sebep olan kaynağın tespit ve teşhisinin elzem olduğunu vurgulamış, bu amaçla sinerjik yaklaşım metodunu kullanarak, radar ve uydu görüntülerini meteorolojik, oşinografik veriler ile Otomatik Tanımlama Sistemi (OTS) vb. teşhis sistemlerinden sağlanan bilgiler ile birleştirmişlerdir. Açık denizlerden elde edilen akıntı, sıcaklık, tuzluluk gibi değerlerin kirlilik yayılma modellerinin içine direk ya da hidrodinamik modellerle vasıtasıyla sokulmasına yönelik örnekler sunan Hackett, Comerma, Daniel ve Ichikawa (2009), bu değerlerin toplanması ve işlenmesinde küre-sel çapta rol oynayan "Global Ocean Data Assimilation Experiment (GODAE)" verilerinin yayılım modellerinin tahmin doğruluğunu artırdığını vurgulamıştır. Bukin, Proschenko, Chekhlenok ve Korovets-kiy (2019), denizel çevre ekosistemlerinin insansız hava araçları vasıtasıyla gözetlenmesinde yeni teknolojilerin uygulama sonuçlarını sunmuşlardır. Bu kapsamda yakıt kirliliklerinin tespitinde, yapay zekanın kullanıldığı yazılım-donanım komplekslerini açıklamış, kirliliğin teşhisinde kullandıkları Laser Endüklü Floresan-Laser Induced Fluorescence (LIF) metodu ile yukarı yönlü "Solar Radyasyon Spektrum Kaydı" metodlarının laboratuvar sonuçlarını ortaya koymuşlardır. Tek parametre hesaplamalı modelden üç boyutlu nümerik hesaplamalı kompleks sistemlere varan değişkenlikteki onsekiz adet deniz kirliliği yayılım modelinin incelendiği Keramea, Spanoudaki, Zodiatis, Gikas ve Sylaios (2021)'in çalışmasında, bu simülasyonların; yakıtın fiziksel değişimleri, deniz yüzeyinden deniz dibine kadar olan yer ve miktar değişimleri, ortam değişkenlerinin gerçek zamanlı girdileri ve yayılım tahminlerinin doğruluğu açısından yeterlilik ve etkinlikleri incelenmiştir. Bu kapsamda yeni jenerasyon modellerin özellikle kirliliğe müdahalenin gerçek zamanlı simülasyonunda eksiklik içerdiği vurgulanmıştır. Perkovic ve Sitkov (2008) ise çalışmalarında, bir deniz kirliliği yayılım ve müdahale simülatörü olan "Potential Incident Simulation, Control and Evaluation System – PISCES"ın, denizel çevreye ait diğer tüm dinamikleri monite eden sistemler ile entegrasyonu ve karar destek sistemi olarak kullanımını tanıtmıştır. Ye, Chen, Li, Jing, ve Zeng (2019) çalışmalarında, deniz kirliliğine müdahale cihazlarının tahsisi ve süreç kontrolünde karar verme sürecini desteklemek için entegre simülasyon tabanlı çoklu parçacık sürüsü optimizasyonu (multi-agent particle swarm optimization-SA-PSO) yaklaşımını önermiştir. Bahse konu simülasyonda ilk olarak deniz kirliliğinin yayılımı modellenmiş, daha sonra bu kirliliğe asgari maliyet ve zamanla müdahale edebilmeye yönelik olarak araçların en etkin tahsis ve kullanımı sağlanmıştır. Deniz kirliliğinin yayılımı ve müdahaledeki bilimsel ilerlemelerin, mevcut zorlukların ve geleceğe yönelik öngörülerin kapsamlı bir sentezini sunan Barker vd. (2020) yakıt yayılım tahminlerinin doğruluğunu artırmaya yönelik olarak okyanus akıntıları ve yakıt yayılım modelleri üzerinde çalışmışlardır. Çalışma, uluslararası müdahale merkezlerinin uygulamaları, keşif ve gözetleme ihtiyaçları, yeni yöntemler ile organizasyon protokolleri üzerine yoğunlaşmıştır. Amir-Heidari vd. (2019) ise çalışmalarında, gemi batıklarından kaynaklanan yakıt sızıntılarının olasılık esaslı ve alansal risk değerlendirmesini yapmışlar, risk değerlerini etkileyen faktörleri içerecek şekilde yapısal yeni bir model kullanmışlardır Mohammadiun vd. (2021). deniz kirliliği ile mücadele yönetimine ilişkin sayısal nitelikli çalışmaları derlemiş, kirliliğin tespiti ile sonrasındaki müdahale esaslarının optimizasyonu şeklinde iki bölüme ayırdıkları çalışmalarının sonucunda sayısal tekniklerdeki potansiyel hataları tespit etmiş ve etkin bir mücadele yönetimi için kendi bütüncül sayısal tabanlı modellerini ortaya koymuşlardır.

Konuyla alakalı literatürün taranması neticesinde, deniz kirliliğini tespit ve teşhis etme yöntemleri ile deniz kirliliği yayılımı ve bu kirliliğe müdahale simülasyonları incelenmiş olmakla birlikte, denizde meydana

gelebilecek bir olayda, bu simülasyonların bir karar destek sistemi şeklinde kullanımına yönelik çalışmaların olmadığı, Türkiye'nin kendi dinamikleri çerçevesinde böyle bir sistemin nasıl bir organizasyon dahilinde oluşturulabileceğinin ele alınmadığı tespit edilmiştir.

Geçmişte yaşanan büyük çaplı deniz kazaları ve akabinde oluşan deniz kirlilikleri, özellikle 1989 yılında Alaska Körfezi'nde meydana gelen Exxon Valdez kazası, geliştirilen bu teknolojik imkânların, devletlerin tek başına çabasıyla değil, diğer devletlerle koordinasyon ve kabiliyetlerin karşılıklı paylaşımı sonucunda etkin olabileceğini göstermiştir. Ülkelerin, kirliliğin tespiti, takibi ve müdahaleyi en kısa zamanda gerçekleştirmek üzere oluşturduğu kontrol, değerlendirme ve karar sistemleri bölgesel boyutta diğer ülkelerin imkanlarıyla da entegre edilmiştir. Örneğin Avrupa Deniz Emniyeti Ajansı (EMSA) ve Avrupa Birliği Sivil Korunma Mekanizması üye devletlerin deniz çevresinin güvenliğine yönelik imkanlarının ortak alanda toplanmasını ve çabaların koordinesini sağlamak amacıyla Acil Durum Müdahale Koordinasyon Merkezi (Emergency Response Coordination Centre-ERCC)'ni kurmuş, bu çatı altında yer alan tüm unsurların bilgi paylaşımını ise Ortak Acil Durum Haberleşme ve Bilgi Sistemi (Common Emergency Communication and Information System, CECIS) vasıtasıyla sağlamıştır (AFAD, 2014). Bu gibi bilgi paylaşım ve koordinasyon organizasyonlarının temelini ise ülkelerin gerek bireysel gerekse bölgesel işbirlikleri vasıtasıyla oluşturdukları denizde acil durum simülasyon ve karar destek sistemleri oluşturmaktadır.

Karar destek sistemleri deniz kazaları sonrasında arama kurtarma ve kirliliğe müdahale operasyonlarında karar vericilere, deniz ve hava alanı değişkenlerinin sürekli güncel tutulmasıyla modelledikleri olay sahası resmini sunabilmektedir. Bu modellerin girdilerini teşkil eden değişkenler ise; kirliliğe sebep olan yakıtın buharlaşma, yayılma, doğal parçalanma, viskozite değişimi ile olay sahası hava durumu, deniz durumu, yüzey akıntısı sahanın sahil yapısı, derinliği, ekolojik hassas alanları, müdahale ekipmanları vb. değerler olabilmektedir (Delgado, Kumzerova ve Martynov, 2006). Bu değişkenler içerisinde, meteorolojik şartlar, yüzey akıntısı, deniz durumu, olay sahasındaki diğer gemiler vb. dinamik olanlarının sistemlere gerçek zamanlı olarak girdilerinin sağlanabilmesi, kararların etkin ve süratli verilebilmesinde hayati rol oynamaktadır. Bu kapsamda bahse konu değişkenleri tespit eden, işleyen, depolayan kurum ve kuruluşların sistemlerinin gerçek zamanlı ve 7/24 olacak şekilde denizde acil durum karar destek sistemlerine entegrasyonları da elzem hale gelmektedir.

2. Materyal ve Yöntem

2.1. Araştırmanın Amacı

Bu çalışmanın amacı; Türkiye'nin deniz kirliliği acil durum karar destek sistemine yönelik, karar vericilere gerçek zamanlı olay sahası resmini sağlayacak ağ merkezli bir organizasyon yapısı hakkında perspektif sunmaktır. Ortaya konulan bu organizasyon yapısı sayesinde Türkiye'nin deniz çevresinde meydana gelebilecek herhangi bir olayda, hâlihazırda birbirinden bağımsız vaziyette bulunan karar verici makamların bütünleşik bir yapı içerisinde aynı deniz resmine sahip olmaları sağlanmaktadır. Bununla birlikte çalışma, konuya yönelik yeni ve yaratıcı bir bakış açısı sunması açısından önem arz etmektedir.

2.2. Araştırmada Kullanılan Yöntem

Bu araştırmada, konu ile ilgili literatür taraması yapılarak deniz kirliliği yayılım modellemeleri ile Türkiye'nin deniz kazalarına müdahale organizasyonu ve sorumlu makamlar hakkında bilgi toplanmıştır. Kalitatif nitelikte olan bu çalışma kaynak tarama yöntemi kullanılarak yapılmıştır. Bu kapsamda perspektifi sunulan Türkiye'nin denizel çevre yönetimi karar destek sistemine veri sağlayacak kurumların kabiliyetleri incelenmiş, sistem entegrasyonlarının mevcut durumu ortaya konmuş, etkinliği artıracak bir organizasyona yönelik teklifte bulunulmuştur.

3. Bulgular ve Tartışma

3.1. Denizel Çevre Yönetimi ve Karar Süreci

Denizel çevre kirliliği ile mücadelede karar mekanizması incelenmeden önce buna kaynak teşkil eden denizel çevrenin kapsamının belirlenmesi gerekmektedir. Uluslararası mevzuat incelendiğinde denizel çevrenin kapsamı belirlenmemiş olmakla birlikte Birleşmiş Milletler Üçüncü Deniz Hukuku Konferansında ülkelerin bu konudaki önerileri çalışmalara temel teşkil edebilmektedir. Buna göre; "Deniz çevresi, deniz

yüzeyi, üzerindeki hava, altındaki su kolonu ve içindeki ona bağlı biyosistemler de dahil olmak üzere denizin en çok yükseldiği hattın ötesindeki deniz yatağından ibarettir”

Kapsamı bu derece geniş olan bir çevrenin kirlenmesine neden olan kaynakların da mücadelenin etkinliğini sağlamak amacıyla, sağlıklı bir şekilde ortaya konması gerektiği değerlendirilmektedir. Bu konuda yine aynı konferansta; deniz hayatının deniz çevresi kapsamı içerisinde yer aldığı, kirlilik söz konusu olduğunda sadece yüzey kaynaklı değil denizin çevresiyle bağlantılı olduğu ortamlar da dahil “denizel çevrenin kirlenmesi” olarak daha geniş algılandığı belirtilmiştir. 1982 tarihli Birleşmiş Milletler Deniz Hukuku Sözleşmesi Kısım 1, Md.1 Parag.4’de yer alan tanımlamada “Deniz çevresinin kirlenmesinden, canlı kaynaklara ve deniz yaşamına zarar verme, insan sağlığı için tehlike oluşturma, balıkçılık ve denizlerin diğer yasal amaçlarla kullanımı da dahil olmak üzere, denizcilik faaliyetlerini engelleme, deniz suyunun niteliğini değiştirme ve güzellikleri bozma gibi zararlı etkileri olan veya olabilecek maddelerin veya enerjinin, insan tarafından doğrudan doğruya veya dolaylı olarak, haliçler de dahil olmak üzere, deniz çevresine dahil edilmesi anlaşılmaktadır”. Tütüncü (2004) ise çalışmasında deniz kirlenmesini; “İnsanların her türlü faaliyetleri sonucu, denizlerde meydana gelen olumsuz gelişmelerle ekolojik dengenin bozulması ve aynı faaliyetler sonucu ortaya çıkan koku, gürültü ve atıkların deniz çevresinde meydana getirdiği arzu edilmeyen sonuçlardır” şeklinde tanımlamıştır.

Denizel çevre içerisinde meydana gelen kaza, kirliliğe müdahale, arama kurtarma vb. operasyonlarda sürecin takibi, kontrolü ve karar verme aşamalarında destek sağlayan sistemlerin girdileri de bahse konu çevrenin değişkenleri paralelinde çeşitlilik arz etmektedir.

3.2. Denizel Çevre Yönetimi Karar Süreci

Denizel çevrenin kirlenmesine yol açan kaynaklar ele alındığında sadece gemiler değil, açık deniz platformları ile zararlı kimyasal ve nükleer atıkların deniz dibine depolanması da göz önünde bulundurulmalıdır Tütüncü (2004). Ancak bunların arasında gemi kazaları, neticesinde oluşan can ve mal kayıpları ile deniz kirliliğinin boyutları açısından öne çıkmaktadır. Büyük ölçekte ekonomik, sosyal ve çevresel etkiler yaratan bu kazalarda, olay sahnesinin büyüklüğü ve ortamdaki değişkenlerin fazlalığı oluşan kayıpların azaltılmasına yönelik müdahaleyi de zorlaştırmaktadır. Bu kapsamda; gerek can ve mal kayıplarının önlenmesine yönelik arama kurtarma, gerekse deniz kirliliğinin etkilerini azaltmaya yönelik müdahale faaliyetlerinin koordineli ve süratli yapılması gerekmektedir. Bunu sağlamak üzere acil durum müdahale planları, personel organizasyonu ve eğitimi sağlanmalıdır. Gerçek şartlar altında bu organizasyon ve eğitimi sağlamak zor ve maliyetli olup, “simülasyon” bu dezavantajları ve büyük ölçüde kirleticiyi ortadan kaldırmaya yönelik stratejilerin geliştirilmesi için önemli bir araç olmaktadır (Nicolae, Perkovic, Ristea, ve Cotorcea, 2016). Bu kapsamın sadece deniz kirliliği boyutu ele alındığında ise petrol, kazaların deniz yaşamı üzerinde en yıkıcı etkiyi yarattığı ve müdahaleye yönelik en zor şartları oluşturduğu bir biçimi olarak ortaya çıkmaktadır. Süratli müdahale, dökülen petrolün etkilerini azaltacağından, yayılma ve akıbetini tahmin etme becerisine sahip simülasyon sistemleri geliştirilmiştir.

Petrol yayılımı tahmini, tipik olarak denizdeki petrolün ayrışması ve hareketinin sayısal bir modeli kullanılarak gerçekleştirilir. Buharlaştırma, emülsifikasyon, doğal dispersiyon ve diğer petrole özgü süreçleri içeren ayrışma, ortamdaki çevresel koşulların etkisi altında petrol tipinin kimyasal özellikleri tarafından belirlenir.

Denizde yaşanan kazalar neticesinde oluşan can ve mal kayıpları, deniz kirliliği, hava kirliliği, kıyı kirliliği gibi etkilerin hepsinin simüle edilebildiği, gerçek şartlarda ise olay sahası resminin takip edilebildiği karar destek sistemleri, olayların asgari kayıpla sonlandırılması için karar vericilere sürat ve etkinlik sağlamaktadır. Yapılan tüm operasyonlarda (Arama kurtarma, deniz ve hava kirliliğine müdahale, ekolojik, ekonomik ve sosyal hassas alanların korunması vb.), yüzer ve uçar unsurların mevkilerini göstermeye yönelik radar, Otomatik Tanımlama Sistemi-OTS (Automatic Identification System-AIS) bilgileri ile, deniz ve hava kirliliği takibine yönelik meteorolojik, oşinografik, hidrografik değerlerin gerçek zamanlı girdilerinin sağlanması ve bu sistemlerinin karar verici kurumlarda 7/24 çalışması gerekmektedir.

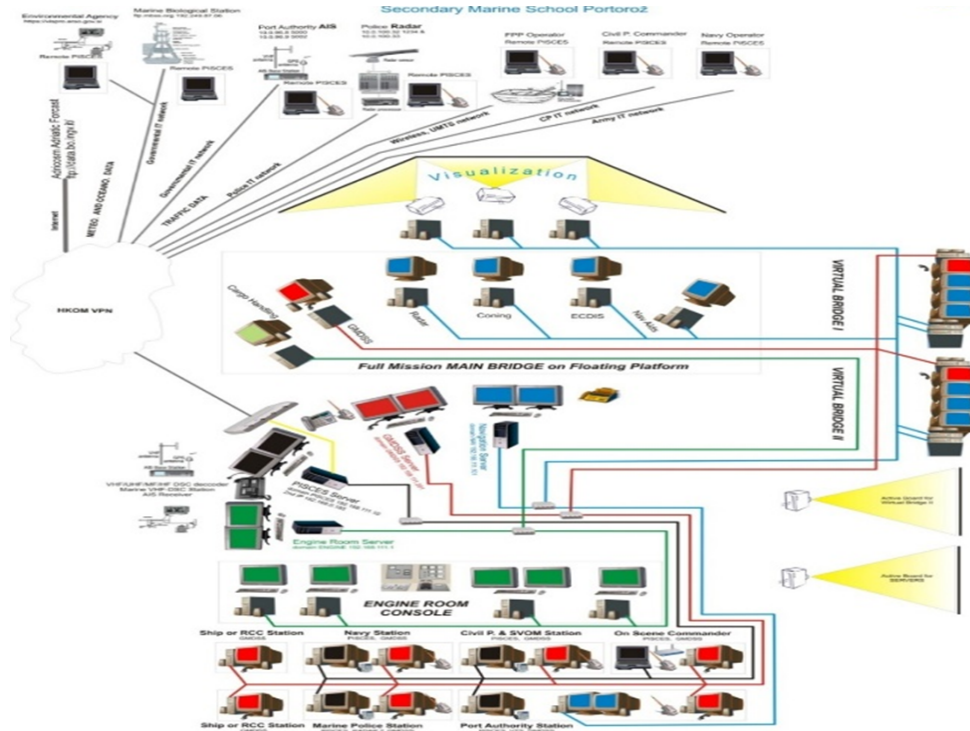
3.3. Karar Destek Sistemleri

Denizde meydana gelen kazaların yarattığı kayıplar gerek taşımacılık ve petrol endüstrisini gerekse karar verici makamları, kirliliğin oluşmasını engellemeye, meydana geldiğinde ise müdahalenin etkinliğini artırmaya yönelik sistemler kurmaya sevk etmiştir. Bu kapsamda kirleticilerin deniz ve hava ile etkileşimi neticesinde kimyasal yapılarında meydana gelen değişiklikler ile denizel çevredeki dinamikleri üzerine

çalışmalar yapılmış, neticesinde karar destek sistemleri geliştirilmiştir. Hidrokarbon kimyası ve akışkanlar mekaniği üzerine inşa edilen bu sistemler, birleştirilmiş bir dizi veri tabanı ve modeller sayesinde kullanıcıların acil durum müdahale planları geliştirmelerine olanak sağlamakta olup;

- Hedefler ve niceliksel tedbirlerin belirlenmesi,
- Maliyet etkinlik analizi, teknik ekipman tedarik ve mekân tahsisine yönelik rasyonalizasyon ve optimizasyon,
- Müdahale personelinin eğitimi,
- Müdahale operasyonlarına destek,
- Alternatif müdahale stratejileri ile lojistiğinin değerlendirilmesi,
- Çevresel risk ve etki değerlendirmesi,
- Dispersant (Kimyasal müdahale) çevresel etki değerlendirmesi vb. ihtiyaçlara cevap vermek üzere dizayn edilmiştir (Reed, Aamo ve Daling, 1995).

Bu kapsamda, Norveç IKU Petrol Araştırmaları Enstitüsü Çevre Teknolojileri Bölümü tarafından geliştirilen Oil Spill Contingency and Response (OSCAR) sistemi (Reed vd., 1995), Türkiye Bilimsel ve Teknolojik Araştırma Kurumu (TÜBİTAK) tarafından geliştirilen Yardım Arama Kurtarma ve Acil Müdahale Otomasyon Sistemi (YAKAMOS), Potential Incident Simulation Control and Evaluation System (PISCES) vb. sistemler, denizde acil durum müdahalesinin etkin ve süratli icrasına yönelik karar vericilere destek sağlarken meteoroloji (rüzgar, hava ve deniz suyu sıcaklığı, vb.), oşinografi (deniz suyu yoğunluğu, yüzey akıntısı, dalga durumu, derinlik vb.), deniz trafiği dinamik verileri ile kirleticiler ve müdahale ekipmanları verilerini (viskozite, yoğunluk, bariyer yüksekliği, yağ sıyırıcı kapasitesi vb.) kullanmaktadır. Statik verilerin önceden sisteme sokulması ve güncel tutulmasının yanı sıra dinamik verilerin gerçek zamanlı girdisi, olay sahnesinin de doğru bir şekilde resmedilmesinde hayati öneme sahiptir. Dolayısıyla bu verileri sağlayan kurum/kuruluşların (meteoroloji dairesi, oşinografi/hidrografi dairesi, sahil güvenlik radarları, deniz trafik hizmetleri radarları/OTS-AIS'leri, polis radarları, uydu gözetleme sistemleri vb.) karar verici sistemlere gerçek zamanlı veri entegrasyonu yapılması elzem olmaktadır. Şekil-1'de bu tarz bir sistemin örnek resmi sunulmuştur.



Şekil 1. Deniz trafiği yönetim, denizde haberleşme, yük elleçleme, makine kontrol, deniz kirliliği simülasyonlarının entegrasyon konsepti (Perkovic ve Sitkov, 2008).

Şekil-1'de deniz çevresinde meydana gelebilecek herhangi olayda sahanın tüm dinamik verilerini (akıntı, rüzgar, sıcaklık, trafik vb) sağlayan sistemler ile bu verileri sağlayan makamlar (Hidrografi Ajansı, Polis ve Sahil Güvenlik, Meteoroloji Ajansı, Komuta Kontrol Merkezi) internet tabanlı olarak birbirlerine entegre edilmiş olup, Komuta Kontrol Merkezinde bulunan makina, köprüüstü ve deniz kirliliği simülatörleri ağ merkezli bir yapıya kavuşturulmuş ve karar destek sistemi meydana getirilmiştir. Yine internet tabanlı yapı sayesinde karar makamlarının bu destek sisteminin sağladığı deniz resmine eş zamanlı olarak ulaşmaları sağlanmıştır.

3.4. Türkiye'nin Denizel Çevre Kirliliğine Müdahale Organizasyonu

Deniz kirliliği ile mücadelenin uluslararası hukuksal tabanı 1954 tarihli Denizlerin Petrol ile Kirlenmesini Önlemeye İlişkin Uluslararası Sözleşme (OILPOL-International Convention for the Prevention of Pollution of the Sea by Oil) ile oluşmaya başlamış, özellikle ülkeler ve kurumlar arası koordinasyon ile ülkelerin bireysel organizasyon ve planlarının oluşturulmasında 1990 tarihli Petrol Kirliliğine Karşı Hazırlıklı Olma, Müdahale ve İşbirliği Uluslararası Sözleşmesi (OPRC 1990- International Convention on Oil Pollution Preparedness, Response and Co-operation) öncü rol oynamıştır. Türkiye taraf olduğu OPRC 1990 sözleşmesi paralelinde kendi denizel çevresinin korunmasına yönelik 5312 sayılı "Deniz Çevresinin Petrol ve Diğer Zararlı Maddelerle Kirlenmesinde Acil Durumlarda Müdahale ve Zararların Tazmini Esaslarına Dair Kanunun Yürütme Yönetmeliğini" 2006 yılında yürürlüğe sokmuştur. Bahse konu Kanun'un amacı; "deniz emniyetinin sağlanması ve deniz kirliliğinin önlenmesi konusundaki uluslararası hukuk ve iç hukuktan doğan hak ve yükümlülükler göz önünde bulundurularak;

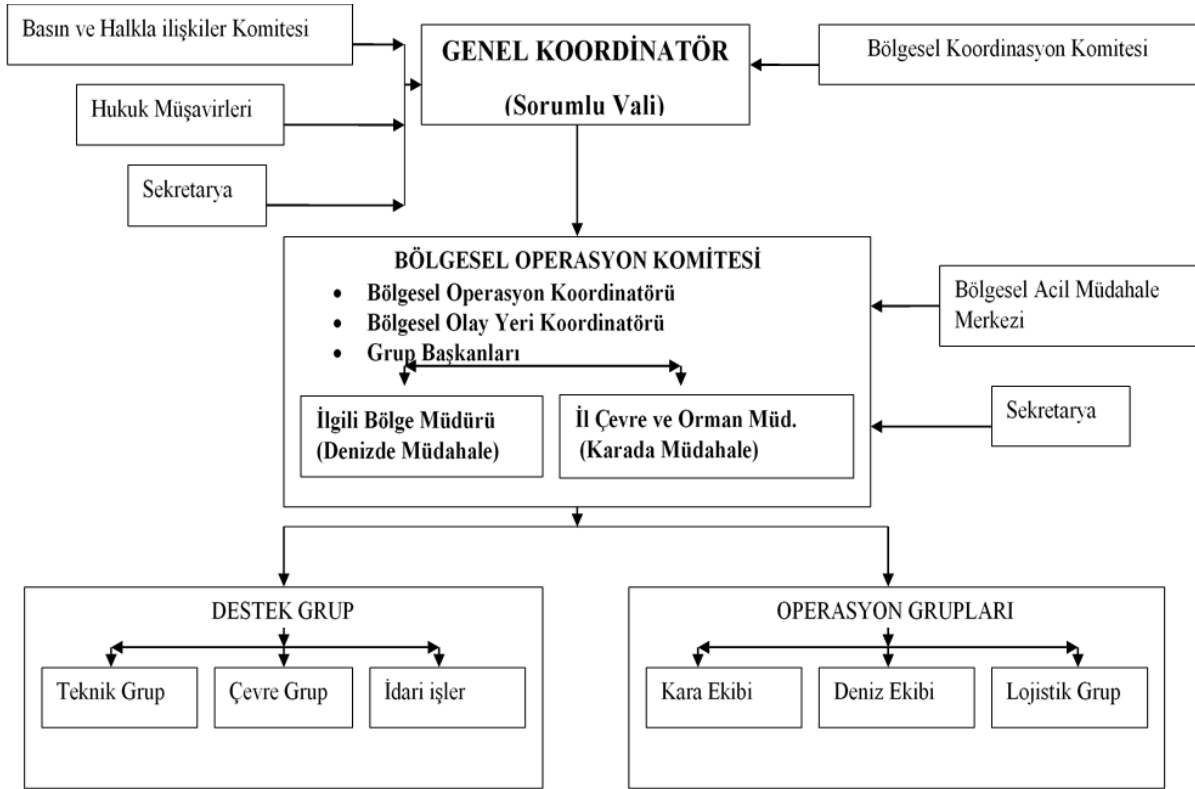
- Acil durumlarda gemilerden ve kıyı tesislerindeki faaliyetlerden kaynaklanan kirlenme tehlikesini ortadan kaldırmak veya kirlenmeyi azaltmak, sınırlamak ve gidermek üzere uygulanacak müdahale ve hazırlıklı olma esaslarını,
- Olay sonucu ortaya çıkan zararların tespit ve tazmin esaslarını,
- Uluslararası yükümlülüklerin yerine getirilmesi esaslarını,
- Kanun kapsamına giren kişilerle kurum, kuruluş, gemi ve tesislerin Kanunda belirtilen ilgililerinin yetki, görev ve sorumluluklarını, belirlemektir" (5312 Sayılı Kanun, 2006).

Aynı mevzuatta yer alan kuruluşların yetki, görev ve sorumlulukları kapsamında Çevre, Şehircilik ve İklim Değişikliği Bakanlığı, Ulaştırma ve Altyapı Bakanlığı (UAB), Sahil Güvenlik Komutanlığı, kirliliğin seviyesine bağlı olarak, valilikler, belediyeler, ilgili bakanlık il müdürlükleri, kıyı emniyeti genel ve bölge müdürlükleri ile ilgili kurumlar, olası deniz kirliliğini önleme ve müdahalede planlı reaksiyonlar için görevlendirilmiş durumdadır.

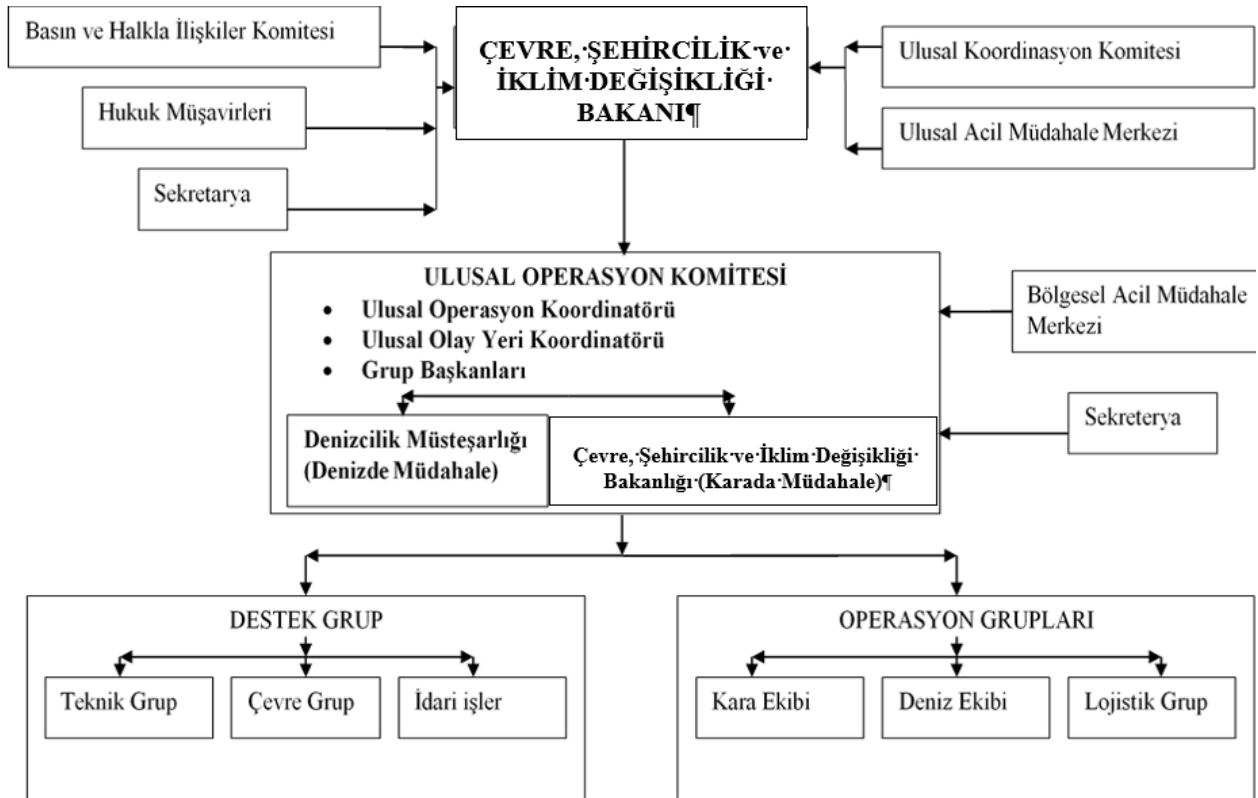
Ulaştırma ve Altyapı Bakanlığı (UAB)'nın Acil Müdahale Merkezleri Projesi kapsamında; Türkiye kıyılarında bölgesel ve ulusal seviyede meydana gelebilecek muhtemel kazalara karşı kurulacak istasyonlardan müdahale imkânı planlanmıştır. Ulusal Acil Müdahale Sistemi Türkiye denizleri ve kıyılarını petrol ve diğer zararlı maddelerden kaynaklı deniz kirliliklerine karşı korumak amacıyla Tekirdağ'da bulunan Ulusal Deniz Emniyeti ve Acil Müdahale Merkezi (UDEM), Antalya'da bulunan Bölgesel Acil Müdahale Merkezi ve kurulması planlanan Acil Müdahale İstasyonlarını kapsamaktadır (UAB, 2018).

Büyük deniz kirliliklerinde koordinasyon ve operasyon merkezi olarak görev yapacak UDEM, bu işlevini yerine getirebilmek için gerek tatbikat gerekse gerçek zamanlı olay sahası resmini gösterecek bir karar destek sistemine sahip olacaktır. Bu sistemin bahse konu resme sahip olması ve 5312 sayılı Kanun kapsamında karar verici ve operasyonel makamlar tarafından gerçek zamanlı paylaşılması gerekmektedir. Kirliliğin seviyesine bağlı olarak üç aşamalı bir eylem planı öngören bahse konu Kanun'un öngördüğü müdahale organizasyonu Şekil 2 ve Şekil 3'te sunulmuştur.

Denizde meydana gelebilecek bir kirlilik, kıyı tesisinin müdahale edebileceği boyutta ise Seviye 1 olarak sınıflandırılmakta, aksi durumda ise Seviye 2 olarak değerlendirilmekte, görevlendirilen İl Valisi koordinatörlüğünde Şekil 2'de yer alan makamların işbirliği ile bölgesel boyutta müdahale organizasyonu teşkil edilmektedir. Kirlilik, bölgesel imkânları da aşan daha büyük boyutta gerçekleştiği takdirde ise Seviye 3 olarak değerlendirilmektedir.



Şekil 2. Türkiye deniz çevresinin petrol ve diğer zararlı maddelerle kirlenmesinde bölgesel acil müdahale teşkilat şeması (5312 sayılı kanun, 2006).

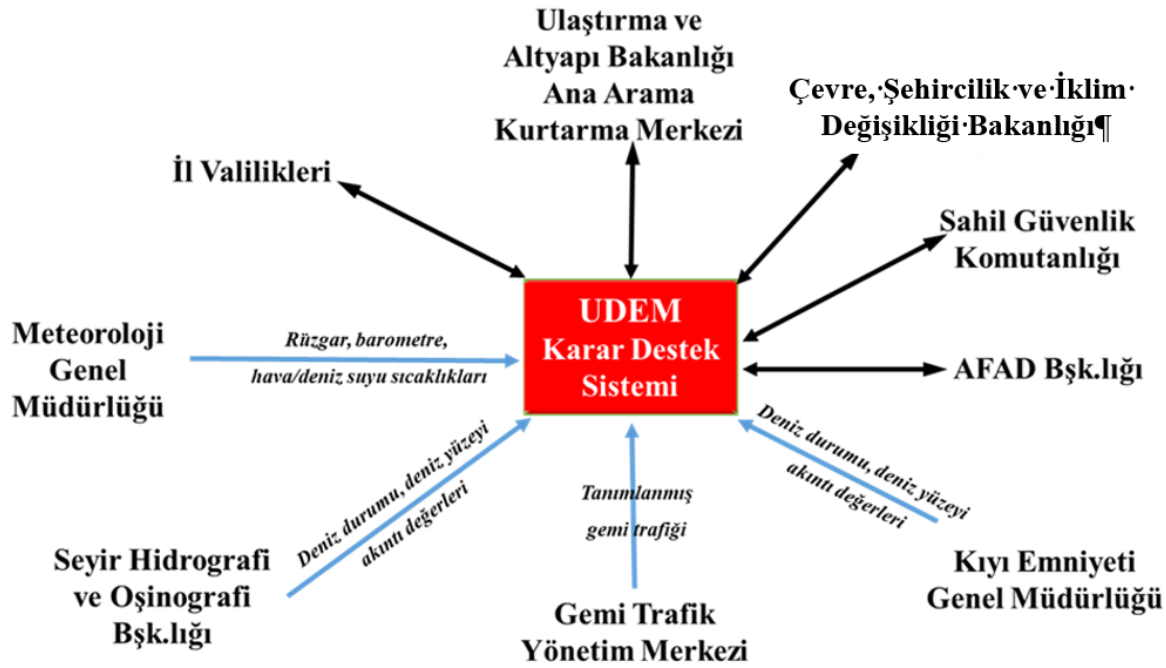


Şekil 3. Türkiye deniz çevresinin petrol ve diğer zararlı maddelerle kirlenmesinde ulusal acil müdahale teşkilat şeması (5312 sayılı kanun, 2006).

3'üncü Seviye kirlilik ulusal boyutta bir müdahaleyi gerekli kılmakta, bu durumda Çevre ve Şehircilik Bakanı'nın başkanlık ettiği, denizdeki kirlilik için Ulaştırma ve Altyapı ve Bakanlığı bağlısı Denizcilik Genel Müdürlüğü, karadaki kirlilik içinse Çevre ve Şehircilik Bakanlığı'nın sorumlu olduğu ve ilgili diğer makamların katıldığı Şekil 3'te yer alan organizasyon oluşturulmaktadır.

Bölgesel ve Ulusal boyutta bu organizasyonlar kurulmakla birlikte, makamların birbirleriyle bütünlük yapı içerisinde olmadıkları, olay sahasının gerçek zamanlı resmini ortak olarak paylaşmadıkları, deniz çevresini dinamik verilerine (rüzgâr, akıntı vb.) gerçek zamanlı olarak sahip olmadıkları tespit edilmiştir.

Bu doğrultuda veri akışı ve bilgi paylaşımının hangi makamlar tarafından sağlanabileceğine dair bir öngörü 4'te sunulmuştur.



Şekil 4. Denizde acil durum karar destek sistemi kullanıcı/veri entegrasyon öngörüsü.

Şekil 4'teki yapı kapsamında; deniz çevresi dinamik verilerinin, halen var olan ve gerektiğinde tesis edilecek sensörler vasıtasıyla rüzgâr, barometre, hava/deniz suyu sıcaklıklarının Meteoroloji Genel Müdürlüğü tarafından, deniz durumu, deniz yüzeyi akıntı değerlerinin Seyir Hidrografi ve Oşinografi Dairesi Başkanlığı ile Kıyı Emniyeti Genel Müdürlüğü tarafından, radarlar ve OTS tarafından elde edilen veriler ışığında tanımlanmış gemi trafiğinin Gemi Trafik Yönetim Merkezi tarafından sağlanması ve bu verilerin Marmara Ereğlisi/Tekirdağ'da konuşlu bulunan Ulusal Deniz Emniyeti Merkezi (UDEM) bünyesinde tesis edilecek PISCES, YAKAMOS, vb. bir karar destek sistemine internet tabanlı, gerçek zamanlı ve 7/24 esaslı bir entegrasyonla iletilmesi, bu karar destek sisteminde oluşan gerçek zamanlı deniz resminin yine internet tabanlı bir entegrasyon vasıtasıyla, karar verici makamlar olan Çevre, Şehircilik ve İklim Değişikliği Bakanlığı, Ulaştırma ve Altyapı Bakanlığı, ilgili İl valilikleri, Sahil Güvenlik Komutanlığı, AFAD Başkanlığı ile sorumlu alt kademe makamları tarafından eş zamanlı paylaşılması öngörülmüştür.

4. Sonuçlar

Küreselleşmeyle birlikte artan deniz ticaret hacmi, denizlerde meydana gelebilecek kaza, can ve mal kaybı ile kirlilik riskini de artırmaktadır. Bahse konu kazalar neticesinde oluşabilecek kayıpların azaltılmasına yönelik tedbirler, teknolojinin gelişmesiyle birlikte daha etkin olmakta, bununla birlikte bu tedbirlerin uygulayıcı makamları arasında süratli, akıcı ve etkin koordinasyon ihtiyacını da beraberinde getirmektedir. Deniz kazaları akabinde can ve mal kayıplarını önlemeye yönelik arama kurtarma, kirliliği önlemeye/

azaltmaya yönelik ise müdahale operasyonları da bu gelişmiş tedbirlere ve etkin koordinasyona ihtiyaç duymaktadır. Gerek kazalardan sonra operasyonların etkinliğini artırmak, gerekse öncesinde alınabilecek tedbirlere yönelik karar destek/simülasyon sistemleri büyük yarar sağlamaktadır. Bu sistemlerin karar vericilere olay sahasının doğru resmini güncel olarak sunabilmesi operasyonların süratli ve etkin icrasında gerek şartı oluşturmaktadır. Olay sahasının güncel resmi ortam değişkenlerinin sistemlere gerçek zamanlı aktarılmasıyla mümkün olabilmekte, bahse konu resmin karar verici paydaşların hepsinde aynı zamanlı paylaşımı ise operasyonların, koordineli ve etkin icrasına olanak sağlamaktadır. Türkiye'nin 5312 sayılı Deniz Çevresinin Petrol ve Diğer Zararlı Maddelerle Kirlenmesinde Acil Durumlarda Müdahale ve Zararların Tazmini Esaslarına Dair Kanun gereği, Çevre, Şehircilik ve İklim Değişikliği Bakanlığı, Ulaştırma ve Altyapı Bakanlığı, Sahil Güvenlik Komutanlığı, İl Valilikleri, AFAD Başkanlığı, UDEM ana paydaşlar olmak üzere alt bağlularıyla birlikte deniz kazalarına müdahalede karar verme mekanizmasını oluşturmaktadırlar. Yapılan literatür taramasında, destek sistemlerinin bireysel bazda nasıl ve hangi teknolojik altyapıyla çalıştığı, ne gibi katkılar sağladığına yer verilmiş ve bu husus durum senaryolarıyla örneklendirilmiştir. Ancak bu sistemlere Türkiye'de hangi makamlar tarafından veri beslemelerinin yapılacağı, hangi makamların ana karar verici olarak sisteme entegre edilmesi gerektiğine dair bir çalışma olmadığı tespit edilmiştir. Bu çalışmanın amacı kapsamında Şekil 4'te, UDEM bünyesinde tesis edilen bir karar destek sistemine, denizel çevre dinamik verilerinin sağlayıcısı makamlar olan Kıyı Emniyeti Genel Müdürlüğü, Gemi Trafik Yönetim Merkezi, Seyir Hidrografi ve Oşinografi Dairesi Başkanlığı ve Meteoroloji Genel Müdürlüğü tarafından gerçek zamanlı veri akışının sağlanması öngörülmüş, deniz kazaları sonrasında müdahaleden sorumlu makamların süratli ve etkin karar vermelerini sağlayacak bir entegrasyon ve bu sayede olay sahası resminin sürekli ve güncel takip edilebileceği bir organizasyon oluşturulmuştur.

Bu çalışma sayesinde ortaya konan taslak sistemin, ana sorumlu makam olan Çevre, Şehircilik ve İklim Değişikliği Bakanlığı tarafından yapılacak daha detaylı çalışma ve bu sayede alt sorumlu makamların da katılmasıyla, etkin ve kapsamlı bir karar destek sistemi haline geleceği değerlendirilmektedir.

Yazar Katkıları

Cihat Aşan: Çalışmayı planlamış, verileri toplamış, örnekleme yapılmış ve makaleyi yazmıştır.

Çıkar Çatışması

Yazar çıkar çatışması bildirmemiştir.

Kaynaklar

- AFAD, (2014). 2014-2023 Deniz Kirliliğine Neden Olan Kazalar Yol Haritası Belgesi. Erişim adresi: https://www.afad.gov.tr/kurumlar/afad.gov.tr/3912/xfiles/denizcilik_kazalari_son1.pdf
- Amir-Heidari, P., Arneborg, L., Lindgren, J. F., Lindhe, A., Rosén, L., Raie, M., Axell, L., ve Hassellöv, I. M. (2019). A state-of-the-art model for spatial and stochastic oil spill risk assessment: A case study of oil spill from a shipwreck. *Environment International*, 126, 309–320. <https://doi.org/10.1016/j.envint.2019.02.037>
- Barker, C. H., Kourafalou, V. H., Beegle-Krause, C. J., Boufadel, M., Bourassa, M. A., Buschang, S. G., Androulidakis, Y., Chassignet, E. P., Dagestad, K. F., Danmeier, D. G., Dissanayake, A. L., Galt, J. A., Jacobs, G., Marcotte, G., Özgökmen, T., Pinardi, N., Schiller, R. v., Socolofsky, S. A., Thrift-Viveros, D., Zheng, Y. (2020). Progress in operational modeling in support of oil spill response. In *Journal of Marine Science and Engineering* (Vol. 8, Issue 9, pp. 1–55). MDPI AG. <https://doi.org/10.3390/jmse8090668>
- Bukin, O. A., Proschenko, D. Y., Chekhlenok, A. A., ve Korovetskiy, D. A. (2019). Methods for Optical Monitoring of Oil Pollution of Sea Water Basins Using Unmanned Aerial Vehicles. *Atmospheric and Oceanic Optics*, 32(4), 459–463. <https://doi.org/10.1134/S102485601904002X>
- Delgado, L., Kumzerova, E., ve Martynov, M. (2006). Simulation of oil spill behaviour and response operations in PISCES. *WIT Transactions on Ecology and the Environment*, 88, 279–292. <https://doi.org/10.2495/CENV060271>

- Fingas, M. (2014). The basics of oil spill cleanup. In *International Journal of Environmental Analytical Chemistry* (3.rd ed., Vol. 94, Issues 14–15). CRC Press, Taylor and Francis Group. <https://doi.org/10.1080/03067319.2014.974591>
- Garello, R., ve Kerbaol, V. (2017). Oil pollution monitoring: An integrated approach. *2017 IEEE Workshop on Environmental, Energy, and Structural Monitoring Systems, EESMS 2017-Proceedings, 2003*. <https://doi.org/10.1109/EESMS.2017.8052689>
- Hackett, B., Comerma, E., Daniel, P., ve Ichikawa, H. (2009). Marine oil pollution prediction. *Oceanography*, 22(SPL.ISS. 3), 168–175. <https://doi.org/10.5670/oceanog.2009.75>
- Keramea, P., Spanoudaki, K., Zodiatis, G., Gikas, G., ve Sylaios, G. (2021). *Oil spill modeling: A critical review on current trends, perspectives, and challenges*. Journal of Marine Science and Engineering. <https://doi.org/10.3390/jmse9020181>
- Mohammadiun, S., Hu, G., Gharahbagh, A. A., Li, J., Hewage, K., ve Sadiq, R. (2021). Intelligent computational techniques in marine oil spill management: A critical review. In *Journal of Hazardous Materials* (Vol. 419). Elsevier B.V. <https://doi.org/10.1016/j.jhazmat.2021.126425>
- Nicolae, F., Perkovic, M., Ristea, M., ve Cotorcea, A. (2016). Method for monitoring the space-Time development of oil spilled in marine environment using Pisces II simulation software. *Journal of Environmental Protection and Ecology*, 136–145.
- Perkovic, M., ve Sitkov, A. (2008). “Oil spill modeling and combat,” Soares, C. G., and Kolev, P. N. (eds.), Maritime Industry, Ocean Engineering and Coastal Resources, Vols. 1 and 2: Proceedings and Monographs in Engineering Water and Earth Sciences, 1161-1169.
- Reed, M., Aamo, O. M., ve Daling, P. S. (1995). Quantitative analysis of alternate oil spill response strategies using OSCAR. *Spill Science and Technology Bulletin*, 2(1), 67–74. [https://doi.org/10.1016/1353-2561\(95\)00020-5](https://doi.org/10.1016/1353-2561(95)00020-5)
- Tütüncü, A. N. (2004). *Gemi kaynaklı deniz kirlenmesinin önlenmesi, azaltılması ve kontrol altına alınmasında devletin yetkisi* (3rd ed.). Kırklareli: Beta Basım A.Ş.
- UAB. (2020). Ulaştırma ve Altyapı Bakanlığı, Ulaşan ve Erişen Türkiye 2020. Erişim adresi: <https://www.uab.gov.tr/uploads/pages/bakanlik-yayinlari/revize-ulasan-ve-erisen-turkiye-2020-20210319-100631.pdf>.
- Ye, X., Chen, B., Li, P., Jing, L., ve Zeng, G. (2019). A simulation-based multi-agent particle swarm optimization approach for supporting dynamic decision making in marine oil spill responses. *Ocean and Coastal Management*, 172, 128–136. <https://doi.org/10.1016/j.ocecoaman.2019.02.003>
- 5312 Sayılı Kanun. (2006). Deniz Çevresinin Petrol Ve Diğer Zararlı Maddelerle Kirlenmesinde Acil Durumlarda Müdahale Ve Zararların Tazmini Esaslarına Dair Kanunun Uygulama Yönetmeliği, T.C. Resmi Gazete, 21 Ekim 2006, 26326



Determination of seed yield, quality and fixed oil components of different basil (*Ocimum basilicum* L.) genotypes: Evaluation of fatty acid profile by PCA biplot analysis

Musa Türkmen^{1*}, Yılmaz Eren¹, Yusuf Ziya Aygün¹, Esra Nermin²

¹Department of Fields Crops, Faculty of Agriculture, Hatay Mustafa Kemal University, Hatay, Türkiye

²Vocational School, Medicinal and Aromatic Plants Program, Antalya AKEV University, Antalya, Türkiye

Article History

Received: 04.01.2022

Accepted: 05.05.2022

Published: 25.09.2022

Research Article

Abstract – Basil (*Ocimum basilicum* L.) plants are generally grown for different properties and produce seed with a considerable amount at the end of the growing season. This study was carried out to determine the seed yield, quality and fixed oil components of eight different basil (B) genotypes with purple (PB) and green (GB) leaf color obtained from different countries. In other words, seed yield and quality, fixed oil components, the seed yield, 1000 seed weight, oil content, oil yield, crude protein, ash, linoleic acid, linolenic acid, oleic acid, palmitic acid, stearic acid, hexadecatrienoic acid properties, ethyl linolate and trace oil contents were investigated. Seed yield, 1000 seeds weight and oil yield were significant statistically among the genotypes. While the best result in terms of seed and oil yield was obtained from GB1, the highest 1000 seeds weight was recorded in GB4. Palmitic acid and trace oil contents of genotypes were significant statistically. The highest palmitic acid content was detected in GB2, whereas the maximum trace oil contents were obtained from GB5. In results of principal components analysis (PCA) purple and green basil types demonstrated different features in terms of fixed oil components. GB2, GB4 and GB5 basil genotypes which have green leaf types were superior according to the PCA. GB2 genotype obtained from Hungary was the better in terms of seed yield and fixed oil components among the purple and green basil genotypes used in this research.

Keywords – Basil, fixed oil, , genotype, *Ocimum basilicum* L., seed

1. Introduction

Ocimum basilicum L. (basil) grown up to 60 cm height is an annual plant. The roots of these plants are thin and grow by branching. Basil leaves are different oval and elongated forms and the basil flowers are at the top of the main axis. Basil seeds are oval and nut-shaped and maintain the germination vigour (Dachler & Pelzmann, 1999). Basil flowers bloom from bottom to top. Therefore, first matured seeds are at the bottom of the flower. Due to periodic ripening and delayed harvest, seeds matured about 20-25% separate as a by-product and then the basil plants are harvested. Another option to obtain seed is waiting till plant fully matures (Domokos & Perédi, 1993). The origin of basil plants is unknown. However, since many basil plants are similar to the species grown in Africa, it is assumed to be of African origin. On the other hand, it is estimated that India and Asia can also be its origin (Small, 2006). Basil cultivation was widely performed in Turkey, Iran, Japan and China (Sadeghi, Rahnavard, and Ashravi, 2009).

Basil seeds have been traditionally used in the treatment of indigestion, ulcer, diarrhea, sore throat and kidney ailments (Rezapour, Tarzi, and Movahed, 2016). Also, gum obtained from basil seeds has been used for many purposes such as a fiber source, pharmaceutical drug additive, suspending agent, anti-diabetic agent, growing plant seedlings and biodegradable film (Tabasi & Razavi, 2017). Fixed oils are glycerol esters commonly found in both animals and plants (Asil & Bozdoğan-Konuşkan, 2021). These oils have

¹ turkmenmusa@hotmail.com

² eren47959@gmail.com

³ yusufziyaaygun@mku.edu.tr

⁴ nermin.kucukors@hotmail.com

*Corresponding Author

been widely used in the food, lubrication, soap, paint, polish and fuel industries (Behera, Nagarajan, and Rao, 2004; Kadam, Yadav, Shivatare, Bhilwade, and Patil, 2012). Seed oils differ significantly in fatty acid composition at different taxonomic and typical differentiations (Zhang, Zhang, Zhang, and Kitajim, 2015). Fatty acid compositions in the seed oils can be found at different levels among the species and genotypes and within species (Motojest, Ogunlaja, and Amos, 2011; Zhang et al., 2015; Idris et al., 2020). Despite this popularity, few current studies have evaluated the seed oil yield and compositions of basil (Angers et al., 1996; Sadeghi et al., 2009; Tarchoune et al., 2013; Mostafavai et al., 2019; Idris, Nour, Ali, Erwai Ishag, and Nour, 2020). Therefore, this study aimed to investigate the seed and oil yield, chemical characteristics and fatty acid compositions of different basil genotypes to rise the economical usage.

2. Materials and Methods

2.1. Plant Material

The origins of the eight different green and purple basil genotypes used in this study were given in Table 1. One purple and three green basil genotypes were obtained from Garafarm Corporation from Hungary. The Arapgir genotype (purple basil) marked geographically in Turkey was obtained from Malatya province. Genotypes originating from France were provided via Turkish Vilmorin Seed Corporation.

Table 1

Knowledge about the basil genotypes used in this study

Abbreviations	Genotypes	Colour of Leaves	Leaf Types	Origin
PB1	Arapgir	Purple	Elongation	Turkey
PB2	Piros	Purple	Oval	Hungary
PB3	Midnight	Purple	Oval	France
GB1	Fahéj illatú	Green	Elongation	Hungary
GB2	Magas	Green	Elongation	Hungary
GB3	Törpe	Green	Oval	Hungary
GB4	Compact	Green	Elongation	France
GB5	Large Sweet	Green	Oval	France

2.2. Growing the Basil Seedlings, Experimental Design, Climatic Conditions and Soil Properties

Purple and green basil seeds obtained from different countries were sown in viol including 1:1 peat and perlite mediums on 7 March in 2020. First seedling emergences were determined five days after sowing. Seedlings reaching a period of 4-5 leaves were planted in experimental field at Hatay Mustafa Kemal University on 22 March 2020. The experimental design was laid out the randomized completed blocks with three replications. The plants were planted by setting 40 cm space among the plants in rows and 50 cm space among the rows in experimental field. The row length was 5 m. Before planting, the field was fertilized with 3 kg nitrogen and 5 kg phosphorus. Plants were irrigated with a drip irrigation system according to their water needs during the growing period. Plants were again fertilized with 3 kg nitrogen at pre-flowering stage. The climatic conditions were given in Table 2. While precipitation decreased significantly in all months compared to the LYA (long year averages) climatic conditions, the temperature increased considerably. The soil of the experimental field was clay-loam texture and slightly alkaline reaction (pH: 7.60), also the organic matter content was 2.30% (Yılmaz, Hür, and Ertekin, 2018; Ertekin, Atış, and Yılmaz, 2020).

2.3. LYA: Long Year Averages (Anonimous, 2020) Harvest and Yield

Twenty basil plants randomly selected from each parcel were harvested on 15 September 2020 when the seeds were fully mature. Samples filled separately in sacks were laid out on the drying table at room

Table 2

The climatic conditions of the province of Hatay where the experiment was conducted

Months	Year and LYA	Precipitation (mm)	Temperature (°C)	Relative Humidity (%)
March	2020	49.4	14.9	82.1
	LYA	143.3	13.0	-
April	2020	38.2	18.1	75.0
	LYA	103.9	17.2	-
May	2020	13.8	23.2	63.4
	LYA	81.1	21.2	-
June	2020	0.4	25.2	67.4
	LYA	32.0	24.8	-
July	2020	0.0	29.5	68.3
	LYA	16.0	27.2	-
August	2020	0.0	29.6	64.7
	LYA	18.2	27.8	-
September	2020	0.0	29.6	65.6
	LYA	41.1	25.7	-

LYA: Long Year Averages (Anonymous, 2020)

temperature conditions. The dried samples were collected after one week and filled in sacks. To remove seeds from flowers, the plants in the sacks were chewed and hammered. The seeds removed from flowers were cleaned from plant residues via sieves. Seeds for each genotype and replicate were counted and weighed four times with groups of a hundred. 1000 seed weights of genotypes were determined in this way. The seed yield of genotypes was calculated over twenty plants randomly selected and harvested with the number of plants grown per decare.

2.4. Chemical Analyzes, Oil Extraction and Determination of Oil Components

100 g seed obtained from genotypes was ground in a mill with 1 mm sieve diameter (Ertekin, Çeliktas, Can, and Kızılsimsek, 2017; Kızılsimsek, Ozturk, Yanar, Ertekin, Ozkan, and Kamalak, 2017; Ertekin, Atiş, Yılmaz, Can, and Kızılsimsek, 2019; Ertekin and Kızılsimsek, 2020). Nitrogen (N) content of seeds was analyzed by the Kjeldahl method (AOAC, 2019). Crude protein (CP) contents were calculated as $N \times 6.25$. Ash content was determined by burning in the muffle furnace at 550 °C for 4 hours (AOAC, 2005). Oil extraction of seeds was performed extraction method via soxhlet extractor according to the AOAC (2005). Also, oil ratio and oil yield of genotypes was calculated. After taking 100 µl of oils obtained from basil seeds and adding 3 ml of N-Heptane and 400 µl of 2N methanolic KOH solution, esterification was applied and the components of the oils were analyzed by GC / MS. Determination of fixed oil components was carried out under the following conditions with Thermo Scientific ISQ Single Quadrupole model gas chromatograph device. A column with a TR-FAME MS model, 5% Phenyl Polysilphenylene-silohexane, 0.25 mm inner diameter × 60 m length, 0.25 µm film thickness was used. Helium (99.9%) was used as carrier gas at a flow rate of 1 mL min⁻¹. The ionization energy was set at 70 eV and the mass range m/z 1.2-1200 amu. Scan Mode was used for data collection. Temperatures of MS transfer line, MS ionization, injection port and initially column were 250, 220, 220 and 120 °C, respectively. The 1 µL of the esterified sample was taken by the autosampler and placed in the injection port. Samples in initially column temperature were kept for 1 min. Column temperature increased by 10 °C per minute to 175 °C and samples were kept there for 10 min. Column temperature rose by 5 °C per minute to 210 °C and the samples were kept there for 5 minutes. Then, the column temperature increased by 5 °C per minute to 230 °C and the analysis was concluded by waiting for 6 minutes here. Total analysis time was 38.5 minutes. The structure of each compound was identified with the Xcalibur program using mass spectra (Türkmen & Koçer 2021).

2.5. Statistical Analyses

Analysis of variance was performed to compare the seed yield, seed chemical characteristics and fixed oil components of different basil genotypes. Significance among the means was evaluated by using the LSD test ($p \leq 0.05$). Also, standard error means of the data were presented. Principle component analysis (PCA) was carried out using XLSTAT to examine relationships between basil genotypes and fixed oil components detected via GC/MS.

3. Results and Discussion

3.1. Yield and Chemical Characteristics

Means of properties of seed yield, 1000 seeds weight, oil ratio, oil yield, crude protein and ash content were given in [Table 3](#). Basil genotypes had significant effect on the seed yield, 1000 seeds weight and oil yield, but not on the oil ratio, crude protein and ash. Seed yield ranged from 178.89 to 606.67 kg da⁻¹. The highest seed yield was obtained from GB1, whereas the lowest value was detected in PB2. 1000 seeds weight varied between 1.03 and 1.48 g. While the highest 1000 seeds weight was determined in GB4, the lowest value was found in GB3. Oil yield values ranged from 24.36 to 97.34 kg da⁻¹. The maximum oil yield was achieved in the GB1, while the minimum value was recorded in PB3. The oil ratio values varied between 12.17 and 17.08%. The maximum oil ratio was found in PB1, whereas the lowest was determined in GB5. Crude protein contents of genotypes ranged from 15.70-19.30%. The highest crude protein ratio was obtained from GB2, while the lowest value was detected in GB5. The ash contents of genotypes varied between 8.99 and 10.46%. The maximum ash content was recorded in PB2, whereas the minimum ash content was achieved in GB2. The seed yield, 1000 seeds weight and oil yield properties, as affected by different basil genotypes, were determined to investigate yield and these features changed highly among the genotypes. [Egata, Geja, and Mengesha \(2017\)](#) reported that the seed yield per plant varied between 1.88 and 14.03 among the Ethiopian sweet basil genotypes. In addition, another study described that the seed yield per plant ranged from 9.26 to 44.84. ([Gowda, Dorajerao, Madvai, and Suneetha, 2019](#)). [Nassar, El-Segai, and Mohamed \(2013\)](#) reported that the 1000 seeds weight was 1.396 g in basil. Results obtained

Table 3

Effects of genotypes on seed yield, 1000 seeds weight, oil ratio, oil yield, crude protein and ash contents

Genotypes	Seed Yield (kg/da)	1000 seeds weight (g)	Oil Yield (kg/da)	Oil ratio (%)	Crude protein (%)	Ash (%)
PB1	256.67±58.97 ^b	1.37±0.03 ^{ab}	43.59±9.63 ^{bc}	17.08±0.23	18.21±0.45	9.34±0.12
PB2	178.89±17.88 ^b	1.21±0.06 ^c	28.59±2.61 ^c	16.02±0.35	16.42±0.57	10.46±0.48
PB3	181.11±15.44 ^b	1.13±0.03 ^{cd}	24.36±1.95 ^c	13.46±0.25	16.93±0.22	9.74±0.12
GB1	606.67±173.60 ^a	1.33±0.04 ^b	97.34±21.12 ^a	16.76±2.06	18.19±1.06	9.56±0.72
GB2	300.00±42.21 ^b	1.43±0.06 ^{ab}	41.15±0.78 ^{bc}	14.23±1.86	19.30±1.03	8.99±0.21
GB3	228.89±41.16 ^b	1.03±0.03 ^d	34.19±7.62 ^{bc}	14.73±0.62	15.88±0.31	9.68±0.13
GB4	406.67±24.57 ^{ab}	1.48±0.01 ^a	60.05±4.82 ^b	14.81±1.18	18.55±1.19	9.53±0.25
GB5	382.22±103.79 ^{ab}	1.34±0.04 ^b	45.65±11.67 ^{bc}	12.17±0.56	15.70±1.06	10.18±0.34
Mean	317.64	1.29	46.86	14.91	17.40	9.69
Significance	*	***	**	ns	ns	ns
P value	0.04	<.0001	<.01	0.13	0.07	0.25
LSD	249.87	0.12	30.99	3.60	2.59	1.15

ns: non-significant; *:0.05≥p>0.01; **:0.01≥p>0.001; ***: 0.001≥p; ^{abcd}Row means with common superscripts do not differ.

from this study about seed yield and 1000 seeds weight was to similar literature reports. Also, while the GB1 was superior in term of seed yield, the GB4 was the highest in terms of 1000 seeds weight. There was no literature report about basil seed oil yield. Safflower seed yield varies between 60 and 100 kg da⁻¹ (Kolsarıcı, Gür, Başalma, İşler, and Kaya, 2005). Seed oil yield results obtained from this study was similar to safflower seed oil yield. Nour, Elhussein, Osman, and Nour (2009) reported that the oil ratio of 14 different basil genotypes was between 8.8-30%. Moreover, a study determined that the oil ratio was between 12.4 and 21.6% (Kakaraparthi, Srinivas, Kumar, and Kumar, 2015). Sarfraz, Anjum, Khan, Arshad, and Nadeem (2011) found that the crude protein content of basil was 11.4. The crude protein content of genotypes used in this study was higher than the results of Sarfraz et al. (2011). Sarfraz et al. (2011) reported that the ash content of basil was 6.3. Ash content obtained from this study was higher than the findings of Sarfraz et al. (2011). The main reason for these results may be the difference in genotypes.

3.2. Fixed Oil Components

Means of components of oil obtained from genotypes were given in Table 4. Our results indicated that the basil genotypes had a significant effect on the palmitic and trace oil acids, but not on the others. Linoleic acid component fixed oils obtained from different basil genotypes ranged from 21.05 to 25.62%. The maximum linoleic acid was achieved in PB1, while the minimum value was recorded in GB5. Purple basil genotypes gave generally better linoleic acid content than green basil genotypes. Linolenic acid determined as the major component varied between 47.77 and 51.00%. The highest linolenic acid content was detected in GB2, whereas the lowest value was determined in GB3. The oleic acid component ranged from 10.56 to 15.72%. The highest value was obtained from GB1, while the lowest was determined in PB1. Palmitic acid contents of basil fixed oils ranged from 8.31 to 9.78%. The maximum palmitic acid content was obtained from GB4 while the lowest value was detected in PB2. The stearic acid component varied between 2.10 and 3.23%. The maximum stearic acid content was achieved in PB2, whereas the minimum value was recorded in GB5. The hexadecatrienoic acid content of genotypes ranged from 0.50 to 1.01%. The highest hexadecatrienoic acid content was obtained from PB3, while the lowest value was found in GB1. The ethyl linoleate content varied between 0.50 and 0.79%. The maximum ethyl linoleate was detected in GB5, whereas the minimum ethyl linoleate was recorded in GB3. The trace oil acids varied between 0.78 and 1.37%. The highest value among the trace oil acids was determined in GB5 but PB1, PB3 and GB2 were statistically in the same group. The lowest value among the trace oil acids was recorded in GB3. Fixed oil components of different basil genotypes were investigated to determine the fixed oil quality. Angers, Morales, and Simon (1996) reported that the linoleic acid content of basil genotypes was between 18.3 and 21.7%. On the other hand, Domokos and Perédi (1993) found that linoleic acid content varied between 17 and 25%. Furthermore, Matthaus, Vosmann, Pham, and Aitzetmüller (2003) reported that the linoleic acid content in basil was 22% and 24.89%, respectively. Although results of linoleic acid content obtained from this study were similar to literature findings, some genotypes gave the higher linoleic acid content than literature results. Many researchers reported that the linolenic acid content in basil ranged from 50 and 63% (Domokos & Perédi, 1993; Angers et al., 1996; Matthaus et al., 2003). Linolenic acid contents of the genotypes used in this study were lower than the literature reports except for the GB2 basil genotype. Angers et al. (1996) found that the oleic acid content was between 18.3 and 21.7%. Also, Domokos & Perédi (1993) and Matthaus et al. (2003) determined that the oleic acid content was 9-15%, 15% and 7.43, respectively. Oleic acid content of GB1 basil genotype used in this study was higher than the results of these researches. Domokos & Perédi, (1993) reported that the palmitic acid content in basil was between 6 and 9%. Palmitic acid contents of the GB2, GB4 and GB5 basil genotypes used in this study were higher than the Domokos & Perédi (1993)'s results. Angers et al. (1996) detected that the stearic acid content in basil ranged from 2.0 to 2.8%. Except for the GB2, GB4 and GB5, stearic acid content in the study was higher than the literature results in five basil genotypes.

3.3. Principal Components Analysis for Fixed Oil Components

The eigenvalues and eigenvectors obtained as a result of the principle components analysis related to the fix oil components of different basil genotypes examined in this study were given in Table 5 and Figure

Table 4

Effects of genotypes on fixed oil components in different purple and green basil

Genotypes	Linoleic acid (%)	Linolenic Acid (%)	Oleic Acid (%)	Palmitic Acid (%)	Stearic Acid (%)	Hexadecatrienoic Acid (%)	Ethyl Linoleate (%)	Trace (%)
PB1	25.62±0.74	48.91±1.26	10.56±2.12	8.91±0.44 ^{bcd}	2.90±0.30	0.55±0.06	0.60±0.05	1.09±0.14 ^{abc}
PB2	25.35±0.75	48.37±0.66	11.91±2.06	8.31±0.27 ^d	3.23±0.14	0.60±0.23	0.57±0.10	0.91±0.12 ^{bc}
PB3	24.90±0.84	48.81±1.52	10.84±2.00	8.85±0.42 ^{bcd}	2.95±0.42	1.01±0.44	0.61±0.06	1.06±0.08 ^{abc}
GB1	24.67±1.21	45.51±1.42	15.72±1.76	8.51±0.05 ^{bcd}	2.89±0.32	0.50±0.24	0.63±0.09	0.81±0.10 ^c
GB2	21.70±1.92	51.00±2.10	11.46±2.10	9.78±0.19 ^a	2.77±0.12	0.67±0.20	0.62±0.13	1.28±0.06 ^{ab}
GB3	23.29±0.83	47.77±1.43	14.19±2.63	8.40±0.14 ^{cd}	2.86±0.52	0.78±0.44	0.50±0.23	0.78±0.08 ^c
GB4	22.38±1.44	48.56±0.79	14.55±1.24	9.25±0.30 ^{abc}	2.15±0.53	0.57±0.27	0.75±0.06	0.83±0.17 ^c
GB5	21.02±1.23	49.77±0.95	14.33±1.95	9.27±0.12 ^{ab}	2.10±0.26	0.61±0.09	0.79±0.15	1.37±0.21 ^a
Mean	23.62	48.59	12.95	8.91	2.73	0.66	0.63	1.02
Significance	ns	ns	ns	*	ns	ns	ns	*
P value	0.11	0.31	0.54	0.03	0.28	0.87	0.50	0.03
LSD	3.71	4.17	6.35	0.87	1.02	0.75	0.29	0.38

ns: non-significant; *:0.05≥p>0.01; ^{abcd}Row means with common superscripts do not differ.

1 and in Table 6, respectively. When the eigenvalues were investigated, eigenvalue of Factor 1 (F1) and Factor 2 (F2) was over 1. Also, F1 and F2 explained the variation at the rate of 79.06 (Table 5 and Figure 1). Correlation analysis methods were used to select the influential features to indirect selection of best genotypes (Yaldiz & Camlica, 2020). In this context, principle components analysis (PCA) is a suitable multivariate technique to determine the genotypes. To detect the appropriate genotype in terms of fixed oil components, PCA method was used according to the literature evaluations (Leilah & Al-Khateeb, 2005; Golparvar, Ghasemi-Pirbalouti, and Madani, 2006). According to the PCA, GB1, GB4 and GB5 genotypes were superior in terms of fixed oil components.

Table 5

Eigenvalues of principal components analysis for fixed oil contents obtained from different basil genotypes

	F1	F2	F3	F4	F5	F6	F7
Eigenvalue	3.94	2.39	0.80	0.42	0.26	0.15	0.04
Variability (%)	49.20	29.86	10.02	5.23	3.31	1.83	0.55
Cumulative %	49.20	79.06	89.08	94.31	97.63	99.45	100.00

As the eigenvectors (Table 6), it was found that the components of palmitic acid and ethyl linoleate for F1 and oleic acid and ethyl linoleate for F2 should be evaluated. In the biplot analysis graph of basil genotypes presented in Figure 2, the F1 axis (49.20%) was formed with palmitic acid and ethyl linoleate, and the F2 axis (29.86%) with oleic acid and ethyl linoleate contents. In the positive direction of the F1 axis, it was observed that the GB5 genotype was superior in terms of ethyl linoleate component. Also, in the positive direction of F2 axis, it was determined that the GB4 was excellent in term of oleic acid content. GB2 and GB5 genotypes gave the good results in term of palmitic acid content. Basil genotypes circled in the principal component analysis biplot graph were found superior in terms of fixed oil contents.

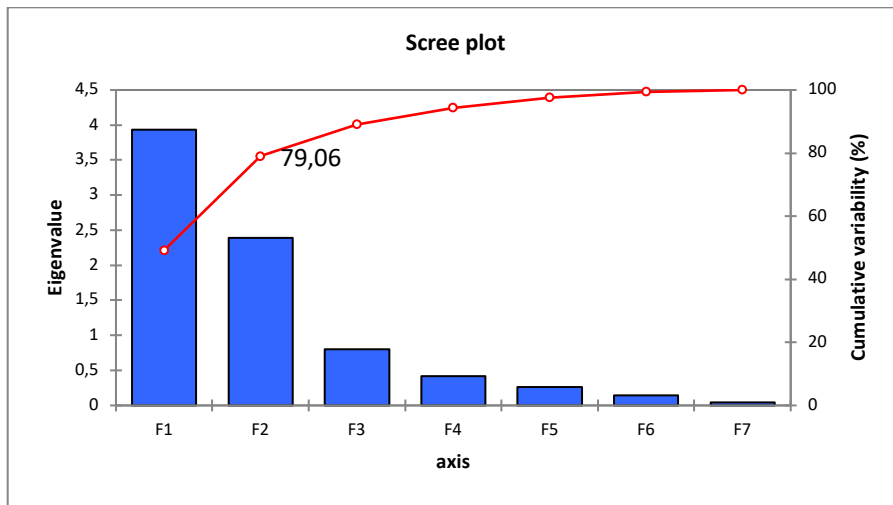


Figure. 1. Principle component factors based on eigenvalues line chart

Table 6

Eigenvectors of principle components analysis for fixed oil contents obtained from different basil genotypes

	F1	F2	F3	F4	F5	F6	F7
Linoleic Acid	-0.43	-0.14	-0.32	0.53	-0.17	0.09	-0.21
Linolenic Acid	0.36	-0.42	-0.04	-0.24	-0.16	-0.53	0.27
Oleic Acid	0.04	0.61	0.26	-0.21	0.30	0.16	0.10
Palmitic Acid	0.45	-0.15	-0.08	-0.17	-0.43	0.73	-0.07
Stearic Acid	-0.42	-0.30	-0.19	-0.24	0.26	0.34	0.68
Hexadecatrienoic Acid	-0.07	-0.39	0.85	0.30	0.04	0.14	0.06
Ethyl linoleate	0.40	0.26	-0.10	0.65	-0.04	-0.01	0.57
Trace	0.37	-0.32	-0.21	0.15	0.77	0.13	-0.27

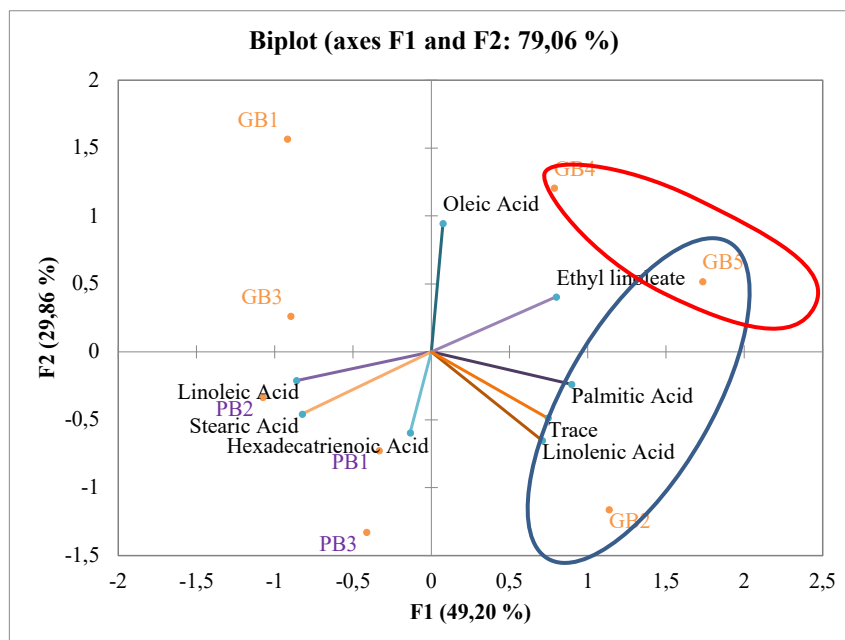


Figure. 2. Biplot distribution graph of principal components analysis for fixed oil contents obtained from different basil genotypes

4. Conclusion

This study aimed to investigate seed yield and quality and fixed oil components of different basil genotypes including purple and green plant types. The best seed yield was determined in GB1 which was obtained from Hungary and had green and elongation leaf types. It was found significant differences in terms of oil components among the basil genotypes. Purple and green basil types demonstrated different features in terms of fixed oil components. In results of principle components analysis, GB2, GB4 and GB5 basil genotypes which have green leaf type were superior. As a result of this study, we deduced that the GB2 genotype obtained from Hungary was the better in terms of seed yield and fixed oil components among the purple and green basil genotypes used in this research. The genotype of GB2 is not used due to its high linolenic acid, its oil quick oxidation and time to time oil bitterness. However, it can be recommended to be consumed directly as food and included in diets because this fatty acid is an omega 3 fatty acid.

Acknowledgement

This study was funded by the Scientific Research Projects Agency Coordination of Hatay Mustafa Kemal University with the Project Number: 20.M.022.

Author Contributions

Musa TÜRKMEN: Planned the study, contributed to the administer of the study, designed and performed the analyses, determined the final version of the article.

Yılmaz EREN: Planned the study, designed and performed the analyses, collected the data

Yusuf Ziya AYGÜN: Planned the study, designed and performed the analyses, collected the data

Esra Nermin ERTEKİN: Planned the study, designed and performed the analyses, Performed statistical analysis, wrote the paper

Conflicts of Interest

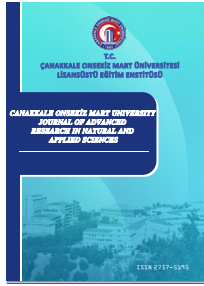
The authors declare no conflict of interest.

References

- Angers, P., Morales, M.R., & Simon J.E. (1996). Fatty acid variation in seed oil among *Ocimum* species. *Journal of the American Oil Chemists' Society*, 73, 393-395. <https://doi.org/10.1007/BF02523437>
- Anonimous (2020). Hatay Meteoroloji İl Müdürlüğü, Yıllık İklim Verileri.
- AOAC. (2005). Official methods of analysis. *Association of Official Analytical Chemists*. Arlington, VA, (USA).
- AOAC. (2019). 21st edition. official methods of analysis 2019 *AOAC International*.
- Asil, H., Bozdoğan-Konuşkan, D. (2021). Farklı yağlı tohumlardan soğuk pres yöntemiyle elde edilen sabit yağların yağ asidi kompozisyonlarının araştırılması. *Mustafa Kemal Üniversitesi Tarım Bilimleri Dergisi*, 26(3), 670-678. <https://doi.org/10.37908/mkutbd.959699>
- Behera, S., Nagarajan, S. & Rao L.J.M. (2004). Microwave heating and conventional roasting of cumin seeds (*Cuminum cyminum* L.) and effect on chemical composition of volatiles. *Food Chemistry*, 87, 25-29. <https://doi.org/10.1016/j.foodchem.2003.10.012>
- Dachler, M. & Pelzmann, H. (1999). Arznei- und Gewürzpflanzen, Österreichischer Agrarverlag, Klosterneuburg, 2. Auflage.
- Domokos, J. & Perédi, J. (1993). Studies on the seed oils of basil (*Ocimum basilicum* L.) and summer savory (*Satureja hortensis* L.). *Acta Horticulturae*, 344, 312-314. <https://doi.org/10.17660/ActaHortic.1993.344.35>
- Egata, D.F., Geja, W. & Mengesha, B. (2017). Agronomic and bio-chemical variability of Ethiopian sweet basil (*Ocimum basilicum* L.) accessions. *The Academic Research Journal of Agricultural Science and Research*, 5, 489-508. <https://doi.org/10.14662/ARJASR2017.078>

- Ertekin, İ., Atış, İ. & Yılmaz Ş. (2020). The effects of different organic fertilizers on forage yield and quality of some vetch species. *Mustafa Kemal University Journal of Agricultural Sciences*, 25, 243-255. <https://doi.org/10.37908/mkutbd.739805>
- Ertekin, İ., Atış, İ., Yılmaz, Ş., Can, E., & Kızıllımsımsek M. (2019). Comparison of shrub leaves in terms of chemical composition and nutritive value. *KSU Journal of Natural Sciences*, 22, 781-786. <https://doi.org/10.18016/ksutarimdog.v22i45606.530946>
- Ertekin, İ., Çelikleş, N., Can, E. & Kızıllımsımsek M. (2017). Silage quality and nutritional features determination for alfalfa by FT-NIRS. *KSU Journal of Natural Sciences*, 20, 88-92. <https://doi.org/10.18016/ksudobil.348931>
- Ertekin, İ. & Kızıllımsımsek, M. (2020). Effects of lactic acid bacteria inoculation in pre-harvesting period on fermentation and feed quality properties of alfalfa silage. *Asian-Australasian Journal of Animal Sciences*, 33, 245-253. <https://doi.org/10.5713/ajas.18.0801>
- Golparvar, A.R., Ghasemi-Pirbalouti, A. & Madani H. (2006). Genetic control of some physiological attributes in wheat under drought stress conditions. *Pakistan Journal of Biological Sciences*, 9, 1442-1446. <https://scialert.net/abstract/?doi=pjbs.2006.1442.1446>
- Gowda, M.P., Dorajeerao, A.V.D., Madvai, M. & Suneetha D.R.S. (2019). A study on genetic variability for yield and its attributes in sacred basil (*Ocimum tenuiflorum* L.). *Journal of Crop and Weed*, 15, 1-6. <https://doi.org/10.22271/09746315.2019.v15.i3.1227>
- Idris, A.A., Nour, A.H., Ali, M.M., Erwa, I.Y., Ishag, O.A.O. & Nour A.H. (2020). Physicochemical properties and fatty acid composition of *Ocimum basilicum* L. seed oil. *Asian Journal of Physical and Chemical Sciences*, 8, 1-12. <https://doi.org/10.9734/ajopacs/2020/v8i130104>
- Kadam, P.V., Yadav, K.N., Shivatare, R.S., Bhilwade, S.K. & Patil M.J. (2012). Comparative studies on fixed oil from *Ocimum sanctum* and *Ocimum basilicum* seeds. *Inventi Rapid: Planta Activa*, 4, 1-5. <https://www.researchgate.net/publication/306393614>
- Kakaraparthi, P.S., Srinivas, K.V.N., Kumar, J.K. & Kumar A.N. (2015). Composition of herb and seed oil and antimicrobial activity of the essential oil of two varieties of *Ocimum basilicum* harvested at short time intervals. *Journal of Plant Development*, 22, 59-76. <https://plant-journal.uaic.ro/docs/2015/7.pdf>
- Kizilsimsek, M., Ozturk, C., Yanar, K., Ertekin, I., Ozkan, C.O. & Kamalak A. (2017). Associative effects of ensiling soybean and corn plant as mixtures on the nutritive value, fermentation and methane emission. *Fresenius Environmental Bulletin*, 26, 5754-5760. <https://www.researchgate.net/publication/320563801>
- Kolsarıcı, Ö., Gür, A., Başalma, D. İşler, N. & Kaya, M.D. (2005). Yağlı tohumlu bitkiler üretimi. *Türkiye Ziraat Mühendisliği VI. Teknik Kongresi* 3-7 Ocak 2005. Milli Kütüphane, Ankara. 1. Cilt, 409-429. <https://kutuphane.tarimorman.gov.tr/vufind/Record/1177118>
- Leilah, A.A., & Al-Khateeb S.A. (2005). Statistical analysis of wheat yield under drought conditions. *Journal of Arid Environments*, 61, 483-496. <https://doi.org/10.1016/j.jaridenv.2004.10.011>
- Matthaus, B., Vosmann, K., Pham, L.Q. & Aitzetmüller K. (2003). FA and tocopherol composition of vietnamese oilseeds. *Journal of the American Oil Chemists' Society*, 80, 1013-1020. <https://doi.org/10.1007/s11746-003-0813-y>
- Mostafavai, S., Gharneh, H.A. & Miransari, M. (2019). The phytochemical variability of fatty acids in basil seeds (*Ocimum basilicum* L.) affected by genotype and geographical differences. *Food Chemistry*, 276, 700-706. <https://doi.org/10.1016/j.foodchem.2018.10.027>
- Motojest, O., Ogunlaja, S. & Amos, O. (2011). Variation in lipid composition of the seed oil *Parinari polyandra* Benth. *Asian Journal of Applied Sciences*, 4, 195-201. <https://doi.org/10.3923/ajaps.2011.195.201>
- Nassar, M.A., El-Segai, M.U. & Mohamed S.N. (2013). Botanical studies on *Ocimum basilicum* L. (Lamiaceae). *Research Journal of Agriculture and Biological Sciences*, 9, 150-163. <https://scholar.cu.edu.eg/?q=usamasegai/publications/botanical-studies-ocimum-basilicum-l-lamiaceae>
- Nour, A.H., Elhoussein, S.A., Osman, N.A. & Nour, A.H. (2009). Characterization and chemical composition of fixed oil of fourteen basil (*Ocimum basilicum*) accessions grown in Sudan. *International Journal of Chemistry and Technology*, 1, 52-58. <https://dx.doi.org/10.3923/ijct.2009.52.58>

- Rezapour, R., Tarzi, B.G. & Movahed S.(2016). The effect of adding sweet basil seed powder (*Ocimum basilicum* L.) on rheological properties and staling of baguette bread. *Journal of Food Biosciences and Technology*, 6, 41-46. https://jfbt.srbiau.ac.ir/article_8909_b128abae50248cb36ba53fd3f012b1cc.pdf
- Sadeghi, S., Rahnavard, A. & Ashrabi Z.Y. (2009). The effect of plant-density and sowing-date on yield of Basil (*Ocimum basilicum* L.) in Iran. *Journal of Agricultural Science and Technology*, 5, 413-422. http://ijat-aatsea.com/pdf/Nov_v5_n2_09/19-IJAT2008_26F.pdf
- Sarfraz, Z., Anjum, F.M., Khan, M.I., Arshad, M.S. & Nadeem, M. (2011). Characterization of basil (*Ocimum basilicum* L.) parts for antioxidant potential. *African Journal of Food Science*, 2, 204-213. <http://www.interestjournals.org/AJFST>
- Small, E. (2006). Culinary herbs, NRC Research Press, Ottawa, 2. Auflage. https://link.springer.com/chapter/10.1007/978-3-030-30314-3_15
- Tabasi, S.N. & Razavi S.A. (2017). Functional properties and applications of basil seed gum: An overview. *Food Hydrocoll*, 73, 313-325. <https://doi.org/10.1016/j.foodhyd.2017.07.007>
- Tarchoune, I., Baâtour, O., Harrathi, J., Hamdaoui, G., Lachaâl, M., Ouerghi, Z. & Marzouk, B. (2013). Effects of two sodium salts on fatty acid and essential oil composition of basil (*Ocimum basilicum* L.) leaves. *Acta Physiologiae Plantarum*, 35, 2365-2372. <http://dx.doi.org/10.1007/s11738-013-1271-4>
- Türkmen, M. & Koçer, O. (2021). Variation of components in laurel (*Laurus nobilis* L.) fixed oil extracted by different methods. *International Journal of Chemistry and Technology*, 5(2), 167-171. <https://doi.org/10.32571/ijct.1006137>
- Yaldiz, G. & Camlica M. (2020). Agro-morphological and phenotypic variability of sweet basil genotypes for breeding purposes. *Crop Science*, 61, 621-642. <https://doi.org/10.1002/csc2.20391>
- Yılmaz, Ş., Hür, N. & Ertekin İ. (2018). Determination of forage yield and quality in some selected bermudagrass (*Cynodon dactylon* (L.) Pers. var. dactylon) lines. *MKU Journal of Agricultural Faculty*, 23, 232-241. <https://dergipark.org.tr/pub/mkuzfd/issue/41577/419818>
- Zhang, J.L., Zhang, S.B. Zhang, Y.P. Kitajim K. (2015). Effects of phylogeny and climate on seed oil fatty acid composition across 747 plant species in China. *Industrial Crops and Products*, 63, 1-8. http://sourcedb.kib.cas.cn/yw/papers/201603/t20160329_4576068.html



Ensemble Based Box-Cox Transformation via Meta Analysis

Muhammed Ali Yılmaz¹, Osman Dag^{1,*}

¹Department of Biostatistics, School of Medicine, Hacettepe University, Ankara, Türkiye.

Article History

Received: 18.12.2021
Accepted: 30.03.2022
Published: 25.09.2022

Research Article

Abstract – Normal distribution has a vital role for the most of statistical methods. Box-Cox power transformation is the most usually applied method when the distribution of data is not normal. In this study, a novel algorithm is proposed assembling different Box-Cox transformation estimates of the well performed six techniques through random effect model in meta analysis. These techniques include the use of goodness-of-fit tests for normality; Anderson–Darling, Lilliefors, Cramer-von Mises, Shapiro–Wilk, Jarque–Bera and Shapiro–Francia tests. For the estimation of Box-Cox parameter, we assemble all possible combinations (63 combinations) of estimates calculated by these six methods. A Monte-Carlo simulation study is implemented to investigate which combination performs better compared to the rest. The simulation study states that the combination of Shapiro–Wilk, Jarque–Bera and Anderson–Darling tests performs well in most of the simulation scenarios constructed under different transformation parameters and sample sizes. In this study, this combination is proposed as ensemble based Box-Cox transformation via meta analysis. The proposed approach is implemented on white blood count data of leukaemia patients which are not normally distributed. Also, the proposed methodology is provided in AID R package with “boxcoxmeta” function for public use.

Keywords – Data transformation, meta analysis, normality, searching algorithms, statistical software

1. Introduction

Normal distribution has an essential role for statistical approaches. The reason why the normality assumption has a fundamental role is that it constructs the basis of the approaches, such as t-test and ANOVA. When this assumption is violated, the most widely utilized solution is Box-Cox power transformation (Box and Cox, 1964). Data are not normally distributed in general while analysing data in application. Box-Cox transformation has been carried out in different areas, such as medical studies. Liu et al. (2021) used Box-Cox power transformation to transform the distribution of stay length of type 2 diabetes mellitus patients in public hospital to normal one. Roy et al. (2021) applied Box-Cox transformation for non-normality in brainstem dose-volume histogram points. Singh et al. (2021) applied Box-Cox transformation to normalize absolute insulin dosing. Nelson et al. (2022) used Box-Cox transformation on outcome of cancer-related self-efficacy. In the original article, Box and Cox (1964) used maximum likelihood as an estimation technique of transformation parameter. Dag et al. (2014) proposed a methodology including the usage of an artificial covariate for the estimation of transformation parameter. Rahman and Pearson (2008) and Rahman (1999) used normality tests, Anderson Darling and Shapiro Wilk tests, to estimate the power. Asar et al. (2017) extended the use of normality tests in parameter estimation and included searching algorithm to optimize the parameter. Their study includes well-know seven normality tests; namely, Anderson-Darling, Shapiro-Wilk, Lilliefors (Kolmogorov-Smirnov), Jarque-Bera, Cramer-von Mises, Shapiro-Francia, Pearson chi-square tests. In this study, we propose a novel approach to estimate power transformation parameter. According to the simulation results of the work done by Asar et al. (2017), Pearson chi-square test performed worse compared to the other methods for the parameter estimation. Therefore, we include the other six normality tests in this study. We assemble different Box-Cox transformation estimates through random effect model in meta analysis. Specifically, we assemble all possible combinations (63 combinations) of six methods for the

¹ yilmazmuhammedali@outlook.com.tr

² osman.dag@hacettepe.edu.tr

*Corresponding Author

estimation of Box-Cox parameter. We compare all possible combinations via a simulation study. We observe that the combination of Jarque-Bera, Anderson-Darling and Shapiro-Wilk tests performs well in most of the simulation scenarios. Therefore, we propose this combination as ensemble based Box-Cox transformation via meta analysis. The organization of this paper is as follows. Some information regarding Box-Cox power transformation and our proposed methodology are placed in [Section 2](#). The steps of simulation study and its results are placed in [Section 3](#). Moreover, the application of our proposed method is carried out on data of leukaemia patients and the implementation of the proposed approach is placed in [Section 3](#). The article is completed in [Section 4](#).

2. Materials and Methods

Box-Cox power transformation was proposed by [Box and Cox \(1964\)](#). The transformation on y_i ($i = 1, 2, \dots, n$) is as follows.

$$Z_i = \begin{cases} \frac{(y_i + \lambda_2)^\lambda - 1}{\lambda}, & \text{if } \lambda \neq 0 \\ \log(y_i + \lambda_2), & \text{if } \lambda = 0 \end{cases} \quad (1)$$

Here, y_i are the data to be transformed, λ is the transformation parameter to be estimated, Z_i are the data on which Box-Cox power transformation is applied and n is the size of sample. λ_2 is the specified fixed value to add each y_i making them positive if $y_i \leq 0$. The power transformation given in [Equation \(1\)](#) is equivalent to

$$Z_i^* = \begin{cases} (y_i + \lambda_2)^\lambda, & \text{if } \lambda \neq 0 \\ \log(y_i + \lambda_2), & \text{if } \lambda = 0 \end{cases} \quad (2)$$

since [Equation \(1\)](#) is the linear transformation of [Equation \(2\)](#) ([Box and Cox 1964](#)).

The objective of this paper is to propose an ensemble based Box-Cox transformation by assembling the estimates found by Shapiro-Wilk, Jarque-Bera and Anderson-Darling tests via random effect model in meta analysis. Information on estimation process via these tests is available in the work done by [Asar et al. \(2017\)](#). The algorithm of the proposed algorithm can be followed:

- i. The possible λ values are specified such as $\lambda = -3, -2.99, -2.98, \dots, 3$.
- ii. Any observations in data are not allowed to be negative. If yes, the value is specified to make all observations larger than zero ([Box and Cox, 1964](#)).
- iii. The estimates via Shapiro-Wilk, Jarque-Bera and Anderson-Darling tests are obtained using the algorithm proposed by [Asar et al. \(2017\)](#).
- iv. Standard errors of the estimates are obtained via non-parametric bootstrap.
- v. The estimates found in (iii) are assembled using the standard errors obtained in (iv) with random effect model in meta analysis.

The proposed methodology can be reached in [AID](#) R package with “boxcoxmeta” function. The estimates via Shapiro-Wilk, Jarque-Bera and Anderson-Darling tests are obtained via “boxcoxnc” function in [AID](#) package. The estimates are assembled via meta package ([Balduzzi, 2019](#)). All applications and codes are conducted in R environment ([R Development Core Team, 2020](#)). The figures are drawn using ggplot2 R package ([Wickham, 2016](#)).

3. Results and Discussion

In this part, we implement a Monte Carlo simulation for the comparison of our proposed method with the other existing methods. The simulation scenarios are provided with their results in this section. Our proposed method is demonstrated on data of leukaemia patients. Brief information is presented together with results. The implementation of the proposed method is provided in the last subsection.

3.1. Monte Carlo Simulation Study

A simulation study is implemented to make a comparison for the estimation performance with our proposed method (OM) with other methods; Shapiro-Francia (SF), Cramer-von Mises (CVM), Shapiro-Wilk (SW), Jarque-Bera (JB), Anderson-Darling (AD), Lilliefors test (LT). The algorithm of simulation scenarios is as follows.

- i. Simulate a random data set from $N(\mu = 0, \sigma = 5)$ with different sample size ($n = 20, 30, 50, 100, 500$).
- ii. If generated variable (Z) includes any non-positive value, add a specified fixed value to make all observations larger than zero.
- iii. Make inverse transformation $Z^{(\lambda)}$ stated in Equation (2) with Box-Cox parameter ($\lambda = -5, -2, -1, 0, 2, 5$).
- iv. Estimate λ by all methods.
- v. Repeat all steps for 10,000 runs.

When all steps are ended, the performance measures; namely, bias, mean square error (MSE) and standard error (SE) are obtained.

In this section, the performances of methods are investigated through bias, MSE and SE. All results are not reported here for the content integrity, but available at yunus.hacettepe.edu.tr/~osman.dag/supp_materials/ensemble_boxcox.xlsx. We provide the performances in Figure 1 and Table 1.

In general perspective, biases and MSEs get smaller as the magnitude of λ decreases as expected. For example, under the scenario of $n = 50$, absolute biases and MSEs are within a range of 0.005-0.105 and 1.631-2.869 for $\lambda = 5$, respectively; on the other hand, absolute biases and MSEs are found to be in an interval of 0.001-0.043 and 0.266-0.514 for $\lambda = 2$, respectively.

Bias and MSE values become smaller as the number of observations raises. The performances of the methods are similar especially for large sample size. However, as the sample size gets smaller, the differences among the estimation techniques become clear. In most scenarios, our proposed method performs better compared to other estimation techniques. To illustrate, for $n = 30$ and $\lambda = 2$, absolute bias and MSE of our method are 0.001 and 0.449, respectively. Under the same condition, the absolute biases and their MSEs of the other methods are within a range of 0.008-0.054 and 0.412-0.752, respectively.

Table 1

Comparison of our method with six different methods

n	true		λ_{SW}	λ_{AD}	λ_{CVM}	λ_{SF}	λ_{LT}	λ_{JB}	λ_{OM}
20	-5	Bias	0.020	-0.103	-0.130	-0.133	-0.061	0.077	-0.001
		MSE	3.287	3.704	4.232	3.391	4.666	3.579	3.440
	-2	Bias	-0.012	-0.073	-0.098	-0.078	-0.087	-0.005	-0.030
		MSE	0.622	0.748	0.914	0.656	1.078	0.748	0.681
	-1	Bias	-0.007	-0.038	-0.051	-0.040	-0.049	-0.006	-0.017
		MSE	0.159	0.194	0.241	0.168	0.287	0.199	0.176
50	0	Bias	0.000	0.000	0.000	0.000	0.001	0.000	0.000
		MSE	0.003	0.003	0.004	0.003	0.005	0.003	0.003
	2	Bias	0.012	0.073	0.098	0.078	0.087	0.005	0.030
		MSE	0.622	0.748	0.914	0.656	1.078	0.748	0.681
	5	Bias	-0.020	0.103	0.130	0.133	0.061	-0.077	0.001
		MSE	3.287	3.704	4.232	3.391	4.666	3.579	3.440

Table 1
 Comparison of our method with six different methods (Continued)

n	true		λ_{SW}	λ_{AD}	λ_{CVM}	λ_{SF}	λ_{LT}	λ_{JB}	λ_{OM}
30	-5	Bias	0.041	-0.064	-0.076	-0.097	-0.017	0.105	0.029
		MSE	2.357	2.805	3.339	2.436	3.703	2.569	2.503
	-2	Bias	0.008	-0.041	-0.054	-0.049	-0.038	0.028	-0.001
		MSE	0.412	0.514	0.642	0.432	0.752	0.472	0.449
	-1	Bias	0.003	-0.021	-0.027	-0.025	-0.021	0.013	-0.002
		MSE	0.104	0.130	0.162	0.109	0.190	0.120	0.113
	0	Bias	0.000	0.000	-0.001	-0.001	-0.001	-0.001	-0.001
		MSE	0.002	0.002	0.002	0.002	0.003	0.002	0.002
	2	Bias	-0.008	0.041	0.054	0.049	0.038	-0.028	0.001
		MSE	0.412	0.514	0.642	0.432	0.752	0.472	0.449
	5	Bias	-0.041	0.064	0.076	0.097	0.017	-0.105	-0.029
		MSE	2.357	2.805	3.339	2.436	3.703	2.569	2.503
50	-5	Bias	0.014	-0.074	-0.086	-0.105	-0.026	0.070	0.005
		MSE	1.631	2.070	2.524	1.701	2.869	1.744	1.748
	-2	Bias	0.004	-0.033	-0.042	-0.043	-0.025	0.024	-0.001
		MSE	0.266	0.345	0.435	0.279	0.514	0.290	0.287
	-1	Bias	0.002	-0.017	-0.021	-0.023	-0.014	0.012	-0.001
		MSE	0.067	0.087	0.109	0.070	0.129	0.073	0.072
	0	Bias	-0.001	0.000	0.000	-0.001	0.000	-0.001	-0.001
		MSE	0.001	0.001	0.001	0.001	0.001	0.001	0.001
	2	Bias	-0.004	0.033	0.042	0.043	0.025	-0.024	0.001
		MSE	0.266	0.345	0.435	0.279	0.514	0.290	0.287
	5	Bias	-0.014	0.074	0.086	0.105	0.026	-0.069	-0.005
		MSE	1.631	2.070	2.524	1.701	2.869	1.744	1.748
100	-5	Bias	0.012	-0.034	-0.043	-0.079	-0.021	0.062	0.014
		MSE	0.925	1.265	1.568	0.961	1.856	0.964	0.997
	-2	Bias	0.005	-0.014	-0.019	-0.032	-0.011	0.024	0.005
		MSE	0.149	0.205	0.256	0.155	0.307	0.156	0.161
	-1	Bias	0.002	-0.007	-0.010	-0.016	-0.007	0.010	0.002
		MSE	0.038	0.052	0.065	0.040	0.077	0.039	0.040
	0	Bias	0.000	0.000	0.000	0.000	0.000	0.000	0.000
		MSE	0.000	0.000	0.000	0.000	0.000	0.000	0.000
	2	Bias	-0.005	0.014	0.019	0.032	0.011	-0.024	-0.005
		MSE	0.149	0.205	0.256	0.155	0.307	0.156	0.161
	5	Bias	-0.012	0.035	0.043	0.079	0.021	-0.062	-0.014
		MSE	0.925	1.265	1.568	0.961	1.856	0.964	0.997

Table 1

Comparison of our method with six different methods (Continued)

n	true		λ_{SW}	λ_{AD}	λ_{CVM}	λ_{SF}	λ_{LT}	λ_{JB}	λ_{OM}
500	-5	Bias	-0.012	-0.016	-0.017	-0.052	-0.009	0.008	-0.006
		MSE	0.273	0.400	0.480	0.280	0.571	0.277	0.293
	-2	Bias	-0.005	-0.006	-0.007	-0.021	-0.004	0.003	-0.003
		MSE	0.045	0.065	0.077	0.046	0.091	0.045	0.047
	-1	Bias	-0.003	-0.004	-0.003	-0.011	-0.003	0.000	-0.002
		MSE	0.012	0.017	0.020	0.012	0.023	0.012	0.012
	0	Bias	0.000	0.000	0.000	0.000	0.000	0.000	0.000
		MSE	0.000	0.000	0.000	0.000	0.000	0.000	0.000
	2	Bias	0.005	0.006	0.007	0.021	0.004	-0.003	0.003
		MSE	0.045	0.065	0.077	0.046	0.091	0.045	0.047
	5	Bias	0.012	0.016	0.017	0.052	0.009	-0.008	0.006
		MSE	0.273	0.400	0.480	0.280	0.571	0.277	0.293

When lambda is close to zero, all estimation techniques perform similar. For instance, the absolute bias and MSE values of all tests are lower than 5×10^{-3} for all scenarios.

When the data generated under the normal distribution with sample size $n = 20$ for $\lambda = -2, -1, 2, JB$ and SW techniques have smaller bias compared to our proposed method.

In brief, our proposed method seems to be more effective than other methods for estimating Box-Cox transformation parameter in most scenarios. However, JB and SW might be preferable when sample size is small and estimated transformation parameter is close to 0.

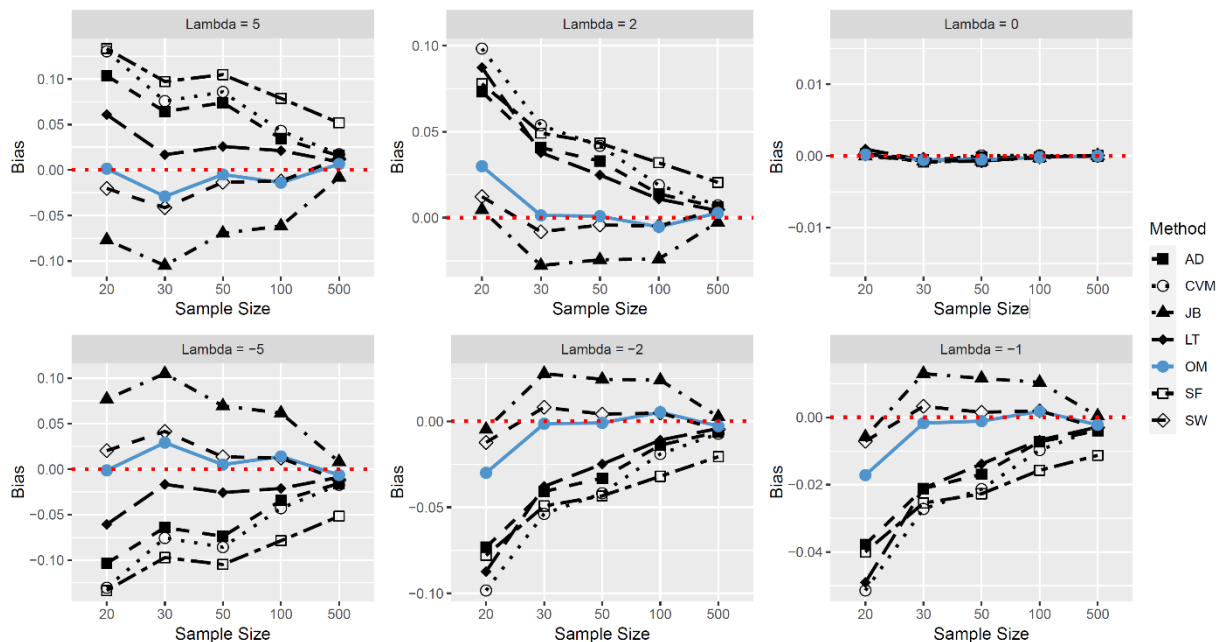


Figure 1. Biases of Methods

3.2. Data of Leukaemia Patients

This dataset involves 33 patients having died from acute myelogenous leukaemia. The data set includes three variables; namely, white blood count, test result and survival time. The data set can be reached in

MASS R package (Venables and Ripley, 2002). For our analysis, the distribution of white blood count (wbc) is examined. This variable shows positively skewed distribution (Figure 2); moreover, the normality tests (Jarque-Bera, Anderson-Darling and Shapiro-Wilk tests) indicate that the distribution of white blood count is non-normal (e.g.. Shapiro-Wilk normality test: $p\text{-value} = 1.986 \times 10^{-6}$).

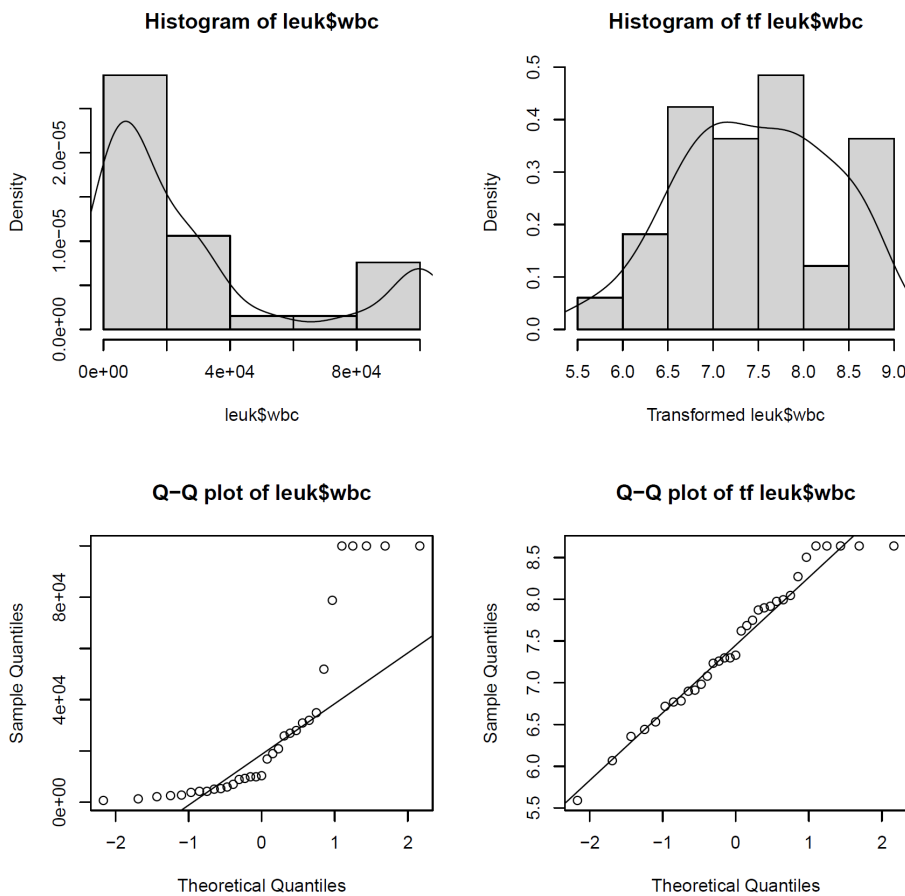


Figure 2. Left: Histogram (upper) and Q-Q (lower) plot of white blood count before Box-Cox transformation; Right: Histogram (upper) and Q-Q plot (lower) of white blood count after Box-Cox transformation.

Our aforementioned method is performed for the estimation of unknown parameter. The estimate is found to be -0.05333092 . When we apply Box-Cox transformation with this lambda estimate, we can easily see transformed data are distributed normally (Figure 2). Moreover, the results of normality tests are provided along with p-values in following part.

3.3. Implementation

The proposed methodology is released in “boxcoxmeta” function under **AID** R package. The estimate of λ for white blood count can be acquired with R codes presented below.

```
R> library(AID)
R> library(MASS)

R> set.seed(1)
R> result <- boxcoxmeta(leuk$wbc, lambda = seq(-3,3,0.01), nboot = 100, lambda2 = NULL,
plot = TRUE, alpha = 0.05, verbose = TRUE)
```

Box-Cox power transformation via meta analysis

data : leuk\$wbc

lambda.hat : -0.05251743

Normality tests for transformed data (alpha = 0.05)

	<i>Test</i>	<i>Statistic</i>	<i>P.Value</i>	<i>Normality</i>
1	<i>Shapiro-Wilk</i>	<i>0.9596797</i>	<i>0.2531485</i>	<i>Not reject</i>
2	<i>Anderson Darling</i>	<i>0.3500850</i>	<i>0.4515463</i>	<i>Not reject</i>
3	<i>Jarque-Bera</i>	<i>0.9444637</i>	<i>0.6236089</i>	<i>Not reject</i>

Here, lambda.hat is the estimate of λ . After transformation, three normality tests assess the normality of the variable. Since all p-values are larger than alpha, the normality of transformed white blood count is suggested by Shapiro-Wilk, Jarque-Bera and Anderson Darling tests.

In boxcoxmeta function, lambda is the vector of plausible transformation parameter. This vector is fixed to -3:3 (with increment 0.01) as a default. The nboot argument is the number of non-parametric bootstrap samples. Default is set to 100. The lambda2 is the constant to add each value making them positive. The plot option draws a figure given in Figure 2. Default is set to TRUE. The alpha argument is the significance level to check whether normality holds or not after Box-Cox transformation. The alpha argument is set to 0.05 as a default.

Box-Cox transformation is used to transform non-normal variable to a normal one. Therefore, symmetric confidence interval is not appropriate for non-normal data. After transformation, we calculated mean and confidence interval for transformed data. After that, we back transform mean and confidence interval to the original scale. For this reason, asymmetric confidence interval is appropriate for non-normal data. The confInt function is developed and released under **AID** package to obtain asymmetric confidence interval since the original data is asymmetric. This function returns mean, lower confidence limit (LCL) and upper confidence limit (UCL) for original scale of data.

R> confInt(result, level = 0.95)

Back transformed data

	Mean	2.5%	97.5%
leuk\$wbc	13064.64	8148.229	21200.45

The usage of mean and confidence interval for such a non-normal data set sometimes becomes inappropriate. We reported different usages of mean and confidence interval (CI) in Table 2 to emphasize the difference among them.

In our case, the distribution of white blood count is positively skewed in original scale. Moreover, there exist possible outliers at right tail of the data (Figure 2). Therefore, mean (2.5% - 97.5% CI) of white

Table 2

Difference among the usages of mean and confidence interval

Scale of data	Mean	LCL (2.5%)	UCL (97.5%)
Original data	29165.15	16935.75	41394.56
Transformed data	7.47	7.18	7.76
Back transformed data	13064.64	8148.23	21200.45

blood count moves to right. This does not reflect the central tendency of the data. For transformed data, the distribution of the data is normal and confidence interval is symmetric; however, scale of the data is not interpretable in clinic. For back transformed data, scale of back transformed data is same with original data. Compared to LCL (2.5%), UCL (97.5%) is further to mean since the original data set is positively skewed. Therefore, this usage reflects the central tendency of the data.

4. Conclusion

In this study, a novel technique for the estimation of Box-Cox parameter is proposed. Box-Cox transformation parameter estimates are assembled via random effect model in meta analysis. We assemble the estimates of the well performed six techniques proposed by [Asar et al. \(2017\)](#). These techniques include use of normality tests, Cramer-von Mises, Shapiro–Wilk, Lilliefors, Anderson–Darling, Jarque–Bera and Shapiro–Francia tests. For the estimation of Box-Cox parameter, we assemble not only all estimates by these methods, but also all possible combinations (63 combinations) of estimates calculated by these six methods.

We implement a simulation study. The combination of Shapiro–Wilk, Jarque–Bera and Anderson–Darling tests performs well in most of the simulation scenarios. Therefore, we propose this combination. We call this combination ensemble based Box-Cox transformation via meta analysis. Results show that our proposed method seems to be more effective than other methods for estimating Box-Cox transformation parameter. For an estimate closer to 0, the estimation based on Jarque-Bera and Shapiro-Wilk test might be preferable when sample size is small.

The proposed method is released in **AID** R package under “boxcoxmeta” function. Its implementation is conducted on data of leukaemia patients.

Author’s Contributions

Muhammed Ali Yilmaz: Developing codes, Simulation study, Figures, Table(s), Data analysis, Writing the paper.

Osman Dag: Designing the study, Developing codes, Simulation study, Writing the paper.

Conflicts of Interest

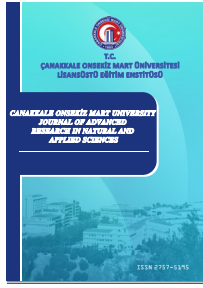
There is no conflict of interest declared by the authors.

References

- Asar, O., Ilk, O., & Dag, O. (2017). Estimating Box-Cox power transformation parameter via goodness-of-fit tests. *Communications in Statistics – Simulation and Computation*, 46(1), 91-105. DOI: <https://doi.org/10.1080/03610918.2014.957839>
- Balduzzi, S., Rucker, G., & Schwarzer, G. (2019). How to perform a meta-analysis with R: a practical tutorial. *Evidence-Based Mental Health*, 22, 153-160. DOI: <https://doi.org/10.1136/ebmental-2019-300117>
- Box, G.E.P., & Cox, D.R. (1964). An analysis of transformations (with discussion). *Journal of Royal Statistical Society, Series B (Methodological)*, 26(2), 211-243. DOI: <https://doi.org/10.1111/j.2517-6161.1964.tb00553.x>
- Dag, O., Asar, O., & Ilk, O. (2014). A methodology to implement Box-Cox transformation when no covariate is available. *Communications in Statistics – Simulation and Computation*, 43(7), 1740-1759. DOI: <https://doi.org/10.1080/03610918.2012.744042>
- Liu, W., Shi, J., He, S., Luo, X., Zhong, W., & Yang, F. (2021). Understanding variations and influencing factors on length of stay for T2DM patients based on a multilevel model. *Plos One*, 16(3), 1-14. DOI:

<https://doi.org/10.1371/journal.pone.0248157>

- Nelson, D., Law, G.R., McGonagle, I., Turner, P., Jackson, C., & Kane, R. (2022). The Effect of Rural Residence on Cancer-Related Self-Efficacy With UK Cancer Survivors Following Treatment. *The Journal of Rural Health, 38*(1), 28-33. DOI: <https://doi.org/10.1111/jrh.12549>
- R Development Core Team (2020). R: A Language and Environment for Statistical Computing. R Foundation for Statistical Computing, Vienna, Austria, Retrieved from <http://www.R-project.org>.
- Rahman, M. (1999). Estimating the Box-Cox transformation via Shapiro-Wilk W statistic. *Communications in Statistics - Simulation and Computation, 28*(1), 223-241. DOI: <https://doi.org/10.1080/03610919908813545>
- Rahman, M., & Pearson, L.M. (2008). Anderson-Darling statistic in estimating the Box-Cox transformation parameter. *Journal of Applied Probability and Statistics, 3*(1), 45-57.
- Roy, A., Widjaja, R., Wang, M., Cutright, D., Gopalakrishnan, M., & Mittal, B.B. (2021). Treatment plan quality control using multivariate control charts. *Medical Physics, 48*(5), 2118-2126. DOI: <https://doi.org/10.1002/mp.14795>
- Singh, S.R., Dhanasekara, C.S., Tello, N., Southerland, P., Saleh, A.A., Kesey, J., & Dissanaikie, S. (2021). Variations in insulin requirements can be an early indicator of sepsis in burn patients. *Burns, 48*(1), 111-117. DOI: <https://doi.org/10.1016/j.burns.2021.02.026>
- Venables, W.N., & Ripley, B.D. (2002). *Modern Applied Statistics with S*. Fourth Edition. Springer: New York. ISBN: 978-0-387-21706-2
- Wickham, H. (2016). *ggplot2: Elegant Graphics for Data Analysis*. Springer-Verlag: New York. ISBN: 978-0-387-98141-3



Kimyasal Tanker Gemilerinde Emniyet Ekipmanlarını Kullanan Personelin Yeterliği

Devran Yazır^{1*}, Sefa Yay²

¹Deniz Ulaştırma İşletme Mühendisliği Bölümü, Sürmene Deniz Bilimleri Fakültesi, Karadeniz Teknik Üniversitesi, Trabzon, Türkiye

²İstatistik ve Bilgisayar Bilimleri Anabilim Dalı, Fen Bilimleri Enstitüsü, Karadeniz Teknik Üniversitesi, Trabzon, Türkiye

Makale Tarihiçesi

Gönderim: 05.12.2021
Kabul: 10.04.2022
Yayın: 25.09.2022
Araştırma Makalesi

Öz – Dünyanın %71'i denizlerle kaplıdır. Denizcilik, sunduğu ekonomik maliyetler nedeniyle uluslararası ticari taşımacılıkta en çok tercih edilen sektördür. Enerji, tıbbi ekipman, ilaç, gıda ve benzeri hammadde ve ürünlerin nakliyesi çoğunlukla deniz yoluyla yapılmaktadır. Bu çalışmada; Denizcilerin bilgi birikimleri ile çalışma performansları ve gemiye uyumları arasındaki ilişkinin incelenmesi amaçlanmaktadır. Bu amaçla alanında uzman kişiler tarafından bir anket formu oluşturularak 740 kişiye gönderilmiş ve 63 anket yanıtlanmıştır. Çalışmada SPSS 23 paket programı kullanılmıştır. Başlıca bulgular şunlardır; Denizcilerin eğitim düzeylerinin çalışma performansını etkilediği gözlemlenmiştir. Acil durumlara hazırlık role talimlerinde personel ve görevlilerin performans not ortalamalarının yüksek olduğu görülmüştür. İlgili kursları başarıyla tamamlamış ve ilk kez gemide çalışan bir denizcinin bilgisinin, performansını etkilediği sonucu elde edilmiştir. Uyum sürecinin yabancı bir denizcinin performansını etkilediği görülmüştür. Denizcilik eğitimlerinin denizcilerin çalışma performansını ve ilgili acil durumlarda sorumluluk duygularını artırdığı görülmüştür. İstatistiksel analizlerle tespit edilen durumlar için gerekli öneriler ve tavsiyelerde bulunulmuştur. Role talimi gibi hayatı önem taşıyan eğitimlerin etkisi belirlenmiş ve eğitimlerin ciddiyetinin korunması önerilmektedir. İlk kez gemide görev alacak olan personellerin ve yabancı uyruklu personellerin bilgi ve adaptasyonlarını arttıracak etkinliklere önem verilmesi gerektiği önerilmektedir.

Anahtar Kelimeler – Denizcilik, emniyet ekipmanları, gemiadamı eğitimleri, kimyasal tankerler, spss

Competency of Personnel Using Safety Equipment on Chemical Tanker Ships

¹Department of Maritime Transportation and Management Engineering, Sürmene Faculty of Marine Sciences, Karadeniz Technical University, Trabzon, Türkiye

²Department of Statistics and Computer Sciences, Graduate School of Science and Engineering, Karadeniz Technical University, Trabzon, Türkiye

Article History

Received: 05.12.2021
Accepted: 10.04.2022
Published: 25.09.2022
Research Article

Abstract – %71 of the world is covered by seas. Due to the economic costs it offers, maritime is the most preferred sector in international commercial transportation. The transportation of energy, medical equipment, medicine, food, and similar raw materials and products are mostly transported by sea. In this study; it is aimed to examine the relationship between seafarers' knowledge, working performance, and adaptation to the ship. For this purpose, a questionnaire form was created by experts in the field and sent to 740 people, and 63 questionnaires were answered. SPSS 23 package program was used in the study. The main findings are as; it has been observed that the education level of seafarers affects their working performance. It has been observed that personnel and officers have high-performance grade averages in role drills for emergency preparedness. It has been obtained that the knowledge of a seafarer who has successfully completed the relevant courses and embarked for the first time affects his performance. It has been seen that the adaptation process affects the performance of a foreign seafarer. It has been observed that maritime training increases the working performance of seafarers and their sense of responsibility in related emergencies. Necessary suggestions and recommendations were made for the situations determined by statistical analysis. The effect of vital trainings such as role training has been determined and it is recommended to maintain the seriousness of the trainings. It is suggested that importance should be given to activities that will increase the knowledge and adaptation of the personnel and foreign personnel who will be on the ship for the first time.

Keywords – chemical tankers, maritime, safety equipment, seafarers training, spss.

¹ dyazir@ktu.edu.tr*

² 362503@ogr.ktu.edu.tr

*Sorumlu Yazar / Corresponding Author

1. Giriş

Dünya'nın %71'i, kara alanının yaklaşık 2,5 katı okyanuslarla kaplıdır (Bozkurt ve Arslan, 2017). Denizler, tüm ulusların birbirleriyle iletişim kurmalarını sağlayan en önemli unsurlardır (Çetin, 2009). Denizcilik, uluslararası rekabet koşullarının geçerli olduğu, yorucu çalışma koşullarının ve karada çalışmaya nazaran çok daha farklı çalışma ortamlarının olduğu bir sektördür (Parker, 2001). Düşük kalitede uyku, uzun çalışma saatleri, çalışma periyotları arasındaki yetersiz dinlenme, aşırı çalışma yükü, gürültü ve titreşim, gece çalışma durumları denizcilerin mesleğinin doğasında vardır (Smith vd., 2006). Dünya ekonomisinin sağlıklı gelişimiyle birlikte, ihtiyaç duyulan enerji, hammadde gibi ürünlerin ithalat yoluyla temini olağanlaşmıştır (Ünsan vd., 2007). Bunun yanında deniz ticaretiyle görevli gemiler, insan ihtiyaçlarına göre çeşitlenmiş; kuru yük, konteyner ve tankerlerin yanında, özel hizmet gemileri, feribotlar ve yolcu gemileri gibi sınıflarda dünya denizlerinde seyretmektedirler (Kaluza vd., 2010). Deniz ticaretinin, dünya ulaşım ve ticaretin artıp gelişmesine katkı sağladığı söylenebilir (Smil, 2007).

Covid-19 gibi dünyayı sarsan bir pandeminin sonucu olarak 2019 yılına göre 2020 yılında azalma olsa bile yine de dünya ticaretinin yaklaşık %90'lık kısmı gemiler tarafından yürütülmektedir (UNCTAD, 2020; ICS, 2021). Denizcilik, birim nakliye maliyeti açısından en avantajlı taşımacılık türü olmakla birlikte, ton-mil yük başına da en avantajlı taşımacılık türüdür. Örneğin bir dökme yük gemisinin taşıyacağı 150 bin ton demirin taşınabilmesi için 4.000 kamyonu ihtiyaç vardır (Demirci, 2019). Ham petrol, otomotiv gibi büyük miktarlardaki devamlı taşımaların deniz yolu ile taşınmasının daha pratik olması, tek seferdeki taşıma kapasiteleri, denizciliğin önemini gözler önüne sermektedir (Gönel, 2013). Dünyanın en büyük filo sıralamasında Türkiye 28,5 milyon DWT toplam kapasitesi ile ilk otuz ülke arasında 15. sırada yer almaktadır (UTİKAD, 2019). Dünya deniz ticaretinde, en yüksek gemi tonajına sahip olan gemiler tanker gemileridir, bu gemiler taşıdıkları yükler sebebiyle riskli olarak görülmüş ve limanda kalış süreleri kısıtlanmıştır. Demir bölgeleri, bekleme yerleri, limanları yerleşim yerlerine uzak olacak şekilde tasarlanmıştır (Cömert, 2008).

Gemiler, faaliyetlerini yerine getirebilmek için, insan gücüne ihtiyaç duyarlar. Gemiadamı, gemide geminin tahsis edildiği amacı yerine getirmesinde doğrudan veya dolaylı bir katkı sağlamak amacıyla o gemide çalışanların genel olarak adıdır. Baltic and International Maritime Council (BIMCO) verilerine göre, 1,5 milyondan fazla insan gemi adamı olarak dünya gemi filosunda çalışmaktadır. Türkiye, 100 bini aktif, 170 bin gemiadamı ile Çin'den sonra en çok gemi adamı yetiştiren ülke olarak belirtilmiştir (BIMCO/ISF, 2010). 'Aktif gemiadamı' terimi son 5 yıl içerisinde liman cüzdanını yenilemiş gemi adamı anlamına gelmektedir. Türkiye Cumhuriyeti Ulaştırma ve Altyapı Bakanlığının yayımına göre 2020 yılında 134.501 aktif gemiadamı vardır. Bunların 40.782'si zabitan sınıfıyken 93.719'u güverte sınıfıdır (Gönel, 2013; T.C. UAB, 2020).

Gemilerde günlük bakım-tutum çalışmaları, yanaşma-kalkma manevraları gibi temel gemicilik aktivitelerinin yanında, gemiadamları sürekli can emniyeti riskleriyle de karşı karşıyadırlar (Fei ve Lu, 2015). Çatma, oturma, yangın gibi gemi bütününe ilgilendiren durumların yanı sıra, gemi içinde yaşanan iş kazaları denizciliğin neden tehlikeli iş kollarından olduğunu açıklar niteliktedir (T.C. UAB, 2002). Ayrıca, gemilerdeki iş kazalarının sonucunda ortaya çıkan ölüm oranlarının, bazen ölümlerle sonuçlanan korsan saldırılarının da denizcilik mesleğinin gerçeklerinden olduğu unutulmamalıdır (Nincic, 2010). Gemide yaşanan iş kazalarına çoğunlukla güverte tayfalarının güvertede çalışırken maruz kaldığı belirtilmiştir (Hansen vd., 2002).

Gerek çalışma temposu ve gerekse karada çalışanlara nispeten farklı bir hayat tarzı ile denizcilik mesleği, hiyerarşi gerektiren mesleklerdendir (Guo vd., 2006). Denizcilik, yaşanan ölümcül kaza ve yaralanma oranlarıyla hata kabul etmeyen bir iş kolu olarak da nitelendirilmektedir (AMSA, 2010). Gemilerin neden olduğu kazaların çoğu, başta gemiadamları olmak üzere insan kaynaklıdır (Er, 2005). European Maritime Safety Agency (EMSA)'nın 2014-2019 verilerine dayanarak hazırladığı raporunda, denizde yaşanan 1.801 kazanın %54'ü insan hatalarından kaynaklanırken, %28'i sistem/ekiptandan kaynaklandığı belirlenmiştir (EMSA, 2020).

Birleşmiş Milletler (BM) ve Uluslararası Denizcilik Örgütü (IMO) tarafından deniz güvenliği ve kazalara yönelik önlemler için kurallar belirlenmiş ve eğitim standartları oluşturmuşlardır (Şahin, 2021). Uluslararası Denizcilik Örgütü (IMO), insan faktörü kaynaklı deniz kazaları sebebiyle eleştirilmiştir. 1993'te üye ülkelerce desteklenen Deniz Emniyet Komitesi Gemiadamlarının Eğitim, Belgelendirme ve Vardiya Tutma Standartları (STCW) Sözleşmesinin detaylı olarak gözden geçirilmesine karar vermiş ve sonuç olarak 1995 yılında STCW Sözleşmesinin düzenlenmesi sağlanmıştır (Fuazudeen, 2008). Denizcilik eğitimi alanında da IMO'da kabul edilen STCW en temel referans kaynak olup tüm denizcilik eğitimlerinin

ve gemiadamı belgelendirmelerinin bu sözleşmeye uygun olması beklenmektedir. Eğitimlerin asgari koşulları IMO tarafından STCW 78/95 kuralları doğrultusunda belirlenmiş olup bu kapsamda 160'tan fazla ülkenin 500'den fazla eğitim kurumunun değişik eğitim seviyesindeki kişilere değişik sürelerde denizcilik eğitimi verilmektedir (Özcan, 2020). 21. yüzyılda tüm dünyada zabitan eğitimi STCW 78/95'te öngörülen standartları karşılamaya yönelik olarak üniversite, akademi, fakülte, enstitü, denizcilik bölümleri ve değişik tipteki okullar tarafından verilmeye başlanmıştır (Öztürk vd., 2020).

Gelişen eğilimlere uygun olarak, gemilerde yüke göre yapısal farklılaşmaya gidilmektedir. Günümüzde taşıyacakları yükler için özel olarak üretilen gemiler mevcuttur ve bu tür gemilerde çalışacak gemiadamlarının donanımlı ve tecrübeli olmaları işletmelerin önkoşulu haline gelmiştir. Bu nedenle nitelikli iş gücüne her zamankinden daha fazla ihtiyaç duyulmaktadır (Pourzanjani vd., 2002). Yine bu durumla doğru orantılı olarak sektörde farklı gemi türlerinde, uzun yıllardır çalışan gemiadamlarının denizcilik firmalarınca tercih edildiği de bilinen bir gerçektir. Gemi ve personelin, denizcilik sektörünün en önemli üretim faaliyetlerinden olması nedeniyle gemilerde yer alacak gemi çalışanların bilgi ve deneyimleri denizcilik sektöründeki işletmelerin rekabet edebilirliği ve devamlılığı açısından büyük öneme sahiptir (Çelik, 2014). Organizasyonu iyi olan düzenli firmalar, gemiadamlarını istihdam etmeden önce yalnızca STCW'ye uygun olarak düzenlenmiş yeterlilik belgelerinin ve sertifikalarının var olup olmadığına bakarak gemiye atama süreci yapmamaktadırlar (Aydm, 1998).

Güverte veya makine tayfası 5 temel STCW sertifika yeterliliğine sahip olmak için her biri 18 saat olmak üzere 90 saat temel sertifika eğitimi almalıdır. Toplamda mesleki eğitim dersleri 180 saattir (T.C. UAB, 2018). Kurslardan almaya hak kazanılan 5 temel sertifika; Denizde Kişisel Can Kurtarma Teknikleri Eğitimi, Yangın Önleme ve Yangınla Mücadele Eğitimi, Temel İlk Yardım Eğitimi, Personel Güvenliği ve Sosyal Sorumluluk Eğitimi, Can Kurtarma Araçlarını Kullanma Yeterliği Eğitimi sertifikalarıdır (STCW, 2017). Bir gemiadamı, çalışacağı gemi tipine hususi olan sertifikaları (tanker, yolcu ve Ro-Ro gemileri gibi) almak için kendi isteği ile bir kursa gitmediği takdirde meslek hayatının sonuna kadar mesleki konularda bir daha eğitim almak mecburiyetinde değildir. Sadece alınan temel sertifikalar için 5 yılda bir sertifika yenileme sınavına girmek yeterlidir (Gönel, 2013). Gemilerde de yine mesleki eğitimler devam etmektedir. Bu sebepten dolayı kursları başarıyla bitirip, gemiadamı cüzdanı almaya hak kazanmış bir denizcinin alacağı eğitimler gemi hayatı süresince devam eder demek yanlış olmaz.

Gemide verilen eğitimler, emniyet ve güvenliğe yönelik eğitimler ve mesleğe yönelik eğitimler olarak ikiye ayrılır. Güvenlik ve emniyete yönelik eğitimler role talimlerini ve gemide yapılan işin içeriğini kapsar. Role talimlerinde tüm gemiadamlarının görevleri açıkça belirtilir ve bu talimler gemiadamlarının acil durumlara hazırlandığı, belli periyotlarla yaptıkları eğitimlerdir. Role talimleri tüm gemiadamlarının katılımlarıyla gerçekleşir. Denize adam düşmesi, yangın, batma, çatışma, karaya oturma, denize yağ veya petrol sızıntısı, dümen kilitlenmesi, gemiyi terk olarak bilinen role talimlerinde, gemiadamlarının her birinin bu durumların yaşanma ihtimaline karşı, sorumlulukları belirlenmiş ve olası kötü bir senaryoda bilinçli bir şekilde görevlerini yerlerine getirmeleri, sorumluluklarının farkında olmaları amaçlanır. Mesleğe yönelik eğitim ise, gemide kazanılan bilgi becerilerin yeni katılmış kişilere usta çırak ilişkisi çerçevesinde aktarılmasıdır (Cömert, 2008).

Literatürde gemiadamlarının aldıkları eğitim ve iş sürecindeki çalışma performanslarına dair yapılmış ayrı ayrı çalışmalar olsa da literatürde yapılan bu çalışmadaki gibi gemiadamlarının eğitimleri, adaptasyonları, role talimindeki bilgi seviyelerinin performanslarını etkileyip etkilemedikleri gibi birleştirici, karşılaştırmalı bir çalışma olmamıştır. Bu çalışmayla gemiadamlarının eğitim performans yönünden karşılaştırılması yapılarak literatüre katkıda bulunulmuştur. Bunun için alanında uzman kişilerin görüşleri doğrultusunda anket formları hazırlanarak gemi kaptanlarına gönderilmiştir. Anketlerden elde edilen verilere SPSS 23 paket programı ile istatistiksel testler uygulanarak sonuçlar elde edilmiştir.

2. Literatür Taraması

Kimyasal tanker gemiler tehlikeli, zehirli sıvı yükleri limanlar arasında taşıyan gemilerdir. Taşıdıkları yüklerin tehlikeli yük sınıfına girmesi, çalışan gemiadamlarının da farkındalık seviyelerinin yüksek olmasını ve bu gemilerdeki çalışma koşullarına yönelik eğitimler almalarını gerektirmektedir. Literatürde gemiadamlarının aldıkları eğitimler ve bu eğitimlerin geliştirilmesi ile ilgili çeşitli araştırmalar yapılmıştır. (Asyalı vd., (2004) ISO Kalite Yönetim Sistemi (KYS)'nin, STCW Kod A-I/8 gereklerini de kapsayacak şekilde aktif eğitimle entegrasyonundan oluşan, eğitimde toplam kalite yönetiminin oluşturulması deneyiminin paylaşılmasına

yönelik yaptıkları çalışmada; bir yükseköğrenim süreci olarak güverte öğrencilerinin eğitiminde andragojik öğrenme ilkelerinin göz önüne alınmasının, aktif eğitimde üst düzey kalitenin oluşturulmasında önemli bir gereklilik olduğu belirtilmiştir. Diğer bir görüşe göre gemiadamları küresel ihtiyaca göre yetiştirilmelidir. Dil yeterliliği, mesleki yeterlilik konusunda eksiklerin giderilmesi için düzenlemeler, çalışmalar yapılmalıdır. Böylelikle yeni yetişen gemiadamları çok uluslu gemilerde, şirketlerde günümüz denizcilik kültürüne uyum sağlayacak bir programla eğitilmiş olacaktır. Sürekli eğitim merkezleri ile gemiadamlarının gelişimi desteklenmelidir. Özel istihdam büroları gemiadamları için sürekli eğitim modelleri geliştirebilir, aday bulma seçme ve yerleştirme işlemlerinin yapılmasında doğru işe doğru gemiadamının yerleştirilmesi sürecine gemiadamının sürekli eğitimi aracılığıyla başarılı bir şekilde katkı sunabilir (Muslu, 2018).

Türkiye’de gemi zabıtlarının aldıkları eğitimler araştırıldığında lisans düzeyinde faaliyet gösteren denizcilik okullarında 149 akademisyenin görev aldığı görülmüştür ve bu akademisyenlerden 46’sı denizcilik lisans eğitimi almıştır. MEB’e bağlı okullarda ise 83 eğitimciden 56’sı denizci eğitimci olarak nitelendirilmekteyken bu eğitimcilerin %42’si Balıkçılık Teknolojisi Mühendisi bölümü lisans mezunu iken %12’si Deniz Ulaştırma ve İşletme Mühendisliği, %2’si Gemi Makineleri İşletme Mühendisliği mezunudur. İncelemelerde %68’inin herhangi bir gemi adamı yeterliliği olmadığı göze çarpan bu eğitimcilerin, %1’i uzakyol kaptan, %12’sinin uzakyol vardiya zabiti ve %3’ünün uzakyol vardiya mühendisi olduğu görülmüştür. Yaklaşık 1000 adet fakülte veya yükseköğretim öğrencisi olduğu düşünüldüğünde, her bir öğretim elemanı başına yaklaşık 4 öğrenci ve her denizci kökenli öğretim elemanı başına 22 öğrenci düşüğü görülmektedir (Öztürk vd., 2020).

Denizde çalışma koşulları, gemilerdeki iş yükü ve çalışma ortamlarının gemiadamları üzerindeki olumsuz etkileri araştırıldığında, 1999-2008 yılları arasında mezun olmuş Dokuz Eylül Üniversitesi Denizcilik Fakültesi Deniz Ulaştırma ve İşletme Mühendisliği Bölümünden mezun olan uzakyol vardiya zabıtlarına yönelik bir çalışmada, “bol kazançlı bir meslek olması” denizcilik mesleğini seçme nedenlerinin başında olduğu görülmüştür. Bir diğer göze çarpan durum ise büyük bir oranın denizdeki kariyerlerini sonlandırmadan önce Uzakyol Kaptan yeterliliğine ulaşmayı hedefledikleridir. Olumsuz etkenlerin ise günden güne artan iş stresi, aileden uzak kalma, limandaki kısıtlı süre, iş yükünün fazlalığı, denetimlerin artması ve sorumlulukların artması olduğu görülmüştür (Köseoğlu vd., 2015).

Gemilerde ölümlü iş kazaları karadaki iş kazalarına nazaran 10 kat daha fazladır. Araştırmalarda iş kazalarının en yoğun yaşandığı yerler gemilerin güverteleriyken iş kazalarından en çok güverte tayfalarının etkilendiği görülmüştür. 1986-1995 yılları arasında Hong-Kong bayraklı gemilerde meydana gelen kazalarda ölüm vakalarının sayısı 123 olarak tespit edilmiştir ve %56,1’i deniz kazaları sonucunda yaşanırken %17,1’i hastalıktan, %10,6’sı bireysel meslek kazası sonucu, %7,3’ü denizde kaybolma, %3,3’ü cinayet, %3,3’ü de intihar olarak belirlenmiştir (Nielsen, 1999).

Literatür incelemesi yapılmış ve gemiadamlarının aldıkları eğitimlerin ve bu yöndeki tavsiyelerin yanında gemideki çalışma koşulları ve iş kazalarına yönelik çalışmaların olduğu görülmüştür. Bu çalışmada kimyasal tankerlerde çalışan gemiadamlarının gemi kaptanları tarafından değerlendirildiği anketler üzerinden SPSS ile analizler gerçekleştirilmiştir. Analizlerde gemide çalışan gemiadamlarının eğitim, performans ve sorumluluk düzeyleri arasındaki etkiler araştırılmıştır. Eğitim seviyelerinin performans etkisi, role talimlerdeki seviyelerinin tespiti ve performans etkisi, ilk defa çalışan gemiadamlarının eğitim bilgileri ve performanslarının belirlenmesi için istatistiksel analizler gerçekleştirilmiştir. Ayrıca yabancı personellerin adaptasyonlarının role talim performanslarının ve sorumluluklarının etkilenip etkilenmedikleri araştırılmıştır.

3. Yöntem

Çalışmanın amacı kimyasal tankerlerde çalışan gemi çalışanları, güverte zabıtları ve makine zabıtlarının aldıkları role talimlerinin uygun istatistiksel analizlerle belirlenmesidir. Çalışmada, SPSS 23 paket programı kullanılmıştır. Toplanan veriler için tanımlayıcı istatistikler ve frekans analizinden sonra verilerin türü ve dağılım tipine uygun olan testler uygulanmıştır. Çalışmanın hazırlık aşamasında belirlenen hipotezlere göre gerekli karşılaştırma ve ilişki testleri ile analizler yapılmış ve sonuçları yorumlanmıştır.

3.1. Veri Toplama

Araştırmanın konusu itibarıyla gemiadamlarının değerlendirilmesine yönelik yapılacak istatistiksel analiz için Google formlar aracılığıyla anket formu tasarlanmıştır. Anket formları, kurumların, gemi personellerini

değerlendirebilmeleri için Karadeniz Teknik Üniversitesi Deniz Ulaştırma İşletme Mühendisliği Mezunlar Derneği (KTÜDUİMMMD) ve Kılavuz Kaptanlar Derneği üzerinden kimyasal tanker gemilerinde görev yapan kaptanlara yönlendirilmiştir. Bu iki dernekten sadece KTÜDUİMMMD aracılığı ile anketlere yanıt verilmiştir. Anketler 740 kişiye iletilmiş sadece 63 yanıtlanan anket formu olmuştur. Anket sonuçları analiz edilirken %90 güvenilirlik seviyesinde %10'luk hata payı ile gerçekleştirilmiştir.

3.2. Veri Analizi

Toplanan verilerle betimsel istatistikler gerçekleştirilmiş, dağılımları kontrol edilmiştir. Elde edilen verilerin normal dağılım göstermeleri uygulanacak testin seçiminde önemli rol oynamaktadır. Verilerin boyutunun 30'dan büyük olması, normal dağılımı olması ve homojen olması halinde parametrik testlerin uygulanmasını gerektirecektir. Dağılımın normal olup olmadığına karar vermek için basıklık (kurtosis) ve çarpıklık (skewness) değerlerine bakılmıştır. Bu değerlerin +/-2 arasında olması halinde verilerin normal dağılım gösterdikleri sonucuna varılmıştır (Bhattacharya ve Habtzghi, 2002).

Hipotezlere uygun olarak skorlaştırılmış değişkenler seçilerek uygun testler uygulanmıştır. Değişkenleri nicelleştirebilmek için öncelikle SPSS 23 paket programında ilgili değişkenler seçildikten sonra skor hesabı yapılarak nicel veri elde edilmiştir. Toplanan verilerin normal dağılım göstermeleri ve kategorik değişkenlerin skor hesabı yapılarak nicel veri tipine dönüştürülmesi nedeniyle bağımsız değişkenlerde t-Testi ve regresyon testleri uygulanmıştır.

Test sonuçlarının anlamlı olup olmadığına kararına anlamlılık düzeyine yani p değerine bakılarak karar verilmiştir. p değeri, anlamlı bir farklılığın var olmasının ve kanıt seviyesinin belirlenmesi amacı ile kullanılmıştır. p değerini 0,05 ($p < 0,05$) olarak baz alıp analizlere karar verilmiştir (Kul, 2014). p değerinin yorumlanması Tablo 1'e göre yapılmıştır (Rosner, 2010).

Tablo 1

p değer aralıklarının yorumlanması

p Değeri	Yorumu
$p < 0,001$	Çok yüksek düzeyde istatistiksel anlamlılık
$0,001 \leq p < 0,01$	Yüksek düzeyde istatistiksel anlamlılık
$0,01 \leq p < 0,05$	İstatistiksel anlamlılık
$0,05 \leq p < 0,10$	Anlamlılık eğilimi (sınırdan anlamlılık)
$p > 0,10$	Fark tesadüfen ileri gitmiştir (istatistiksel olarak anlamlı farklılık saptanmamıştır)

4. Bulgular

Türk gemilerinde gemiadamlarının performans ve eğitimlerinin değerlendirilmesine yönelik hazırlanmış anket verilerinin SPSS paket programında analizi gerçekleştirilmiştir. Anket katılımcılar tarafından her bir soruyu 1 ile 10 arasında değerlendirebileceği şekilde hazırlanmıştır. Anketin doğru bir analizden geçirilebilmesi için keşifsel faktör analizi yapılmıştır. Tablo 2'de ifade edilen Kaiser-Meyer-Olkin (KMO) test sonucu ve Bartlett'in Küresellik test sonucuna göre faktör analizine uygun verilere sahip bir anket olduğu belirlenmiştir. SPSS'teki ismiyle *Açıklanan Toplam Varyans* tablosunda 6 faktör oluşmuş ve faktörlerin varyans toplamı 75,804 olarak hesaplanmıştır. Varyans toplamının 50'den büyük olmasından dolayı oluşan faktörlerin anlamlı olduğu sonucuna varılmıştır. Böylece keşifsel faktör analizi sonucuna göre sorulan 40 sorunun 6 alt boyut içerdiği sonucuna varılmıştır.

Oluşturulan anket genel olarak Cronbach'ın Alpha test sonucuna göre %95 güvenilirlik ile yüksek seviyede bir güvenilirlikle tamamlanmıştır. Anketteki soruların faktör bazlı güvenilirlikleri Tablo 3'te gösterilmiştir. Güvenirlik katsayıları 0,75 ve 0,97 arasında değişmekte olup, tüm faktörlerin güvenilirlik oranlarının kabul edilebilir değer olan 0,70'ten büyük olması nedeniyle hazırlanan anket ölçeğinin güvenilir olduğu sonucuna varılmıştır.

Tablo 2

Kaiser-Meyer-Olkin (KMO) ve Bartlett Test Sonuçları

Kaiser-Meyer-Olkin Örnekleme Yeterliliğinin Ölçüsü		0,758
Bartlett'in Küresellik Testi	Yaklaşık Ki-Kare Değeri	2399,379
	df	595
	Önemlilik	,000

Bu çalışmadaki amacın çözümüne yönelik analiz ve inceleme yapılması için; eldeki veriler, uzman görüşleri ve literatür taraması nihayetinde yazarlar tarafından literatüre katkı sunabileceği düşünülen 6 hipotez belirlenmiştir.

H₁: Çalışan gemi adamlarının eğitim düzeyinin çalışma performansını açıklayıcılığı yüksektir.

H₂: Role talimlerinde görev alan gemi zabıtları, güverte çalışanlarına göre performansları yüksektir.

H₃: Role talimlerinde yer alan gemi zabıtlarının ortalamaları yüksektir.

H₄: Gemiadamlarının role talimlerine yönelik bilgilerinin sorumluluk seviyelerini açıklamaktadır.

H₅: İlk defa görev alan gemi adamlarının bilgileri performanslarını etkilemektedir.

H₆: Yabancı personellerin adaptasyonları role talim performansları ve çalışma performanslarını etkilemektedir.

Tablo 3

Güvenilirlik analizi sonucu belirlenen değişkenler ve Cronbach'ın Alpha değerleri

Değişkenler	Cronbach'ın Alpha
Şirketin verdiği eğitimler	0,97
Yabancı çalışanlar	0,92
Gemide ilk kez çalışanlar	0,88
Emniyet ekipmanlarının kullanımı	0,83
Çalışanların performansı	0,82
Çalışanların eğitimlerinin değerlendirilmesi	0,75

4.1. H₁ Hipotezi; Çalışan Gemi Adamlarının Eğitim Düzeyinin Çalışma Performansını Açıklayıcılığı Yüksek

Tablo 4'e bakıldığında basıklık ve çarpıklık değerlerinin +/-2 arasında değer almış olması testlerde kullanılacak değişkenlerin normal dağıldığını göstermektedir. H₁ hipotezi için kullanılan iki değişkende normal dağılım gösterdikleri için regresyon analizi uygulanmıştır.

Şekil 1 ve Şekil 2'deki grafiklere bakıldığında da verilerin normal dağılım gösterdiği gözlemlenebilmektedir. Veri tipine uygun olan teste karar verilmiş olup Regresyon analizi gerçekleştirilmiştir. Tablo 5'te regresyon analizi uygulanmış hipotezlerin sonuçlarına yer verilmiştir. H₁ hipotezi için uygulanan regresyon analizine göre R² değerine bakıldığında kurulan modelin açıklayıcılığının %61 olduğu bulunmuştur. Yani gemi adamlarının performanslarının %61'inin eğitim düzeyine bağlı olduğu sonucuna varılmıştır. Gemi adamlarının aldıkları eğitimlerin performanslarını açıklayıcılığı önemlilik derecesine göre 0,05 değerinden daha düşük bir değer almıştır. Oluşturulan modele göre gemi adamlarının eğitim düzeyleri performanslarını açıkladığı belirlenmiştir. β Katsayısının 0,669 olduğu ve katsayının önemlilik değerinin 0,05'ten düşük olması model için kullanılabilir olduğu anlaşılmıştır.

4.2. H₂ Hipotezi; Role Talimlerinde Görev Alan Gemi Zabıtları, Güverte Çalışanlarına Göre Performansları Yüksek

Ankette güverte çalışanları ve zabıtlar için role talimlerinin her biri ayrı ayrı sorulmuştur. Role talimlerine katılan güverte ve makine zabıtlarının gemi çalışanları ile aralarındaki farkın analizinden önce

Tablo 4

Hipotezlerdeki değişkenlerin yığılma ve çarpıklık değerleri

	Basıklık	Çarpıklık
Gemiadamlarının Eğitim Değerleri	-0,347	0,222
Gemiadamlarının Performans Değerleri	1,069	-0,705
Role Talimi Alan Gemiadamlarının Skorları	-0,489	-0,112
Role Talimi Alan Zabitlerin Skorları	-0,474	-0,171
Role Talimi Sorumluluk Seviyesi	-0,290	-0,109
Role Talimi Bilgi Seviyesi	-0,602	-0,153
İlk Kez Çalışanların Eğitim Seviyesi	1,273	0,787
İlk Kez Çalışanların Performans Seviyesi	0,398	0,138
Yabancı Uyrukluların Adaptasyon Seviyesi	1,524	-0,699
Yabancı Uyrukluların Performans Seviyesi	1,310	-0,964

Tablo 5

Hipotezler için Regresyon analizlerinin sonuçları

Hipotezler	R ²	Modelin Önemlilik Değeri	Beta (β) Katsayısı	Katsayılar	
				t Değeri	Katsayıların Önemlilik Değeri
H ₁	0,613	0,000	0,669	6,062	0,000
H ₄	0,923	0,000	0,932	27,035	0,000
H ₅	0,519	0,000	0,705	7,196	0,000
H ₆	0,707	0,000	0,853	9,184	0,000

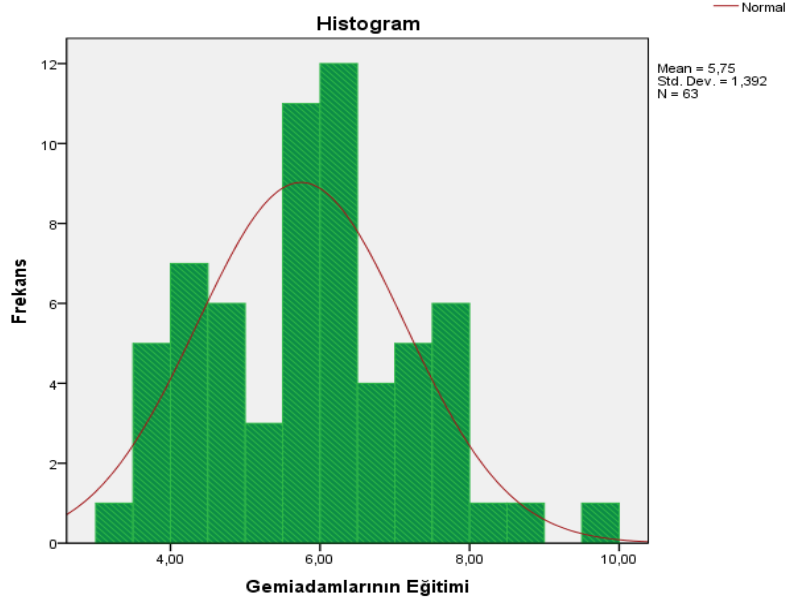
verilerin dağılımı görselleştirilmiştir. Tablo 4'e bakıldığında basıklık ve çarpıklık değerlerinin +/-2 arasında değer almış olması test edilen iki değişkenin normal dağıldığını göstermektedir. Şekil 3 ve Şekil 4'teki grafiklere bakıldığında verilerin normal dağılım gösterdiği gözlemlenebilmiştir.

Role talimlerini alan çalışanlar gemi zabitleri ve gemi çalışanları olmak üzere gruplandırılmıştır. Bu grupların performanslarının istatistiksel olarak anlamlı düzeyde farklılık gösterip göstermediği araştırılmıştır. Bunun için "bağımsız iki örnek için t-Testi" uygulanmıştır. Sonuçlar incelendiğinde zabitler ve gemi çalışanlarının role talimi performansları bakımından önemli bir farklılık göstermediği sonucuna varılmıştır. Çünkü hesaplanan p değeri 0,340 olarak hesaplanmıştır. Bu değer 0,05 olarak kabul ettiğimiz p değerinden oldukça yüksektir. Dolayısıyla zabitlerin role talim performanslarının gemi çalışanlarının performanslarından yüksek olduğu hipotezi reddedilir. Aralarında farklılık olmadığı sonucuna varılmıştır.

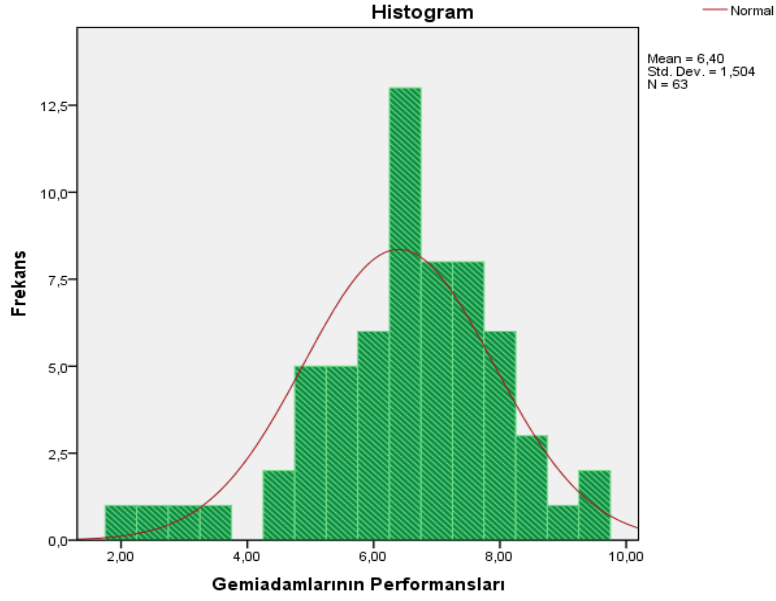
4.3. H₃ Hipotezi; Role Talimlerinde Yer Alan Gemi Zabitlerinin Ortalamaları Yüksek

Analize başlamadan önce kullanılacak olan değişkenin normal dağılıp dağılmadığının kontrol edilmesi gerekmektedir. Kullanılan değişken role talimi alan gemi zabitleri olduğu için Tablo 4'te çarpıklık basıklık değerlerinden ve Şekil 4'teki grafikten normal dağılım gösterdiği sonucuna varılmaktadır.

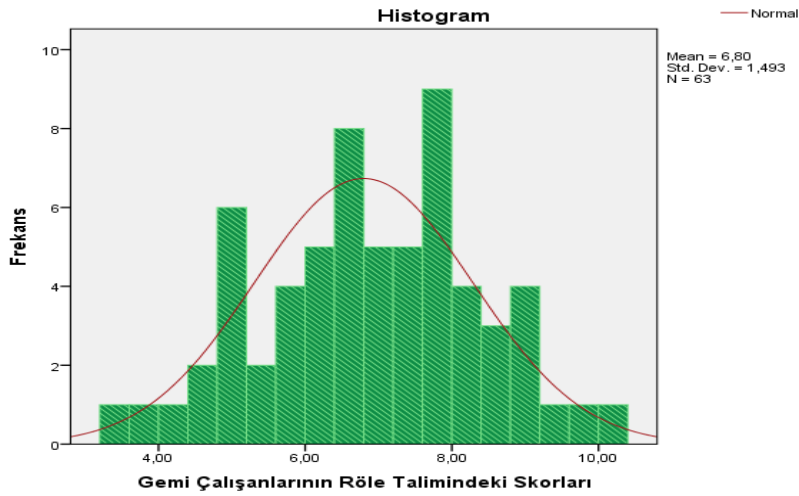
Hipotez 2'de uygulanan "bağımsız örnekler için t-Testi" role talimi alan gemi zabitlerinin değerlendirilmelerinin ortalamadan farklı olup olmadığını ölçmek içinde kullanılmıştır. Ortalamadan düşük yapılan değerlendirmelerin sayısı 6 iken ortalamadan yüksek değer alan zabitlerin sayısı 57'dir. Bu farkın istatistiksel olarak anlamlı olup olmadığı araştırılmıştır. Test sonucuna göre p değeri 0,001 olarak bulunmuştur. Bu değer kabul edilen 0,05 p değerinden düşük olması kurulan hipotezin kabul edilmesi



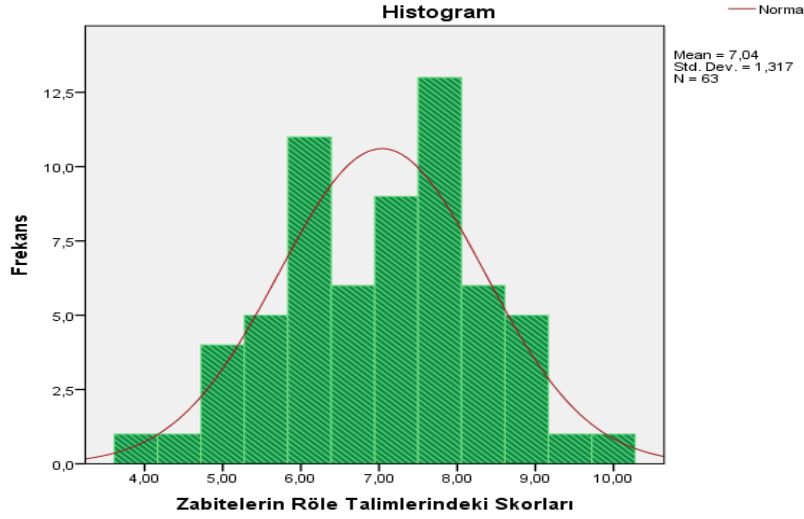
Şekil 1. Gemiadamlarının eğitim skorlarının normal dağıldığını gösteren histogram grafiği



Şekil 2. Gemiadamlarının performanslarının normal dağıldığını gösteren histogram grafiği



Şekil 3. Role talimindeki gemi çalışanlarının skorlarının histogram grafiği



Şekil 4. Role talimindeki gemideki zabitelerin skorlarının histogram grafiği

anlamına gelmektedir. Yani gemi zabitelerinin role talimindeki performansları ortalamadan yüksektir sonucuna varılmıştır.

Hipotez 2’de role talimi alan gemi zabiteleri ile güverte çalışanları arasında bir fark olmadığı anlaşılmıştır. Hipotez 3’teki analizde ise gemi zabitelerinin aldıkları role talimleri için yapılan değerlendirme sonuçlarının ortalamadan yüksek olup olmadığı incelenmiştir ve talimleri yüksek performansla bitirdikleri belirlenmiştir.

4.4. H₄ Hipotezi; Gemiadamlarının Role Talimlerine Yönelik Bilgilerinin Sorumluluk Seviyelerini Açıklamaktadır.

Gemiadamlarına verilen role talimleri sonucunda alınan eğitimin sorumluluk düzeyini ne derece artırdığı veya açıkladığı araştırılmıştır. Çalışanların 1’den 10’a kadar değerlendirildiği anket sonuçları 4 guruba ayrılmıştır. 1-2,5 skorları 1, 2,5-5 skorları 2, 5-7,5 skorları 3, 7,5-10 skorları 4 olarak gruplandırılmıştır. Tablo 6’deki çapraz tabloya bakıldığında çalışan role talimi bilgisi 2 olan 7 kişinin sorumluluk seviyeleri 5 kişinin 2 2 kişinin 3 olarak puanlanmış. Bilgi seviyesi düşük olan kişilerin sorumluluk düzeylerinin de düşük olduğu anlaşılmaktadır. Bilgi seviyesi 4 olan 26 kişinin 6’sı 3, 20’si 4 puan almış olduğu görülmektedir. Role talim bilgi seviyesi artan kişilerin sorumluluk seviyelerinin de artmış olduğu anlaşılmaktadır.

Tablo 6

Role talimi sorumluluk skorları * role talimi bilgi skorları çapraz tablosu

		Role Talimi Bilgi Skorları			Toplam
		2	3	4	
Role Talimi Sorumluluk Skorları	2	5	1	0	6
	3	2	28	6	36
	4	0	1	20	21
Toplam		7	30	26	63

Tablo 6’de görülen bu değişimlerin rastlantı mı yoksa istatistiksel anlamda bir farklılık mı olduğunun analizi gerçekleştirilmiştir.

Tablo 4’te role talimi alan gemiadamlarının sorumluluk ve bilgi skorlarının normal dağılıp dağılmadıkları basıklık ve çarpıklık değerleri ile kontrol edilmiş ve +/-2 değerler aralığında sonuçlar alınmış olması normal dağıldıklarını göstermektedir. Böylece parametrik testlerin uygulanmasına karar verilmiştir.

Role talimi alan gemiadamlarının bilgisinin sorumluluk seviyelerini ne düzeyde açıkladığının, etkilendiğinin araştırılması yapılmıştır. Bunun için veri tipine ve dağılımına uygun olarak lineer regresyon yapılmıştır.

Yapılan regresyon analizinde Tablo 5'teki değerine bakıldığında kurulan modelin açıklayıcılığının %92 olduğu bulunmuştur. Yani gemiadamlarının sorumluluk seviyelerinin %92'sinin role talimi alan gemiadamlarının bilgi düzeyine bağlı olduğu sonucuna varılmıştır. Gemiadamlarının aldıkları role talimlerdeki bilgi düzeyinin sorumluluklarını açıklayıcılığı önemlilik derecesine göre 0,05 değerinden daha düşük bir değer almıştır. Oluşturulan modele göre role talimi alan gemiadamlarının bilgi seviyelerinin artması veya azalması sorumluluk seviyelerini açıkladığı belirlenmiştir. β katsayısı 0,932 olarak hesaplanmış ve katsayının önemlilik değerinin 0,05'ten düşük olarak tespit edilmiştir. Sonuç olarak model için kullanılabilir bir katsayı olduğu anlaşılmıştır.

4.5. H_5 Hipotezi; İlk Defa Görev Alan Gemiadamlarının Bilgileri Performanslarını Etkilemektedir

İlk defa denizde görev alan gemiadamlarının bilgi seviyelerinin denizde aldıkları görevlerindeki performanslarını etkileyip etkilemedikleri araştırılmıştır.

Çalışanların 1'den 10'a kadar değerlendirildiği anket sonuçları 4 guruba ayrılmıştır. 1-2,5 skorları 1, 2,5-5 skorları 2, 5-7,5 skorları 3, 7,5-10 skorları 4 olarak gruplandırılmıştır. Tablo 7'deki çapraz tabloya bakıldığında eğitim skorları 1 olan kişilerin performansı 2 olarak puanlanmış, eğitim skoru 4 olarak puanlanan kişilerin performansları 3 ve 4 olarak puanlanmışlar. Eğitim seviyesinin düşük ve yüksek değerlerine göre performans seviyelerinin de değiştiği gözlemlenmektedir.

Tablo 4'te basıklık ve çarpıklık değerlerinin +/-2 değerleri arasında olmasının eğitim ve performans değişkenlerinin normal dağılım gösterdikleri anlaşılmaktadır. Böylece parametrik testlerin uygulanmasına karar verilmiştir.

İlk defa gemiye çıkan gemiadamlarının bilgi düzeylerinin performans seviyelerini ne düzeyde açıkladığının, etkilendiğinin araştırılması yapılmıştır. Yapılan regresyon analizinde Tablo 5'teki R^2 değerine bakıldığında kurulan modelin açıklayıcılığının %52 olduğu bulunmuştur. Yani ilk defa gemide görev alan gemiadamlarının performanslarının %52'sinin bilgi düzeyine bağlı olduğu sonucuna varılmıştır. Tablo 5'te modelin önemlilik değerinin 0,05'ten düşük olması oluşturulan modelin anlamlı olduğu yönündedir. Yani ilk defa gemide görev alan gemiadamlarının eğitim seviyelerinin performanslarını açıkladığı sonucuna varılmıştır. β Katsayısının 0,961 olduğu ve katsayının önemlilik değerinin 0,05'ten düşük olması model için kullanılabilir bir katsayı olduğu anlaşılmıştır. Tablo 7'de gözlemlenen ilk defa denizde görev alan gemiadamlarının bilgi seviyelerinin artması veya azalması performans seviyelerini açıklamaktadır.

Tablo 7

İlk kez denizde görev alan gemiadamlarının eğitim skorları ile performans skorları çapraz tablosu

		Eğitim Skorları				
		1	2	3	4	Toplam
Performans Skorları	1	0	1	0	0	1
	2	2	20	2	0	24
	3	0	11	9	1	21
	4	0	2	0	2	4
Toplam		2	34	11	3	50

4.6. H_6 Hipotezi; Yabancı Personellerin Adaptasyonları Role Talim Performansları ve Çalışma Performanslarını Etkilemektedir

Yabancı uyruklu gemiadamlarının adaptasyonlarının denizdeki çalışmalarını ve role talimlerdeki performanslarını etkileyip etkilemediği araştırılmıştır.

Çalışanların 1'den 10'a kadar değerlendirildiği anket sonuçları 4 guruba ayrılmıştır. 1-2,5 skorları 1, 2,5-5 skorları 2, 5-7,5 skorları 3, 7,5-10 skorları 4 olarak gruplandırılmıştır. Tablo 8'deki çapraz tabloya bakıldığında eğitim skorları 1 olan kişilerin performansı 1 olarak puanlanmış, eğitim skoru 4 olarak puanlanan kişilerin performansları 3 ve 4 olarak puanlanmışlar. Eğitim seviyesinin düşük ve yüksek değerlerine göre performans seviyelerinin de değiştiği gözlemlenmektedir. Tablo 8'de görülen bu değişimlerin rastlantı mı yoksa istatistiksel anlamda bir farklılık mı olduğunun analizi gerçekleştirilmiştir.

Tablo 8

Yabancı uyruklu gemiadamlarının adaptasyon skorları ile performans skorları çapraz tablosu

		Adaptasyon Skorları				
		1	2	3	4	Toplam
Performans Skorları	1	1	0	0	0	1
	2	0	3	6	0	9
	3	0	1	17	3	21
	4	0	0	2	4	6
Toplam		1	4	25	7	37

Yabancı uyruklu gemiadamların adaptasyonlarının performanslarına etki edip etmediği veya ne düzeyde etki ettiğinin araştırılması gerçekleştirilmiştir. Bunun için veri tipine ve dağılımına uygun olarak lineer regresyon yapılmıştır. Yapılan regresyon analizinde Tablo 5'teki değerine bakıldığında kurulan modelin açıklayıcılığının %70 olduğu bulunmuştur. Yani gemideki yabancı uyruklu gemiadamlarının performanslarının %70'inin adaptasyonlarına bağlı olduğu sonucuna varılmıştır. Tablo 5'te modelin önemlilik değerinin 0,05'ten düşük olması oluşturulan modelin anlamlı olduğu yönündedir. Yani yabancı uyruklu gemiadamlarının adaptasyonlarının performanslarını açıkladığı sonucuna varılmıştır. β Katsayısının 0,853 olduğu ve katsayının önemlilik değerinin 0,05'ten düşük olması model için kullanılabilir bir katsayı olduğu anlaşılmıştır. Yani Tablo 8'de gözlemlenen yabancı uyruklu gemiadamlarının adaptasyon seviyelerinin artması veya azalması performans seviyelerini açıklamaktadır.

5. Sonuçlar

Yapılan literatür araştırmasında gemiadamlarının yetiştiği eğitim kurumları, çalışma ortamları, gemide yaşanan kazalar ve nedenleri ile ilgili çalışmaların olduğu görülmüştür. Bu çalışmada literatürden farklı olarak kimyasal tanker gemilerinde elzem olan eğitim ekipmanlarının kullanımı noktasında gemiadamlarının yeterlilikleri istatistiksel olarak kapsamlı bir şekilde analiz edilmiştir. Bu amaçlarla kimyasal tanker gemilerinde görev alan güverte zabıtları, makine zabıtları, gemi çalışanları, ilk kez görev alan gemiadamları ve yabancı personellerin, eğitimleri, adaptasyonları, role talimindeki bilgi seviyeleri ve performanslarına yönelik yapılan analizlerle istatistiksel bir çalışma gerçekleştirilmiştir. İstatistiksel testleri analiz etmek için SPSS 23 paket programı kullanılmıştır. Yapılan çalışmada istatistiksel kurallara uygun olarak bağımsız örnekler için t-Testi ve regresyon analizi uygulanmıştır. Çalışan gemiadamlarının eğitim düzeyinin çalışma performansının açıklayıcı olduğu kanıtlanmıştır. Yani yüksek seviyede verilecek eğitimler gemilerde doğrudan çalışanların performanslarına yansımakta olduğu belirlenmiştir. Gemilerde işe alımlar için dikkat edilmesi gereken bir faktör olarak eğitim seviyesine yer verilmesi önerilmektedir. Role talimlerinde görev alan gemi zabıtlarının performans ortalamalarının yüksek olduğu belirlenmiştir. Yüksek performansa sahip zabıtlar ile güverte çalışanlarının performansları karşılaştırıldığında bir farklılık olmadığı sonucuna varılmıştır. İki sonuç beraber düşünüldüğünde güverte çalışanlarının da performans olarak yüksek seviyede oldukları anlaşılmaktadır. Role talimlerinde verilen yangın, gemi terk ve denize adam düştü talimlerinin gemiadamları üzerinde etkili olduğu ve sorumluluk seviyelerinde anlamlı bir etki oluşturdukları kanıtlanmıştır. Role eğitimlerinin özenli bir şekilde yapılmasına dikkat edilmesi gerektiği önerilmektedir. Kimyasal tankerler gibi riskli çalışma ortamlarında risk unsurunu azaltmak önemli olacağı göz önüne alındığında ilk kez gemiye çıkan gemi adamları ve yabancı uyruklu gemiadamları üzerine yapılan çalışmalarda yabancılar için adaptasyon, ilk kez gemide çalışmaya başlayanlar için bilgi seviyelerinin artması veya azalması performanslarını etkiledikleri saptanmıştır. Risk unsurunu azaltma noktasında dikkat edilmesi gerektiği sonucuna varılmıştır. İlk kez gemide görev alacak olan personellerin ve yabancı uyruklu personellerin bilgi ve adaptasyonlarını arttıracak etkinliklere önem verilmesi gerektiği önerilmektedir. Bu çalışma spesifik bir konu olması nedeniyle az sayıda katılımcıyla gerçekleştirilmiş olması bir kısıt olarak görülmüştür.

Yazar Katkıları

Devran Yazır: Makale konusunun ve yöntemin belirlenmesi, gerekli verilerin elde edilmesi ve makale yazımının her aşamasında desteklenmesi.

Sefa Yay: Yöntemin uygulanması ve makale yazımı.

Kaynaklar

- Australian Maritime Safety Authority (AMSA). (2010). *Fact finding report into the reported collision involving the New Zealand registered craft Ady Gil and the Japan registered whaling ship Shonan Maru. No.2 in the Southern Ocean on 6 January 2010*. Avustralya Hükümeti.
- Asyalı, E., Tuna, O., ve Cerit, G. A. (2004). *Denizcilikte aktif eğitim ve kalite yönetimi*. 1. Aktif Eğitim Kurultayı Bildiriler Kitabı, 67-75, İzmir.
- Aydın, H. (1998). *Uluslararası güvenlik yönetimi ISM kodu ve uygulaması* (Yüksek Lisans Tezi). Erişim adresi: <https://tez.yok.gov.tr/UlusalTezMerkezi/>
- Bhattacharya, B., ve Habtzghi, D. (2002). *Median of the p value under the alternative hypothesis*. The American Statistician, 56(3), 202-206. <https://doi.org/10.1198/000313002146>
- Birleşmiş Milletler Ticaret ve Kalkınma Konferansı (UNCTAD). (2020). *Review of maritime transport*. Erişim adresi: https://unctad.org/system/files/official-document/rmt2020_en.pdf
- BIMCO/ISF. (2010). *Manpower 2010 update the worldwide demand for and supply of seafarers highlights*. Bagsværd/Denmark. BIMCO/ISF, 1-2.
- Bozkurt, Y., ve Arslan, R. (2017). *Kamusal hizmet sunumunda suyun yeri: Kütahya Belediyesi örneği*. Kastamonu Üniversitesi İktisadi ve İdari Bilimler Fakültesi Dergisi, 201-213. <https://dergipark.org.tr/en/download/article-file/361146>
- Cömert A. (2008). *Türkiye’de gemiadamı piyasası: arz ve istihdam üzerine bir model önerisi* (Doktora Tezi). Erişim adresi: <https://tez.yok.gov.tr/UlusalTezMerkezi/>
- Çelik, B. (2014). *Denizcilik Endüstrisinde İnsan Kaynakları Planlaması: Türk Gemi Adamlarına Yönelik Bir Araştırma* (Yüksek Lisans Tezi). Erişim adresi: <https://tez.yok.gov.tr/UlusalTezMerkezi/>
- Çetin, O. (2009). *Denizcilik sektöründe mukayeseli bir model*. Güvenlik Stratejileri Dergisi, 5(10), 35-58. <https://dergipark.org.tr/en/download/article-file/84531>
- Demirci, E. (2019). *Lojistik ilkeleri*. İstanbul Üniversitesi, Açık ve Uzaktan Eğitim Fakültesi, 332. http://auzefkitap.istanbul.edu.tr/kitap/uluslararasıitlojistikyonetimi_ao/lojistikilkeleri.pdf
- Er, Z. (2005). *Definitions of human factor analysis for the maritime safety management process*. In International Association of Maritime Universities (IAMU) 6th Annual General Assembly and Conference World Maritime University, 235-243. Erişim adresi: <https://trid.trb.org/View/776073>
- European Maritime Safety Agency (EMSA). (2020). *Annual overview of marine casualties and incidents*. 147.
- Fei, J., ve Lu, J. (2015). *Analysis of students’ perceptions of seafaring career in china based on artificial neural network and genetic programming*. Maritime Policy and Management, 42(2), 111–126. <https://doi.org/10.1080/03088839.2013.873545>
- Fuazudeen, M. (2008). *Seafarers’ training and the comprehensive review of the STCW convention and STCW code*, 16th International Maritime Lecturers Association (IMLA) Conference, 14 Ekim, İzmir, Türkiye.
- Gönel, O. (2013). *Gemi adamı arz-talebinin incelenerek gelecekteki istihdam ve eğitimin planlanması* (Yüksek Lisans Tezi). Erişim adresi: <https://tez.yok.gov.tr/UlusalTezMerkezi/>
- Guo, J. L., Liang, G. S., ve Ye, K. D. (2006). *An influence model in seafaring choice for Taiwan navigation students*, Maritime Policy and Management, 33(4), 403-421. <https://doi.org/10.1080/03088830600895725>
- Hansen H., Nielsen D., ve Frydenberg M. (2002). *Occupational accidents aboard merchant ships*, Occupational Environmental Medicine, 59, 85–91. Erişim adresi: <https://oem.bmj.com/content/59/2/85.short>
- International Chamber of Shipping (ICS), *Shipping and world trade overview*, Erişim adresi: <http://www.ics-shipping.org/shipping-facts/shipping-and-world-trade>

- International Maritime Organisation (IMO) (2017). *International convention on standards of training, Certification and Watchkeeping for Seafarers (STCW) consolidated edition 2017*. 4 Albert Embankment, London.
- Kaluza, P., Kölzsch, A., Gastner, M. T., ve Blasius, B. (2010). *The complex network of global cargo ship movements*. Journal of the Royal Society, Interface, 7(48), 1093–1103. <https://royalsocietypublishing.org/doi/10.1098/rsif.2009.0495>
- Köseoğlu, A. M., Ağca, E. O., ve Özbekler, T. M. (2015). *Port management and educational needs of the sector: a study in ports*, Eurasian Academy of Sciences Social Sciences Journal, 6, 1-27.
- Kul, S. (2014). *İstatistik sonuçlarının yorumu: p değeri ve güven aralığı nedir*. Türk Toraks Derneği, 8(1), 11- 13. Erişim adresi: https://www.toraks.org.tr/site/sf/books/pre_migration/c19fa28083ae026a97e3878c26e1b03eaacfd74d114c8d66f832d8d806c56307.pdf
- Muslu, A. (2018). *Importance of Private crew management companies for employment of Turkish seafarer to replace in international maritime labor market*. Gaziantep University Journal of Social Sciences, 17, 291–302. <https://dergipark.org.tr/en/download/article-file/414933>
- Nielsen, D. (1999). *Deaths at sea- a study of fatalities on board HongKong-registered merchant ships (1986-95)*. Safety Science, 32, 121-141. [https://doi.org/10.1016/S0925-7535\(99\)00016-8](https://doi.org/10.1016/S0925-7535(99)00016-8)
- Nincic, D. (2010). *Maritime piracy in africa: the humanitarian dimension*. African Security Review, 18(3), 1–16. <https://doi.org/10.1080/10246029.2009.9627538>
- Özcan, S. (2020). *Denizcilik sektöründe entegre platform kontrol ve izleme sistemlerinin teknoloji kabul modeli ile incelenmesi* (Yüksek Lisans Tezi). Erişim adresi: <https://tez.yok.gov.tr/UlusalTezMerkezi/>
- Öztürk, O. B., Turna, İ., Altınpınar, İ., ve Pirim, A. E. (2020). *Gemiadamı eğitiminde rol alan eğitim kurumlarına yönelik bir çalışma: denizci eğitimciler*. Turkish studies, 15(4), 2877-2891.
- Parker, C. J. (2001). *Shipping and the human factor*, Seaways, The Nautical Institute, 11, 4-8.
- Pourzanjani, M., Schröder, J. U., ve Zade, G. (2002). *Maritime Education and Training (MET) in the european union: how can maritime administrations support MET*. International Association of Maritime Universities (IAMU) Journal, 2(2), 50-56.
- Rosner, B. (2010). *Fundamentals of biostatistics*. 7th edition, Cengage Learning.
- Smil, V. (2007). *The two prime movers of globalization: history and impact of diesel engines and gas turbines*. Journal of Global History, 2(3), 373–394. <https://doi.org/10.1017/S1740022807002331>
- Smith, A., Allen, P., ve Wadsworth, E. (2006). *Seafarer fatigue: the cardiff research programme*. Centre for Occupational and Health Psychology Cardiff University, 87. Erişim adresi: https://orca.cardiff.ac.uk/48167/1/research_report_464.pdf
- Şahin, K. (2021). *Küresel deniz güvenliğine yönelik hukuki tedbirler: Uluslararası Denizcilik Örgütü sözleşme, karar, protokol, kod ve uygulamaları*. Elektronik Siyaset Bilimi Araştırmaları Dergisi, 12(2), 31-45. Erişim adresi: <https://esbadergisi.com/images/sayi23/3kenan-sahin-kuresel-deniz-guvenligi.pdf>
- Türkiye Cumhuriyeti Ulaştırma ve Altyapı Bakanlığı (2002). *Gemilerin gemiadamları ile donatılmasına ilişkin yönerge*. 31/07/2002 gün 24823 sayılı Resmî Gazete. <https://www.kiyemniyeti.gov.tr/userfiles/file/mevzuat/EK-4.pdf>
- Türkiye Cumhuriyeti Ulaştırma ve Altyapı Bakanlığı (2018). *Gemiadamları ve kılavuz kaptanlar eğitim ve sınav yönergesi*. <https://denizcilik.uab.gov.tr/uploads/pages/gemiadamlari-sinav-merkezi/gkkes.pdf>
- Türkiye Cumhuriyeti Ulaştırma ve Altyapı Bakanlığı, (2020). *Ulaşan ve erişen Türkiye*. Erişim adresi: <https://www.uab.gov.tr/uploads/pages/bakanlik-yayinlari/ulasan-ve-erisen-turkiye-2020.pdf>
- UTİKAD. (2019). *Türk denizcilik sektörü için yeni fırsatlar kapıda*. Erişim adresi: <https://www.utikad.org.tr/Detay/Sektor-Haberleri/26485/turk-denizcilik-sektoru-icin-yeni-firsatlar-kapida>
- Ünsan, Y., İnel, M., ve Helvacıoğlu, İ. H. (2007). *Dünya deniz ticareti ve gemi filosu analizi*. 77. Ulaştırma Kongresi, 19-21 Eylül, İstanbul, 426-437. <https://eskisakarya.imo.org.tr/resimler/ekutuphane/pdf/3122.pdf>



Performance Analysis of Dimming Methods in Visible Light Communication Systems

Süleyman Börekoglu¹, Mehmet Sönmez^{1*}

¹Department of Electrical and Electronics Engineering, Faculty of Engineering, Osmaniye Korkut Ata University, Osmaniye, Türkiye

Article History

Received: 27.12.2021
Accepted: 17.03.2022
Published: 25.09.2022

Research Article

Abstract – The Visible Light Communication (VLC) has been taken very attentions from many researchers due to its efficiency substructure. In specially, the VLC systems provide both lighting and data transmission at the same time. This paper has investigated the performance analyses of modulation schemes which support the brightness control for Visible Light Communication. In this sense, it has been focused on performance differences between M-ary VPPM (M-ary Variable Pulse Position Modulation) scheme and VPAPM (Variable Pulse Amplitude Position Modulation) which was proposed to ensure the multilevel transmission for VPPM scheme. In particular, a performance comparison has been given for both techniques with respect to Bit Error Rate by considering the same bit length consisted in a symbol. The investigated M-ary VPPM is modified by generating the signals of two power levels. Moreover, a VPAPM based-transmission model has been proposed to assure the accurate dimming target values under condition of long runs of same bits (1 s or 0 s) that encode the signal amplitude. However, the proposed system has lower data rate when compare to traditional VPAPM. Moreover, a receiver scheme has been suggested to decode received VPAPM signals. The performance of VPAPM demodulator architecture has been observed in terms of BER versus transmission distance between receiver and transmitter.

Keywords – Demodulator design, dimming methods, m-ary vppm, vlc, vpapm

1. Introduction

With the rapid popularization of wireless communication devices, the spectrum regulation for wireless data transmission need to be further improved. Due to the limited wireless channel sharing, it is expected to emerge new transmission links in the wireless data transmission (Chen, Zhang, Hsu, & Chang, 2020). With the continual technological advances in semiconductor devices such as white light-emitting diode (LED), it is claimed that optical communication systems such as visible light communication (VLC) will overcome the limited communication capacity by integrating Radio Frequency (RF) systems (Küçük, Msongaleli, Akbulut, Kavak, & Bayılmış, 2021; Vats, Aggarwal, & Ahuja, 2019; Alnwaimi & Boujemaa, 2021; Kamat, Khosla, & Narayanamurti, 2020). Even though VLC exhibits many solutions for future integrated communication links, there are still essential technical challenges in nowadays.

It has been proposed the several dimming methods to regulate the LED brightness in the literature since the VLC provide both lighting and data transmission at the same time (Lee W.-C. and Kwon M.-J., 2020; Yawale P., Wagh V., and Shaligram A., 2019; Guo J.-N., Zhang J., Zhang Y.-Y., Xin G., and Li L., 2021; Das B., Bardhan S., Maity T., and Mazumdar S., 2020). For the adjusting the LED brightness, the candidate dimming techniques can be grouped into two general categories, these being analogue and digital dimming methods (Zafar F., Karunatilaka D., and Parthiban R., 2015). The analogue dimming methods are based on amplitude of LED driving signal taking account consideration the data bits while the digital dimming methods are performed by adjusted the duty cycle of driving signal (Zafar F., Kala-vally V., Bakaul M., and Parthiban R., 2015).

Many modulation techniques have been modified to provide dimming support in VLC links (Bui T.-C., Singh R., O'Farrell T., and Biagi M., 2018; Wang T., Yang F., Cheng L., and Song J., 2018; Okumura J., Kozawa

¹ suleyman.borekoglu@gmail.com

² mehmetsonmez@osmaniye.edu.tr

*Corresponding Author

Y., Umeda Y., and Habuchi H.,2017; Knobloch F., 2015). Especially, digital dimming methods have been widely explored due to their low complexity in experimental systems (Raj R., Jaiswal S., and Dixit A., 2021). Variable On-Off Keying (VOOK) and Variable Pulse Position Modulation (VPPM) schemes can be indicated as basic modulation schemes (Lee K. and Park H., 2011). The VOOK scheme was constituted by modifying On-Off Keying (OOK) method while VPPM technique adjusts the duty cycle of binary PPM schemes to provide the variable LED brightness. In the following years, it has been aim to increase the data rate of VPPM scheme in the literature. To provide the higher data transmission, VPAPM (Variable Pulse Amplitude Position Modulation) scheme has been proposed to ensure both variable illumination and data transmission at the same time (Yi L. and Lee S. G., 2014). This method encodes the amplitude of transmitted signal against to transmitted data bits. Instead of amplitude, it has been considered that the position can be encoded to increase the data rate of VPPM scheme in the literature. This position based scheme has been referred to as M-ary VPPM (Yoo J.-H., Kim B. W., and Jung S.-Y., 2015). M-VPPM consists of wrapped signal scheme to ensure the target dimming level.

The one of the disadvantages of VPAPM method cannot assure the desired dimming level if there are long runs of same bits (1 s or 0 s) among the transmitted data signal. Similar problem has been appeared for OOK method in the literature since OOK scheme cannot support a target dimming level under condition of long runs of same bits (1 s or 0 s). To cope with the mentioned challenge, it has been suggested a packet transmission model for VPAPM scheme in the paper. Although the proposed model can support the desired dimming level under condition of long runs of same bits it has lower data rate compared with traditional VPAPM. Addition to this, a demodulator scheme has been performed for received VPAPM signals. The proposed demodulator architecture is analysed in terms of BER versus transmission distance between receiver and transmitter. Moreover, M-ary VPPM has been modified by considering the signals of two power levels. In the last framework of the paper, it has been given a performance comparison with respect to BER for modified M-ary VPPM and VPAPM.

2. VPAPM Method

This section gives VPAPM method which has been proposed to data rate binary VPPM scheme. This scheme allows multiple data transmission by encoding the pulse signal according to data signal. If n is defined as bit number by consisted of one symbol, encoded signal number will equal to bit number n . A VPAPM signal sample is given in the Figure 1 against to data bits.

In the Figure 1, a M-n-VPAPM signal sequence is given considering the transmitted data symbol. As shown in the figure, both M and n get 2 value. The n will be used the 2 for all transmitted signals if the VPAPM

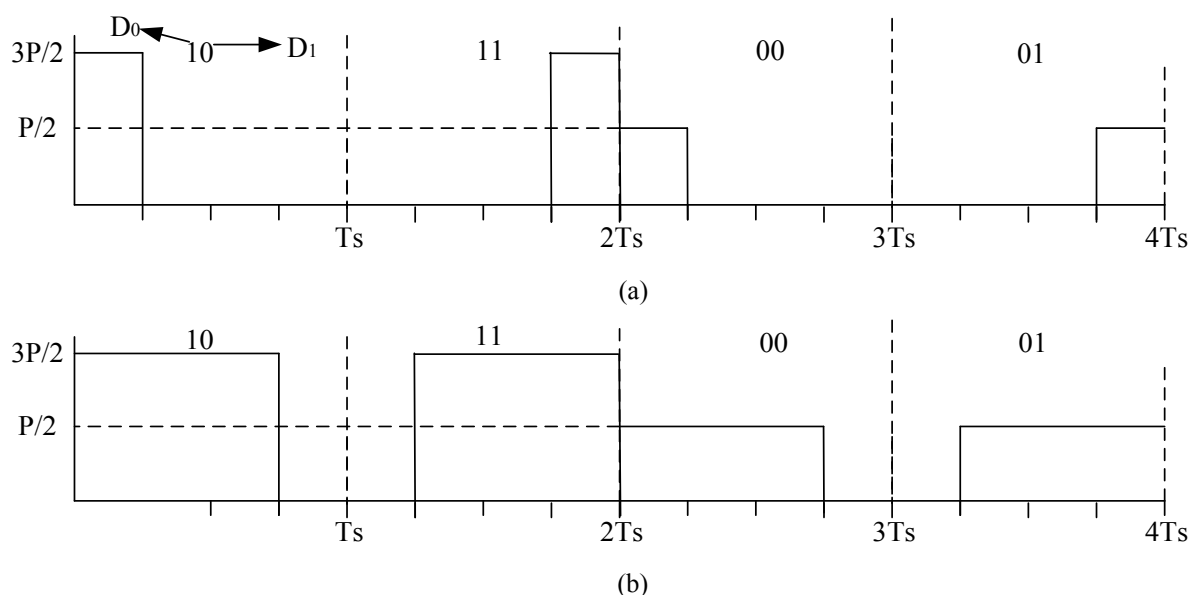


Figure 1. The M-n-VPAPM signal against to data symbols at the dimming ratios of 25 % and 75 %. For 25%. (b) 75%

signal is observed as M-n-VPAPM. The VPAPM method provides higher data rate compared to VPPM scheme since it encodes the amplitude of pulse signal by taking into account data signal. A VPAPM signal can be given by,

$$x(t) = nAP \sum_{k=0}^{n-1} c_k p \left(t - \frac{kT}{n} \right) \tag{2.1}$$

where, $x(t)$ is VPAPM signal. The c_k , T and n are defined as codewords, filled slot duration and chip number. In the Eq.2.1, A is amplitude of modulated signal. The VPAPM signal detected from the photodiode can be decoded by using the receiver algorithm given in the [Figure 2](#).

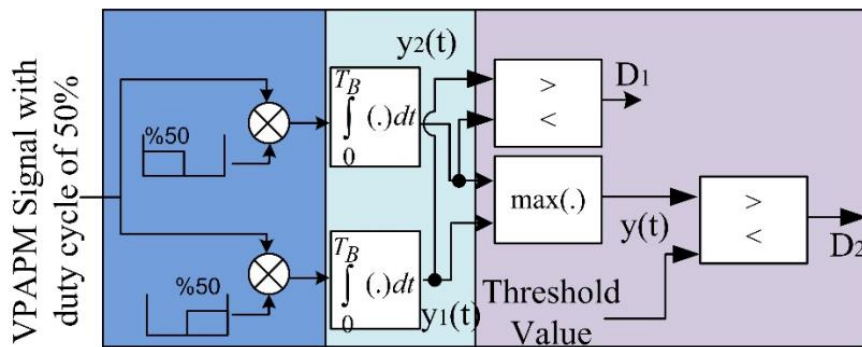


Figure 2. A receiver architecture for the VPAPM

The modified demodulator given in [Figure 2](#) can be considered as a sample architecture for decoding of 2-2-VPAPM signals. In the first stage, the received signal is multiplied by a given masking signals to investigate the position of pulse. Afterwards, the signal is passed through integrator blocks which generates outputs of $y_1(t)$ and $y_2(t)$. In last stage, both signals are applied on a comparison unit. The first bit, which can be referred to as position bit, is appeared at output of comparator block. The two levels including $P/2$ and $3P/2$ is generated to encode the data bit which is $D2$ as depicted in the [Figure 2](#). To determine the level of $D2$, it is necessary a threshold value for M-2-VPAPM. Therefore, an optimum threshold value that can be adjusted as mean value of both transmission level. Under user mobility condition, an adaptive detection threshold method must be applied on receiver system since this condition causes the receiver power being dynamic levels. Addition to this, the received optical power can change under ambient light effect hence threshold level can be dynamic levels. Moreover, the ISI (Intersymbol Interference) problem can be observed when the data rate is increased. The received $x(t)$ signal is added to noise signal at the output of optical detector, hence the outputs of multiplications given in the [Figure 2](#) can be expressed by (Noh J., Lee S., Kim J., Ju M., and Park Y., 2015),

$$y_1(t) = \int_0^{T_s} (x(t) + n(t)) . m_1(t) \tag{2.2}$$

$$y_2(t) = \int_0^{T_s} (x(t) + n(t)) . m_2(t) \tag{2.3}$$

Where (inEqs2.2, 2.3), $y_1(t)$ and $y_2(t)$ are defined as outputs of integrators. The noise signal is depicted by $n(t)$. The $m_1(t)$ and $m_2(t)$ is masking signals which are used to multiply by received M-2-VPAPM signal. The decision can be made as follows:

$$(y_2(t) < y_1(t) \rightarrow D_1 = 1) \wedge (y_2(t) > y_1(t) \rightarrow D_1 = 0) \tag{2.4}$$

Where (inEq2.4), it is performed a comparison of $y_1(t)$ with $y_2(t)$ to decide the level of $D1$. A maximum value is determined in the decision stage. To detect $D2$ bit, it must be compared a threshold value with this maximum value that is chosen from among the $y_1(t)$ and $y_2(t)$. Therefore, $D2$ bit can be determined by

$$y_{max} = \max(y_1(t), y_2(t)) \tag{2.5}$$

$$(th < y_{max} \rightarrow d_{i+1} = 1) \wedge (th > y_{max} \rightarrow d_{i+1} = 0) \tag{2.6}$$

Where (inEqs.2.5, 2.6), y_{max} is described as maximum value that can be determined from among the output values of integrators.

3. M-ary VPPM Method

M-ary VPPM scheme is a digital dimming method while VPAPM is defined as hybrid dimming method that consists of analogue and digital dimming methods. The M-VPPM can adjust the LED brightness by changing duty cycle of modulated signal while VPAPM regulates the amplitude of signal to reach the desired dimming level. Therefore, it can be claimed that M-VPPM has simpler structure than that of VPAPM since it can be considered that the changing of duty cycle is more efficient method to adjust the dimming level of signal compared to setting of signal amplitude. In Figure 3, it is given a M-VPPM signal at the dimming ratio of 50% for $M=4$.

It is shown from the Figure 3 that the filled pulse is rotated by decimal value of transmitted symbol. It is provided the target dimming level under overflow condition. As observed in Figure 3, there is given a M-VPPM signal which has dimming ratio of 50%. The symbol of “11” has caused an overflowing condition. In this condition, the overflow signal is applied on the first slot, hence it is emerged a wrapped signal condition. it is given the traditional M-VPPM demodulator architecture for $M=4$ in the Figure 4. According to the figure, it can be stated that the number of integrator and multiplication block in the traditional M-VPPM demodulator depends on M of modulation order.

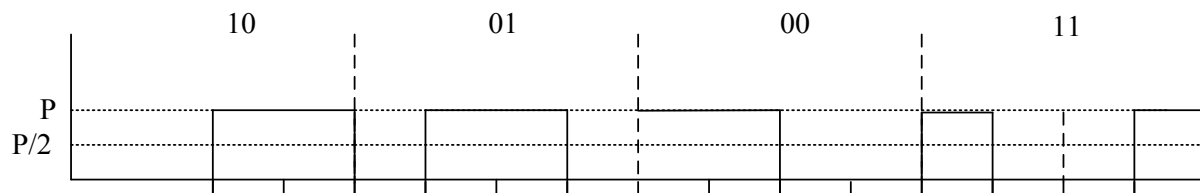


Figure 3. 4-VPPM signal against to data symbol at the dimming ratio of 50%

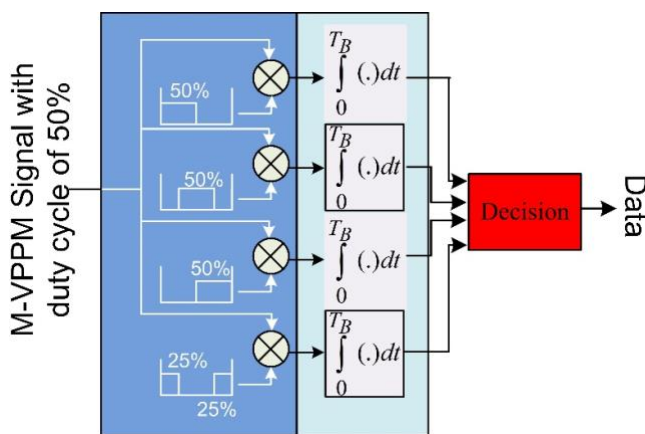


Figure 4. A M-VPPM receiver model for M = 4

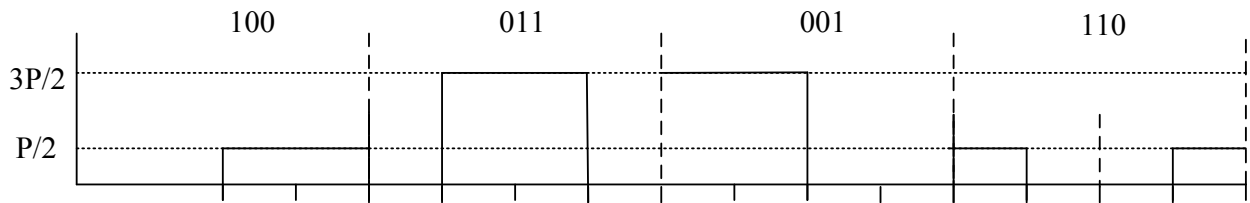


Figure 5. 2-n-VPPM receiver model for n = 4

4. Modified M-ary VPPM method

This section gives a model to increase the transmission performance of M-ary VPPM. In contrast to M-n-VPAPM, the M fixed at the 2. The modified model performs the generating of two amplitude levels while the number of position can get dynamic values. Therefore, modified M-ary VPPM can be defined as M-n-VPPM where the M value gets 2. A M-n-VPPM scheme is given in the Figure 5.

The number of slot can be increased for the architecture given in the Figure 5, instead of amplitude when compare to M-n-VPAPM. Although the signal consists of four slots, it is transmitted by considering the two amplitude levels. Therefore, it is considered that the transmission performance can be increased by fixing the number of amplitude level to 2 when compare to 4-VPPM scheme presented in the Figure 3.

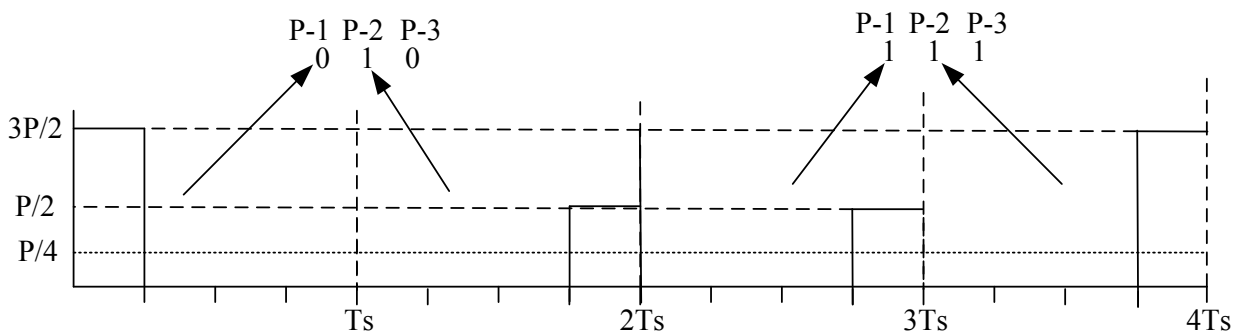


Figure 6. Modified 2-2-VPAPM scheme

As shown in the Figure 6, it is consisted of three data bits in a symbol or a packet while the traditional 2-2-VPAPM can transmits four data bits over two modulated signal. Therefore, 2-2-VPAPM has superior with respect to data rate when compare the modified scheme. However, the modified scheme gives static dimming levels at the transmission during since it consists of serial high and low powers. The optical power can get P/4 for dimming ratio of 25% at the all transmission during. The P3 position bit encodes the positions of signals which have powers of 3P/2 and P/2.

5. Results and Discussion

In this section, it is presented the performance analyses for 2-n-VPAPM and M ary MVPPM in terms of BER and distribution of dimming level. In the first consideration, the 2-2-VPAPM has been investigated at dimming levels between 25% and 75% against the transmission distance between receiver and transmitter. It has been get similar results to VPPM in the simulation. The Figure 7 gives the BER performance of 2-2-VPAPM technique versus transmission distance. The simulation results have been obtained by using the architecture given in the Figure 2. According to simulation results, similar BER performances are observed at the dimming ratios of a% and (100-a)%.

As shown in the Figure 7, it can be performed the 2-2-VPAPM system at the distance of 2.30 m and dimming ratio of 40% instead of the distance of 2.34m and dimming ratio of 50%. The performances at these distance and dimming ratios are close to each other's.

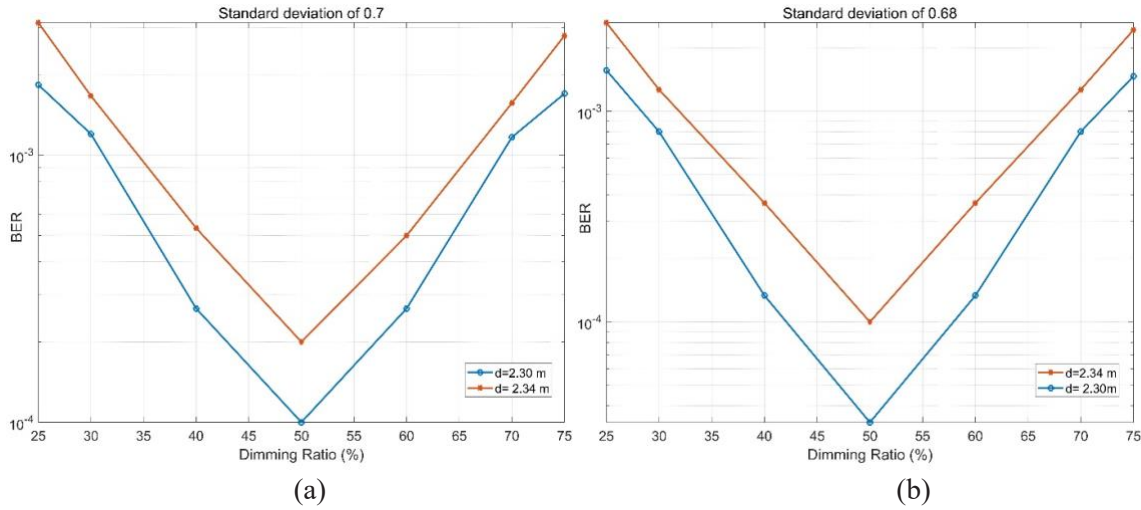


Figure 7. The BER performance of 2-2-VPAPM versus dimming ratios between 25% and 75%. (a) The standard deviation of 0.7 for noise. (b) The standard deviation of 0.68 for noise

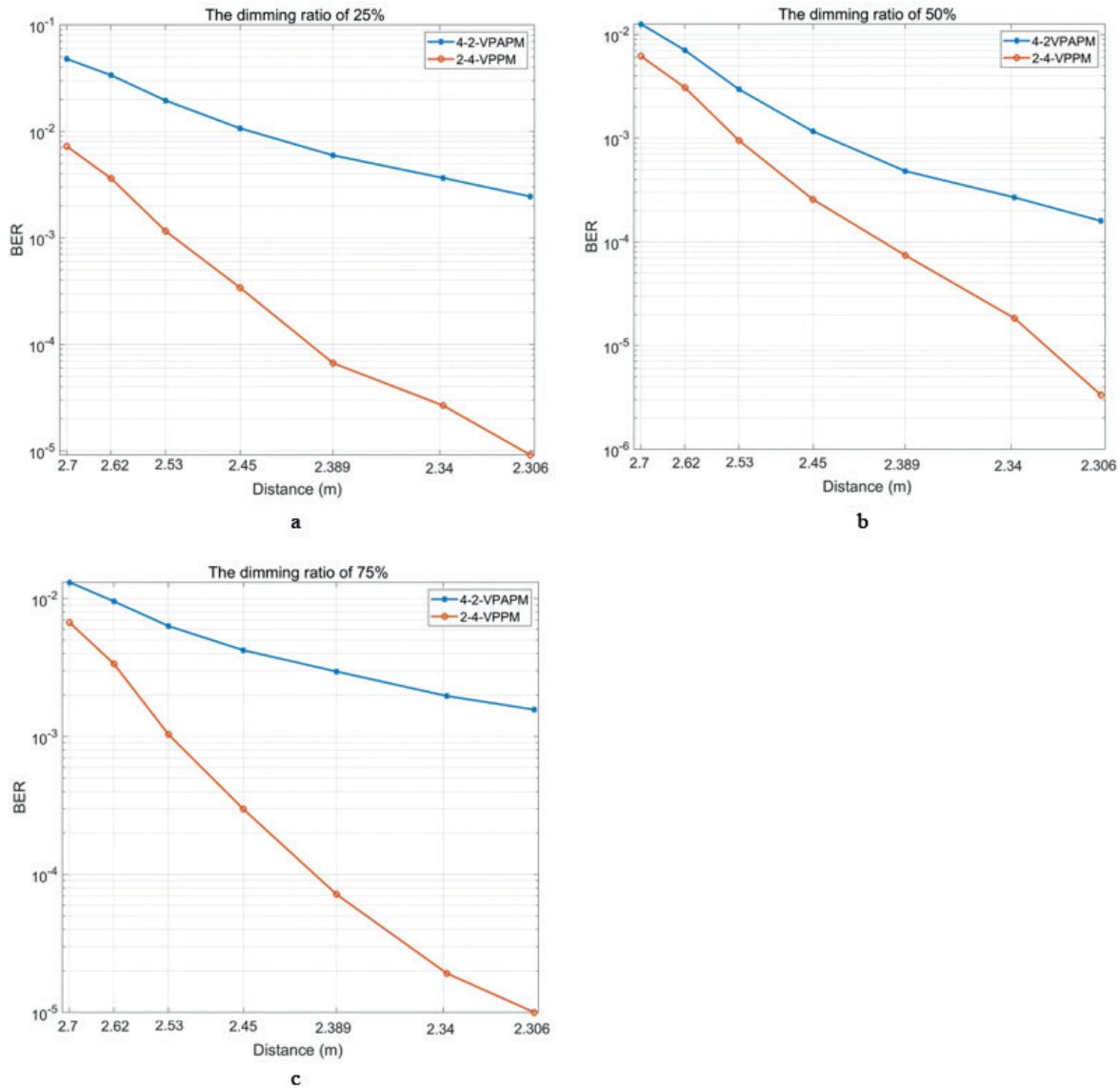


Figure 8. The BER performance comparison of 4-2-VPAPM and 2-4-VPPM versus transmission distance and dimming ratio.(a) Dimming ratio of 25% (b) Dimming ratio of 50% (c) Dimming ratio of 75%

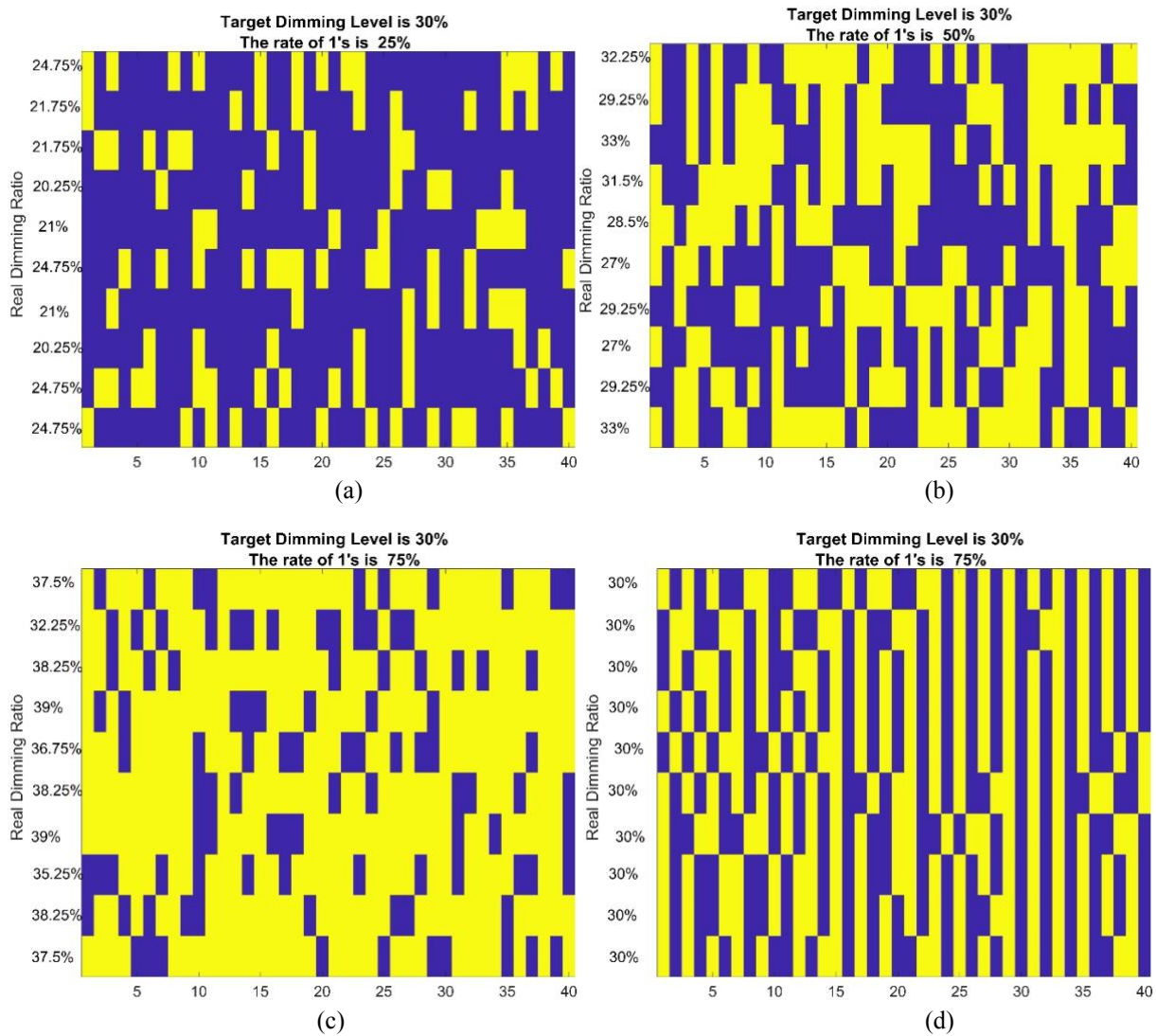


Figure 9. The target dimming performance of 2-2-VPAPM and modified VPAPM in terms of various input ratio of ‘0’ and ‘1’ bits. (a) The input ratio of ‘1’ bits is 25% for 2-2-VPAPM (b) The input ratio of ‘1’ bits is 50% for 2-2-VPAPM (c) The input ratio of ‘1’ bits is 75% for 2-2-VPAPM (c) The input ratio of ‘1’ bits is 75% for the modified VPAPM.

The Figure 8 depicts another performance comparison between 4-2-VPAPM and 2-4-VPPM. As mentioned in previously, the 2-4-VPPM is proposed by modifying the M-ary VPPM scheme. It is illustrated from simulation results that it is growing the difference of BER performance between both systems while the dimming ratio used in the systems is increasing. The similar comparison can be observed between results obtained in the Figure 8 (a) and (c). It can be asserted the 2-4-VPPM can increase the transmission distance at the BER of 10^{-3} and lesser where the system has meaningful BER performance. As shown in the Figure 8 (b), the transmission distance is increased from 2.306m to 2.389m at the BER of 10^{-4} when compare to 4-2-VPAPM. From the simulation results obtained in the Figure 8, it can be claimed that modified M-ary VPPM (2-4-VPPM) has superior in terms of BER performance compared to 4-2-VPAPM. Addition to this, it is shown from simulation results that the modified M-ary VPPM (2-4-VPPM) can be increased the transmission distance under all dimming levels.

In the Figure 9, it is shown that it is given the comparison of dimming ratio performance according to input ratio of input ratio of ‘0’ and ‘1’ bits for 2-2-VPAPM and modified VPAPM. The input ratio of ‘1’ bits has been chosen 25%, 50% and 75%, respectively. It has been adjusted the brightness ratio of 30. However, the system where the input ratio of ‘1’ bits becomes 50% is more close the target dimming of 30%. The real dimming ratio moves away from target dimming level while the input ratio of ‘1’ bits becomes distant from 50%. Compared to 2-2-VPAPM, the modified system provides the target dimming ratio for whole of input ratio of ‘1’ since average dimming ratios of sequential signals are fixed at the target dimming levels.

6. Conclusion

It is considered that M-n-VPAPM scheme has a challenge related to the adjusting of target dimming ratio in the paper. To overcome the problem related to the adjusting target dimming ratio, therefore, it has been proposed a packet transmission model for 2-2-VPAPM scheme in the paper. Although the modified VPAPM scheme can assure the desired dimming level under condition of long runs of same bits it has lower data rate compared with traditional VPAPM. Moreover, a receiver scheme has been presented to decode the received VPAPM signals. The introduced demodulator architecture is analysed in terms of BER versus transmission distance between receiver and transmitter. Addition to these, M-ary VPPM has been modified by taking into account the signals of power levels. The modified M-ary VPPM generates the modulated signal at the two power levels. In this paper, it has been given a performance comparison with respect to BER for modified M-ary VPPM and VPAPM.

Author Contributions

Süleyman Börekoğlu: Conceived and designed the analysis, collected data and performed the analysis.

Mehmet Sönmez: Conceived and designed the analysis, collected data and performed the analysis.

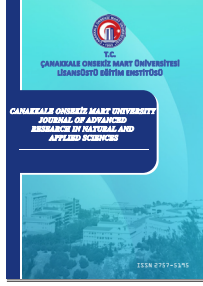
Conflicts of Interest

The authors declare no conflict of interest.

References

- Alnwaimi G. & Boujemaa H. (2021). Hybrid RF/VLC Communications Using Reconfigurable Intelligent Surfaces. *Wireless Personal Communications*. 121, 1533-1545. DOI: <https://doi.org/10.1007/s11277-021-08683-x>
- Bui T.-C., Singh R., O'Farrell T., & Biagi M. (2018). Performance evaluation of generalized optical spatial modulation with dimming support. *IEEE Globecom Workshops (GC Wkshps)*. (pp. 1-6). Abu Dhabi, United Arab Emirates. DOI: <https://doi.org/10.1109/GLOCOMW.2018.8644516>
- Chen Y.-W., Zhang R., Hsu C.-W., & Chang G.-K. (2020). Key enabling technologies for the post-5G era: Fully adaptive, all-spectra coordinated radio access network with function decoupling. *IEEE Communications Magazine*. 58(9), 60-66. DOI: <https://doi.org/10.1109/MCOM.001.2000186>
- Das B., Bardhan S., Maity T., & Mazumdar S. (2020). Variable CCT constant illuminance white LED light communication system with dimming feature. *Results in Optics*.1, 100013. DOI: <https://doi.org/10.1016/j.rio.2020.100013>
- Guo J.-N., Zhang J., Zhang Y.-Y., Xin G., & Li L. (2021). Joint multi-LED dimming control scheme based on the additively uniquely decomposable constellation group. *Optics Communications*. 495, 127053. DOI: <https://doi.org/10.1016/j.optcom.2021.127053>
- Kamat A. S., Khosla R., & Narayanamurti V. (2020). Illuminating homes with LEDs in India: rapid market creation towards low-carbon technology transition in a developing country. *Energy Research & Social Science*. 66, 11488. DOI: <https://doi.org/10.1016/j.erss.2020.101488>
- Knobloch F. (2015). Noncoherent dimming frequency shift On-Off keying scheme for low data rate optical street lighting communication. *17th International Conference on Transparent Optical Networks (ICTON)*. (pp. 1-5). Budapest, Hungary. DOI: <https://doi.org/10.1109/ICTON.2015.7193306>
- Küçük K., Msongaleli D., Akbulut O., Kavak A., & Bayılmış C. (2021). Self-adaptive medium access control protocol for aggregated VLC-RF wireless networks. *Optics Communications*. 488: 126837. DOI: <https://doi.org/10.1016/j.optcom.2021.126837>
- Lee W.-C. & Kwon M.-J. (2020). A Study on the Multiple Control Techniques for LED Dimming of Single Stage LLC Resonant Converter. *Journal of Electrical Engineering & Technology*. 15(2), 693-703. DOI: <https://doi.org/10.1007/s42835-019-00334-3>
- Lee K. & Park H. (2011). Modulations for visible light communications with dimming control. *IEEE photonics technology letters*. 23(16), 1136-1138. DOI: <https://doi.org/10.1109/LPT.2011.2157676>

- Noh J., Lee S., Kim J., Ju M., and Park Y. (2015). A dimming controllable VPPM-based VLC system and its implementation. *Optics Communications*. 343, 34-37. DOI: <https://doi.org/10.1016/j.optcom.2015.01.008>
- Okumura J., Kozawa Y., Umeda Y., & Habuchi H. (2017). Hybrid PWM/DPAM dimming control for digital color shift keying using RGB-LED array. *IEEE Journal on Selected Areas in Communications*. 36(1), 45-52. DOI: <https://doi.org/10.1109/JSAC.2017.2774738>
- Raj R., Jaiswal S., & Dixit A. (2021). Dimming-Based Modulation Schemes for Visible Light Communication: Spectral Analysis and ISI Mitigation. *IEEE Open Journal of the Communications Society*. 2, 1777-1798. DOI: <https://doi.org/10.1109/OJCOMS.2021.3098105>
- Vats A., Aggarwal M., & Ahuja S. (2019). End-to-end performance analysis of hybrid VLC-RF system using decode and forward relay in E-health medical applications. *Optik*. 187, 297-310. DOI: <https://doi.org/10.1016/j.ijleo.2019.03.045>
- Wang T., Yang F., Cheng L., & Song J. (2018). Spectral-efficient generalized spatial modulation based hybrid dimming scheme with LACO-OFDM in VLC. *IEEE Access*. 6, 41153-41162. DOI: <https://doi.org/10.1109/ACCESS.2018.2851076>
- Yawale P., Wagh V., & Shaligram A. (2019). Impact of current controlled dimming on spectral characteristics of high power LEDs. *Optics & Laser Technology*. 115, 289-291. DOI: <https://doi.org/10.1016/j.optlastec.2019.02.010>
- Yi L. & Lee S. G. (2014). Performance improvement of dimmable VLC system with variable pulse amplitude and position modulation control scheme. International Conference on Wireless Communication and Sensor Network. (pp. 81-85). Wuhan, China, DOI: <https://doi.org/10.1109/WCSN.2014.23>
- Yoo J.-H., Kim B. W., & Jung S.-Y. (2015). Modelling and analysis of M-ary variable pulse position modulation for visible light communications. *IET Optoelectronics*. 9(5): 184-190, DOI: <https://doi.org/10.1049/iet-opt.2014.0107>
- Zafar F., Karunatilaka D., & Parthiban R. (2015). Dimming schemes for visible light communication: the state of research. *IEEE Wireless Communications*. 22(2), 29-35. DOI: <https://doi.org/10.1109/MWC.2015.7096282>.
- Zafar F., Kalavally V., Bakaul M., & Parthiban R. (2015). Experimental investigation of analog and digital dimming techniques on photometric performance of an indoor Visible Light Communication (VLC) system. *Fourteenth International Conference on Solid State Lighting and LED-based Illumination Systems, D: International Society for Optics and Photonics*. (pp. 9571-9571). DOI: <https://doi.org/10.1117/12.2187367>.



Tünel Yangınlarında Jet Fan Diziliminin Duman ve Isı Kontrolüne Olan Etkilerinin İncelenmesi

Songül Solmaz¹, Tolga Demircan^{1,*}

¹Makine Mühendisliği Bölümü, Mühendislik ve Mimarlık Fakültesi, Kırıkkale Üniversitesi, Kırıkkale, Türkiye

Makale Tarihiçesi

Gönderim: 01.10.2021
Kabul: 04.02.2022
Yayın: 25.09.2022

Araştırma Makalesi

Öz – Bu çalışmada, bir karayolu tüneline çıkabilecek olası bir yangın sonucu oluşan yüksek ısı ve dumanın kontrolü üzerine çalışılmıştır. Bu kapsamda, tünel girişinden iki farklı konum için olası yangın modelleri oluşturulmuştur. Yangın sonucu oluşacak dumanın tünel dışına atılabilmesi amacıyla, tünel boyunca farklı noktalara üç adet aksiyel jet fanın yerleştirildiği düşünülmüştür. Oluşturulan yangın modelleri için, tünel içerisine yerleştirilmiş olan bu jet fanlarının farklı açıklık kapalılık durumları için farklı yangın senaryoları oluşturularak, sayısal analizler tekrarlanmıştır. Böylelikle yangın konumunun ve fan diziliminin sıcaklık, duman, CO ve O₂ değerlerine olan etkileri incelenmiştir. Sonuç olarak, tünelin girişine yakın bölgelerde çıkan bir yangında tünel içerisinde ki sıcaklık ve duman dağılımının, tünel çıkışına yakın bölgelerde çıkan bir yangına göre daha yoğun olduğu belirlenmiştir. Fanların açıklık ve kapalılık durumunun ise, tünel içerisindeki sıcaklık ve duman dağılımlarını önemli ölçüde etkilediği gözlemlenmiştir. Hiçbir fanın çalışmadığı durumda, tünel içindeki sıcaklık ve duman seviyelerinin çok yükseldiği ve ortamın insan sağlığı için olumsuz özelliklerde olduğu belirlenmiştir. Sadece 3. fanın açık olmasının, yangın kaynaklı duman, sıcaklık, CO ve O₂ değerleri üzerinde ki iyileştirici etkisinin çok düşük düzeyde kaldığı gözlemlenmiştir. Ancak sadece 1. fanın veya sadece 2. fanın açık olması durumlarının, tünel içi duman ve ısı kontrolünde daha efektif sonuçlar verdiği kanaatine varılmıştır. Tüm fanların açık olduğu durumda ise, diğer tüm durumlara göre duman, sıcaklık ve CO değerlerinin minimum seviyede, O₂ değerinin ise maksimum seviyede gerçekleştiği gözlemlenmiştir. Dolayısıyla, incelenen parametre aralığında tüm fanların açık olduğu durumun optimum duman ve ısı kontrolü sağladığı tespit edilmiştir.

Anahtar Kelimeler – Duman kontrolü, jet fan, ısı salınım oranı, tünel yangınları

Investigation of The Effects of Jet Fan Sequence to Smoke and Heat Control for Tunnel Fires

¹Department of Mechanical Engineering, Faculty of Engineering and Architecture, Kırıkkale University, Kırıkkale, Türkiye

Article History

Received: 01.10.2021
Accepted: 04.02.2022
Published: 25.09.2022

Research Article

Abstract – In this study, fire models for two different locations from the tunnel entrance are created. To discharge the smoke due to the fire outside the tunnel, three axial jet fans are considered to be positioned at different points along the tunnel. For the created fire models, different fire scenarios for open and closed positions of these jet fans inside the tunnel are created. Thus, the effects of the fire location and fan sequence on temperature, smoke, CO and O₂ values are investigated. It is observed that the open or closed status of the fans had a significant effect on temperature and smoke distribution inside the tunnel. When none of the fans was open, it is found that the temperature and smoke levels inside the tunnel increased at a high level. It is observed that when only the 3rd fan was open, the improvement effect on fire-induced smoke, temperature, CO and O₂ values were at a very low level. However, when only the 1st fan or only the 2nd fan was open, it is found that smoke and temperature control inside the tunnel was more effective. When all the fans were open, it is observed that smoke, temperature and CO value were at the minimum level and the O₂ value was at the maximum level compared to all other states. Therefore, it is determined that the optimum smoke and heat control was achieved in all fans are open status for the investigated parameter range.

Keywords – Heat release rate, jet fan, smoke control, tunnel fires.

¹ sngl.solmaz@gmail.com

² tolgademircan@gmail.com

*Sorumlu Yazar / Corresponding Author

1. Giriş

Günümüzde, trafikte bulunan araç sayısı her geçen gün artmaktadır. Bu durum, mevcut karayollarının yetersiz kalmasına ve trafik yoğunluğuna sebep olmaktadır. Trafik yoğunluğunun çok fazla olduğu yollarda, hem trafik yoğunluğunu azaltmak hem de zaman ve yakıt tasarrufu sağlamak amacıyla yeraltı tünelleri yapılmaktadır. Ayrıca engebeli bir yapıya sahip yollarda, ulaşımı kolaylaştırması ve ulaşım süresini kısaltmaları sebebiyle yer altında yapılan tünellerin önemi aşikardır. Ancak ulaşımında kullanılan tünel sayısı arttıkça, tünel içerisinde meydana gelen kaza sayısı da artmaktadır. Tünel içerisinde oluşabilecek bir kaza, normal yolda gerçekleşebilecek bir kazaya göre çok daha fazla can ve mal kaybına sebep olabilmektedir. Çünkü uzun tüneller, bir nevi kapalı bir ortam gibi kabul edilebilmektedir. Tünel içerisinde bir kaza olduğunda, tünel içindeki trafik kaza nedeni ile durabilmektedir. Dolayısıyla tünel içerisinde gerçekleşen bir araç kazasında, kazalı aracın alev alması durumunda oluşan bir yangın tünel içerisinde duran diğer araçlara sıçrayabilmekte ve onlarında da yanmasına sebep olabilmektedir.

Tünel içerisinde oluşan yangın sonucu, zehirli gazlardan oluşan duman ve yüksek sıcaklık tünelin içine hızla yayılabilmektedir. Oluşan bu duman görünürlüğü azaltarak, tünel içindeki insanların tüneli terk etmesini, yangın söndürme ve ilkyardım personelinin ise kazazedelere ulaşımını zorlaştırabilmektedir. Ayrıca zehirli gazlar, tünel içerisinde bulunan insanların nefes almasını zorlaştırmakta ve can kaybına sebep olabilmektedir. Tüm bu olumsuzluklar nedeniyle, tünel içerisinde olası bir yangın durumunda, oluşan yüksek ısının ve dumanın kontrollü ve hızlı bir şekilde tünel dışına atılması hayati önem arz etmektedir. Bu amaçla, tünel havalandırma sistemleri kullanılmaktadır. Tünel havalandırma sistemi seçilirken, tünel uzunluğu, kesit büyüklüğü, eğimi ve kullanan araç yoğunluğu vb. faktörler dikkate alınmaktadır. Günümüzde tünel havalandırmasında jet fanlar sıklıkla kullanılmaktadır. Jet fanlar tünel içindeki mevcut havayı üfleyerek tünel çıkışına doğru bir hava akışı sağlamaktadır. Olası bir yangın durumunda, bu hava akışı sayesinde duman ve yüksek sıcaklıklar tünel dışına doğru süpürülerek, tünel içerisinde insan sağlığına uygun bir ortam sağlanmaktadır. Ancak jet fanlarının sayısı ve dizilimi, bu duman kontrolü için önemli bir parametredir.

Karayolu tünellerinde yangını oluşturan ve yangın sonucunu etkileyen pek çok parametre olduğundan dolayı; tünellerde yangını, yangın kaynaklı dumanın hareketini, yangın sonucu meydana gelen zehirli gazların konsantrasyonunu hep birlikte ele almak gerekmektedir. Bu sebeple karayolu tünellerinde çıkan yangın pek çok araştırmacının ilgi odağı ve pek çok araştırmanın konusu olmuştur. Literatür incelendiğinde, araştırmacıların karayolu tünel yangınları konusunda; gerçek boyutta veya ölçeklendirilmiş tünelleri kullanarak, yangın kaynaklı dumanın akış hareketi ve karakteristiği, uygun duman tahliye yönteminin belirlenmesi ve tünel havalandırma metotları gibi hususlar üzerinde deneysel ve sayısal çalışmalar yürüttüğü görülmüştür. Bu çalışmalardan bazılarında aşağıda yer verilmiştir.

Li ve diğerleri, boyuna havalandırma sistemine sahip bir tünel yangınında, kritik hızı ve geri katmanlaşma tabakasının uzunluğu üzerinde çalışmışlardır. Çalışmalarının sonucunda, kritik hızın boyutsuz ısı salım oranının 0,15 değerine yaklaşırken meydana geldiğini belirtmiştir (Li vd., 2010). Ünal çalışmasında, 690 m uzunluğuna ve %1,5 eğime sahip bir karayolu tüneline, yangın olması durumunda bölgedeki hava koşullarının tünel havalandırmasına etkisini sayısal olarak incelemiştir. Tünel çıkışında rüzgar hızının 4 m/s ve 10 m/s olduğu durumlar için 2 farklı senaryo oluşturmuştur. Rüzgar hızının 10 m/s olması durumunda; tünel içindeki görüş mesafesinin daha düşük, zehirli gaz konsantrasyon değerlerinin ise daha fazla olduğunu belirtmiştir (Ünal, 2015). Fan ve diğerleri, dikey shaftlı doğal havalandırma sistemine sahip karayolu tünellerinde, CO yoğunluğu, duman ısı, duman hızı, duman boşaltma etkinliğinin duman boşaltma verimliliğine etkisini ölçmek için deneysel incelemeler yapmışlardır (Fan vd., 2013). Bilgin, hava kirliliği, yanma reaksiyonları, yanma sonucu meydana gelen zararlı gaz emisyonları, bu emisyonların çevreye ve insan sağlığına zararları üzerine çalışmıştır. Tünellerin yapımları, işlevleri ve AB standartlarından bahsetmiştir. Sonuç olarak, karayolu tünellerinde tünel güvenliğinin bir sistem olarak ve AB mevzuatına uygun olarak ele alınması gerektiğini belirtmiştir (Bilgin, 2014). Karaaslan ve diğerleri, at nalı kesitine sahip 300 m uzunluğunda, her biri 3 adet fan içeren 3 adet jet fan grubunun yerleştirilmiş olduğu bir karayolu tüneline incelemişlerdir. Bu amaçla, 10 MW ve 50 MW'lık iki farklı yangın büyüklüğü ve farklı senaryolarda çalıştırılan jet fanlar için CFD analizleri yapmışlardır. Sonuç olarak tünel içi kritik hız değerini 2,46 m/s olarak belirlemişlerdir (Karaaslan vd., 2013).

Tian ve diğerleri, tam ölçekli bir tünelde metanol-benzin karışımı olan çeşitli yakıtlarla gerçekleşen bir yangından kaynaklı dumanın, farklı rüzgar koşulları için tünel içerisindeki sıcaklık dağılımını deneysel olarak

incelemişlerdir (Tian vd., 2017). Alpgiray, enine havalandırma sistemine sahip bir karayolu tüneline 10 MW ısı yayılım oranında olan bir yangın için, emme-basma fan gruplarını tünelin girişine, merkezine ve çıkışına yerleştirilerek inceleme yapmıştır. Sonuç olarak, fanların çalışma sırası, tünel geometrisi, yangın büyüklüğü gibi parametrelerin, tünel havalandırma sisteminin tasarımı için önemli parametreler olduğunu belirtmiştir (Alpgiray, 2016). Wang ve arkadaşları, bir tünel yangınında egzoz çıkış açıklıklarının duman yayılma performansı üzerindeki etkisini incelemişlerdir. Bu amaçla, tam ölçekli bir tünelde gerçekleşebilecek bir yangını üç boyutlu bilgisayar modeli FDS ile simüle ederek, tünelin sıcaklık ve duman dağılımını belirlemişlerdir. Sonuç olarak; duman geri katmanlaşma tabakasının egzoz açıklıklarından önemli derecede etkilendiğini belirtmişlerdir (Wang vd., 2016). Yuan ve diğerleri, tren vagonu içinden çıkan bir yangında, farklı lokasyonlarda yangının çıkması durumunda yangın bölgesinin, duman ve sıcaklık dağılımı üzerine olan etkileri üzerine sayısal olarak çalışmışlardır. Vagonun içinde yangın yerinin önemli bir etkisinin olmadığı kanaatine varmışlardır (Yuan vd., 2015).

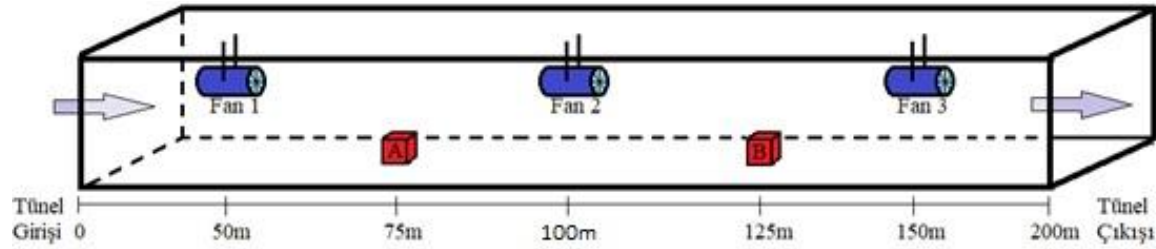
Lin ve diğerleri yapmış oldukları çalışmada, tünel yangınlarında taşıt kaynaklı tünel tıkanıklığının duman kontrol sisteminin performansına etkisini sayısal olarak incelemişlerdir. Sonuç olarak taşıt kaynaklı tıkanıklığın, tünellerde duman kontrolü için faydalı olan kritik hızı düşürdüğünü, tünelin tıkanıklık olan tarafında kütle akış hızının azaldığını ve boşaltımın mümkün olmadığını belirtmişlerdir (Lin vd., 2016). Li ve diğerleri, birleşim kavşağı olan bir karayolu tünellerinde duman kontrolünü sayısal olarak incelemişlerdir. Bu amaçla, ana tünelde duman kontrolünü, farklı yangın güçleri için kritik hızı kullanarak yapmışlardır. Sonuç olarak, ana tünelde duman geri akışının engellenebildiğini fakat birleşim kavşağında duman kontrolünün iyi sağlanamadığını belirtilmiştir (Li vd., 2017). Altay, at nalı kesitine sahip bir karayolu tüneline, 10 MW ve 50 MW ısı salınım oranına sahip yangınlar için farklı senaryoları sayısal olarak incelemiştir. Sonuç olarak, 50 MW ısı salım hızına sahip bir yangında duman tahliyesinin oldukça zor olduğunu, uygun duman tahliyesinin ancak fan gruplarının tünel çıkışına daha yakın bir yerde konumlanması ile mümkün olabileceğini belirtmiştir (Altay, 2016). Fan ve diğerleri, bir karayolu tünellerinde olası bir yangın durumunda enine duman sıcaklık dağılımı ve uzunlamasına duman sıcaklık dağılımı arasındaki farkı incelemek için deneysel çalışmalar yapmışlardır. Bu kapsamda, yangın kaynağının yeri değiştirilerek farklı senaryolar hazırlanmıştır. Sonuç olarak tünel yan duvarlarının bloke edici etkisi nedeniyle, sıcaklık artışının enine bozulma oranının uzunlamasına olandan daha büyük olduğunu gözlemlemişlerdir (Fan vd., 2013).

Yuan ve diğerleri, 1:5 oranında küçültülmüş doğal havalandırılmalı bir tünel yangınında duman yayılım özelliklerini deneysel olarak incelemişlerdir. Yapmış oldukları bu çalışmada tünel içerisinde ısı yayılım oranı, shaft mesafesi, shaft boyutu, tren tıkanıklığı ve duman perdesi gibi bazı faktörlerin etkisini araştırmışlardır (Yuan vd., 2013). Li ve diğerleri, tünellerde eğimin kritik hız üzerindeki etkisini sayısal ve deneysel olarak incelemişlerdir. Sonuç olarak, yangın büyüklüğü ve tünel eğimi arttıkça kritik hızın arttığını belirtmişlerdir (Li vd., 2017). Lee ve diğerleri, tünel yangınlarında tünel en-boy oranının duman hareketi üzerine etkilerini sayısal ve deneysel olarak incelemişlerdir. Sonuç olarak, tünel yangınlarında en-boy oranının dumanın büyüme ve gelişmesini etkilediğini belirtmişlerdir (Lee vd., 2016).

Bu çalışma kapsamında ise, bir karayolu tüneline araç kazası nedeniyle çıkabilecek olası bir yangın sonucu oluşan yüksek ısı ve dumanın kontrolü üzerine çalışılmıştır. Bu kapsamda, tünel girişinden iki farklı konum için olası yangın modeli oluşturulmuştur. Yangın sonucu oluşacak dumanın tünel dışına atılabilmesi amacıyla, tünel boyunca farklı noktalara üç adet aksiyel jet fanın yerleştirildiği düşünülmüştür. Oluşturulan yangın modelleri için, tünel içerisine yerleştirilmiş olan bu jet fanlarının farklı açıklık kapalılık durumları için farklı yangın senaryoları oluşturularak, sayısal analizler tekrarlanmıştır. Böylelikle yangın konumunun ve fan diziliminin yangın kaynaklı dumanın hareketine, tünel içi sıcaklık, CO ve O₂ değerlerine olan etkileri incelenmiştir.

2. Materyal ve Yöntem

Bu çalışma kapsamında, bir tüneline yangın tahliye sisteminin sayısal olarak incelenebilmesi için 8x8x200 m boyutlarında ve duvar kalınlığı 50 cm olan bir karayolu tüneli ele alınmıştır. Bu tünelde, ısı yayılım oranı 5 MW olan ve propanın (C₃H₈) yanması sonucu oluşan olası bir yangın kaynağı, tünel girişinden 2 farklı uzaklık için konumlandırılarak incelemeler yapılmıştır. Bu kapsamda, tünel girişinden farklı uzaklıklara üç adet aksiyel jet fan yerleştirildiği düşünülmüştür. Bu jet fanlarının farklı açıklık kapalılık durumları için farklı yangın senaryoları oluşturularak sayısal analizler tekrarlanmıştır. Bu çalışma kapsamında incelenen tünel geometrisinin şematik gösterimi Şekil 1’de verilmiştir. Şekilde görüldüğü üzere, tünel girişinden 75. metrede çıkan yangının merkezi A ile, 125. metrede çıkan yangının merkezi ise B ile gösterilmiştir.



Şekil 1. İncelenen model tünelin şematik gösterimi

Fanların diziliş şeklinin, tünel içerisindeki duman ve sıcaklık dağılımına etkisini incelemek, yangın sonrasında insanların tüneli tahliye edebilecek görünürlük düzeyine erişebilmesini sağlayıp sağlamadığını analiz edebilmek amacıyla, fan hızı 30 m/s sabit hızda tutularak; bütün fanlar kapalı, sadece birinci fan açık, sadece ikinci fan açık, sadece üçüncü fan açık ve bütün fanlar açık olacak şekilde farklı yangın senaryoları oluşturularak simülasyonlar yapılmıştır. Bu senaryolarda yangının ilk 360 saniyesi zamana bağımlı olarak incelenmiştir. Bu çalışma kapsamında incelenen analiz parametreleri Tablo 1'de verilmiştir.

Tablo 1

Analiz parametreleri

Yangın Konumu	75 m ve 125 m
Fan Konumu	50 m, 100 m ve 150 m
Fan Açık/Kapalı Durumu	Hepsi Kapalı, Sadece 1. fan açık, Sadece 2. fan açık, Sadece 3. fan açık, Hepsi Açık

2.1. Diferansiyel Denklemler

İncelenen yangın modelinin sayısal olarak çözülmesinde kullanılan süreklilik denklemi Denklem 2.1'de, türlerin korunumu denklemi Denklem 2.2'de, momentum denklemi Denklem 2.3'de, enerjinin korunumu denklemi ise Denklem 2.4'de verilmiştir (Chiam, 2005).

Süreklilik denklemi

$$\frac{\partial \rho}{\partial t} + \nabla \cdot \rho u = 0 \quad (2.1)$$

Türlerin korunumu denklemi

$$\frac{\partial}{\partial t} (\rho Y_i) + \nabla \cdot \rho Y_i u = \nabla \cdot \rho D_i \nabla Y_i + \dot{m}_i'' \quad (2.2)$$

Momentum denklemi

$$\rho \left(\frac{\partial u}{\partial t} + (u \cdot \nabla) u \right) = -\nabla p + \nabla \cdot \tau + \rho g + f \quad (2.3)$$

Enerjinin korunumu denklemi

$$\left(\frac{\partial}{\partial t} (\rho h) + \nabla \cdot \rho h u \right) = \left(\frac{\partial p}{\partial t} + u \cdot \nabla p \right) + q''' - \nabla \cdot q_{rad} + \nabla \cdot k \nabla T + \sum_i \nabla \cdot h_i \rho D_i \nabla Y_i \quad (2.4)$$

2.2. Sınır Şartları

Problemin diferansiyel denklemlerinin sayısal olarak çözülebilmesi için, sınır şartlarının bilinmesi gerekmektedir. Bu kapsamda, çözüm başlangıcında tünelin içerisinde 20 °C sıcaklığa sahip durağan ortam havası bulunduğu düşünülmüştür. Tünelin içinde hava akışını sağlayan jet fanların hızlarının 30 m/s olacak şekilde sabit olduğu ve bu fanların açıklık/kapalılık durumunun ise incelenen yangın senaryosuna göre değiştiği kabul edilmiştir. Tünel içerisinde meydana gelen yangının propanın (C₃H₈) yanması sonucu oluştuğu, ısı salınım oranının (HRR) ise sabit 5 MW değerinde olduğu varsayılmıştır. Yanma sonucu ortaya çıkan gazların ise atmosfer basınca sahip bir dış ortama gönderildiği düşünülmüştür.

2.3. Sayısal Yöntem

Bu çalışmada ele alınan tünelin sayısal olarak incelenmesi sırasında çözücü program olarak Fire Dynamics Simulator (FDS) yazılımı kullanılmıştır. Grafik ara yüzü olarak ise Pyrosim programının deneme sürümü tercih edilmiştir. Bu kapsamda FDS ve Pyrosim programlarının 2018 versiyonları kullanılmıştır. Akışı modellemek için Large Eddy Simulation (LES) yaklaşımı ve Smagorinsky–Lilly türbülans modeli kullanılmıştır. Bu modelde türbülans viskozitesi Denklem 2.5 yardımıyla belirlenmektedir. (Yuen vd. 2017, Tian ve Xiao 2020)

$$\mu_T = \rho(C_s \Delta)^2 |\tilde{S}| \quad (2.5)$$

Burada C_s terimi Smagorinsky katsayısıdır ve bu çalışma kapsamında C_s katsayısının değeri 0,15 olacak şekilde sabit tutulmuştur. \tilde{S} ve Δ terimleri ise sırasıyla Denklem 2.6 ve Denklem 2.7 yardımıyla belirlenmektedir. (Yuen vd. 2017, Tian ve Xiao 2020)

$$|\tilde{S}| = \sqrt{2\tilde{S}_{ij}\tilde{S}_{ij}} \quad (2.6)$$

$$\Delta = \sqrt[3]{\Delta x \Delta y \Delta z} \quad (2.7)$$

\tilde{S}_{ij} ise gerinim tensörüdür ve Denklem 2.8 aracılığı ile belirlenmektedir. (Yuen vd. 2017, Tian ve Xiao 2020)

$$\tilde{S}_{ij} = \frac{1}{2} \left(\frac{\partial u_i}{\partial x_j} + \frac{\partial u_j}{\partial x_i} \right) \quad (2.8)$$

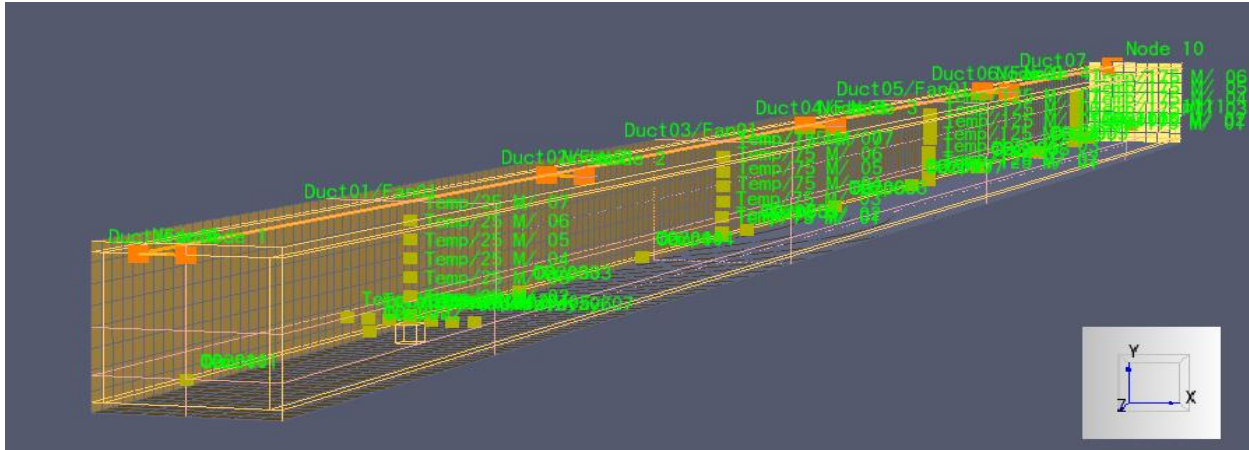
Yanmayı modellemek için ise Karışım Kesri Modeli (Mixture Fraction Model) kullanılmıştır. Sayısal çözümler, zamana bağlı algoritma kullanılarak yangının ilk 360 saniyesi için gerçekleştirilmiştir. FDS yazılımı ve Pyrosim ara yüzü ile yürütülen analizlerden elde edilen sonuçlar, Smokeview görüntüleme ara yüzü aracılığı ile görüntülenmiştir.

Oluşturulan tünelin ağ yapısını da içeren izometrik görünümü Şekil 2’de verilmektedir. İlgili şekilde, sıcaklık, CO, O₂ vb. büyüklüklerin ölçümünün yapıldığı prob noktaları ve jet fanların konumları birlikte görülmektedir. Ağ yapısı oluşturulurken, farklı sayıda eleman sayısına sahip ağ yapıları için deneme simülasyonları yapılmıştır. Tünel girişinden 75 m uzaklıkta gerçekleşen bir yangın için elde edilen maksimum sıcaklığın eleman sayısı ile değişimi Tablo 2’de verilmiştir. Çizelgeden de görüldüğü üzere, eleman sayısının 43200 değerinden sonra, maksimum sıcaklık değeri fazla değişim göstermemektedir. Bundan dolayı 43200 eleman sayısına sahip ağ yapısı optimum ağ yapısı olarak belirlenmiştir. Tüm simülasyonlar bu optimum ağ yapısı kullanılarak gerçekleştirilmiştir.

Tablo 2

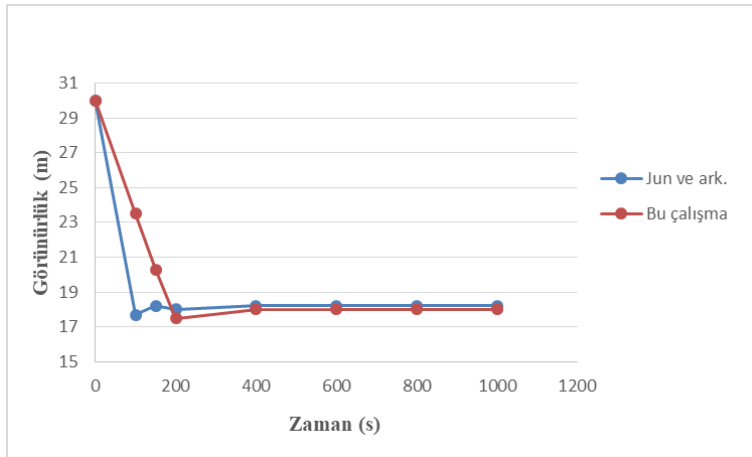
Maksimum sıcaklığın eleman sayısı ile değişimi

Eleman Sayısı	T _{maks}
1600	112,13 °C
12800	123,28 °C
43200	128,86 °C
102400	129,12 °C



Şekil 2. Modelin izometrik görünümü

Bu çalışmada kullanılan sayısal yöntemin ve yapılan kabullerin doğruluğunu ve güvenilirliğini kontrol etmek amacıyla, bu çalışmadan elde edilen sonuçlar literatürde bulunan benzer bir çalışmanın sonuçları ile kıyaslanmıştır. Bu amaçla, literatürde bulunan [Jun vd. \(2013\)](#) tarafından yapılan çalışma, onların geometrisi ve sınır şartları için tekrarlanmıştır. İncelenen tünelin 300-350 m aralığı için her iki çalışmadan elde edilen sonuçlar [Şekil 3](#)'de birlikte verilmektedir. Şekilden görüldüğü üzere, iki çalışma için çizilen eğriler benzer bir profil oluşturmaktadır. Yangının başlangıç anlarında eğriler arasında biraz farklılıklar olmasına rağmen, 200. saniyeden sonra her iki eğri birbiri ile uyum içindedir. Dolayısıyla bu çalışmada ele alınan sayısal yöntem ve kabullerin güvenilir seviyede olduğu söylenebilir.



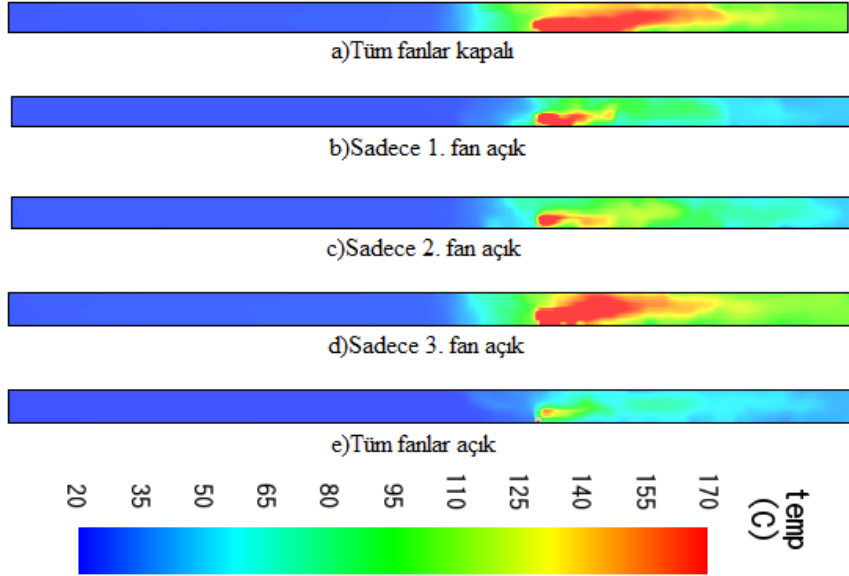
Şekil 3. Bu çalışmanın sonuçları ile literatür ([Jun vd., 2013](#)) sonuçlarının karşılaştırılması

3. Bulgular ve Tartışmalar

Bu çalışma kapsamında, bir karayolu tüneline çıkan olası bir yangın durumu için tünelin yangın tahliye sistemi sayısal olarak incelenmiştir. Bu kapsamda, ısı yayılım oranı 5 MW olan olası bir yangın kaynağının tünel girişinden 2 farklı uzaklık için konumlandırıldığı ve tünel girişinden farklı uzaklıklara üç adet aksiyel jet fanın yerleştirildiği düşünülmüştür. Fan hızı 30 m/s sabit hızda tutularak; bütün fanlar kapalı, sadece 1. fan açık, sadece 2. fan açık, sadece 3. fan açık ve bütün fanlar açık olacak şekilde farklı yangın senaryoları oluşturularak simülasyonlar yapılmıştır. Yapılan analizlerden elde edilen bazı sonuçlar aşağıda verilmiştir.

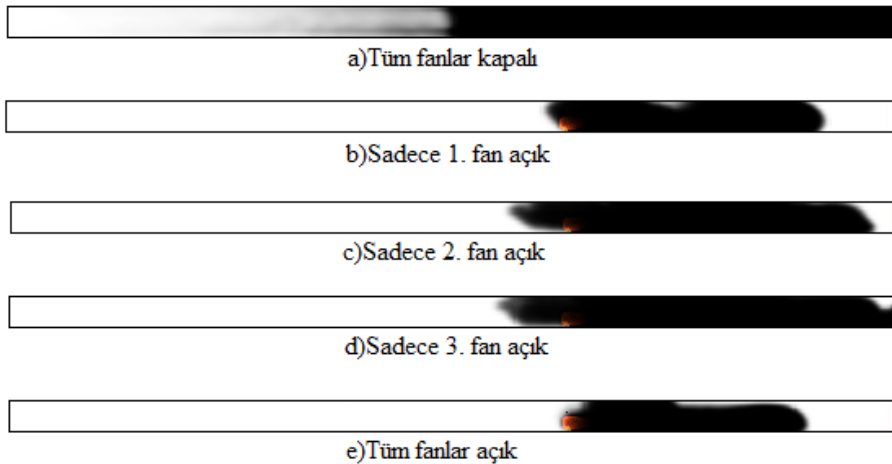
Yangın konumu 125 metre olduğu durumda 360. saniyenin sonunda, farklı fan açıklık senaryoları için elde edilen tünel içi sıcaklık dağılımları [Şekil 4](#)'te görülmektedir. Şekil incelendiğinde; tüm fanlar kapalı iken tünel içi sıcaklık değerlerinin çok yükseldiği, tünel girişinden 125 m uzakta meydana gelen yangın merkezi ve

çevresinden tünel çıkışına doğru can ve mal güvenliği için uygun sıcaklık şartlarının kalmadığı görülmüştür. Buna karşılık tüm fanların açık olması durumunda tünel içi sıcaklık durumunun iyi seviyelere ulaştığı, insanlar için tünelden güvenli bir çıkış alanının oluştuğu gözlemlenmiştir. Sadece 3. fanın açık olması durumunda ise, bu fanın konumunun yangın konumundan daha ileride kalması sebebiyle sıcaklık üzerinde iyileştirici bir etkisi bulunmadığı belirlenmiştir. Ancak sadece 2. fanın açık kalmasının 3. fana kıyasla daha iyi sonuçlar verdiği kanaatine varılmıştır.



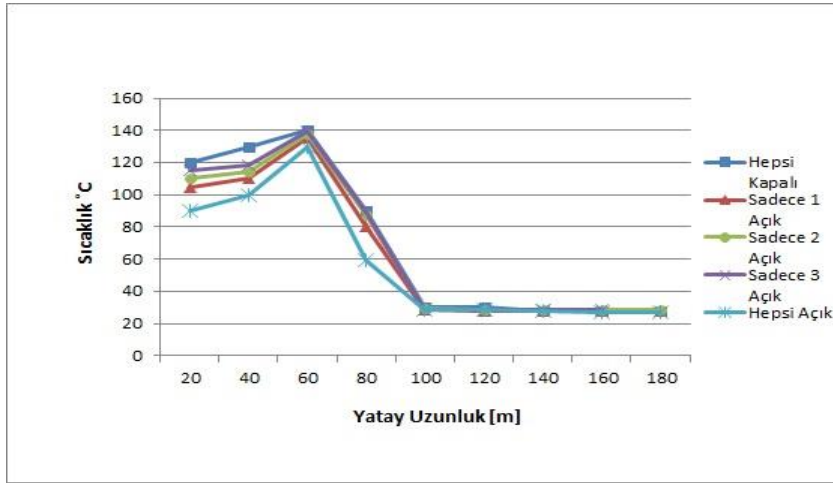
Şekil 4. Yangın konumu 125 m ve $t=360$ s için sıcaklık dağılımı, a) Tüm fanlar kapalı, b) Sadece 1. fan açık, c) Sadece 2. fan açık, d) Sadece 3. fan açık, e) Tüm fanlar açık

Yangın konumu 125 metre olduğu durumda 360. saniyenin sonunda, farklı fan açıklık durumları için elde edilen tünel içi duman dağılımları Şekil 5'te verilmektedir. Şekil incelendiğinde, tüm fanların kapalı olması durumunda tünelin büyük bir bölümünün duman ile kaplandığı, insanlar için görüş mesafesinin oldukça azaldığı, duman miktarının artmasına bağlı olarak zehirli gaz miktarının arttığı ve insan sağlığı için tehlikeli boyutlara ulaşabileceği görülmektedir. Tüm fanların açılmasının duman seviyesini önemli ölçüde azalttığı, görünürlük düzeyini arttırmaya katkı sağladığı ve güvenli bir çıkış için daha fazla alan meydana getirdiği gözlemlenmiştir. Tek bir fanın açık olduğu durumlar karşılaştırıldığında, sadece ilk fanın açık olduğu durumda tünelin büyük bir kısmında görünürlüğün uygun seviyede olduğu gözlemlenmiştir. Sadece üçüncü fanın açılmasının duman dağılımı üzerinde önemli bir katkı sağlamadığı belirlenmiştir. Eğer tünel içerisinde sadece tek bir fan açılacaksa ise, bunun ilk fan olması gerektiği anlaşılmaktadır.



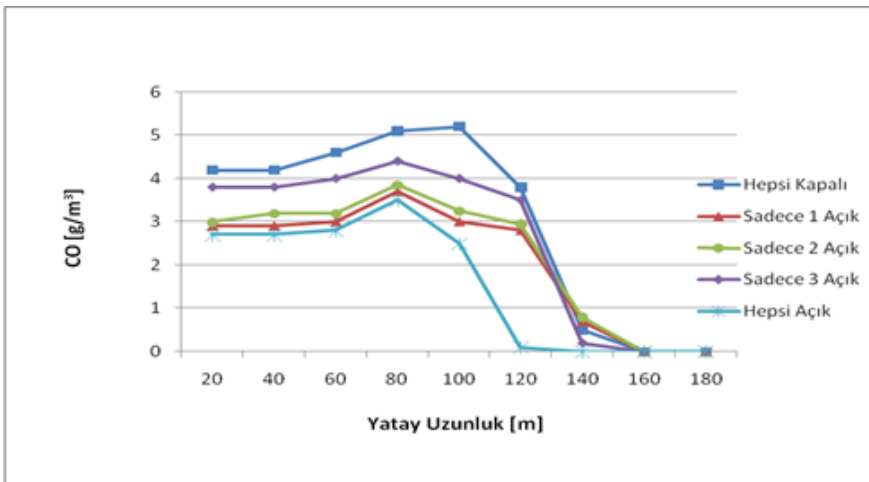
Şekil 5. Yangın konumu 125 m ve $t=360$ s için duman dağılımı, a) Tüm fanlar kapalı, b) Sadece 1. fan açık, c) Sadece 2. fan açık, d) Sadece 3. fan açık, e) Tüm fanlar açık

Şekil 6'da tünel girişinden 75 m uzaklıkta gerçekleşen yangında 360 saniye sonunda, fanların açıklık kapalılık durumlarındaki değişimin tünel boyunca oluşan sıcaklık değerleri üzerindeki etkilerini gösteren eğriler verilmiştir. Şekilden de görüldüğü üzere, yangın merkezinde tüm fan durumları için sıcaklık değerleri en yüksek seviyeye ulaşmış ve yangın merkezinden tünel çıkışına doğru ilerledikçe sıcaklık değerlerinin azalıp tünel çıkışında normal değerlere ulaştığı görülmüştür. Tüm fanlar kapalı olduğu durumda, tünel içi sıcaklık değerlerinin diğer fan durumlarına kıyasla daha yüksek olduğu ve tüm fanların açılmasının sıcaklık değerleri üzerinde iyileştirici etkide bulunduğu anlaşılmıştır. Sadece 1. fanın veya sadece 2. fanın açık olması durumlarının, sıcaklık dağılımı üzerinde olumlu etkide bulunduğu, fakat sadece 3. fanın açık olmasının tüm fanların kapalı olmasıyla neredeyse eş değer sonuçlar verdiği gözlemlenmiştir.



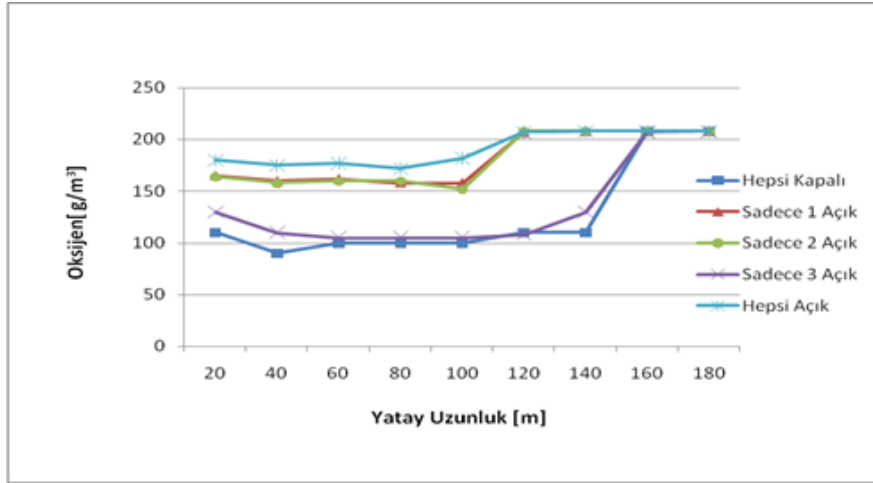
Şekil 6. Yangın konumu 75 m ve $t=360$ sn için, sıcaklığın tünel boyunca değişimi

Şekil 7'de tünel girişinden 75 m uzaklıkta gerçekleşen bir yangın için 360. saniye sonunda, fanların açıklık kapalılık durumlarındaki değişimin tünel boyunca oluşan CO dağılımı üzerindeki etkileri grafiksel olarak verilmiştir. Tüm fan durumları için yangının merkezine yakın bölgelerde CO değerlerinin en yüksek seviyede olduğu gözlemlenmiştir. Bu bölgelerde CO seviyesi insan sağlığı için tehlikeli sınırlara ulaşmıştır. Tünel çıkışına doğru ise CO normal değerlere ulaşmıştır. En kötü durum fanların hepsinin kapalı olduğu durumda gerçekleşmiştir. Fanların açılması tünel içinde oluşan CO değerlerini azaltıcı etkide bulunmuştur. Tek fan açık olması durumunda, sadece 1. veya sadece 3. fanın açık olması benzer bir etkiye sebep olmuştur. Ancak sadece 3. fanın açık olduğu durumda, fanın konumunun yangın merkezinin ilerisinde olması sebebiyle CO seviyesinin diğer durumlara göre daha yüksek olduğu gözlemlenmiştir. Fanların hepsinin açık olduğu durumda ise, tünel boyunca minimum CO seviyesi gerçekleşmiş, özellikle tünelin çıkışına doğru CO değerlerinde ani bir düşüş gözlemlenmiştir.



Şekil 7. Yangın konumu 75 m ve $t=360$ sn için, CO seviyesinin tünel boyunca değişimi

Şekil 8’de tünel girişinden 75 m uzaklıkta gerçekleşen bir yangın için 360. saniye sonunda, fanların açıklık kapalılık durumlarındaki değişimin tünel boyunca oluşan oksijen dağılımı üzerindeki etkileri görülmektedir. Şekil incelendiğinde, fanların hepsinin kapalı ve sadece 3. fanın açık olduğu durumlar için çizilen eğrilerin birbirleri ile oldukça benzer olduğu görülmektedir. Bu iki durumda da, özellikle yangının başlangıç konumuna yakın bölgelerde oksijen seviyesinin düştüğü belirlenmiştir. Tüm fanların açılması durumunda ise, tünel içerisindeki dumanın tünel çıkışına doğru en iyi şekilde tahliye edilebilmesinden dolayı, tünel boyunca O_2 seviyesinin optimum düzeyde tutulabildiği görülmüştür. Sadece 1. fanın ve sadece 2. fanın açık olması durumlarının da, tünel içerisindeki O_2 seviyesine iyileştirici etkide bulunduğu belirlenmiştir.

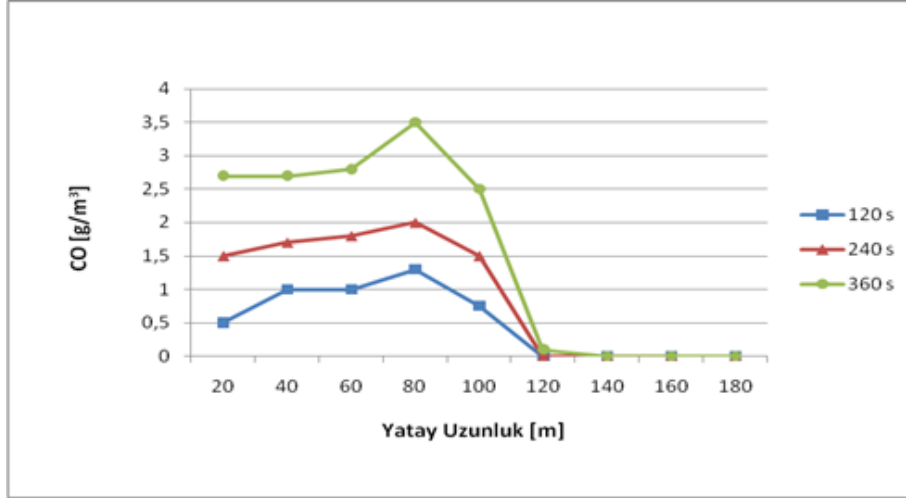


Şekil 8. Yangın konumu 75 m ve $t = 360$ sn için, O_2 seviyesinin tünel boyunca değişimi

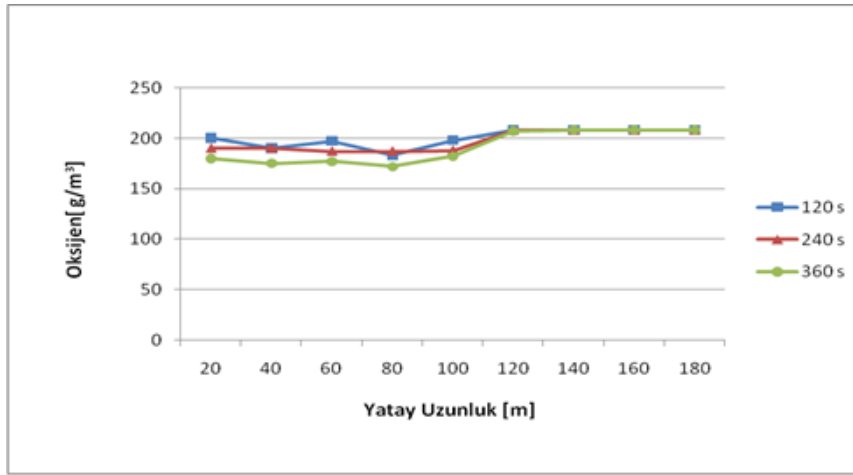
Şekil 9’da ise tünel girişinden 75 m uzaklıkta meydana gelen bir yangında tüm fanların açık olması durumunda, yangın başlangıcından 120, 240 ve 360 saniye sonundaki tünel içi CO ve O_2 değerleri birlikte görülmektedir. Bu kapsamda CO’nun tünel uzunluğu boyunca değişimi Şekil 9a’da, O_2 ’nin tünel uzunluğu boyunca değişimi ise Şekil 9b’de verilmiştir. Zamana bağlı olarak yapılan analizler sonucunda yangın merkezi ve yakın çevresinde, ilerleyen zamana bağlı olarak CO değerlerinin yükseldiği O_2 değerlerinin ise azaldığı görülmüştür. Tünel çıkışına doğru ise zamana bağlı olarak önemli bir değişim olmadığı gözlemlenmiştir.

4. Sonuçlar

Bu çalışmada, bir karayolu tüneline çıkan olası yangın senaryoları için tünelin yangın tahliye sistemi sayısal olarak incelenmiştir. Bu kapsamda, ısı yayılım oranı 5 MW olan olası bir yangın kaynağının tünel girişinden 2 farklı uzaklık için konumlandırıldığı ve tünel girişinden farklı uzaklıklara üç adet aksiyel jet fanın yerleştirildiği düşünülmüştür. Bütün fanlar kapalı, sadece 1. fan açık, sadece 2. fan açık, sadece 3. fan açık ve bütün fanlar açık olacak şekilde farklı yangın senaryoları oluşturularak analizler yapılmıştır. Yapılan analizlerin sonucunda, fanların açıklık kapalılık durumlarının tünel içi görünürülük, duman, sıcaklık, CO ve O_2 seviyelerini önemli ölçüde etkilediği gözlemlenmiştir. Fanların hepsinin kapalı olması durumunda, yangın kaynaklı oluşan CO ve dumanın tünel dışına tahliye edilmesi için gereken taze havanın sağlanamadığı tespit edilmiştir. Bundan dolayı, tünel boyunca sıcaklık ve CO seviyesinin yükseldiği, tünel içi duman yayılımının arttığı ve O_2 seviyesinin ise azaldığı gözlemlenmiştir. Dolayısıyla hiçbir fanın çalışmadığı durum için, olası bir yangın durumunda tünel içindeki ortamın insan sağlığı için olumsuz özelliklerde olduğu belirlenmiştir. Sadece 3. fanın açık olmasının, yangın kaynaklı duman, sıcaklık, CO ve O_2 değerleri üzerinde ki iyileştirici etkisinin çok düşük düzeyde olduğu gözlemlenmiştir. Ancak sadece 1. fanın veya sadece 2. fanın açık olması durumlarının, insan sağlığı için daha efektif sonuçlar verdiği kanaatine varılmıştır. Tüm fanların açık olduğu durumda ise, duman, sıcaklık ve CO değerlerinin minimum seviyede, O_2 değerinin ise maksimum seviyede gerçekleştiği gözlemlenmiştir. Dolayısıyla, incelenen parametre aralığında tüm fanların açık olduğu durumun optimum duman ve ısı kontrolü sağladığı söylenebilir. Ayrıca tünel çıkışına daha yakın bir noktada meydana gelen olası bir yangının duman tahliyesinin, tünel girişine yakın bölgede meydana gelen bir yangına kıyasla daha fazla gerçekleştirilebildiği gözlemlenmiştir.



(a)



(b)

Şekil 9. Yangın konumu 75 m ve tüm fanlar açık olduğu durumda, farklı zaman anları için (a) CO ve (b) O₂ seviyesinin tünel boyunca değişimi

Yazar Katkıları

Songül Solmaz: Literatür taramasını yapmış, model geometriyi oluşturmuş, sayısal doğrulama işlemini yapmış, sayısal analizleri tamamlamış, grafik, tablo ve şekilleri hazırlamıştır.

Tolga Demircan: Çalışma konusunu belirlemiş, çalışmayı planlamış, tasarlamış, yönetmiş ve denetlemiş, elde edilen verileri değerlendirmiş, grafikleri yorumlamış ve makaleyi yazmıştır.

Çıkar Çatışması

Yazarlar çıkar çatışması bildirmemişlerdir.

Kaynaklar

Alpgiray, B. (2016). *Enine havalandırma sistemine sahip bir tünelde yangın kaynaklı dumanın tahliyesinin sayısal yöntemle incelenmesi* (Yüksek Lisans Tezi). Erişim adresi: <https://tez.yok.gov.tr/UlusalTezMerkezi>

Altay, M., (2016). *Tünel yangınlarının modellenmesi ve etkin parametrelerin modellemedeki gerçekçiliğinin incelenmesi* (Yüksek Lisans Tezi). Erişim adresi: <https://tez.yok.gov.tr/UlusalTezMerkezi>

- Bilgin, F. (2014). *Karayolu tünellerinde araç emisyonları havalandırma ve yangın önleme esasları* (Yüksek Lisans Tezi). Erişim adresi: <https://tez.yok.gov.tr/UlusalTezMerkezi>
- Chiam, B.H. (2005). *Numerical simulation of a metro train fire* (Master's thesis). University of Canterbury, Christchurch, New Zealand.
- Fan, C.G., Ji, J., Gao, Z.H. ve Han, J.Y. (2013). Experimental study on transverse smoke temperature distribution in road tunnel fires. *Tunnelling and Underground Space Technology*, 37, 89–95. <https://doi.org/10.1016/j.tust.2013.04.005>
- Fan, C.G., Ji, J., Gao, Z.H., Han, J.Y. ve Sun, J.H. (2013). Experimental study of air entrainment mode with natural ventilation using shafts in road tunnel fires. *International Journal of Heat and Mass Transfer*, 56, 750–757. <https://doi.org/10.1016/j.ijheatmasstransfer.2012.09.047>
- Jun, D., Li, M., Zhen-ping, W., Zhen, X. ve Wei-feng, W. (2013). Simulation study on critical velocity of longitudinal ventilation tunnel fire. *Procedia Engineering*, 52, 67-71. <https://doi.org/10.1016/j.proeng.2013.02.107>
- Karaaslan, S., Hepkaya, E. ve Yücel, N. (2013). Cfd simulation of longitudinal ventilation systems in a scaled short tunnel. *Isı Bilimi ve Teknigi Dergisi*, 33, 1, 63-77.
- Lee, S. R. ve Ryou, H. S. (2016). A numerical study on smoke movement in longitudinal ventilation tunnel fires for different aspect ratio. *Building and Environment*, 41, 719–725. <https://doi.org/10.1016/j.buildenv.2005.03.010>
- Li, J., Deng, Q., Li, Y. ve Wang, Z. (2017). Numerical evaluation on the smoke control strategies and parameters for the road tunnel with converging junctions. *10th International Symposium on Heating, Ventilation and Air Conditioning, ISHVAC2017* (pp. 1858-1863) Jinan-China. <https://doi.org/10.1016/j.proeng.2017.10.262>
- Li, J., Tian, Y., Li, Y., Zhao, Y., ve Huang, Y. (2017). Numerical and experimental study on the effects of the slope on the critical velocity in titled tunnels. *10th International Symposium on Heating, Ventilation and Air Conditioning, ISHVAC2017* (pp. 1864–1870) Jinan-China. <https://doi.org/10.1016/j.proeng.2017.10.265>
- Li, Y.Z., Lei, B. ve Ingason, H. (2010). Study of critical velocity and backlayering length in longitudinally ventilated tunnel fires. *Fire Safety Journal*, 45, 361–370. <https://doi.org/10.1016/j.firesaf.2010.07.003>
- Lin, P., Zhang, Y., Li, T. ve Si, Y. (2016). A numerical study on the impact of vehicles' blockage on the performance of semi-transversal smoke control system in tunnel fire. *Procedia Engineering*, 135, 248 – 260. <https://doi.org/10.1016/j.proeng.2016.01.120>
- Tian, G. ve Xiao, Z. (2020). New insight on large-eddy simulation of flow past a circular cylinder at subcritical Reynolds number 3900. *AIP Advances*, 10, 085321. <https://doi.org/10.1063/5.0012358>
- Tian, X., Zhong, M., Shi, C., Zhang, P. ve Liu, C. (2017). Full-scale tunnel fire experimental study of fire-induced smoke temperature profiles with methanol-gasoline blends. *Applied Thermal Engineering*, 116, 233–243. <https://doi.org/10.1016/j.applthermaleng.2017.01.099>
- Ünal, E. (2015). Acil durum tünel havalandırmasında bölgesel faktörlerin sayısal olarak incelenmesi. *12. Ulusal Tesisat Mühendisliği Kongresi* (pp. 677-686). İzmir.
- Wang, Q., Tang, F., Li, L., Zhang, X. ve Fan, C. (2016). Large eddy simulation on the effect of smoke exhaust openings arrangement on the smoke spread in tunnel fires. *Procedia Engineering*, 135, 309 – 315.
- Yuan, Z., Lei, B. ve Bia H. (2015). The effect of fire location on smoke temperature in tunnel fires with natural ventilation. *Procedia Engineering*, 121, 2119–2124. <https://doi.org/10.1016/j.proeng.2015.09.082>
- Yuan, Z., Lei, B. ve Kashef, A. (2013). Reduced-scale experimental research on fires in tunnels with natural ventilation. *The 9th Asia-Oceania Symposium on Fire Science and Technology*, (pp. 907-915). <https://doi.org/10.1016/j.proeng.2013.08.142>
- Yuen, A.C.Y., Yeoh, G.H., Timchenko, V., Cheung, S.C.P., Chan, Q.N. ve Chen, T. (2017). On the influences of key modelling constants of large eddy simulations for large-scale compartment fires predictions. *International Journal of Computational Fluid Dynamics*, 31(6-8), 324-337. <https://doi.org/10.1080/10618562.2017.1357809>



Morphometric Analysis of Mount Ararat (Eastern Anatolia, Türkiye)

Vedat Avcı^{1,*}, Murat Sunkar², Ahmet Toprak²

¹ Department of Geography, Faculty of Arts and Science, Bingöl University, Bingöl, Türkiye

² Department of Geography, Faculty of Humanities and Social Sciences, Fırat University, Elazığ, Türkiye

Article History

Received: 18.12.2021
Accepted: 10.03.2022
Published: 25.09.2022

Research Article

Abstract – In this study, the morphometric characteristics of Mount Ararat which is a strato-volcano are analyzed. Türkiye's highest Mountain, Mount Ararat, is located in Eastern Anatolia. The Mountain takes the shape of two major volcanic cones after 2500 m height; these volcanic cones are named Greater Mount Ararat (5137 m) and Little Mount Ararat (3896 m). In this study, relief morphometry, basin morphometry, and drainage characteristics are morphometrically analyzed with Geographic Information Systems (GIS) using 10x10 m resolution Digital Elevation Model (DEM). According to the analysis results, there is an increase in the elevation on the high and steep slopes of the main cone and the slope values increase up to 56° in some locations towards the summit. On the other hand, according to the aspect analyses, 19.9% of slope faces are north-east direction, 14.7% of the slopes are north-direction, 9.4% are northwest, 9.8% are west, 10.7% are southeast, and 16.4% of the slopes are east direction. These results support the fact that Mount Ararat extends in NW-SE direction and is formed on the basis of a fault line in this direction. According to the grouping made by the altitude ranges analysis, the decrease in the rate of elevation belts starting from the slopes of the mountain towards the top confirms the structure of volcanic cone. Elevation differences in relative relief analyses range between 0 and 1141 m and this value increases to 1141 m on the slopes surrounding the summit. The cone structure of Mount Ararat was prominent in transverse and longitudinal profile analyses.

Keywords – Eastern anatolia, geographic information systems, mount ararat, morphometric analysis, strato-volcano

1. Introduction

Mount Ararat is at the intersection of the borders between Türkiye, Armenia, Azerbaijan, and Iran. The volcanic mountain is formed on a circular base with a diameter of 30-35 km. Greater Mount Ararat is Türkiye's highest mountain with 5137 m elevation. Mount Ararat is a (strato-volcano) volcano that was formed as a result of the multi-period and accumulation of lava and tuffs on one another (Figure 1). The Cone-shape and high and steep slopes of the Mountain are the results of non-flowing lava that cools and solidifies quickly. The volcanic mass, which is basically formed as a single body, rises as two separate volcanic cones after 2500 m. The cone in the west is Greater Mount Ararat (5137 m) while the cone in the east is Little Mount Ararat (3896 m). Greater Mount Ararat has a relative elevation difference of 4300 m compared to Iğdır plain, which is located in the North, and more than 3000 m compared to Doğubayazıt located in the south (Figure 2).

Increased with altitude, the degree of slope on the Mount Ararat varies between 0° and 56°. There is a distances of 10 km between the summits of Greater Mount Ararat and Little Mount Ararat and they are similar in terms of structure as they were formed in the same period (Atalay, 2017; Kaya, 2017; Şahin, 2011). Mount Ararat, which is a multi-period strato-volcano, consists of acidic lava flows, agglomerates, and tuffs. As a result of the Quaternary volcanism, approximately 3x10¹² tons of volcanic material surfaced (Türkünal, 1980). Agglomerate, volcanic breccia, obsidian, and ashes are common materials on the bases of the cones while the last surfaced materials are tuffs. It is assumed that the cones were formed in two possible

¹ vavci@bingol.edu.tr

² sunkarmurat@gmail.com

³ atoprak@firat.edu.tr

*Corresponding Author

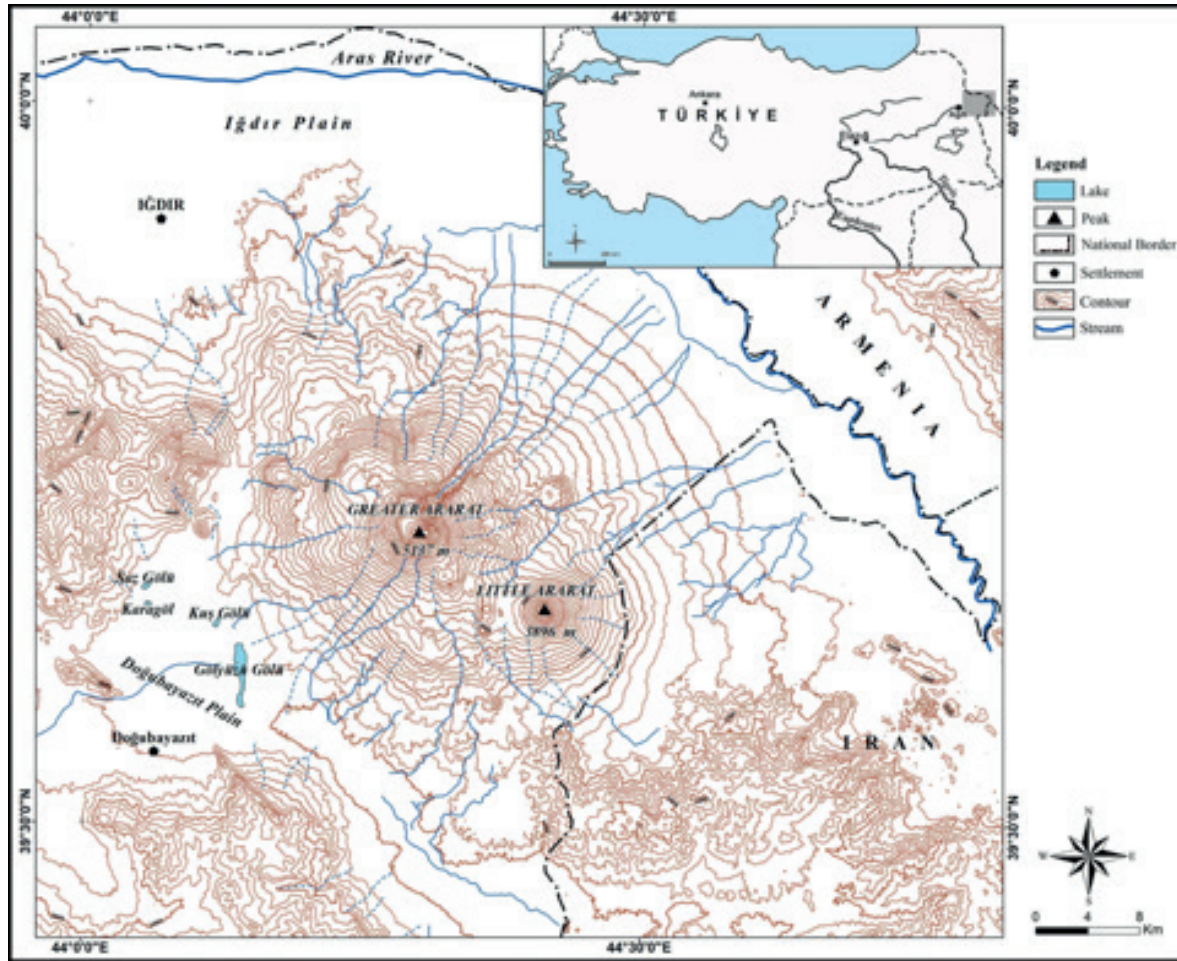


Figure 1. Location map of Mount Ararat.

phases according to their morphological status. According to that assumption, the andesitic structure of the two cones was formed in the Early Quaternary in the first phase while young lava flows and parasitic cones were formed in the Late Quaternary in the second phase (Blumenthal, 1958). Apart from this view, (Güner & Şaroğlu, 1987) state that Mount Ararat consists of 11 different stages (Türkecan, 2017).

Quaternary basalt, andesite, and pyroclastic rocks cover a large surface on Mount Ararat (Şenel & Ercan, 2002). The alluvial materials were carried by the rivers originating from the summit of the Greater and the Little Ararat and created thick deposits in the north-eastern fans (Figure 3). The permanent snow line on Mount Ararat starts at 4000 m and after this elevation, a part covering 1000 m is in the permanent snow limit. The summit of the mountain is covered with a wide ice cap glacier (Erinç, 1953). Besides being the highest summit of Türkiye, Mount Ararat has a current 10 km² ice cap (Arkel, 1973; Imhof, 1956). According to (Blumenthal, 1956, 1958) 11 glacial tongues hanging from the ice cap with lengths varying from 1 to 2,5 km reach to 4200 m on the southern slopes and 3900 m on the northern slopes (Çiner, 2003). Geomorphology studies on the whole mountain haven't been conducted because of the reasons such as the height of Mount Ararat, the area it occupies, transportation and security. However, the glaciers on Mount Ararat have attracted the attention of many researchers for a long time and there are many types of research about glaciers (Arkel, 1973; Blumenthal, 1956, 1958; Çiner, 2003; Erinç, 1953; Imhof, 1956; Sarıkaya, 2012; Azzoni et al., 2017). According to the title of the article prepared by Azzoni et al., (2017) it is thought that the geomorphology of Mount Ararat is investigated. However, by the content of the article it is understood that the glaciers on the mount are studied using satellite images. Apart from the glaciers, catastrophic events having occurred in Ahora Gorge on the mount is evaluated (Azzoni et al., 2019). In the literature, quantitative analyses reflecting its topographic and geomorphological features have not been performed on Mount Ararat.

As it is difficult for today to study the geomorphology of Mount Ararat due to geographical conditions and security issues, the goal of this study is to make morphometric analyses showing geomorphologic features.

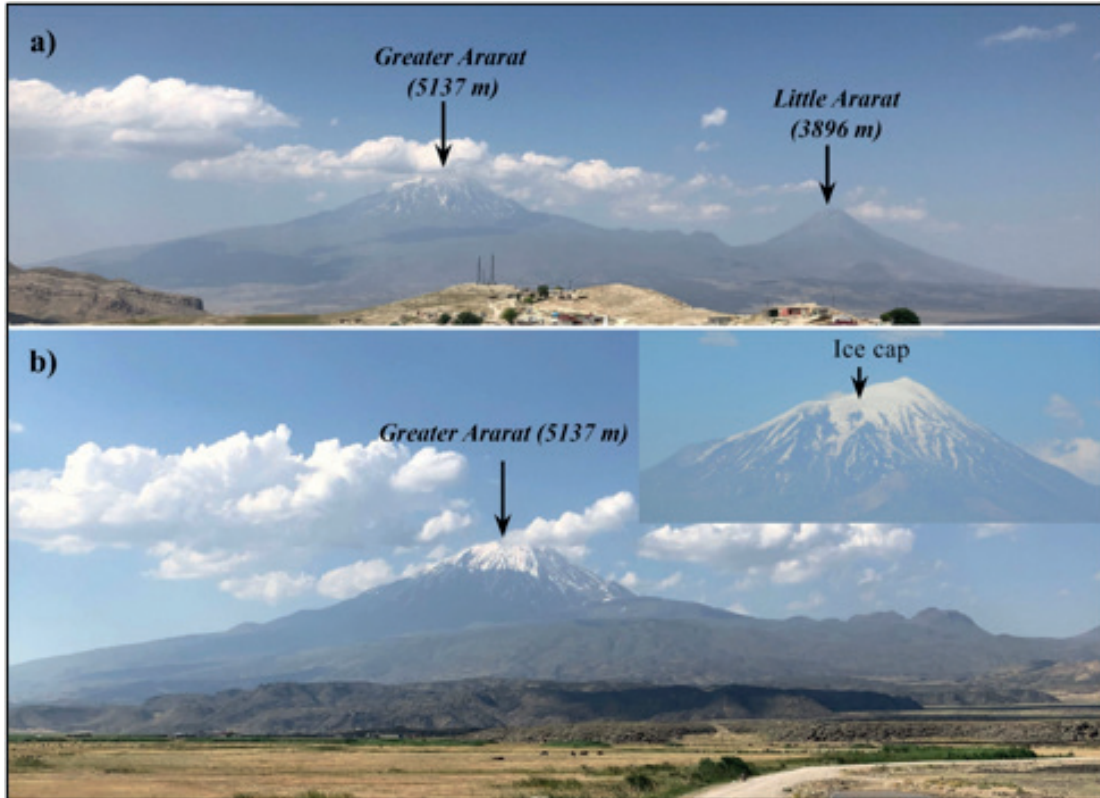


Figure 2. In Eastern Anatolia, Mount Ararat (Ağrı) is located at the intersection of the border between Türkiye and Armenia, Azerbaijan and Iran. The Greater and Little Mount Ararat (a) and glaciers on the Greater Mount Ararat (b).

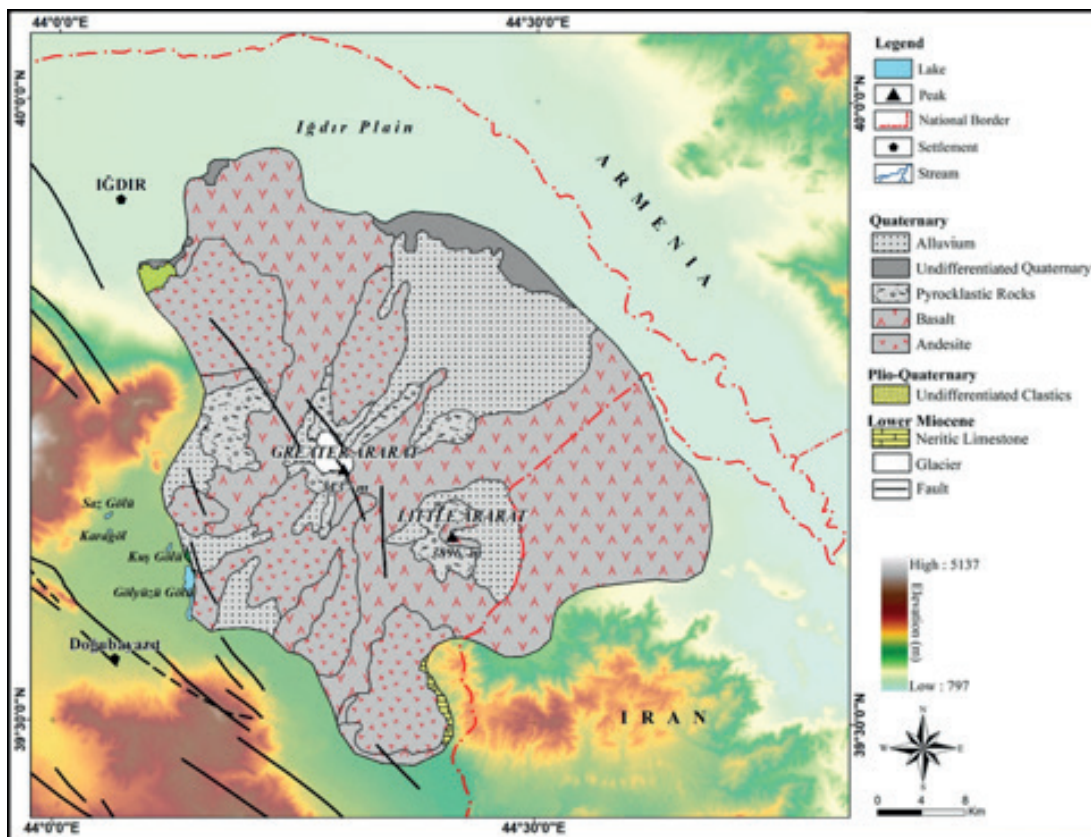


Figure 3. Geological map of Mount Ararat (The figure is drawn on the basis of MTA 1/500.000 scale Geological Map of Türkiye, Van Sheet by (Şenel & Ercan, 2002).

Morphometry is defined as the analysis by using geographic information technologies for the purpose of obtaining data about geomorphologic units on the basis of the altitude values of that region (DEM-Digital Elevation Model). The data obtained with morphometric analyses can provide rapid and reliable information about the drainage development in an area, influence level of the structure and lithology on this development and distribution and properties of structure (Keller, & Pinter, 2002). Because of this advantage of morphometric analysis, the method has been preferred in many recent studies on the issue (Avcı & Sunkar, 2015, 2018; Avcı, Sunkar, & Toprak, 2018; Erginal & Cürebal, 2007; Özşahin, 2015; Topuz & Karabulut, 2016).

2. Materials and Methods

In order to analyze the geomorphological features of Mount Ararat, this article has been prepared using also indices in addition to oral presentation. On the basis of lithology and morphology, the border of the mountain has been determined according to topography, geological maps and satellite images. Analyses, which reveal the cone- or shield-shaped structure of volcanic mountains within these boundaries, have been used. In order to determine the morphometric properties of Mount Ararat, 15 morphometric analyses were performed for analysing relief morphometry, basin morphometry and drainage characteristics (Table 1).

Table 1

Formulas and results used in morphometric analyses of Mount Ararat

No	Morphometric Parameter	Formula	Reference	Result	Unit
1	Stream Order	Hierarchical Rank	(Strahler, 1952a)	1 to 6	Dimensionless
2	1 st Order Stream (Suf)	Suf = N1, N1 = 1 st Order Stream	(Strahler, 1952a)	14.483	Dimensionless
3	Stream Number (Nu)	Nu = N1 + N2 Nn, N1, N2= Number of the streams.	(Horton, 1945)	19.041	Dimensionless
4	Stream Length (Lu)	Lu = L1 + L2 Ln L1, L2= Length of the stream.	(Horton, 1945)	5046,8	km
5	Stream Length Ratio (Lur)	Lur = L1/Lu + 1 Lu= Stream Length (km)	(Horton, 1945)	0,49-0,62	Dimensionless
6	Basin Area (km ²)	It was calculated with calculate geometry tool.	(Schumm, 1956)	1662	km ²
7	Drainage Density (Dd)	Dd = Lu/A Lu= Total drainage length, A= Area.	(Horton, 1932)	3,7	km/km ²
8	Hypsometric Curve	y = h/H, x = a/A, y= Relative Height, x= Relative Area	(Strahler, 1952b)	Concave curve	Dimensionless
9	Hypsometric Integral	Hi = (Hmean - Hmin)/(Hmax - Hmin), Hmean= Mean elevation (m), Hmin= Minimum elevation (m), Hmax= Maximum elevation (m).	(Strahler, 1952b)	0,28	Dimensionless
10	Aspect	Derives aspect from a raster surface. The aspect identifies the downslope direction of the maximum rate of change in value from each cell to its neighbors (Arcgis Desktop Help, 2022).		151,69	(o)

Table 1

Formulas and results used in morphometric analyses of Mount Ararat (Continued)

No	Morphometric Parameter	Formula	Reference	Result	Unit
11	Slope Analysis	Identifies the slope (gradient, or rate of maximum change in z-value) from each cell of a raster surface (<u>Arcgis Desktop Help, 2022</u>)	(<u>Rich, 1916</u>)	0°-56°	(°)
12	Relative Relief	$Rr = H - h$, H= Maximum elevation (m), h= Minimum elevation (m).	(<u>Smith, 1950</u>)	1141	m
13	Topographic Position Index	$Z = \frac{1}{NR} \sum ieRZi$ calculates the difference between the height (z) of point and mean height (m). The Radius is R.	(<u>Jenness, 2006</u>)	-18,2-25,1	Dimensionless
14	Topographic Curvature Analysis	$C = Z_{xx}^2 + Z_{xy}^2 + Z_{yy}^2$ Z= Elevation C= Curvature	(<u>Wilson and Gallant, 2000</u>)	-21,36-24,52	Dimensionless
15	Terrain Ruggedness Index	If each square represents a grid cell on a digital elevation model then, $TRI = Y[\sum(x_{ij} - x_{00})^2]^{1/2}$ where x _{ij} elevation of each neighbor cell to cell (0,0) (<u>Riley, DeGloria, & Elliot, 1999</u>)	(<u>Riley, DeGloria, & Elliot, 1999</u>)	0-2,5	Dimensionless

The DEM data used in these analyses have been created using 1/25000 scale topography maps of General Directorate Mapping (GDM, 2004) and Alos Palsar DEM data (ASF, 2019). DEM created from GDM and Also Palsar data have been combined through Data Management-Raster-Mosaic to New Raster module in the ArcGIS environment. All data in the study have been produced in the UTM WGS 84 Zone 38 projection system. Raster data have been reclassified using Reclassify tool. These reclassified layers have been converted to polygons through Conversion-Raster to Polygon tool. With this process, the area and ratio of the layer sub-groups have been determined. SAGA GIS software was used to obtain DEM data and Topographic Position Index and Terrain Ruggedness Index Maps were created accordingly. The data created by SAGA GIS were saved with File-Grid-Export tool in the file format to be used in ArcMap environment. The study area was divided into the sections of 1 km² grid; relative elevation differences of these grids were calculated by using zonal statistics which show the difference between the highest and the lowest points. On the basis of this difference, a relative relief map was created by using the Inverse Distance Weighted (IDW) method. The IDW method, which is one of the interpolation methods, consists of a calculation based on a logic whose value effect decreases as the distance of control points used in interpolation to the target point increases (Turoğlu, 2011). On the other hand, transverse and longitudinal profile series of Mount Ararat in the NE-SW and NW-SE directions were drawn.

3. Results and Discussion

3.1. Profile Analyses

Topographic profiles are one of the most reliable tools used for accurate description and interpretation of landforms (Erol, 1993). The zigzag shape in a prepared profile shows that the topography in that area is rugged and has been split dissected too much (Bilgin, 2013). Profiles that are drawn for defining and bordering a morphological unit accurately provide highly reliable data in determining the processes through which the shapes are formed. It is usually possible to define topography maps and undefined ground patterns in field studies through these carefully drawn profiles. For this reason, profile analyses, which are under estimated today, are considered as one of the first issues that should be evaluated in geomorphology and

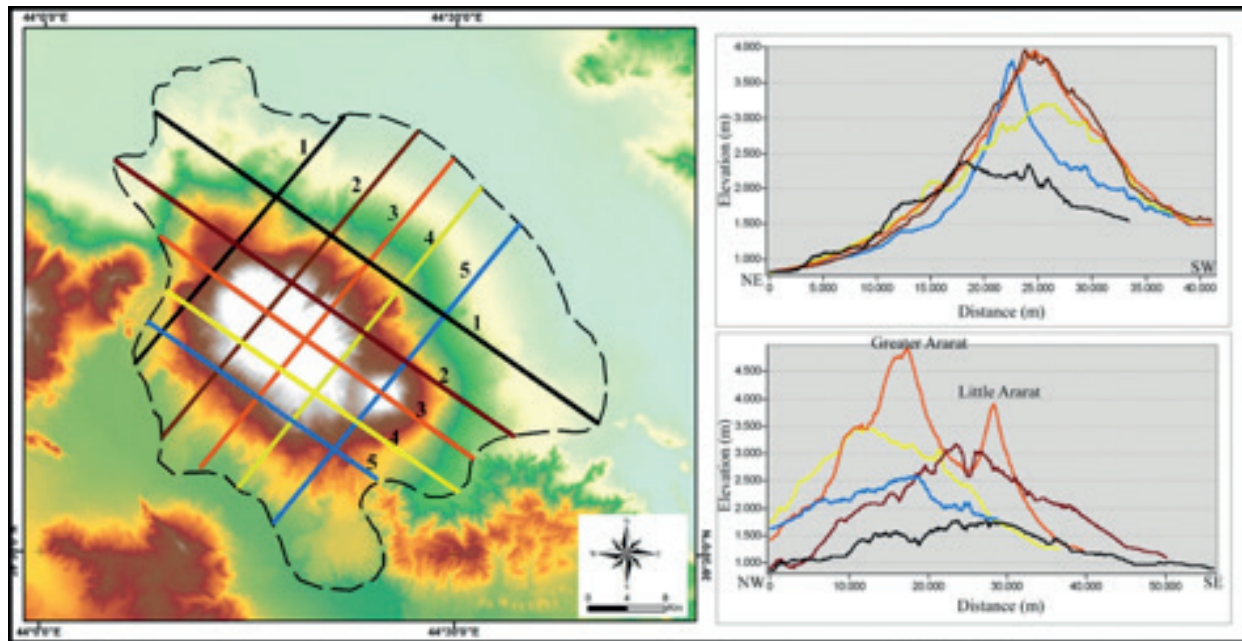


Figure 4. NW-SE and NE-SW directions profile series of Mount Ararat.

morphometry studies. In order to determine the morphological features of Mount Ararat, NW-SE and NE-SW profiles were constructed (Figure 4).

Despite its massive structure, Mount Ararat is made of two high summits. The presence of a smaller summit on the east of the main summit suggests that the mountain extends in the NW-SE direction. In fact, the diameter of the mountain in this direction is higher than that of the other direction. According to the NW-SE direction profiles, the Greater Ararat and Little Ararat cones start after the 2000-2500 m elevation range (Figure 4). On the other hand, according to the transverse and longitudinal profile series, there is a greater elevation difference between the mountain foot and the summit. Cone shape is very prominent in both profile series and the slopes start to incline after 2500 m elevation. It is also determined that the mountain rises on a wide base between 2000-1000 m elevation range.

3.2. Altitude Range Analysis

The altitude range analysis in morphometric analyses is used in the interpretation of topography. In this analysis, the Digital Elevation Model (DEM) is used as the basis. According to the classification, the elevation in the specifically limited area varies between 797 m and 5137 m (Figure 5). The volcanites of Mount Ararat start after 1000 m elevation in İğdir Plain and 1500 m elevation in Doğubayazıt Plain. The base is characterized by lava flows up to 2000 m and takes a typical cone shape after this elevation. There is a steady altitude increase between 2000-3000 m while the altitude increases at much shorter intervals after 3000 m. The areas below the altitude ranges of 2000-3000 m constitute the lower slope of the mountain while the upper areas constitute the cone. The area in this elevation range corresponds to the lower slope of the cone while the areas above this elevation are considered the summit of the Mountain.

DEM data in the studied area are divided into 18 classes; the size of each class is 250 m. In this classification, the area covered by the 797-1000 m altitude range covers the widest area when compared to the other ranges (Figure 6). It is determined that the young lava flows surfaced in the last period of the Mountain spread over İğdir Plain; this process is one of the reasons that contributed to the width of this area. The areas on 1000-1250 m altitude range correspond to the lava flows in İğdir Plain while they correspond to the plain base in Doğubayazıt Plain. The 1500-1750 m altitude range, which is the second widest area, corresponds to the low volcanic plateaus around the mountain. The plateaus at this step are the volcanic terrain formed by the spread of lava flows.

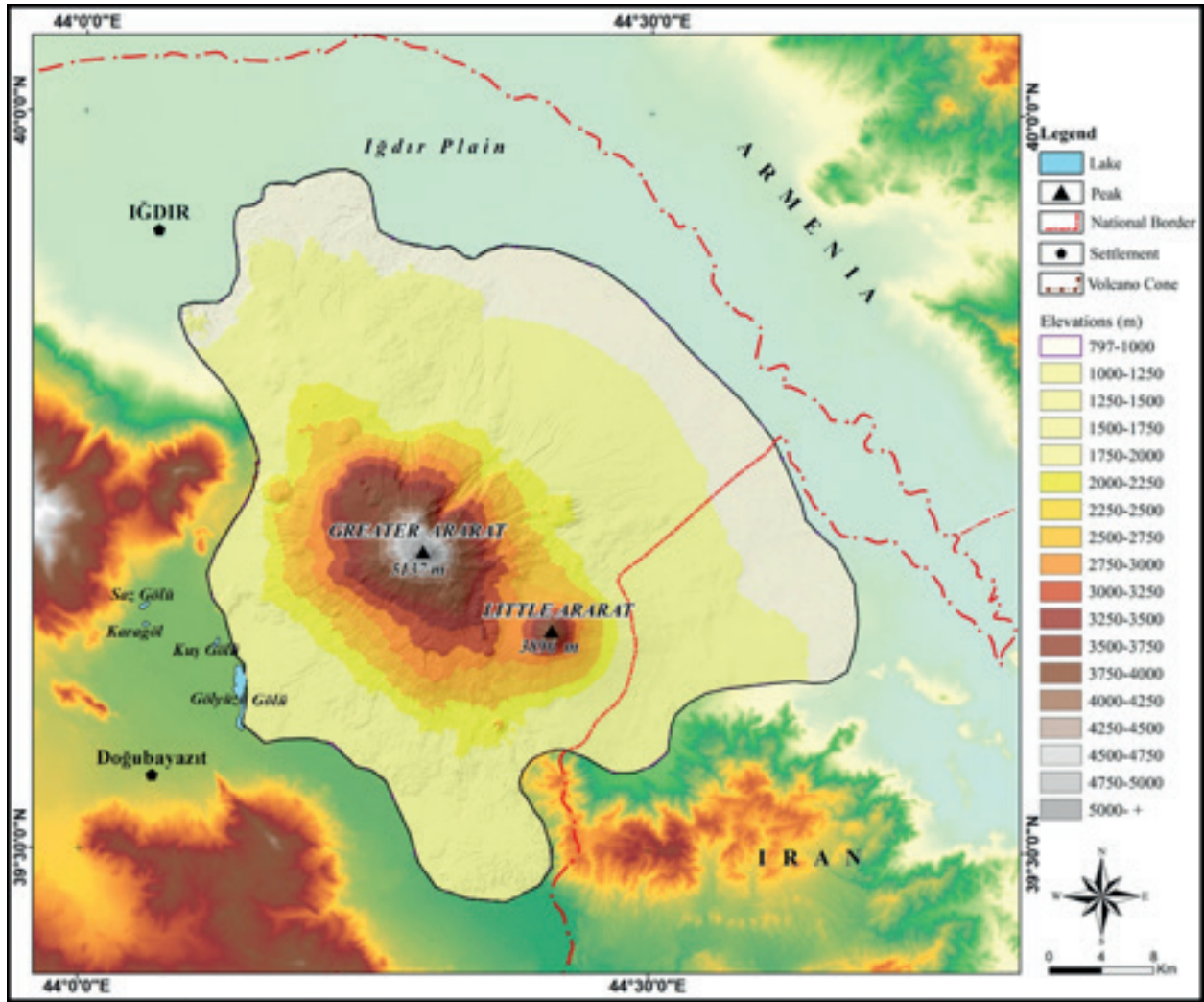


Figure 5. Altitude ranges map of Mount Ararat

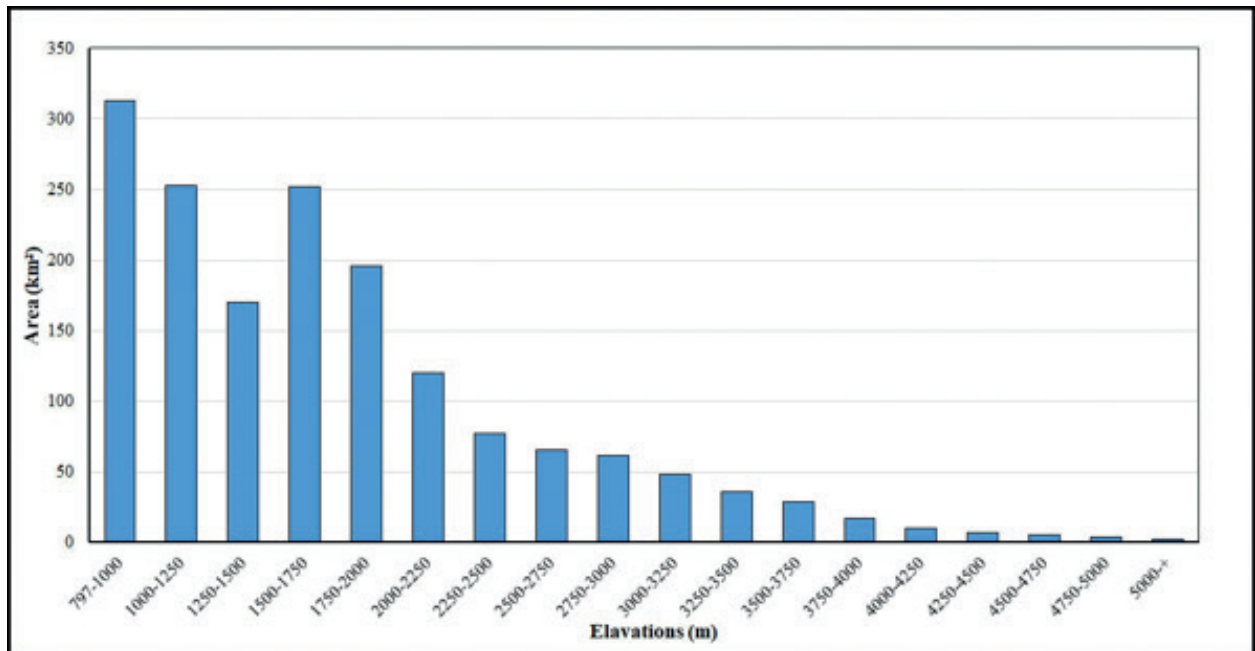


Figure 6. Mount Ararat altitude ranges areal distribution.

The altitude ranges between 797-1500 m have an approximate ratio of 44% in the study area according to the proportional distribution of the altitude ranges. The ranges between 1500-1750 m have a 15% ratio, 1750-2000 m have a 12% ratio, 2000-2250 m have a 7% ratio, 2250-2500 m have a 5% ratio, 2500-2750 m 4%, 2750-3000 m 4%, 3000-3250 m 3%, 3250-3500 m 3%, 3500-3750 m 2% and the ranges between 3750-4000 m have a 1% ratio in the whole area (Figure 7).

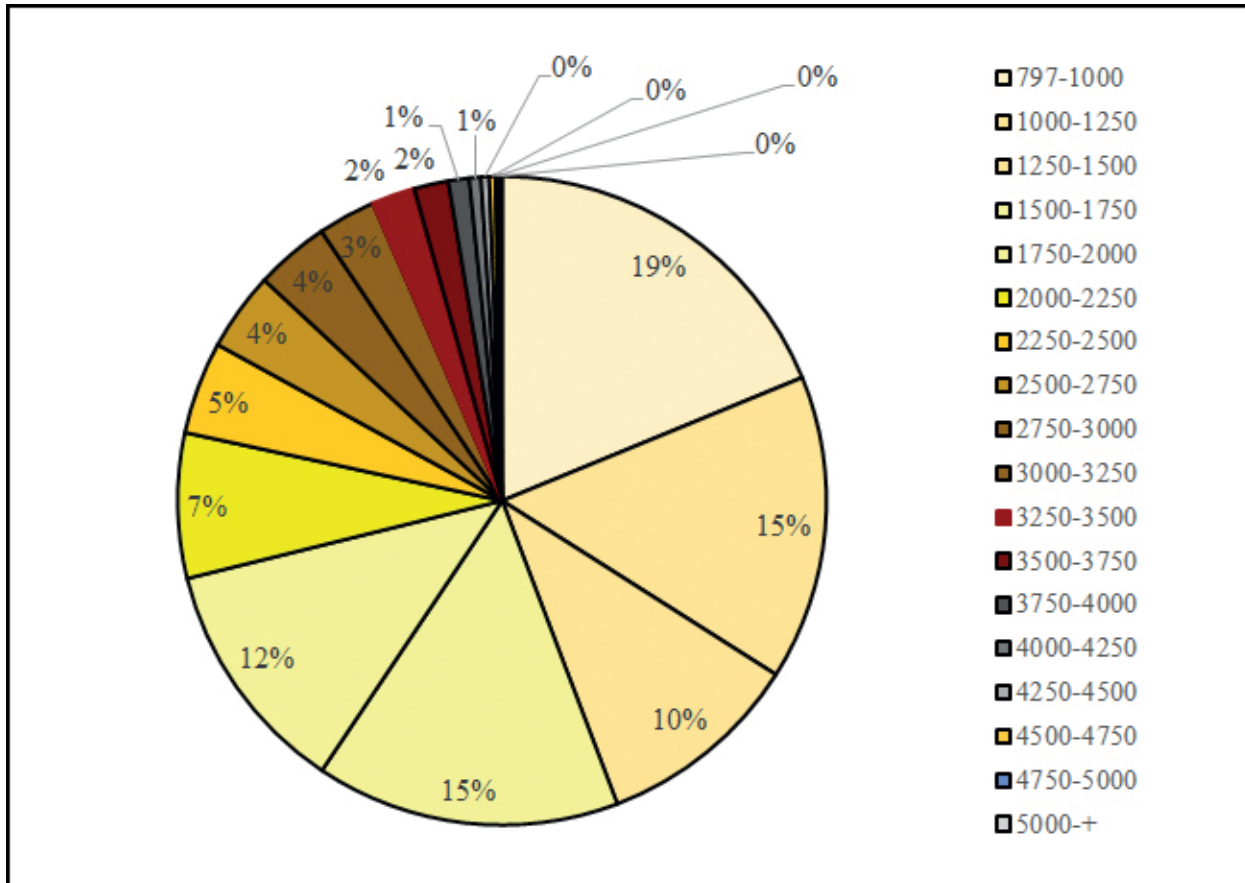


Figure 7. Mount Ararat altitude ranges proportional distribution.

According to the results of the analysis, the rate of the areas with an altitude below 2000 m. in the Mountain is 71% while the areas above this altitude correspond to 29 % of the Mountain. According to the results of this analysis, the areas covered by the altitude ranges surrounding the mountain proportionally decrease towards the summit. This fact confirms that the mountain is morphologically in the form of a volcanic cone.

3.3. Slope Analysis

The most important analysis that reveals the character of topography is slope analysis. The slope values of Mount Ararat vary between 0-56°. It is observed that the slope values generally increase in line with the increase in volcanic cone elevation on the slopes, which generally becomes apparent after 2500 m. The slope towards the summit reaches 56° in the areas over 3500-4000 m elevations (Figure 8). The dominant process that shapes the topography, breaks it up in different proportions, shapes slopes, and ridges which are formed in different directions and causes different slope values is the fluvial processes (Ardel, 1968). However, the effects of volcanic activity and glacial formation are also significant in the formation of a high slope at the summits of the Mountain. There are high slope values in stream valleys located on cone slopes in areas lower than 4000 m. Although the slope increases in line with the increase in elevation, slope values decrease towards the lower slope of the cone. The high inclination difference between the lower slope of the volcanic cone and the summit reflects the typical characteristics of the volcanic cones (Avci et al., 2018).

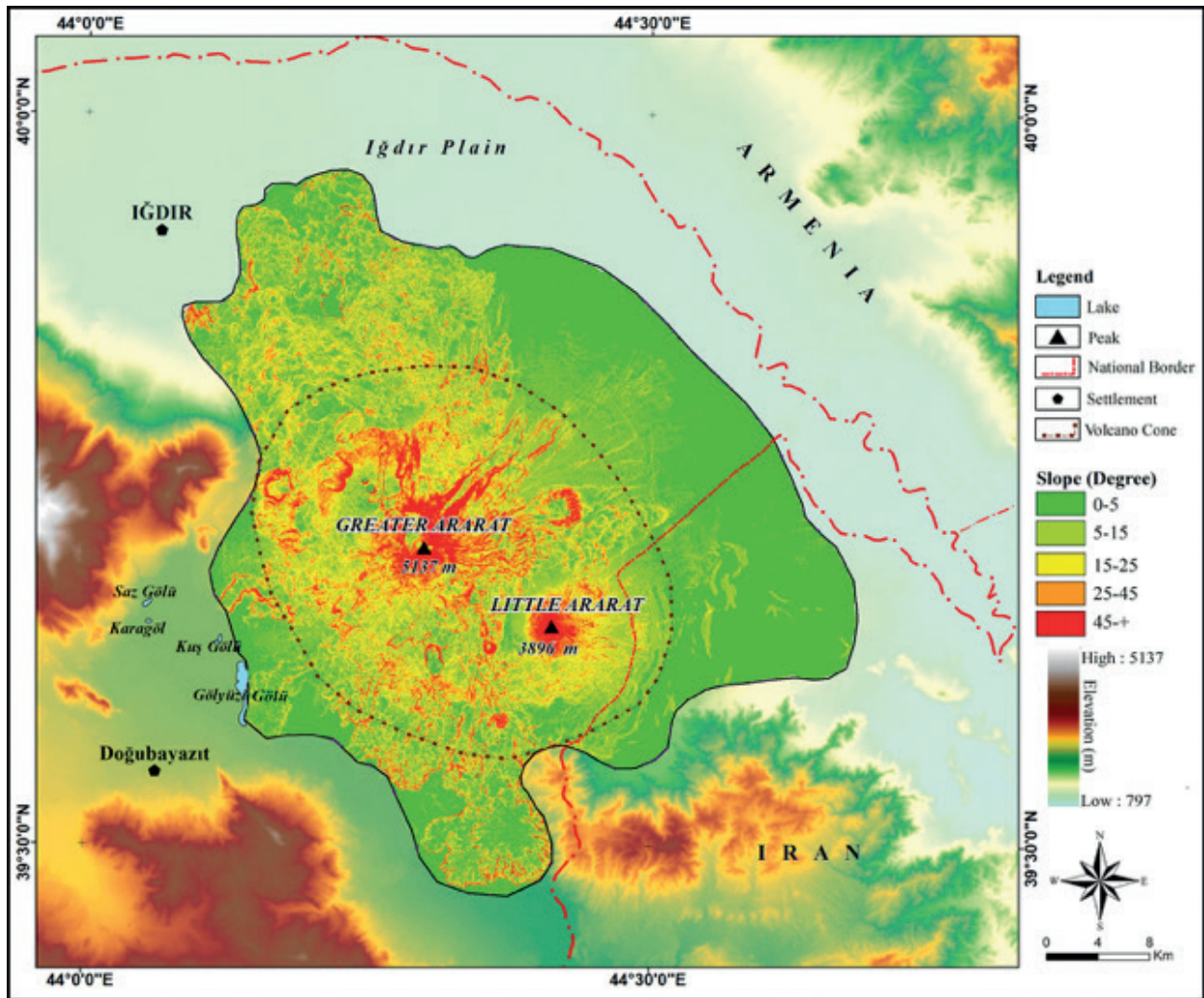


Figure 8. Slope map of Mount Ararat.

According to the slope map of Mount Ararat, there are important differences between the Eastern and Western slopes of the Mountain. The slope values of the west-facing slopes are higher than the East. Increased glacial activity on the East and North-East slopes supported the formation of the valley on these slopes. Thus, the incline in the slopes eroded by glaciers and rivers increased. Apart from this formation, young lava eruptions on the slopes facing northwest and southeast caused the slope to be partially low. When the slope values of Greater Ararat and Little Ararat are compared, it can be seen that the slope of the Mount Ararat regularly increases from the slopes of the cone to the summit. The inclination towards the summit is very high as the cone of Little Mount Ararat is younger and less eroded than the Greater Mount Ararat. On the other hand, as Greater Mount Ararat is older and higher than Little Mount Ararat, the slopes around the summit are eroded by glaciers and streams. Because of this process, slope values around the summit of Greater Mount Ararat are relatively low when compared to Little Mount Ararat. According to the reclassified slope map, nearly half of the researched area, whose slope level varies between 0 and 5°, constitutes 42% of Mount Ararat. Mountainside and the ranges in the mountainsides of Mount Ararat aren't included in the research field; this is why areas with low inclination cover a wide area. On the other hand, the very same data indicates that the mountain starts on a very wide and flat base. The areal and proportional change in slope groups from low to high reflects the typical characteristics of the volcanic cone (Figure 9).

The ratio of the areas in the 0-5° slope group in the limited (study) area is 42%. Areas with a slope between 5-15° are 25%, areas with a slope between 15-25° are 17%, and areas with a slope between 25-45° are 11%

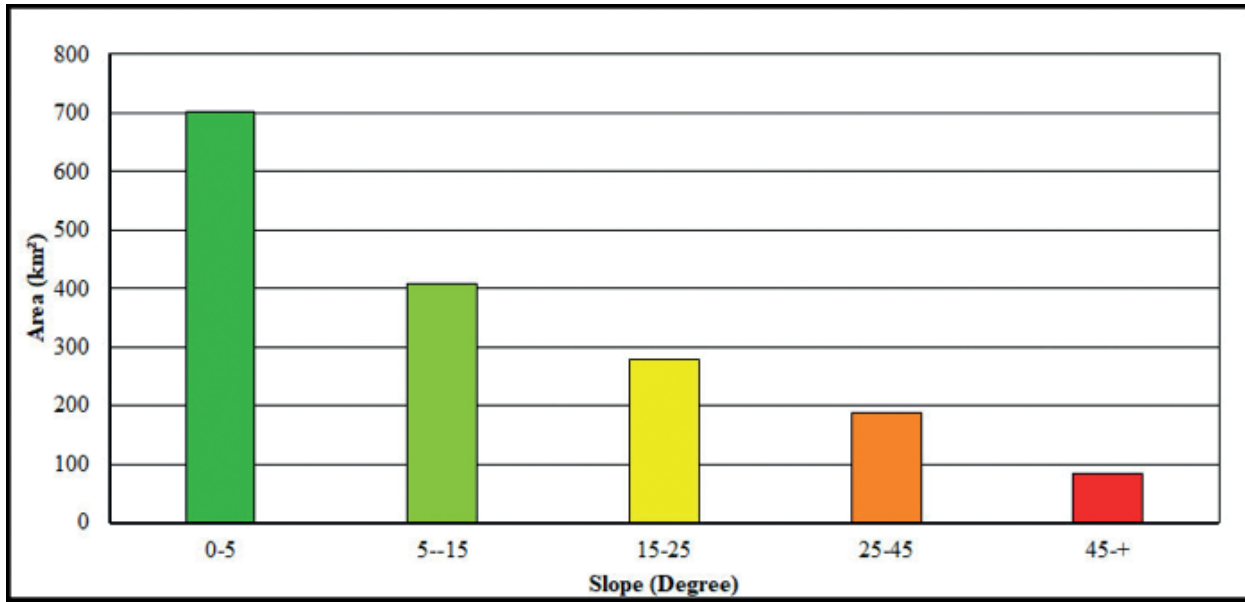


Figure 9. Areal distribution of the slope on Mount Ararat.

of the complete study area (Figure 10). The relative distribution of the slope groups gradually decreases approximately one degree in each group. The volcanic cone is characterized by this decrease; 5% of the slope groups have 45° and higher slope ratio.

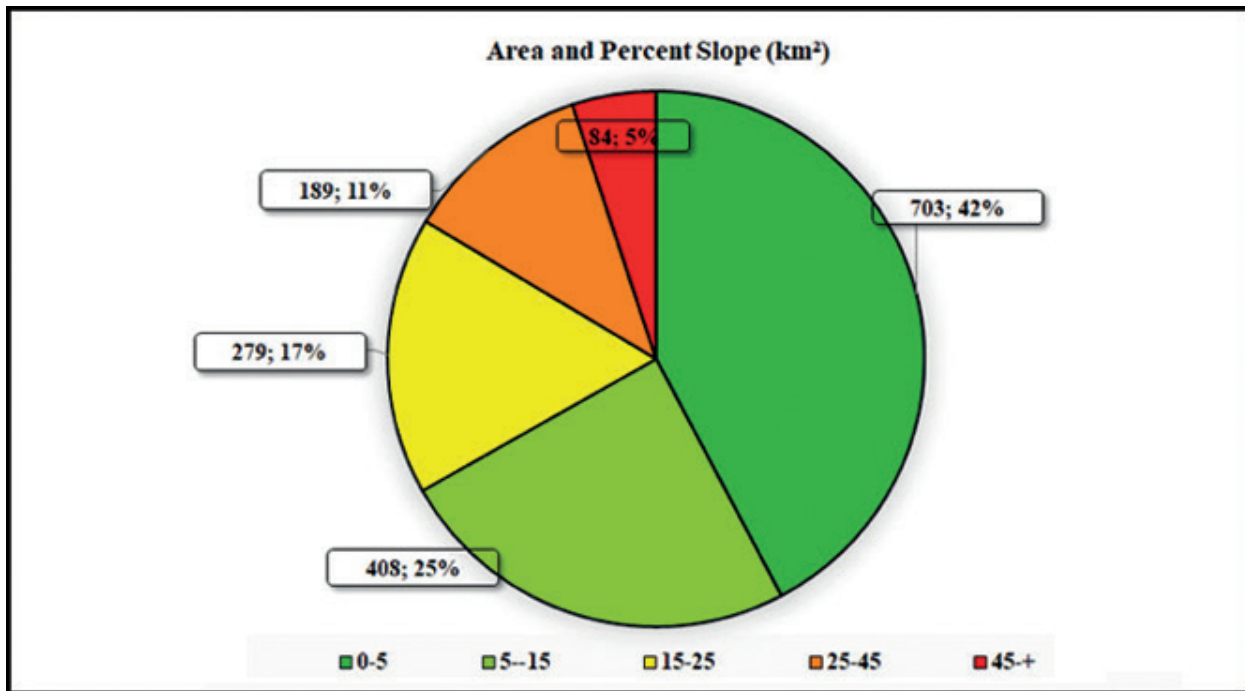


Figure 10. Proportional distribution of the slope in Mount Ararat

According to the slope analyses, the spatial and proportional distributions of the slope in Mount Ararat reflect the characteristics of volcanic cones. The wide and low slopes around the Mountain are dominant up to 2000 m altitude; there is a slow increase in the slope between 2000 m and 3000 m while there is a rapid slope increase after 3000 m towards the summit. The parasite cones on the main volcanic cone and the lava exit points in different areas led to the formation of different slope features on the greater cone. This is clearly observed on the northwest and southeast slopes of the Mountain.

3.4. Aspect Analysis

Aspect can be effective and guiding on environmental features in an area such as sunshine duration, sunshine intensity, humidity, rainfall, and wind, which are some of the climatic elements (Wilson & Gallant, 2000). According to the aspect map, the slopes facing north-northeast and south-southeast cover more areal and proportional areas (Figure 11). This partial difference shows that Mount Ararat extends in the direction of NW-SE. This result is also confirmed when aspect features are compared with the profiles. The reclassified aspect map is converted from raster format to vector format and the area covered by each aspect group is determined. According to the aspect map, the northeast slopes cover 1/5 of the study area. According to the aspect map, the ratio of flat areas is 1.6%, the ratio of the northern slopes is 14.7%, the ratio of the northeast slopes is 19.9%, the ratio of the eastern slopes is 16.4%, the ratio of the southeast slopes is 10.7%, the ratio of the south slopes is 8.7%, the ratio of the southwest slopes is 8.7% the ratio of the western slopes is 9.8% and the ratio of the northwest slopes is 9.4% (Table 2). While the total ratio of the northern slopes is 44%, the ratio of the southern slopes is 28.1% (Figure 12). This distribution shows that the mountain extends in the direction of NW-SE.

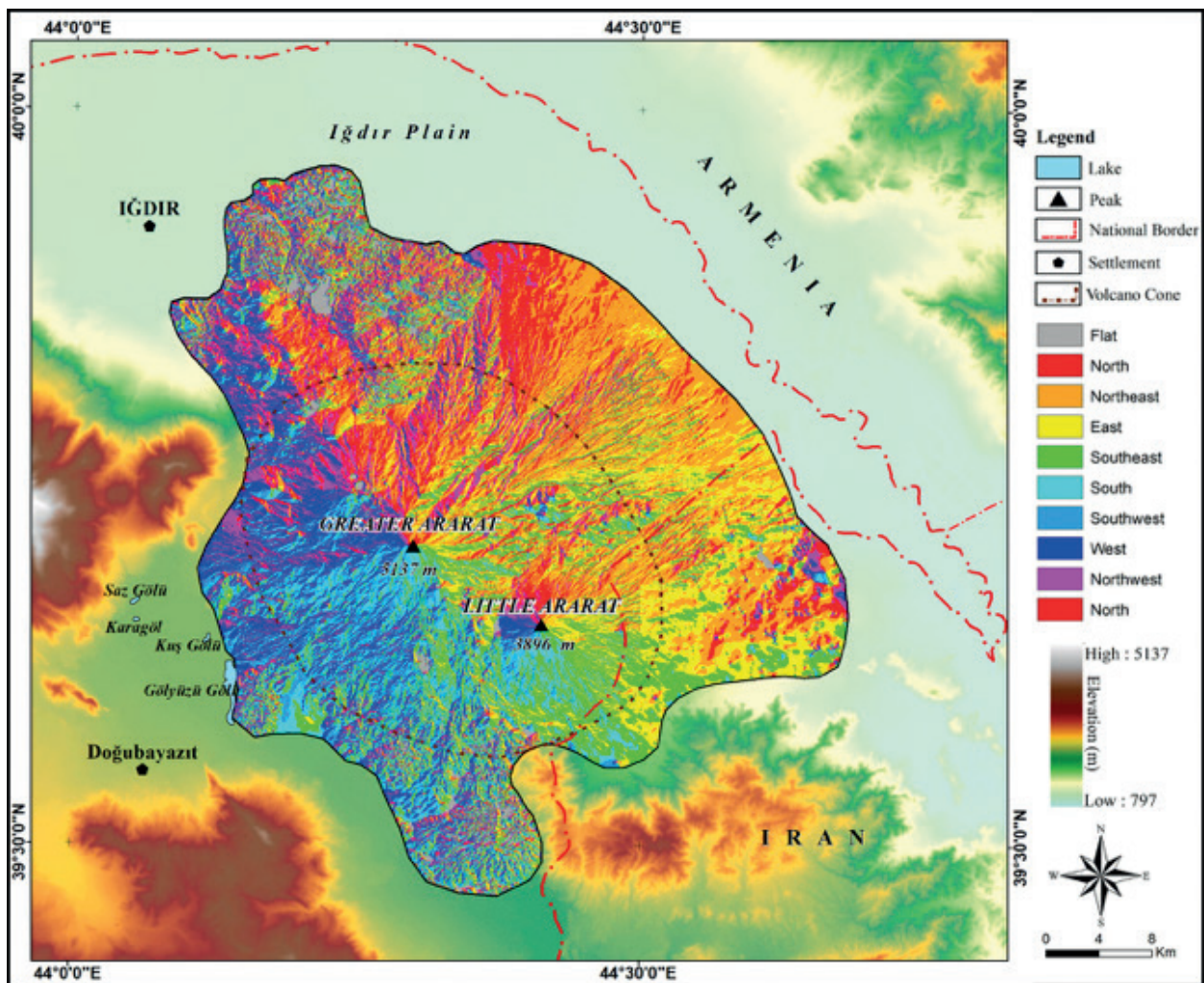


Figure 11. Aspect map of Mount Ararat.

According to the results of the analysis, the aspect is mostly concentrated in the northern sector directions and not distributed equally in all directions. The area covered by the northeast, northwest and southeast slopes of Mount Ararat is wider. The western slopes cover the smallest area. This distribution directed the glaciation on the mountain. Wider north-facing slopes have enabled the glaciers to extend further down the northern slopes.

Table 2

Areal and percentage distribution of aspect groups in Mount Ararat

Aspect reclassification	Area (km ²)	Area (%)
Flat	27	1,6
North	244	14,7
Northeast	331	19,9
East	273	16,4
Southeast	178	10,7
South	144	8,7
Southwest	145	8,7
West	163	9,8
Northwest	157	9,4
Total	1662	100,0

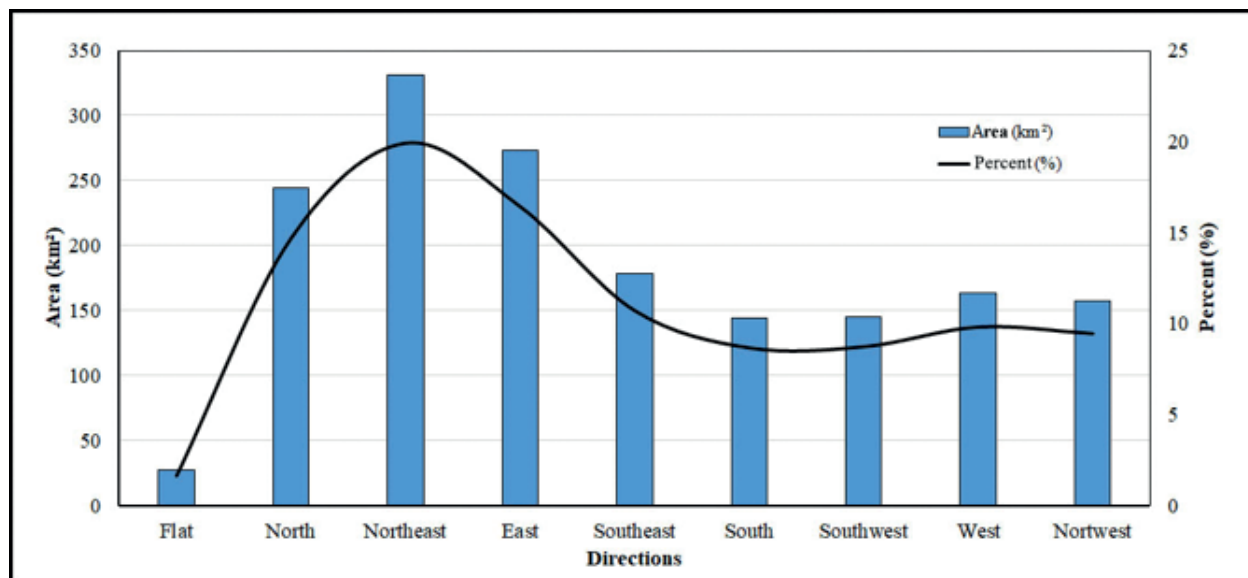


Figure 12. Areal and proportional distribution of aspect classes on Mount Ararat.

3.5. Relative Relief Analyses

Relative relief analyses are based on the calculation of the difference in elevation between the lowest and highest points at a specific place. In the process of morphological development, the rivers deepen their valleys by eroding backwards, towards the area of actual resource. In this way, the elevation difference between valley floors and topography surface or summits where these valleys are buried increases throughout the erosion period. Determining this difference, named relief amplitude, reveals the degree of dissected in an area (Bilgin, 2013). It gives highly reliable results in terms of the specific period of fluvial process and the effect of them in areas where these processes are prominent. According to the results of the analysis, it is possible to reach safe conclusions in volcanic lands. The morphological structure of Mount Ararat is clearly revealed through the relative relief analysis of the mountain. According to the results of the analysis, the altitude difference varies between 0-1141 m per km². This difference in such narrow distances is related to the volcanic formation of the mountain. Relative relief values start increasing after 2500 m and reach high values at very short distances on the slopes of the cone. It is determined that the relative elevation between 3000 m and the summit of the Mountain is very high on all of the slopes on the mountain. This indicates that the Mountain summit is young and has not yet been splitted by rivers.

Greater Mount Ararat relative relief values increase after 3000 m and maximum values are observed between the summit and the elevations higher than this value. On the other hand, there are some decreases and increases in relative relief values on different points of Little Ararat. Decreases in relative relief at some points on the summit of Mount Ararat reflect the impact of glacial, stream and lava flows on this summit (Figure 13). Relative relief values are low as young lava flows cover the surface on the mountainside of both cones. The values decrease to values close to zero since the splitting disappears in the area of transition from the mountain to the plains.

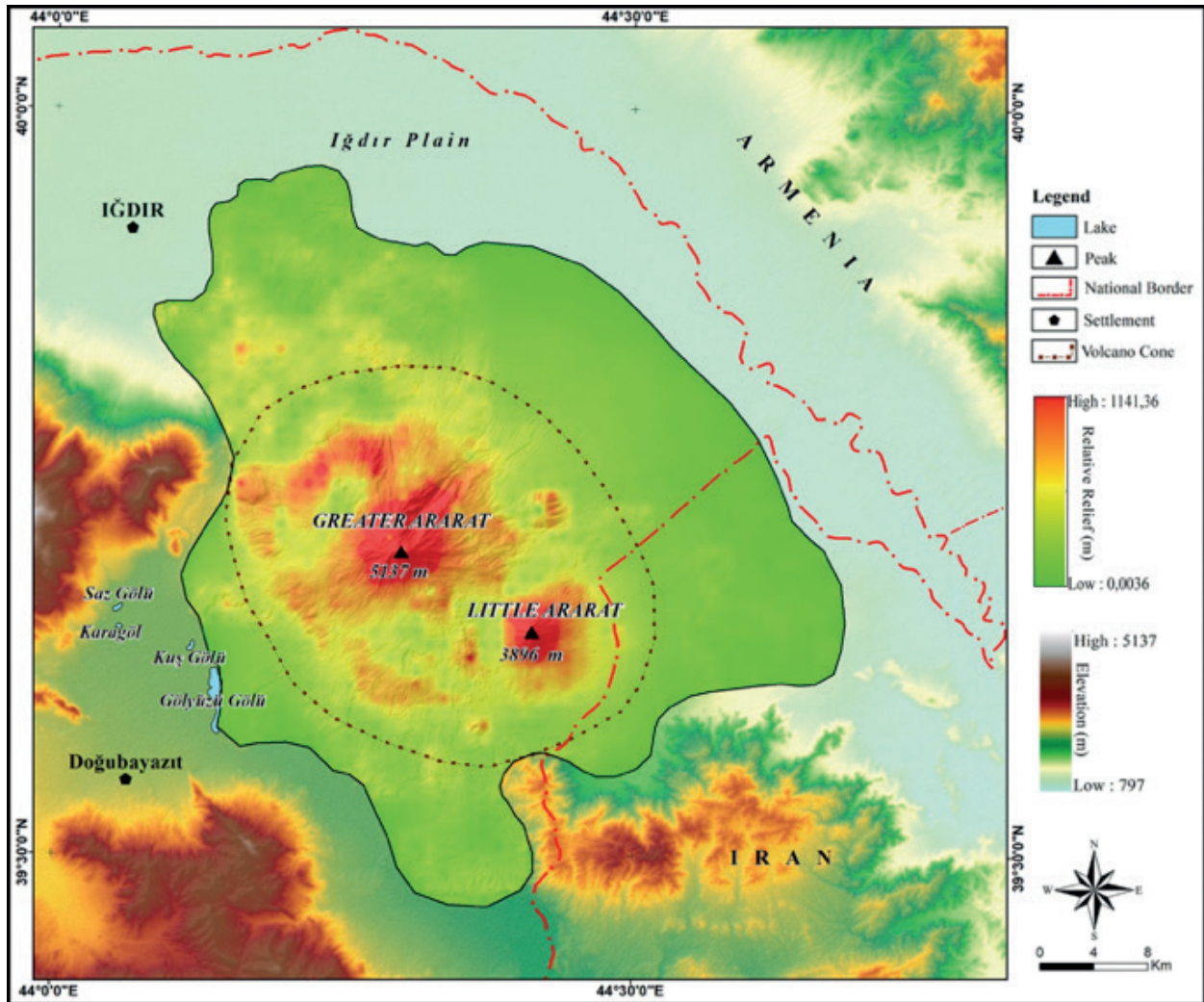


Figure 13. Relative relief map of Mount Ararat.

3.6. Topographic Position Index Analysis (TPI)

The topographic position index (TPI) consists of the processes of classifying and standardizing a terrain according to surface shapes and slope values, using cell values for each elevation step. At the end of the analysis, positive values indicate areas with high elevations such as mountains and hills, negative values indicate lower areas such as canyons and valleys, and index values close to zero indicate the ridges and flat areas (Jenness, 2006; Weiss, 2001). Topographic Position Index is a data analysis produced by the Digital Evaluation Model (DEM). According to the map formed by SAGA GIS software, the index values range from -18.2 to 25.1 (Figure 14). The topographic position index, which is an important source for geomorphologic maps, classifies the landforms. It determines the types of morphological variability in a specific field (Jenness, 2006; Tağıl & Jenness, 2008).

Topographic Position Index values are high at the summit of Mount Ararat because of the morphology while the values are low in the valleys and piedmond created by rivers on the slopes surrounding the cone.

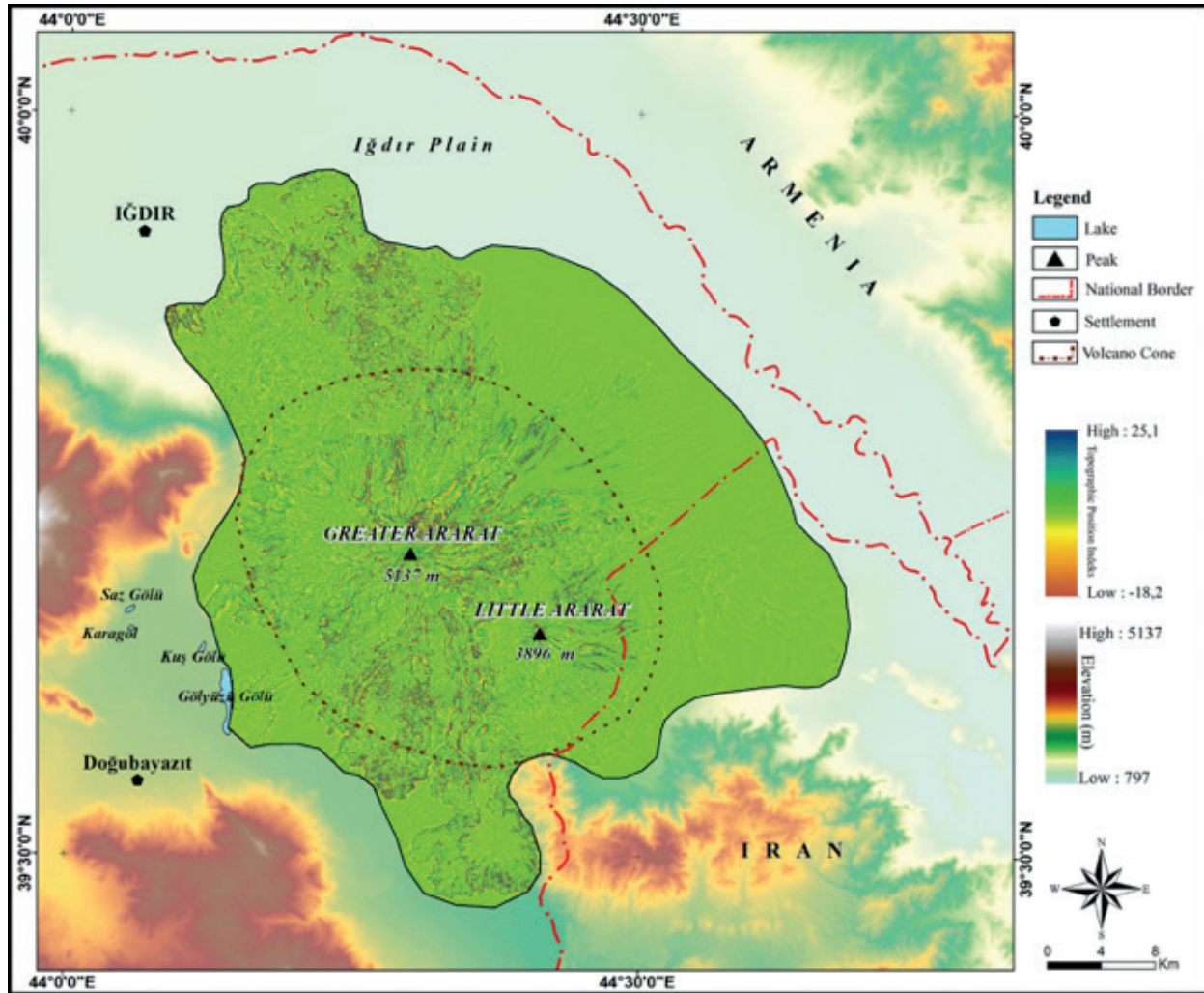


Figure 14. Topographic position index map of Mount Ararat.

According to the results map, there was a considerable amount of lava flow towards Iğdır Plain in the northwest of Mount Ararat and towards Doğubayazıt Plain in the south. On the other hand, there are other valleys on the big cone, including Cehennem creek glacial valley.

3.7. Topographic Curvature Analysis

This analysis shows the rate of slope change as a geomorphologic feature (Figure 15). The curvature function displays the shape or curve of the slope. A portion of a surface may be concave or convex. Curvature analysis can be used for understanding erosion and flow processes and defining basin features of a drainage basin. Profile curvature affects the acceleration and deceleration of flow, and consequently erosion and deposition. In the field, a negative value indicates that the curve is convex, a positive value indicates that the curve is concave while 0 indicates that the curve is linear (Florinsky, 1998; Shary, 1995; Smith, Goodchild, & Longley, 2012).

Positive values morphologically indicate concave shapes such as valleys and canyons while negative values indicate convex profiles such as ridges. In Mount Ararat analyses, important morphological shapes such as valley, ridge, hill, lava flows and plateau plains are seen. Geomorphology studies make an important contribution to limiting and defining shapes by combining topographic position analysis and this analysis and using both methods in narrow distances.

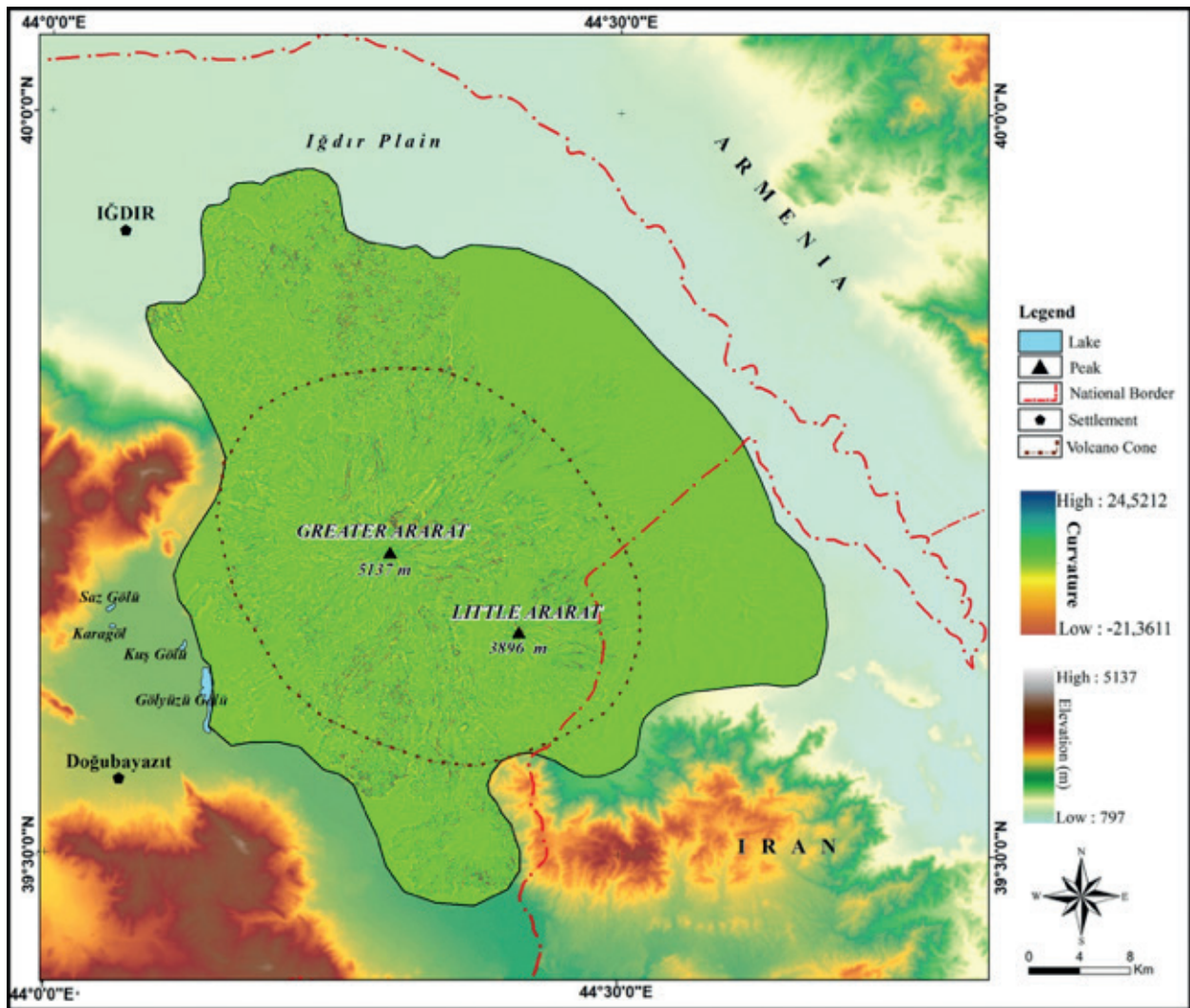


Figure 15. Topographic curvature map of Mount Ararat.

3.8. Terrain Ruggedness Index (TRI)

Terrain Ruggedness Index (TRI) is used to express the amount of the elevation difference between adjacent cells of a digital elevation model (DEM). It is also used as a measure of land heterogeneity (Riley et al., 1999). TRI provides new information about landslide morphology and is suggested to be specifically used for characterizing the accumulated parts of landslides (Leopold, Wolman, & Miller, 1964; Różycka, Migoń, & Michniewicz, 2017). The topographic analysis of Mount Ararat indicates that this analysis can be used for determining volcanic cones, lava flows and other volcanic geographical formations. The volcanic formations in the northwest and south of the Mountain could be accurately determined by this method. According to this result, it can be said that terrain ruggedness index can efficiently be used for identifying landforms on volcanic areas (Figure 16).

3.9. Stream Order Analysis

In the first stage of the drainage basin analysis, procedures for determining the stream orders are performed. Branches of a stream are defined according to the hierarchical place of them in the basin of that stream (Leopold et al., 1964). Strahler system (Strahler, 1964) classifies the smallest tributary as the first stream order. The junction of the two first tributary streams is called the 2nd stream order and one upper upstream is called the 3rd stream order. When different sequences (streams) are combined in this way, the greater sequences (streams) form the upper order while the mainstream forms the stream segment of the highest order (Strahler, 1964). The border based on Mount Ararat distribution volcanic material covers 1662 km². The rivers in this area have a radial drainage network and the main flows are on the sixth order. It is determined that there are 6 main flows and 19,041 smaller flows on Mountain Ararat (Figure 17).

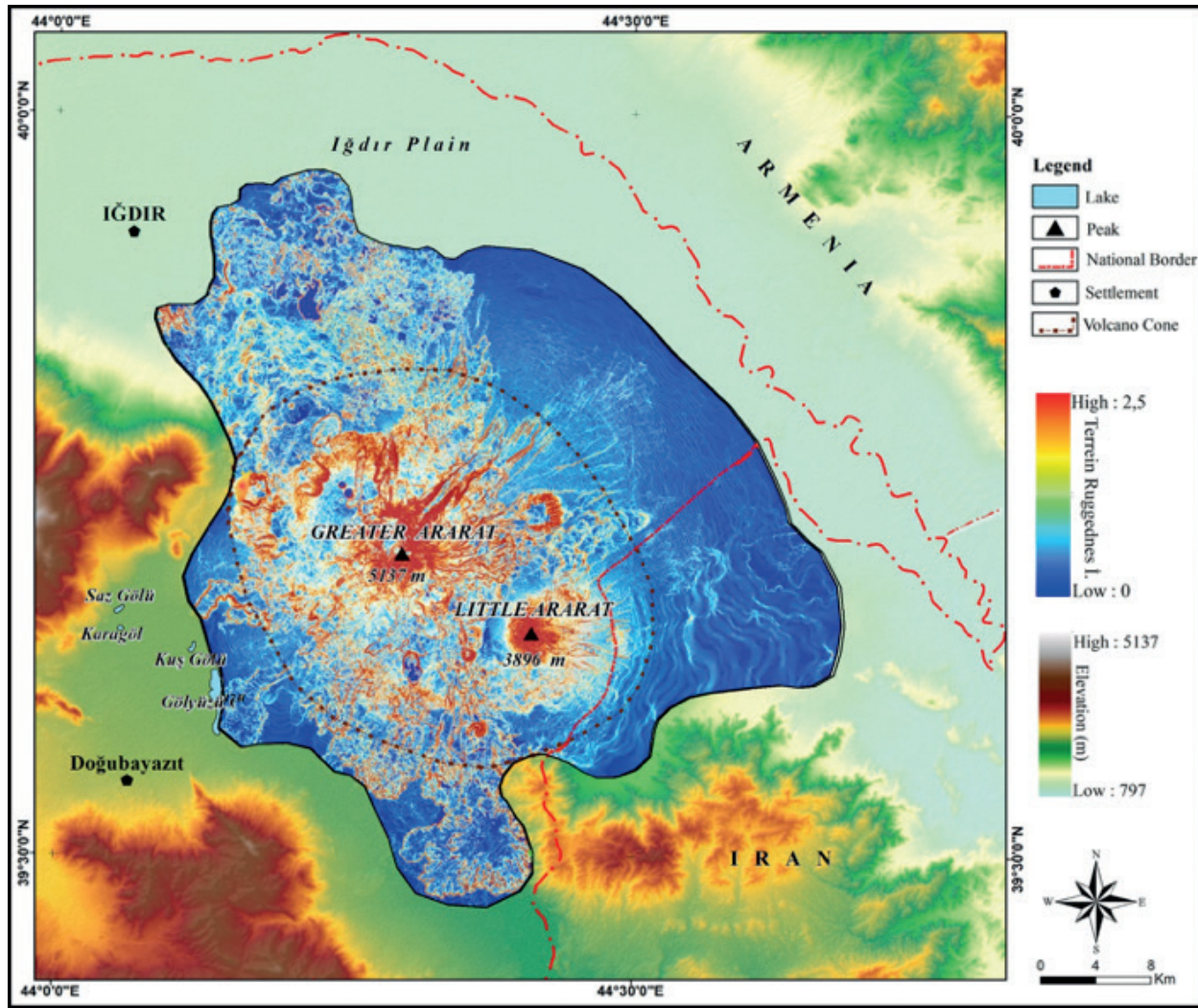


Figure 16. Terrain ruggedness map of Mount Ararat.

According to the analysis results, 1st order streams involve 14.483 flow sections while the 2nd order streams involve 2.337 flow sections. The 6th order streams involve the lowest number of flow sections (8). It is observed that there is a decrease in the stream frequency in line with the increase in the stream order. The flows in the first-order account for 52.3% and the flows in the second-order account for 27.5% of the total number of flows. 1st and 2nd order streams make up more than 75% of the area (Table 3). The 3rd and 4th order streams account for 18%, while the 5th and 6th order streams account for 2.2% of the streams. All of these results are specific to young volcanic cones.

Table 3

Number, length and order ratio of streams in Mount Ararat

Stream Order	Stream Number	Stream Length (km)	Stream Order (%)
1	14.483	2638,8	52,3
2	2.337	1387,4	27,5
3	1.227	588,1	11,7
4	752	319,3	6,3
5	234	107,8	2,1
6	8	5,6	0,1
Total	19.041	5046.9	100

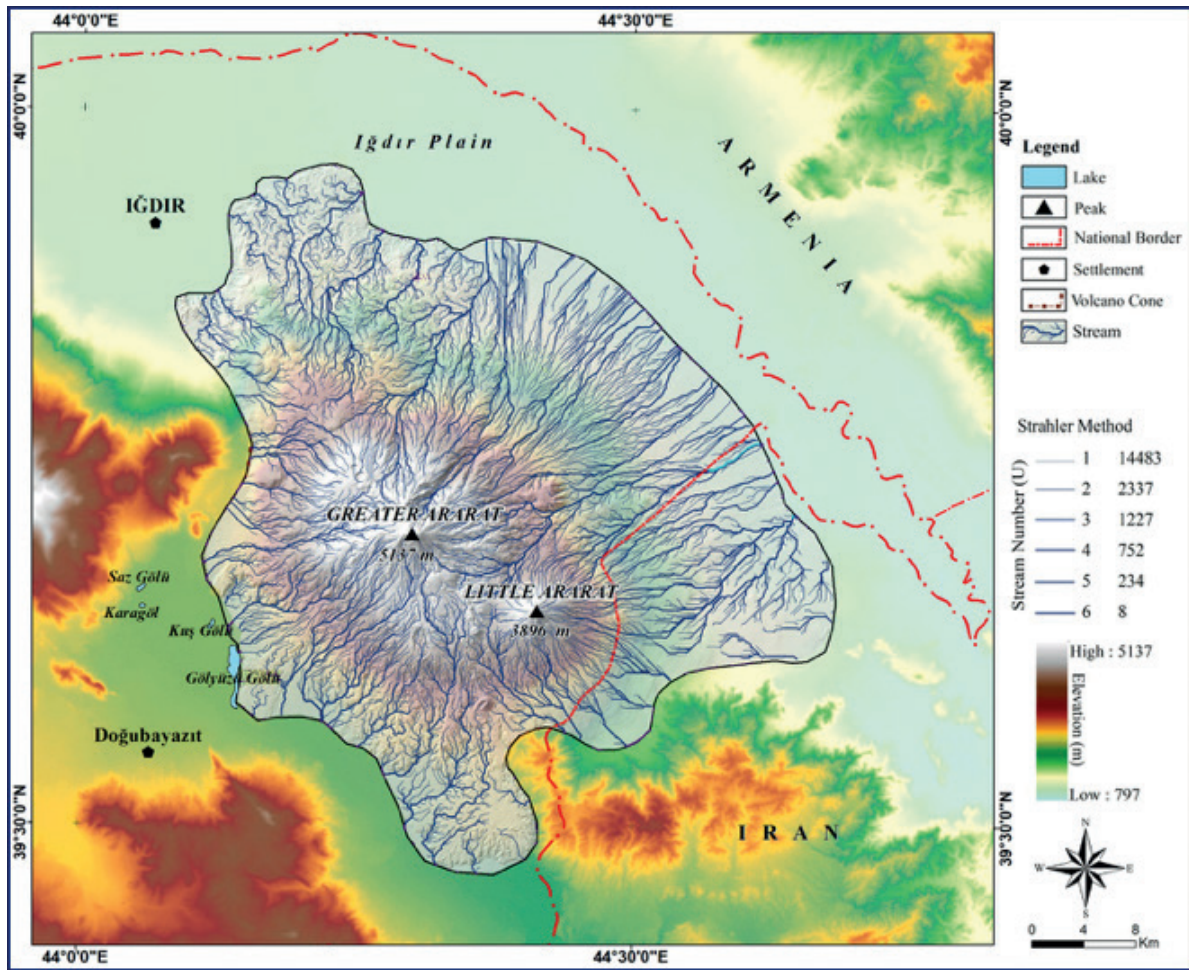


Figure 17. Stream order map of Mount Ararat.

3.10. Drainage Density Analysis

It is known that drainage density varies with the agents such as climate, vegetation, geomorphology, soil and rock characteristics (Kelson & Wells, 1989; Moglen, Eltahir, & Bras, 1998). In this method, values between 0 and 2 indicate low density, values between 2 and 2.5 indicate medium, values between 2.5 and 3 indicate high, and the values between 3 and higher indicate high drainage density (Malik, Bhat, & Kuchay, 2011). According to the analysis results, the drainage density is high in 18% and very high in 82% of the river basins on Mount Ararat. According to these results, river activity was very dominant in the formation of the Mountain. The morphological structure of the mountain and the ice cap glacier at the summit are effective in this very high drainage density level. On the other hand, these results prove the young and high volcano cone structure of the mountain. The northeast mountainside, where the drainage density is very high, corresponding to the wide fans and show the efficacy of torrent streams (Figure 18; Table 4).

Table 4

Drainage Density and Percentage Values of Mount Ararat

Drainage Density (Dd)	Sub-basin	Percentage (%)
Low (0-2)	0	0
Medium (2-2,5)	0	0
High (2,5-3)	11	18,0
Very High (3- +)	50	82,0
Total	61	100

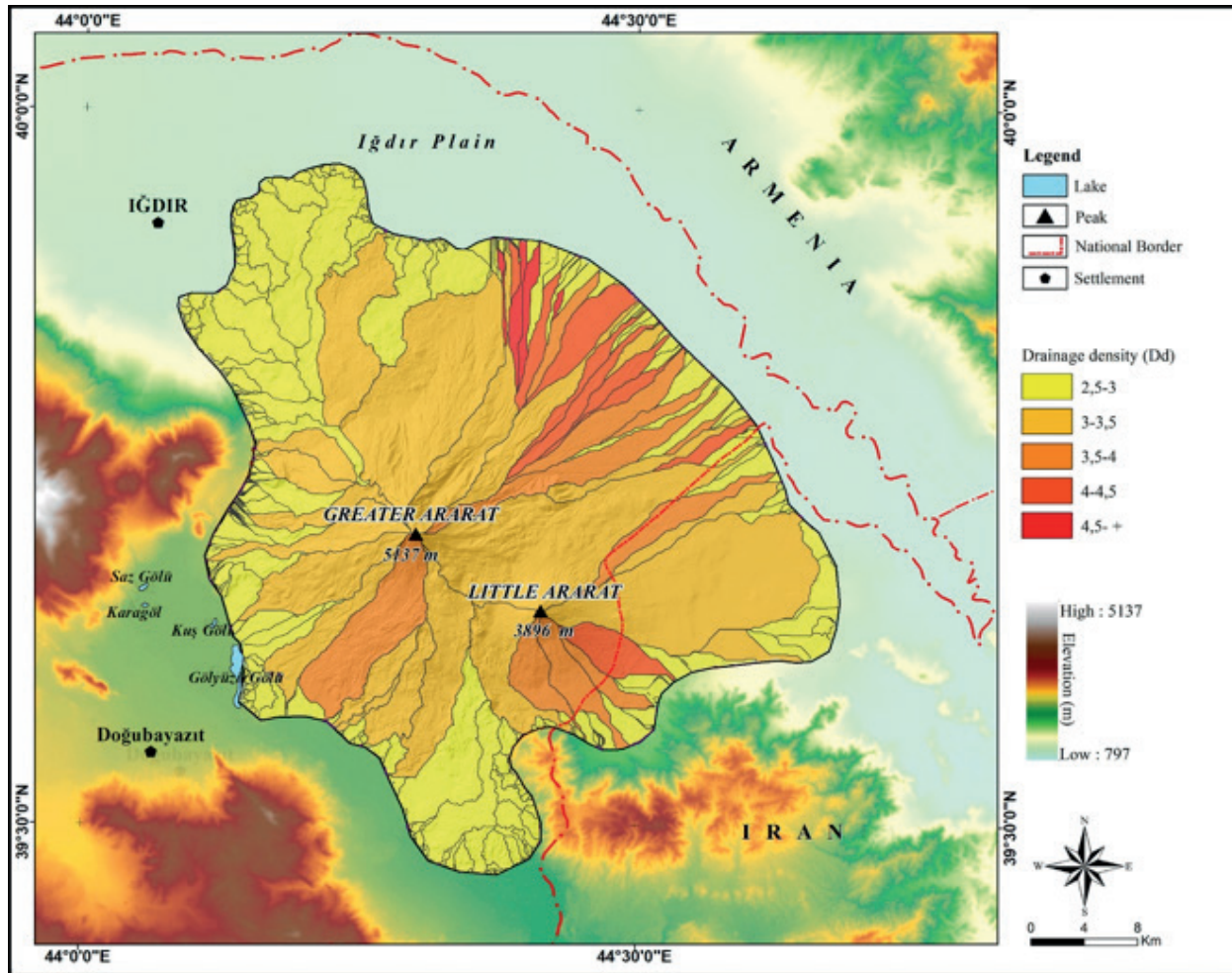


Figure 18. Drainage density map of Mount Ararat

3.11. Hypsometric Curve and Integral

The hypsometric curve shows the distribution of height in a basin and gives information about geological and geomorphological stages of basin development and basin erosion (Garg, 1983; Strahler, 1952b). The hypsometric integral provides data about geomorphological development stages in an area. Integral values vary between 0-1 and the proximity to 0 represents the mature basin and the proximity to 1 represents the young basin (Keller & Pinter, 2002; Strahler, 1952b). For the hypsometric integral analysis of Mount Ararat, the area in the boundary of the volcano cone was evaluated and the integral value was calculated as 0.28. When other morphometric analysis results are compared with this analysis, the presence of wide plains (except cone) on Mount Ararat is observed. According to this value, most of the analysed areas are mature basins. While the slopes of the cone higher than 2500 m mean young topography, there are wide volcanic plains below this elevation. Considering this topographic situation, it can be said that the result is correct (Figure 19).

4. Conclusion

Mount Ararat is the highest mountain in Türkiye. Apart from this feature, it is also important for being an existing ice-capped volcano. It is a strato-volcano formed on a circular area with an average diameter of 30-35 km. The mountain consists of two volcanic cones above an altitude of 2500 m. The decrease in the distance between the elevation ranges according to elevation map, the increase in the slope values at the summit and the relative relief difference of 0-1141 m per km² show the morphological feature of the mountain in the shape of cone. All analyses except that of aspect showing the extent support this result. The volcano cones and the surrounding flats are noticeably separated according to the slope,

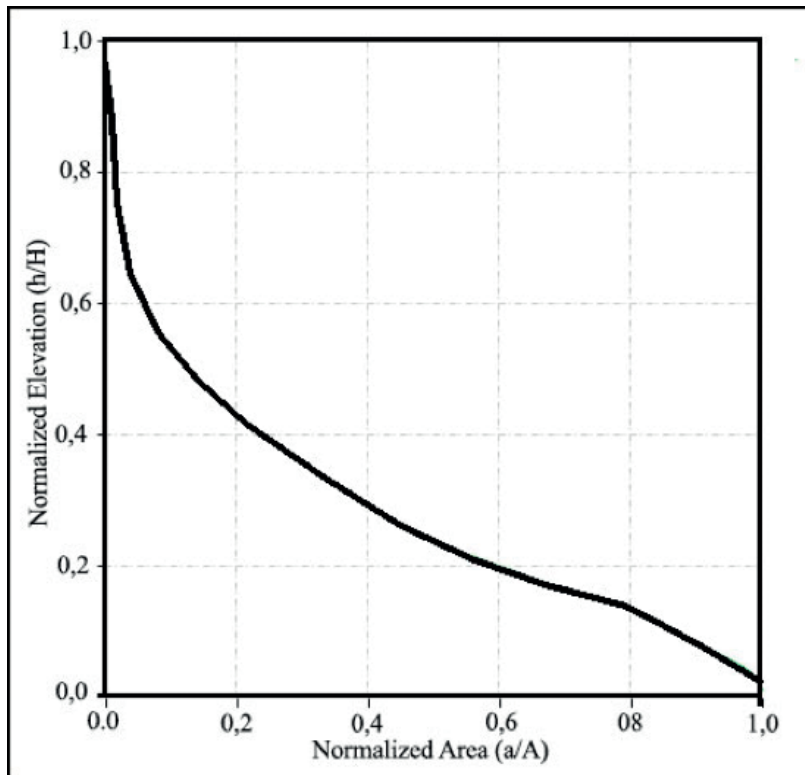


Figure 19. Hypsometric curves of Mount Ararat (Drawn with the Calhypo plugin (Pérez-Peña et al., 2009))

relative relief, topographic position, and topographic curvature analyses. Topographic position and topographic curvature analysis demonstrates all of the main geomorphologic units on the mountainous mass. Terrain ruggedness analysis is a reliable technique for observing and analyzing landslides; it has been determined that the method is also reliable for analyzing volcanic areas. According to the data obtained through this analysis, the boundaries of the lava flows are particularly very clear. The radiant structure of the drainage specific to the volcano cones is evident in the stream order and drainage density analyses. Morphometric analyses helps conducting detailed geomorphology studies in extremely wide, volcanic terrain and topographically rough areas like Mount Ararat. It is clear that these analyses will provide great, reliable support to accurate identification of some morphological units that are not very prominent in the field.

Acknowledgement

Part of this study was presented at the Fourth International Symposium on Mount Ararat and Noah's Ark.

Author Contributions

Vedat Avci: He has planned the study, performed 10 analyses and created the figures and texts under the headings related to these analyses.

Murat Sunkar: He has planned the study, written the summary, introduction and conclusion sections, checked the figures prepared according to the results of analyses and made the arrangements.

Ahmet Toprak: He has contributed to the method section, performed 5 analyses and created the texts under the headings related to these analyses.

Conflicts of Interest

The authors declare no conflict of interest.

References

- ArcGIS Desktop Help. (2022). Environmental Systems Research Institute.
- Ardel, A. (1968). *Jeomorfolojinin Prensipleri, Fasikül I.* İstanbul: İstanbul University Institute of Geography Publication.
- Arkel, N. van. (1973). Die Gegenwärtige Vergletscherung des Ararat (The present-day glaciation of Ararat). *Zeitschrift Für Gletscherkunde Und Glazialgeologie*, (9), 89–103.
- ASF. (2019). *Alaska Satellite Facility Data Search User Manual*. Retrieved from: <https://search.asf.alaska.edu/>
- Atalay, İ. (2017). *Türkiye Jeomorfolojisi*. İzmir: Meta Printing Services.
- Avcı, V., & Sunkar, M. (2015). Morphometric Analyses of Aksu Stream And Batlama Creek Watersheds That Caused Flood and Overflows in Giresun. *Journal of Geography*, (30), 91–119.
- Avcı, V., & Sunkar, M. (2018). Morphometric Analysis of Pazarsuyu, İncüvez, Kara and Bulancak Streams Which Cause Flood and Overflow Events in Bulancak (Giresun). *Fırat University Journal of Social Sciences*, 28 (2), 15–41. Doi: <https://doi.org/10.18069/firatsbed.460907>
- Avcı, V., Sunkar, M., & Toprak, A. (2018). Ağrı Dağı'nın (Ararat) Morfometrik Analizleri. In O. Belli, F. Kaya, İ. Özgül, & V. E. Belli (Eds.), *The Fourth International Mount Ararat And Noah's Ark Symposium (pp. 124-132.)*, Ağrı, Turkey.
- Azzoni, R. S., Zerboni, A., Pelfini, M., Garzonio, C. A., Cioni, R., Meraldi, E., & Diolaiuti, G. A. (2017). Geomorphology of Mount Ararat/Ağrı Dağı (Ağrı Dağı Milli Parkı, Eastern Anatolia, Turkey). *Journal of Maps*, 13(2), 182–190. Doi: <https://doi.org/10.1080/17445647.2017.1279084>
- Azzoni, R. S., Fugazza, D., Garzonio, C. A., Nicoll, K., Diolaiuti, G. A., Pelfini, M., & Zerboni, A. (2019). Geomorphological effects of the 1840 Ahora Gorge catastrophe on Mount Ararat (Eastern Turkey). *Geomorphology*, (332), 10-21. Doi: <https://doi.org/10.1016/j.geomorph.2019.02.0011>
- Bilgin, T. (2013). *Kartoğrafya II*. İstanbul: Filiz Kitabevi.
- Blumenthal, M. M. (1956). Die Vergletscherung des Ararat (Nordöstliche Türkei). *Geographica Helvetica*, 11(4), 263–264.
- Blumenthal, M. M. (1958). Vom Ağrı Dag (Ararat) zum Kaçkar Dag. Bergfahrten in nordost anatolischen Glenzlanden (From Mount Ararat to Mount Kaçkar Mountain trip in the frontier region of northeastern Anatolia). *Die Alpen*, (34), 125–137.
- Çiner, A. (2003). Recent glaciers and late quaternary glacial deposits of Turkey. *Geological Bulletin of Turkey*, 46(1), 56–78.
- Erginal, A. E., & Cürebal, İ. (2007). Soldere Havzasının Jeomorfolojik Özelliklerine Morfometrik Yaklaşım: Jeomorfik İndisler İle Bir Uygulama. *Selçuk Üniversitesi Sosyal Bilimler Enstitüsü Dergisi*, (17), 203–210.
- Erinç, S. (1953). *Doğu Anadolu Coğrafyası*. İstanbul: İstanbul University Geography Institute Publication
- Erol, O. (1993). Ayrıntılı jeomorfoloji haritaları çizim yöntemi. *İstanbul Üniversitesi Deniz Bilimleri ve Coğrafya Enstitüsü Bülteni*, (10), 19–37.
- Florinsky, I. V. (1998). Accuracy of local topographic variables derived from digital elevation models. *International Journal of Geographical Information Science*, 12 (1), 47-62. Doi: <https://doi.org/10.1080/136588198242003>
- Garg, S. K. (1983). *Geology-The science of the earth*. New Delhi: Khanna Publication
- General Directorate Mapping (GDM). (2004). 1/25.000 Ölçekli Topoğrafya Haritaları I52 ve I 53 paftaları. Ankara.
- Güner, Y., & Şaroğlu, F. (1987). Doğu Anadolu'da Kuvaterner volkanizması ve jeotermal enerji açısından önemi. *Türkiye 7. Petrol Kongresi* (371-383). Ankara, Turkey.

- Horton, R. E. (1932). Drainage-basin characteristics. *Eos, Transactions American Geophysical Union*, 13(1), 350–361. Doi: <https://doi.org/10.1029/TR013i001p00350>
- Horton, R. E. (1945). Erosional development of streams and their drainage basins; hydrophysical approach to quantitative morphology. *Geological Society of America Bulletin*, 56(3), 275–370. Doi: [https://doi.org/10.1130/0016-7606\(1945\)56\[275:EDOSAT\]2.0.CO;2](https://doi.org/10.1130/0016-7606(1945)56[275:EDOSAT]2.0.CO;2)
- Imhof, B. (1956). Der Ararat. *Die Alpen*, 32(1), 1–14.
- Jenness, J. (2006). Topographic Position Index extension for ArcView 3. X, v. 1.2., Jenness Enterprises.
- Kaya, F. (2017). *Ağrı Dağı*. Ağrı: Republic of Turkey Agri Governorship Provincial Culture and Tourism Directorate Publications.
- Keller, E. A., & Pinter, N. (2002). *Active tectonics: Earthquakes, uplift, and landscape*. New Jersey: Prentice-Hall.
- Kelson, K. I., & Wells, S. G. (1989). Geologic influences on fluvial hydrology and bedload transport in small mountainous watersheds, northern New Mexico, USA. *Earth Surface Processes and Landforms*, 14 (8), 671–690. Doi: <https://doi.org/10.1002/esp.3290140803>
- Leopold, L. B., Wolman, M. G., & Miller, J. P. (1964). *Fluvial processes in geomorphology*. New York: Dover Publications.
- Malik, M. I., Bhat, M. S., & Kuchay, N. A. (2011). Watershed based drainage morphometric analysis of Lidder catchment in Kashmir valley using geographical information system. *Recent Research in Science and Technology*, 3(4), 118–126. Doi: <https://doi.org/10.25081/rst.2017.9.3355>
- Moglen, G. E., Eltahir, E. A. B., & Bras, R. L. (1998). On the sensitivity of drainage density to climate change. *Water Resources Research*, (34), 855–862. Doi: <https://doi.org/10.1029/97WR02709>
- Özşahin, E. (2015). Geomorphometric Features Of Hoşkoy River Basin (Tekirdag). *International Journal of Social Science*, (33), 99–120. Doi: <http://dx.doi.org/10.9761/JASSS2678>
- Pérez-Peña, J. V., Azañón, J. M., & Azor, A. (2009). CalHypso: An ArcGIS extension to calculate hypsometric curves and their statistical moments. Applications to drainage basin analysis in SE Spain. *Computers & Geosciences*, 35(6), 1214-1223. Doi: <https://doi.org/10.1016/j.cageo.2008.06.006>
- Rich, J. L. (1916). A graphical method of determining the average inclination of a land surface from a contour map. *Transaction Illinois Academy of Science*, (9), 196–199.
- Riley, S. J., DeGloria, S. D., & Elliot, R. (1999). Index that quantifies topographic heterogeneity. *Intermountain Journal of Sciences*, 5(1–4), 23–27.
- Różycka, M., Migoń, P., & Michniewicz, A. (2017). Topographic wetness index and terrain ruggedness index in geomorphic characterisation of landslide terrains, on examples from the Sudetes, SW Poland. *Zeitschrift Für Geomorphologie, Supplementary Issues*, (61), 61–80. Doi: https://doi.org/10.1127/zfg_suppl/2016/0328
- Sarikaya, M. A. (2012). Recession of the ice cap on Mount Ağrı (Ararat), Turkey, from 1976 to 2011 and its climatic significance. *Journal of Asian Earth Sciences*, (46), 190–194. Doi: <https://doi.org/10.1016/j.jseas.2011.12.009>
- Schumm, S. A. (1956). Evolution of drainage systems and slopes in badlands at Perth Amboy, New Jersey. *Geological Society of America Bulletin*, 67(5), 597–646. Doi: [https://doi.org/10.1130/0016-7606\(1956\)67\[597:EODSAS\]2.0.CO;2](https://doi.org/10.1130/0016-7606(1956)67[597:EODSAS]2.0.CO;2)
- Shary, P. A. (1995). Land surface in gravity points classification by a complete system of curvatures. *Mathematical Geology*, 27(3), 373–390. Doi: <https://doi.org/10.1007/BF02084608>
- Smith, K. G. (1950). Standards for grading texture of erosional topography. *American Journal of Science*, 248 (9), 655–668. Doi: <https://doi.org/10.2475/ajs.248.9.655>
- Smith, M. J., Goodchild, M. F., & Longley, P. A. (2012). *Geospatial Analysis: A Comprehensive Guide to Principles, Techniques and Software Tools*. Leicester: Matador Publication. Retrieved from: <https://>

- scholar.google.com/scholar?hl=tr&as_sdt=0%2C5&q=Geospatial+analysis%3A+A+comprehensive+guide%2C+Electronic+book.&btnG=
- Strahler, A. N. (1952a). Dynamic basis of geomorphology. *Geological Society of America Bulletin*, 63 (9), 923–938. Doi: [https://doi.org/10.1130/0016-7606\(1952\)63\[923:DBOG\]2.0.CO;2](https://doi.org/10.1130/0016-7606(1952)63[923:DBOG]2.0.CO;2)
- Strahler, A. N. (1952b). Hypsometric Analysis of Erosional Topography. *Bull. Geol. Soc. Am.* (63), Doi: [https://doi.org/10.1130/0016-7606\(1952\)63\[1117:HAAOET\]2.0.CO;2](https://doi.org/10.1130/0016-7606(1952)63[1117:HAAOET]2.0.CO;2)
- Strahler, A. N. (1964). Quantitative geomorphology of drainage basins and channel net work. New York: In Chow, V.T. (ed.) *Handbook of Applied Hydrology*, McGraw-Hill, 4–76.
- Şahin, C. (2011). *Türkiye Fiziki Coğrafyası* (Extended 4th Edition). Ankara: Daytime Education and Publishing.
- Şenel, M., & Ercan, T. (2002). *1/500.000 Ölçekli Türkiye Jeoloji Haritaları, Van Paftası*. Ankara: Maden Tetkik ve Arama Genel Müdürlüğü.
- Tağıl, Ş., & Jenness, J. (2008). GIS-based automated landform classification and topographic, landcover and geologic attributes of landforms around the Yazoren Polje, Turkey. *Journal of Applied Sciences*, 8(6). Doi: [10.3923/jas.2008.910.921](https://doi.org/10.3923/jas.2008.910.921)
- Topuz, M., & Karabulut, M. (2016). Geomorphometric Analysis Of Limonlu And Alata Watersheds (Erdemli, Mersin, Turkey). *Electronic Turkish Studies*, 11(2), 1231-1250. Doi: <http://dx.doi.org/10.7827/TurkishStudies.9165>
- Turoğlu, H. (2011). *Coğrafi Bilgi Sistemlerinin Temel Esasları*. İstanbul: Çantay Kitabevi.
- Türkecan, A. (2017). Türkiye'nin Doğu Bölgelerinde Gözlenen Kuvaterner Yaşlı Volkanik Etkinlikleri. *Doğal Kaynaklar ve Ekonomi Bülteni*, (22), 63-78.
- Türkunal, S. (1980). *Doğu ve Güneydoğu Anadolu'nun Jeolojisi*. Ankara: Chamber of Geological Engineers Publication.
- Weiss, A. (2001). Topographic position and landforms analysis. *ESRI User Conference*. San Diego, USA. Retrieved from: http://www.jennessent.com/downloads/tpi-postertnc_18x22.pdf
- Wilson, J. P., & Gallant, J. C. (2000). *Terrain analysis: Principles and Applications*. New York: John Wiley & Sons.



The Effect of Vertical Earthquake Motion on Steel Structures Behaviour in Different Seismic Zones

Ercan Işık¹, Fatma Ülker Peker², Aydın Büyüksaraç^{3*}

¹Department of Civil Engineering, Faculty of Engineering and Architecture, Bitlis Eren University, Bitlis, Türkiye

²Department of Civil Engineering, Faculty of Engineering and Natural Sciences, Malatya Turgut Özal University, Malatya, Türkiye

³Çan Vocational School, Çanakkale Onsekiz Mart University, Çanakkale, Türkiye

Article History

Received: 16.11.2021
Accepted: 03.03.2022
Published: 25.09.2022

Research Article

Abstract – Each geographical location has its own seismicity and this affects the seismic behaviour of structures. In this study, four different settlements with different seismicity such as İzmir, Bitlis, Samsun and Konya were considered. Seismic risks and parameters for these provinces were compared. Analyses were carried out separately for a ten-storey steel building with the same structural characteristics in each of these provinces. The sample building model was created by considering the provisions of Principles for the Design, Calculation and Construction of Steel Structures-2016 and Turkish Building Earthquake Code-2018. The nonlinear time history analysis method for the sample steel building was made separately for each province considering different earthquake directions, by using the SAP200 program. Records of the 2020 İzmir earthquake (Mw=6.9) were used in the analyses. The displacement, base shear force and moments were obtained for each province for each direction taken into account. The aim of the study is to reveal the effect of both earthquake direction and different seismic regions. The displacement, rotation, base shear force and moment values obtained in the provinces with higher PGA values were also higher. It was determined that the vertical earthquake effect did not significantly change the results obtained for the horizontal direction in this study.

Keywords – Steel structure, site-specific, tbec-2018, vertical earthquake effect

1. Introduction

Earthquake resistant building design principles should be considered in structures to be built in high earthquake-risk areas. It is inevitable to change and update these principles over time depend on the developments in the civil and earthquake engineering fields (Büyüksaraç et al., 2021; Aksoylu et al., 2020). Studies on Turkey's earthquake hazard map and seismic design codes were initiated after 1939 Erzincan (Mw = 7.9) earthquake, that was known as the largest and most destructive earthquake in the country and continued with earthquakes that induced significant casualties over time (Özmen, 2012; Işık, 2021). The legal earthquake zonation map in Turkey was arranged in 1945, initially. (Özmen and Pampal, 2017). The maps, which were changed in 1945, 1947, 1963, 1972, were updated in 1996 and this map was used until 2018. The earthquake hazard map was also updated and started to be used according to Turkish Building Earthquake Code (TBEC-2018), that was updated in 2018 (Özmen, 2012; Işık et al., 2021a). Turkey earthquake hazard maps used so far are given in Table 1 comparatively.

Table 1

Earthquake hazard maps used in Turkey

Year	Names of Maps	Method Used	Zoning Type	Number of Zones
1945	Earthquake Zones	Damage based	Regional	3
1947	Earthquake Zones	Damage based	Regional	3
1963	Earthquake Zones of Turkey	Deterministic	Regional	4
1972	Earthquake Zones of Turkey	Deterministic	Regional	5
1996	Earthquake Zones of Turkey	Probabilistic	Regional	5
2018	Turkish Earthquake Hazard	Probabilistic	Site-specific	Site-specific

¹ eisik@beu.edu.tr

² fatma.peker@ozal.edu.tr

³ absarac@comu.edu.tr

*Corresponding Author

The six earthquake hazard maps used in Turkey are shown in [Figure 1](#).

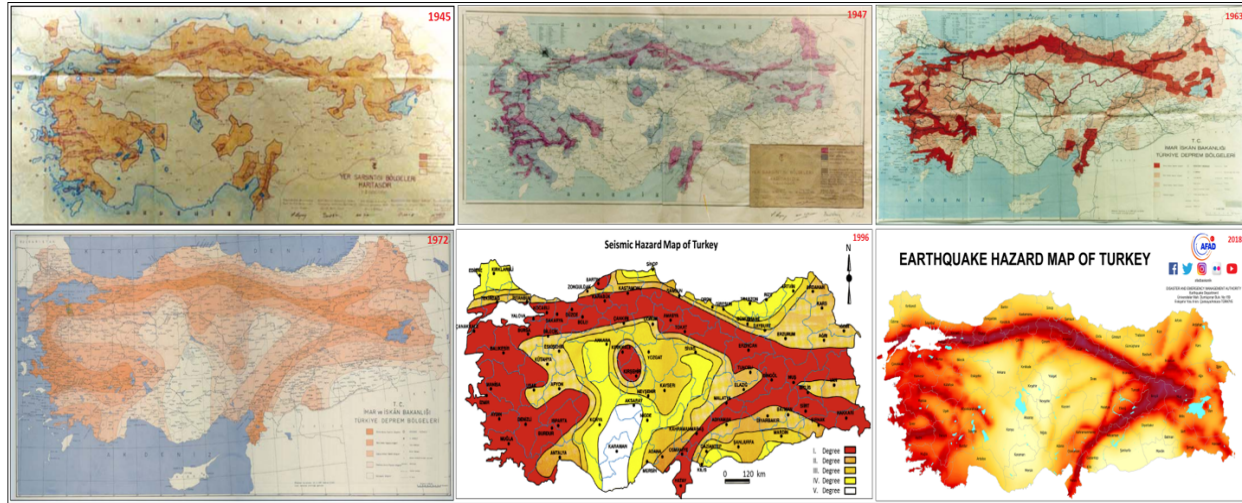


Figure 1. Development of Turkey earthquake hazard maps (adopted from [Özmen and Pampal, 2017](#); [Güneş, 2015](#); [AFAD, 2021](#))

Turkey Earthquake Hazard Map was arranged by AFAD (Disaster and Emergency Management Presidency) within the scope of the project titled Updating the Seismic Hazard Map of Turkey. The concept of seismic region has been removed and replaced by site-specific seismic risk with this map. However, regional-based design spectra have been replaced by design spectra specific to each geographical location ([Akkar et al., 2014](#); [Çeken et al., 2017](#); [Akkar et al., 2018](#); [Akkar et al. 2018a](#); [Karaşin et al., 2020](#); [Işık et al., 2021b](#)). Update has become inevitable not only in earthquake hazard maps, but also in seismic design codes, due to developing technology, scientific innovations and new generation mathematical equations. The ongoing changes and updates on ten different dates were finally completed in 2018 and entered into force in 2019 and was named TBEC-2018. The current seismic design code is much more comprehensive and detailed than previous codes. One of the innovations in the current code, which includes many innovations and updates, is the usage of the vertical earthquake effect in structural analyzes and evaluations.

Buildings are exposed to earthquake movements in three directions under earthquake impact ([Yavaş et al., 2019](#)). The first studies using different earthquake records in order to reveal the vertical effect of the earthquake were made by [Chopra \(1966\)](#); [Newmark et al. \(1973\)](#); [Weichert et al. \(1986\)](#); [Abrahamson and Litehiser \(1989\)](#); [Bozorgnia et al. \(1995\)](#); [Papazoglou and Elnashai \(1996\)](#) and [Ambraseys and Douglas \(2003a\)](#). As a result of field observations, it has been proved that the damage of buildings during the earthquake can be caused not only by exceeding the shear or bending capacity, but also by excessive axial stresses caused by the vertical effect of the earthquake ([Farsangi and Tasnimi, 2016](#)). The vertical earthquake effect is an important factor in increasing the axial forces in the structure ([Papazoglou and Elnashai, 1996](#)). Since the vertical component of the earthquake is smaller than the horizontal component and the vertical loads are more effective, the vertical component effect of the earthquake is ignored in the design of building-type structures ([Doğan ve Elmas, 2004](#)). Unlike other earthquake codes, the vertical effect of the earthquake has been taken into account initially with the updated seismic design regulation in Turkey. Structural analysis were performed by researchers on buildings with dissimilar structural systems regarding the vertical effect of the earthquake, and different results have been obtained ([Gürel and Kısa, 2002](#); [Doğan and Elmas, 2004](#); [Baş et al., 2015](#); [Eren and Beyen 2015](#); [Eren and Beyen, 2017](#); [Kim et al., 2017](#); [Abdolahiparsa et al., 2016](#); [Loghman et al., 2015](#); [Chopra, 1966](#)). It has also been clearly demonstrated in other studies that the vertical component of earthquake effect must be included in the structural analyses for design of earthquake-resistant buildings ([Kalkan and Graizer, 2007](#); [Kunnath et al., 2008](#); [Kadid et al., 2010](#); [Ambraseys and Douglas, 2003b](#); [Jakayev and Aydemir, 2019](#)). These studies have shown that excessive axial stresses occur due to the vertical effect of the earthquake, cause different damage distributions together with the change of axial forces in the columns, significant increases in column shear forces with the addition of the vertical component of the earthquake, and as a result, they may have serious effects on some structural elements.

Structural analyzes were carried out for a steel building selected as an example, taking into account different variables within the scope of this study. Four settlements with different earthquake hazards are one of the variables. In this context, İzmir, which is located in the 1st degree, Bitlis for the 2nd degree, Samsun for the 3rd degree and Konya for the 4th degree seismic zone in the prior earthquake zone map was selected. A random geographical location was chosen in these provinces. Peak ground velocity (PGV), peak ground acceleration (PGA), spectral acceleration coefficients (S_a , S_1) and spectral acceleration coefficients for short and long periods (S_{DS} , S_{D1}) for selected provinces were obtained using the Turkish Earthquake Hazard Map Interactive Web Earthquake Application (TEHMIWA) (AFAD, 2021). The vertical and horizontal design spectrum of these provinces have been obtained and compared. These current values were compared with recommended values in the previous code. Structural analyzes for a 10-storey steel building selected as an example using the obtained spectrum curves were carried out separately for each province with SAP2000 software. The steel building model, designed by the authors, was modeled within the framework of the provisions given in the Principles for the Design, Calculation and Construction of Steel Structures-2016 (PDCCSS-2016) and TBEC-2018. Nonlinear time history analysis was used in all structural analysis. In these analyses, earthquake effects in different directions were obtained separately for each province by using the acceleration records of the 2020 İzmir (Mw = 6.9) earthquake. The displacement, rotation, base shear and moment values for each direction were obtained separately. In this study, the earthquake behaviour of the building was examined for different earthquake directions as well as the different design spectra to be obtained for settlements with different seismicity. The results were evaluated, and interpretations were made.

2. Earthquake Parameters Considered in the Study

It is known that site-specific design spectrum importantly affects the expected target displacements from the structure (Işık et al., 2016; Kutanis et al., 2018; Işık et al., 2020). The design spectra obtained on a regional-based in the prior earthquake code have been replaced by the site-specific design spectrum with the current earthquake code. This study aims to obtain the impact of different design spectra, four different settlements located in different earthquake zones in the 1996 Turkey Earthquake Zones Map, İzmir, Bitlis, Samsun and Konya were selected. The seismicity of these provinces is different from each other. While making the selection, İzmir (Center) as the 1st degree earthquake zone, 2nd degree Bitlis (Güroymak), 3rd degree Samsun (Center) and Konya (Center) as the 4th degree earthquake zone was taken into consideration in the previous earthquake risk map. The representation of these settlements on the Earthquake Zones Map in 1996 is given in Figure 2.

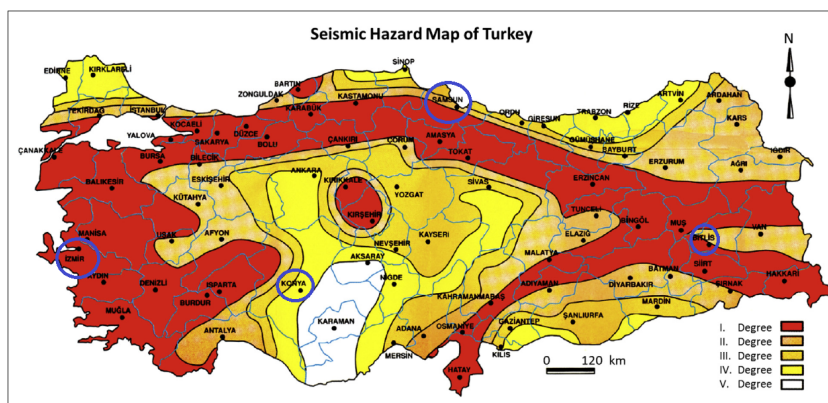


Figure 2. Turkey earthquake zoning map published in 1996 (Güneş, 2015) and selected settlements

A random geographic location from these settlements was chosen. The representation of the locations considered in the research and the current Earthquake Hazard Map of Turkey is given in Figure 3.

In TBEC-2018, which is currently used, the spectrum is defined in standard form or by site-specific earthquake hazard analyzes depending on the map spectral acceleration coefficients and local ground effect coefficients for

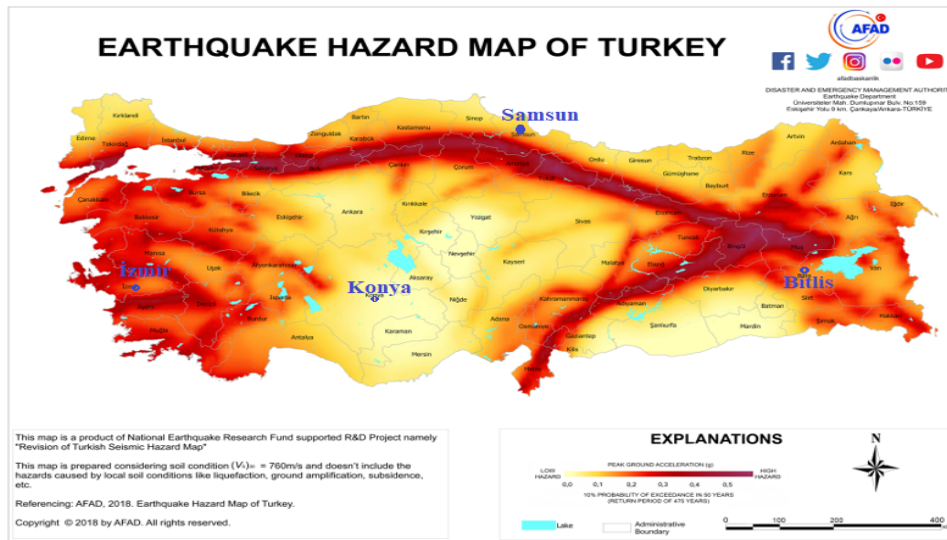


Figure 3. Turkey Earthquake Hazard Map (AFAD, 2021) and selected settlements

5% damping rate based on a certain earthquake ground motion level (TBEC-2018; Koçer et al., 2018). Map spectral acceleration coefficients corresponding to the geometric mean of earthquake effects in two perpendicular horizontal directions, based on the reference ground condition ($V_s=760$ m/s) for a given earthquake ground motion level, dividing the map spectral accelerations by the gravitational acceleration for 5% damping ratio are defined as dimensionless coefficients. Dimensionless map spectral acceleration coefficients are defined within the scope of Turkey Earthquake Hazard Maps for four different earthquake ground motion levels. The map spectral acceleration coefficient (S_s) for the short period (0.2s) and the map spectral acceleration coefficient (S_1) for the long period (1s) can be obtained from the Interactive Web Earthquake Application, except for the ZF ground class. These two coefficients have been used for the first time with the current code. In the previous earthquake code, design spectra were obtained according to the maximum ground acceleration depending on the earthquake region, while in the current code, design spectra are used depending on earthquake parameters such as spectral accelerations in short and long periods to be determined with the help of this application. The map spectral acceleration coefficients S_s and S_1 are converted to the design spectral acceleration coefficients S_{DS} (Equation 2.1) and S_{D1} (Equation 2.2) for short and long periods as follows:

$$S_{DS} = S_s \cdot F_s \tag{2.1}$$

$$S_{D1} = S_1 \cdot F_1 \tag{2.2}$$

where F_s and F_1 are local ground coefficients that are being used for the first time with the current regulation. S_s , PGA, S_1 , F_s , PGV, S_{DS} , F_1 and S_{D1} and vertical/horizontal design spectra have been obtained separately for each of the different exceedance probabilities by using the earthquake web application. The comparison of the PGA and PGV values obtained for the settlements considered in this study at four different earthquake ground motion levels is shown in Table 2.

Table 2
Comparison of PGA and PGV for different exceedance probabilities

Province	PGA (Peak Ground Acceleration) (g)				PGV (Peak Ground Velocity) (cm/s)			
	Probability of exceeding in 50 years				Probability of exceeding in 50 years			
	2%	10%	50%	68%	2%	10%	50%	68%
İzmir (Center)	0.844	0.454	0.174	0.124	52.739	27.621	10.237	7.422
Bitlis (Güroymak)	0.549	0.296	0.118	0.085	32.870	17.748	7.483	5.408
Samsun (Center)	0.422	0.232	0.096	0.067	28.497	16.241	6.798	4.783
Konya (Center)	0.291	0.132	0.044	0.031	14.080	6.633	2.449	1.761

The comparison of S_s , S_1 values for different earthquake ground motion levels is given in [Table 3](#) for each geographical location considered in this study by using the TEHMIWA.

Table 3

Comparison of map spectral acceleration coefficients for different exceedance probabilities

Province	S_s (Short period acceleration coefficient)				S_1 (Map spectral acceleration coefficient for a 1.0 s period)			
	Probability of exceeding in 50 years				Probability of exceeding in 50 years			
	2%	10%	50%	68%	2%	10%	50%	68%
İzmir (Center)	2.127	1.115	0.416	0.297	0.544	0.274	0.104	0.076
Bitlis (Güroymak)	1.355	0.705	0.277	0.199	0.360	0.198	0.083	0.059
Samsun (Center)	1.017	0.549	0.219	0.153	0.345	0.194	0.079	0.055
Konya (Center)	0.681	0.304	0.100	0.070	0.147	0.072	0.027	0.020

One of the important changes in the current code has been in earthquake ground motion levels. While the previous code there was only a design earthquake with a probability of 10% to be exceeded in 50 years, four different earthquake ground motion levels were expressed with the current code as 2%, 10%, 50% and 68% probability of exceedance in 50 years. The spectral coefficients and corner periods of the horizontal and vertical elastic design spectra were shown in [Figure 4](#).

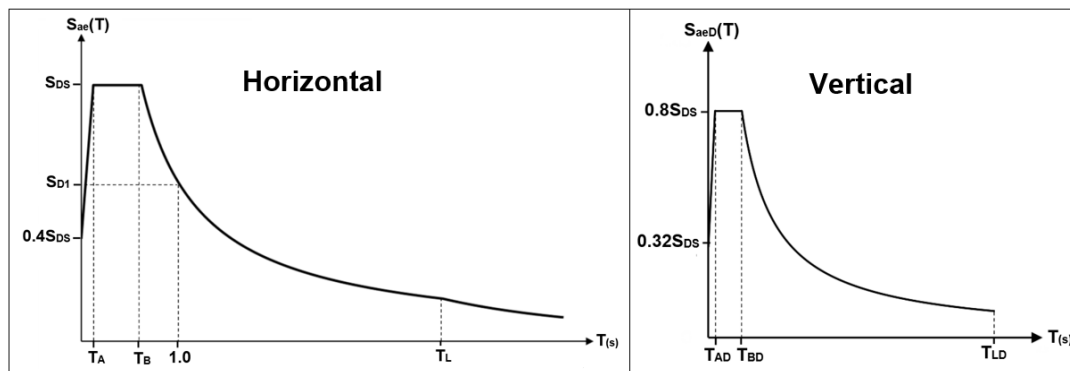


Figure 4. The spectral coefficients and corner periods of the horizontal and vertical elastic design spectra

The spectral acceleration coefficients and corner period values of the design spectra for DD-2 earthquake ground motion level in the last two codes were compared ([Table 4](#)). The same soil class was used in each location to make comparisons of structural analysis results and seismic parameters among six different soil classes envisaged in TBEC-2018. Considering the ZE soil class, both seismic and structural parameters were obtained. As the weakest soil class, the ZE local soil class is considered for comparisons for all locations.

Table 4

Comparison of design spectral acceleration and period values

Province	10% probability of exceedance in 50 years	Spectral Acceleration Coefficients				Horizontal				Vertical		
		All Type Soils				ZE						
		TSDC-2007	TBEC-2018	TSDC-2007	TBEC-2018	T_A	T_B	T_A	T_B	T_{AD}	T_{BD}	T_{AD}
İzmir (Center)	1	0.40	1.124	0.450	0.15	0.90	0.143	0.714	There is no data		0.048	0.238
Bitlis (Güroymak)	0.75	0.30	0.967	0.387	0.15	0.90	0.136	0.679		0.045	0.226	
Samsun (Center)	0.50	0.20	0.890	0.356	0.15	0.90	0.146	0.731		0.049	0.244	
Konya (Center)	0.25	0.10	0.684	0.274	0.15	0.90	0.088	0.442		0.029	0.147	

The comparison of the PGA(g) values is given in [Table 5](#), which have a 10% probability of exceeding in the last two earthquake codes in 50 years.

Table 5

Comparison of PGA values for the last two earthquake codes

Province	PGA (2018)	Earthquake Zone (1996)	PGA (2007)	PGA_{2018}/PGA_{2007}	Change (%)
İzmir (Center)	0.454	1	0.400	1.135	13.50
Bitlis (Güroymak)	0.296	2	0.300	0.987	1.33
Samsun Center)	0.232	3	0.200	1.160	16
Konya (Center)	0.132	4	0.100	1.320	32

The comparison of the horizontal design spectra obtained by using the Interactive Web Earthquake Application for four different settlements is given in [Figure 5](#).

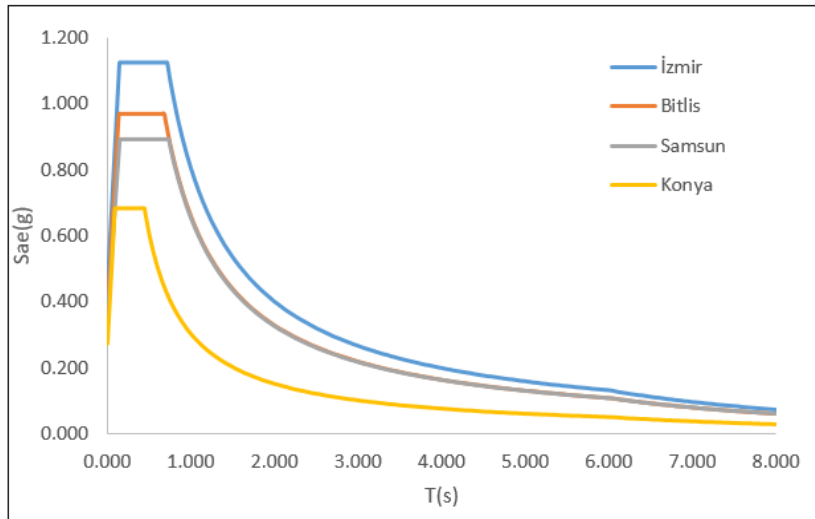


Figure 5. The comparison of horizontal design spectrum

One of the concepts that entered with the updated seismic design code is the vertical elastic design spectrum. In this context, the comparison of the vertical elastic design spectra obtained from the earthquake application for these settlements is given in [Figure 6](#).

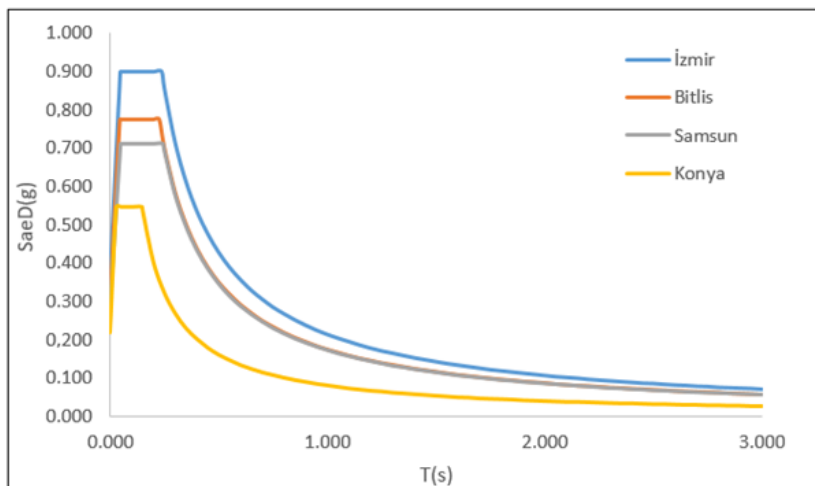


Figure 6. Comparison of vertical elastic design spectra

3. Aegean Sea Earthquake (Mw=6.9) on 30th of October 2020

An earthquake (Mw=6.9) strikes the epicenter of which was off the Aegean Sea, İzmir (Seferihisar) On 30th of October 2020. The earthquake lasted for about 16s and was felt in Greece, a neighboring country to Turkey. The greatest acceleration was measured as 180.16 gal in the N-S component at Kuşadası (Aydın) station (AFAD, 2020a). The station locations and measured acceleration values at the five stations closest to the epicenter of this earthquake are given in [Table 6](#).

Table 6

The five stations closest to the epicenter and the measured acceleration values (AFAD, 2020a)

Station					Acceleration (gal)			Distance
Province	Town	Latitude	Longitude	N-S	E-W	Vertical	km	
İzmir	Seferihisar	38.1968	26.8384	51.035	81.116	34.453	34.75	
Aydın	Kuşadası	37.8600	27.2650	180.164	144.564	87.161	42.95	
İzmir	Urla	38.3232	26.7706	82.072	64.950	43.174	48.94	
İzmir	Menderes	38.2572	27.1302	763.916	46.433	43.701	51.38	
İzmir	Güzelbahçe	38.3706	26.8707	47.418	48.544	35.011	54.57	

This earthquake, which is thought to have caused a 30 km long faulting on the Samos Fault, caused loss of life and property in İzmir city center due to the soil amplification effect and structural defects. 117 people were died and 1032 people were injured after this earthquake (AFAD, 2020b). The acceleration records of the 2020 Aegean Sea Earthquake were used in the structural analyzes for the sample steel building within the scope of this study. The acceleration records of this earthquake in different directions are shown in [Figure 7](#).

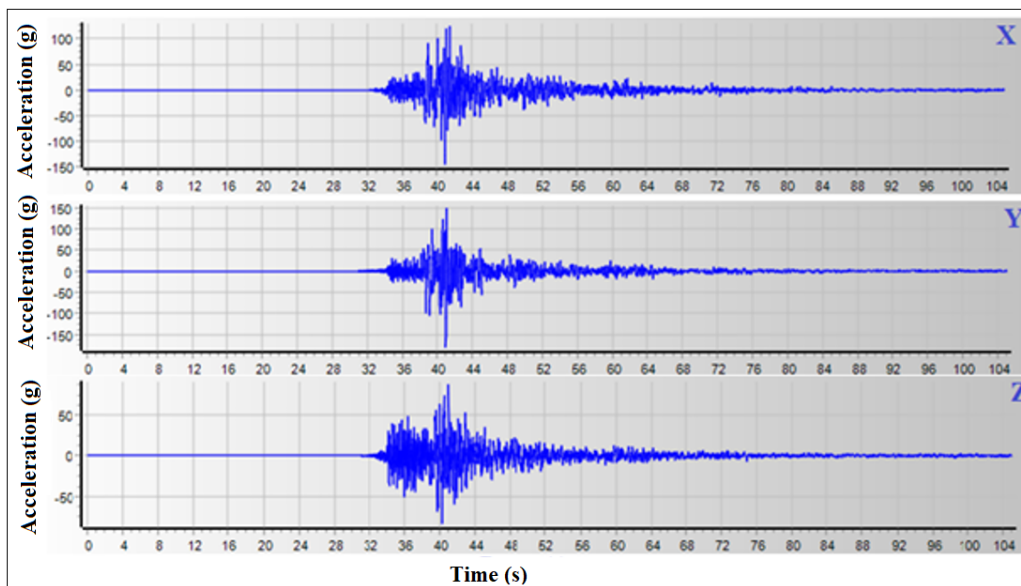


Figure 7. Records of Aegean Sea Earthquake (Mw=6.9) on 30th of October 2020

Izmir (2020) earthquake records were used in the study and the records were obtained from the AFAD database. Considering the horizontal components of the earthquake and the vertical earthquake effect for the earthquake record taken into consideration, dynamic analyzes were carried out by creating functions in the time history with the response spectrums and earthquake records defined in the SAP2000 program in accordance with the TBEC-2018.

4. Results and Discussion

Structural analyzes were carried out by using the SAP2000 software. The directions and freedoms in the software program are shown in [Figure 8](#).

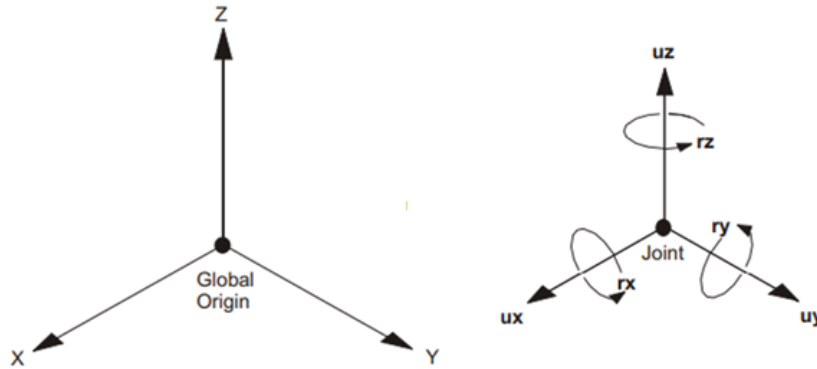


Figure 8. Directions and freedoms in the software used (SAP2000)

When making a definition with the local axis, the numbers 1,2,3 are used, and when defining with the global axis, the X, Y, Z axes are used. Linear and nonlinear structural analyzes were performed within the scope of this study. Time history analysis provides linear or nonlinear assessment of dynamic responses in the structure under varying loading according to a certain time function. The dynamic equilibrium equations specified by [Equation 4.1](#) can be solved using modal or direct integration methods.

$$Ku(t) + C^{d/dt} u(t) + Md^{2/dt} u(t) = r(t) \tag{4.1}$$

Nonlinear direct integration history analysis is a nonlinear dynamic analysis method in which the equilibrium equations of motion are fully integrated while a structure is subjected to dynamic loading. The analysis includes the integration of structural features and behaviors over a series of time steps that are small relative to the loading time ([Tazarv, 2011](#)). This type of analysis was used in this study. The steel building chosen as an example was modeled by the authors considering the provisions of [PDCCSS-2016](#) and [TBEC-2018](#). Structural analyzes were carried out separately using the design spectra obtained for four different settlements considered within the scope of this study and the earthquake acceleration record taken into account. The structure has 5 spans in the X direction and each span is 10 m, and in the Y direction 7 spans and each span is 8 m. The total height of the building is 30 m, the floor heights are equal to each other and are 3 m. The X-Z, Y-Z and X-Z axis sections of this structure are shown in [Figure 9](#). In the steel structure chosen as an example, IPE270 profiles for transverse beams, IPE400 for longitudinal beams, HEB550 for columns, and CHS 114.3×3.6 profiles for cross beams are used.

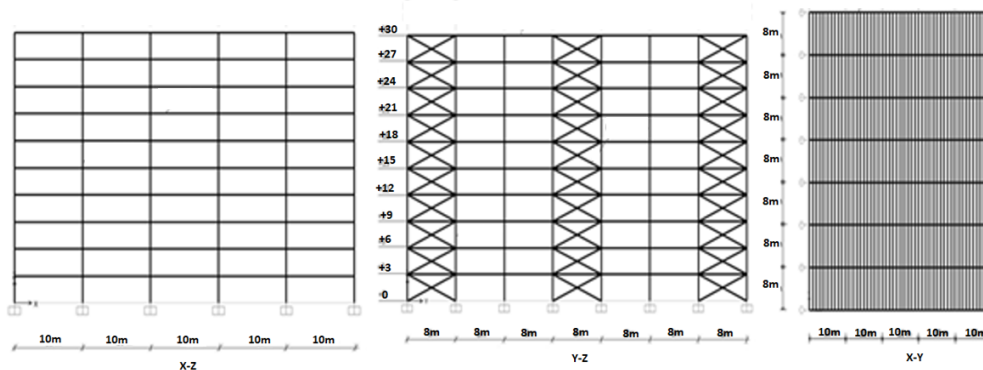


Figure 9. Sections of the sample steel structure model

Nonlinear behavior parameters for steel structures are specified in FEMA 273 Chapter-5. In this regulation, the joint properties that must be defined for columns and beams are defined. The analysis model and behavior properties of the structure in SAP2000 were carried out with the help of plastic hinges defined in FEMA 273, with the intensified plasticity model. Plastic hinge properties were determined by the nonlinear behavior coefficients given in FEMA 273. The properties of plastic hinges were determined with the help of the coefficients given in FEMA 273.

Structural analyzes were carried out separately for each province, taking into account the X, Y, XY, YZ and XYZ directions of earthquake effects in the steel building chosen as an example. Analyzes were made using vertical and horizontal design spectrum which were obtained from the Interactive Web Earthquake Application (TEHMIWA) and acceleration record of the Aegean Sea Earthquake (Mw=6.9) on 30th of October 2020 and the structural analysis results were obtained. The maximum displacement and rotation values obtained for earthquake loads effects in different directions for the provinces considered in this study are shown in [Table 7](#). The maximum displacement, rotation, base shear force and moment values were obtained at the 3764 joint point and comparisons were made considering this joint.

Table 7

Maximum displacement and rotation values obtained for different provinces and directions

Joint	Province	u_1	u_2	u_3	r_1	r_2	r_3
		m	m	m	Radians	Radians	Radians
3764	İZMİR X	0.23802	~0	~0	~0	0.004518	~0
3764	BİTLİS X	0.17307	~0	~0	~0	0.003815	~0
3764	SAMSUN X	0.13716	~0	~0	~0	0.002677	~0
3764	KONYA X	0.13418	~0	~0	~0	0.002616	~0
3764	İZMİR Y	~0	0.176943	0.00896	0.005176	0.000043	~0
3764	BİTLİS Y	~0	0.170053	0.00774	0.004279	0.000027	~0
3764	SAMSUN Y	~0	0.10919	0.0052	0.002839	0.000024	~0
3764	KONYA Y	~0	0.065722	0.00261	0.001862	0.000022	~0
3764	İZMİR XZ	0.23802	~0	0.01539	~0	0.005092	~0
3764	BİTLİS XZ	0.17307	~0	0.01331	~0	0.004824	~0
3764	SAMSUN XZ	0.13716	~0	0.01068	~0	0.003689	~0
3764	KONYA XZ	0.13418	~0	0.00839	~0	0.003108	~0
3764	İZMİR XY	0.23802	0.176943	0.00892	0.005176	0.004523	~0
3764	BİTLİS XY	0.17307	0.170053	0.00776	0.004279	0.003801	~0
3764	SAMSUN XY	0.13716	0.10919	0.00523	0.002839	0.002661	~0
3764	KONYA XY	0.13418	0.065722	0.0026	0.001862	0.002626	~0
3764	İZMİR YZ	~0	0.176943	0.02247	0.005176	0.002271	~0
3764	BİTLİS YZ	~0	0.170053	0.01654	0.004279	0.00164	~0
3764	SAMSUN YZ	~0	0.10919	0.01636	0.002839	0.001097	~0
3764	KONYA YZ	~0	0.065722	0.00969	0.001862	0.001029	~0
3764	İZMİR XYZ	0.23802	0.176943	0.02247	0.005176	0.005086	~0
3764	BİTLİS XYZ	0.17306	0.170053	0.01654	0.004279	0.004827	~0
3764	SAMSUNXYZ	0.13716	0.10919	0.01636	0.002839	0.003698	~0
3764	KONYA XYZ	0.13418	0.065722	0.00972	0.001862	0.003106	~0

In the structural analysis, base shear forces and moment values were also obtained separately for each province in the earthquake directions considered. The maximum base shear forces and moment values obtained were shown in [Table 8](#).

Table 8

Maximum base shear forces and moments obtained for different directions

Joint	Province	F_x kN	F_y kN	F_z kN	M_x kNm	M_y kNm	M_z kNm
3764	İZMİR X	10179	~0	~0	~0	166582.9	278135
3764	BİTLİS X	8557.4	~0	~0	~0	129936	225745
3764	SAMSUN X	7094	~0	~0	~0	99017.21	176770
3764	KONYA X	5962.4	~0	~0	~0	87579.08	174110
3764	İZMİR Y	~0	24081	~0	346149.9	~0	602036
3764	BİTLİS Y	~0	21297	~0	345487.8	~0	532432
3764	SAMSUN Y	~0	13377	~0	205205	~0	334437
3764	KONYA Y	~0	10086	~0	138152.6	~0	252154
3764	İZMİR XZ	10179	~0	153273	4291656	3944923	278135
3764	BİTLİS XZ	8557.4	~0	116602	3264845	2914633	225745
3764	SAMSUN XZ	7094	~0	98305	2752548	2331024	176770
3764	KONYA XZ	5962.4	~0	47179	1321014	1261650	174110
3764	İZMİR XY	10179	21297	~0	3264845	2914633	761694
3764	BİTLİS XY	8557.4	13377	~0	345487.8	166582.9	477177
3764	SAMSUN XY	7094	10086	~0	205205	129936	333662
3764	KONYA XY	5962.4	~0	~0	138152.6	99017.21	174110
3764	İZMİR YZ	~0	24081	153273	4353242	3972752	602036
3764	BİTLİS YZ	~0	21297	116602	3445749	2896088	532432
3764	SAMSUN YZ	~0	13377	98305	2800802	2302348	334437
3764	KONYA YZ	~0	10086	47179	1349552	1153268	252154
3764	İZMİR XYZ	10179	24081	153273	4353242	3944923	761694
3764	BİTLİS XYZ	8557.4	21297	116602	3445749	2914633	699676
3764	SAMSUNXYZ	7093.8	13377	98305	2800802	2331024	477177
3764	KONYA XYZ	5962.4	10086	47179	1349552	1261646	333655

The comparison of the displacement and rotation values obtained for different directions for the province of İzmir, which has the highest PGA value among the provinces considered, is presented in [Table 9](#).

The comparison of the displacement and rotation values obtained for different loading situations in different load conditions in İzmir is shown in [Figure 10](#).

Table 9
Comparison of displacement and rotation values for İzmir

Point	Province	u_1 m	u_2 m	u_3 m	r_1 Radians	r_2 Radians	r_3 Radians
3764	İZMİR X	0.23802	~0	~0	~0	0.004518	~0
3764	İZMİR Y	~0	0.176943	0.00896	0.005176	0.000043	~0
3764	İZMİR XZ	0.23802	~0	0.01539	~0	0.005092	~0
3764	İZMİR XY	0.23802	0.176943	0.00892	0.005176	0.004523	~0
3764	İZMİR YZ	~0	0.176943	0.02247	0.005176	0.002271	~0
3764	İZMİR XYZ	0.23802	0.176943	0.02247	0.005176	0.005086	~0

The comparison of the displacement and rotation values obtained for different loading situations in different load conditions in İzmir is shown in Figure 10.

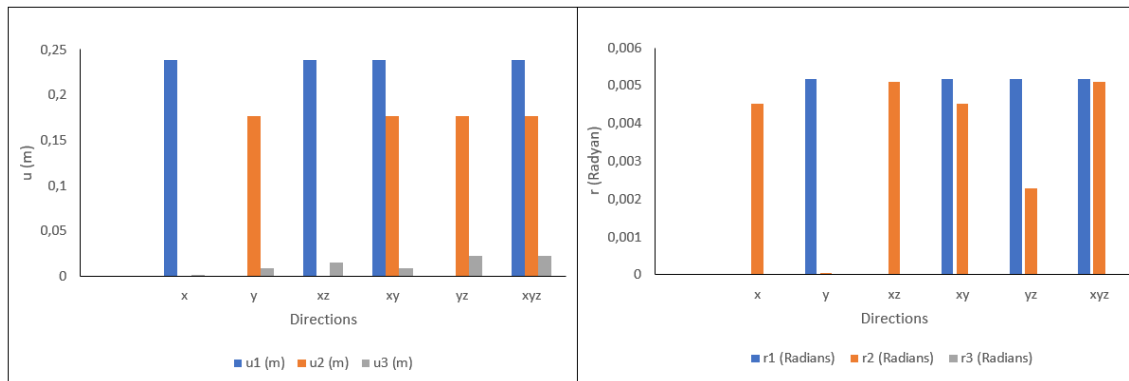


Figure 10. Comparison of displacements and rotations for İzmir

The comparison of the base shear force and moment values obtained for the 3764 joint point for the province of İzmir, which has the highest seismic risk among the provinces considered in this study, is shown in Table 10.

Table 10
Comparison of base shear force and moment values for İzmir

Point	Direction	F_x kN	F_y kN	F_z kN	M_x kNm	M_y kNm	M_z kNm
3764	İZMİR X	10179	~0	~0	~0	166582.9	278135
3764	İZMİR Y	~0	24081	~0	346149.9	~0	602036
3764	İZMİR XZ	10179	~0	153273	4291656	3944923	278135
3764	İZMİR XY	10179	21297	~0	3264845	2914633	761694
3764	İZMİR YZ	~0	24081	153273	4353242	3972752	602036
3764	İZMİR XYZ	10179	24081	153273	4353242	3944923	761694

The comparison of the base shear force and moments obtained for different loading situations in different loads conditions in İzmir is shown in Figure 11.

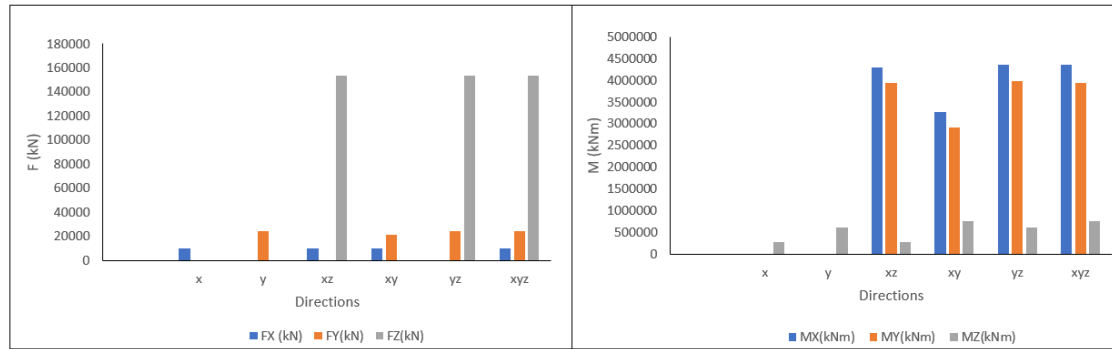


Figure 11. Comparison of base shear force and moment for İzmir

5. Conclusions

Considering major earthquake damages and developments in earthquake engineering, renewal, updating and additions are inevitable in earthquake risk zoning maps and earthquake resistant building design principles. In Turkey, these processes have been carried out in seismic hazard maps and seismic design codes over time. At different times, both earthquake resistant building design principles and the arrangements made in earthquake hazard maps contain very important studies and achievements in reducing earthquake damages. Structural analyzes were carried out for a sample steel building by considering both the current map and the important changes in the regulation, taking into account the provinces with different seismic risks and different earthquake directions within the scope of this study. In the structural analysis, the acceleration records of the Aegean Sea Earthquake ($M_w=6.9$) on 30th of October 2020, which is one of the most important earthquakes in Turkey recently, were used. It has been tried to reveal the effects of different design spectra obtained depending on different earthquake zones and earthquake effects in different directions on the earthquake behavior of the building with this study.

For the provinces considered in this study, the highest PGA value for the earthquake ground motion level, which has a 10% probability of exceeding in 50 years, was calculated for İzmir as 0.454g, while the lowest PGA value was obtained as 0.132 g for the same motion level for Konya. This situation preserved its validity in PGV and map spectral acceleration coefficients, while the highest values were obtained for İzmir and the lowest values for Konya. Since there are randomly selected points, these values may differ according to different geographical locations. The design spectral acceleration coefficients obtained according to the current regulation for all the provinces considered were larger than the values predicted in the previous earthquake regulation. The increase in design spectral acceleration coefficients was 12.4% for İzmir, 28.5% for Bitlis, 78% for Samsun and 174% for Konya. PGA values, on the other hand, increased for the other three provinces, excluding the geographical location selected in Bitlis. There was a small decrease in Bitlis compared to the previous map. Vertical ground dominant periods (T_{AD} , T_{BD}) have been used for the first time with the current regulation. While T_A and T_B values, which are horizontal spectrum corner points, took the same values for the same soil groups in the previous regulation, they take different values for each geographical location in the current regulation. The displacement, rotation, base shear and moment values obtained from the structural analysis results for the province of İzmir, where the PGA value is the highest, have the highest values in all the directions considered in the study. The lowest values were found in Konya, where the PGA value was the lowest. This once again revealed the direct effect of the PGA value on the design spectra and thus on the structural analysis results. In this context, together with the current earthquake code, it reveals the necessity of site-specific design spectra.

The acceleration value measured for the Izmir earthquake was well below the PGA values predicted in the last two earthquake codes and earthquake maps for Izmir. This shows that the current seismic design code and map are sufficient for the province of Izmir. It can be said that it was caused an increase in structural damage due to soil enlargement and insufficient structural characteristics and similar reasons.

All displacement, rotation, base shear force and moment values obtained for four provinces were obtained in complete harmony. With the increase in PGA, the results of the structural analysis obtained for each direction also took higher values. In this context, the highest displacement, rotation, base shear force and moment values were obtained for İzmir, while the lowest values were obtained for Konya. This once

again revealed that the seismic parameters of any region directly affect the structural analysis. For u_1 , the component in the X direction is active and the highest value is taken from the load combination where this component is taken into account. For u_2 , the component in the Y direction is active and the highest value is taken from the load combination where this component is taken into account. The highest values for u_3 were obtained for the loading case YZ and XYZ. In this case, it can be said that the Y and Z components are effective for the displacement in this direction. The r_1 rotation values have their highest value in the loading cases of Y, XY, YZ and XYZ is taken into account. Here, it can be said that the Y component is more effective. While the highest value for r_2 was obtained in XZ loading condition, the highest value was obtained for r_3 in Y and XY loading conditions. Considering all the load combinations, the highest u_1 was obtained for X, XZ, XY, XYZ; for u_2 ; Y, XY, YX, XYZ and u_3 for YZ, XYZ. The highest displacement was calculated as 0.238 m at u_1 . The largest rotation was obtained for r_1 as 0.00517 radians. While the highest values for F_x were obtained from the loads with the component in the X direction, the highest values were obtained from the loads with the Y component in general. The highest values were obtained as a result of the loads in which the Z-direction component was active in F_z . All the results obtained reveal the importance of using all data related to the earthquake when calculating the impact of the earthquake on the structures. The effects of different earthquakes with different components on structures will also be different.

When the displacement, rotation, base shear force and moment values obtained for the provinces and different directions considered in this study were examined, it was determined that the vertical earthquake effect did not significantly change the results obtained for the horizontal direction. Within the scope of this study, only one earthquake record, namely the Aegean Sea Earthquake (Mw=6.9) on 30th of October 2020, was used for a regular steel building without irregularities. These results may vary in earthquakes with different frequency content and structures with irregularity. In addition, the dominance of the horizontal and vertical components of the earthquake, which will be taken into account in the structural analysis, may also affect the results.

Acknowledgements

This study is derived from the presentation titled "Investigation of the Effect of Vertical Earthquake Motion on Structural Behavior in Multi-Storey Steel Buildings According to Turkish Building Earthquake Regulation" presented at the 22nd National Mechanics Congress.

Author Contributions

Ercan Işık: Collected data, planned, and designed the analysis.

Fatma Ülker Peker: Collected and analyzed data.

Aydın Büyüksaraç: Made statistical and seismic analyzes of the study.

Conflict of Interest

The authors declared no conflict of interest.

References

- Abdollahiparsa, H., Homami, P., & Khoshnoudian, F. (2016). Effect of vertical component of an earthquake on steel frames considering soil-structure interaction. *KSCE Journal of Civil Engineering*, 20(7), 2790-2801. <https://doi.org/10.1007/s12205-016-0687-y>
- Abrahamson, N.A., Litehiser, J.J. (1989). Attenuation of vertical peak acceleration. *Bulletin of the Seismological Society of America*, 79(3), 549-580. <https://doi.org/10.1785/BSSA0790030549>.
- AFAD (2021). Türkiye Deprem Tehlike Haritası. <https://tdth.afad.gov.tr/>
- AFAD (2020a). İzmir Seferihisar Depremi-Duyuru 81. Erişim tarihi:07.12.2020, <https://www.afad.gov.tr/izmir-seferihisar-depremiduyuru-81-26112020---2100>

- AFAD Deprem Dairesi Başkanlığı. (2020b). 30 Ekim 2020 Sisam Adası (İzmir Seferihisar Açıkları) Mw 6.6 Depremi Raporu. Erişim Tarihi: 18.12.2020, <https://deprem.afad.gov.tr/depremdokumanlari/2065>
- Akka, S., Kale, Ö., Yakut, A., & Ceken, U. (2018). Ground-motion characterization for the probabilistic seismic hazard assessment in Turkey. *Bulletin of Earthquake Engineering*, 16(8), 3439-3463. <https://doi.org/10.1007/s10518-017-0101-2>
- Akka, S., Azak, T., Çan, T., Çeken, U., Tümsa, M. D., Duman, T. Y., ... & Zülfikar, Ö. (2018a). Evolution of seismic hazard maps in Turkey. *Bulletin of Earthquake Engineering*, 16(8), 3197-3228. <https://doi.org/10.1007/s10518-018-0349-1>
- Akka, S., Azak, Çan, T., Çeken, U., Demircioğlu, M.B., Duman, T., Kartal, R.F., (2014). Türkiye Sismik Tehlike Haritasının Güncellenmesi. (UDAP-Ç-13-06). In *Ulusal Deprem Araştırma Programı; Disaster and Emergency Management Presidency Press: Ankara, Turkey*, Available online: <http://www.deprem.gov.tr/belgeler2016/tsth.Pdf> (2014) (Erişim tarihi: 22 Haziran 2021).
- Aksoylu, C., Mobark, A., Arslan, M.H., Hakkı Erkan, İ. (2020). A comparative study on ASCE 7-16, TBEC-2018 and TEC-2007 for reinforced concrete buildings. *Revista de la construcción*, 19(2), 282-305. <http://dx.doi.org/10.7764/rdlc.19.2.282>
- Ambraseys, N.N., Douglas, J. (2003a). Effect of vertical ground motions on horizontal response of structures. *International Journal of Structural Stability and Dynamics*, 3(02), 227-265. <https://doi.org/10.1142/S0219455403000902>
- Ambraseys, N. N., Douglas, J. (2003b). Near-field horizontal and vertical earthquake ground motions. *Soil Dynamics and Earthquake Engineering*, 23(1), 1-18. [https://doi.org/10.1016/S0267-7261\(02\)00153-7](https://doi.org/10.1016/S0267-7261(02)00153-7).
- Baş, S., Sevinç, M., Kalkan, İ., Aykaç, S. (2015). Düşey deprem etkisi altındaki çok katlı betonarme yapıların davranışının incelenmesi, 3. *Türkiye Deprem Mühendisliği ve Sismoloji Konferansı, İzmir, Türkiye*. http://www.tdmd.org.tr/TR/Genel/pdf2015/TDMSK_063.pdf
- Bozorgnia, Y., Niazi, M., Campbell, K. W. (1995). Characteristics of free-field vertical ground motion during the Northridge earthquake. *Earthquake spectra*, 11(4), 515-525. <https://doi.org/10.1193/1.1585825>.
- Büyüksaraç, A., Işık, E., Harirchian, E. (2021). A case study for determination of seismic risk priorities in Van (Eastern Turkey). *Earthquakes and Structures*, 20(4), 445-455. <https://doi.org/10.12989/eas.2021.20.4.445>
- Chopra, A. K. (1966). The importance of the vertical component of earthquake motions. *Bulletin of the Seismological Society of America*, 56(5), 1163-1175. <https://doi.org/10.1785/BSSA0560051163>
- Çeken, U., Dalyan, İ., Kılıç, N., Köksal, T.S., Tekin, B.M. (2017). Türkiye deprem tehlike haritaları interaktif web uygulaması. 4. *Uluslararası Deprem Mühendisliği ve Sismoloji Konferansı 11-13 Ekim 2017 – Eskişehir*. <http://www.tdmd.org.tr/TR/Genel/4UDMSK/pdf2017/4008.pdf>
- Çelik Yapıların Tasarım, Hesap ve Yapım Esaslarına Dair Yönetmelik, PDCCSS (2016). https://www.imo.org.tr/resimler/dosya_ekler/5ba6a974eb906bf_ek.pdf
- Doğan, E., Elmas, M. (2004). Binalarda düşey deprem etkisinin zaman tanım alanında hesap yöntemi ile incelenmesi. *Sakarya Üniversitesi Fen Bilimleri Enstitüsü Dergisi*, 8(1), 9-17. <http://www.saujs.sakarya.edu.tr/tr/download/article-file/192893>
- Eren, G., Beyen, K. (2015). Düşey deprem etkisinde tipik bir binada gözlenen performansın tartışılması. 8. *UDMK, İstanbul, Türkiye*. s.199-211. https://www.imo.org.tr/resimler/ekutuphane/pdf/17371_51_01.pdf
- Eren, G., Beyen, K., (2017). Tarihi yapı davranışına zemin, mesnet, yatay ve düşey deprem koşullarının etkisi, *Uluslararası Katılımlı 6. Tarihi Yapıların Korunması ve Güçlendirilmesi Sempozyumu, İstanbul, Türkiye*. s.401-410. https://www.imo.org.tr/resimler/ekutuphane/pdf/17952_15_50.pdf
- Farsangi, E. N., Tasnimi, A. A. (2016). The influence of coupled horizontal-vertical ground excitations on the collapse margins of modern RC-MRFs. *International Journal of Advanced Structural Engineering (IJASE)*, 8(2), 169-192. <https://doi.org/10.1007/s40091-016-0122-0>.

- Güneş, O. (2015). Turkey's grand challenge: Disaster-proof building inventory within 20 years. *Case Studies in Construction Materials*, 2, 18-34. <https://doi.org/10.1016/j.cscm.2014.12.003>
- Gürel, M.A., Kısa, M. (2002). Deprem Hareketinin Düşey Bileşeninin Çeşitli Yapı Elemanları Üzerindeki Etkileri ve Hasar Potansiyeli. *Uluslararası Yapı ve Deprem Mühendisliği Sempozyumu ECAS2002, Ankara*, s. 118-125. <http://bupim.com/yayinlar/bupim-pdf/ECAS20.pdf>
- Işık, E., Kutanis, M., Bal, İ.E. (2016). Displacement of the buildings according to site-specific earthquake spectra. *Periodica Polytechnica Civil Engineering*, 60(1), 37-43. <https://doi.org/10.3311/PPci.7661>
- Işık, E. (2021). A comparative study on the structural performance of an RC building based on updated seismic design codes: case of Turkey. *Challenge Journal of Structural Mechanics*, 7(3), 123-134. <https://doi.org/10.20528/cjsmec.2021.03.002>
- Işık, E., Harirchian, E., Bilgin, H., Jadhav, K. (2021a). The effect of material strength and discontinuity in RC structures according to different site-specific design spectra. *Research on Engineering Structures and Materials*. 7(3) 413-430. <http://dx.doi.org/10.17515/resm2021.273st0303>
- Işık, E., Büyüksaraç, A., Ekinci, Y. L., Aydın, M. C., Harirchian, E. (2020). The effect of site-specific design spectrum on earthquake-building parameters: A case study from the Marmara region (NW Turkey). *Applied Sciences*, 10(20), 7247. <https://doi.org/10.3390/app10207247>
- Işık, E., Harirchian, E., Büyüksaraç, A., & Ekinci, Y. L. (2021b). Seismic and structural analyses of the eastern anatolian region (Turkey) using different probabilities of exceedance. *Applied System Innovation*, 4(4), 89. <https://doi.org/10.3390/asi4040089>.
- Jakayev, S., Aydemir, M. E. (2019). Düzenli bir betonarme binada düşey deprem bileşeninin yapısal davranışa etkisi. *Afet ve Risk Dergisi*, 2(1), 1-13.
- Kadid, A., Yahiaoui, D., Chebili, R. (2010). Behavior of reinforced concrete buildings under simultaneous horizontal and vertical ground motions. *Asian Journal Of Civil Engineering (Building And Housing)*, 11(4), 463-476. <https://www.sid.ir/en/journal/ViewPaper.aspx?id=185518>
- Kalkan, E., Graizer, V. (2007). Multi-component ground motion response spectra for coupled horizontal, vertical, angular accelerations and tilt. *ISET Journal of Earthquake Technology*, 44(1), 259-284. <http://home.iitk.ac.in/~vinaykg/Isset485.pdf>
- Karaşin, İ.B., Işık, E., Demirci, A., Aydın, M.C. (2020). Coğrafi konuma özel tasarım spektrumlarının betonarme yapı performansına etkisi. *Dicle Üniversitesi Mühendislik Fakültesi Mühendislik Dergisi*, 11(3), 1319-1330. <https://doi.org/10.24012/dumf.682377>
- Kim, S.J., Holub, C.J., Elnashai, A.S. (2011). Analytical assessment of the effect of vertical earthquake motion on RC bridge piers. *Journal of Structural Engineering*, 137(2), 252-260. [https://doi.org/10.1061/\(ASCE\)ST.1943-541X.0000306](https://doi.org/10.1061/(ASCE)ST.1943-541X.0000306)
- Koçer, M., Nakipoğlu, A., Öztürk, B., Al-hagri, M. G., Arslan, M. H. (2018). Deprem kuvvetine esas spektral ivme değerlerinin TBDY 2018 ve TDY 2007'ye göre karşılaştırılması. *Selçuk-Teknik Dergisi*, 17(2), 43-58. <http://sutod.selcuk.edu.tr/sutod/article/view/437>
- Kunnath, S. K., Erduran, E., Chai, Y. H., Yashinsky, M. (2008). Effect of near-fault vertical ground motions on seismic response of highway overcrossings. *Journal of Bridge Engineering*, 13(3), 282-290. [https://doi.org/10.1061/\(ASCE\)1084-0702\(2008\)13:3\(282\)](https://doi.org/10.1061/(ASCE)1084-0702(2008)13:3(282))
- Kutanis, M., Ulutaş, H., Işık, E. (2018). PSHA of Van province for performance assessment using spectrally matched strong ground motion records. *Journal of Earth System Science*, 127(7), 1-14. <https://doi.org/10.1007/s12040-018-1004-6>
- Loghman, V., Khoshnoudian, F., Banazadeh, M. (2015). Effect of vertical component of earthquake on seismic responses of triple concave friction pendulum base-isolated structures. *Journal of Vibration and Control*, 21(11), 2099-2113. <https://doi.org/10.1177/1077546313503359>
- Newmark, N.M., Blume, J.A., Kapur, K.K. (1973). Seismic Design Spectra for Nuclear Power Plants. *Journal of the Power Division*, 99(02), 287-303. <https://doi.org/10.1061/JPWEAM.0000753>

- Özmen, B. (2012). Türkiye deprem bölgeleri haritalarının tarihsel gelişimi. *Türkiye Jeoloji Bülteni*, 55(1), 43-55. https://www.jmo.org.tr/resimler/ekler/742ef3153c914cf_ek.pdf
- Özmen, B., Pampal, S. (2017). Türkiye Deprem Bölgeleri Haritalarının Evrimi. 4. *Uluslararası Deprem Mühendisliği ve Sismoloji Konferansı*, Eskişehir, Türkiye. <http://www.tdmd.org.tr/TR/Genel/4UDMSK/pdf2017/3708.pdf>
- Papazoglou, A.J., Elnashai, A.S. (1996). Analytical and field evidence of the damaging effect of vertical earthquake ground motion. *Earthquake Engineering & Structural Dynamics*, 25(10), 1109-1137. [https://doi.org/10.1002/\(SICI\)1096-9845\(199610\)25:10<1109::AID-SAP2000>3.0.CO;2-3](https://doi.org/10.1002/(SICI)1096-9845(199610)25:10<1109::AID-SAP2000>3.0.CO;2-3)
- SAP2000, Version 17, Computers and Structures, Inc., Berkeley, California
- Tazarv, M. Linear Time History Analysis of MDOF Structure by Mode Superposition Method. <http://alum.sharif.edu/~tazarv/>
- TBEC-2018. *Türkiye Bina Deprem Yönetmeliği*; T.C. Resmi Gazete: Ankara, Turkey, (2018). <https://www.afad.gov.tr/> (Erişim tarihi:1 Haziran 2021).
- Weichert, D. H., Wetmiller, R. J., Munro, P. (1986). Vertical earthquake acceleration exceeding 2 g? The case of the missing peak. *Bulletin of the Seismological Society of America*, 76(5), 1473-1478. <https://doi.org/10.1785/BSSA0760051473>
- Yavaş, M., Teloğlu, A.N., Celep, Z. (2019). Türkiye Bina Deprem Yönetmeliği'nde binaların taşıyıcı sisteminde tanımlanan düşey deprem etkisi üzerine. In *International Conference on Earthquake Engineering and Seismology (SICEES)*, 8, s.11.